International Journal of MECHANICAL SCIENCES

Volume 2, 1960–61

l. 2
60-61

Editor-in-Chief

W. JOHNSON
(United Kingdom)

Regional Editors

W. RUPPERT
(Germany)

H. KUDO
(Japan)

PERGAMON PRESS

OXFORD • LONDON • NEW YORK • PARIS

INTERNATIONAL JOURNAL OF MECHANICAL SCIENCES

EDITORS

UNITED KINGDOM

W. Johnson (*Editor-in-Chief*), *Department of Mechanical Engineering, The Manchester College of Science and Technology, Manchester* 1, *England*

GERMANY

W. Ruppert, *Frankfurt a. M., Glaubergstrasse* 22, *Germany*

JAPAN

H. Kudo, *The Government Mechanical Laboratory*, 132 *Sumiyoshi, Suginami, Tokyo, Japan*

HONORARY EDITORIAL ADVISORY BOARD

C. B. Biezeno, *Delft*
P. F. Chenea, *Lafayette*
D. G. Christopherson, *London*
W. J. Duncan, ✠ *Glasgow*
R. H. Evans, *Leeds*
G. Ford, *Alberta*
A. M. Freudenthal, *Columbia*
S. Fukui, *Tokyo*
A. J. Gould, *Natal*
R. Grammel, *Stuttgart*
A. S. Hall, *Purdue*
J. P. den Hartog, *M. I. T.*
R. M. Haythornthwaite, *Ann Arbor*
P. G. Hodge, *Illinois Inst. Tech.*
N. J. Hoff, *Stanford*
J. H. Horlock, *Liverpool*
G. A. Horvay, *Schenectady*
J. A. Hrones, *Case*
C. F. Kettleborough, *Sydney*
J. Kolakowski, *Baghdad*
J. Marin, *Penn. State*
D. Mordell, *McGill*
E. Pestel, *Hanover*
H. C. Rothbart, *New York*
B. W. Shaffer, *New York*
M. Shaw, *Queensland*
M. C. Shaw, *M. I. T.*
M. F. Spotts, *Northwestern*
W. T. Thomson, *UCLA*
L. C. Woods, *Oxford*

Sub-Editor: N. S. Barrett, *Journals Department, Pergamon Press Ltd., Headington Hill Hall, Oxford, England*

Publishing Offices: Headington Hill Hall, Oxford, England (Oxford 64881)

Published bi-monthly.

Annual subscriptions (including postage): (A) for libraries, government departments or industrial establishments, £14 0s. 0d. (U.S.A. $40.00); (B) for subscribers who write directly to the publisher certifying that the journal is for their personal use, £5 5s. 0d. (U.S.A. $15.00).

Single issues £2 10s. 0d. (U.S.A. $9.00) each.

Copyright © 1961 Pergamon Press Ltd.

PERGAMON PRESS LTD.

Headington Hill Hall, Oxford, England 122 East 55th Street, New York 22, N.Y.

Vol. 2
1960-61

LIST OF CONTENTS

Numbers 1/2

PAGE

SHARAD A. PATEL, B. VENKATRAMAN and WILLIAM P. VAFAKOS: Analysis of compressibility in creep by the nonlinear elastic analogue 1

P. G. MORGAN and A. SAUNDERS: An experimental investigation of inertia effects in viscous flow 8

A. S. KOBAYASHI and P. R. TRUMPLER: Elastic stresses in a rotating disk of general profile 13

LIU HSIEN-CHOU: Wang Cheng and the first book on mechanical engineering in China (Condensed and translated by S. S. CHANG) 30

G. A. ZIZICAS: Resolution of plastic strains into components of symmetrically isotropic behavior 40

J. H. HORLOCK: Losses and efficiencies in axial-flow turbines (Review) 48

N. I. LEVITSKII and K. K. SHAKVAZIAN: Synthesis of four-element spatial mechanisms with lower pairs (Translated from the Russian by F. FREUDENSTEIN) 76

O. C. ZIENKIEWICZ and R. W. GERSTNER: A stress-function approach to interface and mixed boundary-condition problems (Boundary conditions and finite-difference techniques) 93

H. KUDO: Some analytical and experimental studies of axi-symmetric cold forging and extrusion—I 102

A. M. FREUDENTHAL and M. P. BIENIEK: Test of cylindrical shells in the plastic range 128

Letters to the Editor:

A. L. TITCHENER: Note on stresses in bolts in a bolted bracket 131

B. W. SHAFFER: Comments on A. L. TITCHENER's criticism 132

IRVING U. OJALVO: Criticism of "Small vibrations of thin incomplete circular rings" 132

Book Reviews:

Advanced Propulsion Systems, Edited by MORTON ALPERIN and GEORGE P. SUTTON. (Reviewed by FRANCIS CHEERS) 134

Applied Heat for Engineers, by J.-B. O. SNEEDEN. (Reviewed by G. C. BRIGGS) 134

Principles of Surveying, by J. CLENDINNING. (Reviewed by S. RAYMOND) 135

Papers to be published in future issues 136

Number 3

F. LECKIE and E. PESTEL: Transfer-matrix fundamentals 137

F. KOZIN and J. L. BOGDANOFF: On the statistical analysis of the motion of some simple two-dimensional linear vehicles moving on a random track 168

D. JORTNER, J. F. OSTERLE and C. F. ZOROWSKI: An analysis of cold strip rolling 179

B. M. BOTROS: Residual stresses in cold ironed tubes 195

S. L. LEE and P. BALLESTEROS: Uniformly loaded rectangular plate supported at the corners 206

Papers to be published in future issues 212

Number 4

PAGE

W. F. Riley and A. J. Durelli: Stress distribution on the boundary of an elliptical hole in a large plate during passage of a stress pulse of long duration (Major axis tangent to the wave front) 213

W. Johnson and H. Kudo: The cutting of metal strips between partly rough knife-edge tools 224

R. S. Benson and W. A. Woods: The energy content of exhaust pulses in the exhaust system of a supercharged two-stroke-engine model 231

J. H. Horlock and R. I. Lewis: Shear flows in straight-sided nozzles and diffusers 251

O. C. Zienkiewicz and R. W. Gerstner: The method of interface stress adjustment and its uses in the solution of some plane elasticity problems 267

P. Montague: Load distribution in overhead stranded conductors 277

H. Lippmann, O. Mahrenholtz and W. Johnson: Thin heavy elastic strips at large deflexions 294

Letters to the Editor:

H. H. Pan: On "On the response of the singly free linear oscillator" 311

J. H. Horlock: Further comments on "Losses and efficiencies in axial-flow turbines" 312

H. H. Pan: Note on "The uniformly loaded rectangular plate supported at the corners" 313

Book Reviews:

Engineering Mathematics, by J. Blakey and M. Hutton. (Reviewed by J. Halling) 316

Analytical Quadrics, by B. Spain. (Reviewed by H. B. Shutrick) 316

Machine Drawing and Design, by W. Abbott. (Reviewed by G. R. Schiffer) 316

Thermal Reactor Theory, by A. D. Galanin. (Reviewed by P. H. Price) 317

Tables of Thermodynamic and Transport Properties. (Reviewed by G. S. Cantle) 318

Lectures on Fluid Mechanics, by Sydney Goldstein. (Reviewed by J. K. Royle) 318

AUTHOR INDEX

(B.R. indicates a Book Review)

Ballesteros P.		206	Montague P.		277
Benson R. S.		231	Morgan P. G.		8
Bieniek M. P.		128	Ojalvo I. U.		132
Bogdanoff J. L.		168	Osterle J. F.		179
Botros B. M.		195	Pan H. H.	311,	313
Briggs G. C.	(B.R.)	134	Patel S. A.		1
Cantle G. S.	(B.R.)	318	Pestel E.		137
Cheers F.	(B.R.)	134	Price P. H.	(B.R.)	317
Durelli A. J.		213	Raymond S.	(B.R.)	135
Freudenthal A. M.		128	Riley W. F.		213
Gerstner R. W.	93,	267	Royle J. K.	(B.R.)	318
Halling J.	(B.R.)	316	Saunders A.		8
Horlock J. H.	48, 251,	312	Schiffer G. R.	(B.R.)	316
Hsien-Chou L.		30	Shaffer B. W.		132
Johnson W.	224,	294	Shakvazian K. K.		76
Jortner D.		179	Shutrick H. B.	(B.R.)	316
Kobayashi A. S.		13	Titchener A. L.		131
Kozin F.		168	Trumpler P. R.		13
Kudo H.	102,	224	Vafakos W. P.		1
Leckie F.		137	Venkatraman B.		1
Lee S. L.		206	Woods W. A.		231
Levitskii N. I.		76	Zienkiewicz O. C.	93,	267
Lewis R. I.		251	Zizicas G. A.		40
Lippmann H.		294	Zorowski C. F.		179
Mahrenholtz O.		294			

Vol. 2
1960-61

Int. J. Mech. Sci. Pergamon Press Ltd. 1960. Vol. 2, pp. 1–7. Printed in Great Britain

ANALYSIS OF COMPRESSIBILITY IN CREEP BY THE NONLINEAR ELASTIC ANALOGUE*

SHARAD A. PATEL, B. VENKATRAMAN and WILLIAM P. VAFAKOS
Polytechnic Institute, Brooklyn, N.Y.

(*Received* 17 *January* 1960)

Summary—An elementary device for including compressibility effects on the creep behavior of materials is presented. A hollow sphere subjected to uniform pressures is analyzed to illustrate these effects. The stress solution is presented in closed parametric form.

1. INTRODUCTION

A GENERAL stress–strain law for strain-hardening isotropic materials subject to combined stresses has been established by Prager[1]. The formulation of this law is based on three essential assumptions. Firstly, it is assumed that during an experiment under combined stresses the directions of the principal stresses and the ratios of their magnitudes remain constant. Since the material is considered isotropic, the principal axes of stress and strain must coincide and the ratios of the principal strains may be expected to remain constant. Secondly, it is assumed that the material has identical stress–strain diagrams in pure tension and pure compression so that reversal of signs of all stresses may generally be expected to lead to a mere reversal of the signs of all strains. Finally, it is assumed that the isotropic material is incompressible and consequently a state of hydrostatic pressure could not produce any deformation. It follows from this assumption that two states of stress which differ only by a state of hydrostatic pressure may be expected to produce identical deformations.

That the preceding formulation of the stress–strain law could be readily adapted to problems of creep in materials subject to combined stresses has been shown by Hoff[2,3]. This was achieved by means of the elastic analogue of a uni-dimensional creep law or its suitable generalization.

The primary object of the present paper is an elementary investigation of Prager's[1] stress–strain formulation with the removal of the restriction of incompressibility. While all other assumptions are still considered valid, the material is now assumed compressible. Section 2 discusses such a formulation for a special case. This section also summarizes the use of this stress–strain law as an analogue of the solution of creep problems. With this as basis, the elementary problem of a hollow sphere subjected to uniform internal and external pressure is analysed in Section 3. A similar analysis for an incompressible material has been presented.[4] A brief discussion of the results concludes the paper.

* The results presented in this paper were obtained in the course of research sponsored by the Office of Naval Research under Contract No. Nonr 839(23).

2. STRESS–STRAIN RELATIONS

It has been shown[1] that for an incompressible material the deformations are produced by the deviations of stresses from the hydrostatic state of stress. If on the other hand the material is compressible, there will be deformations even under hydrostatic pressure. For such materials, then, two states of stress which differ only by a hydrostatic pressure will no longer produce identical deformations. The usual definition of stress deviations for incompressible materials has therefore to be discarded, since the deformations do not depend upon these deviations for compressible materials. However, an approach similar to that for incompressible materials appears possible with a modified definition of stress deviations.

Let the stress deviation s_{ij} be defined as

$$s_{ij} = \sigma_{ij} - \alpha\sigma_{kk}\,\delta_{ij} \tag{2.1}$$

where σ_{ij} is the stress tensor, α is the compressibility constant and δ_{ij} is the Kronecker delta. If the strains ϵ_{ij} are required to depend upon the stress deviations as defined in equation (2.1), a simple stress–strain law for an elastic compressible material under combined stresses may be written as

$$\epsilon_{ij} = CJ_2^m\, s_{ij} \tag{2.2}$$

where C and m are material constants and $J_2 = \frac{1}{2}s_{ij}s_{ij}$ is the second invariant of the tensor s_{ij}. It may be verified that the stress–strain law (2.2) has the same form as used by Hoff[3] with the difference that in the present case s_{ij} is defined by equation (2.1).

It may be noted that $\alpha = \frac{1}{3}$ [equation (2.1)] corresponds to an incompressible material as given in Ref. 1. The definition of α and the fact that a hydrostatic pressure cannot increase the volume of the material show that $\alpha \leqslant \frac{1}{3}$. Further, α cannot be negative if the analysis is restricted to materials which do not expand laterally under longitudinal tension. Therefore α must satisfy the condition $0 \leqslant \alpha \leqslant \frac{1}{3}$.

It has been shown by Hoff[3] that the nonlinear elastic law (2.2) is the analogue of the creep law

$$\epsilon_{ij} = CJ_2^m\, s_{ij}\, t^{1/q} \tag{2.3}$$

where q is a constant and t represents time. In other words, the creep–stress distribution in a body governed by the law (2.3) is the same as that in an analogous nonlinear elastic body governed by the law (2.2).

With the preceding analogue as basis, the creep–stress distribution in a hollow sphere subjected to uniform internal and external pressures is investigated in the next section. While the first two postulates stated in the Introduction are assumed to remain valid, the material of the sphere is now considered to be compressible and governed by equation (2.2).

3. PROBLEM OF THE HOLLOW SPHERE

The analysis of a hollow sphere subjected to uniform internal and external pressures is essentially a uni-dimensional problem. While the stress field is characterized by the normal stresses $\sigma_r, \sigma_\vartheta$ and σ_ϕ in the respective spherical

Vol. 2
1960-61

co-ordinate directions r, ϑ and ϕ, point symmetry of the problem shows that $\sigma_\phi = \sigma_\vartheta$ and the independent variable is the radial co-ordinate r. The strains $\epsilon_r = du/dr$ and $\epsilon_\phi = \epsilon_\vartheta = u/r$ readily follow from the radial displacement u.

On the bases of the preceding discussion and the stress–strain law (2.2), the behavior of the hollow sphere is governed by the equilibrium equation

$$(r/2)\, d\sigma_r/dr = \sigma_\vartheta - \sigma_r = s_\vartheta - s_r \tag{3.1}$$

and the relations

$$\epsilon_r = du/dr = CJ_2^m s_r = CJ_2^m [\sigma_r - \alpha(\sigma_r + 2\sigma_\vartheta)] \tag{3.2}$$

$$\epsilon_\vartheta = u/r = CJ_2^m s_\vartheta = CJ_2^m [\sigma_\vartheta - \alpha(\sigma_r + 2\sigma_\vartheta)] \tag{3.3}$$

Equations (3.1), (3.2) and (3.3) determine the stresses σ_r and σ_ϑ and the displacement u.

As a first step in the solution, the displacement u may be eliminated between equations (3.2) and (3.3) to yield the stress relation

$$(\sigma_\vartheta - \sigma_r)/r + (1-2\alpha)\,\sigma_\vartheta' - \alpha\sigma_r' + m(J_2'/J_2)\,[(1-2\alpha)\,\sigma_\vartheta - \alpha\sigma_r] = 0 \tag{3.4}$$

where

$$J_2 = \tfrac{1}{2}(s_r^2 + 2s_\vartheta^2) = \tfrac{1}{2}[\sigma_r^2 + 2\sigma_\vartheta^2 - \alpha(2-3\alpha)\,(\sigma_r + 2\sigma_\vartheta)^2] \tag{3.4a}$$

$$J_2' = \sigma_r\sigma_r' + 2\sigma_\vartheta\sigma_\vartheta' - \alpha(2-3\alpha)\,(\sigma_r + 2\sigma_\vartheta)\,(\sigma_r' + 2\sigma_\vartheta') \tag{3.4b}$$

and the primes denote differentiations with respect to r. The stress distributions σ_r and σ_ϑ may now be obtained by a simultaneous solution of equations (3.1) and (3.4).

Proceeding to solve for the stresses, equation (3.1) is used to express σ_ϑ and σ_ϑ' in terms of σ_r and its derivatives with respect to r. These are then introduced into equation (3.4) together with the values of J_2 and J_2' [equations (3.4a) and (3.4b)]. Simplification of the result finally yields the differential equation in σ_r:

$$4 + r\sigma_r''/\sigma_r' = \frac{m[1 + a(\sigma_r/r\sigma_r')]}{b(\frac{3}{2} + ma)\,(\sigma_r/r\sigma_r')^2 + [(m+1)\,b + 2mac]\,(\sigma_r/r\sigma_r') + (2m+1)\,c} \tag{3.5}$$

where $a = 2(1-3\alpha)/(1-2\alpha)$, $b = 2(1-3\alpha)^2$ and $c = (1 - 4\alpha + 6\alpha^2)/2$. Equation (3.5) is of the second order and may be solved when σ_r is prescribed at the inner and outer boundaries. Before attempting the solution, however, scrutiny of the equation shows that a simplification is possible as follows.

With the definition

$$y = \sigma_r/r\sigma_r' \tag{3.6a}$$

it can be easily shown that

$$4 + r\sigma_r''/\sigma_r' = 3 + 1/y - ry'/y \tag{3.6b}$$

Substitution of these relations into equation (3.5) and simplification yield the following first-order differential equations

$$\frac{dr}{r} = \frac{1 + Dy + Ey^2}{1 + Fy + Gy^2 + Hy^3}\, dy \tag{3.7}$$

$$\frac{d\sigma_r}{\sigma_r} = \frac{1 + Dy + Ey^2}{y(1 + Fy + Gy^2 + Hy^3)}\, dy \tag{3.8}$$

equivalent to equations (3.5) and (3.6a), respectively. Here, the constants have the values

$$D = \frac{2}{2m+1}\left[\frac{2(m+1)(1-3\alpha)^2}{(1-4\alpha+6\alpha^2)} + \frac{2m(1-3\alpha)}{(1-2\alpha)}\right]$$

$$E = \frac{2(1-3\alpha)^2}{(2m+1)(1-4\alpha+6\alpha^2)}\left[3 + \frac{4m(1-3\alpha)}{(1-2\alpha)}\right]$$

$$F = 3 + D - \frac{2m}{(2m+1)(1-4\alpha+6\alpha^2)}$$

$$G = E + 3D - \frac{4m(1-3\alpha)}{(2m+1)(1-2\alpha)(1-4\alpha+6\alpha^2)}$$

$$H = 3E$$

A simultaneous solution of equations (3.7) and (3.8) for given boundary conditions yields the radial stress distribution.

Let it be assumed that the hollow sphere is subjected to a uniform internal pressure $\sigma_r = \sigma_i$ at $r = r_i$ and a uniform external pressure $\sigma_r = \sigma_0$ at $r = r_0$. These conditions must be expressed in terms of the variable y in order to solve equations (3.7) and (3.8). Thus, it is assumed that the transformed boundary conditions are

$$\sigma_r = \sigma_i, \quad r = r_i, \quad \text{when} \quad y = y_i \tag{3.9}$$

$$\sigma_r = \sigma_0, \quad r = r_0, \quad \text{when} \quad y = y_0 \tag{3.10}$$

where σ_i, σ_0, r_i and r_0 are given and the corresponding constants y_i and y_0 are as yet unknown.

The solution of equations (3.7) and (3.8) and the determination of the constants y_i and y_0 are accomplished in the following manner. Firstly, the equations are integrated to yield functional relations of the form

$$Ar = \exp f(y) \tag{3.11}$$

$$B\sigma_r = \exp g(y) \tag{3.12}$$

where A and B are arbitrary constants. Use of boundary conditions (3.9) and (3.10) yield the simultaneous equations

$$r_0/r_i = \exp f(y_0)/\exp f(y_i) \tag{3.13}$$

$$\sigma_0/\sigma_i = \exp g(y_0)/\exp g(y_i) \tag{3.14}$$

in the unknowns y_i and y_0. Once these are determined, it is readily seen that equations (3.11) and (3.12) yield the solutions

$$\begin{aligned} r/r_i &= \exp f(y)/\exp f(y_i) \\ \sigma_r/\sigma_i &= \exp g(y)/\exp g(y_i) \end{aligned} \tag{3.15}$$

or

$$\begin{aligned} r/r_0 &= \exp f(y)/\exp f(y_0) \\ \sigma_r/\sigma_0 &= \exp g(y)/\exp g(y_0) \end{aligned} \tag{3.16}$$

Vol. 2
1960-61

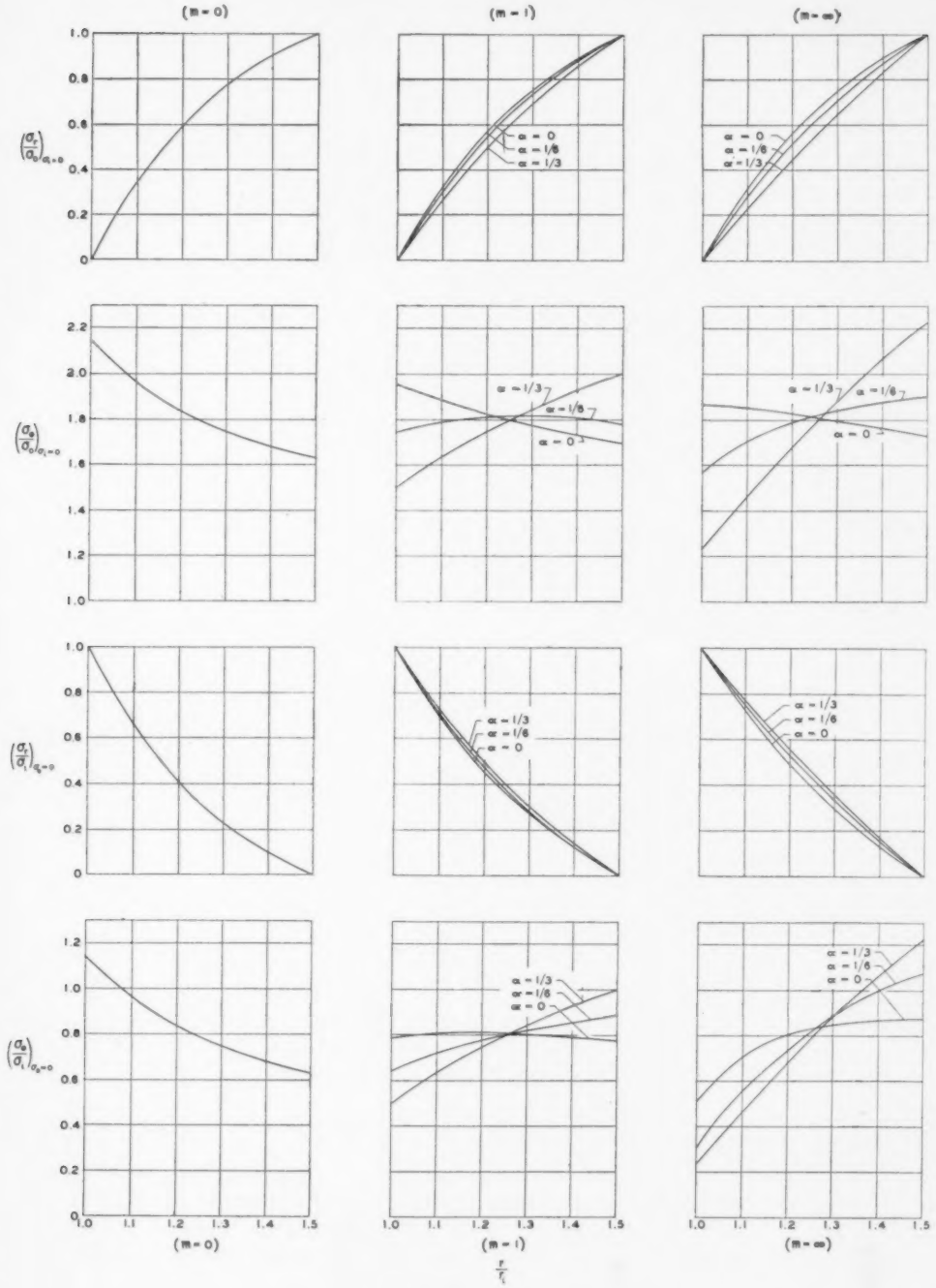

FIG. 1. Distribution of creep stresses.

With the radial stress determined, the equilibrium equation (3.1) and the relation (3.6a) may be used to obtain the circumferential stress

$$\sigma_\vartheta = \sigma_r(1 + 1/2y) \tag{3.17}$$

The functions $f(y)$ and $g(y)$ are the integrals of the right-hand sides of equations (3.7) and (3.8), respectively. These may be easily obtained as

$$f(y) = (a_1/c_1)\log(1+c_1y) + (a_3/2c_3)\log(1+c_2y+c_3y^2) + \frac{2a_2 - a_3(c_2/c_3)}{4c_3 - c_2^2}\tan^{-1}\left[\frac{2c_3y+c_2}{\sqrt{(4c_3-c_2^2)}}\right] \tag{3.18}$$

$$g(y) = \log y + (b_1/c_1)\log(1+c_1y) + (b_3/2c_3)\log(1+c_2y+c_3y^2) + \frac{2b_2 - b_3(c_2/c_3)}{4c_3 - c_2^2}\tan^{-1}\left[\frac{2c_3y+c_2}{\sqrt{(4c_3-c_2^2)}}\right] \tag{3.19}$$

where c_1 is given by the only real root of the cubic equation

$$c_1^3 - Fc_1^2 + Gc_1 - H = 0 \tag{3.20}$$

The other constants in equations (3.18) and (3.19) have the values

$$c_2 = F - c_1, \quad c_3 = H/c_1;$$

$$a_1 = \frac{E - c_1(D - c_1)}{c_3 - c_1(c_2 - c_1)}, \quad a_2 = 1 - a_1, \quad a_3 = \frac{E - a_1c_3}{c_1};$$

$$b_1 = \frac{c_1^2(D-F) - c_1(E-G) - H}{c_3 - c_1(c_2 - c_1)}, \quad b_2 = D - F - b_1, \quad b_3 = \frac{H + b_1c_3}{c_1} \tag{3.21}$$

TABLE 1. (LAMÉ SOLUTION, ALL α); $m = 0$

$\frac{r}{r_i}$	1·0	1·1	1·2	1·3	1·4	1·5
$\frac{\sigma_r}{\sigma_0}$	0	0·345	0·590	0·780	0·902	1
$\frac{\sigma_\vartheta}{\sigma_0}$	2·130	1·963	1·837	1·748	1·680	1·630
$\frac{\sigma_r}{\sigma_i}$	1	0·655	0·410	0·220	0·098	0
$-\frac{\sigma_\vartheta}{\sigma_i}$	1·130	0·963	0·837	0·748	0·680	0·630

It may be pointed out here that when the creep exponent $m = 0$, the stress–strain law (2.2) reduces to a linear law and the right-hand side of equation (3.5) vanishes. The latter equation then is independent of α and yields the well-known Lamé solution. Further, $\alpha = \frac{1}{3}$ applies to incompressible materials and the above equations yield the solutions given in Ref. 4.

Vol. 2
1960-61

For values of $m = 0, 1$ and ∞, a particular sphere having the radius ratio $r_0/r_i = 1{\cdot}5$ and subjected to either internal pressure ($\sigma_0 = 0$) or external pressure ($\sigma_i = 0$) is considered as an illustrative example. The results for $m = 0, 1$ and ∞ are tabulated in Tables 1 and 2 for the three values of $\alpha = 0, \frac{1}{6}$ and $\frac{1}{3}$. These results are shown plotted in Fig. 1.

TABLE 2. (SOLUTIONS, $\alpha = 0, \frac{1}{6}, \frac{1}{3}$); $m = 1, \infty$

	$m = 1$						$m = \infty$						
$\frac{r}{r_i}$	1·0	1·1	1·2	1·3	1·4	1·5	1·0	1·1	1·2	1·3	1·4	1·5	α
$\frac{\sigma_r}{\sigma_0}$	0	0·270	0·505	0·695	0·855	1	0	0·288	0·446	0·642	0·828	1	1/3
	0	0·300	0·549	0·732	0·881	1	0	0·283	0·515	0·708	0·868	1	1/6
	0	0·330	0·573	0·757	0·891	1	0	0·320	0·562	0·745	0·890	1	0
$\frac{\sigma_\vartheta}{\sigma_0}$	1·500	1·638	1·745	1·840	1·930	2	1·233	1·461	1·680	1·880	2·062	2·223	1/3
	1·745	1·788	1·806	1·815	1·810	1·799	1·565	1·700	1·786	1·840	1·879	1·900	1/6
	1·955	1·889	1·828	1·775	1·730	1·695	1·866	1·851	1·822	1·790	1·757	1·726	0
$\frac{\sigma_r}{\sigma_i}$	1	0·730	0·495	0·305	0·145	0	1	0·772	0·554	0·358	0·172	0	1/3
	1	0·708	0·471	0·280	0·127	0	1	0·750	0·528	0·335	0·152	0	1/6
	1	0·700	0·450	0·265	0·123	0	1	0·727	0·486	0·295	0·130	0	0
$-\frac{\sigma_\vartheta}{\sigma_i}$	0·500	0·638	0·745	0·840	0·930	7	0·233	0·461	0·680	0·880	1·062	1·223	1/3
	0·641	0·718	0·780	0·820	0·855	0·886	0·305	0·552	0·737	0·882	0·988	1·075	1/6
	0·788	0·807	0·810	0·800	0·789	0·775	0·513	0·703	0·802	0·848	0·868	0·875	0

4. DISCUSSION

An elementary device for including the effects of compressibility in the creep behavior of materials has been presented. This has been accomplished by a simple modification in the usual definition of the stress deviations. With the modified definition, it has been possible again to relate the strains and the stress deviations. The new stress–strain law thus obtained has been used in the problem of a hollow sphere subjected to uniform internal and external pressures. The resulting nonlinear differential equations have been solved in a closed parametric form.

The numerical results shown in tabular and graphical forms apply to a particular sphere of radius ratio $r_0/r_i = 1{\cdot}5$. It is clear that when the creep exponent $m = 0$, the stress distribution is the Lamé solution and is independent of the compressibility constant α. For other values of m, the radial stress distribution is qualitatively the same for all values of $\alpha (0 \leqslant \alpha \leqslant \frac{1}{3})$. On the other hand, it is clearly seen that the circumferential stress distribution for $m \geqslant 1$ differs radically from that of the Lamé solution.

REFERENCES

1. W. PRAGER, *J. Appl. Phys.* **16**, 837 (1945).
2. N. J. HOFF, *Quart. Appl. Math.* **12**, 49 (1955).
3. N. J. HOFF, *Effets Thermiques dans le Calcul de la Resistance des Structures d'Avions et d'Engins.* AGARD Report No. 52 (1956).
4. S. A. PATEL and K. A. V. PANDALAI, *Creep Analysis of Hollow Spheres Subjected to Uniform Pressures.* PIBAL Report No. 488 (1959).

Int. J. Mech. Sci. Pergamon Press Ltd. 1960. Vol. 2, pp. 8–12. Printed in Great Britain

AN EXPERIMENTAL INVESTIGATION OF INERTIA EFFECTS IN VISCOUS FLOW

P. G. MORGAN and A. SAUNDERS
University of Manchester

(*Received* 15 *October* 1959)

Summary—Experiments are presented concerning the importance of the inertia term in the Navier–Stokes equation for viscous radial flow between parallel plates.

Vol. 2
1960-61

NOTATION

p	static pressure
r, y, θ	cylindrical co-ordinates
u	velocity along the r direction
ρ	density
μ	coefficient of viscosity
v	kinematic viscosity
$2h$	clearance between parallel plates
Q	volume flow rate
u_{mean}	radial velocity at mean radius between pressure tappings p_1 and p_2

1. INTRODUCTION

RECENT work has drawn attention to the importance, in certain applications, of the inertia term in the Navier–Stokes equation. An analysis by Livesey[1] has dealt with the problem of the radial flow between two parallel surfaces, and he shows that the usual Reynolds equation of viscous flow

$$\frac{\partial p}{\partial r} = \mu \frac{\partial^2 u}{\partial y^2} \tag{1}$$

is a particular case of the general equation

$$\rho u \frac{\partial u}{\partial r} = -\frac{\partial p}{\partial r} + \mu \frac{\partial^2 u}{\partial y^2} \tag{2}$$

An exact solution of (2) for the boundary conditions of radial flow between parallel plates has not been obtained, but Livesey gives the solution

$$p_1 - p_2 = \frac{3\mu Q}{4\pi h^3} \ln \frac{r_2}{r_1} - \frac{3\rho Q^2}{80\pi^2 h^2} \left[\frac{1}{r_1^2} - \frac{1}{r_2^2} \right] \tag{3}$$

for the pressure difference between any two points at radii r_1 and r_2. The second term on the right-hand side represents the pressure change due to inertia effects, and is of opposite sign to that of the viscous pressure drop. Livesey suggests that these inertia effects may be significant at low velocities, and that the radial pressure gradient may be reversed at low Reynolds numbers.

A series of tests have now been carried out to examine the radial flow of a fluid between two parallel plates, for the case of a narrow gap between them. Details of the work and the results obtained are given below.

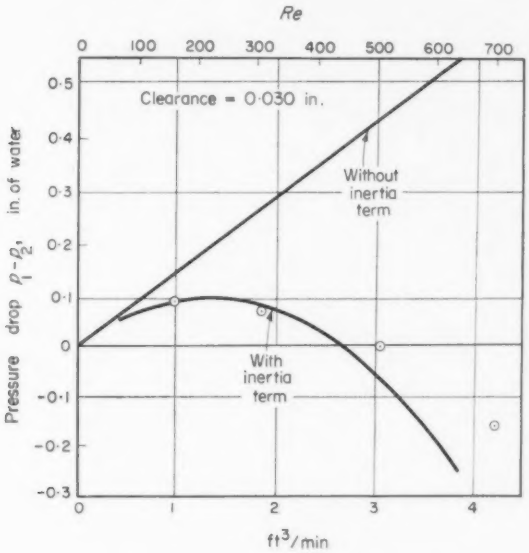

FIG. 1. ○ Experimental points.

2. EQUIPMENT

This consists simply of an accurately machined steel disk, 6 in. dia. and 3/8 in. thickness, supported over a surface plate by three screwed rods attached to a rigid frame. The clearance between the disk and the plate can be varied as required; it is measured by means of three dial gauges, rigidly clamped to the frame and resting on the upper surface of the disk.

Compressed air is supplied to the centre of the disk after passing through a control pressure reducing valve. The static pressure distribution over the surface of the disk is measured by a number of static tappings at different radii, connected to a multi-tube water or mercury manometer.

A number of tests have been carried out for different flow rates and inlet pressures, with different values of the clearance between the two surfaces. In each test, measurements of the pressure distribution over the surface of the disk were made.

3. RESULTS

In order to compare the experimental results with Livesey's theory, it is necessary to determine the pressure drop between two different radial positions, i.e. the pressure gradient in some region, and to examine its variation with flow rate. Figs. 1, 2 and 3 show the results obtained with clearances between the plates of 0·030, 0·015 and 0·010 in. respectively. In each case, curves have been drawn of pressure drop against flow rate for the case when

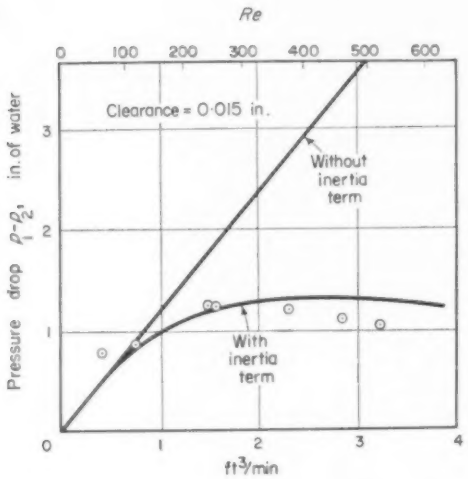

FIG. 2. ○ Experimental points.

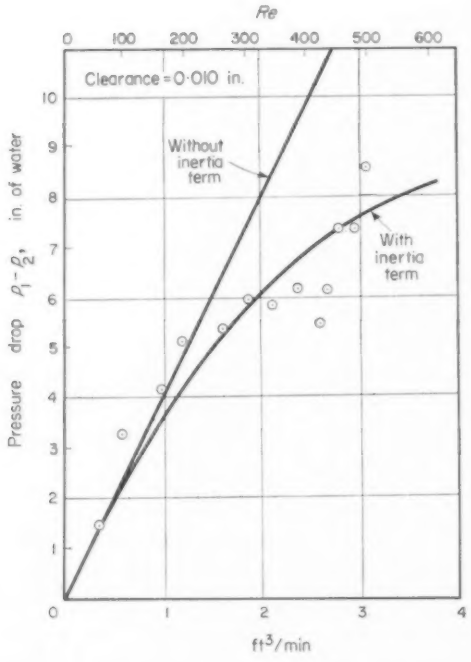

FIG. 3. ⊙ Experimental points.

Vol. 2
1960-61

the inertia terms are neglected, corresponding to

$$p_1 - p_2 = \frac{3\mu Q}{4\pi h^3} \ln \frac{r_2}{r_1} \tag{4}$$

and for the general case, equation (3). The curves are drawn for values of μ, Q and h appropriate to the experiment, while the pressure drop is taken between two points distance 13/16 in. and 37/16 in. from the centre of the disk. The flow rate has been used as the abscissa of the graphs, but a second (Reynolds number) scale has been inserted, where

$$Re = \frac{u_{\text{mean}} 2h}{\nu}$$

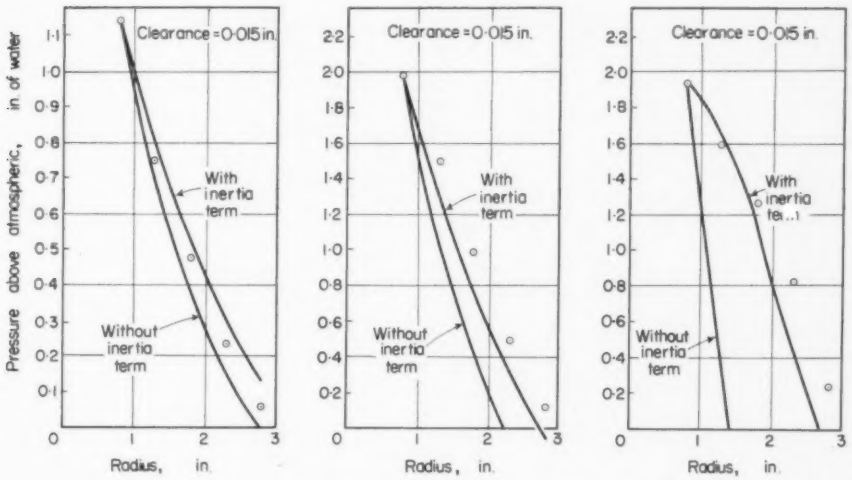

FIG. 4. —— Theoretical curves; ○ experimental points.

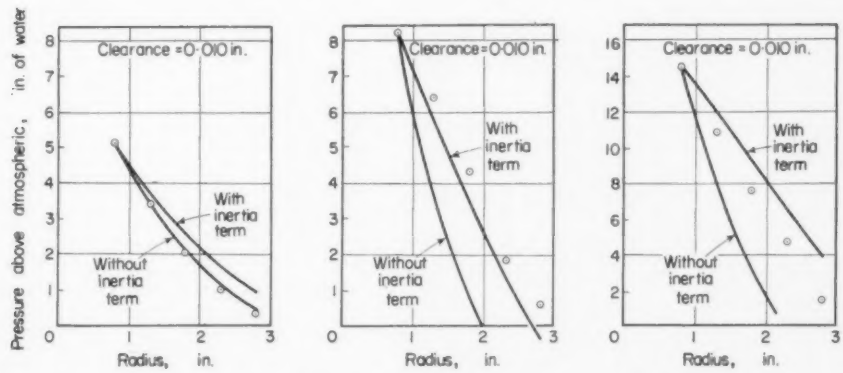

FIG. 5. —— Theoretical curves; ○ experimental points.

Figs. 4 and 5 show the variation with radius of the pressure distribution across the disk for the cases of 0·015 and 0·010 in. clearance between the disks.

4. CONCLUSIONS

The results apparently show that the inertia effects are important in this particular case of viscous radial flow. It should be noted, however, that the Reynolds number can only be considered high or low in relation to some critical value of Reynolds number, and a low Reynolds number immediately implies a value for which the inertia effects are negligible. The experimental evidence is, at the moment, insufficient to confirm Livesey's theory, and further tests using a liquid as the working fluid are in progress.

A further series of tests are planned on the question of the radial flow between parallel surfaces when the surfaces approach one another, i.e. the case of squeeze film lubrication. Considerable differences may occur when the surfaces approach one another at high velocity, as in the case of impact loading.

Acknowledgement—The authors wish to thank Mr. A. Frith for his assistance with the experimental equipment.

Vol. 2
1960-61

REFERENCE

1. J. L. LIVESEY, *Int. J. Mech. Sci.* **1**, 84 (1960).

Int. J. Mech. Sci. Pergamon Press Ltd. 1960. Vol. 2, pp. 13–29. Printed in Great Britain

ELASTIC STRESSES IN A ROTATING DISK OF GENERAL PROFILE*

A. S. KOBAYASHI† and P. R. TRUMPLER‡

(*Received* 10 *August* 1959)

Summary—Known methods of calculating elastic stresses in a rotating disk are plane-stress solutions of the problem. The method used here for calculating elastic stresses in a rotating disk of general profile is a three-dimensional treatment. The method consists of the linear combination of the states of stresses of one basic problem and two residual problems. The basic problem is the known plane-strain problem of a long rotating cylinder. The first residual problem is the elimination of surface tractions acting on a disk which is cut from this rotating cylinder. The second residual problem is the determination of the state of stress due to the prescribed displacements along the disk bore. Southwell stress functions are used to solve these residual problems. The two solutions are obtained numerically by the use of a high-speed digital computer.

NOTATION

THE following nomenclature is used in this paper. The dimensions of all physical quantities are indicated in parentheses.

a = radius of the disk bore, (L)
b = outer radius of the disk, (L)
L = axial length of the disk, (L)
r, θ, z = cylindrical co-ordinates of a point, $(L, 0, L)$
E = modulus of elasticity of the material, (FL^{-2})
ν = Poisson's ratio of the material, (0)
n = angular velocity of the disk, (T^{-1})
w = density of the disk material, $(FL^{-4}T^2)$
$s_{rr}, s_{\theta\theta}, s_{zz}$ = radial, tangential and axial stresses, respectively, (FL^{-2})
$s'_{rr}, s'_{\theta\theta}, s'_{zz}$ = radial, tangential and axial stress coefficients $\frac{s_{rr}}{wb^2n^2}, \frac{s_{\theta\theta}}{wb^2n^2}, \frac{s_{zz}}{wb^2n^2}$ respectively, (0)
$s_{r\theta}, s_{\theta z}, s_{zr}$ = shear stresses, (FL^{-2})
$s'_{r\theta}, s'_{\theta z}, s'_{zr}$ = shear stress coefficients $\frac{s_{r\theta}}{wb^2n^2}, \frac{s_{\theta z}}{wb^2n^2}, \frac{s_{zr}}{wb^2n^2}$ respectively, (0)
u_r, u_θ, u_z = radial, tangential and axial displacements, respectively, (L)
$u'_r = u_r/b$ = radial displacement coefficients, (0)
h = spacing of a rectangular grid network for finite-difference method, (L)
N = number of nodes in a finite-difference grid network
U, V = Southwell stress functions, (F)
U', V' = normalized Southwell stress functions $\frac{U}{wb^2n^2}, \frac{V}{wb^2n^2}$ respectively, (L^2)

$$\vartheta^2 = \frac{\partial^2}{\partial r^2} - \frac{1}{r}\frac{\partial}{\partial r} + \frac{\partial^2}{\partial z^2}$$

* This paper summarizes a thesis submitted by the first author in partial fulfilment of the requirements for the degree of Doctor of Philosophy in Mechanical Engineering in the Graduate School of Illinois Institute of Technology, Chicago.

† Department of Mechanical Engineering, University of Washington.
‡ School of Mechanical Engineering, University of Pennsylvania.

INTRODUCTION

One of the design problems in turbo-machinery is to determine the stresses in turbine disks under operating conditions. Calculation of the elastic stress distribution due to centrifugal force alone is a first step in the determination of such actual stress distributions in these disks. Many papers dealing with this problem have been published to date. Heretofore, most of these problems were treated either as a plane-stress problem[1, 2] or as a plane-strain problem[3] where the variations of stresses in the axial direction and the shear and axial stresses were neglected. An exception to this method of approach is found in a recent paper by Hodge[4] where the variations in radial and tangential stresses in the axial direction of a thin rotating disk were considered but the shear and axial stresses were assumed to be negligible.

In this paper a method is established for computing the elastic stresses in a rotating disk of general profile where the variations of stresses in the axial direction as well as the shear and axial stresses are considered. The developed method is suitable for, but not limited to, iterative computation carried out by high-speed digital computers.

Vol. 2
1960-61

BASIC ASSUMPTIONS

The following assumptions are made in this development.

1. The disk is a body of revolution and rotates at constant speed about its geometrical axis which is fixed in a Newtonian reference frame.
2. The plane region which the disk has in common with any meridional half-plane is simply connected.
3. Any external forces acting on the disk surfaces are rotationally symmetric about the geometrical axis.
4. The disk material is homogeneous and isotropic. Thus, the elastic constants and density remain constant throughout the disk.
5. The temperature remains constant throughout the disk.
6. The linear stress–strain law holds throughout the disk.
7. The deformations are sufficiently small that all loads may be applied to the undeformed body.
8. The effect of the gravitational and magnetic fields on the disk is neglected.

Assumptions 1 to 3 are the geometrical restrictions imposed on the disk for the developed method to be applicable. Assumption 2 is imposed for the unique determination of the stress functions associated with the given state of stress.[5] Assumption 5 indicates that thermal stresses are not considered in this paper. It will be shown later how to compute thermal stresses using this method when the temperature in the disk varies in the radial direction only. Assumptions 4, 6 and 7 are necessary for the linear theory of elasticity to be applicable here.

THEORETICAL DEVELOPMENT

Consider a disk of general profile in its undeformed shape rotating at a constant speed about its geometrical axis as shown in Fig. 1. The origin, O, of a cylindrical co-ordinate system, (r, θ, z), is taken on the axis and at one end of the disk. The disk is assumed to be press-fitted at the bore on a rigid shaft and

therefore radial displacements are prescribed where the disk bore interferes with the surface of the rigid shaft. No shearing force is assumed to exist between the shaft and the disk. The problem now is to determine the stress distribution in such a disk.

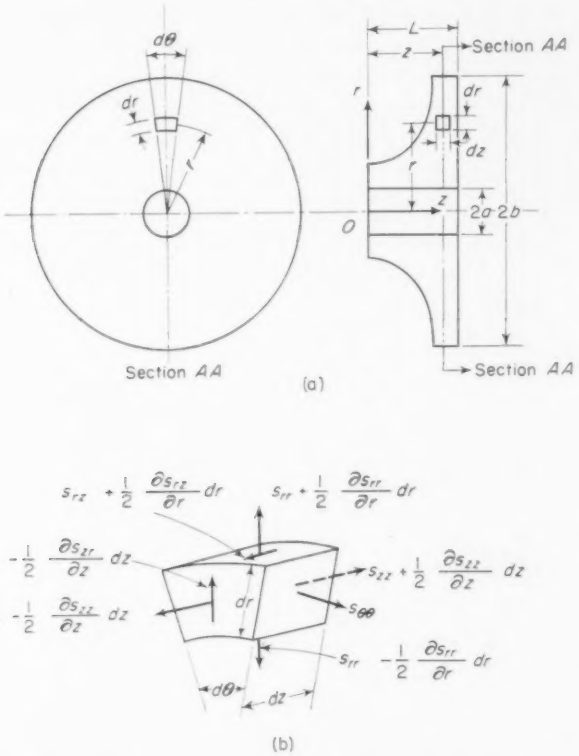

FIG. 1. Cylindrical co-ordinate system and equilibrium of an element in the disk. (a) Cylindrical co-ordinate system applied to a disk of general profile. (b) Equilibrium of an element in a torsionless rotationally symmetric body.

One conceivable method of approach is to solve numerically for the Boussinesq–Papkovitch stress functions* which satisfy three simultaneous Poisson's equations and the given boundary conditions. The displacement field is then obtained in terms of these stress functions and their first derivatives with respect to r and z. Knowing the complete displacement field in the disk, it is then possible to obtain the strain and hence the stress fields by the strain-displacement and the stress–strain relations of elasticity theory. A numerical solution by this approach requires the use of a high-speed computer with a large capacity of memory storage. Unfortunately, the writers did not have such a computer at their disposal and therefore this method of approach was abandoned.

* A note on these functions is given in the Appendix.

In the absence of body force in a rotationally symmetric body, it has been shown that one stress function can be eliminated from the three Boussinesq–Papkovitch stress functions without loss in completeness.[5] With such reduction in the number of stress functions, the amount of numerical work involved would be reduced considerably and the problem becomes manageable by an IBM 650 digital computer. Following this reasoning the method of approach used in this paper was to find a linear combination of different stress fields which satisfies the given field equations and given boundary conditions. This was accomplished by representing the solution of the given problem as the linear superposition of the solution of one basic problem with body forces and the solutions of two residual problems without body forces. As mentioned previously, the latter problems can be solved numerically without much difficulty.

Vol. 2
1960-61

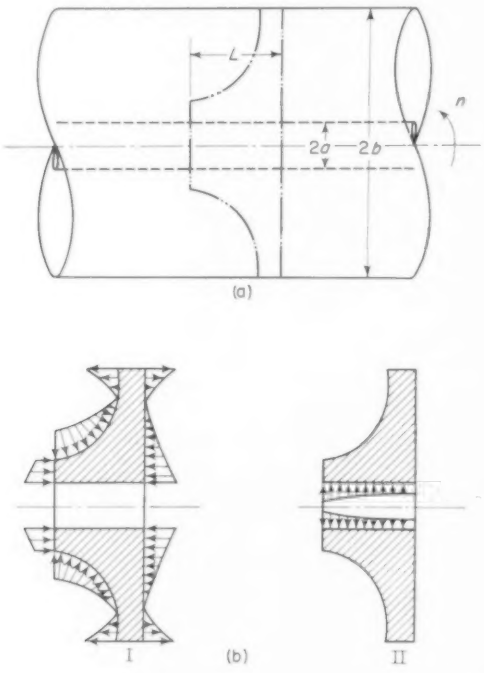

FIG. 2. Schematic drawings of the method of approach for obtaining elastic stresses in a rotating disk of general profile. (a) Basic Problem (long rotating cylinder). (b) Residual Problem I (surface tractions prescribed); Residual Problem II (displacement prescribed).

As shown in Fig. 2, the Basic Problem is the plane-strain problem of a long rotating thick cylinder for which a well-known solution exists. When a disk of general profile is cut from this cylinder, the surface tractions acting on the surfaces of the disk can be calculated by the known formulae.

The elimination of these surface tractions constitutes Residual Problem I. That is, surface tractions of opposite sense to the surface tractions just obtained

are prescribed to the corresponding boundaries of the disk at rest and the stress distribution is computed numerically. The resultant solution obtained by the linear superposition of the solution of the Basic Problem and Residual Problem I is the solution for a rotating disk of general profile which is free of any external surface tractions on its boundaries.

Residual Problem II is to find the stress distribution in the disk due to the radial interference with a rigid shaft at the disk bore. For this purpose, the radial displacements at the bore of the disk are computed from the resultant solution of the Basic Problem and Residual Problem I. Radial displacements which are equal to the amount of radial interference between the rigid shaft and the disk bore are then prescribed onto the bore of the disk at rest and the stress distributions are again computed numerically.

The results of this calculation are then superposed on the results of the previously obtained two solutions and the final solution for a rotating disk shrunk on a rigid shaft is thus obtained.

The two residual problems themselves are solved by solving numerically for a pair of Southwell stress functions for each problem. Southwell stress functions in the form which is used here were first used by Allen[6] to solve the problem of a cylinder of finite length with radial surface tractions prescribed. Southwell did not indicate explicitly the use of the two stress functions U, V in the form shown in the paper, but based his development on a stress function which satisfied the following equation:

$$\partial^4 W = 0$$

This function W is related to U and V in the following manner:

$$\frac{\partial^2 W}{\partial z^2} - (1+\nu)\partial^2 W = V$$

$$\partial^2 W = U$$

Southwell stress functions were used here in place of the aforementioned Boussinesq–Papkovitch stress functions since Southwell stress functions were simpler to handle in numerical computation. This change in stress functions does not alter the generality of the approach. Southwell stress functions are derivable from Boussinesq–Papkovitch stress functions[5] and hence the preceding discussion on the completeness of Boussinesq–Papkovitch stress functions also applies to Southwell stress functions.

The axial cross-section of the disk is replaced by a finite grid network where two unknown stress functions are assigned to each node of the grid. If these nodes are in the interior of the body then the stress functions must satisfy two given field equations which are written in finite-difference form. If the nodes are on the boundaries of the disk, then the stress functions must satisfy the given boundary equations which are also written in finite-difference form. The orderly array of all field and boundary equations for every node of the grid network constitutes a set of linear simultaneous algebraic equations.

These equations are solved for their unknowns, the two stress functions at each node, using the numerical method of iteration by single steps. This iteration process is programmed for and carried out on an IBM 650 digital computer.

Knowing the numerical values of the two Southwell stress functions at each node, the stresses at these nodes are computed for each residual problem.

BASIC EQUATIONS

(1) The six components of the stress coefficients of a plane-strain solution of a rotating cylinder of infinite length with free ends are as follows:

$$\left.\begin{aligned} s'_{rr} &= \frac{1}{8}\frac{3-2\nu}{1-\nu}\left[\frac{a^2}{b^2}+1-\frac{a^2}{r^2}-\frac{r^2}{b^2}\right] \\ s'_{\theta\theta} &= \frac{1}{8}\frac{3-2\nu}{1-\nu}\left[\frac{a^2}{b^2}+1+\frac{a^2}{r^2}-\frac{1+2\nu}{3-2\nu}\frac{r^2}{b^2}\right] \\ s'_{zz} &= \frac{\nu}{4(1-\nu)}\left[\frac{a^2}{b^2}+1-2\frac{r^2}{b^2}\right] \\ s'_{r\theta} &= s'_{z\theta} = s'_{zr} = 0 \end{aligned}\right\} \tag{1}$$

The radial displacement coefficient u'_r along the disk bore, $r = a$, can be computed in terms of the above three stress coefficients as follows:

$$[u'_r]_{r=a} = \frac{wn^2 ab}{E}[s'_{\theta\theta} - \nu(s'_{rr} + s'_{zz})] \tag{2}$$

(2) In the absence of body forces, the stress coefficients in a rotationally symmetric body can be expressed in terms of two normalized Southwell stress functions, U' and V', as follows:

$$\left.\begin{aligned} s'_{rr} &= \frac{1}{r}\left[\frac{\partial U'}{\partial r}+\frac{\partial V'}{\partial r}\right]-\frac{1}{r^2}[V'+(1-\nu)U'] \\ s'_{\theta\theta} &= \frac{\nu}{r}\frac{\partial U'}{\partial r}+\frac{1}{r^2}[V'+(1-\nu)U'] \\ s'_{zz} &= -\frac{1}{r}\frac{\partial V'}{\partial r} \\ s'_{zr} &= \frac{1}{r}\frac{\partial V'}{\partial z} \\ s'_{r\theta} &= s'_{\theta z} = 0 \end{aligned}\right\} \tag{3}$$

where U' and V' satisfy the following two field equations

$$\left.\begin{aligned} \vartheta^2 U' &= 0 \\ \vartheta^2 V' &= \frac{\partial^2 U'}{\partial z^2} \end{aligned}\right\} \tag{4}$$

BOUNDARY EQUATIONS FOR RESIDUAL PROBLEM I

As mentioned in the previous section, for numerical computation, the axial cross-section of a given disk is replaced by a finite-difference grid network of mesh size h. Also in order to reduce the amount of computation, the curved portion of the disk is replaced by the closest step-shaped surface which follows the grids of the network.

Vol. 2
1960-61

Residual Problem I is a boundary-value problem of the first type where surface tractions alone are prescribed to the boundaries. For the step-shaped disk, the prescribed surface tractions derivable from equation (1) can be divided into the following two groups:

(A) s'_{zz} and s'_{zr} prescribed on the plane surfaces perpendicular to the axis.
(B) s'_{rr} and s'_{zr} prescribed on the cylindrical surface parallel to the axis.

Now s'_{zr} is equal to zero along all boundaries of the disk in Residual Problem I as shown by the fourth equation in equation (1). Thus, from the fourth equation in equation (3) it can be seen that V' is a function of r only along all boundaries. Using this result and also from the third equations in equations (1) and (2), the following relation is obtained for V':

$$V' = \frac{\nu}{8(1-\nu)} r^2 \left[1 + \frac{a^2}{b^2} - \frac{r^2}{b^2}\right] - V'(r_A) \tag{5}$$

where $V'(r_A)$ is an integration constant. This integration constant can be set equal to zero without loss in generality provided $U'(r,z)$ is altered simultaneously by a constant value $-V'(r_A)/(1-\nu)$, and for simplicity this is done here. Thus, by equation (5), V' can be computed along all boundaries which belong to either one of the above two cases.

The boundary values for the other stress function, $U'(r,z)$, are not given in such explicit form. As shown in equations (3) and (4), U' is established implicitly by a partial differential equation which involves the values of V' and s'_{rr} or s'_{rz} along the boundaries.

BOUNDARY EQUATIONS FOR RESIDUAL PROBLEM II

Residual Problem II is a mixed–mixed boundary-value problem where normal and tangential surface tractions are prescribed on part of the boundary of the disk. Normal displacements and tangential surface tractions are prescribed on the remaining boundaries of the disk. Following identical development in the previous section, it can be seen that V' vanishes along all boundaries.

Where the radial displacement coefficient, $u'_{r=a}$ is prescribed along the disk bore, $U'_{r=a}$ can be determined by using equations (2) and (3) as follows:

$$U'_{r=a}(r,z) = \frac{E}{1-\nu^2} \frac{a}{b} \frac{u'_{r=a}(r,z)}{wn^2} \tag{6}$$

DETERMINATION OF ELASTIC STRESSES IN TWO ROTATING DISKS

Following the procedure described above, the elastic stresses in two typical turbine rotor disks were determined. Fig. 3 shows the dimensions of the two disks considered here. Fig. 4 shows the step-shaped disks which were substituted in place of the original disks in order to simplify the computation of the finite-difference equations. A total of 88 nodes was used for the grid network of Disk No. 1 with the grid spacing being $\frac{1}{4}$ in. There were 75 nodes in Disk No. 2.

An IBM 650 digital computer was used to carry out the iteration by single-step process to compute the two Southwell stress functions, U' and V', for

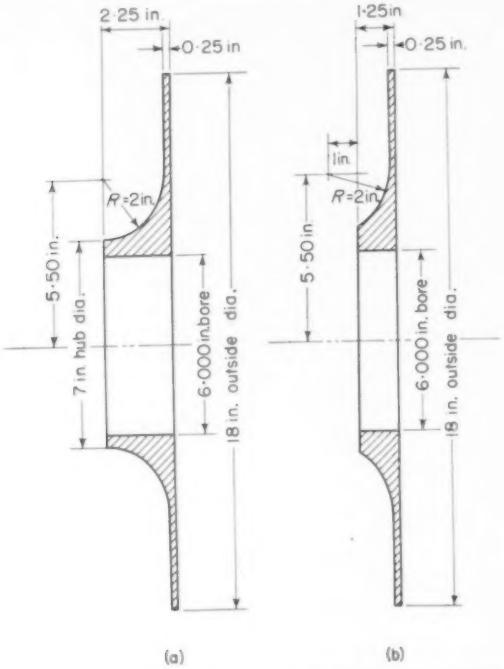

FIG. 3. Dimensions of two disks. (a) Disk No. 1. (b) Disk No. 2.

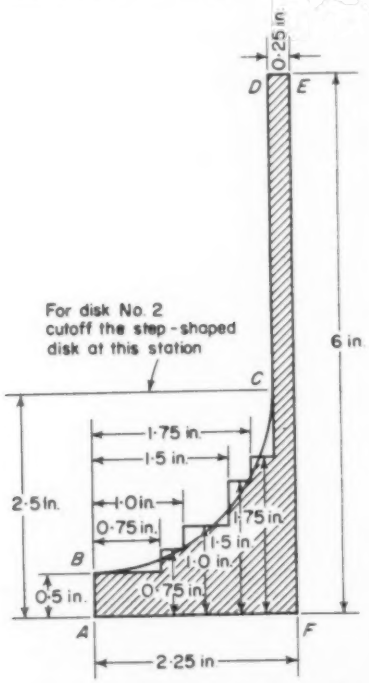

FIG. 4. Dimensions of the step-shaped disks which were used for finite-difference method of computing stress functions.

Vol. 2
1960-61

Residual Problems I and II. The iteration was discontinued when the accuracy of U' and V' was such that the residual surface tractions on the boundaries were less than 3 per cent of the maximum stress at each node. Moreover, for the particular shapes of disks considered here the maximum stress in Residual Problems I and II was less than 10 per cent of the maximum stress in the Basic Problem. Therefore, the overall accuracy of the resultant states of stress was considered to be such that the mismatch in the computed stresses with the prescribed surface tractions at the boundaries was less than one per cent of the maximum stress at the corresponding nodes.

Figs. 5 and 6 show the resultant stress distribution in Disk No. 1 (without shaft) in terms of stress coefficients. The tangential and radial stress coefficients along $ABCD$ in Fig. 6 are not shown for the curved portion of the surface since this curved portion was replaced by a step-shaped boundary.

The two figures show the significant effect of axial variations. The axial stress is no longer negligible. The tangential stress coefficient along the bore is minimum at the hub end and reaches a maximum value at the plate end. This maximum tangential stress coefficient, 0·58 at the plate end of the bore, is about 55 per cent higher than the corresponding tangential stress coefficient which was obtained by the plane stress formula for the corresponding symmetric disk.*

Fig. 7 shows the radial displacements along the bore of the disk in terms of displacement coefficients. The displacements increase at the plate end of the disk, an effect which is sometimes referred to as the result of an "overturning moment" produced by the body forces acting on the non-symmetrical disk.

Figs. 8 and 9 show the resultant stress distribution in Disk No. 2 (without shaft) in terms of the stress coefficients. For the reason mentioned previously, the tangential and radial coefficients along CBA in Fig. 9 are not shown here. The effect of the overturning moment is still significant but the axial stresses are small and the state of stress approaches that of plane stress. The maximum tangential stress coefficient along the bore, 0·63 at the plate end, is 39 per cent higher than the corresponding tangential stress coefficient obtained by the plane-stress formula for the corresponding symmetric disk.

Fig. 10 shows the radial displacements along the bore of Disk No. 2 in terms of the displacement coefficients. Again the increase in displacements towards the plate end of the disk is noted. When comparing the radial displacements at the hub ends of Disk Nos. 1 and 2, Figs. 7 and 10, the effect of the added rigidity at the hub end of Disk No. 1 is also noticeable.

Figs. 11–14 show the stress distributions in the two disks at rest caused by press-fitting rigid shafts with 0·1 per cent radial interference in the disk bores. It should be noted that sharp peaks exist in the stress distribution along the disk bore of Disk No. 1. These sharp peaks exist at two points where the prescribed radial displacements terminate and are points of singularities. No accuracy is claimed for the values of the stresses in the immediate vicinities of these points.

* The method of "small differences"[1] was used here to compute the stresses in rotating disk of symmetric profile.

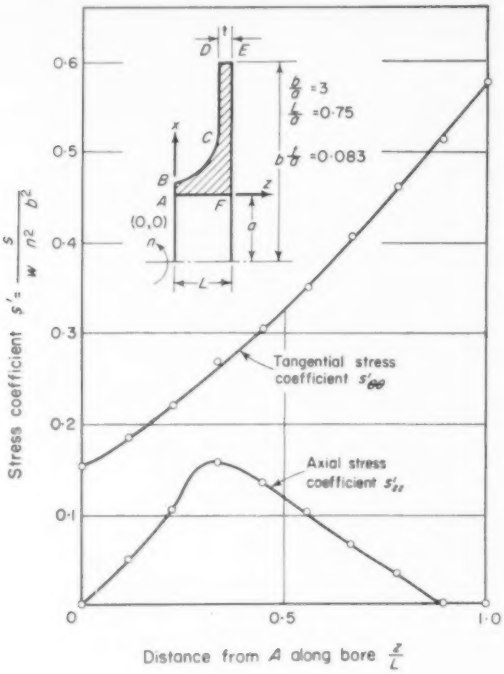

FIG. 5. Stress distribution along the bore of Disk No. 1 (without shaft) rotating at constant speed.

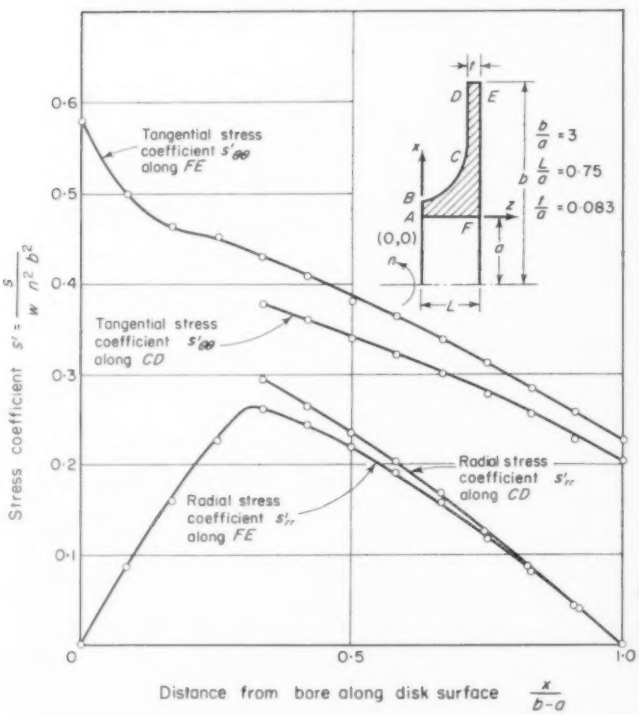

FIG. 6. Stress distribution along two surfaces of Disk No. 1 (without shaft) rotating at constant speed.

Vol. 2
1960-61

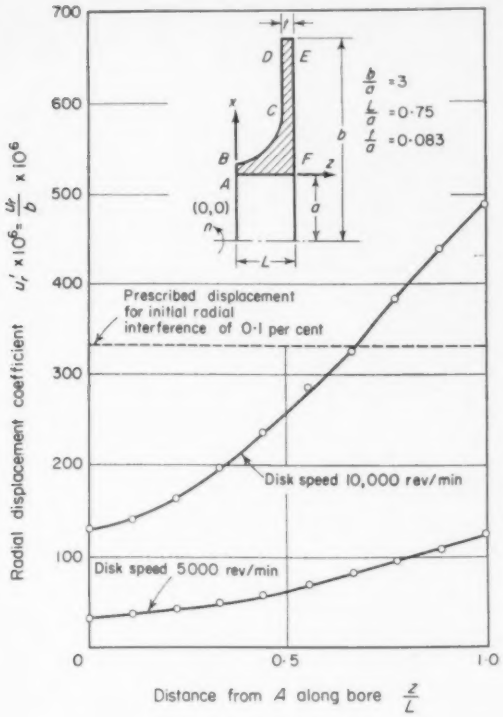

FIG. 7. Radial displacement along the bore of Disk No. 1 (without shaft) rotating at constant speed. Modulus of elasticity, Poisson's ratio and density of the disk material are 26×10^6 lb/in^2, 0·26 and $0{\cdot}751 \times 10^{-3}$ lb-sec^2/in^4 respectively.

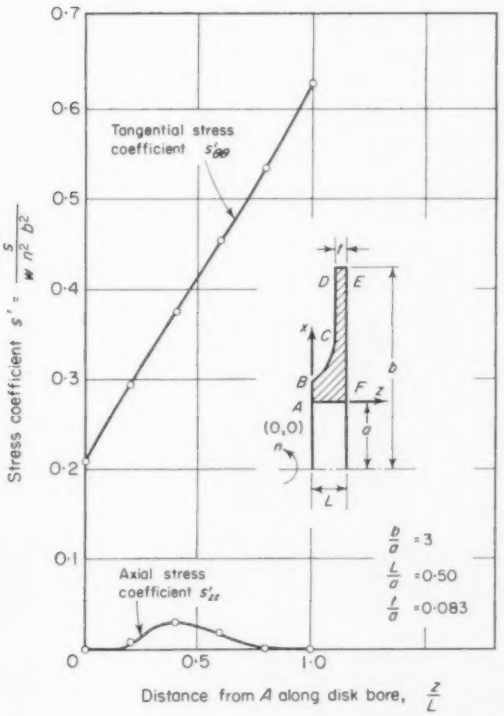

FIG. 8. Stress distribution along the bore of Disk No. 2 (without shaft) rotating at constant speed.

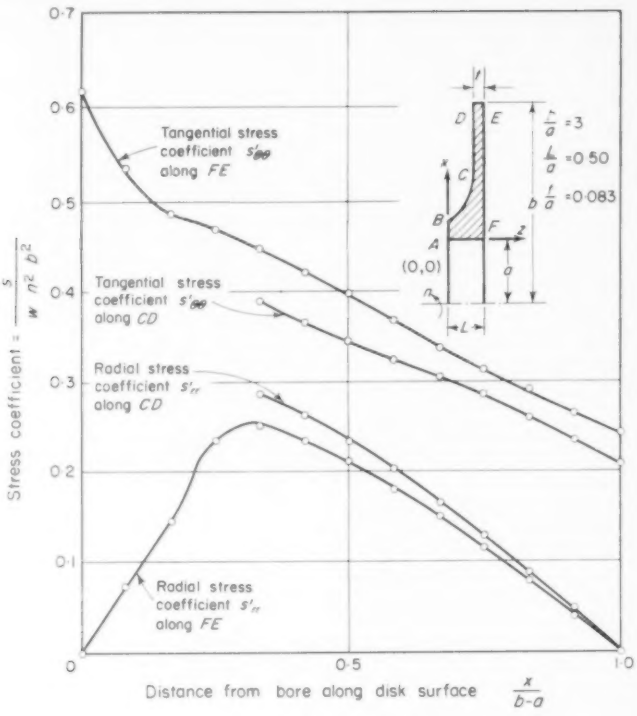
Tangential stress coefficient $s'_{\theta\theta}$ along FE
Tangential stress coefficient $s'_{\theta\theta}$ along CD
Radial stress coefficient s'_{rr} along CD
Radial stress coefficient s'_{rr} along FE
Stress coefficient = $\frac{s}{\omega^2 \rho b^2}$
Distance from bore along disk surface $\frac{x}{b-a}$
$\frac{b}{a}$ = 3
$\frac{L}{a}$ = 0·50
$\frac{t}{a}$ = 0·083

FIG. 9. Stress distribution along two surfaces of Disk No. 2 (without shaft) rotating at constant speed.

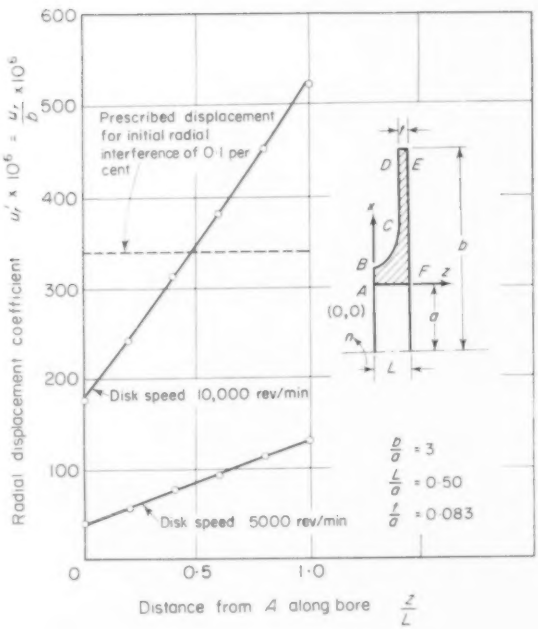
Prescribed displacement for initial radial interference of 0·1 per cent
Disk speed 10,000 rev/min
Disk speed 5000 rev/min
Radial displacement coefficient $u'_r \times 10^6 = \frac{u_r}{b} \times 10^6$
Distance from A along bore $\frac{z}{L}$
$\frac{b}{a}$ = 3
$\frac{L}{a}$ = 0·50
$\frac{t}{a}$ = 0·083

FIG. 10. Radial displacement along bore of Disk No. 2 (without shaft) rotating at constant speed. Modulus of elasticity, Poisson's ratio and density of the disk material are 26×10^6 lb/in^2, 0·26 and $0{\cdot}751 \times 10^{-3}$ lb-sec^2/in^4 respectively.

Vol. 2
1960-61

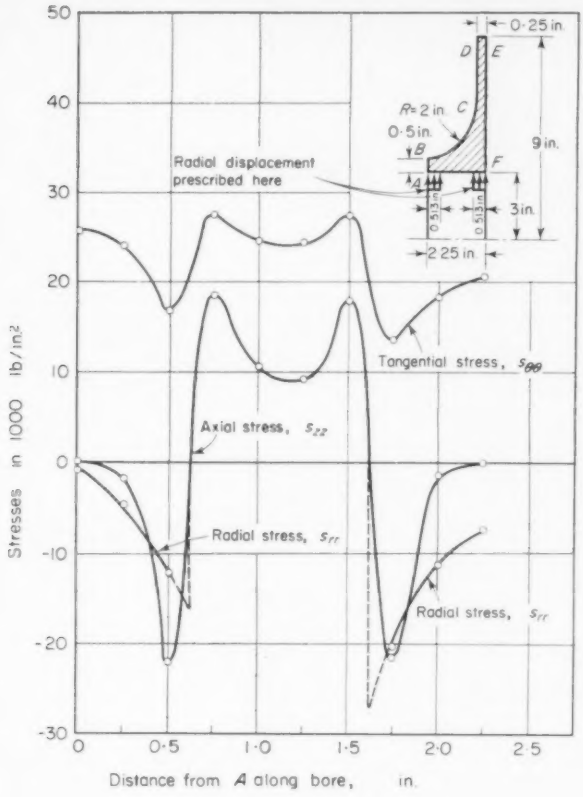

FIG. 11. Stress distribution along the bore of Disk No. 1 (at rest) due to 0·1 per cent radial interference at bore.

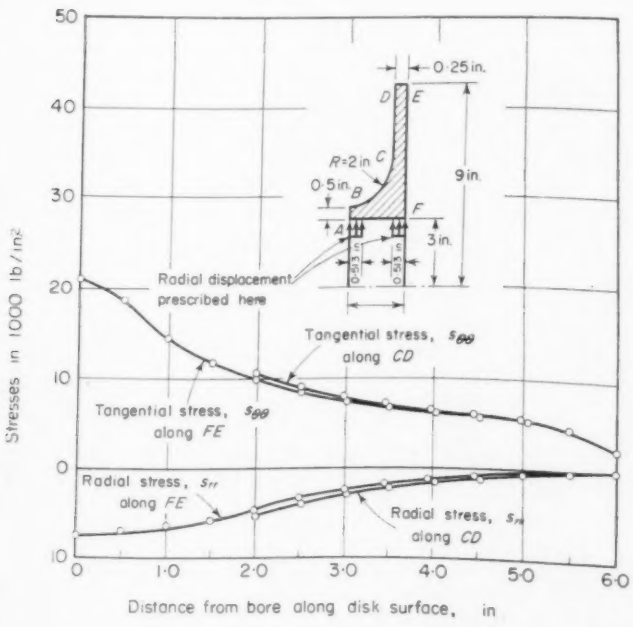

FIG. 12. Stress distribution along the two surfaces of Disk No. 1 (at rest) due to 0·1 per cent radial interference at bore.

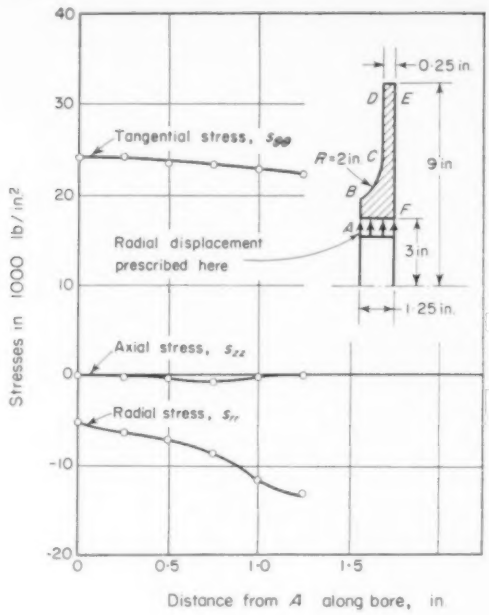

FIG. 13. Stress distribution along the bore of Disk No. 2 (at rest) due to 0·1 per cent radial interference at bore.

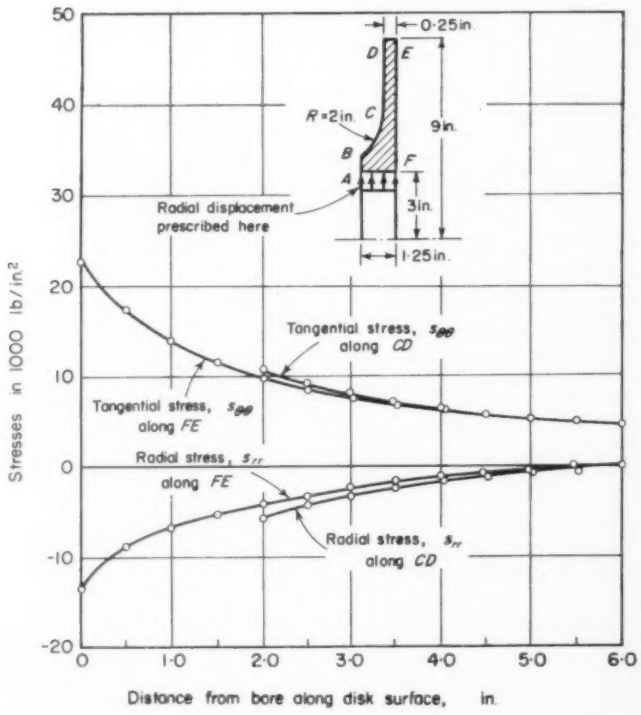

FIG. 14. Stress distribution along two surfaces of Disk No. 2 (at rest) due to 0·1 per cent radial interference at bore.

Vol. 2
1960-61

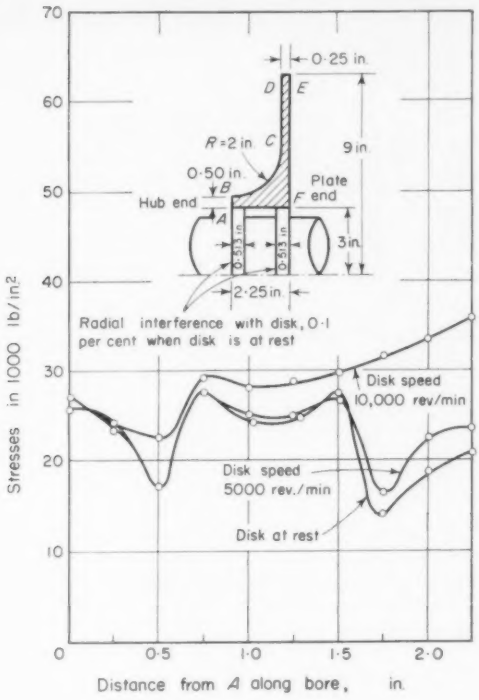

FIG. 15. Tangential stress distributions along the bore of Disk No. 1 at rest and rotating at two different speeds.

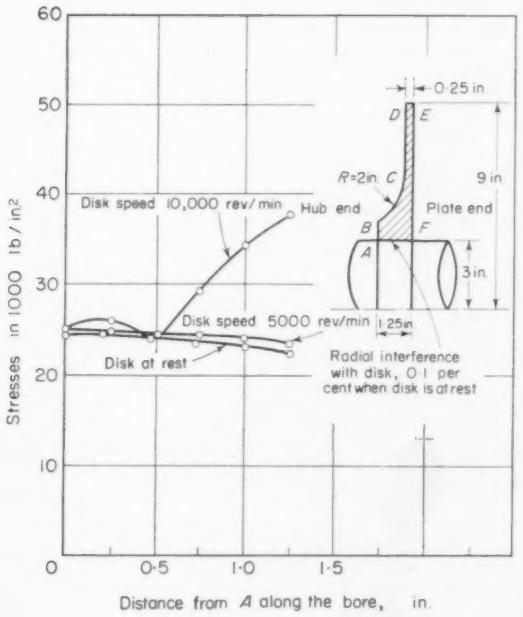

FIG. 16. Tangential stress distributions along the bore of Disk No. 2 at rest and rotating at two different speeds.

Figs. 15 and 16 show the tangential stress distribution along the bores in Disk Nos. 1 and 2 for disk speeds of 0, 5000 and 10,000 rev/min. As shown in Fig. 15, there is little difference in the two tangential stress distributions when Disk No. 1 is at rest and when it is rotating at 5000 rev/min. As shown in Fig. 7 at 10,000 rev/min, the plate-end contact region of the disk bore completely lifts away from the shaft and the disk is in contact with the shaft at the hub end only. Thus, the sharp peak in the tangential stress distribution on the disk-end side of the disk does not exist at this speed of 10,000 rev/min.

As shown in Fig. 16, the tangential stresses along the disk bore in Disk No. 2 are uniformly distributed when the disk is at rest and when the disk is rotating at 5000 rev/min. The stress distribution at 10,000 rev/min shows a large axial stress variation. The disk at this speed is only contacting the shaft along half of its bore length at the hub end as shown in Fig. 10. Thus, the tangential stress increases sharply at this portion of the disk bore.

Vol. 2
1960-61

CONCLUSIONS

The elastic-stress distribution in rotating disks of general profile can be determined by the method presented by the authors. The accuracy of determination is limited by the accuracy associated with the finite-difference method employed here.

As shown by Hodge,[4] the overturning moments, due to the variation of centroidal height with respect to the radius, increase the maximum tangential stress at the plate end of the disk bore. The plane-stress formula for calculating the maximum tangential stress in the corresponding symmetric disk ignores the effect of this overturning moment and can therefore result in an under-design of the disk.

The method can be extended to compute the thermal stresses in a rotating disk of general profile where the temperature in the disk varies in the radial direction only. The known plane-strain solution of thermal stresses in a long cylinder needs only to be superposed on the Basic Problem of the plane-strain solution of the rotating cylinder and the remaining procedure remains identical to that described here.

The approach used in this paper to obtain more precisely the actual elastic-stress distribution in rotating disks should be helpful in establishing the design of such disks. It is perhaps a necessary second step (plane solutions are the first step) to the solution of the elastic–plastic problem on which future design criteria will probably be based.

Acknowledgements—The writers are indebted to Crane Company, Chicago, Illinois, and Armour Research Foundation of Illinois Institute of Technology for making available the IBM 650 digital computers and assisting with machine operation. They are also indebted to Dr. R. A. Eubanks of Borg–Warner Corporation, Des Plaines, Illinois, for his helpful suggestions.

APPENDIX

Boussinesq–Papkovitch stress function

For a point interior of a homogeneous and isotropic elastic body, consider a set of functions, $\phi(\bar{\rho})$ and $\bar{\psi}(\bar{\rho})$, which satisfy the following relations:

$$\left.\begin{aligned} \nabla^2\phi &= \frac{-\bar{\rho}\cdot\bar{F}}{2(1-\nu)} \\ \nabla^2\bar{\psi} &= \frac{\bar{F}}{2(1-\nu)} \end{aligned}\right\} \tag{A-1}$$

where the bar quantities indicate vector quantities and the non-bar quantities indicate scalar quantities.

$\bar{\rho}$ is the position vector of a field point referred to the origin.

$\bar{F} = \bar{F}(\bar{\rho})$ is the body force at the field point.

Consider next a displacement vector, $\bar{u}(\bar{\rho})$, defined as follows:

$$\bar{u} = \frac{1}{2\mu}[\nabla(\phi + \bar{\rho}\cdot\bar{\psi}) - 4(1-\nu)\bar{\psi}] \tag{A-2}$$

where μ is the shear modulus. Then $\bar{u}$ satifies the displacement equation of equilibrium for the body force $\bar{F}(\bar{\rho})$, provided ϕ and $\bar{\psi}$ are class 3 for $\bar{\rho}$ in the body. These functions, ϕ and $\bar{\psi}$, are called Boussinesq–Papkovitch stress functions and the completeness of these functions was proven by Mindlin[8].

For the case of torsionless axial-symmetry, equation (A–1) can be expressed by the following three scalar equations:

$$\left.\begin{aligned} \nabla^2\phi &= -\frac{r\cdot F_r + z\cdot F_z}{2(1-\nu)} \\ \nabla^2\psi_r &= \frac{F_r}{2(1-\nu)} \\ \nabla^2\psi_z &= \frac{F_z}{2(1-\nu)} \end{aligned}\right\} \tag{A-3}$$

and the corresponding displacement equations are

$$\left.\begin{aligned} u_r &= \frac{1}{2\mu}\left[\frac{\partial\phi}{\partial r} + \frac{\partial}{\partial r}(r\cdot\psi_r + z\cdot\psi_z) - 4(1-\nu)\psi_r\right] \\ u_z &= \frac{1}{2\mu}\left[\frac{\partial\phi}{\partial z} + \frac{\partial}{\partial z}(r\cdot\psi_r + z\cdot\psi_z) - 4(1-\nu)\psi_z\right] \end{aligned}\right\} \tag{A-4}$$

REFERENCES

1. A. Stodola, *Steam and Gas Turbines* (English translation of 6th German Ed.) Vol. 1, p. 372. McGraw-Hill, New York (1927).
2. S. S. Manson, *The Determination of Elastic Stresses in Gas-turbine Disks* p. 1. NACA Technical Note No. 1279 (1947).
3. C. C. Wan, *Stress Distribution in a Rotating Shaft.* Ph.D. Thesis, Illinois Institute of Technology (1948).
4. P. G. Hodge, Jr. and J. Papa, *J. Franklin Inst.* **263**, 505 (1957).
5. R. A. Eubanks and E. Sternberg, *On the Completeness of the Boussinesq–Papkovitch Stress Functions.* Government Contract No. N7Onr-32906, Office of Naval Research Department of the Navy (1958).
6. D. N. Allen, *Relaxation Methods* p. 134. McGraw-Hill, New York (1954).
7. R. V. Southwell, *Proc. Roy. Soc.* A **180**, 367 (1942).
8. R. D. Mindlin, *Force at a Point in the Interior of a Semi-Infinite Solid.* Proceedings of the First Midwest Conference on Solid Mechanics, University of Illinois (1953).

Int. J. Mech. Sci. Pergamon Press Ltd. 1960. Vol. 2, pp. 30–39. Printed in Great Britain

WANG CHENG AND THE FIRST BOOK ON MECHANICAL ENGINEERING IN CHINA

LIU HSIEN-CHOU
(Condensed and translated by S. S. CHANG*)

Vol. 2
1960-61

TRANSLATOR'S FOREWORD

ALTHOUGH the Chinese, as early as a few thousand years ago, invented gunpowder, silk, the compass, paper making and printing, their engineering development a few hundred years ago was far behind that of the European countries. The main cause of China's lack of progress in engineering was the ancient Empire's tradition that "all ten thousand professions are of low grade except the study of classical philosophy and literature". Government officials, the rulers of the country, were all chosen from students who had passed examinations in literature. In the sixteenth and seventeenth centuries Western science and technology were imported by a group of European missionaries into China and attracted the attention of some far-sighted people in China, including Wang Cheng who translated some of the European books and himself wrote the first book on mechanical engineering in the Chinese language.

The author of the original paper published in Chinese in the *Chinese Journal of Mechanical Engineering* Vol. 6, No. 3, September 1958, p. 148, is Liu Hsien-Chou, an authority on mechanical engineering science in China. The material included in this comprehensive and lengthy paper had been collected by the author for more than twenty years. In this English translation, much of the non-technical information which is thought to be of less interest to Western readers has been excluded. However, it is believed that this condensed translation still keeps the essentials of the original paper.

BIOGRAPHY

Wang Cheng (portrait shown in Fig. 1), also known as Wang Liang-Fu, Wang Kuei-Hsin and Liao I Tao Jen,† was born in the city of Ching Yang in the province of Shensi on 12 May 1571. His father, Wang Ying-Hsuan (also known as Wang Fu-Pei), was a scholar of high attainment in literature and mathematics; he taught in the villages and had written two books, one in literature and one in mathematics. His mother was a sister of a high-ranking official, Chang Chien, under whose supervision Wang Cheng studied at the age of six in 1577. Influenced by his father and his uncle, Chang Chien, Wang Cheng had the boyhood ambition of devoting himself to his country and its people.

In 1594 at the age of 23, Wang obtained the qualification in literature "Chü Jen" (Translator: probably equivalent to "a degree") and after that he

* National Engineering Laboratory, East Kilbride, Glasgow.

† Translator's note: It was common for a man in the old China to have several names.

l. 2
60-61

FIG. 1. Wang Cheng.

Vol. 2
1960-61

sat the examination in the capital Peking for the qualification of "Chin Shih" (Translator: probably equivalent to "a higher degree") for nine times without success. However, during this period his interest in engineering was fully developed. He became a member of a Christian club in Peking and met Matteo Ricci (1552–1610), an Italian member of the club, and some Chinese scholars with whom he discussed Western science. Inspired by the working principle of clocks imported from the West by Matteo Ricci, etc., Wang invented the siphon, drinking-stork, "wheel-kettle", automatic plough, automatic grinder and self-propelled vehicle. Later on, describing these inventions with illustrations, he wrote a book entitled *Illustrated Machines*. The first edition was dated 1626.

In 1622 he was awarded "Chin Shih" at the age of 51. In 1623 he read a book written by Jules Aleni (1582–1649), a European, and was greatly intrigued by the unusual Western machines described therein. Soon afterwards, he was appointed as an army training officer and wrote a book on military strategy in which he referred to his uncle Chang's previous publications on this subject.

In 1626 he met, in Peking, Nicolas Longobardi (Italian, 1559–1654), Jean Terrenz (Swiss, 1576–1630) and Jean Adam Schall van Bell (German, 1591–1666), who supplied Wang with many European books related to the unusual machines as described in Jules Aleni's book. He was overjoyed and requested their assistance in translating into Chinese those books which described the machines of immediate use in the daily life of the people and the industrialization of the nation. As a result, Wang translated them from dictation given by Jean Terrenz and added appropriate illustrations. The translation, entitled *Illustrated Unusual Western Machines* and bound in three volumes, was completed and printed in 1627, together with the book *Illustrated Machines* (one volume) written by himself. Later the translation was called *Illustrated Unusual Machines*.

From 1627 to 1633, he was appointed as a Magistrate and an Army Commander both at home and abroad. During his service he often saved people's lives and property by fighting against the official corruption and extortion which gripped the whole country towards the end of the Ming Dynasty. In 1634 at the age of 63 he set up in his birthplace a charitable institution which collected periodically a small amount of money from each member to form a fund for the relief of members suffering hardship due to robbery and bereavement.

When the Ming Dynasty was overthrown in 1644, he went on hunger strike to show his loyalty to the Ming Emperor and died, aged 73, after seven days of starvation. In addition to those mentioned above he had written many books on literature, philosophy and military strategy.

THE EAGERNESS OF CHINESE SCHOLARS TO STUDY WESTERN SCIENCE THROUGH CHRISTIAN MISSIONARIES IN THE SIXTEENTH AND SEVENTEENTH CENTURIES

At the end of the sixteenth century and the beginning of the seventeenth century, some Chinese scholars, with Hsu Kuang-Chi as the leader, showed great eagerness in the study of Western science. Books on pure science (such as

astronomy and mathematics) and applied science (such as irrigation, surveying and engineering) were extensively translated into Chinese. A few of those books were translated by the Western missionaries themselves and the rest dictated by them and translated by Chinese scholars. The enthusiasm was maintained in the face of persistent opposition from some conservative Chinese scholars. However, it is regretted that Wang was the only one at that time to translate books on the science of mechanical engineering.

The Western missionaries in China at that time were all highly educated and distinguished. As there was strong anti-foreign feeling it was difficult for them to enter China and to preach religion to the Chinese people. In order to establish their position in the society, they had to make friends with Chinese officials and scholars. They also hoped to win the confidence of the Emperor. Such a difficult duty could be successfully performed only by capable scholars with high personal attainment. For instance, the Swiss preacher Jean Terrenz, as mentioned before, was elected "Fellow of the Accademia dei Lincei" in 1611, the same year as the famous Italian physicist Galileo was elected. Inventions such as levers, pulleys and screws, and their applications were all included in Wang's translation *Illustrated Unusual Machines*. These must have been imported to China by Jean Terrenz before Galileo's death.

Vol. 2
1960-61

In a Russian book *History of Thermal Power* by I. Ya Konfederatov, a drawing is shown which is exactly the same as the Wood-Sawing Illustration No. 1 of *Illustrated Unusual Machines* (see Fig. 4). It is stated in this Russian book that this was an invention made in the seventeenth century. As *Illustrated Unusual Machines* was translated in 1626, it is evident that the Western science imported to China at that time was quite modern and advanced.

ILLUSTRATED UNUSUAL MACHINES (TRANSLATED BY WANG)

The book is generally regarded as consisting of three volumes. Actually preceding the first volume there is another volume equivalent to an introduction in which it is stated that the main text consists of four volumes, on *Gravity*, *Machines*, *Force* and *Motion*. In fact, the volume dealing with force is not extant.

Volume No. 1, entitled *Gravity*, deals with weight, centre of gravity, specific gravity, etc. Volume No. 2, entitled *Machines*, describes the construction and applications of various simple machines such as weighing scales, levers, pulleys, wheels, inclined planes, etc. Volume No. 3 deals with the practical applications of different machines. The volume entitled *Force*, as indicated in the introduction, dealing with the utilization of man power, horse power, wind power, water power and gravitational force, can actually be regarded as being included in this volume. The book contains eleven illustrations on weight lifting, four on weight pulling, nine on water delivery, fifteen on rotating grinders, four on wood sawing, one on each of stone cutting, rotating pestles, sundials, automatic ploughs, and four on water pistols. "Flying man" is listed in the contents but not included in the text.

The machines described consist of the following mechanisms: levers, single and compound pulleys, pinions, wheel axles, capstans, cranks, connecting rods,

gear racks, "walking wheels" (driven by the gravity of a man crawling on the inside or outside of a wheel), cams, chain wheels, gears and gear systems, worms and worm wheels, ratchet gears, flywheels and pumps. The motive power used was provided by animals, human beings, human body weight and dead weights. Elastic force, inertial force, wind force and hydraulic force were also used in some cases. Three examples are shown as below:

1. *Weight-pulling illustration No.* 1 (Fig. 2)

Inside the rectangular framework A, a pinion B with six teeth is turned round by a man. The pinion is matched to a large wheel C which is fixed to a worm D. The latter is, in turn, matched to a gear E which has a common vertical shaft with a small gear G. G drives a large gear F which is on the same shaft as a pulley H. A rope I is wound round the pulley three turns. One end of the rope is fastened to the weight and the other pulled tight by another man. The weight is thus pulled towards the machine.

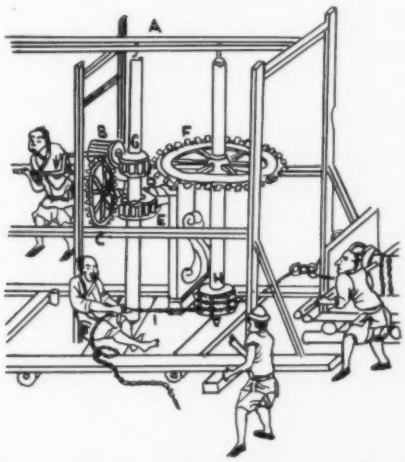

FIG. 2. Weight-pulling illustration No. 1.

2. *Weight-lifting illustration No.* 11 (Fig. 3)

Under the framework A there is a large capstan B with, on its vertical shaft, a gear C in match with a large gear D. The horizontal shaft of gear F is mounted on the top of the frame A and is driven by a small gear E fixed on the same shaft as D. A rope G, with one end fixed to the shaft of F, passes through a pulley H and is fastened to the weight I. The weight is then lifted when the capstan is driven by man power. If the pulley H is located at a lower position the machine can be used for pulling weights.

3. *Wood-sawing illustration No.* 1 (Figs. 4 and 5)

The machine is water driven. Many errors have been found in the original drawing (Fig. 4) and text. The original description of the machine has been corrected with the aid of another diagram of the same machine (Fig. 5) from Konfederatov's *History of Thermal Power* published in 1954. The corrected description is as follows.

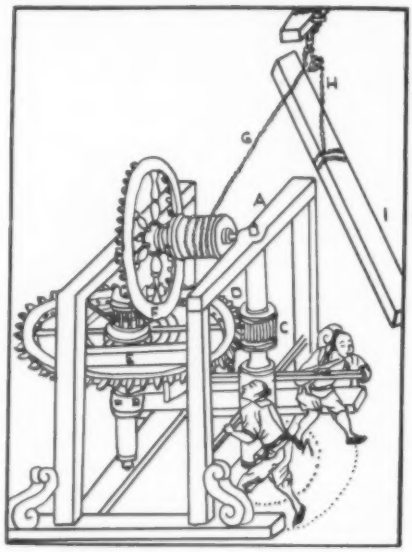

FIG. 3. Weight-lifting illustration No. 11.

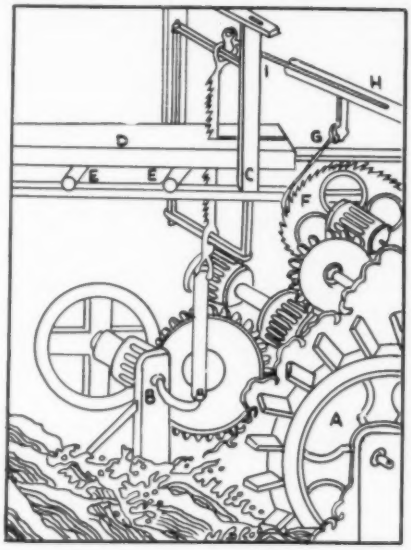

FIG. 4. Wood-sawing illustration No. 1.

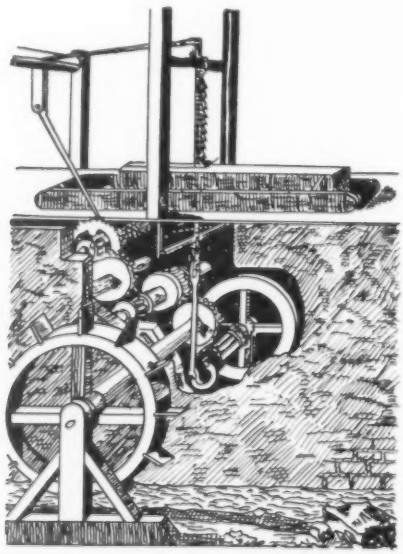

FIG. 5. Hydraulic wood-sawing machine.

As shown in these figures, the water wheel *A* drives the crank *B* which is connected to the lower end of the saw by a vertical rod. When the water wheel is set in motion, vertical movement of the crank *B* causes reciprocating motion of the saw which, together with its frame, slides along two vertical guides *C*. The machine also provides the automatic feeding of wood: The wood *D* is

Vol. 2
1960-61

mounted on a frame which has four rollers E. The uncut end of the wood is connected to the shaft of a ratchet wheel F by means of a rope (not shown in the original diagram). A long rod G with a pawl at the end to drive the ratchet is fixed to the large rotating rod H. A thin rod I connects the rod H and the top end of the saw. When the saw is driven downwards it pushes down the rod I, rotates the rod H and consequently disengages the pawl of the rod G from the ratchet wheel F. When the saw moves upwards the pawl will engage the next ratchet, thus winding up the rope and feeding the wood towards the saw teeth. To prevent the ratchet from returning freely a short rod is used (not shown in the figures).

It can be seen from the above description that the mechanism of a ratchet wheel is used to feed the wood. However, judging from the two diagrams, it should also be feasible to obtain more continuous feeding by using the existing gear system instead of the ratchet wheel.

ILLUSTRATED MACHINES (WRITTEN BY WANG)

Unlike *Illustrated Unusual Machines* (which was entirely translated from Western books) *Illustrated Machines*, bound in one volume, was, according to the preface by Wang himself, his own contribution. It consists of the following items:

1. Water delivering machines: (i) siphoning; (ii) drinking stork.
2. Rotating machines: (i) water wheel; (ii) windmill; (iii) machine driven by dead-weight using the clock mechanism.
3. Self-propelled vehicle using the clock mechanism and weight-operated.
4. "Wheel kettle."
5. Automatic plough.
6. Continuous crossbow.

Three examples are shown as below:

1. *Drinking-stork illustration* (Fig. 6)

This is a long bamboo or wooden slot, with a bucket at the head and its length depends on the water level of the stream from which water is obtained. Underneath the head there is a wooden knife, similar to the rudder of a boat, to ease the flow of water. The slot is provided with two ears in the central portion to accommodate a shaft which rests on a frame located in a piece of high ground between the stream and the rice field to be watered. The bucket will be filled with water when the tail is raised and flows out when the head is lifted. The effort required to irrigate rice fields in this way is only half of that required in the ordinary way.

2. *Automatic grinder illustration* (Fig. 7)

Four wheels A, B, C and D are mounted on a hard-wood frame with their shafts shown as small circles in the figure. The number of teeth for the four gears is 60, 48, 36 and 24 respectively, the gear D being matched to the grinder. The shafts for B, C and D all have six teeth but there is none for A. Mounted on the same shaft as A, and with a smaller diameter than A, is a counter wheel on which a rope carrying a weight is attached. The grinder is then set in motion

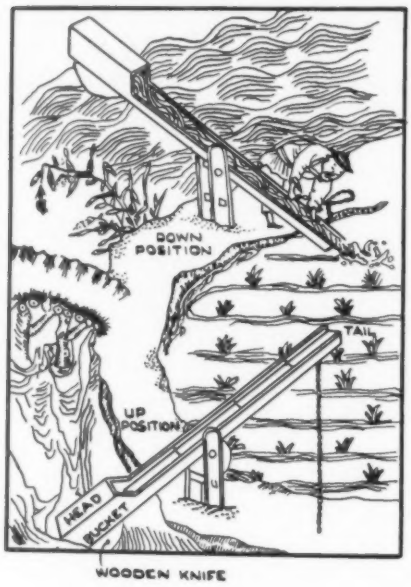

FIG. 6. Drinking stork.

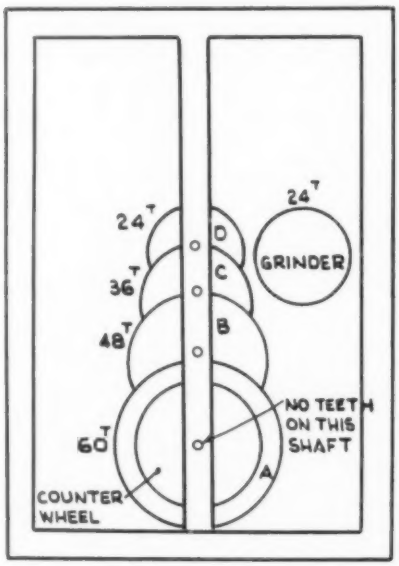

FIG. 7. Automatic grinder.

by the gravity of the weight. For rewinding the rope the counter wheel can be turned easily, even by women, without turning back the wheel A. Through one revolution of the wheel A a picul* of wheat can be ground and if the rope is long enough more than one picul can be done in one setting.

* Chinese unit of capacity.

3. *Self-propelled vehicle illustration* (Fig. 8)

The vehicle has four wheels. The two front wheels are on two separate axles which have no teeth. The two back wheels, twice as big as the front ones, are on a common axle with six teeth made of hard steel. Four gears A, B, C and D, with number of teeth 60, 48, 36 and 24 respectively, form a gear system and match the back-wheel axle. There are six teeth on all gear axles except A. Placing a weight on A to drive it will consequently move the vehicle; the heavier the weight the faster the vehicle travels. Provision is made to raise the weight when its potential energy is exhausted. When running on an uneven road extra driving force is obtained by using some "half-wheel rod" (construction unknown). It carries passengers or goods whose weight provides the driving force. A model was made and travelled 30 (Chinese) feet and a large vehicle should travel 3 (Chinese) miles.

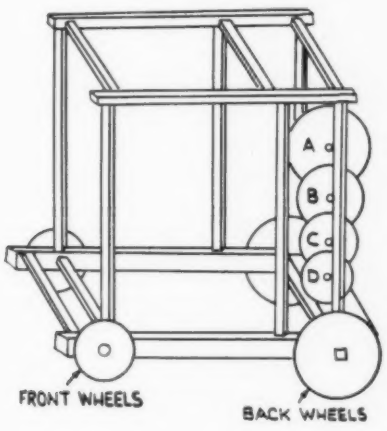

FIG. 8. Self-propelled vehicle.

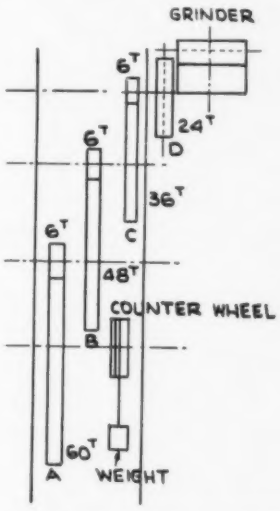

FIG. 9. Layout of gear system in automatic grinder (Fig. 7).

The above three examples are copied from the original book. A careful study of these machines throws some doubt on their practical application. For instance, according to the above description of the gear system in the automatic grinder (Fig. 7), the construction of the machine can be shown schematically as in Fig. 9. For one revolution of the wheel A or the counter wheel which carries the weight, the wheel D should rotate 480 revolutions, i.e. the speed ratio of the whole gear system is 480. Assuming the number of teeth of the grinder is the same as that of the wheel D (not clearly stated in the original book), for one revolution of the counter wheel the grinder should turn 480 revolutions. Thus the weight carried must be considerable to achieve this. Assuming the diameter of the grinder to be the same as the counter wheel (no dimensions are mentioned in the original book) and neglecting any friction, a weight of 4800 catties* is required to give a grinding force of 10 catties. This

* Chinese unit of weight.

obviously conflicts with the statement in the book that the counter wheel can easily be turned, even by women, to lift the weight.

The self-propelled vehicle as shown in Fig. 8 is also unrealistic for the same reason. Fig. 10 shows schematically its construction. Assuming that the wheel *A* is driven by the weight through a gear rack (which is necessary to transform the gravity into torque although not mentioned in the book), the back wheels will rotate 1920 revolutions for each revolution of the wheel *A*. Assuming the diameter of the back wheels to be 2 (Chinese) feet, then, for each revolution of the wheel *A*, the vehicle will travel approximately 11,520 ft, i.e. 6·4 (Chinese) miles. The same two problems exist here as in the case of the automatic grinder: (1) The weight must be very heavy to move the vehicle at all and (2) the difficulty of raising the weight again after travelling a certain distance. These problems need further investigation.

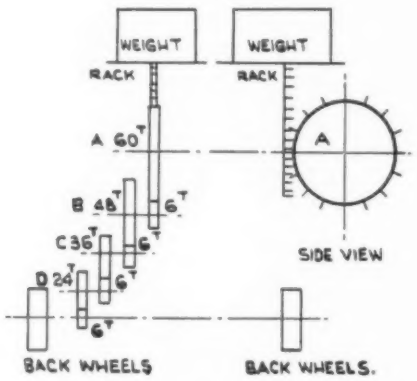

FIG. 10. Layout of gear system in self-propelled vehicle (Fig. 8).

CONCLUSIONS

From the foregoing biography of Wang Cheng and a careful study of his books, the following observations are made:

(1) During the past one or two thousand years most of the intellectuals in China much preferred literature to craft. Anything related to science and technology was classified as a craft and regarded as a low-grade profession not worth pursuing by intellectuals. This prejudice severely affected economic progress in the old China. Only very few people of progressive mind and remarkable patience could rid themselves of this prejudice. From Wang's biography it can be seen that he led a simple life, he was of practical mind and devoted himself to his country and its people. He respected craft as well as literature. In the preface of the book *Illustrated Unusual Machines* he wrote that any knowledge, whether of a high or low profession, should be pursued should it prove to be useful, and that although what had been described in this book was purely technological it was urgently needed in daily practice and in the nation's economic development.

(2) Confusing layout of Wang's books and many printing errors have been found. Firstly, the number of the volume is incorrect in several cases; secondly, some indicating symbols used in the illustrations are inconsistent with the text and, thirdly, the text does not always follow the list of contents. One example of this is that the "flying-man illustration" as listed in the contents does not appear in the text. This book was translated by Wang after Leonardo da Vinci's time and it is possible that books imported from the West at that time already contained the description of the "flying man". It might have been deleted from Wang's book because the discovery was too surprising or because it had no practical value in everyday life. The fact that it still appears in the list of contents shows carelessness in the proof checking.

(3) Some of Wang's inventions as described in his book *Unusual Machines* are based on the working principle of clocks imported from the West, such as the "automatic grinder" and the "self-propelled vehicle", while some others are basically Chinese ancient machines but slightly improved, such as the "continuous crossbow". A careful study of his design on the "automatic grinder" and "self-propelled vehicle" shows that the application of these machines is open to some doubt. The motive force in both cases is the gravity of dead weights and the energy required to drive the machines is much greater than that required for moving two or three hands of a clock. Too light a weight would fail to drive the machine while too heavy a weight would introduce the difficulty of re-lifting the weights after running for a certain period of time. The energy required for this will certainly be greater than what has been gained. Therefore, whilst the construction of the machines is sound, they are not practical.

As an old scholar in China more than 330 years ago, Wang Cheng realized the importance of machines to the people's daily life and the nation's economic development, methodically and systematically translated books most suitable for people to use, wrote the first book on mechanical engineering in China, and continued profound and extensive research until late in life. For this he is certainly admired and respected.

Int. J. Mech. Sci. Pergamon Press Ltd. 1960. Vol. 2, pp. 40–47. Printed in Great Britain

RESOLUTION OF PLASTIC STRAINS INTO COMPONENTS OF SYMMETRICALLY ISOTROPIC BEHAVIOR

G. A. Zizicas
Department of Engineering, University of California, Los Angeles

(*Received* 4 *December* 1959)

Summary—The octahedral shear is resolved into deviatoric components of uniaxial tension and pure shear for which the equality between Lode's variables for stress and strain is insured by symmetry. Then, by superposition, an analysis is developed which correlates the experimental discrepancy between diagrams of octahedral shearing stress versus octahedral shearing strain for tension and torsion with the values of Lode's variables for stress and strain under various loadings.

Vol. 2
1960-61

INTRODUCTION

In most analyses of plasticity it is assumed that the Mohr circle pattern (*not* including the relative location of the origin of stress and strain) of plastic strains e_{ij} or the increments of plastic strains Δe_{ij} and of total stresses s_{ij} are similar. Concisely, this interrelation is expressed by the equality $\nu_\gamma = \nu_\tau$ between the so-called variables of Lode

$$\nu_\tau = \frac{s_1 + s_3 - 2s_2}{s_1 - s_3} \tag{1}$$

$$\nu_\gamma = \frac{e_1 + e_3 - 2e_2}{e_1 - e_3} \quad \text{or} \quad \nu_\gamma = \frac{\Delta e_1 + \Delta e_3 - 2\Delta e_2}{\Delta e_1 - \Delta e_3} \tag{2}$$

which may also be named, respectively, *index of shearing-stress distribution and index of shearing-strain distribution*. Here $s_1 \geqslant s_2 \geqslant s_3$ are the principal stresses, $e_1 \geqslant e_2 \geqslant e_3$ the principal strains and $\Delta e_1 \geqslant \Delta e_2 \geqslant \Delta e_3$ the principal strain increments. Principal strains are used in the so-called total or deformation theories, while strain increments form the basis of the procedures designated as incremental or flow theories. In this paper the sign for the definition of ν_τ and ν_γ is taken opposite to the assumption of Lode[1] to give $\nu_\tau = +1$ for uniaxial tension and $\nu_\tau = -1$ for uniaxial compression in agreement with the usual sign convention for tension and compression in engineering applications.

For materials with macroscopically isotropic behavior, Taylor[2, 3] has pointed out that the equality $\nu_\gamma = \nu_\tau$ is imposed by considerations of symmetry when $\nu_\tau = \pm 1$ and $\nu_\tau = 0$. For other values of ν_τ, however, this equality need not be satisfied. As a matter of fact, experiments of Lode[1] and particularly of Taylor and Quinney[2] have shown a marked and consistent deviation from the relation $\nu_\gamma = \nu_\tau$. Furthermore, one of the implications of such a deviation is that the diagrams of octahedral stress versus octahedral strain for loading

under tension and shear may not coincide. Evidence of such discrepancy has actually been reported in experiments of Taylor and Quinney[2], Osgood[4], Gleyzal[5], Marin[6], Sato[7] and others. Thus, there is available considerable experimental evidence to justify an interest in incorporating departures from the equality $\nu_\gamma = \nu_\tau$ into the analytical theory.

The incremental theory of plasticity with a loading function depending on both stress invariants J_2 *and* J_3 does allow for $\nu_\gamma \neq \nu_\tau$ although the resulting expressions are rather complicated. Stockton and Drucker[8] have actually analyzed on such a basis the results of Taylor and Quinney[2]. As an alternative to the procedure of the incremental theory, it occurred to the author that an arbitrary increment of a stress distribution can always be resolved into hydrostatic stress, uniaxial tension (or compression) and pure shear, and the possibility of superimposing the associated strain increments, at least for sufficiently small stress increments, was worth investigating. Now, hydrostatic stress certainly implies $\nu_\gamma = \nu_\tau$ for isotropic materials and any inequalities between ν_γ and ν_τ must come from the components of the resolved octahedral shear in the directions of tension (or compression) and pure shear. Furthermore, the addition of hydrostatic tension or compression in isotropic materials does *not* affect the relation between ν_γ and ν_τ which may be investigated without considering the effect of hydrostatic stress. By a comparison of the diagrams of octahedral shearing stress versus octahedral shearing strain for simple tension (or compression) and pure shear—which differ when $\nu_\gamma \neq \nu_\tau$—a rather simple and clear correlation with the diagram of ν_γ versus ν_τ is obtained. The results appear in good agreement at least with the presently available experimental data.

To the engineer who is familiar with analyses based on the principle of superposition and who may not be versed in the general theory leading to the formulation of the incremental stress–strain relations, the procedure proposed in the paper may be found visual and attractive.

The paper is restricted to proportional or radial loading for which all the stress components increase simultaneously by the same factor at each instant during loading. It is well known that, under these conditions, the existing analytical theories have been found in good agreement with available experimental data, while unfortunately for variable stress ratios serious discrepancies between theory and experiment have been reported. Since the main purpose of the paper is to establish the basic idea of the proposed procedure, no attempt to apply it to variable stress ratios is made at this time. Nevertheless the analysis of the paper should also be applicable to cases that exhibit only limited deviations from proportional loading; it is well known that under such restrictions the incremental and total theories of plasticity are generally in good agreement between themselves and with experiments.

SHEARING-STRESS RESOLUTION ON OCTAHEDRAL PLANES

If the hydrostatic stress has no effect on the relation between ν_γ and ν_τ, the only significant stress in each surface of an infinitesimal element bounded by the eight octahedral planes is the octahedral shearing stress τ. It forms angles, ω_τ with the projection of the middle principal stress s_2 and ψ_τ with the direction

perpendicular to s_2, which are related to the variable of Lode (or index of shearing-stress distribution) ν_τ by the equality

$$\tan \psi_\tau = \cot \omega_\tau = \pm \nu_\tau \frac{\sqrt{3}}{3} \tag{3}$$

where ν_τ is defined by equation (1). Since $-1 \leqslant \nu_\tau \leqslant +1$, the value of ψ_τ within a multiple of π is

$$-\frac{\pi}{6} \leqslant \psi_\tau \leqslant \frac{\pi}{6} \tag{4}$$

and the vector τ is always located within the shaded area of the octahedral plane or the region symmetrical to it about the centroid of the triangular surface element, Fig. 1. The value $\psi_\tau = 0$, namely $\nu_\tau = 0$, corresponds to pure

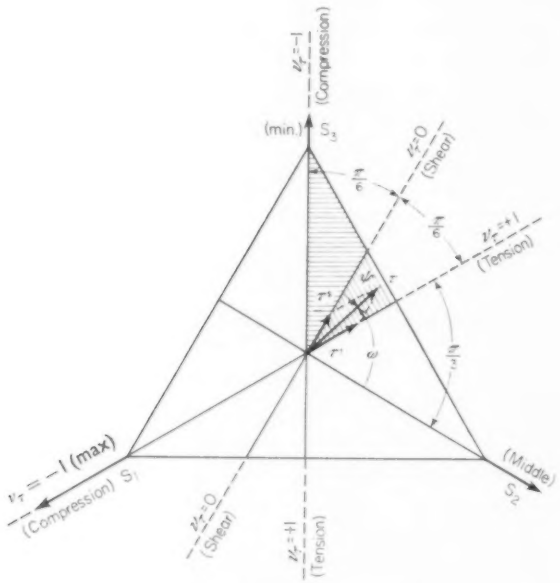

FIG. 1. Shear resolution on octahedral planes.

shear and $\nu_\tau = \pm 1$, or $\psi_\tau = \pm \pi/6$, implies uniaxial tension or compression as indicated on Fig. 1; in either case an undetermined amount of hydrostatic stress may also be present. The relation of the direction of τ to the value ν_τ was apparently first established by Geiringer and Prager[9] and has also been discussed by Sokolovskii[10], Hill[11], Westergaard[12] and Zizicas[13].

Now let the components of an arbitrary τ in the direction $\nu_\tau = 0$ (pure shear) and $\nu_\tau = 1$ (uniaxial tension) or $\nu_\tau = -1$ (uniaxial compression) be τ^s and τ^l and τ^c respectively. They are related to τ and ψ_τ by the sine relations of the triangle of stresses τ^s, τ^l and τ, which are, according to Fig. 1,

$$\frac{\tau^s}{\sin(\pi/6 - \psi_\tau)} = \frac{\tau^l}{\sin \psi_\tau} = \frac{\tau}{\sin 5\pi/6} \tag{5}$$

When τ possesses a compressive instead of a tensile component, τ^t may be designated by τ^c; otherwise there is no change in relations (5). From equations (5) it follows that

$$\tau^s = \tau(\cos\psi_\tau - \sqrt{3}\sin\psi_\tau) \tag{6}$$

$$\tau^t = 2\tau\sin\psi_\tau \tag{7}$$

These relations are also true for infinitesimal increments $\Delta\tau^s$, $\Delta\tau^t$ and $\Delta\tau$, in which case they become

$$\Delta\tau^s = \Delta\tau(\cos\psi_\tau - \sqrt{3}\sin\psi_\tau) \tag{8}$$

$$\Delta\tau^t = 2\Delta\tau\sin\psi_\tau \tag{9}$$

Vol. 2
960-61

SHEARING-STRAIN RESOLUTION ON OCTAHEDRAL PLANES

The mathematical analogy between distributions of stresses and small strains allows one to write immediately

$$\gamma^s = \gamma(\cos\psi_\gamma - \sqrt{3}\sin\psi_\gamma) \tag{10}$$

$$\gamma^t = 2\gamma\sin\psi_\gamma \tag{11}$$

or

$$\Delta\gamma^s = \Delta\gamma(\cos\psi_\gamma - \sqrt{3}\sin\psi_\gamma) \tag{12}$$

$$\Delta\gamma^t = 2\Delta\gamma\sin\psi_\gamma \tag{13}$$

Here γ is the octahedral shearing strain and γ^s and γ^t, respectively, its components along $\nu_\gamma = 0$ (pure shearing strain) and along $\nu_\gamma = +1$ (uniaxial extension); $\Delta\gamma^s, \Delta\gamma^t$ and $\Delta\gamma$ refer to increments and in such a case ψ_γ is also associated with these increments. When γ possesses a component along $\nu_\gamma = -1$ (uniaxial compression) it suffices to designate γ^t or $\Delta\gamma^t$ by γ^c or $\Delta\gamma^c$ correspondingly. The angle ψ_γ is measured from the direction $\nu_\gamma = 0$ which is perpendicular to the projection of the middle strain e_2 or middle strain increment Δe_2 on the octahedral plane. Moreover, Lode's variable (or index of shearing strain distribution) ν_γ is related to ψ_γ by the analogue of equation (3) which is

$$\tan\psi_\gamma = \cot\omega_\gamma = \pm\nu_\gamma\frac{\sqrt{3}}{3} \tag{14}$$

The definition of ν_γ was already given in equation (2). Except when $\nu_\gamma = \nu_\tau$, the angles ψ_γ and ψ_τ need not be equal.

STRESS–STRAIN RELATIONS FOR SHEAR AND TENSION

Available experimental data for pure shear (torsion) and uniaxial tension may be plotted in Cartesian co-ordinates of octahedral stress τ versus octahedral strain γ. Neglecting any effect that the elastic deformation may have on permanent distortion, one may choose for γ the plastic components of strain

only. The resulting curves, Fig. 2, need not coincide in general. On the basis of the secant moduli at the appropriate level of strain hardening, these curves allow for a relation between octahedral stress and octahedral strain as follows

$$\tau^s = E^s_{\text{sec}}\,\gamma^s, \quad \tau^t = E^t_{\text{sec}}\,\gamma^t \tag{15}$$

For increments and in terms of the tangent moduli one has

$$\Delta\tau^s = E^s_{\text{tan}}\,\Delta\gamma^s, \quad \Delta\tau^t = E^t_{\text{tan}}\,\Delta\gamma^t \tag{16}$$

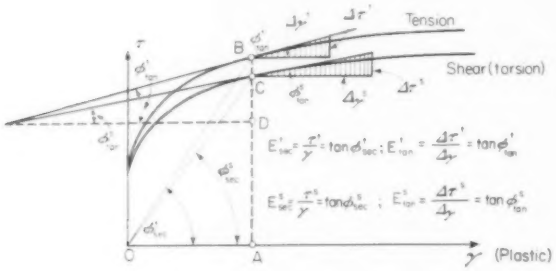

FIG. 2. Secant and tangent moduli for tension and shear.

Geometrically, Fig. 2 shows that for shear and tension respectively

$$E^s_{\text{sec}} = \tan\phi^s_{\text{sec}}, \quad E^t_{\text{sec}} = \tan\phi^t_{\text{sec}} \tag{17}$$

$$E^s_{\text{tan}} = \tan\phi^s_{\text{tan}}, \quad E^t_{\text{tan}} = \tan\phi^t_{\text{tan}} \tag{18}$$

and the ratios

$$\eta_{\text{sec}} = \frac{E^t_{\text{sec}}}{E^s_{\text{sec}}}, \quad \eta_{\text{tan}} = \frac{E^t_{\text{tan}}}{E^s_{\text{tan}}} \tag{19}$$

may be evaluated readily. Thus, from Fig. 2, η_{sec} is equal to the ratio of the segments AB/AC. Similarly η_{tan} is given by the ratio of the segments BD and CD, specified with the help of the point D located on the line parallel to the γ-axis through the point of intersection of the two tangents to the tension and shear curves. The points A, C, B and D correspond to the specified amount of octahedral strain $OA = \gamma$. Then equations (15) and (16) give

$$\frac{\gamma^s}{\gamma^t} = \frac{\tau^s}{\tau^t}\,\eta_{\text{sec}}, \quad \frac{\Delta\gamma^s}{\Delta\gamma^t} = \frac{\Delta\tau^s}{\Delta\tau^t}\,\eta_{\text{tan}} \tag{20}$$

RELATION BETWEEN LODE'S VARIABLES

It is now a simple matter to establish a relation between ν_γ, ν_τ and η by substituting in equation (20) the values of $\tau^s, \tau^t, \gamma^s, \gamma^t$ or $\Delta\tau^s, \Delta\tau^t, \Delta\gamma^s, \Delta\gamma^t$ given in equations (6), (7), (10) and (11), or (8), (9), (12) and (13). The result is

$$\frac{\cos\psi_\gamma - \sqrt{3}\sin\psi_\gamma}{2\sin\psi_\gamma} = \frac{\cos\psi_\tau - \sqrt{3}\sin\psi_\tau}{2\sin\psi_\tau}\,\eta \tag{21}$$

Vol. 2
1960-6

where η is obtained by the one of equations (19) applicable in the case under investigation. If the numerator and denominator of each fraction in equation (21) is divided by the proper cosine and equations (3) and (14) are taken into account, the relation

$$\frac{1-\nu_\gamma}{\nu_\gamma} = \frac{1-\nu_\tau}{\nu_\tau}\eta \tag{22}$$

follows; it has been obtained on the assumption that a tensile rather than a compressive component of τ is present and therefore holds for $\nu_\tau > 0$. Solving for ν_γ yields

$$\nu_\gamma = \frac{\nu_\tau}{(1-\nu_\tau)\eta + \nu_\tau}, \quad 0 \leqslant \nu_\tau \leqslant 1 \tag{23}$$

It is readily found that when compressive components are present, the corresponding relation is

$$\nu_\gamma = \frac{\nu_\tau}{(1+\nu_\tau)\eta + \nu_\tau}, \quad -1 \leqslant \nu_\tau \leqslant 0 \tag{24}$$

At $\nu_\tau = 0$, the derivative of equation (23) from the right is equal to the derivative of equation (24) from the left so that the two equations (23) and (24) define a continuous smooth curve for the entire range $-1 \leqslant \nu_\tau \leqslant +1$. Moreover these equations show that

$$\nu_\gamma(-\nu_\tau) = -\nu_\gamma(\nu_\tau) \tag{25}$$

indicating a symmetry of the curve ν_γ versus ν_τ about the origin $\nu_\gamma = \nu_\tau = 0$. Curves representing equations (23) and (24) are given in Fig. 3.

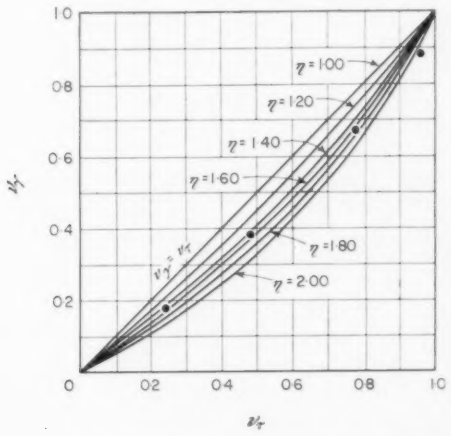

FIG. 3. Curves of ν_γ versus ν_τ for various η.
(●—experimental data of Taylor and Quinney for copper.)

COMPARISON WITH EXPERIMENTAL DATA

Data of Taylor and Quinney[2] for copper have been inserted in Fig. 3. They suggest a value of $\eta = 1{\cdot}60$. In Fig. 4 are reproduced curves of τ versus γ for uniaxial tension and torsion (shear) for the same material reported by the

same investigators; these curves contain a constant scale factor for stresses and strains which, nevertheless, does not affect the value of η. The strain-hardening level at which the data of ν_γ versus ν_τ appearing in Fig. 3 were obtained is roughly 30,000 lb/in^2 in tension. At this level, Fig. 4 gives for increments of stress and strain $\eta = BD/CD = 1{\cdot}65$. This compares favorably with value $\eta = 1{\cdot}60$ obtained from Fig. 3 for the same material. It must be remarked that Taylor and Quinney[2] used the work done rather than the octahedral shearing strain as a measure of strain hardening. This, however, should not affect significantly the foregoing comparison. If anything, it can only raise a question as to the location of the point on the strain axis at which η is to be evaluated.

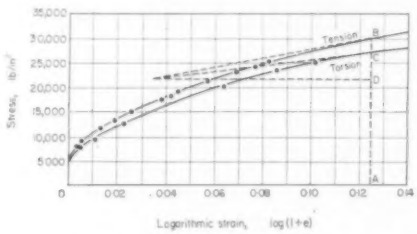

Fig. 4. Experimental data of Taylor and Quinney[2].

There are several other experimental results indicating a discrepancy between the diagrams of τ versus γ for tension and torsion. The results of Osgood[4], Gleyzal[5], Marin[6] and Sato[7] were already mentioned. Unfortunately, the published data in these cases do not include information about the relation between ν_γ and ν_τ to allow a further check of the present theory. Also, Lode's[1] data indicated the same deviations from $\nu_\gamma = \nu_\tau$ that were found subsequently by Taylor and Quinney[2].

CONCLUDING REMARKS

The analysis of the paper suggests that the experimental curves for tension and torsion (shear) may be considered macroscopically as giving information independent of one another even for isotropic materials. Such a conclusion is not any more unexpected than the fact that two independent moduli characterize the behavior of elastic materials (multi-constant theory).

It also becomes clear that an evaluation of the τ versus γ curves for tension and shear in conjunction with data of the associated relation between ν_γ and ν_τ may be desirable. Such information was obtained by Taylor and Quinney[2]. Were it to be made available for the data in Refs. 4–7 it could shed additional light on to the difficult problem of stress–strain relations in the plastic range.

REFERENCES

1. W. Lode, *Z. Phys.* **36**, 913 (1926).
2. G. I. Taylor and H. Quinney, *Phil. Trans.* A **230**, 323 (1931).
3. G. I. Taylor, *Proc. Roy. Soc.* A **191**, 441 (1947).
4. W. R. Osgood, *J. Appl. Mech.* **14**, 147 (1947).
5. A. N. Gleyzal, *J. Appl. Mech.* **15**, 288 (1948).

Vol. 2
1960-6

6. J. Marin, *J. Franklin Inst.* **248**, 231 (1949).
7. Y. Sato, *Bull. Jap. Soc. Mech. Engrs.* **2**, 107 (1959).
8. F. D. Stockton and D. C. Drucker, *J. Colloid Sci.* **5**, 239 (1950).
9. H. Geiringer and W. Prager, *Ergebn. exakt. Naturw.* **13**, 310 (1934).
10. V. V. Sokolovskii, *Izv. Akad. Nauk SSSR* **61**, 223 (1948).
11. R. Hill, *The Mathematical Theory of Plasticity* p. 18. Oxford University Press (1950).
12. H. M. Westergaard, *Theory of Elasticity and Plasticity* p. 73. Wiley, New York (1952).
13. G. A. Zizicas, *J. Appl. Mech.* **24**, 478 (1957).

Vol. 2
960-61

Int. J. Mech. Sci. Pergamon Press Ltd. 1960. Vol. 2, pp. 48–75. Printed in Great Britain

REVIEW

LOSSES AND EFFICIENCIES IN AXIAL-FLOW TURBINES

J. H. Horlock
Department of Mechanical Engineering, University of Liverpool

(*Received* 16 *October* 1959)

Summary—Calculations of efficiencies of axial-flow steam turbines have been based for many years upon experimentally determined velocity coefficients. A great amount of uncorrelated data is available. Efficiency calculations for axial-flow gas turbines have been based on loss coefficients obtained from two-dimensional cascade tests, and some correlation of this data has been attempted, notably by Ainley and Mathieson[1]. The present paper attempts to bring together the two sets of data and the differing nomenclature and approaches of the steam-turbine designer and the gas-turbine designer. Areas are indicated where further research would be useful.

Vol. 2
1960-61

1.0 NOTATION

P	force
ρ	density
A	area
c	velocity
c_x	axial velocity
c_θ	tangential velocity
w	relative velocity
w_θ	relative tangential velocity
η	efficiency
η_n	nozzle efficiency
m	mass flow rate
ϕ	velocity coefficient (stators)
ψ	velocity coefficient (rotors)
p	pressure
p_0	stagnation pressure
h	enthalpy
h_0	stagnation enthalpy
U	blade speed
ξ	"enthalpy-loss" coefficient
Y	loss coefficient based on stagnation-pressure loss
s	entropy
C_L	lift coefficient
C_{L_a}	tangential-force coefficient
C_D	drag coefficient
α	air angle (absolute)

β air angle (relative)
α' blade angle (absolute)
β' blade angle (relative)
T temperature
R reaction
v_{is} blade-speed ratio (based on isentropic velocity)
v blade-speed ratio (based on nozzle velocity)
π blade-loading coefficient
ΔW work output
μ viscosity
a velocity of sound
S blade spacing
L blade chord
o blade throat
b blade axial-chord
H blade height
t blade thickness
δ blade clearance
δ_1 boundary-layer thickness at entry
A.R. $= H/b$ aspect ratio
Re Reynolds number
γ specific-heat ratio
$\bar{R}$ gas constant
M Mach number
D_h hydraulic mean diameter
ϵ deflexion

Subscripts and superscripts

1 upstream of nozzle
2 between nozzle and rotor
3 downstream of rotor
TS total-to-static
TT total-to-total
p profile
s secondary
c clearance
m mean
$'$,$''$ referring to loss-coefficient correlation
$*$ "nominal"
is isentropic
e trailing edge

2.0 INTRODUCTION

Much of the early information on flows in steam-turbine nozzles and blades has been brought together in the works of Stodola[2] and Kearton[3]. In these books the values of leaving-angles and losses are presented for a wide variety

of impulse stators (both nozzles and blades) and impulse rotors (or buckets), and for Parsons (50 per cent) reaction blading.

In the gas turbine the sharp distinction between impulse and reaction (50 per cent) disappears, for the reaction varies along the blade, which is usually twisted from root to tip. The reaction may approach zero (impulse) at the root and exceed 50 per cent at the tip. Gas-turbine designers have used tests of blade aerofoils in cascades to provide data on leaving-angles and losses.

Experimental data on losses obtained from static tests on steam nozzles have usually been presented in the form of a velocity coefficient, the ratio of the "observed" velocity to the so-called "isentropic steam velocity"—the velocity obtained in a hypothetical isentropic expansion to the exhaust back pressure. The "observed" velocity is usually based on a force measurement (the impulsive force of the jet on a plate, or the reactive force on the nozzle row) and a flow measurement. The force is

$$P = \int \rho c^2 \, dA$$

and the flow rate is

$$m = \int \rho c \, dA$$

The "observed" velocity

$$\bar{c} = \frac{P}{m} = \frac{\int \rho c^2 \, dA}{\int \rho c \, dA}$$

and is the velocity of a uniform stream having the same mass flow and the same momentum as the actual stream. The velocity coefficient is

$$\phi = \frac{\bar{c}}{c_{is}} = \frac{\int \rho c^2 \, dA}{c_{is} \int \rho c \, dA}$$

Kearton[3] and Keenan[4] have pointed out that the energy of such a uniform stream ($\frac{1}{2}\rho \bar{c}^3 A$) is not the same as the energy of the actual stream $\left(\int \frac{1}{2}\rho c^3 \, dA\right)$. The nozzle efficiency in three-dimensional flow

$$\eta_{n_3} = \frac{\int \rho c^3 \, dA}{c_{is}^2 \int \rho c \, dA}$$

is therefore not the square of the velocity coefficient in a three-dimensional flow. Kearton quotes experiments by Hodkinson and Devey[5] in which the following values of the discrepancy between $\sqrt{\eta_{n_3}}$ and ϕ were obtained:

ϕ	1	0·98	0·96	0·94
$\frac{\sqrt{(\eta_{n_3})} - \phi}{\phi}$ %	0	0·3	0·6	0·9

Vol. 2
1960-6

Oakden[6] pointed out that in a "strip theory" of the flow through a turbine stage (in which the axial velocity profile remains unaltered across the rotor) the work delivered by the stage is the same as that delivered by a stage with uniform nozzle velocity $\bar{c}$. In fact, the variation of work along the blade will alter the velocity profile considerably.

Experimental data on losses obtained from gas-turbine cascades are usually presented in the form of a mean stagnation pressure loss across the cascade. (Wirt[7] and Ackeret *et al.*[8] were among the first to test turbine blading in a wind tunnel, and the latter pointed out the limitations of using such data in steam turbines. These limitations are discussed later.) The mean stagnation pressures are based on flow averages,

$$\bar{p}_0 = \frac{\int \rho c_x p_0 \, dA}{\int \rho c_x \, dA}$$

A stagnation pressure loss, based on such averaged stagnation pressures, is the loss of a uniform stream with the same mass flow and overall losses as those observed in the experiment.

While the early steam-turbine designers recognized the existence of secondary losses and clearance losses at root and tip, the nature of the experimental data available to them (an overall force measurement, which is related to a mean velocity coefficient) meant that they were not able to split down the losses into separate components. The gas-turbine designers, and later steam-turbine designers, have had more information on which to base correlations of the separate components of the losses.

A third method of obtaining design data on losses in turbines is to assemble information on the overall efficiencies of a wide variety of turbines and to calculate back to the individual blade-row component losses. This has been attempted by Soderberg[9], and it is his correlation, as used by Stenning[10], which is used as a basis for comparison in this paper.

Differences of approach also exist in the statements and definitions of efficiency and in the relations between measured losses and the efficiency. These are due largely to the use of the concept of stagnation enthalpy and pressure by the gas-turbine designer, instead of the use of "carry-over" kinetic energy.

This paper attempts to re-define the efficiencies and relate the differing terms and concepts. Further, an attempt is made to bring together data on losses known to the author. Inevitably there will be omissions in this attempt, for much industrial data remain unpublished, and any further information which would increase the scope and usefulness of this work would be welcome.

3.0 TURBINE EFFICIENCY

Definitions and analyses of turbine efficiency are presented below, using the concepts of stagnation enthalpy, pressure and temperature. All flows are assumed to be adiabatic, and the stagnation enthalpy remains constant across

a stationary row. Across a moving row, the "absolute" stagnation enthalpy drop is equal to the shaft-work output.

3.1. *The enthalpy–entropy diagram for a turbine stage*

The stagnation enthalpy relative to the moving row remains constant across that row. This may be illustrated by reference to Fig. 1, which shows a set of velocity triangles for a turbine in which the streamlines may move radially. (The angles are measured from the axial direction, and the sign convention is such that angles and tangential velocities are taken as positive as drawn.) The work output per unit-flow rate is

$$h_{02}-h_{03}=U_2c_{\theta_2}+U_3c_{\theta_3} \tag{1}$$

where

$$\left.\begin{aligned}h_{02}&=h_2+c_2^2/2\\ h_{03}&=h_3+c_3^2/2\end{aligned}\right\} \tag{2}$$

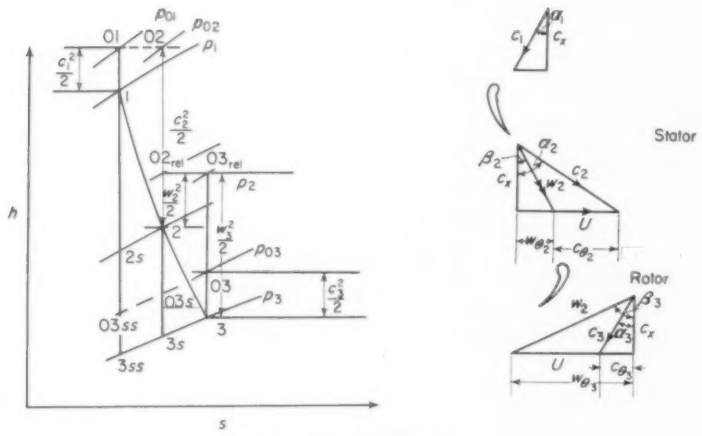

FIG. 1. Notation.

If the relative stagnation enthalpies are defined as

$$\left.\begin{aligned}h_{02_{\mathrm{rel}}}&=h_2+w_2^2/2\\ h_{03_{\mathrm{rel}}}&=h_3+w_3^2/2\end{aligned}\right\} \tag{3}$$

then

$$h_{02_{\mathrm{rel}}}-h_{03_{\mathrm{rel}}}=U_2c_{\theta_2}+U_3c_{\theta_3}+\frac{w_2^2}{2}-\frac{w_3^2}{2}-\frac{c_2^2}{2}+\frac{c_3^2}{2} \tag{4}$$

From the velocity triangles

$$\begin{aligned}w^2&=c_x^2+w_\theta^2,\\ c^2&=c_x^2+c_\theta^2,\\ w^2-c^2&=w_\theta^2-c_\theta^2,\end{aligned}$$

and

$$\begin{aligned}w_2^2-c_2^2&=(c_{\theta_2}-U_2)^2-c_{\theta_2}^2\\ &=U_2^2-2U_2c_{\theta_2},\\ w_3^2-c_3^2&=U_3^2+2U_3c_{\theta_3}\end{aligned} \tag{5}$$

Vol. 2
1960-6

and

$$h_{02_{rel}} - h_{03_{rel}} = U_2 c_{\theta_2} + U_3 c_{\theta_3} + \frac{U_2^2}{2} - U_2 c_{\theta_2} - \frac{U_3^2}{2} - U_3 c_{\theta_3} = U_2^2/2 - U_3^2/2 \qquad (6)$$

If the radial shift is small, as in an axial turbine, then $U_2 = U_3$ and $h_{02_{rel}} = h_{03_{rel}}$.

The enthalpy–entropy diagram for a stage may now be drawn and is illustrated, in Fig. 2, for the stage with velocity triangles as shown in Fig. 1. The stagnation enthalpy remains constant across the nozzle or stationary row ($h_{01} = h_{02}$), although the stagnation-pressure may drop. The stagnation-enthalpy relative to the moving row remains constant, although the relative stagnation-pressure (the pressure that would be obtained after complete isentropic diffusion of the relative velocity) will drop.

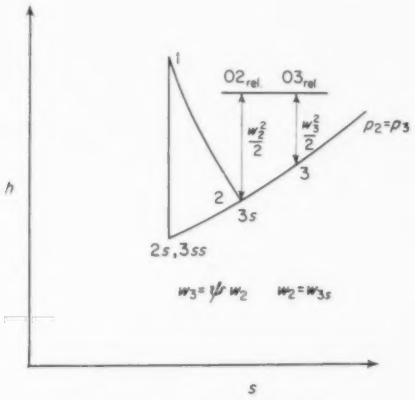

FIG. 2. h–s diagram (impulse).

3.2. *Irreversibility and losses*

The irreversibilities in the flow through stators and rotors may be expressed in a number of ways:

(1) The velocity coefficients (ϕ, ψ for stator and rotor respectively) which are defined as the ratio of the actual velocity to the velocity that would be obtained in isentropic flow to the same back-pressure

$$\phi = \frac{c_2}{c_{2s}} = \sqrt{\left(\frac{h_{01} - h_2}{h_{01} - h_{2s}}\right)}, \quad \psi = \frac{w_3}{w_{3s}} = \sqrt{\left(\frac{h_{02_{rel}} - h_3}{h_{02_{rel}} - h_{3s}}\right)} \qquad (7)$$

(2) The nozzle efficiency (η_n) which may be defined in three ways (Kearton[3]):

$$\text{(i)}\ \eta_{n_1} = \frac{\text{The gain in kinetic energy}}{\text{The gain in kinetic energy in isentropic expansion to the same back pressure}} = \frac{h_1 - h_2}{h_1 - h_{2s}} \qquad (8)$$

$$\text{(ii)}\ \eta_{n_2} = \frac{\text{Final kinetic energy}}{\text{Maximum kinetic energy obtained in an isentropic expansion to the same back pressure}} = \frac{h_{01} - h_2}{h_{01} - h_{2s}} \qquad (9)$$

(iii) $\eta_{n_s} = \dfrac{\text{Final kinetic energy—"carry-over" kinetic energy}}{\text{The gain in kinetic energy obtained in an isentropic expansion to the same back pressure}}$

$$= \frac{(h_{01}-h_2)-\eta_c(h_{01}-h_1)}{(h_1-h_{2s})} \tag{10}$$

where η_c is the efficiency of conversion of the inlet kinetic energy.

(3) The "enthalpy-loss"—the difference between the static enthalpies h_2 and h_{2s}, and h_3 and h_{3s}—and the "enthalpy-loss" coefficients

$$\xi_N = \frac{h_2-h_{2s}}{\frac{1}{2}c_2^2} = \frac{h_2-h_{2s}}{h_{01}-h_2}$$

$$\xi_R = \frac{h_3-h_{3s}}{\frac{1}{2}w_3^2} = \frac{h_3-h_{3s}}{h_{02_{\text{rel}}}-h_3} \tag{11}$$

(4) The increase in entropy

$$s_2-s_1 = s_2-s_{2s}$$

$$s_3-s_2 = s_3-s_{3s}$$

(5) The stagnation losses

$$Y_p = \frac{p_{01}-p_{02}}{\frac{1}{2}\rho_2 c_2^2}, \quad \frac{p_{02_{\text{rel}}}-p_{03_{\text{rel}}}}{\frac{1}{2}\rho_3 w_3^2}$$

(6) The blade-drag coefficients

$$C_D = \frac{\text{Drag}}{\frac{1}{2}\rho_2 c_2^2} \quad \text{or} \quad \frac{\text{Drag}}{\frac{1}{2}\rho_3 w_3^2} \tag{12}$$

These various forms of expressing the irreversibility may be related as follows:

$$\eta_{n_s} = \phi^2 \tag{13}$$

$$\xi_N = \frac{c_{2s}^2-c_2^2}{c_2^2} = \frac{1}{\phi^2}-1 \tag{14}$$

$$\phi = \frac{1}{\sqrt{(1+\xi_N)}} \tag{15}$$

$$s_2-s_{2s} \simeq \frac{h_2-h_{2s}}{T_2} = \frac{\xi_N c_2^2}{2T_2} = \frac{\xi_N \gamma R M_2^2}{2} \tag{16}$$

$$\frac{p_{01}}{p_{02}} = \frac{p_{01}}{p_{2s}}\frac{p_2}{p_{02}} = \left(\frac{T_{01}}{T_{2s}}\right)^{\gamma/(\gamma-1)}\left(\frac{T_2}{T_{02}}\right)^{\gamma/(\gamma-1)} \doteqdot \frac{1}{1-\dfrac{(h_2-h_{2s})\gamma}{C_p T_2(\gamma-1)}} \tag{17}$$

$$\frac{\Delta p_0}{p_{01}} = \frac{\gamma(h_2-h_{2s})}{C_p T_2(\gamma-1)} = \frac{\xi_N M_2^2 \gamma}{2} \tag{18}$$

$$Y = \frac{\Delta p_0}{\frac{1}{2}\rho_2 c_2^2} = \xi_N\left[1+\frac{\gamma-1}{2}M_2^2\right]^{\gamma/(\gamma-1)} \tag{19}$$

$$\doteqdot \xi_N\left[1+\frac{\gamma M_2^2}{2}\right] \quad \text{for} \quad M_2<1 \tag{19a}$$

$$\doteqdot \xi_N, \text{ for incompressible flow} \tag{19b}$$

$$C_D = \frac{\Delta p_0}{\frac{1}{2}\rho c_2^2}\frac{S}{L}\frac{\cos^3\alpha_m}{\cos^2\alpha_2} \doteqdot \xi_N \frac{S}{L}\frac{\cos^3\alpha_m}{\cos^2\alpha_2}, \text{ for incompressible flow} \tag{20}$$

Vol. 2
1960-6

where

$$\alpha_m = \tan^{-1}\left(\frac{\tan\alpha_1 + \tan\alpha_2}{2}\right)$$

Here the different forms of expressing the losses in the stator row have been related by assuming the fluid to be a perfect gas. Similar relationships in terms of relative properties may be obtained for the rotor. These loss coefficients are for an imaginary, uniform, two-dimensional flow having the same flow rate and overall losses as the actual stream. The differences between η_{n_2} and ϕ^2 in a three-dimensional flow, for example, are ignored.

3.3. *Definitions of efficiency*

The definition of the stage efficiency depends on the application. In a multi-stage machine the efficiency is best defined as a "total-to-total" efficiency,

$$\eta_{TT} = \frac{\text{Actual work output}}{\text{Maximum adiabatic work output in operation to the same back pressure}} = \frac{h_{01}-h_{03}}{h_{01}-h_{03_{ss}}} \qquad (21)$$

[The difference between $h_{03_{ss}}$ (at p_{03}, s_1 as indicated on Fig. 1) and $(h_{3_{ss}} + c_{3_{ss}}^2/2)$ is usually neglected. In isentropic expansion to the pressure p_3, the density $(\rho_{3_{ss}})$ and therefore the velocity $(c_{3_{ss}})$ leaving the stage would be slightly different from ρ_3, c_3, and the stagnation-pressure would not be p_{03}.]

This efficiency may be expressed in terms of the work done and the loss coefficients for stator and rotor, ξ_N and ξ_R, (Hawthorne[11]):

$$\eta_{TT} = \left[1 + \left\{\frac{\frac{\xi_N c_2^2}{2} + \frac{T_3}{T_2}\frac{\xi_R w_3^2}{2}}{h_{01}-h_{03}}\right\}\right]^{-1} \simeq \left[1 + \left\{\frac{\xi_N c_2^2 + \xi_R w_3^2}{2(h_{01}-h_{03})}\right\}\right]^{-1} \qquad (22)$$

Further, the loss coefficients are for the complete flow process through each row. The separation of the losses into a "carry-over" loss and a blade loss is artificial, for the boundary-layer behaviour within the nozzle is strongly dependent upon the entry flow.

If the exhaust kinetic energy is not used (e.g. as in a single-stage turbine without an exhaust diffuser) then the efficiency should be defined as a total-to-static efficiency, the ratio of the actual work to the isentropic work obtained in expansion to the exhaust back-pressure at zero-leaving velocity, for this is the maximum work that could be obtained in adiabatic flow.

Thus

$$\eta_{TS} = \frac{h_{01}-h_{03}}{h_{01}-h_{3_{ss}}} = \left[1 + \left\{\frac{\frac{\xi_N c_2^2}{2} + \frac{T_3}{T_2}\xi_R\frac{w_3^2}{2} + \frac{T_3}{T_2}\frac{c_3^2}{2}}{h_{01}-h_{03}}\right\}\right]^{-1} \qquad (23)$$

These separate concepts of turbine efficiency are not new, for both Stodola[2] and Kearton[3] present efficiency curves on the two bases.

The concept of blading or diagram efficiency is useful only in the case where the exhaust kinetic energy is not used.

The diagram efficiency η_D is defined as

$$\eta_D = \frac{\text{Work output}}{\text{Kinetic energy available to the blades}} \tag{24}$$

If the second definition of nozzle efficiency is used, then the diagram efficiency may be related to the total-to-static efficiency *for an impulse-turbine stage* (a stage with zero pressure drop across the moving blades—Fig. 2)

$$\begin{aligned}\eta_{TS} &= \frac{h_{01}-h_{03}}{h_{01}-h_{3_s}} \\ &= \frac{h_{01}-h_{03}}{h_{01}-h_2} \times \frac{h_{01}-h_2}{h_{01}-h_{3_s}} \\ &= \eta_D \times \eta_{n_s}\end{aligned} \tag{25}$$

The blading efficiency for the impulse stage can be related to the basic loss coefficients described above

$$\eta_D = \frac{h_{01}-h_{03}}{h_{01}-h_2} = \left[1 + \left\{\frac{(\xi_R w_3^2)/2 + c_3^2/2}{(h_{01}-h_{03})}\right\}\right]^{-1} \tag{26}$$

4.0 REACTION

The classical definition of reaction is related to the pressure drop across moving and stationary rows. The impulse condition, in which the force on the moving blades is impulsive and results from change in tangential momentum across the blades, is then defined as one of zero reaction—there is no pressure drop across the moving blades.

The author considers that it is more useful to define reaction, which is effectively only a statement on blading geometry, as the ratio of the static *enthalpy*-drop through the moving blades to the static enthalpy-drop through the stage, i.e.

$$R = \frac{h_2-h_3}{h_1-h_3} \tag{27}$$

If the velocity leaving the stage (c_3) is the same as that entering the stage (c_1), then

$$\begin{aligned}R &= \frac{h_2-h_3}{h_{01}-h_{03}} \\ &= \frac{w_3^2-w_2^2}{2U(c_{\theta_2}+c_{\theta_3})}\end{aligned} \tag{28}$$

and if the axial velocity remains constant through the stage

$$\begin{aligned}R &= \frac{w_{\theta_3}^2-w_{\theta_2}^2}{2U(c_{\theta_2}+c_{\theta_3})} \\ &= \frac{w_{\theta_3}-w_{\theta_2}}{2U} \\ &= \frac{c_x}{2U}(\tan\beta_3-\tan\beta_2) \\ &= \tfrac{1}{2}+\frac{c_x}{2U}(\tan\beta_3-\tan\alpha_2)\end{aligned} \tag{29}$$

If $\beta_3 = \beta_2$ the reaction is zero, and if $\beta_3 = \alpha_2$ the reaction is 50 per cent.

Vol. 2
1960-6

The (h, s) diagram for a stage of zero reaction defined on this basis is shown in Fig. 3. There is a pressure drop across the moving row, and the stage is not truly impulse. The (h, s) diagram for an "impulse" stage of zero pressure-drop is shown in Fig. 2. There is an enthalpy increase across the moving row, and the stage is strictly one of negative reaction on the above definition of reaction.

It should be noted that in a reversible stage the definitions of reaction, based on pressure- and enthalpy-drop, are identical, but only by basing the definition on enthalpy-drop is it possible to relate the reaction directly to the blading angles and the flow coefficient c_x/U.

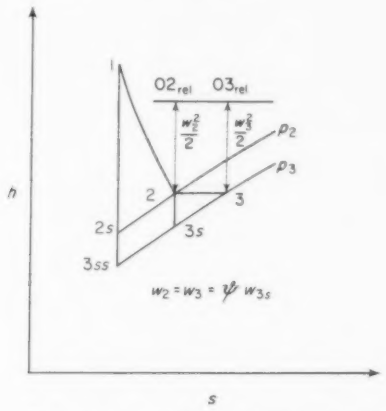

FIG. 3. h–s diagram (zero reaction).

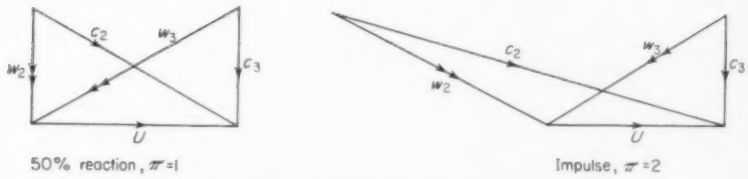

FIG. 4. Velocity triangles for maximum η_{TS}.

5.0 THE BLADE-SPEED RATIO

The blade-speed ratio is widely used by steam-turbine designers. The definition is taken as the ratio of blade speed to the velocity that would be obtained in isentropic expansion through the stage pressure-drop,

$$v_{is} = \frac{U}{c_{is}} = \frac{U}{\sqrt{(h_1 - h_{3_{ss}})}} \tag{30}$$

or sometimes as the ratio of blade speed to nozzle-leaving velocity $v = U/c_2$. These parameters are widely used in choosing the operating condition of a turbine.

The maximum total-to-static efficiency of a reversible turbine is obtained when the leaving velocity is axial. For example, Fig. 4 shows the velocity triangles for zero and 50 per cent reaction designs with axial leaving velocity.

The work done in the two cases is $2U^2$ and U^2 respectively. Assuming there is no change in kinetic energy across the stage, the static enthalpy-drops are $2U^2$ and U^2 and

$$v_{is} = \frac{U}{\sqrt{4U^2}} = \tfrac{1}{2} \text{ (impulse)}$$

$$v_{is} = \frac{U}{\sqrt{2U^2}} = \frac{1}{\sqrt{2}} \text{ (50 per cent reaction)}$$

These well-known results have been modified to give the velocity ratios for maximum total-to-static efficiency, using nozzle- and blade-velocity coefficients which are assumed to be constant (e.g. Kearton[3] pp. 180, 213). Essentially, such analyses give the optimum reaction for a given work loading on the stage, but only if the total-to-static efficiency is the criterion of performance.

A further point may be made concerning the use of the velocity ratio. Not only are the usual plots of efficiency against the velocity ratio (e.g. Keenan[12] p. 156) for total-to-static efficiency, but also they are *design*-efficiency plots. They do not represent the off-design performance of turbines designed for the conditions of maximum efficiency. For example, one of the plots of total-to-static efficiency given later in Fig. 17 is for a zero-reaction stage, and all points on the curve represent possible designs for zero reaction. But a turbine stage designed at $(v) = 0{\cdot}5$ would be required to operate at reactions other than zero off-design, and the curve does not represent its off-design performance.

In the majority of turbine applications it is the "total-to-total" efficiency which is important, and the variation of efficiency with reaction at a given stage-loading is not too critical (see Section 7).

The gas-turbine designer usually uses a blade-loading criterion

$$\pi = \frac{\Delta W}{U^2} = \frac{h_{01} - h_{03}}{U^2} \doteq \frac{h_1 - h_3}{U^2} = \eta_{TT}/2v_{is}^2 \tag{31}$$

or $\pi = 1/(2v^2)$ for an impulse stage

$= 1/v^2$ for a 50 per cent reaction stage

6.0 CORRELATION OF LOSS COEFFICIENTS

For incompressible flow through a row of blades the stagnation pressure loss might be expected to be a function of several parameters,

$\Delta p_0 = f$ (blade geometry, S, L, H, ρ, t, c_2, μ, δ, entry-boundary-layer parameters and turbulence level),

or $\dfrac{\Delta p_0}{\frac{1}{2}\rho c_2^2} = f$ (Re, blade geometry, S/L, t/L, H/L, δ/L, entry-boundary-layer parameters and turbulence level). **(32)**

Vol. 2
1960-6

In compressible flow of a perfect gas the "enthalpy loss" $(h_2 - h_{2s})$ will be a function of the same parameters plus others allowing for changes in density:

$$\Delta h_s = f \text{ (blade geometry, } S, L, H, t, \rho_2, c_2, \mu, \delta, \gamma, \bar{R}, a_2, \text{ entry-boundary-layer parameters and turbulence level),}$$

$$\text{or } \frac{\Delta h_s}{\frac{1}{2}c_2^2} = f \text{ (}Re\text{, blade geometry, } S/L, t/L, H/L, \delta/L, M_2, \gamma, \bar{M}\text{, entry-boundary-layer parameters and turbulence level).} \quad (33)$$

In early work the Reynolds number was based on the exit velocity and the hydraulic mean diameter at the throat section,

$$D_h = 2HS\cos\alpha_2/(S\cos\alpha_2 + H)$$

This implies that the flow is similar to a pipe flow, and that a Reynolds number defined in such a way might be used to correlate losses, eliminating parameters such as H/L from the correlation. In fact, the losses are boundary-layer phenomena and at least two parameters, such as $Re = \rho c_2 L/\mu$ and H/L, must be used. In this paper the Reynolds number based on the hydraulic mean diameter has been retained, but only because most data on the variation of losses with Re is presented in this way.

6.1. *Soderberg's correlation*

Soderberg[9] has correlated the losses on a basis of space-chord ratio, Reynolds number, aspect ratio, thickness ratio and blading geometry.

Soderberg uses the work of Zweifel[13] to obtain the optimum space-chord ratio for a given change of direction through a cascade. Zweifel suggests that the lift coefficient based on the tangential loading

$$C_{L_a} = (2S/b)(\tan\alpha_2 - \tan\alpha_1)\cos^2\alpha_2 \quad (34)$$

should be approximately 0·85. The optimum space-chord ratio is obtained from this equation, for given gas flow angles α_1 and α_2.

For turbine rows operating at this design tangential-lift coefficient (at a Reynolds number of 10^5 and with an aspect ratio (H/b) of 3 : 1), the "nominal" loss-coefficient is ξ^* and is related to gas deflexion $\epsilon = \alpha_1 + \alpha_2$ alone by the relation plotted in Fig. 5. For turbine rows operating at zero incidence, the basis of Soderberg's correlation, the gas deflexion is little different from the blading deflexion $(\alpha_1^1 + \alpha_2^1)$, since the deviations $(\alpha_2 - \alpha_2^1)$ are, in general, small (see sub-section 6.9).

For aspect ratios other than 3 : 1

$$\xi' = (1 + \xi^*)\left(0{\cdot}975 + 0{\cdot}075\frac{b}{H}\right) - 1 \quad (35)$$

and for Reynolds numbers other than 10^5

$$\xi'' = \left(\frac{10^5}{Re}\right)^{\frac{1}{4}}\xi' \quad (36)$$

Soderberg's correlation implies that the effect of profile shape is limited. Fig. 5 shows how the basic $\xi^* - \epsilon^*$ correlation is affected by thickness-chord ratio, but no effect of trailing-edge thickness is included. Further, it is implied that the degree of reaction (or stagger) is unimportant, so long as the optimum space-chord ratio is chosen.

A correction on the efficiency for clearance losses is included by multiplying the final calculated stage-efficiency by the ratio of "blade" area to total area, including leakage space.

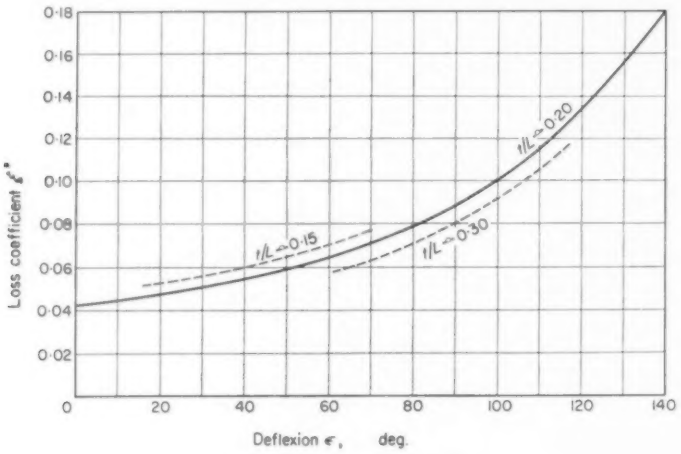

FIG. 5. Soderberg's correlation.

Soderberg's correlation is somewhat oversimplified because the effect of reaction, the Mach number and the non-dimensional parameters of the fluid (specific-heat ratio and molecular weight) have been neglected. Further, the aspect ratio alone cannot be expected to be the only important parameter in the secondary loss-correction, for the entry-boundary layer and the blade geometry must be vital parameters.

However, it is understood that the correlation gives turbine efficiencies to within 3 per cent over a wide range of Reynolds number and aspect ratio, and the method followed here is to compare it with other data.

Hawthorne[11] refers briefly to a correlation similar to Soderberg's. Apparently an analytical simplification of Soderberg's work, the correlation may be written

$$\xi_p = 0{\cdot}025\left[1 + \left(\frac{\epsilon}{90}\right)^2\right] \tag{37}$$

$$\xi = \xi_p\left[1 + 3{\cdot}2\,\frac{b}{H}\right] \tag{38}$$

This implies that the secondary loss $(\xi - \xi_p)$ is equal to the profile loss (ξ_p) at an aspect ratio of 3·2, for all reactions and deflexions. The analytical expression fits Soderberg's curve well at low deflexion but is inaccurate for high-deflexion impulse-blading.

Vol. 2
960-61

6.2. *Ainley's correlation*

Ainley and Mathieson[1] first correlate the profile drag. Figs. 6 and 7 show the profile drag for nozzles and impulse-blading at various values of the outlet angle and various space-chord ratios. For blading of the same space-chord ratio but between impulse and reaction the profile loss is given by

$$Y_{p(i=0)} = Y_{p(\alpha_1=0)} + (\alpha_1/\alpha_2)^2 \left(Y_{p(\alpha_1=\alpha_2)} - Y_{p(\alpha_1=0)}\right) \left(\frac{t/L}{0{\cdot}2}\right)^{\alpha_1/\alpha_2} \tag{39}$$

where the correlation for thickness-chord ratios away from $t/L = 0{\cdot}2$ is also included.

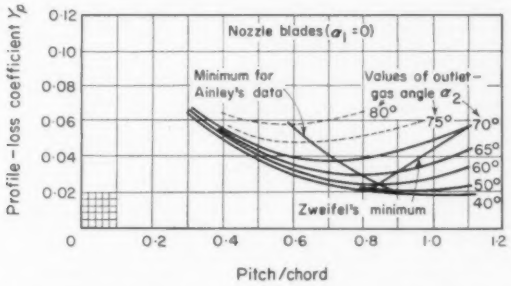

FIG. 6. Profile loss for conventional section-blades at zero incidence ($t/L = 20$ per cent; $Re = 2 \times 10^5$; $M < 0{\cdot}6$) (Ainley and Mathieson).

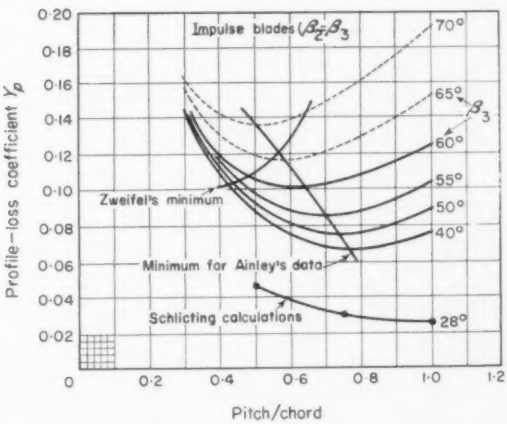

FIG. 7. Profile loss for conventional section-blades at zero incidence ($t/L = 20$ per cent; $Re = 2 \times 10^5$; $M < 0{\cdot}6$) (Ainley and Mathieson).

Ainley correlates secondary and clearance losses ($Y_s + Y_c$) on the basis of lift coefficient,

$$Y_s + Y_c = \left(\lambda + B\frac{\delta}{H}\right)[C_L/(S/L)]^2 \frac{\cos^2 \alpha_2}{\cos^3 \alpha_m} \tag{40}$$

where (i) λ is a function of

$$\frac{(A_2/A_1)^2}{1 + (\text{inner dia.}/\text{outer dia.})}$$

(Fig. 8), A_1 and A_2 being the areas normal to the entering and leaving flow, and (ii) B is 0·5 for a radial clearance and 0·25 for a shroud clearance.

Ainley's data are for a mean Reynolds number (based on blade chord) of 2×10^5. He suggests that the stage losses $(1-\eta_{TT})$ vary as $Re^{-1/5}$ down to Reynolds numbers of 5×10^4.

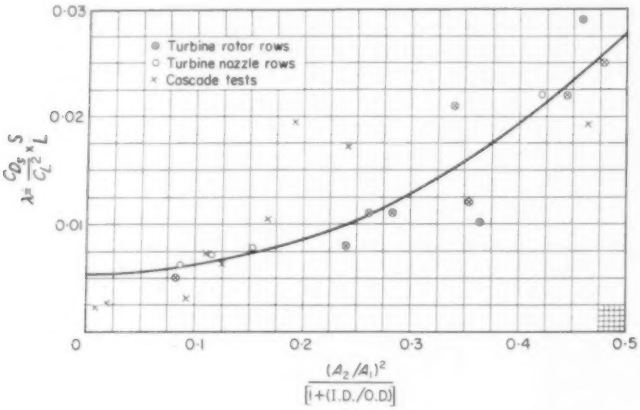

FIG. 8. Secondary losses in turbine blade-rows (Ainley and Mathieson).

6.3. *Comparison of the data of Ainley and Soderberg*

A first comparison is made between the data of Ainley and Soderberg's correlation. This is shown in Fig. 9, in which Soderberg's loss coefficients for $Re = 10^5$ and an aspect ratio of 3 : 1 are shown compared with the minimum profile losses picked off Figs. 6 and 7.

On Figs. 6 and 7 are shown the calculated space-chord ratios for minimum loss as estimated from Zweifel's[13] formula for the tangential-lift coefficient. The profile losses given by Ainley for these space-chord ratios are also plotted in Fig. 9.

Also shown is the Soderberg loss-correlation corrected for infinite aspect ratio, and to a Reynolds number of 2×10^5. It should be noted that Ainley's data are for a mean Reynolds number of 2×10^5, based on the blade chord. At large aspect ratios the hydraulic mean diameter becomes

$$2S \cos \alpha_2 = [2(S/L) \cos \alpha_2] L$$

The factor $2(S/L) \cos \alpha_2$ varies from approximately 0·2 to 1·4 for the minima of Ainley's data.

It is clear that the Zweifel[13] relation for the optimum space-chord ratio is at variance with Ainley's cascade data, although the trends of increased loss with deflexion are similar. The minimum losses for impulse and nozzle blades of the same deflexion (80°) are of the same order, but it would be unwise to conclude from this one result that, for the chosen optimum spacing, the reaction has no effect on the losses.

Vol. 2
1960-6

It should be pointed out again that the Soderberg loss coefficient is essentially a "compressible" irreversibility estimate being based on high-speed-turbine data while Ainley's cascade data are for Mach number less than 0·6. Other evidence (see below) suggests that for the aerofoil-type cascades there is little variation in loss coefficient with Mach numbers in the range 0·6–1·0.

A comparison of the secondary and other losses cannot be made generally, because of the difference in the method of correlation, but two examples given by Ainley are calculated on the Soderberg basis and the results compared. The Reynolds number based on the hydraulic mean diameter is $1{\cdot}8 \times 10^5$ in each example, if the Reynolds number based on the blade chord is 2×10^5. A comparison is made on the basis of both Reynolds numbers being 2×10^5, and for zero clearance.

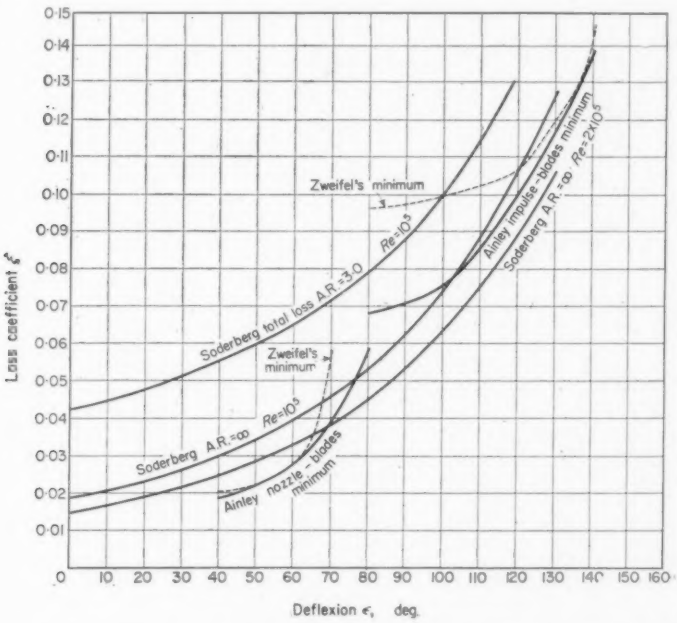

FIG. 9. Comparison between the correlations of Ainley and Soderberg.

Example 1. Nozzle row

$$\alpha_1 = 0, \quad \alpha_2 = 63{\cdot}5, \quad S/L = 0{\cdot}739, \quad t/L = 0{\cdot}20,$$

$$\text{aspect ratio} = H/(L \cos 32^\circ) = 1{\cdot}5.$$

Ainley gives

$$Y_p = \xi_p = 0{\cdot}0288,$$

$$Y_s = \xi_s = 0{\cdot}0295,$$

$$Y = 0{\cdot}0583.$$

Soderberg gives ξ^* as 0·064 for a Reynolds number of 10^5 and an aspect ratio of 3 : 1. For an infinite aspect ratio, ξ_p^* at this Reynolds number would be 0·039 and, at a Reynolds number of $2{\cdot}0 \times 10^5$, $\xi_p = 0{\cdot}033$. The aspect-ratio

correction for an aspect ratio of 1·5 at $Re = 2 \times 10^5$ gives the overall loss coefficient (ξ) as 0·0765, of which $0{\cdot}0765 - 0{\cdot}033 = 0{\cdot}0435$ may be assumed to be secondary loss (ξ_s), if the aspect-ratio correction is assumed to be valid up to large aspect ratios.

The total loss is greater on the Soderberg correlation, although the division between secondary and profile loss is approximately the same.

Example 2. Rotor row

$$\beta_2 = 36°, \quad \beta_3 = 48{\cdot}6,$$

$$S/L = 0{\cdot}749, \quad \beta_2/\beta_3 = 0{\cdot}074, \quad t/L = 0{\cdot}15.$$

Ainley gives

$$Y_p = \xi_p = 0{\cdot}041,$$

$$Y_s = \xi_s = 0{\cdot}091.$$

Soderberg gives

	Re	A.R.
$\xi^* = 0{\cdot}074$	10^5	3 : 1
$\xi_p^* = 0{\cdot}049$	10^5	∞
$\xi_p = 0{\cdot}041$	2×10^5	∞
$\xi = 0{\cdot}084$	2×10^5	1·5
$\xi_s = 0{\cdot}043$	2×10^5	1·5

The profile losses are comparable, but the Soderberg correlation gives a very small secondary loss for this impulse-type blade.

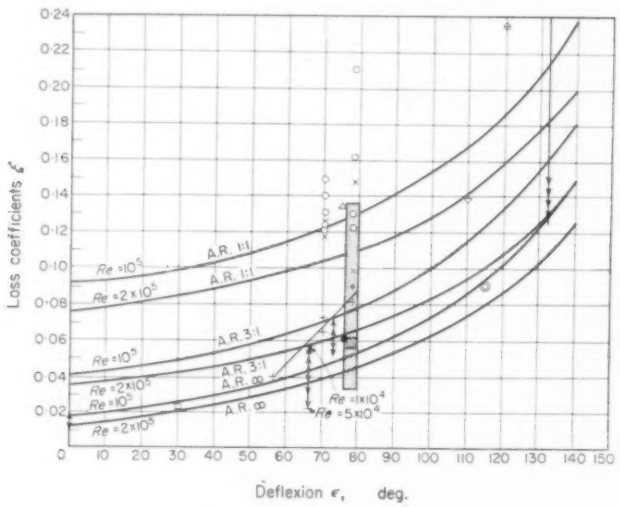

FIG. 10. Steam-turbine data.

6.4. *Steam-turbine data*

There are numerous experimental results obtained from tests of steam-turbine nozzles and blade rows. In general, the data are difficult to compare with that of Soderberg and Ainley, for the testing was not done with reference to Reynolds number or aspect ratio as important parameters.

Vol. 2
1960-6

Vol. 2
1960-61

TABLE for Fig. 10

	Experimenter	Aspect ratio	S/L	Symbol	Re (based on hydraulic diameter)	Remarks
Nozzles	Kraft	0·33–1·0 1·0–4·25	0·55–0·80	⩻	$1{\cdot}4–4{\cdot}5 \times 10^5$	Loss coefficients appear to be generally low
	Steam Nozzles Research Committee	of order unity	of order 0·4–0·7	⊙ (First series of tests) × (Second series of tests increased radius of curvature)	of order $2–2{\cdot}6 \times 10^5$	Consistent with Ainley and Soderberg
	Ackeret *et al.*	?	0·46	●	10^5	Range of Reynolds number and blade surfaces. Consistent with Ainley and Soderberg
	Guy	of order unity	of order 0·4–0·7	+	of order $2–2{\cdot}6 \times 10^5$	Losses appear to be generally low and variation with deflexion to be too large
	Faltin	0·8	0·5	△	?	—
	Scholz	∞	1·0	◎	$8{\cdot}10^4$ (chord)	Consistent with Ainley and Soderberg
	Stodola	of order 1·0	?	↓	$2–3 \times 10^5$	Losses appear to be low
Impulse blades	Kearton	1·5	0·5	▽	$1{\cdot}6–2{\cdot}4 \times 10^5$	Consistent with Ainley and Soderberg
	Brown Boveri	?	?	⊕	?	Consistent with Ainley and Soderberg
	Faltin	0·28	0·6	↓	?	Loss coefficients vary greatly due to variation of incidence. Minimum loss-coefficient consistent with Ainley and Soderberg at small positive reaction. Large variation with Mach number
	Brilling Rateau Christlein					Results not shown. Losses very high for reasons given in text
Nozzles and blades, model turbines	Dollin	?	?	↓	$1 \times 10^5–5 \times 10^4$	Losses appear to be generally low
	Schlicting (calculation)	—	1·0	⊡	10^6 (chord)	Boundary layer assumed fully turbulent
Straight nozzles	Steam Nozzles Research Committee	—	—	↓	?	Circular and square straight nozzles

The presentation adopted here is to convert the velocity coefficients to loss coefficients and to plot the results on a graph of ξ^* against ϵ^* (Fig. 10) together with a grid based on Soderberg's correlation. Where the Reynolds number and aspect ratio are known they are stated in the associated table. In comparing results the following points should be borne in mind:

(i) Most of the steam results are based on force measurements; the velocity coefficient is essentially a measure of the total irreversibility, and the loss coefficients calculated are total-loss coefficients.

(ii) The steam results are usually presented in the form of velocity coefficient against the isentropic exit-velocity (e.g. Fig. 11, which is a typical result from Kraft's[15] paper). Most of the results for "convergent" blade rows designed for subsonic and transonic operation show that the velocity coefficient is constant over a wide range,† from exit Mach numbers of the order of 0·6 up to well beyond the sonic speed. They indicate that it is possible, for subsonic and transonic operation of convergent rows, to ignore the effect of Mach number in equation (33). The velocity coefficients presented in Fig. 10 are mean values taken over the range $0{\cdot}6 < M_2 < 1{\cdot}0$. There is some disagreement on the variation in velocity coefficient at lower Mach number (Kearton[3] p. 160).

Vol. 2
1960-6

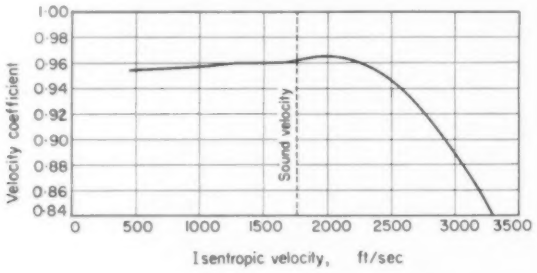

FIG. 11. Nozzle velocity coefficient (Kraft).

Some of the very early data (e.g. that of Christlein[16] and Faltin[17]) show considerable variations with Mach number, presumably because of the bluff profile shapes. In these cases the maximum-velocity coefficient is used.

(iii) Equation (33) shows that the compressible-loss coefficient is dependent upon the fluid molecular weight and the specific-heat ratio. This dependence is usually ignored, for results with air at low velocities ($\gamma = 1{\cdot}4$, $\bar{M} \doteqdot 28{\cdot}8$) are used in steam turbines ($\gamma \doteqdot 1{\cdot}3$, $\bar{M} = 18$) and in gas turbines ($\gamma \doteqdot 1{\cdot}33$, $\bar{M} \doteqdot 29$ at high temperatures).

(iv) Most of the steam-turbine cascade or "lattice" data were obtained with three or four blades in the cascade. It is unlikely that uniform conditions along the span were established in such tests. Further, some of the blade shapes have large thickness-chord ratios and trailing-edge thicknesses when judged by modern standards.

† Equation (15) shows that if the velocity coefficient is constant, then the "compressible" loss coefficient ξ is constant. But equation (19) shows that the coefficient Y, based on stagnation pressure loss, will not be constant but will vary with the Mach number.

The main sources of data are (i) the work of the Steam Nozzles Research Committee[18] and that of Metropolitan Vickers[19], both reported extensively by Kearton, (ii) the Swiss work reported by Stodola[2], (iii) the work of Dollin[20] at Parsons, and (iv) the work of Kraft[15] at the General Electric Company of America.

The latter is the most comprehensive but also the most difficult to interpret and to correlate. For example, tests by Kraft which are stated to show the variation of loss with aspect ratio, in fact show the variation with aspect ratio and Reynolds number combined, for as the aspect ratio was changed, so too was the Reynolds number.

Further results of Ackeret *et al.*[8], Kearton[3], Scholz[21] and Faltin[17] are shown.

Data obtained by Rateau[22], Christlein[16] and Briling[23] on impulse-type blades are open to some criticism and are not plotted. Rateau's blades had very large trailing-edge thickness and Briling and Christlein worked with a large difference in height between nozzles and blades.

In general, it appears that for nozzle-type rows the data of Soderberg, Ainley and the Steam Nozzle Research Committee are reasonably consistent. For the impulse type blades the data of Soderberg, Ainley, Brown Boveri[13] and Kearton are similarly consistent, although there is less experimental data available.

Some of Kraft's experiments at low aspect ratios are comparable with the nozzle data listed above, but most of his results, together with those of Guy[19] (correlated by Kearton and reproduced in Fig. 10) and those of Dollin[20] at low Reynolds number (1×10^4–5×10^4) give considerably lower losses than the main body of the data.

The minimum of the impulse data of Faltin[17] appears consistent with results of other workers, but the losses obtained by Christlein, Briling and Rateau are high, probably for the reasons given above.

6.5. *Effect of Reynolds number*

Workers who have studied the effect of Reynolds number on losses include Ackeret *et al.*[8], Dollin[20], Kearton[3] and Armstrong[24]. Cheshire[25] also gives data on the effect of Reynolds number. Some losses are shown in Fig. 12, together with the Soderberg's Reynolds-number correlation, which is a correction for the *total* loss. Both Armstrong's and Ackeret's cascade results are for profile loss alone; the results of Dollin and Kearton are for the total loss.

It is clear that the simple relation

$$\xi = \xi\left(\frac{10^5}{Re}\right)^{\frac{1}{4}}$$

is quite a good approximation at Reynolds numbers less than 10^5, although Dollin's work shows a greater variation than this. However, it gives no indication of a "critical" Reynolds number above which the loss is substantially constant. The existence of such a critical Reynolds number (based on D_h) around 10^5 is implied in Kearton's data, and in Ackeret's work with smooth blades. Ackeret further showed a lower "transition" Reynolds number for

rougher blades. Only Cheshire's cascade tests show substantial variation above $Re = 10^5$.

Armstrong tested a cascade-section similar to a steam-turbine impulse blade of large deflexion. He found little variation in loss between $2{\cdot}5 \times 10^5 < Re(\text{chord}) < 4 \times 10^5$, but a very large increase in Y_p (up to 0·5) at Reynolds numbers below 2×10^5. The peculiar performance of this cascade may be related to the blade profile which was made up of circular arcs and straight lines, with a "transition" between arc and straight line half-way along the chord on the suction surface.

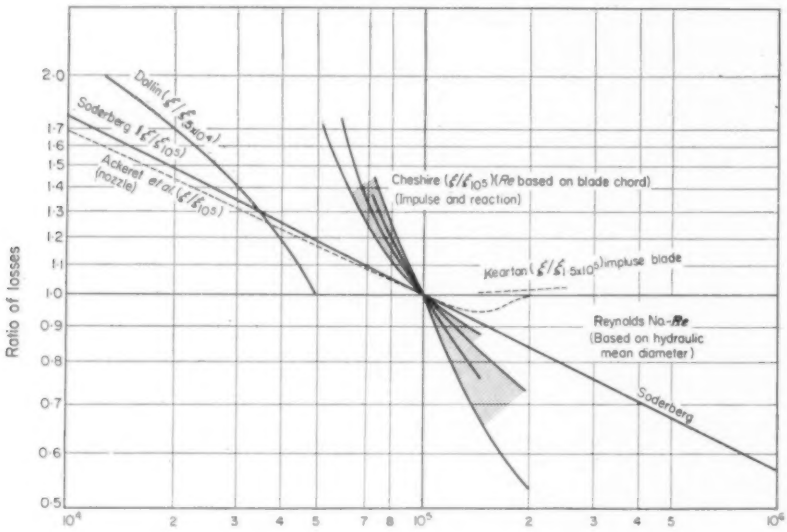

FIG. 12. Effect of Reynolds number on losses.

6.6. *Calculation of the profile losses*

Schlicting[26] has calculated the pressure distributions around turbine blades in cascade, and has estimated the growth of the boundary-layer momentum thickness over the blade surfaces. Results of such calculations for low-camber impulse blades ($\epsilon = 28°$) are shown in Fig. 7 for varying space-chord ratio. The results appear consistent with Ainley's cascade data. The minimum, calculated, profile-loss coefficient is also shown on Fig. 10, and is of the order of that given by Soderberg for low-camber blades.

6.7. *Secondary losses and the effect of aspect ratio*

The secondary flow in turbine rows is an extremely complex phenomenon. Detailed experiments on the nature of the secondary flows in a nozzle have recently been performed by Senoo[27], and in an impulse-type blade by Armstrong[28].

Senoo suggests that the rapid acceleration in a nozzle row may laminarize the boundary layer and he is able to calculate the secondary velocities in the nozzle.

Armstrong has found very large secondary motions in the main stream associated with the growth of secondary vorticity, which may be predicted quite accurately. The vorticity in the wake region is made up of two components, a trailing-filament vorticity transmitted through the row from upstream, and a shed vorticity associated with change of lift along the blade. Large contra-rotating vortices are observed downstream of the cascade.

While the secondary motions can be predicted using inviscid analyses (Hawthorne and Armstrong[29]) no attempt has been made to estimate the loss coefficients. Hawthorne[30] has shown that the drag coefficient associated with the induced velocities (i.e. the loss associated with viscous dissipation of these velocities) may be expressed as analytical functions of the following parameters for small deflexions

$$C_D \propto \frac{\epsilon^2 (S/L)^2}{H/L} f\left(\frac{\delta^1}{S \cos \alpha_2}\right)$$

where δ^1 is the inlet boundary-layer thickness. In practice the secondary losses are far greater than the losses associated with the dissipation of the induced velocities, but the expression gives a guide to an empirical correlation of losses.

Soderberg's correlation may be written, for a given Reynolds number,

$$1 + \xi = (1 + \xi^*)\left\{1 - 0{\cdot}025\left(1 - \frac{3b}{H}\right)\right\}$$

At infinite aspect ratio $\xi_p \doteq \xi^* - 0{\cdot}025$

so that $$\xi_s = \xi - \xi_p \doteq \frac{0{\cdot}075}{H/b}$$

In Ainley's correlation of secondary loss, the factor λ increases with reduced aspect-ratio, and the loss is proportional to the square of the lift coefficient

$$\left\{\text{i.e. to } (\tan \alpha_1 + \tan \alpha_2)^2,\ Y_s = \xi_s = \frac{\lambda C_L^2}{(S/L)^2} \frac{\cos^2 \alpha_2}{\cos^3 \alpha_m}\right\}$$

(The lack of dependence on deflexion in Soderberg's correlation is a weakness, and is illustrated in the examples calculated above.)

The predominant effect of aspect ratio is clear in Kraft's tests, which are replotted in Fig. 13. Most of the data is for nozzles with outlet angles in the range of $\alpha_2 = 76$–$80°$, so no clue is given to the variation of secondary loss with deflexion. But the variation with aspect ratio is substantially as Soderberg predicts, although the total losses are much lower. The variations with Reynolds number also appear to be along the lines of Soderberg's predictions.†

† Mr. D. G. Ainley has informed the author that he and Mr. G. C. R. Mathieson analysed Kraft's results in an earlier paper, *An Examination of the Flow and Pressure Losses in Blade Rows in Axial Flow Turbines* A.R.C. R & M 2891 (1955). Ainley concludes that the increase in loss coefficient at low aspect ratio observed by Kraft (and Scholz) is not an aspect-ratio effect as such, but an effect due to changing the ratio δ_1/H.

Scholz[21], on the basis of a series of tests with varying aspect ratio, has suggested that the overall loss-coefficient may be written

$$\xi = \xi_p + \frac{\xi_{\text{wall}}}{H/L}$$

This is basically the same as Soderberg's expression. The latter implies that ξ_{wall} is constant, and indeed, Scholz's experiments show that ξ_{wall} is constant over a large range of deflexions, for aspect ratios of 1, 3 and 5.

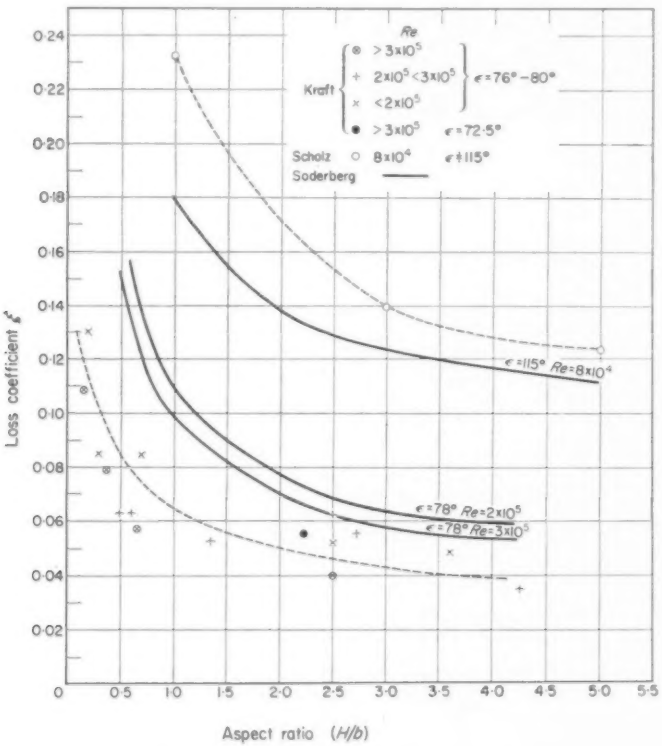

FIG. 13. Effect of aspect ratio on losses.

Scholz's results have been added to Figs. 10 and 13. Soderberg's prediction gives a greater loss than that observed by Scholz, particularly at the lowest aspect ratio, but a criticism of Scholz's work is that the loss coefficient is based upon area integration rather than mass-flow integration.

6.8. *Effect of incidence variation*

Variation of loss away from the zero-incidence condition is given by Ainley as a function of $(i - i_s)$ where i_s is the stalling incidence (this may be obtained from Ainley's paper). Soderberg's prediction is simpler (Fig. 14), the rate of variation with incidence being controlled by the thickness-chord ratio. Two of Ainley's cascade results are shown on the same graph for comparison.

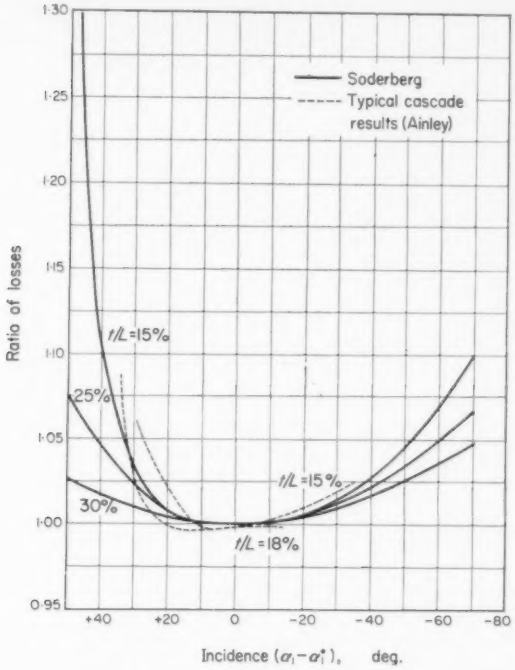

FIG. 14. Effect of incidence on losses.

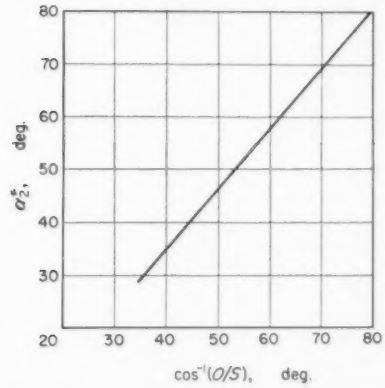

FIG. 15. Relationship between gas-outlet angles and $\cos^{-1}(O/S)$ for "straight-backed" blades operating at low Mach numbers ($M_2 < 0{\cdot}5$, $Re = 2 \times 10^5$) (Ainley and Mathieson).

6.9. *Effect of trailing-edge thickness*

Ainley observed a substantial variation of loss with the trailing-edge thickness–space ratio as indicated on Fig. 15. Kraft made two tests with different thickness–space ratios of 0·95 per cent and 3·2 per cent, all other parameters remaining the same. The loss increased by 28 per cent in the latter case. Ainley's correlation suggests that the increase should be 16 per cent for these cascades.

6.10. *Angle variation*

For the subsonic operation ($0 < M_2 < 0{\cdot}5$) of cascades such as those considered here, Ainley and Mathieson provide Fig. 16, showing the variation in outlet angle with $\cos^{-1}(o/S)$. They suggest that $\cos\alpha_2 = o/S$ at $M_2 = 1$, and that α_2 varies linearly between $M_2 = 0{\cdot}5$ and $M_2 = 1{\cdot}0$.

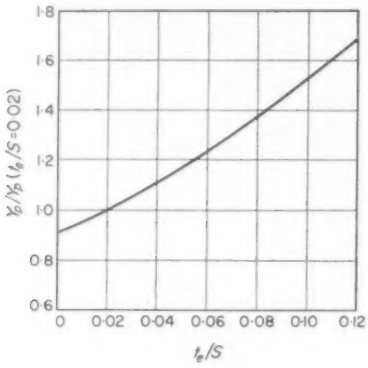

FIG. 16. Effect of trailing-edge thickness on blade-loss coefficients (Ainley and Mathieson).

6.11. *Clearance loss*

Soderberg's correlation, as used by Stenning[10], suggests that a correction for clearance loss is obtained simply by multiplying the calculated efficiency for zero clearance by the ratio of ("blade" area)/("blade" area plus clearance space). Ainley's clearance loss is

$$Y_c = \frac{B\delta}{H} C_L \left(\frac{S}{L}\right)^2 \frac{\cos^2\alpha_2}{\cos^3\alpha_m}$$

where B is 0·5 for a radial clearance and 0·25 for a shroud clearance.

7.0 DISCUSSION

The surprising conclusion from the assembly of loss data for turbine rows is that correlations such as that devised by Soderberg, on the basis of relatively few parameters, can be reasonably accurate. Some of the steam-cascade data is consistent with Ainley's and Soderberg's work, but the data of Guy[19], Kraft[15] and Dollin[20] appear to be optimistic. The following general conclusions emerge:

(i) Zweifel's[13] criterion for optimum space-chord ratio is not consistent with Ainley's work, although large increases in loss are not involved with use of Zweifel's criterion.

(ii) The minimum profile-losses for impulse and reaction blades are strongly dependent upon overall gas deflexion. Soderberg and Ainley agree on this statement.

(iii) The weak effect of Mach number was established by early investigators, for subsonic-type nozzles and blades.

Vol. 2
1960-6

(iv) A Reynolds number dependence $\xi/\xi_{10^5} \propto Re^{-n}$, where $0{\cdot}2 < n < 0{\cdot}35$, appears to be substantiated by several results. It appears that there is less variation of ξ with Re for $Re > 10^5$.

(v) The secondary and clearance losses are difficult to correlate, and there is a considerable diversity in predictions based on Ainley's work and Soderberg's data. The predominant effect of aspect ratio is clearly indicated in Kraft's data and Scholz's data.†

Finally, it is of interest to use Soderberg's correlation to calculate the total-to-total and total-to-static efficiencies for turbine stages of given stage-loading ($\pi = \Delta W/U^2$) and varying reaction (Fig. 17). It is apparent that the simple analyses referred to in Section 5.0 give a valuable guide to the best reaction for a given loading when the total-to-static efficiency is important (when the exhaust kinetic energy is not used) but that the choice of reaction is not critical in most multi-stage-turbine applications, when total-to-total efficiency is the criterion which should be used.

Vol. 2
960-61

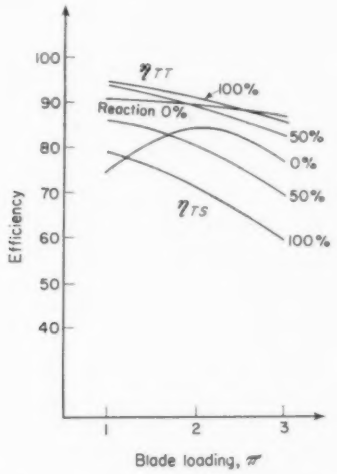

FIG. 17. Efficiency as a function of blade-loading and reaction.

8.0 RECOMMENDATIONS FOR RESEARCH

Date on profile losses and Reynolds-number effects below $Re = 10^5$ appear to be readily available, although there is some doubt about the variation of loss with Re in the $Re = 1\text{–}2 \times 10^5$ range. Further experiments to establish the Reynolds-number effect in this range would be useful. Cheshire's[25] and Armstrong's[24] results serve as a warning that losses may increase rapidly at Reynolds numbers below a critical value, for some blade profiles.

It is clear that the secondary losses require further investigation. The effect of profile shape is considered to be of little importance in the profile loss at high Reynolds numbers, owing to the high acceleration (although it must

† Stenning's experiments with axial-flow turbines of low aspect ratio indicate that Soderberg's prediction of secondary loss is pessimistic for aspect ratios less than unity.

be more significant in the low-reaction blading). However, it is probable that profile shape and even local twisting may produce drastic changes in the secondary loss. (Martin[31], working with the author, has shown that the secondary losses in a low-stagger, low-deflexion compressor cascade may be substantially reduced by reducing the deflexion through the boundary-layer region.) The relation between the clearance losses and the secondary losses requires further investigation.

The most useful work that could be done would be to correlate interstage traverses on turbines with the data given here.

The old controversy, on the effect of the centrifuging of the surface boundary layer (an outward movement on most rotor blades and an inward movement on the stator blades) and the effect upon profile and secondary losses, remains to be settled.

REFERENCES

1. D. G. AINLEY and G. C. R. MATHIESON, *A Method of Performance Estimation for Axial-flow Turbines*. Aeronautical Research Council, R. & M. 2974 (1957).
2. A. STODOLA, *Dampf- und Gas-Turbinen* (6th Ed.). Peter Smith, New York (1945).
3. W. J. KEARTON, *Steam Turbine Theory and Practice* (7th Ed.). Pitman, London (1958).
4. J. H. KEENAN, *Trans. Amer. Soc. Mech. Engrs.* **71**, 773 (1949).
5. B. HODKINSON and A. E. DEVEY, *J. Instn. Mech. Engrs.* **120**, 609 (1931).
6. J. C. OAKDEN, *J. Instn. Mech. Engrs.* **120**, 603 (1931).
7. H. L. WIRT, *Gen. Elect. Rev.* **27**, 780 (1924); *Trans. Amer. Soc. Mech. Engrs.* **46**, 981 (1924).
8. J. ACKERET, C. KELLER and F. SALZMANN, *Schweiz. Bauztg.* **104**, 259, 275, 292 (1934).
9. C. R. SODERBERG, Gas Turbine Laboratory, Massachusetts Institute of Technology. Unpublished Note (1949).
10. A. H. STENNING, *Design of Turbines for High Energy Fuel, Low Power Output Applications*. D.A.C.L. Report 79, Massachusetts Institute of Technology (1953).
11. W. R. HAWTHORNE, *Thermodynamics of Cooled Turbines. Part I: The Turbine Stage*. A.S.M.E. paper 55–A–186 (1955).
12. J. H. KEENAN, *Thermodynamics*. Wiley, New York (1941).
13. O. ZWEIFEL, *The Spacing of Turbo-Machine Blading Especially with Large Angular Deflection*. Brown Boveri Review, December (1945).
14. W. R. HAWTHORNE, *Some Formulae for the Calculation of Secondary Flow in Cascades*. Aeronautical Research Council Report No. 17,519 (1955).
15. H. KRAFT, *Trans. Amer. Soc. Mech. Engrs.* **71**, 781 (1949).
16. P. CHRISTLEIN, *Z. Ver. dtsch. Ing.* **55**, 2081 (1911).
17. H. FALTIN, *Z. Ver. dtsch. Ing.* **70**, 1582 (1926).
18. Reports of the Institution of Mechanical Engineers, Steam Nozzles Research Committee. *J. Instn. Mech. Engrs.* **1**, 1 (1923) (Report No. 1); **1**, 311 (1923) (No. 2); **1**, 455, **2**, 715 (1924) (No. 3); **2**, 747 (1925) (No. 4); **1**, 31 (1928) (No. 5); **1**, 215 (1930) (No. 6).
19. H. L. GUY, *J. Instn. Civ. Engrs.* **13**, 91 (1939).
20. F. DOLLIN, *Proc. Inst. Mech. Engrs., Lond.* **144**, 147 (1941).
21. N. SCHOLZ, *J. Aero. Sci.* **21**, No. 10, 107 (1954).
22. A. RATEAU, *Mode du Calcul des Turbines à Vapeur*. Association Technique Maritime, Paris (1909).
23. N. BRILING, *Z. Ver. dtsch. Ing.* **54**, 265, 352, 389, 474 (1910).
24. W. D. ARMSTRONG, *The Non Uniform Flow of Air Through Cascades of Blades*. Ph.D. Thesis, Cambridge University (1954).
25. L. J. CHESHIRE, *Gas Turbine Principles and Practice* (Edited by Sir H. ROXBEE COX) Section 8. Newnes, London (1955).
26. H. SCHLICTING, *J. Aero. Sci.* **21**, No. 3, 163 (1954).
27. Y. SENOO, *Trans. Amer. Soc. Mech. Engrs.* **11**, 1711 (1958).

Vol. 2
1960-6

28. W. D. Armstrong, *The Secondary Flow in a Cascade of Turbine Blades.* Aeronautical Research Council, R. & M. 2979 (1957).
29. W. R. Hawthorne and W. D. Armstrong, *Quart. J. Mech.* **8**, 280 (1955).
30. W. R. Hawthorne, *Quart. J. Mech.* **8**, 266 (1955).
31. P. M. E. Martin, *Secondary Flow through a Cascade of Twisted Blades.* Aeronautical Research Council Report No. 19,986 (1958).

Vol. 2
960-61

Int. J. Mech. Sci. Pergamon Press Ltd. 1960. Vol. 2, pp. 76–92. Printed in Great Britain

SYNTHESIS OF FOUR-ELEMENT SPATIAL MECHANISMS WITH LOWER PAIRS*†

N. I. Levitskii and K. K. Shakvazian‡

TRANSLATOR'S PREFACE

This paper is the first account in English of the method of least squares developed by N. I. Levitskii for purposes of mechanisms synthesis. Three-dimensional kinematical research represents one of the active fields in the subject at present, and the accuracy obtained in the logarithmic linkage is noteworthy. The paper bears also on related work in the United States, notably by J. Denavit and R. S. Hartenberg.

Vol. 2
1960-6

INTRODUCTION

This work considers one of the basic problems in the synthesis of four-element space mechanisms with lower pairs—the determination of the parameters of the kinematic diagram of the mechanism when a given relationship between the motion of the driving and the driven elements is prescribed.

The analytic solution of this problem for the special case of crank-and-rocker mechanism with driving and driven elements moving on mutually perpendicular planes has been developed by Novodvorskii[1]. Stepanoff[2] attacked the same problem but, even in the general case of non-perpendicular planes of motion of the driving and driven elements, he proposed a graphic solution with analytical refinements of three or four parameters. Finally, Zinovieff[3] gives a method for the analytical evaluation of five parameters in the general case.

The present work studies a method of analytical computation of six, seven and eight parameters of the kinematic diagram for the general case of crank-and-slider mechanism; the solution is carried out to the evaluation of the maximum number of parameters. Furthermore, the present work considers the analytical solution of the same problem for the case of spatial crank-and-rocker mechanism.

1. STATEMENT OF THE PROBLEM

Let us consider a four-element space mechanism in which the driving element AB and the follower CD are connected to a support by means of turning pairs, and to the rod BC by means of spherical pairs (Fig. 1). The superfluous degree of freedom corresponding to the freedom of the rod BC to rotate about its own axis will not be taken into account in the synthesis. We shall select the co-ordinate planes so that the plane of motion of the driven element always coincides with the xoy-plane and the plane of motion of the driving element always coincides with the surface Q which is specified by

* Translated from: Trudi Seminara Po Teorii Mashin i Mekhanizmov, *Akad. Nauk SSSR* **14**, No. 54, pp. 5–24 (1954).

† Translated from the Russian by Professor F. Freudenstein, Columbia University, New York.

‡ Institute of Machine Design, Academy of Sciences of the U.S.S.R.

means of the following three parameters: the angle γ formed by the x-axis and the line of intersection of the Q-plane and the xoz-plane; the angle η, i.e. the angle of inclination of the Q-plane with respect to the xoz-plane, and the distance DK from the origin of co-ordinates to the point of intersection of the x-axis and the Q-plane.[2] All angles are measured in the counterclockwise direction.

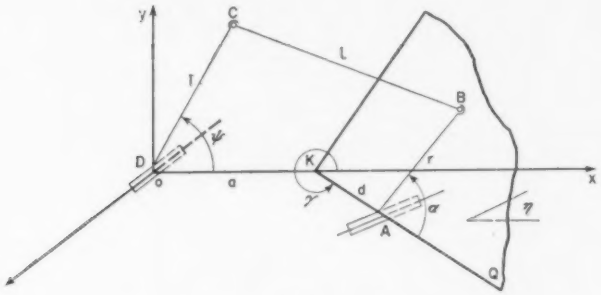

FIG. 1. Four-link spatial mechanism.

In the given system of co-ordinates the space mechanism under consideration is specified by means of the following nine absolute parameters: $AB, BC, CD, DK, KA, \gamma, \eta, \psi_0$ and α_0. ψ_0 and α_0 are the initial values of the angles of inclination of the driving and driven elements. The relative lengths of the elements are sufficient to specify the dependence between the motion of the elements DC and AB and, consequently, the maximum number of relative parameters required to define the given mechanism is equal to eight. Indeed, taking the length of the driven element DC as unity we have the following parameters

$$\frac{AB}{DC} = r; \quad \frac{BC}{DC} = l; \quad \frac{AK}{DC} = d; \quad \frac{DK}{DC} = a$$

and the angles γ, η, α_0 and ψ_0.

Any deviation from the given law $\psi = f(\alpha)$ is given by the equation

$$\Delta\psi = \psi - \psi_M \tag{1}$$

where ψ is the angle of inclination of the driven element for any value of the inclination angle of the driving element (α) as required by the specified law, and ψ_M is the actual angle of inclination of the driven element corresponding to the same angle α.

In order to simplify the problem, besides the quantity $\Delta\psi$, we might consider a function which characterizes the deviations from the given law. Such a function could be the weighted difference Δq which is the difference between the square of the length of the rod l and the square of the variable distance between points B and C for given values of the angles α and ψ.

The analytical expression for the weighted difference Δq in the case under examination has the form[2]

$$\Delta q = a^2 + d^2 + 2ad\cos\gamma + 1 + r^2 - l^2 - 2r(\cos\psi\cos\alpha\cos\gamma - \\ - \cos\psi\sin\alpha\cos\eta\sin\gamma + \sin\alpha\sin\eta\sin\psi) + 2dr\cos\alpha - \\ - 2a\cos\psi - 2d\cos\psi\cos\gamma + 2ar(\cos\alpha\cos\gamma - \sin\alpha\sin\gamma\cos\eta) \qquad (2)$$

If the quantities Δq and $\Delta\psi$ are assumed small, the relation between them is the following[4]

$$\Delta\psi = -\Delta q \Big/ \frac{\partial\Delta q}{\partial\psi}$$

or

$$\Delta\psi = \frac{-\Delta q}{2(B\sin\psi - r\sin\alpha\sin\eta\cos\psi)} \qquad (3)$$

where $B = r\cos\alpha\cos\gamma - r\sin\alpha\cos\eta\sin\gamma + a + d\cos\gamma$.

The desired parameters will be evaluated from the conditions of minimization of the difference Δq and the value of the deviation will be estimated from equation (3).

Analogously we can examine a spatial crank-and-slider mechanism (Fig. 2) whose driving element is AB and whose driven element is the slider T. The slider moves along the X-axis and the driving crank moves on the plane Q.

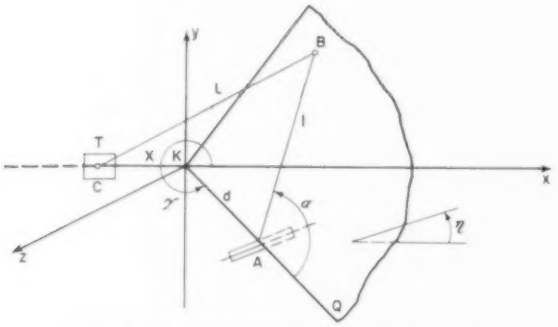

FIG. 2. Spatial slider-crank mechanism.

Taking the length of the driving element AB as unity, we find that six parameters are necessary to define the mechanism: $d, l, \gamma, \eta, \alpha_0, x_0$, where x_0 is the initial value of the distance x from the slider to the origin of co-ordinates.

The expression for the weighted difference Δq is of the form[2]

$$\Delta q = x^2 + d^2 + 1 - l^2 + 2d\cos\alpha + 2x(d\cos\gamma + \cos\alpha\cos\gamma - \cos\eta\sin\alpha\sin\gamma) \qquad (4)$$

The deviation from the given law is

$$\Delta x = x - x_M \qquad (5)$$

where x is the quantity which characterizes the desired position of the slider at any given value of α, and x_M is the quantity which characterizes the actual position of the slider in the mechanism at any value of α.

Vol. 2
1960-6

The relation between Δx and Δq is

$$\Delta x = \frac{-\Delta q}{2(x + d\cos\gamma + \cos\alpha\cos\gamma - \cos\eta\sin\alpha\sin\gamma)} \tag{6}$$

If the slider is considered to be the driving element, then the deviation from the desired law of motion is

$$\Delta\alpha = \alpha - \alpha_M \tag{7}$$

where the quantity $\Delta\alpha$ is related to Δq by

$$\Delta\alpha = \frac{\Delta q}{2(d\sin\alpha + x\cos\gamma\sin\alpha + x\cos\eta\sin\gamma\cos\alpha)} \tag{8}$$

We are going to evaluate the necessary parameters from the condition of minimizing the difference Δq. With this aim in mind, we can represent Δq in relation to the number of computed parameters in the form of the following generalized polynomials

$$\Delta q = A\{F(\alpha) - p_0\phi_0(\alpha) - p_1\phi_1(\alpha) - \ldots - p_n\phi_n(\alpha)\} \tag{9}$$

or

$$\Delta q = a\{F(\alpha) - p_0\phi_0(\alpha) - p_1\phi_1(\alpha) - \ldots - p_n\phi_n(\alpha) - p_0p_1\phi_{n+1}(\alpha) - p_1p_2\phi_{n+2}(\alpha)\} \tag{10}$$

where $A, p_0, p_1, \ldots, p_2$ are coefficients dependent only on the computed parameters of the mechanism.

The solution can be divided into two basic steps.[5]

(1) Computation of the coefficients $p_0, p_1, \ldots, p_n$ by one of the well-known methods of function approximation.

These coefficients are evaluated by interpolation from the condition that the difference Δq be zero at a number of points equal to the number of evaluated parameters; otherwise they are evaluated by quadratic approximation from the condition that the sum

$$S = \sum_{i=0}^{i=m} \{\Delta q(\alpha_i)\}^2 \tag{11}$$

be a minimum or, in the best approximation, from the condition that the maximum absolute value of the difference $\Delta\psi$ be a minimum.

The simplest method of approximate evaluation of the coefficients is by interpolation. If the obtained approximation is not satisfactory then one of the other methods has to be used. The best approximation should be used in the cases where the difference $\Delta\psi$ has to remain within certain predetermined limits.

The quadratic approximation should be used when the average value of the difference $\Delta\psi$ is required to remain within certain limits.

(2) After the coefficients $p_0, p_1, \ldots, p_n$ have been evaluated the parameters are computed from the relations between them and the coefficients.

The computations connected with the first step are examined in detail in work.[5] For this reason, later on we will carry out only the methods of representation of the difference Δq in polynomial form for the various cases of computation of the parameters of a mechanism and we will determine these parameters from the system of equations which connect them to the coefficient $p_0, p_1, \ldots, p_n$.

2. EVALUATION OF SIX PARAMETERS OF THE CRANK-AND-ROCKER MECHANISM

The choice of the number of parameters to be evaluated is made on the basis of the accuracy required in the approximation to the desired law of motion. The higher the accuracy, the larger the number of parameters to be evaluated, the maximum number of parameters being necessary when we have to exploit all the possibilities of the mechanism in decreasing the value of the quantity $\Delta\psi$.

For the evaluation of six parameters we group the terms of the expression for the weighted difference [equation (2)] so that it assumes the form of a generalized polynomial

$$\Delta q = A\{F(\alpha) - p_0\phi_0(\alpha) - p_1\phi_1(\alpha) - p_2\phi_2(\alpha) - p_3\phi_3(\alpha) - p_4\phi_4(\alpha) - p_5\phi_5(\alpha)\} \tag{12}$$

where A is a constant coefficient; $F(\alpha), \phi_0(\alpha), \phi_1(\alpha) \ldots$ are functions of the variable argument α, which do not contain the computed parameters; $p_0, p_1, p_2, \ldots, p_5$ are coefficients depending on the computed parameters.

For example, let it be required to compute the relative dimensions a, d, l, r and the angles γ and η.

Then the weighted difference (2) can be represented in the following form:

$$\begin{aligned}\Delta q = 2r\cos\eta\sin\gamma\Bigg\{&\cos\psi\sin\alpha - a\sin\alpha \\ &- \frac{\cos\gamma}{\cos\eta\sin\gamma}\cos\psi\cos\alpha - \frac{\sin\eta}{\cos\eta\sin\gamma}\sin\alpha\sin\psi \\ &+ \left(\frac{d}{\cos\eta\sin\gamma} + \frac{a\cos\gamma}{\cos\eta\sin\gamma}\right)\cos\alpha - \left(\frac{a + d\cos\gamma}{r\cos\eta\sin\gamma}\right)\cos\psi \\ &- \frac{l^2 - a^2 - d^2 - 1 - r^2 - 2ad\cos\gamma}{2r\cos\eta\sin\gamma}\Bigg\}\end{aligned} \tag{13}$$

In accordance with the symbols used in formula (12) we have

$$\left.\begin{aligned} &F(\alpha) = \cos\psi\sin\alpha; \quad \phi_0(\alpha) = \sin\alpha; \quad \phi_1(\alpha) = \cos\psi\cos\alpha \\ &\phi_2(\alpha) = \sin\alpha\sin\psi; \quad \phi_3(\alpha) = 1; \quad \phi_4(\alpha) = \cos\alpha \\ &\phi_5(\alpha) = \cos\psi \end{aligned}\right\} \tag{14}$$

$$A = 2r\cos\eta\sin\gamma \tag{15}$$

$$\left.\begin{aligned} &p_0 = a; \quad p_1 = \frac{\cos\gamma}{\cos\eta\sin\gamma}; \quad p_2 = \frac{\sin\eta}{\cos\eta\sin\gamma} \\ &p_3 = \frac{l^2 - a^2 - d^2 - 1 - r^2 - 2ad\cos\gamma}{2r\cos\eta\sin\gamma} \\ &p_4 = -\frac{d + a\cos\gamma}{\cos\eta\sin\gamma}; \quad p_5 = \frac{a + d\cos\gamma}{r\cos\eta\sin\gamma} \end{aligned}\right\} \tag{16}$$

Vol. 2
1960-6

The functions $F(\alpha), \phi_0(\alpha), \ldots, \phi_5(\alpha)$ are known, since the relation $\psi = f(\alpha)$ is assumed to be known. The coefficients $p_0, \ldots, p_5$ depend on the parameters we are computing. To determine them we can utilize any of the methods of function approximation which we have developed in Section 1.

Substituting the values of $p_0, \ldots, p_5$ in equations (16) we can find the parameters which define the kinematic diagram of the mechanism.

For this purpose we transform the system of equations (16) to the following form

$$p_0 = a \tag{17}$$

$$\cos\eta \sin\gamma\, p_1 = \cos\gamma \tag{18}$$

$$\cos\eta \sin\gamma\, p_2 = \sin\eta \tag{19}$$

$$-\cos\eta \sin\gamma\, p_4 = d + a\cos\gamma \tag{20}$$

$$r\cos\eta \sin\gamma\, p_5 = a + d\cos\gamma \tag{21}$$

$$2r\cos\eta \sin\gamma\, p_3 = l^2 - a^2 - d^2 - 1 - r^2 - 2ad\cos\gamma \tag{22}$$

We have six equations to determine six parameters. Equation (17) directly determines parameter a

$$a = p_0$$

Dividing equation (18) by $\cos\gamma$, and equation (19) by $\cos\eta$, we obtain

$$\tan\gamma \cos\eta = \frac{1}{p_1} \tag{23}$$

$$\tan\eta = p_2 \sin\gamma \tag{24}$$

Let us define $1/p_1 = p$ so that equation (23) gives

$$\frac{\tan^2\gamma}{p^2} - 1 = \tan^2\eta \tag{25}$$

Equation (24) gives

$$\tan^2\eta = p_2^2 \sin^2\gamma \tag{26}$$

From equations (25) and (26) it follows that

$$\frac{\tan^2\gamma}{p^2} - 1 = p_2^2 \sin^2\gamma$$

After the appropriate transformations we obtain a biquadratic equation in $\sin\gamma$

$$p^2 p_2^2 \sin^4\gamma + (1 + p^2 - p^2 p_2^2)\sin^2\gamma - p^2 = 0 \tag{27}$$

As a consequence it is possible in general to obtain four different values for the parameter γ. All the possible values of the parameter γ have to be considered when computing the other parameters of the mechanism so that no possible variants are overlooked.

When we substitute a value of γ in equation (24) we can obtain a value of the angle η.

Knowing parameters a, γ, η, from equation (20) we obtain d

$$d = -a\cos\gamma - \cos\eta \sin\gamma\, p_4 \tag{28}$$

Vol. 2
960-61

From equation (21) we can find parameter r

$$r = \frac{a + d\cos\gamma}{p_5 \cos\eta \sin\gamma} \tag{29}$$

Now, substituting the values for r, d, a, γ and η in equation (22) we can find the value of the parameter l

$$l = (a^2 + d^2 + 1 + r^2 + 2ad\cos\gamma + 2r\cos\eta\sin\gamma\, p_3)^{\frac{1}{2}} \tag{30}$$

3. EVALUATION OF SEVEN PARAMETERS OF THE CRANK-AND-ROCKER MECHANISM

We have to go into the evaluation of seven parameters of a mechanism when the evaluation of six parameters does not satisfy the requirements of accuracy we desire in the approximation of the law of motion to be obeyed by the mechanism.

Let us, for instance, undertake the evaluation of the parameters a, d, l, r, γ, η and ψ_0.

Grouping the terms of the expression for the weighted difference (2) we obtain

$$\begin{aligned}\Delta q = A\{&F(\alpha) - p_0\phi_0(\alpha) - p_1\phi_1(\alpha) - p_2\phi_2(\alpha) - p_3\phi_3(\alpha) \\ &- p_4\phi_4(\alpha) - p_5\phi_5(\alpha) - p_6\phi_6(\alpha) - p_0 p_1 \phi_7(\alpha)\}\end{aligned} \tag{31}$$

where

$$\left.\begin{array}{lll} F(\alpha) = -\cos\alpha\cos\psi_s; & \phi_0(\alpha) = \cos\alpha\sin\psi_s; & \phi_1(\alpha) = \cos\psi_s \\ \phi_2(\alpha) = \sin\alpha\cos\psi_s; & \phi_3(\alpha) = 1; & \phi_4(\alpha) = \sin\alpha\sin\psi_s \\ \phi_5(\alpha) = \cos\alpha; & \phi_6(\alpha) = \sin\alpha; & \phi_7(\alpha) = \sin\psi_s \end{array}\right\} \tag{32}$$

$$A = 2r\cos\gamma\cos\psi_0 \tag{33}$$

$$\left.\begin{array}{ll} p_0 = \tan\psi_0; & p_1 = \dfrac{a}{r\cos\gamma} + \dfrac{d}{r} \\ p_2 = -\dfrac{\sin\gamma\cos\eta}{\cos\gamma} + \dfrac{\sin\eta\sin\psi_0}{\cos\gamma\cos\psi_0}; & p_3 = \dfrac{l^2 - d^2 - r^2 - a^2 - 1 - 2ad\cos\gamma}{2r\cos\gamma\cos\psi_0} \\ p_4 = \dfrac{\sin\gamma\cos\eta\sin\psi_0}{\cos\gamma\cos\psi_0} + \dfrac{\sin\eta}{\cos\gamma}; & p_5 = -\left(\dfrac{d}{\cos\gamma\cos\psi_0}\,\dfrac{a}{\cos\psi_0}\right) \\ p_6 = \dfrac{a\sin\gamma\cos\eta}{\cos\gamma\cos\psi_0} & \end{array}\right\} \tag{34}$$

Having determined the coefficients $p_0, p_1, \ldots, p_6$ by one of the methods already explained, we can compute the dimensions of the mechanism by means of equations (34).

From the first equation of system (34) we can evaluate directly the value of $\tan\psi_0$, and from this the value of the angle ψ_0.

Vol. 2
1960-6

The remaining six equations can be rewritten in the following form

$$\left.\begin{aligned} r\cos\gamma\, p_1 &= a + d\cos\gamma \\ -\cos\gamma\cos\psi_0\, p_2 &= \cos\eta\sin\gamma\cos\psi_0 - \sin\eta\sin\psi_0 \\ \cos\gamma\cos\psi_0\, p_4 &= \cos\eta\sin\gamma\sin\psi_0 + \sin\eta\cos\psi_0 \\ -\cos\gamma\cos\psi_0\, p_5 &= d + a\cos\gamma \\ \cos\gamma\cos\psi_0\, p_6 &= a\sin\gamma\cos\eta \\ 2r\cos\gamma\cos\psi_0\, p_3 &= l^2 - d^2 - r^2 - a^2 - 1 - 2ad\cos\gamma \end{aligned}\right\} \tag{35}$$

From the second and third equations of system (35) we obtain

$$-\frac{p_2}{p_4} = \frac{\cos\eta\sin\gamma\cos\psi_0 - \sin\eta\sin\psi_0}{\cos\eta\sin\gamma\sin\psi_0 + \sin\eta\cos\psi_0} \tag{36}$$

Hence
$$\sin\gamma = \tan\eta\,\frac{\sin\psi_0 - (p_2/p_4)\cos\psi_0}{\cos\psi_0 + (p_2/p_4)\sin\psi_0} \tag{37}$$

Defining
$$k = \frac{\sin\psi_0 - (p_2/p_4)\cos\psi_0}{\cos\psi_0 + (p_2/p_4)\sin\psi_0} \tag{38}$$

we obtain
$$\sin\gamma = k\tan\eta \tag{39}$$

Substituting the resulting value of $\sin\gamma$ into the second equation of system (35) and raising to the second power, we have

$$(1 - k^2\tan^2\eta)\, p_2^2\cos^2\psi_0 = \sin^2\eta(k\cos\psi_0 - \sin\psi_0)^2$$

After transformations we obtain a biquadratic expression in $\sin\gamma$:

$$\begin{aligned}(k\cos\psi_0 - \sin\psi_0)^2\sin^4\eta - \{&(1+k^2)\, p_2^2\cos^2\psi_0 \\ &- (k\cos\psi_0 - \sin\psi_0)^2\}\sin^2\eta + p_2^2\cos^2\psi_0 = 0\end{aligned} \tag{40}$$

It is therefore possible to obtain, in the general case, four different values for the parameter η. All of them have to be taken into consideration when evaluating the remaining parameters if we want to be sure to have studied all the possible variants of the mechanism.

Substituting the value of η in equation (39) we can derive the value of the angle γ. Then, from the fifth equation of system (35) we can obtain parameter a, from the fourth equation parameter d, from the first equation parameter r and from the sixth equation parameter l.

Therefore the problem is completely solved.

4. EVALUATION OF EIGHT PARAMETERS OF THE CRANK-AND-ROCKER MECHANISM

Let us undertake the determination of the relative dimensions a, d, l, r and the angles γ, η, α_0 and ψ_0. Grouping terms in the expression for the weighted difference [equation (2)], we obtain

$$\begin{aligned}\Delta q = 2A\{&F(\alpha) - p_0\phi_0(\alpha) - p_1\phi_1(\alpha) - p_2\phi_2(\alpha) - p_3\phi_3(\alpha) \\ &- p_4\phi_4(\alpha) - p_5\phi_5(\alpha) - p_6\phi_6(\alpha) - p_7\phi_7(\alpha)\}\end{aligned} \tag{41}$$

Defining $\alpha = \alpha_0 + \alpha_s$ and $\psi = \psi_0 + \psi_s$ we have

$$\left.\begin{aligned} &F(\alpha) = \sin\psi_s; && \phi_0(\alpha) = \cos\alpha_s\cos\psi_s; && \phi_1(\alpha) = \sin\alpha_s\cos\psi_s \\ &\phi_2(\alpha) = \cos\alpha_s\sin\psi_s; && \phi_3(\alpha) = 1; && \phi_4(\alpha) = \sin\alpha_s\sin\psi_s \\ &\phi_5(\alpha) = \cos\alpha_s; && \phi_6(\alpha) = \sin\alpha_s; && \phi_7(\alpha) = \cos\psi_s \end{aligned}\right\} \quad (42)$$

$$A = a\sin\psi_0 + d\sin\psi_0\cos\gamma \quad (43)$$

$$\left.\begin{aligned} p_0 &= \frac{r\cos\psi_0\cos\alpha_0\cos\gamma - r\cos\psi_0\sin\alpha_0\cos\eta\sin\gamma + r\sin\alpha_0\sin\psi_0\sin\eta}{A} \\ p_1 &= \frac{r\cos\alpha_0\sin\psi_0\sin\eta - r\cos\psi_0\sin\alpha_0\cos\gamma - r\cos\psi_0\cos\alpha_0\cos\eta\sin\gamma}{A} \\ p_2 &= \frac{r\sin\alpha_0\cos\psi_0\sin\eta - r\sin\psi_0\cos\alpha_0\cos\gamma + r\sin\psi_0\sin\alpha_0\cos\eta\sin\gamma}{A} \\ p_3 &= \frac{l^2 - a^2 - d^2 - r^2 - 1 - 2ad\cos\gamma}{2A} \\ p_4 &= \frac{r\sin\psi_0\sin\alpha_0\cos\gamma + r\sin\psi_0\cos\alpha_0\cos\eta\sin\gamma + r\cos\alpha_0\cos\psi_0\sin\eta}{A} \\ p_5 &= \frac{ar\sin\alpha_0\cos\eta\sin\gamma - dr\cos\alpha_0 - ar\cos\alpha_0\cos\gamma}{A} \\ p_6 &= \frac{dr\sin\alpha_0 + ar\sin\alpha_0\cos\gamma + ar\cos\alpha_0\cos\eta\sin\gamma}{A} \\ p_7 &= \frac{a\cos\psi_0 + d\cos\psi_0\cos\gamma}{a\sin\psi_0 + d\sin\psi_0\cos\gamma} \end{aligned}\right\} \quad (44)$$

The functions $F(\alpha), \ldots, \phi_7(\alpha)$ are known since the desired law of motion $\psi = \phi(\alpha)$ is assumed known. To determine the coefficients $p_0, \ldots, p_7$ we can utilize any one of the methods previously mentioned.

After substitution of the resulting values of the coefficients $p_0, \ldots, p_7$ into the equations of the system (44) we can solve for the parameters of the mechanism. To do this we rearrange system (44) in the following form

$$\left.\begin{aligned} A(p_0\cos\alpha_0 - p_1\sin\alpha_0) &= r\cos\psi_0\cos\gamma \\ A(p_2\cos\alpha_0 - p_4\sin\alpha_0) &= -r\sin\psi_0\cos\gamma \\ A(p_5\cos\alpha_0 - p_6\sin\alpha_0) &= -ar\cos\gamma - dr \\ A(p_0\sin\alpha_0 + p_1\cos\alpha_0) &= -r\cos\psi_0\cos\eta\sin\gamma + r\sin\psi_0\sin\eta \\ A(p_2\sin\alpha_0 + p_4\cos\alpha_0) &= r\cos\eta\sin\psi_0\sin\gamma + r\cos\psi_0\sin\eta \\ A(p_5\sin\alpha_0 + p_6\cos\alpha_0) &= ar\cos\eta\sin\gamma \\ Ap_7 &= a\cos\psi_0 + d\cos\psi_0\cos\gamma \\ 2Ap_3 &= l^2 - a^2 - d^2 - 1 - r^2 - 2ad\cos\gamma \end{aligned}\right\} \quad (45)$$

Vol. 2
1960-6

From the seventh equation of system (45) we obtain

$$\tan\psi_0 = \frac{1}{p_7} \tag{46}$$

Dividing the second equation of system (45) by the first we find

$$\frac{p_2\cos\alpha_0 - p_4\sin\alpha_0}{p_0\cos\alpha_0 - p_1\sin\alpha_0} = -\tan\psi_0$$

Dividing the left-hand side of this equation by $\cos\alpha_0$ and utilizing (46),

$$\frac{p_2p_7 + p_0}{p_4p_7 + p_1} = \tan\alpha_0 \tag{47}$$

Transforming the fourth and fifth equations of system (44), we find

$$A(k_0\cos\psi_0 - k_1\sin\psi_0) = -r\cos\eta\sin\gamma \tag{48}$$

$$A(k_0\sin\psi_0 + k_1\cos\psi_0) = r\sin\eta \tag{49}$$

where

$$k_0 = p_0\sin\alpha_0 + p_1\cos\alpha_0$$

$$k_1 = p_2\sin\alpha_0 + p_4\cos\alpha_0 \tag{50}$$

Dividing equation (49) by equation (48) and equation (48) by the first equation of system (45), we see that

$$\tan\eta = -\sin\gamma\left(\frac{k_0\sin\psi_0 + k_1\cos\psi_0}{k_0\cos\psi_0 - k_1\sin\psi_0}\right)$$

$$\tan\gamma\cos\eta = -\cos\psi_0\left(\frac{k_0\cos\psi_0 - k_1\sin\psi_0}{p_0\cos\alpha_0 - p_1\sin\alpha_0}\right)$$

or

$$\tan\eta = k_2\sin\gamma \tag{51}$$

$$\tan\gamma\cos\eta = k_3 \tag{52}$$

From equation (52) we obtain

$$\tan^2\gamma - k_3^2 = \tan^2\eta k_3^2 \tag{53}$$

From equation (51) we have

$$k_2^2\sin^2\gamma = \tan^2\eta \tag{54}$$

Substituting the value of $\tan^2\eta$ obtained from equation (54) into equation (53) we produce a biquadratic equation in $\sin\gamma$.

Then by means of equations (49) or (48) and the third and sixth equations of system (45) we can determine r, d, a.

Substituting the values of seven parameters into the last equation of system (45) we can derive the value of l.

5. EXAMPLE OF EVALUATION OF EIGHT PARAMETERS OF THE CRANK-AND-ROCKER MECHANISM

As an example let us undertake the task of evaluating eight parameters in the design of a computing mechanism which could represent the function $y = \log x$ in the interval $x = 1$ to $x = 10$.

The same example has been used[1, 5] to illustrate the solution of the problem of synthesis of plane mechanisms.

The comparison of the results obtained in this paragraph and those obtained in the mentioned examples should show that the accuracy of the approximation is increased by the use of a larger number of computed parameters.

As in Refs. 2 and 3, we will set the angles of rotation of the driving and driven elements

$$\alpha_m - \alpha_0 = 55^\circ; \quad \psi_m - \psi_0 = 90^\circ$$

Consequently the scale of the graph of $y = f(x)$ will be

$$\mu_\psi = \frac{y_m - y_0}{\psi_m - \psi_0} = -\frac{1}{90}\frac{1}{\text{deg.}}$$

$$\mu_\alpha = \frac{X_m - X_0}{\alpha_m - \alpha_0} = \frac{9}{55}\frac{1}{\text{deg.}}$$

On the graph of the assigned function $y = \log x$ we choose 21 points equally spaced along the yy-axis.

The co-ordinates of these points are shown in Table 1.

This table contains the values of $x_s = x - x_0$ and $y_s = y - y_0$ and also the values of α_s and ψ_s obtained by dividing the quantities x_s and y_s by the scale factors μ_α and μ_ψ.

Computation of angles α_s and ψ_s

$$y_0 = 0; \quad x_0 = 1; \quad \frac{1}{\mu_\psi} = -90^\circ = -1{\cdot}57079\,\text{rad}; \quad \frac{1}{\mu_\alpha} = \frac{55^\circ}{9} = 0{\cdot}10666\,\text{rad}$$

TABLE 1

i	$y = y_s$	$x = 10^y$	$x_s = x - x_0$	$\psi_s = y_s\, 1/\mu_\psi$		$\alpha_s = x_s\, 1/\mu_\alpha$	
				rad	deg.	rad	deg.
0	0	1	0	0	0°	0	0°00′00″
1	0·05	1·1220	0·1220	−0·07854	− 4°30′	0·01301	0°44′43″
2	0·1	1·2589	0·2589	−0·15708	− 9°	0·02761	1°34′55″
3	0·15	1·4125	0·4125	−0·23562	−13°30′	0·04400	2°31′16″
4	0·2	1·5849	0·5949	−0·31416	−18°	0·06238	3°34′26″
5	0·25	1·7783	0·7783	−0·39270	−22°30′	0·08301	4°45′22″
6	0·3	1·9953	0·9953	−0·47124	−27°	0·10616	6°04′55″
7	0·35	2·2387	1·2387	−0·54978	−31°30′	0·13212	7°34′12″
8	0·4	2·5119	1·5119	−0·62832	−36°	0·16126	9°14′20″
9	0·45	2·8184	1·8184	−0·70686	−40°30′	0·19395	11°06′45″
10	0·5	3·1623	2·1623	−0·78540	−45°	0·23063	13°12′50″
11	0·55	3·5481	2·5481	−0·86393	−49°30′	0·27178	15°34′19″
12	0·6	3·9811	2·9811	−0·94247	−54°	0·31796	18°13′05″
13	0·65	4·4668	3·4668	−1·02101	−58°30′	0·36977	21°11′11″
14	0·7	5·0119	4·0119	−1·09955	−63°	0·42791	24°31′01″
15	0·75	5·6234	4·6234	−1·17809	−67°30′	0·49313	28°15′16″
16	0·8	6·3096	5·3096	−1·25663	−72°	0·56632	32°26′53″
17	0·85	7·0795	6·0795	−1·33517	−76°30′	0·64844	37°09′11″
18	0·9	7·9433	6·9433	−1·41371	−81°	0·74057	42°25′55″
19	0·95	8·9125	7·9125	−1·49225	−85°30′	0·84395	48°21′17″
20	1	10	9	−1·57079	−90°	0·95993	55°00′00″

Vol. 2
1960-6

Coefficients $p_0, p_1, \ldots, p_7$ will be computed by the method of interpolation. Choosing the points of interpolation by Chebichev's method we obtain the following points: 0, 2, 5, 8, 12, 15, 18, 20.

If we now utilize formula (42) to compute the functions $F(\alpha), \phi_0(\alpha), \ldots, \phi_7(\alpha)$, imposing that the difference Δq be equal to zero at the points of interpolation, we obtain the following equations

$$p_0 + p_3 + p_5 + p_7 = 0$$

$$0{\cdot}98931\,p_0 + 0{\cdot}02727\,p_1 - 0{\cdot}15637\,p_2 + p_3 - 0{\cdot}00432\,p_4 + 0{\cdot}99962\,p_5 + 0{\cdot}02761\,p_6 + 0{\cdot}98769\,p_7 = -0{\cdot}15643$$

$$0{\cdot}92070\,p_0 + 0{\cdot}07660\,p_1 - 0{\cdot}38136\,p_2 + p_3 - 0{\cdot}03173\,p_4 + 0{\cdot}99656\,p_5 + 0{\cdot}08291\,p_6 + 0{\cdot}92388\,p_7 = -0{\cdot}38268$$

$$0{\cdot}79853\,p_0 + 0{\cdot}12989\,p_1 - 0{\cdot}58017\,p_2 + p_3 - 0{\cdot}09437\,p_4 + 0{\cdot}98703\,p_5 + 0{\cdot}16055\,p_6 + 0{\cdot}80902\,p_7 = -0{\cdot}58779$$

$$0{\cdot}55832\,p_0 + 0{\cdot}18376\,p_1 - 0{\cdot}76846\,p_2 + p_3 - 0{\cdot}25292\,p_4 + 0{\cdot}94987\,p_5 + 0{\cdot}31263\,p_6 + 0{\cdot}58779\,p_7 = -0{\cdot}80902$$

$$0{\cdot}33709\,p_0 + 0{\cdot}18115\,p_1 - 0{\cdot}81381\,p_2 + p_3 - 0{\cdot}43735\,p_4 + 0{\cdot}88086\,p_5 + 0{\cdot}47338\,p_6 + 0{\cdot}38268\,p_7 = -0{\cdot}92388$$

$$0{\cdot}11546\,p_0 + 0{\cdot}10554\,p_1 - 0{\cdot}74892\,p_2 + p_3 - 0{\cdot}66640\,p_4 + 0{\cdot}73808\,p_5 + 0{\cdot}67471\,p_6 + 0{\cdot}15643\,p_7 = -0{\cdot}98769$$

$$-0{\cdot}57358\,p_2 + p_3 - 0{\cdot}81915\,p_4 + 0{\cdot}57358\,p_5 + 0{\cdot}81915\,p_6 = -1$$

Applying the usual methods of solution of a system of linear equations we find the following values for the coefficients

$$p_0 = 0{\cdot}0811402; \quad p_1 = 0{\cdot}2649784; \quad p_2 = 0{\cdot}9245966$$

$$p_3 = -0{\cdot}6451103; \quad p_4 = -0{\cdot}5390084; \quad p_5 = 0{\cdot}6030679$$

$$p_6 = -0{\cdot}7471119; \quad p_7 = -0{\cdot}0390978$$

Now we can find the value of the quantity $\Delta q/2A$ by formula (41) for each of the 21 chosen points. At all points the quantity $\Delta q/2A$ had at least five figures equal to zero after the decimal point.

After this we determine the values of the desired parameters.

We determine the value of the angle ψ_0 from equation (46)

$$\tan\psi_0 = -\frac{1}{0{\cdot}0390978} = -25{\cdot}5769; \quad \psi_0 = -87^\circ\,45'\,37''$$

From formula (47) we find the value of the angle α_0

$$\tan\alpha_0 = \frac{p_2 + p_0\tan\psi_0}{p_4 + p_1\tan\psi_0} = \frac{1{\cdot}15077191}{7{\cdot}3163339} = 0{\cdot}1572808$$

$$\alpha_0 = 8^\circ\,56'\,17''$$

Utilizing formulae (51) and (52), we can determine the values of the angles γ and η

$$\tan\eta = -0{\cdot}7659085\sin\gamma; \quad \tan\gamma\cos\eta = 0{\cdot}3787081$$

Solving these equations we obtain a biquadratic expression in $\sin\gamma$. One of the roots of this equation is $\gamma = 21^\circ\,28'\,14''$, to which corresponds a value

$$\eta = -15^\circ\,39'\,36''$$

Then we determine the values of the parameters r, d and a from equations (45) and (49).

$$a = -1{\cdot}705554; \quad d = 0{\cdot}923165; \quad r = 0{\cdot}906669$$

Finally, from the last equation of system (45) we obtain

$$l = 1{\cdot}25000$$

The magnitude of the maximum deviation from the desired function can be evaluated from formula (3).

In our case the quantity $\Delta q/2A$ is equal to zero with five-figure accuracy. For this reason we can evaluate the deviation $\Delta\psi$ by means of the approximate formula assuming the ratio $\Delta q/2A$ to be equal to 0·00001 at all points; that is, we use the higher limit of the values assumed by this quantity.

We first evaluate $\partial\Delta q/\partial\psi$ at 11 points (Table 2).

From Table 2 it follows that in order to evaluate the higher limit of the maximum value of the deviation we have to use $\partial\Delta q/\partial\psi = 0{\cdot}131$.

TABLE 2

i	0	2	4	6	8	10	12	14	16	18	20
$\partial\Delta q/\partial\psi$	0·131	0·143	0·216	0·202	0·230	0·258	0·279	0·287	0·256	0·263	0·38

Using the fact that $A = 0{\cdot}848$, we obtain

$$\Delta\psi = \frac{0{\cdot}00001 \times 2 \times 0{\cdot}848}{0{\cdot}131} = 0{\cdot}00013$$

As a percentage of the total range of the angle we have

$$\Delta_{\text{rel}} = \frac{0{\cdot}00013}{1{\cdot}57} \times 100 = 0{\cdot}008 \text{ per cent}$$

Thus the maximum deviation cannot exceed 0·008 per cent over the whole range. For this reason there is less necessity to use the methods of optimal and quadratic approximation.

Moreover, it is interesting to evaluate the resulting mechanism according to the maximum transmission angle, i.e. the angle between the direction of the force acting on the driven element and the velocity of its point of application. In our example the maximum angle of action considering CD as the driven element is equal to 85° (determined graphically). Taking AB as the driven element the angle of action can assume a maximum value of 57°.

Vol. 2
1960-6

6. EVALUATION OF THREE PARAMETERS OF A SPATIAL CRANK-AND-SLIDER MECHANISM

In order to evaluate three parameters we group the terms of the expression for the weighted difference (4) so that they assume the form of a generalized polynomial

$$\Delta q = A\{F(\alpha) - p_0\phi_0(\alpha) - p_1\phi_1(\alpha) - p_2\phi_2(\phi)\} \tag{55}$$

As an example, let it be required to evaluate the relative dimensions d and l and the angle η. Then the weighted difference can be expressed in the following way

$$\Delta q = x^2 + 2x\cos\alpha\cos\gamma + 2d(\cos\alpha + x\cos\gamma) - 2x\sin\gamma\sin\alpha\cos\eta + d^2 + 1 - l^2 \tag{56}$$

According to the notations assumed in formula (55) we have

$$\left.\begin{aligned} &F(\alpha) = x^2 + 2x\cos\alpha\cos\gamma; \quad \phi_0(\alpha) = \cos\alpha + x\cos\gamma \\ &\phi_1(\alpha) = x\sin\alpha; \qquad\qquad \phi_2(\alpha) = 1 \end{aligned}\right\} \tag{57}$$

$$A = 1; \quad p_0 = -2d; \quad p_1 = 2\sin\gamma\cos\eta; \quad p_2 = l^2 - d^2 - 1 \tag{58}$$

To evaluate the coefficients p_0, p_1 and p_2 we can use any of the methods of Section 1.

After this has been done we make use of formula (58) to determine the desired values of the dimensions of the mechanism

$$d = -p_0/2 \tag{59}$$

$$\cos\eta = p_1/2\sin\gamma \tag{60}$$

$$l = (d^2 + 1 - p_2)^{\frac{1}{2}} \tag{61}$$

7. EVALUATION OF FOUR PARAMETERS OF A SPATIAL CRANK-AND-SLIDER MECHANISM

To evaluate four parameters we group the terms of the weighted difference (4) in the form

$$\Delta q = A\{F(\alpha) - p_0\phi_0(\alpha) - p_1\phi_1(\alpha) - p_2\phi_2(\alpha) - p_3\phi_3(\alpha) - p_0p_1\phi_4(\alpha)\} \tag{62}$$

As an example, let it be required to evaluate the relative dimensions d and l and the angles γ and η. Then the weighted difference can be expressed in the following way

$$\Delta q = 2\{x^2/2 + xd\cos\gamma + \cos\gamma\, x\cos\alpha - x\sin\gamma\cos\eta\sin\alpha + d\cos\alpha + (d^2 + 1 - l^2)/2\} \tag{63}$$

In accordance with the notation of formula (62) we have

$$\left.\begin{aligned} &F(\alpha) = x^2/2; \quad \phi_0(\alpha) = \cos\alpha; \quad \phi_1(\alpha) = x\cos\alpha \\ &\phi_2(\alpha) = x\sin\alpha; \quad \phi_3(\alpha) = 1; \quad \phi_4(\alpha) = -x; \quad A = 2 \end{aligned}\right\} \tag{64}$$

$$\left.\begin{aligned} p_0 &= -d; \\ p_1 &= -\cos\gamma; \\ p_2 &= \sin\gamma\cos\eta; \\ p_3 &= -(d^2+1-l^2)/2 \end{aligned}\right\} \tag{65}$$

After having determined the coefficients p_i by the usual methods, we use formula (65) to find the desired parameters of the mechanism.

From the second equation of system (65)

$$\cos\gamma = -p_1 \tag{66}$$

from the first equation

$$d = -p_0 \tag{67}$$

from the third equation

$$\cos\eta = p_2/(1-p_1^2)^{\frac{1}{2}} \tag{68}$$

Finally, substituting the resulting values into the fourth equation we determine the value of the parameter l:

$$l = (d^2+1+2p_3)^{\frac{1}{2}}$$

8. EVALUATION OF FIVE PARAMETERS OF A SPATIAL CRANK-AND-SLIDER MECHANISM

In order to evaluate five parameters we group the terms of the expression for the weighted difference (4) so that they assume the form

$$\begin{aligned} \Delta q = A\{&F(\alpha) - p_0\phi_0(\alpha) - p_1\phi_1(\alpha) - p_2\phi_2(\alpha) - p_3\phi_3(\alpha) \\ &- p_4\phi_4(\alpha) - p_0p_2\phi_5(\alpha) - p_0p_3\phi_6(\alpha)\} \end{aligned} \tag{69}$$

Let us, for example, evaluate the parameters d, l, γ, η, x_0.

In this case the weighted difference (4) can be written in the following way:

$$\begin{aligned} \Delta q = 2\{&x_s^2/2 + x_0x_s + (x_0^2+d^2+1-l^2)/2 + x_0d\cos\gamma \\ &+ x_sd\cos\gamma + d\cos\alpha + x_0\cos\alpha\cos\gamma + x_s\cos\alpha\cos\gamma \\ &- x_0\sin\alpha\sin\gamma\cos\eta - x_s\sin\alpha\sin\gamma\cos\eta\} \end{aligned} \tag{70}$$

where

$$x_s = x - x_0$$

$$\left.\begin{aligned} F(\alpha) &= x_s^2/2; & \phi_2(\alpha) &= x_s\cos\alpha; & \phi_5(\alpha) &= -\cos\alpha \\ \phi_0(\alpha) &= x_s; & \phi_3(\alpha) &= x_s\sin\alpha; & \phi_6(\alpha) &= -\sin\alpha \\ \phi_1(\alpha) &= \cos\alpha; & \phi_4(\alpha) &= 1 \end{aligned}\right\} \tag{71}$$

$$A = 2 \tag{72}$$

$$\left.\begin{aligned} p_0 &= -x_0 - d\cos\gamma; & p_1 &= -d; & p_2 &= -\cos\gamma \\ p_3 &= \sin\gamma\cos\eta; & p_4 &= (l^2-1-d^2-x_0^2-2x_0d\cos\gamma)/2 \end{aligned}\right\} \tag{73}$$

After having determined the unknown parameters p_0, p_1, p_2, p_3 and p_4, we can evaluate the desired parameters of the mechanism by means of formulae (73).

Vol. 2
1960-6

From the second equation of system (73)

$$d = -p_1 \tag{74}$$

from the third equation

$$\cos\gamma = -p_2 \tag{75}$$

From the first equation

$$x_0 = -p_0 - d\cos\gamma \tag{76}$$

the value of the parameter η can be determined from the fourth equation of system (73)

$$\cos\eta = p_3/\sin\gamma$$

Finally, substituting the obtained values of the parameters into the fifth equation of system (73), we can find the value of the parameter l.

9. EVALUATION OF SIX PARAMETERS OF A SPATIAL CRANK-AND-SLIDER MECHANISM

In order to evaluate six parameters we will group the terms of the expression of the weighted difference (4) in the form of a generalized polynomial

$$\Delta q = 2\{F(\alpha) - p_0\phi_0(\alpha) - p_1\phi_1(\alpha) - p_2\phi_2(\alpha) - p_3\phi_3(\alpha) - p_4\phi_4(\alpha) - p_5\phi_5(\alpha)\} \tag{77}$$

Let it be desired to determine the following parameters of the mechanism: x_0, d, l, γ, η and α_0. Then the weighted difference (4) can be written in the form

$$\begin{aligned}\Delta q/2 = {} & x_s^2/2 - \cos\alpha_s(x_0\cos\eta\sin\gamma\sin\alpha_0 - d\cos\alpha_0 \\ & - x_0\cos\alpha_0\cos\gamma) - \sin\alpha_s(d\sin\alpha_0 + x_0\sin\alpha_0\cos\gamma \\ & + x_0\cos\eta\sin\gamma\cos\alpha_0) - x_s\cos\alpha_s(\cos\eta\sin\gamma\sin\alpha_0 \\ & - \cos\alpha_0\cos\gamma) - x_s\sin\alpha_s(\sin\alpha_0\cos\gamma + \cos\eta\sin\gamma\cos\alpha_0) \\ & + x_s(x_0 + d\cos\gamma) + \frac{(x_0^2 + d^2 + 1 - l^2 + 2dx_0\cos\gamma)}{2}\end{aligned} \tag{78}$$

where $\alpha = \alpha_0 + \alpha_s; \quad x = x_0 + x_s$

In correspondence with the notation used in formula (77), we have

$$\left.\begin{aligned} &F(\alpha) = x_s^2/2; \quad \phi_0(\alpha) = \cos\alpha_s; \quad \phi_1(\alpha) = \sin\alpha_s \\ &\phi_2(\alpha) = x_s; \quad \phi_3(\alpha) = 1; \quad \phi_4(\alpha) = x_s\cos\alpha_s \\ &\phi_5(\alpha) = x_s\sin\alpha_s \end{aligned}\right\} \tag{79}$$

$$\left.\begin{aligned} p_0 &= x_0\cos\eta\sin\gamma\sin\alpha_0 - d\cos\alpha_0 - x_0\cos\alpha_0\cos\gamma \\ p_1 &= d\sin\alpha_0 + x_0\sin\alpha_0\cos\gamma + x_0\cos\eta\sin\gamma\cos\alpha_0 \\ p_2 &= -(x_0 + d\cos\gamma) \\ p_3 &= (l^2 - x_0^2 - d^2 - 1 - 2dx_0\cos\gamma)/2 \\ p_4 &= \cos\eta\sin\gamma\sin\alpha_0 - \cos\gamma\cos\alpha_0 \\ p_5 &= \sin\alpha_0\cos\gamma + \cos\eta\sin\gamma\cos\alpha_0 \end{aligned}\right\} \tag{80}$$

After having evaluated the coefficients $p_0, p_1, \ldots, p_5$, we can determine the values of the desired parameters by means of system (80).

In order to do this we transform system (80) to the following form:

$$p_0 \sin \alpha_0 + p_1 \cos \alpha_0 = x_0 \cos \eta \sin \gamma \tag{81}$$

$$p_0 \cos \alpha_0 - p_1 \sin \alpha_0 = -x_0 \cos \gamma - d \tag{82}$$

$$p_4 \sin \alpha_0 + p_5 \cos \alpha_0 = \cos \eta \sin \gamma \tag{83}$$

$$p_4 \cos \alpha_0 - p_5 \sin \alpha_0 = -\cos \gamma \tag{84}$$

$$-p_2 = x_0 + d \cos \gamma \tag{85}$$

$$p_3 = (l^2 - x_0^2 - d^2 - 1 - 2dx_0 \cos \gamma)/2 \tag{86}$$

The sequence of solution of these equations can be the following:

(1) Obtain the quantity $\cos \eta \sin \gamma$ from equations (81) and (83) and eliminate it from them.

(2) Eliminate the quantity d from equations (82) and (85).

(3) Eliminate the quantity $\cos \gamma$ by equation (84).

(4) Eliminate the quantity x_0 from the remaining two equations.

(5) Find the quantity α_0 from the resulting equation.

Having the value of the parameter α_0, we can obtain the value of γ from equation (84), and the value of the angle η from equation (83). Then equation (81) will yield the value of the parameter x_0 and equation (85) parameter d. Finally, substituting all the obtained values of the parameters in equation (86), we are able to determine the value of l.

REFERENCES

1. E. P. NOVODVORSKII, A method of synthesis of mechanisms. Transactions of the Seminar on the Theory of Machines and Mechanisms, *Akad. Nauk SSSR* **42** (1951).
2. B. I. STEPANOFF, Design of spatial transmission mechanisms with lower pairs. Transactions of the Seminar on the Theory of Machines and Mechanisms, *Akad. Nauk SSSR* **45** (1951).
3. V. A. ZINOVIEFF, *Spatial Mechanisms with Lower Pairs*. Izdatelstvo Akademii Nauk, Moscow–Leningrad (1952).
4. I. SH. PINSKER, Approximate synthesis of mechanisms with lower pairs. Transactions of the Seminar on the Theory of Machines and Mechanisms, *Akad. Nauk SSSR* **18** (1948).
5. N. I. LEVITSKII, *Design of Plane Mechanisms with Lower Pairs*. AH CCCP Izdatelstvo Akademii Nauk, Moscow–Leningrad (1950).

Vol. 2
1960-

Int. J. Mech. Sci. Pergamon Press Ltd. 1960. Vol. 2, pp. 93–101. Printed in Great Britain

A STRESS-FUNCTION APPROACH TO INTERFACE AND MIXED BOUNDARY-CONDITION PROBLEMS (BOUNDARY CONDITIONS AND FINITE-DIFFERENCE TECHNIQUES)

O. C. Zienkiewicz and R. W. Gerstner
Northwestern University, Evanston, Illinois

(*Received* 23 *November* 1959)

Vol. 2
1960-61

Summary—Special conditions which have to be imposed on the stress function for boundaries on which displacements are specified or for an interface separating materials with different elastic properties are derived. The striking similarity of these conditions with those occurring in slabs subject to flexure on lines where a sudden change of thickness occurs is demonstrated.

The application of finite-difference techniques and of relaxation methods to problems falling within the above categories is discussed and some details of the finite-difference operators are presented. An example illustrating the application of such techniques is quoted.

1. INTRODUCTION

The solution of the biharmonic stress-function equation (governing the stress distribution in two-dimensional problems) by finite-difference techniques is well known for cases of given boundary stresses and has been described in numerous publications.[1–4] The problems presented by an interface, sharply separating parts of the body with different elastic constants, as well as problems in which displacements are specified on a part of the boundary, are considerably more difficult. For the latter, it has been suggested that a treatment in terms of the displacement equations is more advantageous.[1, 5] This may not be the case when the major part of the boundary is subject to known stresses, and it is proposed to derive here the boundary conditions which would have to be satisfied by the Airy stress function on the portion of a boundary for which the displacements are specified as well as similar conditions for an elastic interface.

These relations are believed to be new and show some striking analogies with the boundary conditions of transversely loaded plates as could indeed be anticipated from the aspects of the analogy already known.

2. INTERFACE DISPLACEMENT CONDITIONS

Let the line AB in Fig. 1 denote an interface between two regions of different elastic properties for a body with known tractions on the external boundary. On this interface no slippage is possible and therefore the stresses in each region must be such that "perfect fit" of the displacements is assured. In other words, if u_1 and v_1 represent the displacements in the x and y directions respectively for region 1, and u_2, v_2 the similar displacements for the region 2, then these displacements can differ on the interface only by the components of

a rigid-body displacement, i.e.

$$u_1 = u_2 + \alpha y + \beta \tag{1}$$

$$v_1 = v_2 - \alpha x + \delta \tag{2}$$

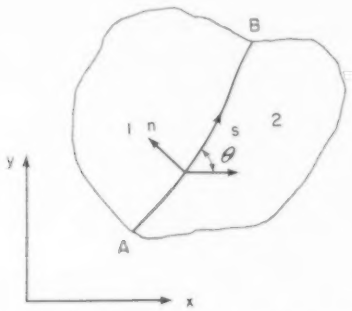

FIG. 1. An interface between two elastic media.

To eliminate the constants of this rigid-body movement, successive differentiation, with respect to s, the interface, and elimination of α, β and δ yield

$$\frac{\partial u_1}{\partial s}\cos\theta + \frac{\partial v_1}{\partial s}\sin\theta = \frac{\partial u_2}{\partial s}\cos\theta + \frac{\partial v_2}{\partial s}\sin\theta \tag{3}$$

and

$$-\frac{\partial^2 u}{\partial s^2}\sin\theta + \frac{\partial^2 v_1}{\partial s^2}\cos\theta = -\frac{\partial^2 u_2}{\partial s^2}\sin\theta + \frac{\partial^2 v_2}{\partial s^2}\cos\theta \tag{4}$$

in which

$$\theta = \tan^{-1}\left(\frac{dy}{dx}\right)$$

along the interface s.

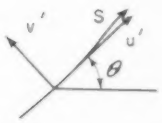

FIG. 2. Tangential and normal displacements.

It can be shown that further differentations and elimination yield only conditions which are already implicit in relations (3) and (4) and these therefore give all the necessary conditions which can be derived from (1) and (2).

These equations between the displacements can be expressed in terms of their tangential and normal components (u' and v'—Fig. 2).

Noting that

$$u = u'\cos\theta - v'\sin\theta$$

and

$$v = u'\sin\theta + v'\cos\theta$$

substitution into (3) and (4) yields the following

$$\frac{\partial u_1'}{\partial s} - \frac{v_1'}{\rho} = \frac{\partial u_2'}{\partial s} - \frac{v_2'}{\rho} \tag{5}$$

Vol. 2
1960-6

and
$$\frac{\partial^2 v_1'}{\partial s^2}+\frac{\partial u_1'}{\partial s}+u_1'\frac{\partial}{\partial s}\left(\frac{1}{\rho}\right)=\frac{\partial^2 v_2'}{\partial s^2}+\frac{\partial u_2'}{\partial s}+u_2'\frac{\partial}{\partial s}\left(\frac{1}{\rho}\right) \tag{6}$$

in which $1/\rho=\partial\theta/\partial s$ represents the curvature of the boundary.

In each region the stresses can be expressed in the usual way by the appropriate stress functions ϕ_1 and ϕ_2, which will define the stresses as

$$\sigma_x=\frac{\partial^2\phi}{\partial y^2},\quad \sigma_y=\frac{\partial^2\phi}{\partial x^2},\quad \tau_{xy}=-\frac{\partial^2\phi}{\partial x\,\partial y}$$

and the strains as
$$\frac{\partial u}{\partial x}=A\left(\frac{\partial^2\phi}{\partial y^2}-B\frac{\partial^2\phi}{\partial x^2}\right)$$

$$\frac{\partial v}{\partial y}=A\left(\frac{\partial^2\phi}{\partial x^2}-B\frac{\partial^2\phi}{\partial y^2}\right)$$

$$\frac{\partial u}{\partial y}+\frac{\partial v}{\partial x}=-2A(1+B)\frac{\partial^2\phi}{\partial x\,\partial y} \tag{7}$$

In which
$$A=\frac{1}{E}$$

$$B=\nu\quad\text{for plane stress}$$

and
$$A=\frac{(1-\nu^2)}{E}$$

$$B=\frac{\nu}{1-\nu}\quad\text{for plane strain}$$

Expansion of expressions (3) and (4) with substitution of the strains results in the following identities (now written without the suffix specifying the region)

$$\frac{\partial u'}{\partial s}-\frac{v'}{\rho}\equiv A\left\{\left(\frac{\partial^2\phi}{\partial y^2}-B\frac{\partial^2\phi}{\partial x^2}\right)\cos^2\theta+\left(\frac{\partial^2\phi}{\partial x^2}-B\frac{\partial^2\phi}{\partial y^2}\right)\sin^2\theta-(1+B)\frac{\partial^2\phi}{\partial x\,\partial y}\sin 2\theta\right\}$$
$$\equiv A\left\{\frac{\partial^2\phi}{\partial n^2}-B\left(\frac{\partial^2\phi}{\partial s^2}-\frac{1}{\rho}\frac{\partial\phi}{\partial n}\right)\right\} \tag{8}$$

and
$$\frac{\partial^2 v'}{\partial s^2}+\frac{\partial u'}{\partial s}+u'\frac{\partial}{\partial s}\left(\frac{1}{\rho}\right)\equiv A\left[\frac{\partial^3\phi}{\partial x^3}\{\sin\theta+(1+B)\sin\theta\cos^2\theta\}\right.$$
$$-\frac{\partial^3\phi}{\partial x^2\,\partial y}\{\cos\theta+(1+B)(\cos^3\theta-2\sin^2\theta\cos\theta)\}$$
$$+\frac{\partial^3\phi}{\partial x\,\partial y^2}\{\sin\theta+(1+B)(\sin^3\theta-2\sin\theta\cos^2\theta)\}$$
$$-\frac{\partial^3\phi}{\partial y^3}\{\cos\theta+(1+B)\sin^2\theta\cos\theta\}$$
$$\left.+\frac{1}{\rho}(1+B)\left\{\left(\frac{\partial^2\phi}{\partial x^2}-\frac{\partial^2\phi}{\partial y^2}\right)(\cos^2\theta-\sin^2\theta)+\frac{\partial^2\phi}{\partial x\,\partial y}2\sin 2\theta\right\}\right]$$
$$\equiv -A\left\{\frac{\partial}{\partial n}(\nabla^2\phi)+(1+B)\frac{\partial}{\partial s}\left(\frac{\partial^2\phi}{\partial n\,\partial s}\right)\right\} \tag{9}$$

in which $\partial/\partial n$ represents the differentiation with respect to the normal shown in Fig. 1.

Two necessary conditions in terms of the stress functions thus become apparent on the interface

$$A_1\left\{\frac{\partial^2\phi_1}{\partial n^2}-B_1\left(\frac{\partial^2\phi_1}{\partial s^2}-\frac{1}{\rho}\frac{\partial\phi_1}{\partial n}\right)\right\}=A_2\left\{\frac{\partial^2\phi_2}{\partial n^2}-B_2\left(\frac{\partial^2\phi_2}{\partial s^2}-\frac{1}{\rho}\frac{\partial\phi_2}{\partial n}\right)\right\} \tag{10}$$

and

$$-A_1\left\{\frac{\partial}{\partial n}(\nabla^2\phi_1)+(1+B)\frac{\partial}{\partial s}\left(\frac{\partial^2\phi_1}{\partial n\,\partial s}\right)\right\}=-A_2\left\{\frac{\partial}{\partial n}(\nabla^2\phi_2)+(1+B)\frac{\partial}{\partial s}\left(\frac{\partial^2\phi_2}{\partial n\,\partial s}\right)\right\} \tag{11}$$

3. INTERFACE STRESS CONDITIONS

In addition to the displacement conditions given above it is necessary that the normal and tangential stresses in both regions be equal on the interface. The value of the normal stress in terms of the stress function is

$$\sigma_n\equiv\frac{\partial^2\phi}{\partial x^2}\cos^2\theta+\frac{\partial^2\phi}{\partial y^2}\sin^2\theta+\frac{\partial^2\phi}{\partial x\,\partial y}\sin 2\theta\equiv\frac{\partial^2\phi}{\partial s^2}-\frac{1}{\rho}\frac{\partial\phi}{\partial n} \tag{12}$$

and similarly the stress tangential to the boundary is

$$\tau_{ns}\equiv\left(\frac{\partial^2\phi}{\partial x^2}+\frac{\partial^2\phi}{\partial y^2}\right)\tfrac{1}{2}\sin 2\theta-\frac{\partial^2\phi}{\partial x\,\partial y}\cos 2\theta\equiv-\frac{\partial^2\phi}{\partial n\,\partial s} \tag{13}$$

Thus the stress equality interface conditions become

$$\frac{\partial^2\phi_1}{\partial s^2}-\frac{1}{\rho}\frac{\partial\phi_1}{\partial n}=\frac{\partial^2\phi_2}{\partial s^2}-\frac{1}{\rho}\frac{\partial\phi_2}{\partial n} \tag{14}$$

and

$$\frac{\partial^2\phi_1}{\partial n\,\partial s}=\frac{\partial^2\phi_2}{\partial n\,\partial s} \tag{15}$$

These conditions may be simplified if, arbitrarily, the equality of the two stress functions and their slopes is imposed at some point (this is always possible, as an addition of any linear function of x and y to either stress function does not alter the stresses). In such a case, as can be easily shown,

$$\phi_1=\phi_2 \tag{16}$$

$$\frac{\partial\phi_1}{\partial n}=\frac{\partial\phi_2}{\partial n} \tag{17}$$

replace conditions (14) and (15).

4. SLAB ANALOGY

It is of interest to compare here the results achieved with some expressions occurring in the theory of thin elastic plates subject to flexure. If M_n represents the bending moment per unit length of a boundary s, and M_{ns} and Q_n the twisting moment and shear force respectively, then the external forces required to support this boundary are a moment $M_n^*=M_n$ and a normal force

$$V^*=Q_n-\frac{\partial M_{ns}}{\partial s}$$

(see Ref. 8). These well-known conditions, when expressed in terms of the lateral

Vol. 2
1960-6

slab deflexion w, become

$$M_n^* = -D\left\{\frac{\partial^2 w}{\partial n^2} + \nu\left(\frac{\partial^2 w}{\partial s^2} - \frac{1}{\rho}\frac{\partial w}{\partial n}\right)\right\} \tag{18}$$

and

$$V^* = -D\left\{\frac{\partial}{\partial n}(\nabla^2 w) + (1-\nu)\frac{\partial}{\partial s}\left(\frac{\partial^2 w}{\partial n\,\partial s}\right)\right\} \tag{19}$$

where D is the flexural rigidity of the slab.

The above relationships show a striking similarity with expressions (8) and (9).

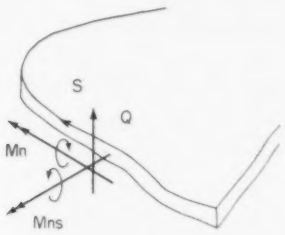

FIG. 3. Edge stress resultants on a slab.

If a problem of a slab with a discontinuity of thickness along a line s is considered, then (excluding of course the local stress-variation effects near such a discontinuity) the relations which have to be satisfied take on the form of the previous interface conditions (10, 11, 16 and 17) with appropriate changes in notation:

$$\phi \to w, \quad A \to D \quad \text{and} \quad B \to -\nu$$

The first two relationships ensure equality of the force resultants while the latter two are simple statements of the continuity of the deflected shape.

From the remarks given above it follows that the method of attack suitable for dealing with interface problems becomes applicable to appropriate slab calculation. It is of interest to note, especially if visualization of the similarity is required, that the region of the two-dimensional-stress problem with a higher elastic modulus corresponds to the slab region with smaller rigidity and vice versa. Further aspects of the analogy are discussed in detail by Southwell[6] and Mindlin[7].

5. DISPLACEMENT CONDITIONS AT A BOUNDARY

If the line AB in Fig. 1 represents, instead of an interface, an external boundary of region 1 for which certain displacements are specified, then the boundary conditions are given directly by relations (8) and (9) with u' and v' representing the imposed boundary displacements and ϕ the stress function defined in region 1. If, for example, the boundary is such that all displacements are suppressed then

$$\frac{\partial^2 \phi}{\partial n^2} - B\left(\frac{\partial^2 \phi}{\partial s^2} - \frac{1}{\rho}\frac{\partial \phi}{\partial n}\right) = 0 \tag{20}$$

and

$$\frac{\partial}{\partial n}(\nabla^2 \phi) + (1+B)\frac{\partial}{\partial s}\left(\frac{\partial^2 \phi}{\partial n\,\partial s}\right) = 0 \tag{21}$$

A comparison of these equations with the expressions for the edge forces on a slab shows that this is directly analogous to a free edge of a slab.

If the boundary tractions are such that the stress function and its gradients can be evaluated from arbitrarily assumed initial values by the usual process of integration, then, by analogy with the slab problem, the above conditions are not only necessary but also sufficient for a unique determination of stresses. In some problems it may happen that displacements are specified on two or more unconnected portions of a boundary. If this is the case, then it is impossible to determine the stress function and its gradients uniquely unless the total resultants of the forces imposed by the displacement boundaries are known. If these are not known, then auxiliary integrals of displacement are required (in a manner similar to the analysis of redundant structures) to determine the boundary values of the stress function.

Such special problems will not be discussed further here as their numerical treatment by the stress-function approach does not appear advantageous.

Vol. 2
1960-6

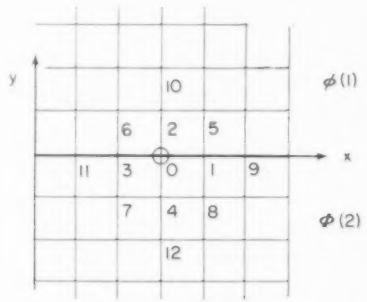

FIG. 4. Straight interface.

6. FINITE-DIFFERENCE TREATMENT

The interface and boundary conditions derived earlier can be expressed in terms of their finite-difference approximations, and the solution to the problem by relaxation (or by direct solution of the simultaneous equations involved) can be carried out. For curved boundaries or interfaces such approximations are somewhat complex, but the frequently encountered straight interface is relatively easy to handle. Let Fig. 4 represent such a straight interface between two regions in which stress functions ϕ and Φ are defined and which have elastic constants A_1, B_1 and A_2, B_2 respectively. The following conditions result from equations (10), (11), (14) and (15), and have to be satisfied on the interface

$$\phi = \Phi$$

$$\frac{\partial \phi}{\partial y} = \frac{\partial \Phi}{\partial y}$$

$$A_1\left\{\frac{\partial^2 \phi}{\partial y^2} - B_1 \frac{\partial^2 \phi}{\partial x^2}\right\} = A_2\left\{\frac{\partial^2 \Phi}{\partial y^2} - B_2 \frac{\partial^2 \Phi}{\partial x^2}\right\}$$

$$-A_1\left\{\frac{\partial^3 \phi}{\partial y^3} + (2+B_1)\frac{\partial^3 \phi}{\partial x^2\, \partial y}\right\} = -A_2\left\{\frac{\partial^3 \Phi}{\partial y^3} + (2+B_2)\frac{\partial^3 \Phi}{\partial x^2\, \partial y}\right\} \qquad (22)$$

and in addition the usual biharmonic equation has to be satisfied by each of the stress functions

$$\nabla^4 \phi = 0$$

$$\nabla^4 \Phi = 0 \tag{23}$$

These conditions can now be written down as their finite-difference approximations in terms of the real and "fictitious" values of the two functions[1] and, by elimination of such "fictitious" values, special equations governing the stress function can be derived for the mesh line on the interface and the two adjacent mesh lines. Although there is nothing novel in such a procedure, the tedious algebra involved justifies the presentation of the special operators involved. These are given in general terms below:

For point O on the interface

$$\begin{aligned}
&\phi_0\left[20+\frac{1}{(A_1+A_2)^2}\{(A_2B_2-A_1B_1)\,8(A_2-A_1)-6(A_2B_2-A_1B_1)^2-4(A_2-A_1)^2\}\right]\\
&\quad+(\phi_1+\phi_3)\left[-8+\frac{4(A_2B_2-A_1B_1)}{(A_1+A_2)^2}\{(A_2B_2-A_1B_1)-(A_2-A_1)\}\right]\\
&\quad+\phi_2\left[-8+\frac{1}{(A_1+A_2)^2}\{4A_1(A_2B_2-A_1B_1)+(A_2-A_1)(8A_2+4A_1)\}\right]\\
&\quad+\Phi_4\left[-8-\frac{1}{(A_1+A_2)^2}\{4A_2(A_2B_2-A_1B_1)+(A_2-A_1)(4A_2+8A_1)\}\right]\\
&\quad+(\phi_5+\phi_6)\left[2-\frac{2}{(A_1+A_2)^2}\{(A_2B_2-A_1B_1)A_1+(A_2-A_1)(A_1+A_2)\}\right]\\
&\quad+(\Phi_7+\Phi_8)\left[2+\frac{2}{(A_1+A_2)^2}\{(A_2B_2-A_1B_1)A_2+(A_2-A_1)(A_1+A_2)\}\right]\\
&\quad+(\phi_9+\phi_{11})\left\{1-\frac{1}{(A_1+A_2)^2}(A_2B_2-A_1B_1)^2\right\}\\
&\quad+\phi_{10}\left(1-\frac{A_2-A_1}{A_2+A_1}\right)+\Phi_{12}\left(1+\frac{A_2-A_1}{A_2+A_1}\right)=0
\end{aligned} \tag{24}$$

For a point O, one mesh line above the interface (suitable change in notation results immediately in a similar equation for a point below the interface)

$$\begin{aligned}
&\phi_0\left(20+\frac{A_2-A_1}{A_2+A_1}\right)-8(\phi_1+\phi_2+\phi_3)\\
&\quad+\phi_4\left[-8+\frac{2}{A_1+A_2}\{A_2B_2-A_1B_1+A_1-A_2\}\right]\\
&\quad+2(\phi_5+\phi_6)+(\phi_7+\phi_8)\left(2-\frac{A_2B_2-A_1B_1}{A_1+A_2}\right)\\
&\quad+\phi_9+\phi_{10}+\phi_{11}+\Phi_{12}\left(1+\frac{A_2-A_1}{A_1+A_2}\right)=0
\end{aligned} \tag{25}$$

From the above operators the finite-difference equations applicable on a rigid boundary follow by making either A_1 or A_2 equal to zero.

The relationships given above have been used with success in a study of dams constructed on foundations with different elastic properties. The full results of this investigation will be presented elsewhere but, to illustrate the application

		15438		12098	10642	9359	8284	7456	6913	6691	6819						
		15432		12092	10627	9340	8270	7451	6917	6686	6820						
		15428	13702	12088	10615	9320	8244	7424	6898	6683	6818		7329				
		15054		11714	10210	8853	7685	6749	6086	5731	5711	6048					
		15052		11712	10211	8863	7711	6790	6134	5771	5732	6049	6754				
		15045	13333	11705	10190	8828	7655	6740	6088	5738	5716	6048	6750				
ϕc																	
		14801		11461	9892	8444	7171	6121	5338	4855	4698	4881					
ϕb		14809		11464	9926	8515	7279	6257	5483	4982	4783	4913					
		14798	13104	11458	9893	8458	7204	6173	5400	4913	4737	4895	5406	6280			
ϕa																	
		14678		11338	9677	8117	6725	5554	4648	4041	3757	3807	4186		4855	(4861)	
		14709		11364	9771	8290	6971	5833	4968	4338	3985	3930	4206		4882	(4866)	
		14691	13026	11351	9721	8205	6858	5723	4834	4216	3890	3876	4193		4864	(4873)	
		14673		11333	9543	7848	6333	5024	3993	3263	2857	2783	3034	3580	4374		
		14740		11390	9729	8171	6774	5571	4589	3846	3356	3132	3196	3590	4413	(4718)	
18855	16706	14713	13107	11373	9650	8055	6619	5388	4393	3655	3189	3011	3136	3586	4399		
				11405	9452	7607	5942	4510	3351	2497	1970	1777	1912	2349		3041	
				11623	9764	8136	6673	5401	4341	3508	2909	2551	2442	2597	3041		
19178	17058	15118	13358	11486	9674	7889	6476	5165	4080	3238	2651	2329	2278	2508	3041	3801	4501
	17386	15389	13499	11625	9827	8156	6699	5316	4193	3286	2601	2139	1904	1903	2157	2726	3411
	17385	15388	13488	11575	9722	7990	6424	5052	3898	2973	2288	1853	1671	1750	2094	2704	3394
	17728	15658	13689	11771	9993	8240	6692	5317	4143	3173	2415	1872	1543	1438	1578	1477	2532
	17724	15647	13657	11708	9830	8071	6472	5054	3848	2858	2097	1576	1294	1254	1476	1422	2502
	18124	15977	13922	11938	10037	8257	6637	5181	3935	2897	2067	1479	1110	976	1077	1389	1846

FIG. 5(a). Stress-function value near the foundation of a dam.
a—E (dam) = E (foundation); *b*—E (dam) = 3 E (foundation) $\nu = 0{\cdot}2$;
c—Rigid foundation, $u = 0$.

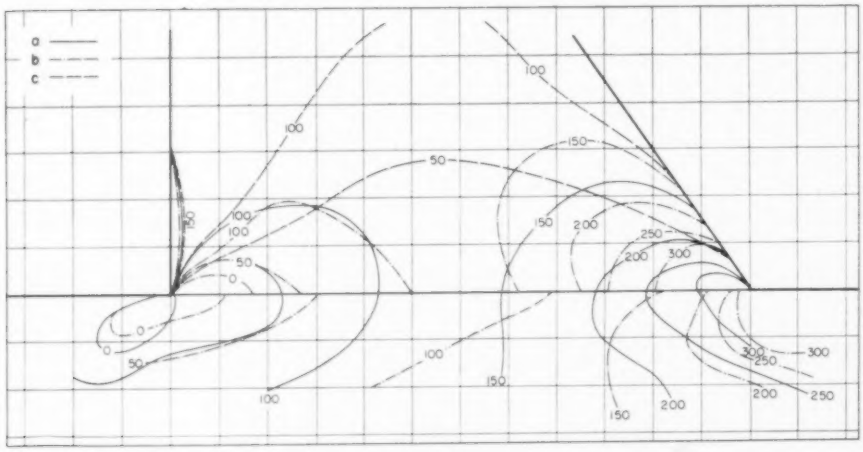

FIG. 5(b). Contour of equal horizontal stress ($\sigma \times 180/wH$).

of the method, Fig. 5(a) shows the values of stress functions obtained for different ratios of the elastic properties of the dam and its foundation and also the contours of equal horizontal stress in the vicinity of the foundation. The values

of the stress function for the case of the same elastic constants are quoted from a previous work by one of the authors,[4] which formed the basis from which the new solutions were derived. The solution of equations was carried out by a relaxation technique which, although more tedious than that involved in a straightforward biharmonic solution (owing to the special patterns involved), showed a reasonable degree of convergence. Stresses plotted in Fig. 5(b) show clearly the discontinuity arising at the interface.

A similar problem has recently been attempted by Lardy[9] and a solution of a dam with radial symmetry resting on a rigid foundation was completed by Allen[10]. The latter used the technique of displacement equations in his computations. It appears to the authors that the technique presented here is advantageous for such cases.

Vol. 2
1960-61

REFERENCES

1. D. N. DE G. ALLEN, *Relaxation Methods*. McGraw-Hill, New York (1955).
2. R. V. SOUTHWELL, *Relaxation Methods in Theoretical Physics*, Vol. II. Clarendon Press, Oxford (1956).
3. L. FOX and R. V. SOUTHWELL, *Phil. Trans.* C **1**, 15 (1941).
4. O. C. ZIENKIEWICZ, *J. Instn. Civ. Engrs.* **27**, 244 (1947).
5. L. FOX, *Proc. Roy. Soc.* A **189**, 535 (1947).
6. R. V. SOUTHWELL, *Quart. J. Mech.* **3**, 257 (1950).
7. R. D. MINDLIN, *Quart. Appl. Math.* **4**, 279 (1946).
8. A. E. H. LOVE, *A Treatise on the Mathematical Theory of Elasticity*. Clarendon Press, Oxford (1926).
9. P. LARDY, "Les Contraintes des Barrages Poids", *Proceedings of the Fourth Congress of the International Association of Bridge Structure Engineering* p. 393. Cambridge (1952).
10. D. N. DE G. ALLEN, L. CHITTY, A. J. S. PIPPARD and R. J. SEVERN, *Proc. Instn. Civ. Engrs.* **5**, 198 (1956).

Int. J. Mech. Sci. Pergamon Press Ltd. 1960. Vol. 2, pp. 102–127. Printed in Great Britain

SOME ANALYTICAL AND EXPERIMENTAL STUDIES OF AXI-SYMMETRIC COLD FORGING AND EXTRUSION—I

H. KUDO*

Aeronautical Research Institute, Tokyo University, Japan

(*Received* 11 *September* 1959)

Summary—(i) In order to obtain upper-bound solutions for the axi-symmetric forging and extrusion of metals following the Mises yield criterion and the Levy–Mises stress–strain-rate relations, two types of admissible velocity fields are examined. The internal rate of energy dissipation associated with them is obtained without numerical integration if the material is assumed perfectly plastic.

(ii) To facilitate the calculation for a specific working problem, the conception of a unit cylindrical deforming region is introduced. The least rates of energy dissipation as determined from the two types of velocity field possible are graphed for individual unit regions having a wide range of dimensions and various frictional boundary conditions.

(iii) An upper-bound solution for problems with Coulomb friction is proposed. This is proved to be a better upper bound than Drucker's in certain cases.

(iv) A modification of upper-bound solutions as determined for a perfectly plastic material, for non-steady working processes of work-hardening material, is proposed.

(v) Several forging and extrusion problems with the tools having flat working surfaces are analysed by dividing the material into several unit regions and by using prepared diagrams of least rate of energy dissipation. These are the compression of a cylinder and an annulus, extrusion, piercing, extrusion-forging and symmetrically opposed extrusion-forging.

(vi) The results for the working pressure either agree with or improve on the analytical results of other investigators. They also agree with the experimental results obtained by others. The most suitable velocity fields well explain the internal deformations and extrusion defects observed hitherto.

1. INTRODUCTION

THE exact mathematical analysis of axi-symmetrical plastic deformation problems, even for rigid–perfectly-plastic materials, is at present possible only when an additional assumption concerning the state of stress is made.[1, 2] Moreover, this analysis is usually very laborious compared with the plane-strain analysis.

It has been shown recently that, by using the Limit Theorems, the analysis of several three-dimensional problems has been greatly simplified, the results being sufficiently accurate for all practical purposes.[3-6]

In many forging and extrusion processes in which most of the work-piece surface is rigidly constrained by the tools, good upper bounds for the working pressure can be obtained easily from considerations of only geometrical configuration; but this is not the case for the lower bounds. In the present paper, therefore, only upper-bound solutions are treated. Instead of obtaining the lower-bound solution, two types of velocity field have been adopted so as to obtain better results. This upper-bound approach has recently been proved very useful in the analysis of plane-strain problems by Johnson[7-10], Johnson and Kudo[11], and Kudo[12].

* Present address: The Government Mechanical Laboratory, 132 Sumiyoshi, Suginami, Tokyo, Japan.

In the present work, the concept of a "unit deforming region" is introduced to reduce the labour of calculation. The worked material is assumed to be non-hardening and rigid–plastic and follows the Mises yield criterion as well as the Levy–Mises stress–strain-rate relations.

Attempts are also made to obtain upper bounds to the working pressure when Coulomb friction between the tools and the material exists and when the material work-hardens.

The most suitable admissible velocity fields and related upper bounds for working pressure are obtained for the compression of a cylinder and an annulus between two flat dies, for extrusion, piercing, non-steady extrusion-forging and symmetrically opposed extrusion-forging of cylindrical billets with flat dies or punches perpendicular to the direction of tool advance.

These results are compared with the experimental results obtained by the author using aluminium, copper, lead and brass, together with those by other investigators.

Vol. 2
1960-61

Experimental work has also been performed to determine the working pressure, the deformation and the onset of the formation of the extrusion-defect in material in various two-orifice extrusion-forgings as well as in closed-die coining. The axi-symmetrical solutions for these problems have not been obtained, but the experimental results are interpreted with the help of results obtained for the corresponding plane-strain problems.

In the final part of the present paper, some results are presented of measurements of the average internal pressure acting on extrusion and coining containers and on the projections of certain coining dies. These results could be used to aid a general understanding of pressure distribution, but this subject is not investigated analytically in the present work.

2. UPPER-BOUND SOLUTION FOR UNIT CYLINDRICAL DEFORMING REGION

To simplify the analysis of complicated problems and to reduce the labours of calculation, the concept of the "unit cylindrical deforming region" analogous to the "unit rectangular deforming region" in plane-strain analysis[12] is used. This region has a rectangular section, Fig. 1, the sides of which are parallel and perpendicular to the axis of symmetry respectively. Two modes of deformation will be considered for this region having an outer radius of unity, inner radius b and height to outer radius ratio of a. In Fig. 1(a) the region is assumed to deform in such a manner that its top surface 13 descends vertically due to an external force with a unit velocity which causes the inner side surface 34 to move inwards as a straight line. The surroundings to this region may be regarded as either a rigid tool or a rigid part of the material, the parts in contact with the outer and bottom surfaces 12 and 24 being at rest. The external body in contact with the inner surface 34 is assumed to move freely only in a radial and horizontal direction.

Another deformation mode is that shown in Fig. 1(b) which differs from the first mode only in that the inner surface does not move whilst the outer surface 12 moves radially outwards, remaining cylindrical. Again, the external body in

contact with the outer surface 12 is assumed to move out freely only in a radial and horizontal direction.

The slip resistance per unit area of boundary between the deforming region and the surrounding body or per unit surface area of tangential-velocity discontinuity is denoted by F or fY, f being termed "the slip-resistance ratio" in the following discussion. Y is the uniaxial yield stress of material. On a perfectly lubricated smooth contact surface between material and tool, f is, of course, zero. On the other hand, on a perfectly rough contact surface or on a surface of velocity discontinuity inside the material, f is equal to $1/\sqrt{3}$ in accordance with the Mises yield criterion.

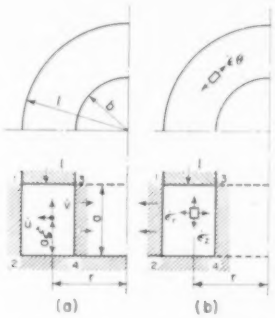

FIG. 1. Unit cylindrical deforming regions.

In the present paper, two types of admissible velocity fields are considered for a unit region. One of them is such that the strain-rate of the material element is independent of its vertical co-ordinate. This type of velocity field has been used extensively in the elementary analysis of axi-symmetrical forging problems and will be referred to henceforth as the parallel velocity field. The surface of velocity discontinuity lies on the boundary of the unit region in this velocity field.

Another type of velocity field considered is shown in Figs. 2, 3 and 4. In these, the unit deforming region consists of two or three annular parts which appear triangular in section. All sides of triangular sections which are lines of velocity discontinuity are assumed to move as straight lines without changing their inclinations. Moreover, the radial velocity component in each part is assumed independent of the z co-ordinate. This means that a straight vertical line in a meridial section of each part remains straight and vertical after deformation. This velocity field will be called the "triangular velocity field".

The internal rate of energy dissipation in these velocity fields is given by

$$\dot{E} = \sqrt{\tfrac{2}{3}}\, Y \int_V (\dot{\epsilon}_r^2 + \dot{\epsilon}_\theta^2 + \dot{\epsilon}_z^2 + \tfrac{1}{2}\dot{\gamma}_{rz}^2)^{\frac{1}{2}}\, dV + Y \int_S f|\dot{s}|\, dS \qquad (1)$$

The first integration is carried out throughout the entire volume of the material which deforms continuously, and the second over the whole surface of velocity discontinuity, both inside the material and on the boundary between the

material and the tool. $\dot{s}$ denotes the rate of relative slip on a discontinuity surface; the other symbols have their usual meanings in plasticity theory.

In the following a non-dimensional magnitude e will be introduced for the unit region.

$$e = \frac{\dot{E}}{\pi Y(1-b^2).1} \tag{2}$$

The denominator of the above formula is a product of Y, the surface area of pressing and the pressing speed on a unit region. This magnitude will be called "the coefficient of internal-energy dissipation". It is to be noted that this quantity remains unchanged if the same unit ring is compressed radially and horizontally on its cylindrical surface, thus resulting in a raising up of its top surface in contact with a rigid external body which moves freely in the vertical direction.

Vol. 2
960-61

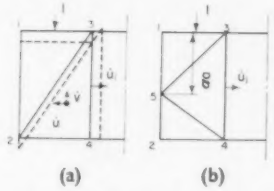

FIG. 2. Triangle velocity fields for unit region of Fig. 1(a).

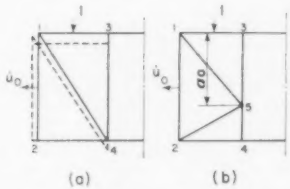

FIG. 3. Triangle velocity fields for unit region of Fig. 1(b).

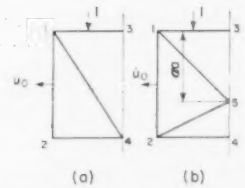

FIG. 4. Triangle velocity fields for unit region of solid cylinder.

(i) *Parallel velocity field*

With the assumptions described above, the admissible parallel velocity field in a unit cylindrical region which deforms according to Fig. 1(a) is

$$\dot{u} = -\frac{1-r^2}{2ar}, \quad \dot{v} = -\frac{z}{a} \equiv -\xi \tag{3}$$

The coefficient of internal-energy dissipation is then obtained by using equation (1) and the expressions for strain-rate,

$$e = M(b) + (f_{13}+f_{24})\,N_1(b)\,\frac{1}{a} + \frac{f_{12}+f_{34}\,b}{1-b^2}\,a \tag{4}$$

$$\left.\begin{aligned} &\text{where} \quad M(b) = \frac{1}{\sqrt{3}}\,\frac{1}{1-b^2}\left[2 - \ln 3 - \sqrt{(3b^4+1)} + \ln\frac{1+\sqrt{(3b^4+1)}}{b^2}\right] \\ &\text{and} \quad N_1(b) = \frac{1}{3}\,\frac{2-b-b^2}{1+b} \end{aligned}\right\} \tag{5}$$

f_{ij} stands for the slip-resistance ratio on boundary surface ij and is assumed to be constant. $M(b)$ approaches infinity as b reduces, and approaches $2/\sqrt{3}$ as b approaches 1.

Similarly, for the deformation mode of Fig. 1(b),

$$\dot{u} = \frac{r^2-b^2}{2ra}, \quad \dot{v} = -\frac{z}{a} \equiv \xi \tag{6}$$

and

$$e = M\left(\frac{1}{b}\right) + (f_{13}+f_{24})\,N_2(b)\,\frac{1}{a} + \frac{f_{12}+f_{34}\,b}{1-b^2}\,a \tag{7}$$

where

$$N_2(b) = \frac{1}{3}\,\frac{1+b-2b^2}{1+b} \tag{8}$$

$M(1/b)$ approaches 1 as b proceeds to zero.

(ii) *Triangular velocity field*

For a simple triangular field such as that shown in Fig. 2(a) which deforms according to the mode of Fig. 1(a), the admissible velocity components in annulus 234 are given by

$$\dot{u} = -\frac{1-b}{2a}\,\frac{1+r}{r}, \quad \dot{v} = \frac{1-b}{2}\,\frac{\xi}{r} \tag{9}$$

The other annulus 123 moves as a rigid body. The volume integration in equation (1) for the present field seems to be impossible to perform analytically and is done using an expansion in polynomial form. It is found that

$$e = \frac{1}{1-b^2}\left\{H_1(b) + K_1(b)\,a^2 + \frac{1}{2\sqrt{3}}\,(1-b)^2(3+b)\,(1+\sqrt{3}f_{24})\,\frac{1}{a} + \frac{1}{2\sqrt{3}}\,[3+b+4\sqrt{3}f_{12}+\sqrt{3}f_{34}(1-b)]\,a\right\} \tag{10}$$

$$\left.\begin{aligned} &\text{where} \quad H_1(b) = \frac{1}{\sqrt{3}}\left[2\ln\frac{1+b}{2b} - b(1-b)\right] \\ &\text{and} \quad K_1(b) = \frac{1}{4\sqrt{3}(1-b)^2}\left[\frac{1}{3}\ln b - \frac{8}{3}\ln\frac{2}{1+b} + \frac{7}{6} - \frac{4}{3}b + \frac{1}{6}b^2\right] \end{aligned}\right\} \tag{11}$$

The above expression for e can be proved to have an accuracy of 1 per cent for typical ranges of a and b. Both $H_1(b)$ and $K_1(b)$ reduce to zero as b approaches unity. $K_1(b)\,a^2$ is negligible for $b \geqslant 0{\cdot}3$ if a is not very much larger than unity.

Vol. 2
1960-6

For the velocity field of Fig. 2(b), the coefficient of internal energy dissipation can be obtained from equation (10). Here, however, the vertical velocity component on the boundary 34 is

$$\dot{v}_{34} = -\frac{1-b^2}{2b}\left(\frac{1-\alpha}{1-b} - \frac{\xi}{1+b}\right) \tag{12}$$

It changes its sign at a point on the boundary for a certain range of α. If it is assumed that there is no sign change in $\dot{v}_{34}$, then, neglecting $K_1(b)\,a^2$

$$e = \frac{1}{1-b^2}\left\{H_1(b) + \frac{3+b}{2\sqrt{3}}\left[2\frac{(1-b)^2}{a} + (1-2\alpha+2\alpha^2)\,a\right] + 2f_{12}\,\alpha a + \tfrac{1}{2}f_{34}[1+3b-2\alpha(1+b)]\,a\right\} \tag{13}$$

By differentiating the above equation with respect to α, the expression for α which minimizes e is obtained, and thence the minimum value of e is found.

For the deformation mode of Fig. 1(b) the admissible velocity field of type Fig. 3(a) in annulus 124 is given by

$$\dot{u} = \frac{1-b}{2a}\,\frac{b+r}{r}, \quad \dot{v} = \frac{1-b}{2}\,\frac{\xi}{r} \tag{14}$$

Summing the volume integral for annulus 124 and the surface integrals for boundaries 12, 24, 34 and 14, the coefficient of internal energy dissipation is

$$e = \frac{1}{1-b^2}\left\{H_2(b) + K_2(b)\,a^2 + \frac{1}{2\sqrt{3}}(1+3b)\left[(1+\sqrt{3}f_{24})\frac{(1-b)^2}{a} + a\right] + \frac{1}{2\sqrt{3}}[4\sqrt{3}f_{34}\,b + \sqrt{3}f_{12}(1-b)]\,a\right\} \tag{15}$$

where
$$H_2(b) = \frac{1}{\sqrt{3}}\left[(1-b) - 2b^2\ln\frac{2}{1+b}\right]$$

and
$$K_2(b) = \frac{1}{4\sqrt{3}\,(1-b)^2}\left(\frac{8}{3}b^2\ln\frac{1+b}{2b} - \frac{1}{3}b^2\ln\frac{1}{b} + \frac{1}{6} - \frac{4}{3}b + \frac{7}{6}b^2\right) \tag{16}$$

$H_2(b)$ and $K_2(b)$ are zero when $b = 0$ and the term $K_2(b)\,a^2$ is negligible for all values of b if a is not much larger than unity.

Similarly, for the velocity field Fig. 3(b),

$$e = \frac{1}{1-b^2}\left\{H_2(b) + \frac{1}{2\sqrt{3}}(1+3b)\left[\frac{2(1-b)^2}{a} + (1-2\alpha+2\alpha^2)\,a\right] + 2f_{34}\,\alpha b a + f_{12}\left[\frac{3}{2} + \frac{b}{2} - \alpha(1+b)\right]a\right\} \tag{17}$$

The above expressions (15) and (17) are in excess by more than 1 per cent because of the use of an approximate expansion for the volume integration in equation (1), where b is near to zero and a is larger than 2.

This volume integration, however, can be performed analytically when $b = 0$, i.e. when the unit region has the form of a solid cylinder [Fig. 4(a)]. In this instance,

$$e = I(a) + \frac{1}{2\sqrt{3}}(1+\sqrt{3}f_{12})a + \frac{1}{2\sqrt{3}}(1+\sqrt{3}f_{24})\frac{1}{a} \tag{18}$$

where

$$I(a) = \frac{1}{\sqrt{3}}\left\{\frac{1}{2}\sqrt{\left(1+\frac{a^2}{4}\right)} + \frac{1}{a}\ln\left[\frac{a}{2} + \sqrt{\left(1+\frac{a^2}{4}\right)}\right]\right\} \tag{19}$$

For the velocity field of Fig. 4(b),

$$e = \alpha I(\alpha a) + (1-\alpha)I[(1-\alpha)a] + \frac{1}{2\sqrt{3}}\left[\frac{2}{a} + (1-2\alpha+2\alpha^2)a + \sqrt{3}f_{12}(3-2\alpha)a\right] \tag{20}$$

The value of α which minimizes equation (20) is $\frac{1}{2}$ when $f_{12} = 0$ and is very nearly unity when $f_{12} = 1/\sqrt{3}$.

(iii) *Comparison of parallel and triangular velocity fields*

When all slip resistances on the boundary surfaces are zero, it is clear that the parallel velocity field yields a lower rate of energy dissipation than does the triangular field. When the slip resistance is $Y/\sqrt{3}$, on at least one boundary plane, the triangular velocity field having the most suitable value of α results in lower values of e over a small range of values of $a/(1-b)$ in the vicinity of unity. Outside this range the parallel field gives better results. It appears that triangular velocity fields consisting of a larger number of annuli would yield lower rates of internal energy dissipation than would the parallel field for a wider range of $a/(1-b)$. This is to be expected by virtue of a similar comparison available from the study of plane-strain velocity fields.[12] In the following analysis, only the simple velocity fields examined above are used.

It is to be noted that all results derived above agree with the corresponding results for plane strain obtained by the author, if b is made unity.

By preparing graphs of the lowest values of e against a for various sets of frictional boundary conditions, using b as a parameter, the numerical calculations associated with each particular metal-working problem are greatly facilitated.

3. UPPER-BOUND SOLUTION UNDER CONDITION OF COULOMB FRICTION

When Coulomb friction exists between the contact surface of a tool and the material, the rate of frictional energy dissipation is usually not determinate because the slip resistance of the frictional stress is unknown. Drucker[13] has suggested that an upper bound for working pressure obtained with the assumption that the surface of Coulomb friction is perfectly rough is also an upper bound for the present case. This obviously leads to an excessive overestimate of the actual working pressure, especially when the coefficient of friction is small.

An alternative upper bound to the mean working pressure on the advancing tool $\bar{p}'_{af}$ is

$$\left.\begin{aligned}\bar{p}'_{af} &= \bar{p}_{ao} + \frac{\bar{F}}{A_a \dot{V}} \int_A \dot{s}_0 \, dA \\ \mu &= \frac{\bar{F}}{\bar{q}'_{f\max}}\end{aligned}\right\} \tag{21}$$

$\bar{p}_{ao}$ is the mean pressure when $\mu = 0$, $\dot{V}$ is the speed of tool advance, $\dot{s}_0$ the actual rate of relative slip when $\mu = 0$. $\dot{s}_0 dA$ has to be integrated over the whole contact surface between the material and the tool. $\bar{F}$ represents the assumed mean slip resistance on the contact surface and $\bar{q}'_{f\max}$ is the highest upper bound for the mean normal pressure on the individual tool surface along which the material flows in one direction. For instance, in the working processes, such as are shown in Fig. 5(a)–(c), $\bar{q}'_{f\max}$ is the upper bound for the mean normal pressure on the top die surface which is perpendicular to the tool advance and is equal to $\bar{p}'_{af}$, whilst in Fig. 5(d) $\bar{q}'_{f\max}$ is applied on the surface of the bottom extrusion die.

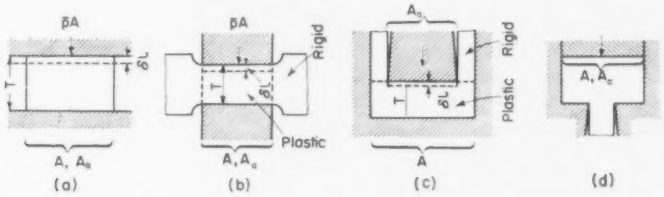

FIG. 5. Several examples of simple working processes to consider the effect of Coulomb friction and work-hardening.

To obtain the relation between $\bar{p}'_{af}$ and μ, for a particular problem, it is necessary first to assume a value of $\bar{F}$ and calculate a value of $\bar{p}_{af}$ using the first equation of (21) and the known values of $\bar{p}_{ao}$ and $\dot{s}_0$. After choosing a proper value for $\bar{q}'_{f\max}$, a corresponding coefficient of friction is calculated from the second equation of (21).

The value of $\bar{p}'_{af}$ can be proved to be an upper bound of $\bar{p}_{af}$ for the value of μ in equations (21) if the assumption is made that on the individual tool surfaces the actual normal pressure q_f does not increase in the direction in which $\dot{s}_0$ increases, as is usually the case. Using this assumption for a contact surface of area A_i,

$$\int_{A_i} \mu q_f \dot{s}_0 \, dA \leqslant \mu A_i \bar{q}_f \bar{\dot{s}}_0 \tag{22}$$

where $\bar{q}_f$ denotes the integral of the mean normal pressure and $\bar{\dot{s}}_0$ the integral of the mean $\dot{s}_0$ over the surface. On the other hand, an inequality for the actual mean working pressure has been suggested by Yamada[14]

$$\bar{p}_{af} \leqslant \bar{p}_{ao} + \frac{1}{A_a \dot{V}} \int_A F \dot{s}_0 \, dA \tag{23}$$

where F stands for the actual frictional stress.

Vol. 2
1960-61

Since $F \leqslant \mu q_f$ and $\bar{q}'_{f_{\max}} \geqslant \bar{q}_f$, it follows from inequalities (22) and (23) that

$$\bar{p}_{af} \leqslant \bar{p}_{ao} + \frac{\mu}{A_a \bar{V}} \sum_i \bar{q}_f \bar{\dot{s}}_0 A_i \leqslant \bar{p}'_{af} \tag{24}$$

An example of the application of equation (21) to the plane-strain compression of a plate between two parallel flat dies [Fig. 5(b)] will be shown below. The actual mean die pressure in relation to μ and the actual rate of slip $\dot{s}_0$ for this problem are known for values of W/T equal to 3 and 7.[15] In the present case, $\bar{q}'_{f_{\max}} = \bar{p}'_{af}$. Consequently, from equation (21),

$$\left.\begin{aligned} \bar{p}'_{af}/2k &= 1/(1-\tfrac{4}{3}\mu), \quad \text{for } W/T = 3 \\ &= 1/(1-\tfrac{24}{7}\mu), \quad \text{for } W/T = 7 \end{aligned}\right\} \tag{25}$$

Fig. 6 indicates that the results given by equations (25) (solid line) locate above the slip-line solution (dotted line) and they are seen to be good approximations to the latter for small values of μ. If instead of the second equation in (21), the frictional stress is assumed to be μq_0 (q_0 is the contact pressure when $\mu = 0$) as were the cases in several of the classical analyses, the resulting mean compressive pressures are such as shown by the dash-dot lines in Fig. 6. These are again good approximations when μ is very small, but are no longer upper bounds when μ becomes large.

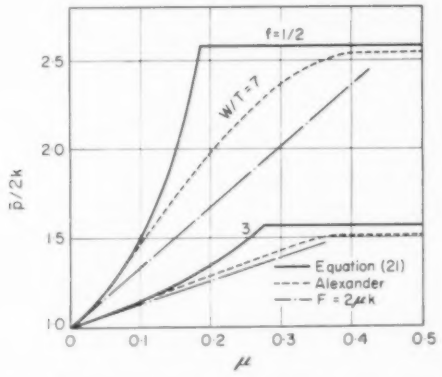

FIG. 6. Proposed upper-bound solution for mean compressive pressure in parallel-die compression accompanied by Coulomb friction.

In general, the exact solutions, i.e. $\bar{p}_{ao}$ and $\dot{s}_0$, for $\mu = 0$ are unknown. Therefore, on calculating the upper bound in Coulomb friction problems, upper bounds for working pressure $\bar{p}'_{ao}$ and relative slip rates $\bar{\dot{s}}'_0$ derived from an admissible velocity field for $\mu = 0$ are used instead of $\bar{p}_{ao}$ and $\bar{\dot{s}}_0$ in equation (21). It is probably true that such a modification would not result in an underestimate of the working pressure.

4. UPPER BOUNDS FOR WORK-HARDENING MATERIALS

A method of obtaining the working pressure for a work-hardening material from a rigid–perfectly-plastic solution has been given by Hill[1] and has been

proved to be effective in extrusion experiments by Johnson[16] and Dodeja and Johnson[17]. This method is used in Part II of this paper for estimating the pressure during steady-state deformations such as extrusion and the piercing of relatively long billets.

A method for the case of non-steady deformation is suggested below. In the examples shown in Fig. 5, the volume of deforming material will be nearly equal to that lying between the top and bottom dies, the type of working shown in Fig. 5(b) being a plane-strain compression.

For simplicity, assumptions are made that the deforming region of material has a height T and a constant cross-sectional area A, and the incremental work done by the tool is uniformly distributed throughout the deforming volume. An additional assumption adopted by Hill will also be made, that the average strain remains unchanged regardless of the work-hardening characteristics of the material used.

Vol. 2
1960-61

For the working problems of Fig. 5, with relatively small initial heights, the deforming material is seen to have been embodied in the deforming volume from the beginning of working. The mean value of the work done per unit volume of the material in the deforming region is given by

$$w_m = \int_0^l \frac{\bar{p}}{T} dl \tag{26}$$

where l denotes the amount of tool advance. On the other hand, for a Levy–Mises material, the yield locus radius which is a function of the total plastic work done on the material

$$Y = \Phi\left(\int Y \, d\bar{\epsilon}\right) \tag{27}$$

or very nearly

$$Y = \Psi\left(\int d\bar{\epsilon}\right) \tag{28}$$

The function Ψ is obtainable directly from the yield stress versus compressive logarithmic strain relation of the material. The term in the parenthesis of equation (28) will be hereafter called total equivalent strain and denoted by $\bar{\epsilon}$.

From the assumptions, the mean total equivalent strain of the deforming material is

$$\bar{\epsilon}_m = \int_0^l \left(\frac{\bar{p}_n}{Y_n}\right) \frac{dl}{T_0 - l} \tag{29}$$

if it is also assumed that the work done by the tool is all converted into plastic work. In equation (29) $\bar{p}_n$ denotes the mean working pressure as determined for the non-hardening material having a constant yield stress Y_n and T_0 the initial height of the deforming region. In the case of the compression of a cylinder between flat smooth dies, equation (29) reduces to the logarithmic compressive strain. If the yield stress Y_m taken from the yield-stress curve of the material corresponding to the logarithmic strain $\bar{\epsilon}_m$, Fig. 7, is taken to be the mean yield stress of the deforming material at a certain stage of working, the mean working pressure $\bar{p}$ can be estimated by $(\bar{p}_n / Y_n) \times Y_m$.

Another type of non-steady deformation is found in the initial stages of the extrusion of a long work-hardening billet, Fig. 8. When the reduction in area is large, it has been found from plane-strain analysis[18] that the rigid–perfectly-plastic solution for the steady state held also for the initial stage of extrusion. In such cases, denoting the depth of the steady-state deforming region by G and assuming that the increment of work done by the tool is distributed uniformly to the material embodied in the instantaneous deforming volume AG, the incremental work done per unit volume of the deforming region is

$$dw_m = (\bar{p} - w_m)\frac{dl}{G} \tag{30}$$

Accordingly,

$$\bar{\epsilon}_m = \frac{\bar{p}_n}{Y_n}(1 - e^{-l/G}) \tag{31}$$

The magnitude of the above equation increases with increasing l, and the Hill[1] steady-state estimate should be used when this estimate exceeds it.

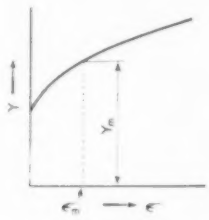

FIG. 7. Relation between mean yield stress and mean total-equivalent strain in non-steady working processes.

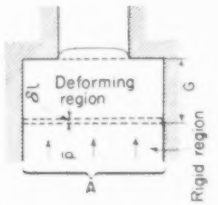

FIG. 8. Initial stage of extrusion process.

A closer approximation for the working of work-hardening materials could be obtained by determining, step by step, the distribution of total equivalent strain in the deforming region using the non-hardening solution.

5. COMPRESSION OF CYLINDER AND ANNULUS

(i) *Compression of solid cylinder*

An upper bound for the mean working pressure for the compression of a solid cylinder, of diameter D_0 and height T, between two flat parallel dies over which Coulomb friction acts, is derived at once using the parallel velocity field

for $\mu = 0$. From equations (7) and (21), e being equal to $\bar{p}/Y$ in the present case, the upper bound is

$$\frac{\bar{p}}{Y} = \frac{\bar{p}'_{af}}{Y} = 1 + \tfrac{1}{3}\mu\frac{D_0}{T} + \frac{1}{9}\left(\mu\frac{D_0}{T}\right)^2 \tag{32}$$

in which the terms of higher order than $(\mu D_0/T)^2$ are neglected.

This expression reduces to Siebel's formula[19] if the third term on the right-hand side is neglected. Moreover, the expression (32) is very close to the formula given by Schroeder and Webster[20] for non-sticking compression.

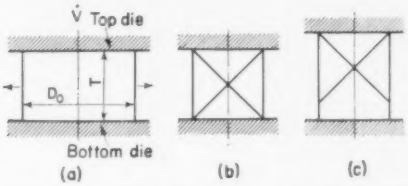

FIG. 9. Compression of cylinder between parallel dies.

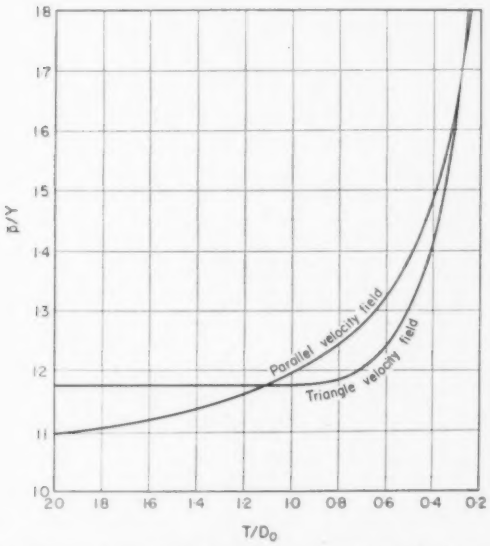

FIG. 10. Upper bound for mean pressure in cylinder compression between rough dies.

For perfectly rough dies, putting $f_{12} = 0$, $f_{13} = f_{24} = 1/\sqrt{3}$, $a = 2T/D_0$ and $b = 0$ in equation (7), the same equation will be obtained as that derived by Schroeder and Webster for the case of complete sticking. For the case of rough dies, however, the triangular velocity field shown in Fig. 9(b) yields better results than the parallel field does for a certain range of T/D_0. Thus, putting $\alpha = 0{\cdot}5$, $f_{12} = 0$ and $a = 2T/D_0$ in equation (20), it becomes

$$\frac{\bar{p}}{Y} = I\left(\frac{T}{D_0}\right) + \frac{1}{2\sqrt{3}}\left(\frac{D_0}{T} + \frac{T}{D_0}\right) \tag{33}$$

Vol. 2
1960-61

where the function I is given by equation (19). Equation (33) takes a minimum value 1·175 at $T/D_0 \simeq 0{\cdot}92$. Therefore, for T/D_0 larger than 0·92, the type of velocity field shown in Fig. 9(c), in which part of the length of the cylinder remains undeformed, gives the minimum upper bound for $\bar{p}/Y$ of 1·18.

In Fig. 10 the upper bounds for the case of rough dies calculated from the above two types of velocity fields are shown. It will be seen that among the velocity fields examined here, the parallel field gives the better results for both large and small values of T/D_0.

The results in Fig. 10 can be applied also to the incipient flow pressure in upsetting an intermediate part of a length of round bar, the other parts being held in die cavities. Some of the experimental results of Kobayashi *et al.*[21] are seen to be closer to the present upper bounds derived from the triangular field than those based on the parallel field.

The buckling type of deformation which is expected for large T/D_0 is not considered in the present paper.

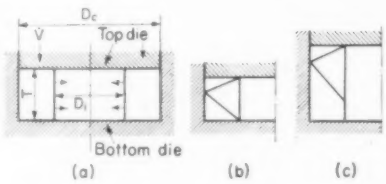

FIG. 11. Compression of annulus in container between parallel dies.

(ii) *Constrained compression of an annulus in a container*

The upper bounds for mean compression pressure over the contact surface between the top die and the material, the outward flow of material being constrained by the container wall, Fig. 11, is obtained directly from equation (4) for the parallel field and equation (10) for the triangular field [Fig. 11(b)], e being equal to $\bar{p}/Y$ in this case. The calculated lowest upper bounds are shown in Fig. 12, in which the surfaces of the tool are assumed either perfectly smooth ($f = 0$) or rough ($f = 1/\sqrt{3}$). For the case of rough tools, the container and the bottom die were assumed to be at rest, the top die moving downwards. In Fig. 12 the solid lines relate to the parallel field and the broken lines to the triangular field. It will be seen from the figure how the compression pressures are affected by the inner–outer-diameter ratio and the height–outer-diameter ratio of the work-piece.

(iii) *Free compression of the annulus*

The problem of the compression of an annulus between two flat parallel dies under the condition of Coulomb friction has been treated by Kunogi[22] and Kudo[23], both using the parallel velocity field (Fig. 13). Assuming the stress and strain distribution to be uniform in the axial direction and the Levy–Mises law to apply, Kunogi has solved the equation of equilibrium by numerical

integration. Kudo has used the upper-bound-approach method and calculated that deformation of the annulus which minimized the total rate of internal energy dissipation, with an assumption that the frictional stress on the contact surface between the tool and material was equal to μY.* Their results showed fair agreement.

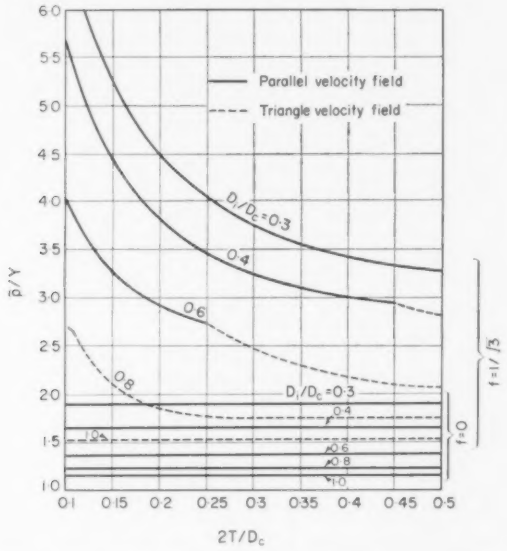

FIG. 12. Upper bound for mean die pressure in compression of annulus in container.

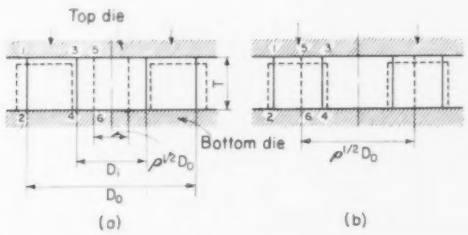

FIG. 13. Compression of annulus between parallel dies.

In the present paper, the upper bounds for the compression pressure ratio for the deformation of an annulus were calculated using the same field as before together with equation (21) which takes account of the effect of Coulomb friction. The results are shown in Fig. 14, in which the co-ordinate $(D_n/D_i)^2$ stands for the square of the no-slip circle diameter to inner diameter ratio. Kunogi's results are reproduced by the crosses in the figure. It will be seen that both results are closer than was hitherto the case, showing that the upper-bound solution is greatly improved by the use of equation (21).

* Equation (14) of Kudo's paper is, incidentally, wrong.

6. EXTRUSION AND PIERCING

(i) *Backwards extrusion of round bar*

To obtain upper bounds for the mean pressure during steady-state backwards extrusion, consider two unit cylindrical deforming regions [1] and [2] inside the material, the radial velocity of their interface 34 being uniform, Fig. 15(a).

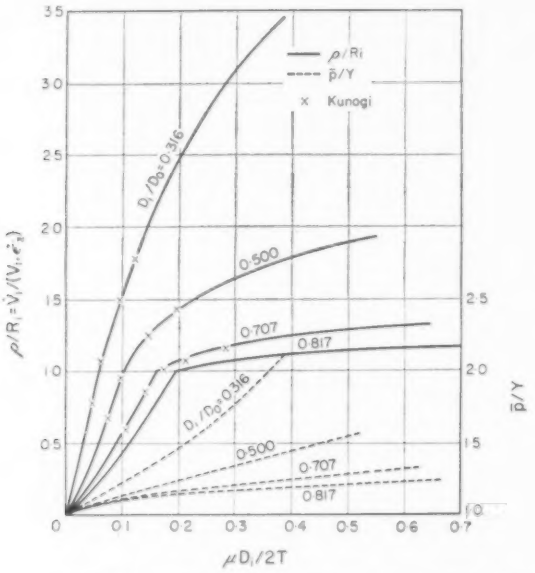

FIG. 14. Upper bound for mean die pressure and most suitable diameter of neutral circle in annulus compression.

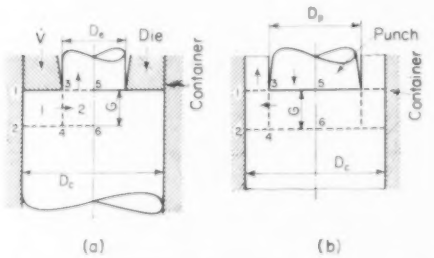

FIG. 15. Assumed configurations of unit cylindrical deforming regions inside material under extrusion or piercing.

The material underlying the deforming region and that which has passed through the die orifice will be regarded as rigid. The modes of deformation of regions [1] and [2] are, then, equivalent to that of the unit regions shown in Fig. 1 (a) and (b) respectively, for the latter b being zero and the direction of deformation being reversed. If the downward speed of the extrusion die is $\dot{V}$, then using the condition of volumetric constancy, the inward radial speed of the boundary 34 becomes $(D_c^2 - D_e^2)\,\dot{V}/4GD_e$ and the speed of the top surface 35

of region [2] is $(D_c^2 - D_e^2)\dot{V}/D_e^2$. For each unit region Table 1 gives the quantities associated with a height–outer-radius ratio a_i, inner–outer-radii ratio b_i, pressing area A_i and speed $\dot{V}_i$. These are analogous to those used in

TABLE 1. HEIGHT–OUTER-RADIUS RATIO, INNER–OUTER-RADII RATIO, PRESSING AREA AND SPEED FOR UNIT CYLINDRICAL DEFORMING REGIONS IN MATERIAL DURING EXTRUSION

Region	Height–outer-radius ratio a_i	Inner–outer-radii ratio b_i	Pressing area A_i	Pressing speed $\dot{V}_i$
[1]	$\frac{2G}{D_c}$	$\frac{D_e}{D_c}$	$\frac{\pi}{4}(D_c^2 - D_e^2)$	$\dot{V}$
[2]	$\frac{2G}{D_e}$	0	$\pi G D_e$	$\frac{(D_c^2 - D_e^2)}{4GD_e}$

Vol. 2
1960-61

plane-strain analysis.[18] The total rate of energy dissipation in a velocity field consisting of several unit regions is given by

$$\dot{E} = Y \sum_i e_i A_i \dot{V}_i \tag{34}$$

from the definition of the coefficient of internal-energy dissipation. In equation (34) e_i stands for the coefficient of energy dissipation in region $[i]$.

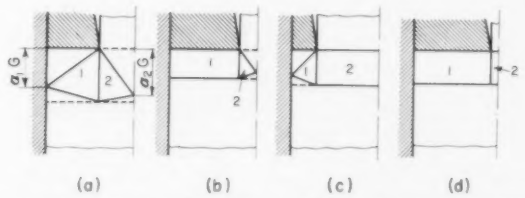

FIG. 16. Possible combinations of parallel and triangle velocity fields inside material under extrusion.

An upper bound for the mean extrusion pressure over the whole sectional area of the billet is obtained from

$$\frac{\bar{p}}{Y} = \frac{\dot{E}}{\pi D_c^2 Y \dot{V}/4} \tag{35}$$

Combining equations (34) and (35) and using Table 1, it is easy to show that

$$\frac{\bar{p}}{Y} = (e_1 + e_2) R \tag{36}$$

where R denotes the fractional reduction in area $[1 - (D_e/D_c)^2]$. Expression (36) is identical with that for plane-strain extrusion obtained by the author.

In the present case, it is necessary to examine the direction of vertical velocity component v on each side of the boundary 34, because the velocity in region [1] may change its direction along the boundary, see equation (12). It is possible to show that for any combination of the velocity fields in Fig. 16, the expressions for e obtained in the preceding section can be substituted into

equation (36) without modification. It is only necessary to take $f_{12} = f_{13} = 0$, $f_{24} = f_{34} = 1/\sqrt{3}$ for region [1] and $f_{34} = f_{35} = f_{46} = 1/\sqrt{3}$ for region [2] when the tool surfaces are smooth. With rough tools, f_{12} and f_{13} must be changed into $1/\sqrt{3}$.

Having available the lowest e versus a diagrams, for each boundary condition and b, it is easy to minimize numerically equation (36) with respect to $a_1(= 2G/D_e)$, for a given reduction in area. The minimization can only be performed analytically when the parallel velocity fields alone are used, as is shown in Fig. 16(d).[24] The minimum upper bounds thus obtained are shown in Fig. 17 by the solid lines. The two curves are represented with errors less than $\pm$ 5 per cent for $R = 0{\cdot}3 \sim 0{\cdot}97$ by

$$\frac{\bar{p}}{Y} = 0{\cdot}88 - 1{\cdot}30\ln(1-R) \quad \text{for smooth tools} \tag{37}$$

and

$$\frac{\bar{p}}{Y} = 1{\cdot}06 - 1{\cdot}55\ln(1-R) \quad \text{for rough tools.} \tag{38}$$

This form of relationship between $\bar{p}/Y$ and R has been confirmed by many experimenters.

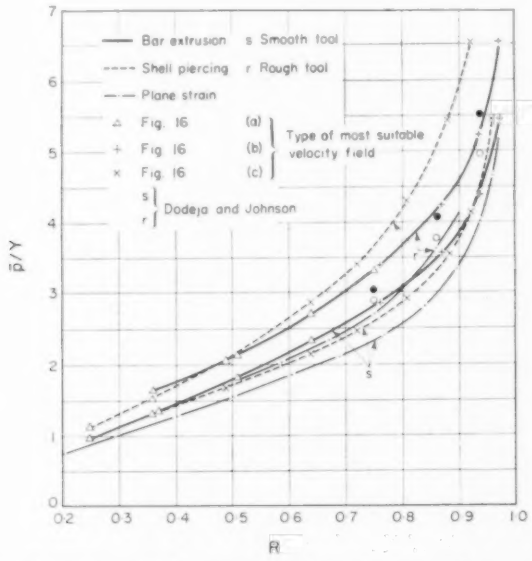

FIG. 17. Upper bounds for mean steady extrusion and piercing pressure.

A comparison is also made in Fig. 17 of the pressures for axi-symmetric and plane-strain extrusion upper bounds, the latter being reproduced from Kudo's upper-bound solution.[18] It is interesting to note that Dodeja and Johnson's[17] results with pure lead in forward extrusion which are represented by hollow circles (smooth tools) and solid circles (rough tools) plot in the close vicinity of the present upper-bound curves. The relations between the upper-bound curves for axi-symmetrical and plane-strain extrusion as derived above also agree with their findings.

The depth of the deforming regions associated with minimized $\bar{p}/Y$ values appear to give an approximate indication of the actual depth of deformation in steady-state extrusions and are shown in Fig. 18 by the solid-line curves. The fact that the depth of the deforming region increases with decreasing reduction larger than about 0·75 (i.e. $D_e/D_c = 0{\cdot}5$) agrees again with the experimental observations. However, the mean depths of deforming regions taken from the experimental results of Thomsen and Frisch[25] are considerably higher than those predicted, the main reason for this discrepancy seeming to be the work-hardening and strain-rate dependent properties of the actual metal. The condition of the existence of dead metal over the extrusion die is found in the present analysis to be $R < 0{\cdot}65$ for smooth tools and $R < 0{\cdot}75$ for rough tools. Stream lines and temperature rise determined from the most suitable velocity field in a frictionless extrusion with $R = 0{\cdot}5$ are illustrated in a paper by Johnson and Kudo[11]. It is interesting to see that the figure is very similar to that found by Thomsen and Frisch experimentally.

Vol. 2
1960-61

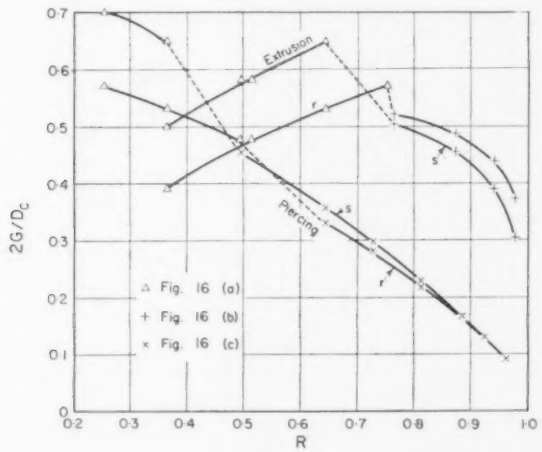

FIG. 18. Most suitable depths of deforming region in extrusion and piercing.

(ii) *Backwards piercing of circular tubes*

Upper-bound solutions for the backwards piercing of long billets [Fig. 15(b)] are obtainable by the same method as that used for the extrusion problem. In the present case it is assumed for simplicity that no frictional work is done between the extruded material and the container wall.

The process of axi-symmetric extrusion and piercing are quite similar as is the case in the plane-strain problem. In particular, the flow of material in both processes should be identical when the extrusion die and the piercing punch are both perfectly rough and the diameters of die orifice and punch are equal, the only difference being the sign of the velocity. In such cases, an upper bound for the mean piercing pressure with a reduction R can be derived

from the upper bound $(\bar{p})_e$ for mean extrusion pressure with a reduction $(1-R)$ by

$$(\bar{p})_p = \frac{R}{1-R}(\bar{p})_e \tag{39}$$

The above equation indicates that the mean extrusion die and piercing punch pressures are identical. For other cases, it is similarly easy to obtain results using the previous method.

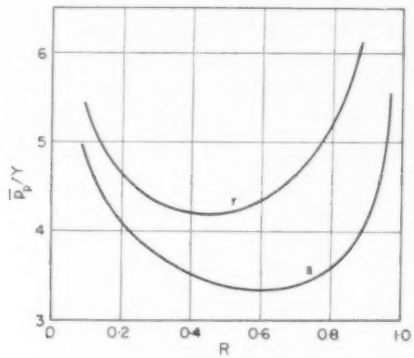

FIG. 19. Upper bounds for mean steady piercing punch pressure.

The calculated results are shown in Fig. 17. Comparison of the present results and those previously obtained with only the parallel velocity field[24] shows that the former is much better, especially for small reductions. It is interesting to note that the upper bounds for lubricated extrusion and piercing with an identical reduction do not differ by more than 8 per cent for the whole range of reduction examined. This confirms the experimental results with non-circular extrusion orifices and multi-hole dies.[17, 26] On the other hand, with rough tools they are equal only when $R = 0{\cdot}5$. The upper bound for piercing increases more steeply than that for extrusion as the reduction increases. This fact indicates the importance of good lubrication for the impact extrusion of thin-walled tubes.[27] The results in Fig. 17 may be expressed as

$$\frac{\bar{p}}{Y} = 0{\cdot}66 - 1{\cdot}41\ln(1-R), \quad \text{for smooth tools} \tag{40}$$

and

$$\frac{\bar{p}}{Y} = 0{\cdot}42 - 2{\cdot}41\ln(1-R), \quad \text{for rough tools} \tag{41}$$

for the range $0{\cdot}3 < R < 0{\cdot}96$ with an accuracy of ± 5 per cent.

The upper bound for the mean punch pressure plotted against the reduction exhibits a minimum, Fig. 19. This has been observed by other investigators.[28, 29] The condition for the formation of a false head over the whole of the punch surface as revealed by the present upper-bound analysis is $R < 0{\cdot}4$ for smooth tools and $R < 0{\cdot}6$ for rough. This agrees approximately with Kunogi's observation.

The depth of the deforming region in steady-state piercing is also shown in Fig. 18, and is again seen to decrease with increasing reduction for $R > 0{\cdot}25$.

7. EXTRUSION-FORGING

In this section round-bar extrusion and hollow cylinder piercing from comparatively short slugs are treated. Two-way extrusion and piercing having a symmetrical geometry with respect to a plane perpendicular to the direction of working will also be included.

(i) *Extrusion-forging of circular bar having end flange*

When a comparatively short slug is extruded, Fig. 20(a), or at the final stage of long-billet extrusion, the whole volume of material between the extrusion die and the bottom flat die comprises the deforming region, the process no longer being one of steady-state. Upper bounds for such processes

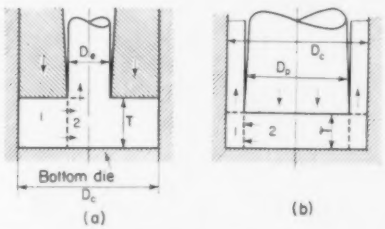

FIG. 20. Assumed configurations of unit regions inside material under extrusion- or piercing-forging.

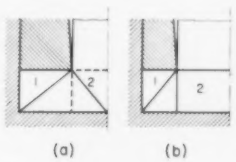

FIG. 21. Other possible combinations of velocity fields than those of Fig. 16.

can be obtained by regarding the non-deforming material underneath the deforming region in Fig. 15(a) to be a rigid bottom die. In the present problem, however, f_{24} and f_{46} should be taken as zero for smooth tools. Table 1 is valid also for the present case, the instantaneous length T of the slug being substituted for G. $\bar{p}/Y$ is determined uniquely from equation (36) using the lowest e versus a diagrams. It is to be noted that the velocity fields shown in Fig. 21 give better results than those in Fig. 16 for certain geometrical configurations when the bottom die is smooth. The type of velocity field shown in Fig. 21(a) explains the phenomenon of surface-skin inclusion on the slug bottom which is known empirically.[30]

(ii) *Cavity formation*

To investigate the cause of cavity formation on the bottom surface which is usually observed on slugs extruded to an extreme degree, a velocity field, shown in Fig. 22(a), similar to that used in the plane-strain analysis by Johnson[9]

and the author[18] is examined. Assuming that the part of the material above the discontinuity surface 37 is rigid, a coefficient of internal-energy dissipation for this velocity field is obtained by substituting $f_{34}=0$, $f_{12}=1/\sqrt{3}$ and $f_{24}\equiv f_{46}$ in equation (15), thus

$$e=\frac{1}{1-b^2}\left\{H_2(b)+K_2(b)\,a^2+\frac{1}{2\sqrt{3}}(1+3b)\left[(1+\sqrt{3}f_{46})\frac{(1-b)^2}{a}+a\right]\right.$$
$$\left.+\frac{1}{2\sqrt{3}}(1-b)\,a\right\} \qquad (42)^*$$

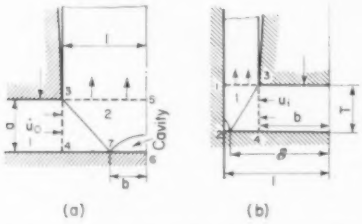

FIG. 22. Triangle velocity fields which result in cavity-formation during extrusion- or piercing-forging.

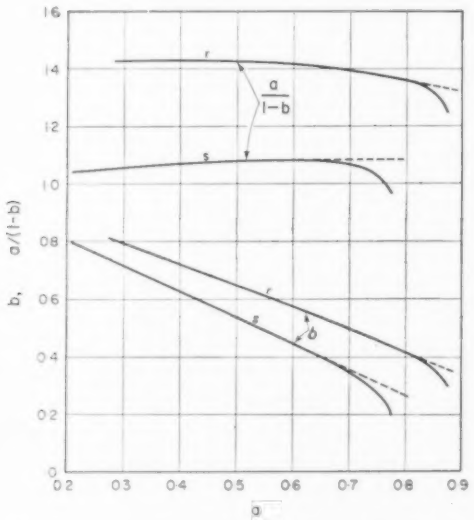

FIG. 23. Most suitable dimension of bottom cavity during extrusion-forging.

Neglecting the term $K_2(b)\,a^2$ and differentiating the above equation with respect to b, the relation between the inclination $a/(1-b)$ of surface 37 and a, which makes e a minimum, is obtained as shown in Fig. 23. The corresponding

* This coefficient of energy dissipation is applicable only to the radial compression of the region and not to the reverse case, i.e. the vertical compression.

values of the inclination in the plane-strain analysis[8] were 1·00 and 1·414 for smooth and rough tools respectively. It is to be noted that, as has been mentioned already, the expression (42) is fairly accurate only for b larger than, say, 0·2.

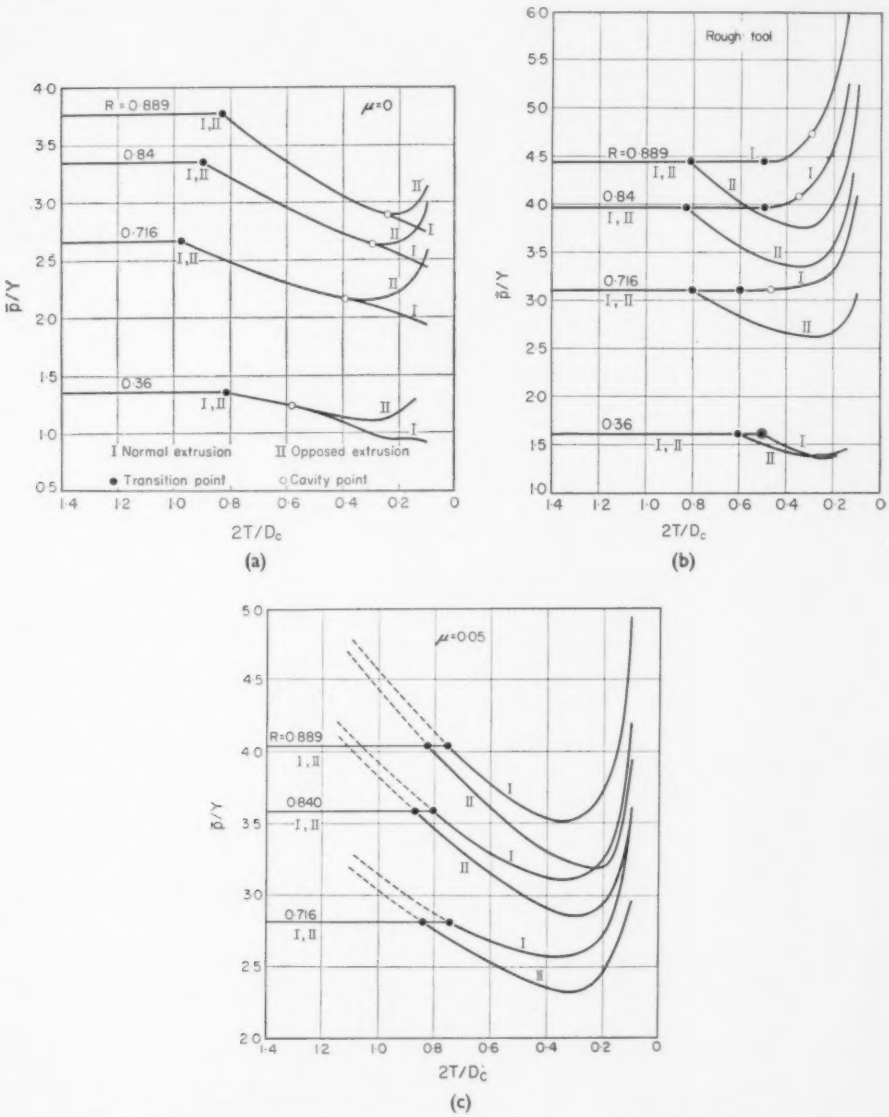

FIG. 24. Upper bounds for mean working pressure during extrusion-forging in relation to slug thickness: (a) smooth tool; (b) rough tool (backwards extrusion); (c) $\mu = 0{\cdot}05$.

In order to predict the beginning of cavity formation, comparisons are made between the minimum value of e given by equation (42) and that derived from the usual velocity field having no cavity, and it is found that the former yields

a lower value for $a < 0{\cdot}73$ when the tool is smooth and for $a < 0{\cdot}88$ when the tool is rough. This indicates a possibility that the diameter of the cavity is of finite size from the beginning.

The upper bounds for $\bar{p}/Y$ are plotted against $2T/D_c$ for several reductions in Fig. 24 by the solid-line curves I, in which the solid circle indicates the transition point between the steady and non-steady processes whilst the hollow circle indicates the beginning of cavity formation. When the tool is smooth, it is seen that the working pressure decreases with $2T/D_c$ in the non-steady region while the opposite is the case when the tool is rough. The upper bounds for working pressure are also calculated for $\mu = 0{\cdot}05$ and are shown in Fig. 24(c). The occurrence of a minimum in the curves agrees with the general tendencies of the autographic diagrams obtained in many experiments with lubricated tools.

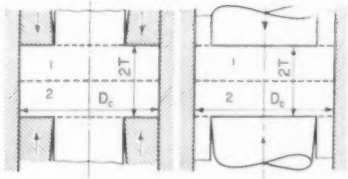

FIG. 25. Symmetrically opposed extrusion- or piercing-forging.

(iii) *Opposed extrusion forging of circular bar having an intermediate flange*

In Fig. 25(a), a symmetrically opposed two-way extrusion is illustrated. For a long billet the process would be identical with that which occurs in the usual extrusion. For a short billet, all the material between the two dies should deform plastically. In such cases, the whole process can be considered to be composed of two identical extrusion-forgings with perfectly smooth flat bottom dies. Consequently, when a smooth tool is used, the $\bar{p}/Y$ versus $2T/D_c$ relations in the one-way and opposed extrusion-forgings should be identical if cavity formation does not occur and if the total length of the remaining slug is represented by $2T$, Fig. 24(a), curves II.

Whether the tool is either perfectly or imperfectly rough, it is necessary to assume that the container is allowed to move freely in order to maintain complete symmetricality of the process. For such cases, the upper bound for working pressure is easily obtained in the same manner as before and is shown in Fig. 24(b) for a perfectly rough tool and in Fig. 24(c) for $\mu = 0{\cdot}05$ by the curves II. It is evident from the figures that the steady to non-steady transition point occurs at a larger $2T/D_c$ value than that of the one-way extrusion when friction exists.

Another difference between the one-way and opposed extrusion-forgings will be seen from the comparison of curves I and II in Fig. 24(a) for very small $2T/D_c$. This is due to the fact that the cavity is allowed to form in the former case whilst this is usually not so in the latter instance. This fact suggests that if the energy required to develop a crack inside the material is relatively small, as is the case for brittle or severely work-hardened material, a crack would

appear in the centre of the material during the opposed extrusion-forging when $2T/D_c$ is smaller than the values indicated by the hollow circle points in Fig. 24. Indeed, this kind of crack was found in experiments with aluminium and copper, as will be reported in Part II of the present work.

(iv) *Piercing-forging of a cylindrical container*

This problem is analysed in the same manner as that used for the extrusion-forging of a circular bar. Corresponding to the velocity field for cavity formation shown in Fig. 22(a), a type of velocity field for region [1] as shown in Fig. 22(b), which results in a lifting-up of the bottom corner of the slug, is examined. The coefficient of internal energy dissipation for this field is, from equation (10), given by

$$e = \frac{1}{1-\epsilon^2}\left[H_1(\epsilon)+\frac{1}{2\sqrt{3}}(1-\epsilon)^2(3+\epsilon)(1+\sqrt{(3)}f_{24})\frac{b}{a\epsilon}\right.$$
$$\left.+\frac{1}{2\sqrt{3}}\left(4+4\sqrt{(3)}f_{12}\frac{\epsilon^2}{b^2}\right)\frac{a\epsilon}{b}\right] \qquad (44)$$

where $\epsilon \equiv b/\delta$. This coefficient of energy dissipation is applicable only to the radial compression of the region, not to the reversed case, i.e. the vertical compression. The most advantageous inclination $a/(\delta-b)$ of the surface of velocity discontinuity 24 can be obtained without difficulty when $f_{12}=0$. In Fig. 26 the result is shown for $f_{12}=f_{24}=0$. From the figure, the value of a at the initiation of lifting up for a given b is also read off by regarding δ as equal to 1. This well explains the defects on the bottom corner of pierced cups which have been reported by Fukui *et al.*[27] and others.

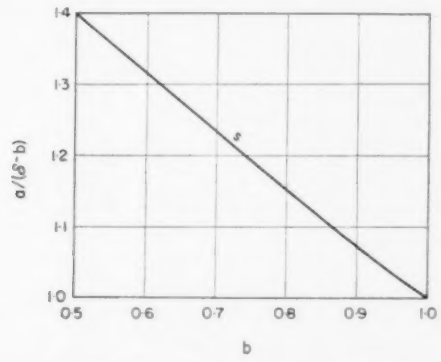

FIG. 26. Most suitable dimension of edge defect during piercing-forging with smooth tool.

The upper bounds for the working pressures are shown in Figs. 27 by the solid-line curves. The solid and hollow circles in the figures have the same meaning as those used in Fig. 24.

(v) *Opposed piercing-forging of hollow cylinders having an intermediate base*

A symmetrically opposed piercing-forging as shown in Fig. 25(b) can be treated similarly. The results are shown in Fig. 27 by solid lines II. It is to be

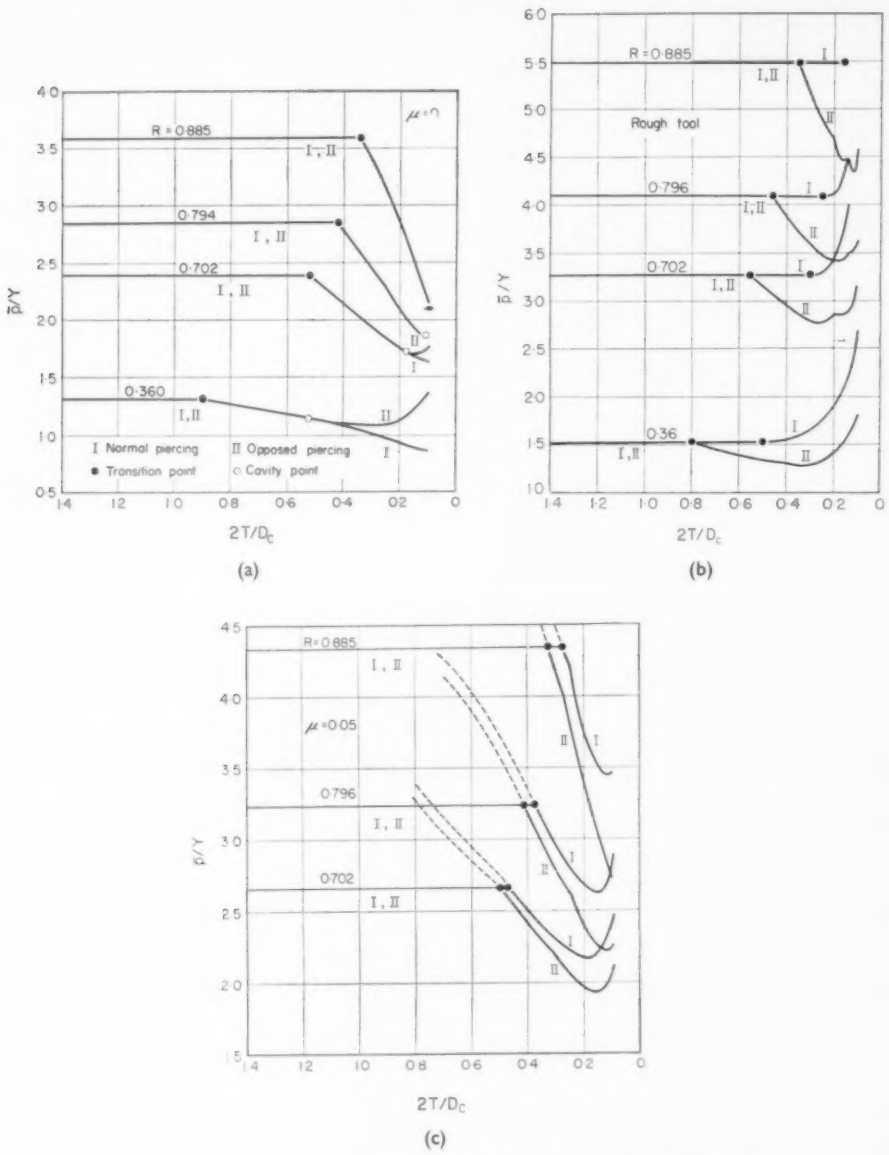

FIG. 27. Upper bounds for mean working pressure during piercing-forging in relation to slug thickness: (a) smooth tool; (b) rough tool (backwards piercing); (c) $\mu = 0{\cdot}05$.

noted that a velocity field analogous to that suggested by Johnson[8] in his study on gudgeon-pin manufacture would give better results when $2T/D_c$ is very small. Such a velocity field, as Johnson has pointed out, results in a circumferential groove round the outer surface of the cylinder at its middle height, the defect actually being observed in manufacture.

REFERENCES

1. R. Hill, *The Mathematical Theory of Plasticity*. Clarendon Press, Oxford (1950).
2. R. T. Shield, *Proc. Roy. Soc.* A**233**, 267 (1955).
3. R. T. Shield and D. C. Drucker, *J. Appl. Mech.* **20**, 453 (1953).
4. R. T. Shield, *Quart. Appl. Math.* **13**, 27 (1955).
5. E. Levin, *Quart. Appl. Math.* **13**, 133 (1955).
6. E. W. Ross, *J. Appl. Mech.* **23**, 244 (1956).
7. W. Johnson, *Third U.S. National Congress on Applied Mechanics* p. 571, Over-estimates of loads for some two-dimensional forging operations (1958).
8. W. Johnson, *Appl. Sci. Res., Hague* 8A, 52 (1959).
9. W. Johnson, *Appl. Sci. Res., Hague* 8A, 228 (1959).
10. W. Johnson, *Proc. Inst. Mech. Engrs., Lond.* **173**, 61 (1959).
11. W. Johnson and H. Kudo, *Int. J. Mech. Sci.* **1**, 175 (1960).
12. H. Kudo, *Int. J. Mech. Sci.* **1**, 57 (1960).
13. D. C. Drucker, *J. Appl. Mech.* **21**, 71 (1954).
14. Y. Yamada, *Kikai-no-Kenkyu, Tokyo* **10**, 621 (1958). (In Japanese.)
15. J. M. Alexander, *J. Mech. Phys. Solids* **3**, 233 (1955).
16. W. Johnson, *J. Inst. Met.* **85**, 403 (1956).
17. L. C. Dodeja and W. Johnson, *J. Mech. Phys. Solids* **5**, 281 (1957).
18. H. Kudo, *Int. J. Mech. Sci.* **1**, 229 (1960).
19. E. Siebel, *Stahl u. Eisen, Düsseldorf* **43**, 1295 (1923).
20. W. Schroeder and D. A. Webster, *J. Appl. Mech.* **16**, 289 (1949).
21. S. Kobayashi, R. Herzog, J. T. Lapsly and E. G. Thomsen, *Trans. Amer. Soc. Mech. Engrs.* B**81**, 228 (1959).
22. M. Kunogi, *Rep. Sci. Res. Inst., Tokyo* **30**, 63 (1954). (In Japanese, with English summary.)
23. H. Kudo, *Proceedings of the 5th Japanese National Congress on Applied Mechanics* p. 75, An analysis of plastic compression deformation of lamella between rough plates by the energy method (1955).
24. H. Kudo, *Proceedings of the 7th Japanese National Congress on Applied Mechanics* p. 57, A computation of required pressure for extrusion-forging circular shells (1957).
25. E. G. Thomsen and J. Frisch, *Trans. Amer. Soc. Mech. Engrs.* **80**, 117 (1958).
26. J. Frisch and E. G. Thomsen, *Trans. Amer. Soc. Mech. Engrs.* B**81**, 207 (1959).
27. S. Fukui, H. Kudo and J. Seino, *Rep. Inst. Sci., Tokyo* **11**, 91 (1957).
28. E. Siebel and E. Fangmeier, *Mitt. K.-Wilh.-Inst. Eisenforsch.* **13**, 29 (1931).
29. M. Kunogi, *Trans. Japan Inst. Mech. Engrs.* **22** IV, 429 (1957). (In Japanese.)
30. C. E. Pearson, *The Extrusion of Metals*. Chapman and Hall, London (1944).

Vol. 2
1960-61

Int. J. Mech. Sci. Pergamon Press Ltd. 1960. Vol. 2. pp. 128–130. Printed in Great Britain

TEST OF CYLINDRICAL SHELLS IN THE PLASTIC RANGE*

A. M. Freudenthal and M. P. Bieniek
Civil Engineering Department, Columbia University, New York

(*Received* 28 *April* 1960)

Summary—Experiments determining the plastic deformation undergone by cylindrical shells having one end fixed and the other free, when subject to internal pressure, are reported and show that certain theoretical analyses lead to erroneous conclusions.

In recent papers[1, 2] dealing with the problem of thin cylindrical shells under internal pressure strained beyond the elastic limit, various simplifying assumptions have been made with respect to the deformational response of the material, in order to establish the analytical approach to the problem. The diversity of assumptions has necessarily resulted in a diversity of solutions; these differ, however, mainly in the deformed shape of the cylinder and in the resulting bending moments near a fixed or free end, while for long cylinders the ultimate (bursting) pressure is practically independent of this shape.

The purpose of the tests reported in the present paper was to obtain an experimental basis against which the validity of different assumptions might be checked. The cylinder with one clamped and one free end was selected as instructive experimentally as well as analytically. The tests extended over a fairly wide range of deformation (up to about 15 per cent) and are thus fairly representative of the total range of deformational behavior, from purely elastic to "plastic collapse" conditions. It should be noted that no quantitative measures and observations were taken, such as relations between pressure and deformation. The objective of these tests was an essentially qualitative investigation of the kinematics of the deformation of the cylinder of an elastic–plastic material with sharp yield-point and, considering the unavoidable, very small strain-hardening.

The shells, with dimensions shown in Fig. 1, were machined out of a solid mild-steel bar so that the fixed-end condition could be achieved without the imposition of initial or residual stresses or local changes of mechanical properties. The leather gasket closing the upper end of the cylinder and supported by the compression plate of a large testing machine, with a clearance of 10^{-3} to 2×10^{-3} in. that was carefully maintained during the test, provided the proper boundary condition at the free end. The internal pressure was produced with the aid of an oil pump.

The deformational response of the material is defined by the following properties: modulus of elasticity $E = 29{\cdot}00 \times 10^6$ lb/in^2, sharply defined

* This research was supported by the United States Air Force under Contract AF 33(616)-6112, monitored by the Materials Laboratory, Wright Air Development Center, Wright-Patterson Air Force Base, Ohio.

yield-point stress $\sigma_0 = 24 \times 10^3$ lb/in^2, average strain-hardening modulus $H = 0{\cdot}36 \times 10^6$ lb/in$^2 \simeq 0{\cdot}0125E$ up to strains of $\epsilon = 3{\cdot}6 \times 10^{-2}$.

Elastic and small plastic deformations were measured with the aid of strain-gages; beyond the range of applicability of strain-gages, micrometer screws were used.

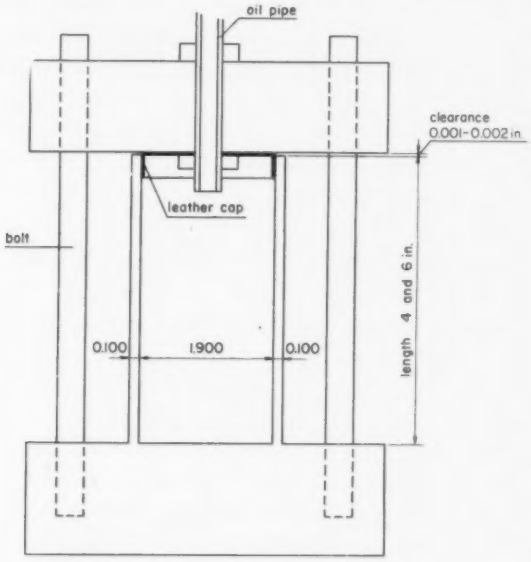

FIG. 1. Tested cylinder.

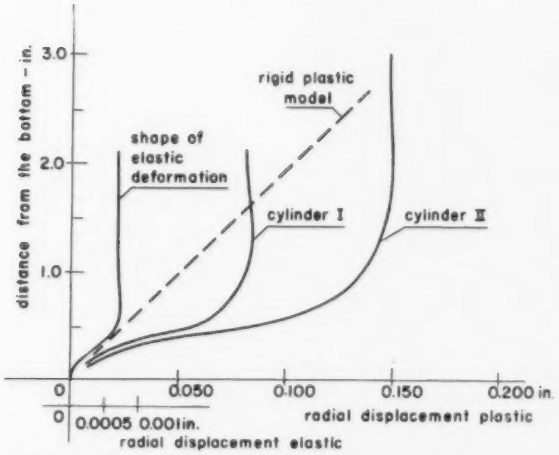

FIG. 2. Radial displacements of tested cylinders.

Typical diagrams of the measured radial displacements along a generatrix of the cylinder as obtained in tests on two cylinders are presented in Fig. 2, and compared with the theoretical deflections of an ideal elastic cylinder (thin full line) and of a rigid–plastic cylinder. Fig. 3 shows a photograph of a longitudinal section of one of the deformed cylinders.

Vol. 2
1960-61

The following conclusions seem justified on the basis of the test results.

(1) The assumption of rigid–plastic behavior of the shell, which implies a conical shape of the deformed cylinder, does not produce an approximation of the real deformed shape of the cylinder.

(2) The replacement of solid walls in bending by an idealized "sandwich" structure does not seem to represent a satisfactory approximation of the real behavior of such walls. The sandwich-type walls (similarly as ideal I-section of beams) imply plastic bending concentrated in narrow rings, while in these tests regions of plastic bending spread over relatively large portions of the longitudinal cross-sections.

(3) The consideration of the elastic deformations seems to be necessary in order to reproduce the behavior of the cylinders of the type tested. This applies to circumferential strains as well as to bending strains.

(4) Even a very mild strain-hardening ($H \approx 0{\cdot}01E$) significantly affects the deformed shape of the cylinder and invalidates the deformed shape resulting from the assumption of rigid–plastic behavior. It is the strain-hardening effect (for circumferential strains) that causes the approximately uniform radial displacements of the upper parts of the walls.

Since in sufficiently long shells the ultimate pressure does not significantly depend on the end-conditions, this pressure will be almost unaffected by discrepancies between the assumed and the real shape of the deformed shell. In short shells, however, such discrepancy will lead to significant differences between the ultimate pressures associated with the different assumptions of deformation response.

Acknowledgement—The assistance of Professor R. A. Heller in the performance of the experiments is gratefully acknowledged.

REFERENCES

1. P. G. HODGE, JR., *J. Appl. Mech.* **21**, 336 (1954); **23**, 73 (1956).
2. E. T. ONAT, *Quart. Appl. Math.* **13**, 63 (1955).

Vol. 2
1960-

Vol. 2
1960-61

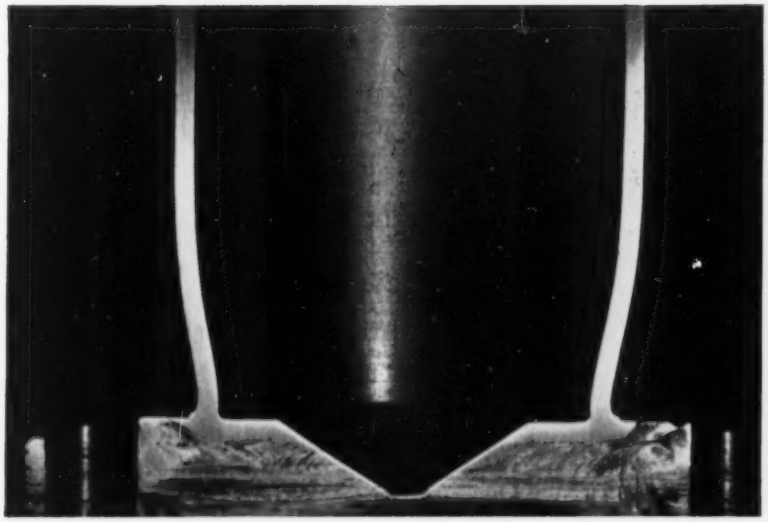

FIG. 3. Longitudinal section of the deformed cylinder.

Vol. 2
1960-

Int. J. Mech. Sci. Pergamon Press Ltd. 1960. Vol. 2, pp. 131–133. Printed in Great Britain

LETTERS TO THE EDITOR

Note on stresses in bolts in a bolted bracket

(*Received* 25 *June* 1960)

SHAFFER[1] reviews the conventional (elastic) analysis[2] of the forces in bolts of a bolted bracket subjected to a moment, and extends the analysis to plastic conditions in the bolts. The original analysis and its extension are based on the assumption that bracket and anchorage are both rigid. Neither the conventional analysis nor the extension due to Shaffer takes account of the real conditions in the bolts. There is an initial load in each bolt due to tightening. By accident or by design this load may even exceed the original yield load of the bolt material.

Vol. 2
1960-61

If the mating parts of a joint subjected to an external tensile load and clamped by a bolt under initial tension are rigid or approximately so, the load in the bolt is either the initial load due to tightening or the applied load, whichever is the greater. If the applied load is greater than the initial load, the joint is open. While this condition need not represent collapse, it almost invariably represents failure.

The situation is not essentially different in bolts clamping a bracket against a pure moment, as discussed by Shaffer. Loading to the level discussed by Shaffer opens the joint and therefore cannot be tolerated in most assemblies. It is not even desirable to absorb an emergency overload in this way, since the plastic strain so engendered will leave the joint permanently open when the load returns to its normal lower level.

A rational design procedure is one based on obtaining in the bolts a predetermined initial tension which exceeds the expected applied load (whether due to a moment or to direct tension) by a properly chosen safety margin. The bolt may be intentionally tightened to an initial load which causes it to yield and work-harden appreciably. The applied load may then be set at a level commensurate with the raised yield strength of the bolt. By designing the bolt to yield in the shank and not in the threads it is, in principle, possible to pre-tension the bolt to any stress up to the ultimate tensile stress of the bolt material. The applied load that could then be sustained would be greater than that pictured by Shaffer, and yet would not cause opening of the joint.

The practical limits to which the bolt may be tensioned and subsequently loaded are governed by the rather variable nature of the relation between the tightening torque applied to the bolt (or nut) and the resulting initial tension.

School of Engineering
The University of Auckland
New Zealand

A. L. TITCHENER

REFERENCES

1. B. W. SHAFFER, *Int. J. Mech. Sci.* **1**, 135 (1960).
2. A. VALLANCE and V. L. DOUGHTIE, *Design of Machine Members* p. 162. McGraw-Hill, New York (1951).

Professor Shaffer's comments (26 *July* 1960): The effect of initial tightening is important in the general analysis of the bolted-bracket problem, but so are the effects of gaskets, spring washers and relative stiffness of the bracket and its support. All these effects were purposely omitted from the original paper because their inclusion would have complicated the analysis and thereby be contrary to the presentation of an introductory elastic–plastic analysis of a problem familiar to most design engineers.

One may extend the present analysis to include the aforementioned effects. The extension would show that if the effect of an applied bending moment is less than that caused by initial tightening, the stresses in the bolts are unaffected by the external load. On the other hand, if the effect of the applied bending moment is greater than that caused by initial tightening, a new set of equations would be required to describe the stress in the bolts. The new set of equations may be derived by an analysis similar to the one presented in the present paper.

BERNARD W. SHAFFER

Department of Mechanical Engineering
College of Engineering
New York University
University Heights
New York 53, *N.Y.*

Vol. 2
1960-

Criticism of "Small vibrations of thin incomplete circular rings"

(*Received* 24 *April* 1960)

PROFESSOR ARCHER has presented a fundamental contribution to the classical theory of the vibration of circular beams (Vol. 1, No. 1, p. 45). Recently, I had the opportunity of discussing this work with him and it appears that several comments of an elucidative nature are in order.

The eigenvalue problem treated in the paper's Appendix, although a member of a general class, is not contained in many standard reference texts. The difference exists in that the eigenvalues, λ_n^2, are coefficients of $y - y'' = \{N[y(\theta)]\}$ rather than simply $y(\theta)$. Equations of this type are discussed by such authors as Crandall[1] and Collatz[2]. Thus, the eigenvalue expansion and orthogonality properties necessary for equations (21) and (27) are contained within the framework of a general theory. In addition I was unable to establish the positive definiteness of $M_{2m}(y) = \lambda^2 N_{2n}(y)$, necessary so that the λ_n^2 are real and greater than zero as has been assumed.

It is noticed that the author separates the eigenvalues into three distinct regions:

$$0 < \lambda_{n1}^2 < 0{\cdot}113401 < \lambda_{n2}^2 < 17{\cdot}6366 < \lambda_{n3}^2 < \infty$$

This results from the solution of (A-4) which may be reduced to a cubic equation, the roots of which depend upon its discriminant[3] Δ. From this it follows that λ_{n1}^2 and λ_{n3}^2 yield eigenvectors of the type (A–6) which correspond to $\Delta < 0$. For $\Delta > 0$, the eigenvectors assume the form (A-5) and correspond to

the λ_{n2}^2. If $\Delta = 0$, the solutions assume still a third form,

$$y(\theta) = A_1 \cos \sigma_1 \theta + (A_2 + A_3 \theta) \cosh \sigma_{23} \theta + B_1 \sin \sigma_1 \theta + (B_2 + B_3 \theta) \sinh \sigma_{23} \theta$$

This matches the condition $\lambda_n^2 = 0{\cdot}113401$ or $17{\cdot}6366$.

Continuing with the discussion of the Appendix, I would assume that the third paragraph from the end alludes to the possible multiplicity of the eigenvalues, in which case more than one mode shape is possible for a particular natural frequency.

An interesting contribution of this work is in the use of (19) as a solution to (6) and (18). Although a similar procedure was introduced by Mindlin and Goodman[4], whom the author cites, a variation of their method is used. The selection of $F(\theta)$ as the ring's statical deflection, rather than a polynomial as suggested in reference (4), presents some physical insight into the method. The total solution, (19), may now be viewed as consisting of two components. A homogeneous eigenvalue part superimposed upon a nonhomogeneous quasi-static solution. This method finds its direct counterpart in the treatment of linear, nonhomogeneous differential equations for which general and particular solutions are sought.

Another point of interest is in the use of the same damping constant for both the radial and tangential motions of the ring. Although this may not be physically achievable, the aculeated fact remains, a solution through the use of separation of variables is possible only if this assumption is made.

My final comment is concerned with the obvious typographical error which appears in equation (9), in which w^2 is written instead of the intended ω^2.

IRVING U. OJALVO

Department of Engineering Mechanics
College of Engineering
New York University

REFERENCES

1. S. H. CRANDALL, *Engineering Analysis* Sections 5.2 and 5.3. McGraw-Hill, New York (1956).
2. L. COLLATZ, *Eigenwertprobleme und Ihre Numerische Behandlung*. Chelsea (1948).
3. R. S. BURLINGTON, *Mathematical Tables and Formulas* (3rd Ed.) p. 7. Handbook (1958).
4. R. L. MINDLIN and L. E. GOODMAN, *J. Appl. Mech.* **17**, 377 (1950).

Vol. 2
1960-61

Int. J. Mech. Sci. Pergamon Press Ltd. 1960. Vol. 2, pp. 134–135. Printed in Great Britain

BOOK REVIEWS

MORTON ALPERIN and GEORGE P. SUTTON (Editors): **Advanced Propulsion Systems.** Pergamon Press, New York, 1959. 237 pp., 42s.

THIS book consists of papers presented at a symposium in Los Angeles at the end of 1957. They range widely over the field of propulsion, from jet and rocket engines using enriched fuels to ion rockets and plasma jets, and from the liquid propellants of the present to such potential sources of energy as nuclear reactors, free radicals and solar heating. One paper discusses human hazards of space flight; another discusses whether electrostatic generators may be suitable for converting mechanical to electrical energy for ion propulsion systems. Two others deal with direct power conversion.

Such diversity leads inevitably to unevenness in content and presentation. Some of the papers which look furthest into the future do no more than offer suggestions. Others, no less advanced, give the impression that a full-scale engine could be designed almost immediately. Those authors who deal with development of existing engines clearly know their possibilities, but tend to ask questions rather than answer them. Anyone who is directly concerned with this work will find little that is new to him, but the research worker in fluid dynamics or engineering physics might find ideas for new projects.

The otherwise excellent production of the book is marred by an incredible number of typographical errors.

FRANCIS CHEERS

J.-B. O. SNEEDEN: **Applied Heat for Engineers** (3rd Ed.). Blackie, Glasgow, 1959. 380 pp., 25s.

THE first edition of Dr. Sneeden's book was issued in 1947 and at that time deservedly received favourable press comment and review. In this extended third edition, the first fifteen chapters are identical with those of the first edition and are, therefore, now outdated, both in the factual data given and in the style of presentation. It is unfortunate that the opportunity for a certain amount of revision was not taken, and a book more suited to the needs of present-day students so produced.

In a very short chapter allocated to "Pressure and its Measurement" the author concludes by briefly dealing with mechanical engine indicators, whilst optical and modern electronic instruments are ignored and considered beyond the scope of his book. On the other hand, in the next, lengthy chapter, "Thermometry" is comprehensively treated and includes a great deal of information regarding practice and instrumentation in this field.

The Preface states that greater emphasis has been placed upon the application of principles rather than on theoretical and experimental proofs. Nevertheless, a clear exposition of the fundamentals of thermodynamics is most essential for all young engineering students and the main weakness and source of criticism of this book lies in the archaic presentation and treatment of these fundamentals. In comparison with other contemporary publications, the failure to revise this section is most regrettable.

The added chapter on refrigeration forms a useful addition but its layout could be improved.

For university students in the first year of an engineering degree course, this book is far from adequate, but for those at Technical Schools and those reading for the examination in Applied Heat of some of the professional institutions it should prove entirely satisfactory.

G. C. BRIGGS

J. CLENDINNING: **Principles of Surveying** (2nd Ed.). Blackie, Glasgow, 1960. 376 pp., 30s.

THE second (1959) edition of Mr. Clendinning's *Principles and Use of Surveying Instruments* was recently reviewed in this journal,* and the book presently reviewed, which forms the companion volume, has also now been issued in its second edition. In its original form the book gave a concise outline of the fundamentals of surveying and in particular formed a useful primer for student use. The main criticism which could be made of this first edition was that no treatment was given of field astronomy, whilst there were some omissions in the section on aerial surveying, the reason for this being that these items were not then present in the syllabus of the Associate Membership of the Institution of Civil Engineers. The Institution's syllabus has been amended and Mr. Clendinning has taken the opportunity in this second edition to add to the scope of his original text by covering the additions to the syllabus.

The second edition contains eighteen chapters, the first twelve being taken from the 1950 edition and forming Part I. In the two appendices to this part, notes are given *inter alia* on the Wiesbach triangle and on the adjustment of braced quadrilaterals; in addition, brief comment is made of the slotted templet method of plotting air surveys. The last six chapters, which comprise Part II of the new edition, are completely new and give a fairly full treatment of field astronomy, including observations of latitude, longitude and azimuth. The treatment is modern, making use of the *Star Almanac* exclusively, and the additional text is lucidly written. In its new edition this book can be confidently recommended to students and engineers.

S. RAYMOND

* S. RAYMOND, *Int. J. Mech. Sci.* **1**, 400 (1960).

Vol. 2
1960-61

PAPERS TO BE PUBLISHED IN FUTURE ISSUES

F. Leckie and E. Pestel: Transfer-matrix fundamentals

B. M. Botros: Residual stresses in cold ironed tubes

H. Kudo: Experimental and theoretical investigation into axi-symmetrical extrusion and forging—II

F. Kozin and J. L. Bogdanoff: On the statistical analysis of the motion of some simple two-dimensional linear vehicles moving on a random track

D. Jortner, J. F. Osterle and C. F. Zorowski: An analysis of cold strip rolling

R. S. Benson and W. A. Woods: The energy content of exhaust pulses in the exhaust system of a supercharged two-stroke-engine model

J. H. Horlock and R. I. Lewis: Shear flows in straight-sided nozzles and diffusers

S. L. Lee and P. Ballesteros: Uniformly loaded rectangular plate supported at the corners

O. C. Zienkiewicz and R. W. Gerstner: The method of interface stress adjustment and its uses in the solution of some flame elasticity problems

P. Montague: Load distribution in overhead stranded conductors

H. Lippmann, O. Mahrenholtz and W. Johnson: Thin elastic strips at large deflexions

E. Volterra: A second approximation of the method of internal constraints and its applications to problems of plates and bars

J. C. Maltbaek: The influence of a concentrated mass on the free vibrations of a uniform beam

Int. J. Mech. Sci. Pergamon Press Ltd. 1960. Vol. 2, pp. 137–167. Printed in Great Britain

TRANSFER-MATRIX FUNDAMENTALS

F. LECKIE* and E. PESTEL†

(*Received* 10 *February* 1960)

Summary—In the past ten years several authors[1-11] have developed the method of transfer matrices for the vibration and stability analysis of complicated elastic systems. This paper is an attempt to generalize and unify the method, and it is hoped that as a result many further problems‡ will fall within the scope of this method. We shall limit our discussion to the natural vibration of elastic systems, but once this has been established it is possible to extend the method to cover forced vibrations and statics.

Vol. 2
1960-61

1. THE STATE VECTOR AND THE TRANSFER MATRIX

THE state vector at a point i of an elastic system is a column vector whose components are the generalized displacements of the point i, and the corresponding generalized forces. In the simple case of a spring–mass system the generalized displacement at point i is simply the linear displacement x_i and the corresponding generalized force is the direct force T_i in the spring. In this special case, the state vector $\mathbf{z}_i$ has the two components x_i and T_i and in matrix notation $\mathbf{z}_i$ has the form

$$\mathbf{z}_i = \begin{bmatrix} x \\ T \end{bmatrix}_i$$

Another more complicated case is that of a beam with longitudinal and flexural elasticity. The three displacements are the longitudinal displacement u, the lateral displacement w and the slope ψ, the corresponding forces being the longitudinal force T, the shear force Q and the bending moment M. The state vector in this case is

$$\mathbf{z}_i = \begin{bmatrix} u \\ w \\ \psi \\ \cdots \\ M \\ Q \\ T \end{bmatrix}_i$$

* University of Cambridge, England.
† Institute of Mechanics, Technical University, Hanover, Germany.
‡ For a complete coverage of the problems treated so far by transfer matrices see Ref. 12.

We should note that a displacement and its corresponding force are in positions which are symmetrical about the centre of the column. The advantage of this arrangement is that it gives rise to matrices symmetrical about the cross diagonal.

Having defined the state vector, we define the transfer matrix as the matrix which relates two state vectors at different positions in the elastic system, i.e.

$$\mathbf{z}_{i+1} = \mathbf{F}_i \mathbf{z}_i$$

where $\mathbf{F}_i$ is the transfer matrix. Obviously, if there are n components in the column matrix the transfer matrix is square and of order n. When i and $i+1$ are different points of a continuous system the transfer matrix relating the state vectors at those points is known as a field matrix. Other occasions arise when a discontinuity in either force or displacement occurs; then the transfer matrix relating the state vectors on either side of the discontinuity is known as a point matrix.

An example of a field matrix, which can be found very easily by statics and simple strength of materials, is that for a massless beam with longitudinal and flexural elasticity [Fig. 1(a)]. The matrix relation between the state vectors at the extremities of a beam of length l is given by

$$\begin{bmatrix} u \\ -w \\ \psi \\ M \\ Q \\ T \end{bmatrix}_{i+1} = \begin{bmatrix} 1 & 0 & 0 & 0 & 0 & l/AE \\ 0 & 1 & l & l^2/2EI & l^3/6EI & 0 \\ 0 & 0 & 1 & l/EI & l^2/2EI & 0 \\ 0 & 0 & 0 & 1 & l & 0 \\ 0 & 0 & 0 & 0 & 1 & 0 \\ 0 & 0 & 0 & 0 & 0 & 1 \end{bmatrix} \cdot \begin{bmatrix} u \\ -w \\ \psi \\ M \\ Q \\ T \end{bmatrix}_i \tag{1}$$

where AE is the longitudinal stiffness and EI the flexural stiffness. The convention for positive displacement and force is indicated in Fig. 1(a), and the sign of w is negative so that all the elements of the field matrix may be positive.

The point matrix relating the state vectors left and right of the point mass m_i [Fig. 1(b)] is given by

$$\begin{bmatrix} u \\ -w \\ \psi \\ M \\ Q \\ T \end{bmatrix}_i^R = \begin{bmatrix} 1 & 0 & 0 & 0 & 0 & 0 \\ 0 & 1 & 0 & 0 & 0 & 0 \\ 0 & 0 & 1 & 0 & 0 & 0 \\ 0 & 0 & 0 & 1 & 0 & 0 \\ 0 & m_i\omega^2 & 0 & 0 & 1 & 0 \\ -m_i\omega^2 & 0 & 0 & 0 & 0 & 1 \end{bmatrix} \cdot \begin{bmatrix} u \\ -w \\ \psi \\ M \\ Q \\ T \end{bmatrix}_i^L \tag{2}$$

where ω is the angular frequency of the free vibration, and when the beam is

supported by a spring of stiffness k [Fig. 1(c)] the matrix relation is

$$\begin{bmatrix} u \\ -w \\ \psi \\ M \\ Q \\ T \end{bmatrix}_i^R = \begin{bmatrix} 1 & 0 & 0 & 0 & 0 & 0 \\ 0 & 1 & 0 & 0 & 0 & 0 \\ 0 & 0 & 1 & 0 & 0 & 0 \\ 0 & 0 & 0 & 1 & 0 & 0 \\ 0 & -k & 0 & 0 & 1 & 0 \\ 0 & 0 & 0 & 0 & 0 & 1 \end{bmatrix} \cdot \begin{bmatrix} u \\ -w \\ \psi \\ M \\ Q \\ T \end{bmatrix}_i^L \tag{3}$$

These point matrices are found by using equilibrium equations. Many other examples of transfer matrices have been compiled in a catalogue.[12, 13]

Vol. 2
1960-61

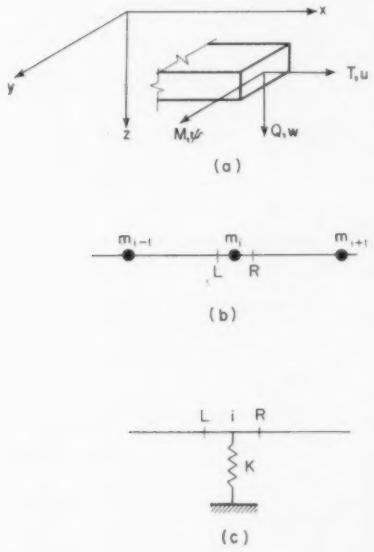

FIG. 1.

2. THE USE OF TRANSFER MATRICES AS AN ELIMINATION PROCESS

We shall illustrate the procedure with reference to the simply supported beam (Fig. 2) in plane bending vibrations, following the well-known Myklestad technique of replacing the distributed mass of the beam by a number of concentrated masses.* Since the field and point matrices for a massless beam and a concentrated mass are already known, we have the relations

$$\mathbf{z}_1^L = \mathbf{F}_1 \mathbf{z}_0 \quad \text{and} \quad \mathbf{z}_1^R = \mathbf{P}_1 \mathbf{z}_1^L \quad \text{so that} \quad \mathbf{z}_1^R = \mathbf{P}_1 \mathbf{F}_1 \mathbf{z}_0$$

* This is done here only for simplicity's sake. Elastic systems with continuous mass distribution offer no basic difficulty when treated by the transfer-matrix method.

Similarly we find that

$$\mathbf{z}_2^L = \mathbf{F}_2\mathbf{P}_1\mathbf{F}_1\mathbf{z}_0 \quad \mathbf{z}_2^R = \mathbf{P}_2\mathbf{F}_2\mathbf{P}_1\mathbf{F}_1\mathbf{z}_0$$

and so on, so that the state vectors at all points along the beam can be calculated in terms of the state vector $\mathbf{z}_0$, and in particular we have the relation between $\mathbf{z}_5$ and $\mathbf{z}_0$,

$$\mathbf{z}_5 = \mathbf{F}_5\mathbf{P}_4\mathbf{F}_4\mathbf{P}_3\mathbf{F}_3\mathbf{P}_2\mathbf{F}_2\mathbf{P}_1\mathbf{F}_1\mathbf{z}_0 = \mathbf{A}\mathbf{z}_0 \tag{4}$$

Written in full this relation is,

$$\begin{bmatrix} -w \\ \psi \\ M \\ Q \end{bmatrix}_5 = \begin{bmatrix} a_{11} & a_{12} & a_{13} & a_{14} \\ a_{21} & a_{22} & a_{23} & a_{24} \\ a_{31} & a_{32} & a_{33} & a_{34} \\ a_{41} & a_{42} & a_{43} & a_{44} \end{bmatrix} \cdot \begin{bmatrix} -w \\ \psi \\ M \\ Q \end{bmatrix}_0$$

Applying the boundary conditions $w_0 = M_0 = w_5 = M_5 = 0$, we find that

$$a_{12}\psi_0 + a_{14}Q_0 = 0$$

$$a_{32}\psi_0 + a_{34}Q_0 = 0$$

from which we obtain the frequency condition

$$\begin{vmatrix} a_{12} & a_{14} \\ a_{32} & a_{34} \end{vmatrix} = 0$$

the determinant being known as the frequency determinant. In practice the frequency determinant is plotted for different values of angular frequency, zero values of the determinant corresponding to the natural frequencies of the system.

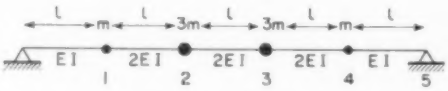

FIG. 2.

In the example we have chosen, we note that $w_0 = M_0 = 0$ so that the first and third columns of the matrices are multiplied by zero, and consequently it is unnecessary to compute these columns. Hence equation (4) may be rewritten in the form,

$$\mathbf{z}_5 = \mathbf{F}_5\mathbf{P}_4\mathbf{F}_4\mathbf{P}_3\mathbf{F}_3\mathbf{P}_2\mathbf{F}_2\mathbf{P}_1\overline{\mathbf{F}}_1\mathbf{v}_0$$

where $\overline{\mathbf{F}}_1$ is the matrix $\mathbf{F}_1$ with the first and third columns missing, and $\mathbf{v}_0$ is the column matrix consisting of the unknowns ψ and Q at the point 0. In general, if the problem is described by an ordinary differential equation of nth order, the initial column vector contains $n/2$ unknowns.

Vol. 2
1960-

Returning to the example under discussion, the dimensionless form of the transfer matrix for a massless beam of length l and flexural rigidity EI is

$$\begin{bmatrix} -\bar{w} \\ \bar{\psi} \\ \bar{M} \\ \bar{Q} \end{bmatrix}_{i+1} = \begin{bmatrix} 1 & 1 & \frac{1}{2} & \frac{1}{6} \\ 0 & 1 & 1 & \frac{1}{2} \\ 0 & 0 & 1 & 1 \\ 0 & 0 & 0 & 1 \end{bmatrix} \cdot \begin{bmatrix} -\bar{w} \\ \bar{\psi} \\ \bar{M} \\ \bar{Q} \end{bmatrix}_i$$

where

$$\bar{w} = w/l, \quad \bar{\psi} = \psi, \quad \bar{M} = \frac{l.M}{EI}, \quad \bar{Q} = \frac{l^2 Q}{EI}$$

and the point matrix for the mass m is given by

$$\begin{bmatrix} -\bar{w} \\ \bar{\psi} \\ \bar{M} \\ \bar{Q} \end{bmatrix}_i^R = \begin{bmatrix} 1 & 0 & 0 & 0 \\ 0 & 1 & 0 & 0 \\ 0 & 0 & 1 & 0 \\ \frac{m\omega^2 l^3}{EI} & 0 & 0 & 1 \end{bmatrix} \cdot \begin{bmatrix} -\bar{w} \\ \bar{\psi} \\ \bar{M} \\ \bar{Q} \end{bmatrix}_i^L$$

An efficient layout for multiplication of matrices on the desk computer is shown below, the field and the point matrices being combined into a convenient form (known as shifted column)[14,15] which eliminates unnecessary writing. On the right-hand side the numerical calculation for $m\omega^2 l^3/EI = 0{\cdot}1$ is reproduced. The matrices are multiplied by multiplying the columns of the matrix on top by the rows of the matrix to the side, and the matrix thus found is in a convenient position to be multiplied further. In the first multiplication the values for w_1, ψ_1 and M_1, which are continuous over point 1, are found by multiplying in the standard manner; the value of Q_1^R however is found by multiplying the column vector

$$\begin{bmatrix} -\bar{w}_0^L \\ \bar{\psi}_0^L \\ \bar{M}_0^L \\ \bar{Q}_0^L \\ \cdots \\ -\bar{w}_1^L \end{bmatrix}$$

by the bottom row

$$\begin{bmatrix} 0 & 0 & 0 & 1 & \frac{\omega^2 m l^3}{EI} \end{bmatrix}$$

It can be readily checked that this procedure gives the same result as multiplying by first the field and then the point matrix.

Vol. 2
1960-61

$$\begin{bmatrix} 0 & 0 \\ 1 & 0 \\ 0 & 0 \\ 0 & 1 \end{bmatrix} \quad \begin{bmatrix} \bar{\psi} \\ \bar{Q} \end{bmatrix}_0 = \mathbf{z}_0$$

$$\downarrow$$

$$\left[\begin{array}{cccc:c} 1 & 1 & \frac{1}{2} & \frac{1}{6} & 0 \\ 0 & 1 & 1 & \frac{1}{2} & 0 \\ 0 & 0 & 1 & 1 & 0 \\ 0 & 0 & 0 & 1 & \frac{\omega^2 m l^3}{EI} \end{array}\right] \rightarrow \begin{bmatrix} & \\ & \\ & \\ & \end{bmatrix} \quad \begin{bmatrix} \bar{\psi} \\ \bar{Q} \end{bmatrix}_0 = \mathbf{z}_1^R$$

$$\downarrow$$

$$\left[\begin{array}{cccc:c} 1 & 1 & \frac{1}{4} & \frac{1}{12} & 0 \\ 0 & 1 & \frac{1}{2} & \frac{1}{4} & 0 \\ 0 & 0 & 1 & 1 & 0 \\ 0 & 0 & 0 & 1 & \frac{3\omega^2 m l^3}{EI} \end{array}\right] \rightarrow \begin{bmatrix} & \\ & \\ & \\ & \end{bmatrix} \quad \begin{bmatrix} \bar{\psi} \\ \bar{Q} \end{bmatrix}_0 = \mathbf{z}_2^R$$

$$\downarrow$$

$$\left[\begin{array}{cccc:c} 1 & 1 & \frac{1}{4} & \frac{1}{12} & 0 \\ 0 & 1 & \frac{1}{2} & \frac{1}{4} & 0 \\ 0 & 0 & 1 & 1 & 0 \\ 0 & 0 & 0 & 1 & \frac{3\omega^2 m l^3}{EI} \end{array}\right] \rightarrow \begin{bmatrix} & \\ & \\ & \\ & \end{bmatrix} \quad \begin{bmatrix} \bar{\psi} \\ \bar{Q} \end{bmatrix}_0 = \mathbf{z}_3^R$$

$$\downarrow$$

$$\left[\begin{array}{cccc:c} 1 & 1 & \frac{1}{4} & \frac{1}{12} & 0 \\ 0 & 1 & \frac{1}{2} & \frac{1}{4} & 0 \\ 0 & 0 & 1 & 1 & 0 \\ 0 & 0 & 0 & 1 & \frac{\omega^2 m l^3}{EI} \end{array}\right] \rightarrow \begin{bmatrix} & \\ & \\ & \\ & \end{bmatrix} \quad \begin{bmatrix} \bar{\psi} \\ \bar{Q} \end{bmatrix}_0 = \mathbf{z}_4^R$$

$$\downarrow$$

$$\left[\begin{array}{cccc:c} 1 & 1 & \frac{1}{2} & \frac{1}{6} & 0 \\ 0 & 1 & 1 & \frac{1}{2} & 0 \\ 0 & 0 & 1 & 1 & 0 \\ 0 & 0 & 0 & 1 & 0 \end{array}\right] \rightarrow \begin{bmatrix} a_{12} & a_{14} \\ a_{22} & a_{24} \\ a_{32} & a_{34} \\ a_{42} & a_{44} \end{bmatrix} \quad \begin{bmatrix} \bar{\psi} \\ \bar{Q} \end{bmatrix}_0 = \mathbf{z}_5 = \begin{bmatrix} 0 \\ \bar{\psi} \\ 0 \\ \bar{Q} \end{bmatrix}_5$$

$$\Delta = \begin{vmatrix} a_{12} & a_{14} \\ a_{32} & a_{34} \end{vmatrix}$$

$$\begin{bmatrix} 0{\cdot}0000 & 0{\cdot}0000 \\ 1{\cdot}0000 & 0{\cdot}0000 \\ 0{\cdot}0000 & 0{\cdot}0000 \\ 0{\cdot}0000 & 1{\cdot}0000 \end{bmatrix} \cdot \begin{bmatrix} \bar{\psi} \\ \bar{Q} \end{bmatrix}_0 = \mathbf{z}_0$$

$$\downarrow$$

$$\left[\begin{array}{cccc:c} 1 & 1 & \frac{1}{2} & \frac{1}{6} & 0 \\ 0 & 1 & 1 & \frac{1}{2} & 0 \\ 0 & 0 & 1 & 1 & 0 \\ 0 & 0 & 0 & 1 & 0{\cdot}1 \end{array}\right] \rightarrow \begin{bmatrix} 1{\cdot}0000 & 0{\cdot}1667 \\ 1{\cdot}0000 & 0{\cdot}5000 \\ 0{\cdot}0000 & 1{\cdot}0000 \\ 0{\cdot}1000 & 1{\cdot}0167 \end{bmatrix} \cdot \begin{bmatrix} \bar{\psi} \\ \bar{Q} \end{bmatrix}_0 = \mathbf{z}_1^R$$

$$\downarrow$$

$$\left[\begin{array}{cccc:c} 1 & 1 & \frac{1}{4} & \frac{1}{12} & 0 \\ 0 & 1 & \frac{1}{2} & \frac{1}{4} & 0 \\ 0 & 0 & 1 & 1 & 0 \\ 0 & 0 & 0 & 1 & 0{\cdot}3 \end{array}\right] \rightarrow \begin{bmatrix} 2{\cdot}0083 & 1{\cdot}0014 \\ 1{\cdot}0250 & 1{\cdot}2542 \\ 0{\cdot}1000 & 2{\cdot}0167 \\ 0{\cdot}7025 & 1{\cdot}3171 \end{bmatrix} \cdot \begin{bmatrix} \bar{\psi} \\ \bar{Q} \end{bmatrix}_0 = \mathbf{z}_2^R$$

$$\downarrow$$

$$\left[\begin{array}{cccc:c} 1 & 1 & \frac{1}{4} & \frac{1}{12} & 0 \\ 0 & 1 & \frac{1}{2} & \frac{1}{4} & 0 \\ 0 & 0 & 1 & 1 & 0 \\ 0 & 0 & 0 & 1 & 0{\cdot}3 \end{array}\right] \rightarrow \begin{bmatrix} 3{\cdot}1168 & 2{\cdot}8695 \\ 1{\cdot}2506 & 2{\cdot}5918 \\ 0{\cdot}8025 & 3{\cdot}3338 \\ 1{\cdot}6375 & 2{\cdot}1780 \end{bmatrix} \cdot \begin{bmatrix} \bar{\psi} \\ \bar{Q} \end{bmatrix}_0 = \mathbf{z}_3^R$$

$$\downarrow$$

$$\left[\begin{array}{cccc:c} 1 & 1 & \frac{1}{4} & \frac{1}{12} & 0 \\ 0 & 1 & \frac{1}{2} & \frac{1}{4} & 0 \\ 0 & 0 & 1 & 1 & 0 \\ 0 & 0 & 0 & 1 & 0{\cdot}1 \end{array}\right] \rightarrow \begin{bmatrix} 4{\cdot}7045 & 6{\cdot}4763 \\ 2{\cdot}0612 & 4{\cdot}8032 \\ 2{\cdot}4400 & 5{\cdot}5118 \\ 2{\cdot}1080 & 2{\cdot}8256 \end{bmatrix} \cdot \begin{bmatrix} \bar{\psi} \\ \bar{Q} \end{bmatrix}_0 = \mathbf{z}_4^R$$

$$\downarrow$$

$$\left[\begin{array}{cccc:c} 1 & 1 & \frac{1}{2} & \frac{1}{6} & 0 \\ 0 & 1 & 1 & \frac{1}{2} & 0 \\ 0 & 0 & 1 & 1 & 0 \\ 0 & 0 & 0 & 1 & 0 \end{array}\right] \rightarrow \begin{bmatrix} 8{\cdot}3370 & 14{\cdot}5063 \\ 5{\cdot}5552 & 11{\cdot}7278 \\ 4{\cdot}5480 & 8{\cdot}3374 \\ 2{\cdot}1080 & 2{\cdot}8256 \end{bmatrix} \cdot \begin{bmatrix} \bar{\psi} \\ \bar{Q} \end{bmatrix}_0 = \mathbf{z}_5$$

$$\Delta = \begin{vmatrix} 8{\cdot}3370 & 14{\cdot}5063 \\ 4{\cdot}5480 & 8{\cdot}3374 \end{vmatrix} = 3{\cdot}5343$$

The plot of the frequency determinant against angular frequency is shown in Fig. 3(a) and the first two angular frequencies are given by

$$\omega_1^2 = 0{\cdot}120\frac{EI}{ml^3} \quad \omega_2^2 = 2{\cdot}54\frac{EI}{ml^3}$$

The normal modes corresponding to the first two natural frequencies are shown in Fig. 3(b) and (c).

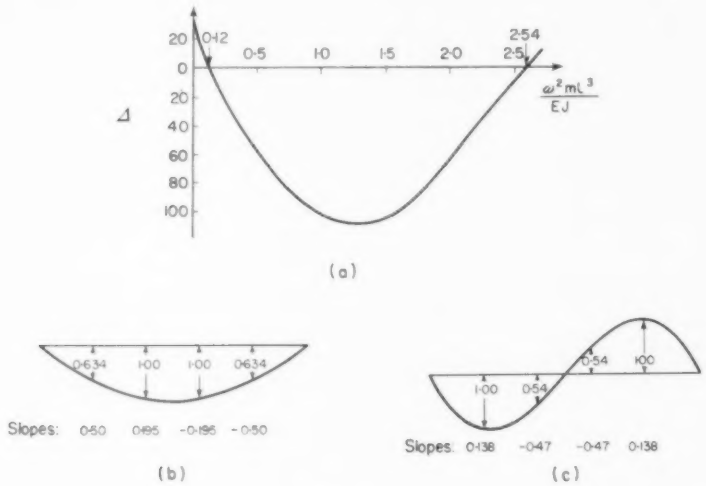

FIG. 3.

3. THE SPRING MATRIX

In the previous section we saw how transfer matrices may be applied very readily to "straight through" systems, and, as the next step, the question of how to deal with branched systems naturally presents itself.[16] Suppose we have an elastic system ABC of order n with an elastic branch DB rigidly connected at B, as represented in Fig. 4. By use of transfer matrices it is possible to find the state vector at the point B_L in terms of the $n/2$ unknowns at the point A; let us say $\mathbf{z}_B^L = \mathbf{F}\mathbf{v}_A$. We now wish to find the state vector $\mathbf{z}_B^R$. It is clear that, while the deflexions are continuous, there is a discontinuity in the stress resultants, the magnitude of the discontinuity depending on the displacements at B and the character of the branch BD. With $\bar{\mathbf{v}}_D$ denoting* the $n/2$ unknowns at the point D, the state vector $\bar{\mathbf{z}}_B$ is given by $\bar{\mathbf{z}}_B = \mathbf{R}\bar{\mathbf{v}}_D$, where $\mathbf{R}$ is the known transfer matrix of the size $n/2 \times n$. This relationship can also be written in the form

$$\begin{bmatrix} \bar{\boldsymbol{\delta}} \\ \cdots \\ \bar{\mathbf{K}} \end{bmatrix}_B = \begin{bmatrix} \mathbf{R}_1 \\ \cdots \\ \mathbf{R}_2 \end{bmatrix} \bar{\mathbf{v}}_D$$

* Quantities referring to the branch shall be indicated by a bar over the symbol.

where $\bar{\boldsymbol{\delta}}_B$ are the displacements at the end B and $\overline{\mathbf{K}}_B$ are the corresponding forces, while $\mathbf{R}_1$ and $\mathbf{R}_2$ are $n/2 \times n/2$ matrices. From this equation we obtain the relations $\bar{\boldsymbol{\delta}}_B = \mathbf{R}_1 \bar{\mathbf{v}}_D$ and $\overline{\mathbf{K}}_B = \mathbf{R}_2 \bar{\mathbf{v}}_D$ so that when $\bar{\mathbf{v}}_D$ is eliminated the relation between the forces and the displacements at the extremity B of the branch is found to be

$$\overline{\mathbf{K}}_B = \mathbf{R}_2 \mathbf{R}_1^{-1} \bar{\boldsymbol{\delta}}_B$$

FIG. 4.

The co-ordinates of the vectors $\overline{\mathbf{K}}_B$ and $\bar{\boldsymbol{\delta}}_B$ are now transferred to the co-ordinates of the main system ABC by the matrix operations

$$\bar{\boldsymbol{\delta}}_B = \mathbf{G}_1 \boldsymbol{\delta}_B \quad \text{and} \quad \overline{\mathbf{K}}_B = \mathbf{G}_2 \mathbf{K}_B$$

The matrix $\mathbf{G}_2$ is such that the forces $\mathbf{K}_B$ coincide with the positive forces on the positive face of ABC (Fig. 5). With these transformations the forces applied at the extremity of the branch in terms of the displacements at point B are given by

$$\mathbf{K}_B = \mathbf{G}_2 \mathbf{R}_2 \mathbf{R}_1^{-1} \mathbf{G}_1 \boldsymbol{\delta}_B \tag{5}$$

The forces acting on ABC are equal and opposite so that in addition to the relation $\boldsymbol{\delta}_B^R = \boldsymbol{\delta}_B^L$ the relation between the forces is

$$\mathbf{K}_B^R = \mathbf{K}_B^L + \mathbf{K}_B = \mathbf{K}_B^L + \mathbf{G}_2 \mathbf{R}_2 \mathbf{R}_1^{-1} \mathbf{G}_1 \boldsymbol{\delta}_B^L$$

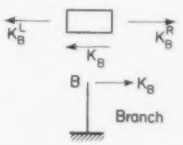

FIG. 5.

Thus, the transfer matrix relating the state vectors to the left and right of the branch junction point is given by

$$\begin{bmatrix} \boldsymbol{\delta} \\ \cdots \\ \mathbf{K} \end{bmatrix}_B^R = \left[\begin{array}{c:c} \mathbf{I} & 0 \\ \cdots\cdots\cdots\cdots & \cdots \\ \mathbf{G}_2 \mathbf{R}_2 \mathbf{R}_1^{-1} \mathbf{G}_1 & \mathbf{I} \end{array}\right] \begin{bmatrix} \boldsymbol{\delta} \\ \cdots \\ \mathbf{K} \end{bmatrix}_B^L \tag{6}$$

The matrix $\mathbf{G}_2 \mathbf{R}_2 \mathbf{R}_1^{-1} \mathbf{G}_1$ is known as the spring matrix $\mathbf{S}_B$ of the branch BC. Using this method we may reduce the effect of a branch of an elastic system to that of an equivalent spring. This concept is shown diagrammatically in Fig. 6.

If several branches are joined to the main branch at one point then the resulting spring matrix is the sum of the individual spring matrices since

$$\mathbf{K}_1 = \mathbf{S}_1 \boldsymbol{\delta}_B, \quad \mathbf{K}_2 = \mathbf{S}_2 \boldsymbol{\delta}_B \ldots \mathbf{K}_n = \mathbf{S}_n \boldsymbol{\delta}_B$$

and therefore

$$\Sigma \mathbf{K}_i = (\Sigma \mathbf{S}_i)\, \boldsymbol{\delta}_B$$

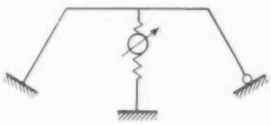

FIG. 6.

Example

As an example let us consider that Fig. 4 represents a plane frame which can vibrate in its own plane. We shall find the spring matrix of the branch DB, assuming for simplicity's sake, that the branch is without mass, although in practice the introduction of mass causes no difficulty. The transfer matrix for a massless beam with longitudinal and flexural elasticity is already given in equation (1).

Since $\bar{u}_D = 0, \bar{w}_D = 0$ and $\bar{\psi}_D = 0$, and with $\bar{\mathbf{v}}$ the unknown vector we have that

$$\begin{bmatrix} \bar{u} \\ -\bar{w} \\ \bar{\psi} \\ \bar{M} \\ \bar{Q} \\ \bar{T} \end{bmatrix}_B = \begin{bmatrix} 0 & 0 & l/AE \\ l^2/2EI & l^3/6EI & 0 \\ l/EI & l^2/2EI & 0 \\ 1 & l & 0 \\ 0 & 1 & 0 \\ 0 & 0 & 1 \end{bmatrix} [\bar{\mathbf{v}}]$$

from which

$$\mathbf{R}_1 = \begin{bmatrix} 0 & 0 & l/AE \\ l^2/2EI & l^3/6EI & 0 \\ l/EI & l^2/2EI & 0 \end{bmatrix}; \quad \mathbf{R}_2 = \begin{bmatrix} 1 & l & 0 \\ 0 & 1 & 0 \\ 0 & 0 & 1 \end{bmatrix}$$

$$\text{and} \quad \mathbf{R}_1^{-1} = \begin{bmatrix} 0 & 6EI/l^2 & -2EI/l \\ 0 & -12EI/l^3 & 6EI/l^2 \\ AE/l & 0 & 0 \end{bmatrix}$$

Also, referring to Fig. 7(a), the matrices required to change co-ordinates are

$$\begin{bmatrix} M \\ Q \\ T \end{bmatrix} = \begin{bmatrix} 1 & 0 & 0 \\ 0 & 0 & -1 \\ 0 & 1 & 0 \end{bmatrix} \begin{bmatrix} \bar{M} \\ \bar{Q} \\ \bar{T} \end{bmatrix} \quad \text{and} \quad \begin{bmatrix} \bar{u} \\ -\bar{w} \\ \bar{\psi} \end{bmatrix} = \begin{bmatrix} 0 & 1 & 0 \\ -1 & 0 & 0 \\ 0 & 0 & 1 \end{bmatrix} \begin{bmatrix} u \\ -w \\ \psi \end{bmatrix}$$

Therefore the spring matrix $\mathbf{S} = \mathbf{G}_2\mathbf{R}_2\mathbf{R}_1^{-1}\mathbf{G}_1$ is found to be

$$\mathbf{S} = \begin{bmatrix} 6EI/l^2 & 0 & 4EI/l \\ 0 & -AE/l & 0 \\ 12EI/l^3 & 0 & 6EI/l^2 \end{bmatrix} \tag{7}$$

so that the matrix relation between state vectors $\mathbf{z}_B^L$ and $\mathbf{z}_B^R$ is now given as in equation (6).

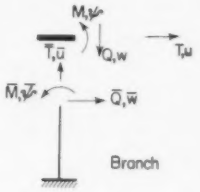

FIG. 7(a).

4. THE SPRING MATRIX FOR A BRANCH WITH A RELEASE

A release is defined as a discontinuity in the system which makes the system incapable of transmitting a particular load. In the case of Fig. 7(b), for example, the branch DB is unable to transmit a bending moment at B on account of the hinge, or in the case of Fig. 7(c) the shear is zero because of the frictionless guide connexion. When the branch is rigidly connected, the end displacements are the same as those of the main system. However, in Fig. 7(b) and (c), it is evident that the displacements complementary to the "force" which is zero are different for the branch and the main system. In the previous section we found that the spring matrix operating on the deflexions of the main system gives the discontinuity in the forces, i.e. $\mathbf{K}_S = \mathbf{G}_2\mathbf{R}_2\mathbf{R}_1^{-1}\mathbf{G}_1\boldsymbol{\delta}_B = \mathbf{S}\boldsymbol{\delta}_B$. Suppose now that the branch has a release at its join with the main system. Rewriting equation (5) in longhand

$$\begin{bmatrix} K_n \\ K_{n-1} \\ \vdots \\ \bar{K}_{m+1} \\ \vdots \\ K_1 \end{bmatrix} = \begin{bmatrix} s_{11} & s_{12} & \cdots & s_{1,m+1} & \cdots & s_{1n} \\ s_{21} & s_{22} & \cdots & s_{2,m+1} & \cdots & s_{2n} \\ \vdots & & & & & \vdots \\ s_{n-m,1} & s_{n-m,2} & \cdots & s_{n-m,m+1} & \cdots & s_{n-m,n} \\ \vdots & & & & & \vdots \\ s_{n,1} & s_{n,2} & \cdots & s_{n,m+1} & \cdots & s_{n,n} \end{bmatrix} \begin{bmatrix} \delta_1 \\ \delta_2 \\ \vdots \\ \bar{\delta}_{m+1} \\ \vdots \\ \delta_n \end{bmatrix} \tag{8}$$

The force which is zero because of the release is represented by $\bar{K}_{m+1}$ and its corresponding displacement by $\bar{\delta}_{m+1}$ which, of course, is different from the corresponding displacement of the main system. Using the fact that $\bar{K}_{m+1} = 0$

we obtain the equation,

$$\{s_{n-m,1} \quad s_{n-m,2} \quad \cdots \quad s_{n-m,m+1} \quad \cdots \quad s_{n-m,n}\} \begin{bmatrix} \delta_1 \\ \delta_2 \\ \vdots \\ \delta_{m+1} \\ \vdots \\ \delta_n \end{bmatrix} = 0$$

which yields

$$\delta_{m+1} = -\frac{1}{s_{n-m,m+1}} \{s_{n-m,1}, s_{n-m,2}, \ldots, \underset{\substack{\uparrow \\ (m+1)\text{th column}}}{0}, \ldots s_{n-m,n}\} \begin{bmatrix} \delta_1 \\ \delta_2 \\ \vdots \\ \delta_{m+1} \\ \vdots \\ \delta_n \end{bmatrix}$$

Using this expression for δ_{m+1} in equation (8) we then find the relation

$$\begin{bmatrix} K_n \\ K_{n-1} \\ \vdots \\ \bar{K}_{m+1} \\ \vdots \\ K_1 \end{bmatrix} = \begin{bmatrix} s_{11}, & s_{12}, & \ldots, & \underset{\downarrow}{0}, & \ldots, & s_{1n} \\ s_{21}, & s_{22}, & \ldots, & 0, & \ldots, & s_{2n} \\ \vdots & \vdots & & \vdots & & \vdots \\ s_{n-m,1}, & s_{n-m,2}, & \ldots, & 0, & \ldots, & s_{n-m,n} \\ \vdots & \vdots & & \vdots & & \vdots \\ s_{n1}, & s_{n2}, & \ldots, & 0, & \ldots, & s_{nn} \end{bmatrix} \begin{bmatrix} \delta_1 \\ \delta_2 \\ \vdots \\ \delta_{m+1} \\ \vdots \\ \delta_n \end{bmatrix}$$

$$-\frac{1}{s_{n-m,m+1}} \begin{bmatrix} s_{1,m+1} \\ s_{2,m+1} \\ \vdots \\ s_{n-m,m+1} \\ \vdots \\ s_{n,m+1} \end{bmatrix} \{s_{n-m,1}, \quad s_{n-m,2}, \quad \ldots, \quad \underset{\downarrow}{0}, \quad \ldots, \quad s_{n-m,n}\} \begin{bmatrix} \delta_1 \\ \delta_2 \\ \vdots \\ \delta_{m+1} \\ \vdots \\ \delta_n \end{bmatrix}$$

$$= \begin{bmatrix} |1, n-m;\ 1, m+1|, & |1, n-m;\ 2, m+1|, & \ldots, & |1, n-m;\ n, m+1| \\ |2, n-m;\ 1, m+1|, & |2, n-m;\ 2, m+1|, & \ldots, & |2, n-m;\ n, m+1| \\ \vdots & \vdots & & \vdots \\ |n, n-m;\ 1, m+1|, & |n, n-m;\ 2, m+1|, & \ldots, & |n, n-m;\ n, m+1| \end{bmatrix} \cdot \begin{bmatrix} \delta_1 \\ \vdots \\ \delta_{m+1} \\ \vdots \\ \delta_n \end{bmatrix} \tag{9}$$

where $|p,q;\,r,s|$ represents the determinant

$$\frac{1}{s_{qs}}\begin{vmatrix} s_{pr} & s_{qr} \\ s_{ps} & s_{qs} \end{vmatrix}$$

and then, of course, when $p=q$ or $r=s$ the determinant vanishes. From this follows that in (9) the elements in the $(n-m)$th row and the $(m+1)$th column are zero. Hence, when a branch has a release at its point of connexion with the main system the spring matrix must be modified according to the rule above.

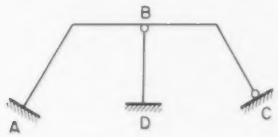

FIG. 7(b).

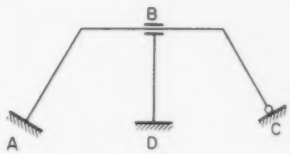

FIG. 7(c).

Example

Find the spring matrix for the branch DB when it is pinned at B. The spring matrix when the branch is rigidly connected to the main system has already been found [equation (7)]

$$\begin{bmatrix} M \\ Q \\ T \end{bmatrix} = \begin{bmatrix} 6EI/l^2 & 0 & 4EI/l \\ 0 & -AE/l & 0 \\ 12EI/l^3 & 0 & 6EI/l^2 \end{bmatrix} \begin{bmatrix} u \\ -w \\ \psi \end{bmatrix}$$

In this case, $M=0$ and the discontinuity at deflexion occurs in the slope ψ. Hence $n=3, n-m=1$ and $m+1=3$ so that the new spring matrix is

$$\begin{bmatrix} M \\ Q \\ T \end{bmatrix} = \begin{bmatrix} |1,1;\,1,3| & |1,1;\,2,3| & |1,1;\,3,3| \\ |2,1;\,1,3| & |2,1;\,2,3| & |2,1;\,3,3| \\ |3,1;\,1,3| & |3,1;\,2,3| & |3,1;\,3,3| \end{bmatrix} \begin{bmatrix} u \\ -w \\ \psi \end{bmatrix}$$

$$= \begin{bmatrix} 0 & 0 & 0 \\ 0 & \dfrac{-AE}{l} & 0 \\ \dfrac{3EI}{l^3} & 0 & 0 \end{bmatrix} \begin{bmatrix} u \\ -w \\ \psi \end{bmatrix}$$

5A. RELEASES AND RIGIDITIES

The definition of a release has been given in the previous section. Whereas a release causes a discontinuity in displacement on account of the inability of the system to transmit a corresponding force, a rigidity causes a discontinuity in force on account of the inability of the system to deflect. Examples of both are indicated in Fig. 8. The methods of relating the state vector on either side of a release or a rigidity are identical, and shall now be developed. We have

Vol. 2
1960-61

seen how a state vector can be found in terms of a transfer matrix and an unknown column vector.

$$\begin{bmatrix} \delta_1 \\ \delta_2 \\ \vdots \\ \delta_m \\ \vdots \\ \delta_{n/2} \\ \cdots \\ K_{n/2} \\ \vdots \\ K_m \\ \vdots \\ K_2 \\ K_1 \end{bmatrix}_i^L = \begin{bmatrix} a_{11} & a_{12} & a_{13} & \cdots & a_{1n/2} \\ a_{21} & a_{22} & a_{23} & \cdots & a_{2n/2} \\ \vdots & \vdots & \vdots & & \vdots \\ a_{m1} & a_{m2} & a_{m3} & \cdots & a_{mn/2} \\ \vdots & \vdots & \vdots & & \vdots \\ \vdots & \vdots & \vdots & & \vdots \\ \vdots & \vdots & \vdots & & \vdots \\ \vdots & \vdots & \vdots & & \vdots \\ \vdots & \vdots & \vdots & & \vdots \\ \vdots & \vdots & \vdots & & \vdots \\ \vdots & \vdots & \vdots & & \vdots \\ a_{n,1} & a_{n,2} & a_{n,2} & \cdots & a_{nn/2} \end{bmatrix} \begin{bmatrix} v_1 \\ v_2 \\ \vdots \\ \vdots \\ v_{n/2} \end{bmatrix} \tag{10}$$

Suppose now that we wish to cross the rigidity (or release) at point i, at which point $\delta_m = 0$. A discontinuity shall be introduced in the corresponding force K_m. From the fact that $\delta_m = 0$ we can obtain the relation

$$\delta_m = 0 = \{a_{m1}\, a_{m2}\, a_{m3} \cdots a_{m,\, n/2}\} \begin{bmatrix} v_1 \\ v_2 \\ \vdots \\ v_{n/2} \end{bmatrix}$$

from which we can solve for any one of the unknown v's in terms of the remaining v's. Let us choose arbitrarily $v_{n/2}$ so that

$$v_{n/2} = -\frac{1}{a_{m,\, n/2}} \{a_{m1}\, a_{m2} \cdots a_{m,\, n/2-1}\} \begin{bmatrix} v_1 \\ v_2 \\ \vdots \\ v_{n/2-1} \end{bmatrix} \tag{11}$$

and introducing this relation into equation (10) we obtain

$$\begin{bmatrix} \delta_1 \\ \vdots \\ \delta_m \\ \vdots \\ \delta_{n/2} \\ \cdots \\ K_{n/2} \\ \vdots \\ \vdots \\ K_1 \end{bmatrix} = \begin{bmatrix} |1,m;\, 1,n/2|, \ldots |1,m;\, n/2-1,n/2|, 0 \\ \vdots \\ |m,m;\, 1,n/2|, \ldots |m,m;\, n/2-1,n/2|, 0 \\ \vdots \\ \vdots \\ \vdots \\ \vdots \\ \vdots \\ |n,m;\, 1,n/2|, \ldots |n,m;\, n/2-1,n/2|, 0 \end{bmatrix} \begin{bmatrix} v_1 \\ \vdots \\ \vdots \\ v_{n/2-1} \\ \cdots \\ 0 \end{bmatrix}$$

On crossing over the rigidity we must introduce the unknown reaction $\bar{K}_i$ and doing so we find the state vector $\mathbf{z}_i^R$ to be given by

$$\begin{bmatrix} \delta_1 \\ \vdots \\ \delta_m \\ \vdots \\ \delta_{n/2} \\ \cdots \\ K_{n/2} \\ \vdots \\ \vdots \\ K_1 \end{bmatrix} = \begin{bmatrix} |1,m;\,1,n/2|, & \ldots, & |1,m;\,n/2-1,n/2|, & 0 \\ \vdots & & \vdots & \vdots \\ |m,m;\,1,n/2|, & \ldots, & |m,m;\,n/2-1,n/2|, & 0 \\ \vdots & & \vdots & \vdots \\ \vdots & & \vdots & \vdots \\ \vdots & & \vdots & \vdots \\ \vdots & & \vdots & \vdots \\ |n-m+1,m;\,1,n/2|, & \ldots, & |n-m+1,m;\,n/2-1,n/2|, & 1 \\ \vdots & & \vdots & \vdots \\ |n,m;\,1,n/2|, & \ldots, & |n,m;\,n/2-1,n/2|, & 0 \end{bmatrix} \begin{bmatrix} v_1 \\ \vdots \\ \vdots \\ v_{n/2-1} \\ \cdots \\ \bar{K}_i \end{bmatrix} \tag{12}$$

The full $n/2$ components of the unknown vector have been restored and the process continues in the usual manner. The same theory applies for a release, the value of m being shifted accordingly. If more than one rigidity or release occurs at the same point, the above technique can be extended to cover the particular case.

FIG. 8.

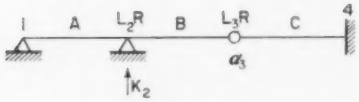

FIG. 9.

Example

It is required to find the natural frequencies of the beam illustrated in Fig. 9. The beam is rigidly supported at point 2 and has a moment release at point 3. Let us suppose that the transfer field matrices A, B and C relating adjacent state vectors of the beam are known, so that

$$\mathbf{z}_2^L = \mathbf{A}\mathbf{z}_1 \quad \mathbf{z}_3^L = \mathbf{B}\mathbf{z}_2^R \quad \text{and} \quad \mathbf{z}_4 = \mathbf{C}\mathbf{z}_3^R$$

The schematic solution is indicated below, the elimination process being carried out according to the result of equation (12). It is useful when computing the normal modes that the expression (11) for the eliminated unknown should be noted.

$$\begin{bmatrix} a_{11} & a_{12} \\ a_{21} & a_{22} \\ a_{31} & a_{32} \\ a_{41} & a_{42} \end{bmatrix} \qquad \begin{bmatrix} \psi \\ Q \end{bmatrix}_1 = \begin{bmatrix} -w \\ \psi \\ M \\ Q \end{bmatrix}_2^L \qquad \text{Condition } w_2 = 0$$

$$\begin{bmatrix} |1,1;\,1,2|\ 0 \\ |2,1;\,1,2|\ 0 \\ |3,1;\,1,2|\ 0 \\ |4,1;\,1,2|\ 1 \end{bmatrix} \qquad \begin{bmatrix} \psi_1 \\ K_2 \end{bmatrix} = \begin{bmatrix} -w \\ \psi \\ M \\ Q \end{bmatrix}_2^R$$

Eliminate Q_1 by noting $m = 1, n = 2$

$$Q_1 = -\frac{1}{a_{12}}(a_{11})\psi_1$$

Introduce reaction K_2 at the point 2

$$\downarrow$$

$$\begin{bmatrix} b_{11}\,b_{12}\,b_{13}\,b_{14} \\ b_{21}\,b_{22}\,b_{23}\,b_{24} \\ b_{31}\,b_{32}\,b_{33}\,b_{34} \\ b_{41}\,b_{42}\,b_{43}\,b_{44} \end{bmatrix} \rightarrow \begin{bmatrix} d_{11} & d_{12} \\ d_{21} & d_{22} \\ d_{31} & d_{32} \\ d_{41} & d_{42} \end{bmatrix} \qquad \begin{bmatrix} \psi_1 \\ K_2 \end{bmatrix} = \begin{bmatrix} -w \\ \psi \\ M \\ Q \end{bmatrix}_3^L \qquad \text{Condition } M_3 = 0$$

$$\begin{bmatrix} |1,3;\,1,2|\ 0 \\ |2,3;\,1,2|\ 1 \\ |3,3;\,1,2|\ 0 \\ |4,3;\,1,2|\ 0 \end{bmatrix} \qquad \begin{bmatrix} \psi_1 \\ \alpha_3 \end{bmatrix} = \begin{bmatrix} -w \\ \psi \\ M \\ Q \end{bmatrix}_3^R$$

Eliminate K_2 by noting $m = 3, n = 2$

$$K_2 = -\frac{d_{31}}{d_{32}}\psi_1$$

Introduce discontinuity in angle α at point 3

$$\downarrow$$

$$\begin{bmatrix} c_{11}\,c_{12}\,c_{13}\,c_{14} \\ c_{21}\,c_{22}\,c_{23}\,c_{24} \\ c_{31}\,c_{32}\,c_{33}\,c_{34} \\ c_{41}\,c_{42}\,c_{43}\,c_{44} \end{bmatrix} \rightarrow \begin{bmatrix} e_{11} & e_{12} \\ e_{21} & e_{22} \\ e_{31} & e_{32} \\ e_{41} & e_{42} \end{bmatrix} \qquad \begin{bmatrix} \psi_1 \\ \alpha_3 \end{bmatrix} = \begin{bmatrix} -w \\ \psi \\ M \\ Q \end{bmatrix}_4 \qquad \text{Conditions } w_4 = 0,\ \psi_4 = 0$$

The frequency determinant is

$$\begin{vmatrix} e_{11} & e_{12} \\ e_{21} & e_{22} \end{vmatrix} = 0$$

When computing normal modes, we assume that $\psi_1 = 1$, then

$$\alpha_3 = -\psi_1 \frac{e_{11}}{e_{12}} = -\frac{e_{11}}{e_{12}};\quad K_2 = -\psi_1 \frac{d_{31}}{d_{32}} = -\frac{d_{31}}{d_{32}};$$

$$Q_1 = -\psi_1 \frac{a_{11}}{a_{12}} = -\frac{a_{11}}{a_{12}};$$

The calculation of the normal modes can then be completed.

5B. SPECIAL CASE OF A BEAM ON A SERIES OF RIGID SUPPORTS

This important case (Fig. 10) leads to a transfer matrix of particularly simple form.[11] Let F be the transfer matrix relating the state vector $\mathbf{z}_i^R$ and $\mathbf{z}_{i+1}^L$ so that written in full we have relations

$$\begin{aligned}
-w_{i+1}^L &= f_{11}(-w_i^R)+f_{12}\psi_i^R+f_{13}M_i^R+f_{14}Q_i^R \\
\psi_{i+1}^L &= f_{21}(-w_i^R)+f_{22}\psi_i^R+f_{23}M_i^R+f_{24}Q_i^R \\
M_{i+1}^L &= f_{31}(-w_i^R)+f_{32}\psi_i^R+f_{33}M_i^R+f_{34}Q_i^R \\
Q_{i+1}^L &= f_{41}(-w_i^R)+f_{42}\psi_i^R+f_{43}M_i^R+f_{44}Q_i^R
\end{aligned}$$

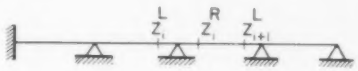

FIG. 10.

Noting that $w_i^L = w_i^R = 0$; $\psi_i^L = \psi_i^R$; $M_i^L = M_i^R$ and $Q_i^L = Q_i^R - K_i$ where K_i is the support reaction, we have then

$$\begin{aligned}
0 &= f_{12}\psi_i^L+f_{13}M_i^L+f_{14}(Q_i^L+K_i) \\
\psi_{i+1}^L &= f_{22}\psi_i^L+f_{23}M_i^L+f_{24}(Q_i^L+K_i) \\
M_{i+1}^L &= f_{32}\psi_i^L+f_{33}M_i^L+f_{34}(Q_i^L+K_i) \\
Q_{i+1}^L &= f_{42}\psi_i^L+f_{43}M_i^L+f_{44}(Q_i^L+K_i)
\end{aligned}$$

Eliminating $(Q_i^L+K_i)$ from these equations we find that

$$\begin{aligned}
\psi_{i+1}^L &= |2,1;2,4|\psi_i^L+|2,1;3,4|M_i^L \\
M_{i+1}^L &= |3,1;2,4|\psi_i^L+|3,1;3,4|M_i^L \\
Q_{i+1}^L &= |4,1;2,4|\psi_i^L+|4,1;3,4|M_i^L
\end{aligned}$$

The vectors ψ_{i+1}^L, M_{i+1}^L and Q_{i+1}^L can be determined from the two vectors ψ_i^L and M_i^L, and introducing the new state vector

$$\begin{bmatrix} \psi \\ M \end{bmatrix}_i$$

we obtain the matrix relation

$$\begin{bmatrix} \psi \\ M \end{bmatrix}_{i+1}^L = \begin{bmatrix} |2,1;2,4| & |2,3;3,4| \\ |3,1;2,4| & |3,1;2,4| \end{bmatrix} \begin{bmatrix} \psi \\ M \end{bmatrix}_i^L$$

Q_{i+1} need not be included in the state vector since it is a linear function of ψ_{i+1} and M_{i+1} so that the transfer matrix has been reduced to one of size 2×2.

6. THE COUPLING MATRIX

As in the case of the branched system with its spring matrix, it is possible to find a coupling matrix for the elastic coupling between two elastic systems.

Vol. 2
1960-61

Let us consider two elastic systems, I and II, which are coupled together by an elastic tie at points A and B (Fig. 11). In the usual way we can proceed along members I and II finding the state vectors at different points in terms of the unknown vectors, until the coupling between A and B is reached. In passing from left to right at the coupling tie, the displacements remain unchanged, but the coupling introduces discontinuities in the forces, their magnitude

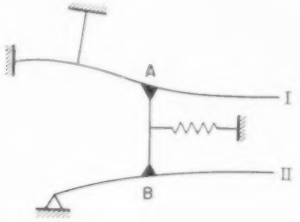

FIG. 11.

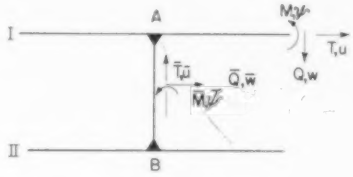

FIG. 12.

depending on the deflexions at the extremities of the coupling and the elastic properties of the coupling. It should be noted that the coupling may possess mass so that its properties shall be a function of the angular frequency. Let us suppose that the transfer matrix relating the state vectors at the extremities of the coupling A and B is known, i.e. $\bar{\mathbf{z}}_A = \mathbf{F}\bar{\mathbf{z}}_B$ when the bars again denote the state vectors in the co-ordinates of the coupling. Rewriting this equation in the form

$$\begin{bmatrix} \bar{\boldsymbol{\delta}}_A \\ \cdots \\ \overline{\mathbf{K}}_A \end{bmatrix} = \begin{bmatrix} \mathbf{F}_1 & \vdots & \mathbf{F}_2 \\ \cdots & \vdots & \cdots \\ \mathbf{F}_3 & \vdots & \mathbf{F}_4 \end{bmatrix} \begin{bmatrix} \bar{\boldsymbol{\delta}}_B \\ \cdots \\ \overline{\mathbf{K}}_B \end{bmatrix}$$

where $\mathbf{F}_1, \mathbf{F}_2, \mathbf{F}_3$ and $\mathbf{F}_4$ are square matrices of order $n/2$, we can then obtain the equations

$$\bar{\boldsymbol{\delta}}_A = \mathbf{F}_1\bar{\boldsymbol{\delta}}_B + \mathbf{F}_2\overline{\mathbf{K}}_B$$
$$\overline{\mathbf{K}}_A = \mathbf{F}_3\bar{\boldsymbol{\delta}}_B + \mathbf{F}_4\overline{\mathbf{K}}_B$$

With the co-ordinate transformations (cf. Section 3) $\bar{\boldsymbol{\delta}}_A = \mathbf{G}_1\boldsymbol{\delta}_A$, $\bar{\boldsymbol{\delta}}_B = \mathbf{G}_3\boldsymbol{\delta}_B$, $\mathbf{K}_A = \mathbf{G}_2\overline{\mathbf{K}}_A$ and $\mathbf{K}_B = \mathbf{G}_4\bar{\mathbf{K}}_B$ it is possible to find the expressions for the discontinuities in the forces of the main system at A and B. This relation is

$$\begin{bmatrix} \mathbf{K}_B \\ \mathbf{K}_A \end{bmatrix} = \begin{bmatrix} \mathbf{G}_4\mathbf{F}_2^{-1}\mathbf{G}_1 & -\mathbf{G}_4\mathbf{F}_2^{-1}\mathbf{F}_1\mathbf{G}_3 \\ \mathbf{G}_2\mathbf{F}_4\mathbf{F}_2^{-1}\mathbf{G}_1 & \mathbf{G}_2(\mathbf{F}_3 - \mathbf{F}_4\mathbf{F}_2^{-1}\mathbf{F}_1)\mathbf{G}_3 \end{bmatrix} \cdot \begin{bmatrix} \boldsymbol{\delta}_A \\ \boldsymbol{\delta}_B \end{bmatrix} = \mathbf{C}\begin{bmatrix} \boldsymbol{\delta}_A \\ \boldsymbol{\delta}_B \end{bmatrix} \quad (13)$$

and consequently the matrix relation between the state vectors right and left of the coupling is given by

$$\begin{bmatrix} \boldsymbol{\delta}_{\mathrm{I}} \\ \boldsymbol{\delta}_{\mathrm{II}} \\ \cdots \\ \mathbf{K}_{\mathrm{II}} \\ \mathbf{K}_{\mathrm{I}} \end{bmatrix}_R = \begin{bmatrix} \mathbf{I} & \vdots & \mathbf{O} \\ \cdots & \vdots & \cdots \\ \mathbf{C} & \vdots & \mathbf{I} \end{bmatrix} \cdot \begin{bmatrix} \boldsymbol{\delta}_{\mathrm{I}} \\ \boldsymbol{\delta}_{\mathrm{II}} \\ \cdots \\ \mathbf{K}_{\mathrm{II}} \\ \mathbf{K}_{\mathrm{I}} \end{bmatrix}_L \quad (14)$$

Vol. 2
1960-

Example

Find the coupling matrix for two parallel beams connected together by a massless beam of flexural rigidity EI and longitudinal stiffness EA (Fig. 12).

The matrix relating the state vectors at the extremities of the branch AB is given in equation (1).

$$\begin{bmatrix} \bar{u} \\ -\bar{w} \\ \bar{\psi} \\ \bar{M} \\ \bar{Q} \\ \bar{T} \end{bmatrix}_A = \begin{bmatrix} 1 & 0 & 0 & 0 & 0 & l/EA \\ 0 & 1 & l & l^2/2EI & l^3/6EI & 0 \\ 0 & 0 & 1 & l/EI & l^2/2EI & 0 \\ 0 & 0 & 0 & 1 & l & 0 \\ 0 & 0 & 0 & 0 & 1 & 0 \\ 0 & 0 & 0 & 0 & 0 & 1 \end{bmatrix} \cdot \begin{bmatrix} \bar{u} \\ -\bar{w} \\ \bar{\psi} \\ \bar{M} \\ \bar{Q} \\ \bar{T} \end{bmatrix}_B$$

Vol. 2
1960-61

In this case

$$\mathbf{F}_1 = \begin{bmatrix} 1 & 0 & 0 \\ 0 & 1 & 1 \\ 0 & 0 & 1 \end{bmatrix}; \quad \mathbf{F}_2 = \begin{bmatrix} 0 & 0 & l/EA \\ l^2/2EI & l^3/6EI & 0 \\ l/EI & l^2/2EI & 0 \end{bmatrix}; \quad \mathbf{F}_3 = \begin{bmatrix} 0 & 0 & 0 \\ 0 & 0 & 0 \\ 0 & 0 & 0 \end{bmatrix};$$

$$\mathbf{F}_4 = \begin{bmatrix} 1 & l & 0 \\ 0 & 1 & 0 \\ 0 & 0 & 1 \end{bmatrix}$$

and the co-ordinate transformation matrices are

$$\mathbf{G}_1 = \mathbf{G}_3 = \begin{bmatrix} 0 & 1 & 0 \\ -1 & 0 & 0 \\ 0 & 0 & 1 \end{bmatrix}; \quad \mathbf{G}_2 = -\mathbf{G}_4 = \begin{bmatrix} 1 & 0 & 0 \\ 0 & 0 & -1 \\ 0 & 1 & 0 \end{bmatrix}$$

Computing the coupling matrix according to (13) we obtain the result

$$\mathbf{C} = \begin{bmatrix} 6EI/l^2 & 0 & 2EI/l & -6EI/l^2 & 0 & 4EI/l \\ 0 & EA/l & 0 & 0 & -EA/l & 0 \\ -12EI/l^3 & 0 & -6EI/l^2 & 12EI/l^3 & 0 & -6EI/l^2 \\ 6EI/l^2 & 0 & 4EI/l & -6EI/l^2 & 0 & 2EI/l \\ 0 & -EA/l & 0 & 0 & EA/l & 0 \\ 12EI/l^3 & 0 & 6EI/l^2 & -12EI/l^3 & 0 & 6EI/l^2 \end{bmatrix} \tag{15}$$

7. COUPLING MATRIX WITH A RELEASE

The coupling with a release follows exactly the case of a release in a spring matrix. The displacement corresponding to the force which is released is eliminated and the resulting coupling matrix is given by equation (9). Consider the previous example with the coupling beam pinned at point A. Noting that $\bar{M}_A = 0$, the coupling matrix for the case of the pin release at A becomes, with

the use of (15) in (9), where $n-m=4$ and $m+1=3$,

$$\begin{bmatrix} M_{II} \\ Q_{II} \\ T_{II} \\ M_{I} \\ Q_{I} \\ T_{I} \end{bmatrix}_R = \begin{bmatrix} 3EI/l^2 & 0 & 0 & -3EI/l^2 & 0 & 3EI/l \\ 0 & EA/l & 0 & 0 & -EA/l & 0 \\ -3EI/l^3 & 0 & 0 & 3EI/l^3 & 0 & -3EI/l \\ 0 & 0 & 0 & 0 & 0 & 0 \\ 0 & -EA/l & 0 & 0 & EA/l & 0 \\ 3EI/l^3 & 0 & 0 & -3EI/l^3 & 0 & 3EI/l^2 \end{bmatrix} \cdot \begin{bmatrix} u_{I} \\ -w_{I} \\ \psi_{I} \\ u_{II} \\ -w_{II} \\ \psi_{II} \end{bmatrix}_L$$

8. COUPLING RIGIDITY

We saw that if a spring support is of infinite stiffness (i.e. rigid) the normal spring matrix no longer holds and an elimination process must be used. A similar situation arises when two elastic systems are connected by a rigid tie, so that certain displacements are constrained to be equal.[11] We shall now consider this case.

Again we express the state vector just before the point of rigid connexion in terms of the transfer matrix and the unknown vector.

$$\begin{bmatrix} \delta_1 \\ \delta_2 \\ \vdots \\ \delta_p \\ \vdots \\ \delta_q \\ \vdots \\ \delta_n \\ \cdots \\ K_n \\ \vdots \\ K_q \\ \vdots \\ K_p \\ \vdots \\ K_1 \end{bmatrix} \begin{bmatrix} a_{11} & a_{12} & \cdots & a_{1n} \\ a_{21} & a_{22} & \cdots & a_{2n} \\ \vdots & \vdots & & \vdots \\ a_{p1} & a_{p2} & \cdots & a_{pn} \\ \vdots & \vdots & & \vdots \\ a_{q1} & a_{q2} & \cdots & a_{qn} \\ \vdots & \vdots & & \vdots \\ a_{n1} & a_{n2} & \cdots & a_{nn} \\ & & & \\ a_{n+1,1} & a_{n+1,2} & \cdots & a_{n+1,n} \\ \vdots & \vdots & & \vdots \\ a_{2n+1-q,1} & a_{2n+1-q,2} & \cdots & a_{2n+1-q,n} \\ \vdots & \vdots & & \vdots \\ a_{2n+1-p,1} & a_{2n+1-p,2} & \cdots & a_{2n+1-p,n} \\ \vdots & \vdots & & \vdots \\ a_{2n,1} & a_{2n,2} & \cdots & a_{2n,n} \end{bmatrix} \begin{bmatrix} v_1 \\ v_2 \\ \vdots \\ \vdots \\ \vdots \\ v_n \end{bmatrix} \tag{16}$$

Let δ_p and δ_q be the deflexions which are constrained to be equal on account of the rigid coupling, and let the corresponding forces be K_p and K_q. Equating δ_p and δ_q, the vector element v_n can be found in terms of the remaining $(n-1)$ vector elements. The relation is

$$v_n = -\frac{1}{a_{pn}-a_{qn}} \{(a_{p1}-a_{q1})(a_{p2}-a_{q2}) \dots (a_{p,n-1}-a_{q,n-1})\,0\} \begin{bmatrix} v_1 \\ v_2 \\ \vdots \\ v_{n-1} \\ \cdots \\ 0 \end{bmatrix}$$

Substituting this expression in equation (16) we obtain the relation

$$\begin{bmatrix} \delta_1 \\ \delta_2 \\ \vdots \\ \delta_p \\ \vdots \\ \delta_q \\ \vdots \\ \delta_n \\ \cdots \\ K_n \\ \vdots \\ K_q \\ \vdots \\ K_p \\ \vdots \\ K_1 \end{bmatrix} = \begin{bmatrix} a_{11} & a_{12} & \cdots & a_{1,n-1} & 0 \\ a_{21} & a_{22} & \cdots & a_{2,n-1} & 0 \\ \vdots & \vdots & & \vdots & \vdots \\ a_{p1} & a_{p2} & \cdots & a_{p,n-1} & 0 \\ \vdots & \vdots & & \vdots & \vdots \\ a_{q1} & a_{q2} & \cdots & a_{q,n-1} & 0 \\ \vdots & \vdots & & \vdots & \vdots \\ a_{n1} & a_{n2} & \cdots & a_{n,n-1} & 0 \\ & & & & \\ a_{n+1,1} & a_{n+1,2} & \cdots & a_{n+1,n-1} & 0 \\ \vdots & \vdots & & \vdots & \vdots \\ a_{2n+1-q,1} & a_{2n+1-q,2} & \cdots & a_{2n+1-q,n-1} & 0 \\ \vdots & \vdots & & \vdots & \vdots \\ a_{2n+1-p,1} & a_{2n+1-p,2} & \cdots & a_{2n+1-p,n-1} & 0 \\ \vdots & \vdots & & \vdots & \vdots \\ a_{2n,1} & a_{2n,2} & \cdots & a_{2n,n-1} & 0 \end{bmatrix} \cdot \begin{bmatrix} v_1 \\ v_2 \\ \vdots \\ \vdots \\ \vdots \\ \vdots \\ \vdots \\ \vdots \\ v_{n-1} \\ \cdots \\ 0 \end{bmatrix}$$

$$= -\frac{1}{a_{pn}-a_{qn}} \begin{bmatrix} a_{1n} \\ a_{2n} \\ \vdots \\ a_{p,n} \\ \vdots \\ a_{q,n} \\ \vdots \\ a_{n,n} \\ a_{n+1,n} \\ \vdots \\ a_{2n+1-q,n} \\ \vdots \\ a_{2n+1-p,n} \\ \vdots \\ a_{2n,n} \end{bmatrix} \{(a_{p1}-a_{q1})(a_{p2}-a_{q2}) \cdots (a_{p,n-1}-a_{q,n-1})\, 0\} \begin{bmatrix} v_1 \\ v_2 \\ \vdots \\ \vdots \\ \vdots \\ \vdots \\ \vdots \\ \vdots \\ v_{n-1} \\ \cdots \\ 0 \end{bmatrix}$$

$$= \begin{bmatrix} \|1,1\| & \|1,2\| & \|1,3\| & \cdots & \|1,n-1\| & 0 \\ \|2,1\| & \|2,2\| & \|2,3\| & \cdots & \|2,n-1\| & 0 \\ \|3,1\| & \|3,2\| & \|3,3\| & \cdots & \|3,n-1\| & 0 \\ \vdots & \vdots & \vdots & & \vdots & \vdots \\ \vdots & \vdots & \vdots & & \vdots & \vdots \\ \vdots & \vdots & \vdots & & \vdots & \vdots \\ \vdots & \vdots & \vdots & & \vdots & \vdots \\ \vdots & \vdots & \vdots & & \vdots & \vdots \\ \|2n,1\| & \|2n,2\| & \|2n,3\| & \cdots & \|2n,n-1\| & 0 \end{bmatrix} \cdot \begin{bmatrix} v_1 \\ v_2 \\ \vdots \\ \vdots \\ v_{n-1} \\ \cdots \\ 0 \end{bmatrix}$$

Vol. 2
1960-61

where

$$\|1,1\| = |1,p;\ 1,n| - |1,q;\ 1,n| \quad \text{and} \quad \|r,s\| = |r,p;\ s,n| - |r,q;\ s,n|, \text{ etc.}$$

In transferring the state vector from left to right at the rigidity, the unknown force K_i in the rigid tie must be introduced so that the transfer matrix for the rigid coupling becomes

$$\begin{bmatrix} \delta_1 \\ \delta_2 \\ \vdots \\ \delta_n \\ \cdots \\ K_n \\ \vdots \\ K_q \\ \vdots \\ K_p \\ \vdots \\ K_1 \end{bmatrix} = \begin{bmatrix} \|1,1\| & \|1,2\| & \cdots & \|1,n-1\| & 0 \\ \|2,1\| & \|2,2\| & \cdots & \|2,n-1\| & 0 \\ \vdots & \vdots & & \vdots & \vdots \\ \vdots & \vdots & & \vdots & \vdots \\ \|2n+1-q,1\| & \|2n+1-q,2\| & \cdots & \|2n+1-q,n-1\| & 1 \\ \vdots & \vdots & & \vdots & \vdots \\ \|2n+1-p,1\| & \|2n+1-p,2\| & \cdots & \|2n+1-p,n-1\| & -1 \\ \vdots & \vdots & & \vdots & \vdots \\ \|2n,1\| & \|2n,2\| & \cdots & \|2n,n-1\| & 0 \end{bmatrix} \cdot \begin{bmatrix} v_1 \\ v_2 \\ \vdots \\ \vdots \\ \vdots \\ \vdots \\ \vdots \\ v_{n-1} \\ \cdots \\ K_i \end{bmatrix} \tag{17}$$

9. MODIFIED TRANSFER-MATRIX METHOD[18]

In order to demonstrate the numerical difficulties with the ordinary transfer-matrix method, let us consider the homogeneous fixed hinged beam of Fig. 13. The natural frequencies and eigen-modes of the beam can be determined by the following matrix equation (cf. Refs. 12 and 13).

$$\begin{bmatrix} -w \\ \psi \\ M \\ Q \end{bmatrix}_B = \begin{bmatrix} c_0 & lc_1 & bl^2 c_2 & bl^3 c_3 \\ \mu\omega^2 bl^3 c_3 & c_0 & blc_1 & bl^2 c_2 \\ \mu\omega^2 l^2 c_2 & \mu\omega^2 l^3 c_3 & c_0 & lc_1 \\ \mu\omega^2 lc_1 & \mu\omega^2 l^2 c_2 & \mu\omega^2 bl^3 c_3 & c_0 \end{bmatrix} \cdot \begin{bmatrix} -w \\ \psi \\ M \\ Q \end{bmatrix}_A \tag{18}$$

$$\left.\begin{aligned} c_0 &= \frac{1}{2}(\cosh\lambda + \cos\lambda) \\ c_1 &= \frac{1}{2\lambda}(\sinh\lambda + \sin\lambda) \\ c_2 &= \frac{1}{2\lambda^2}(\cosh\lambda - \cos\lambda) \\ c_3 &= \frac{1}{2\lambda^3}(\sinh\lambda - \sin\lambda) \end{aligned}\right\} \quad \left.\begin{aligned} &\lambda^4 = \mu\omega^2 bl^4 \\ &b = \frac{1}{EI_y} \\ &\mu = \text{mass per unit length} \end{aligned}\right. \tag{19}$$

Vol. 2
1960-6

With the boundary conditions $w_A = M_A = w_B = M_B = 0$ the frequency determinant is

$$0 = \Delta = \begin{vmatrix} lc_1 & bl^3 c_3 \\ \mu\omega^2 l^3 c_3 & lc_1 \end{vmatrix} = l^2 c_1^2 - \overbrace{\mu\omega^2 bl^4}^{\lambda^4} . l^2 c_3^2 \tag{20}$$

$$0 = \Delta = l^2\{c_1^2 - \lambda^4 c_3^2\} = l^2\left\{\frac{1}{4\lambda^2}(\sinh\lambda + \sin\lambda)^2 - \frac{1}{4\lambda^2}(\sinh\lambda - \sin\lambda)^2\right\}$$

$$0 = \Delta = \frac{l^2}{4\lambda^2}[4\sinh\lambda\sin\lambda],$$

i.e. $\sin\lambda = 0$; $\lambda_i = i\pi$; $\omega_i = \dfrac{i^2\pi^2}{\sqrt{(\mu bl^4)}}$ $(i = 1, 2, 3, \ldots)$

Fig. 13.

It is obvious that $\sin\lambda$ is responsible for the zero of the frequency determinant. When carrying out a numerical computation, however, the elements in the matrix of equation (18), and thus in the frequency determinant (20), are numbers. Therefore, the influence of $\sin\lambda$ is lost when λ is large and insufficient digits are carried along in the computation, because then

$$c_0 \approx \tfrac{1}{2}\cosh\lambda, \text{ etc. [see equation (19)]}$$

Since λ is proportional to $\sqrt{\omega}$, it may become impossible to determine the zeros of the frequency determinant for high frequencies. For example, when λ equals 17 we have,

$$\sinh\lambda = \sinh 17 = 12077476\ldots$$

This means that when only 8 digits are carried along on the computer the influence of the sine functions is lost. Since for a simple beam the sixth eigenfrequency corresponds to $\lambda = 18{\cdot}85$ it is impossible to find more than the lowest five frequencies with an eight-digit numerical computation.

This consideration leads to a simple estimate for the number of digits that have to be carried along for a numerical computation: The number of digits carried along must be larger than the number of digits of

$$\sinh\lambda \simeq \cosh\lambda \simeq \frac{e^\lambda}{2} *$$

In the determination of λ the overall length of the beam, average mass distribution and average bending stiffness may be used.

Although the use of so-called delta matrices[4, 6, 18] offers a satisfactory solution to the problem of numerical accuracy, besides being a convenient means for the consideration of intermediate conditions, it will most probably be limited to fourth-order problems because of the enormous increase in the number of

* This rule was first stated by Schumpich (unpublished).

elements when cases of higher order have to be dealt with. It seemed, therefore, desirable to find another generally applicable approach.[19]

As we had seen in the beginning of this section, the numerical difficulties arise chiefly from the fact that, with rising frequency, the frequency determinant becomes a small difference of large numbers. Furthermore, numerical computations show that the numbers of the matrix elements increase with each successive matrix multiplication. This dilemma could be solved if it were possible to estimate the elements in the initial state vector $\mathbf{z}_0$ close to their actual values which, of course, change with ω. In order to allow a correction of the estimated values, correction terms should be added so that, for the nth order problem in which the initial state vector $\mathbf{z}_0$ contains in general $n/2$ elements equal to zero, $\mathbf{z}_0$ would be written as follows

$$\mathbf{z}_0 = \begin{bmatrix} 0 \\ 0 \\ \vdots \\ 0 \end{bmatrix}_{n/2} \begin{matrix} \\ \\ \\ \\ 1 \\ \lambda_1 \\ \lambda_2 \\ \vdots \\ \vdots \\ \vdots \\ \lambda_{n/2-1} \end{matrix} + k_1 \begin{bmatrix} 0 \\ 0 \\ \vdots \\ 0 \end{bmatrix}_{n/2} \begin{matrix} \\ \\ \\ \\ 0 \\ 1 \\ 0 \\ \vdots \\ \vdots \\ \vdots \\ 0 \end{matrix} + k_2 \begin{bmatrix} 0 \\ 0 \\ \vdots \\ 0 \end{bmatrix}_{n/2} \begin{matrix} \\ \\ \\ \\ 0 \\ 0 \\ 1 \\ \vdots \\ \vdots \\ \vdots \\ 0 \end{matrix} + \ldots + k_{n/2-1} \begin{bmatrix} 0 \\ 0 \\ \vdots \\ 0 \end{bmatrix}_{n/2} \begin{matrix} \\ \\ \\ \\ 0 \\ 0 \\ 0 \\ 0 \\ . \\ 0 \\ 1 \end{matrix} \tag{21}$$

In this scheme the letters λ_i represent actual numbers which are estimated values for the corresponding physical quantities constituting the state vector $\mathbf{z}_0$, whereas the correction factors k_λ are unknown. Since we consider a problem of free vibrations, one of the elements is arbitrarily taken equal to unity. Furthermore, the elements are arranged in such a way that the elements equal to zero on account of the boundary conditions are assembled in the upper half of the state vector.*

With the initial state vector according to equation (21) we obtain on account of the boundary conditions the following system of $n/2$ non-homogeneous linear equations for k_i $(i = 1, 2, \ldots, n/2-1)$

$$\begin{aligned}
&[1] \quad p_{11}(\lambda_1+k_1)+\ldots+p_{1i}(\lambda_i+k_i)+\ldots+p_{1s}(\lambda_s+k_s)+\ldots \\
&\qquad \ldots p_{1,\,n/2-1}(\lambda_{n/2-1}+k_{n/2-1})+p_1=0 \\
&\vdots \\
&[i] \quad p_{i1}(\lambda_1+k_1)+\ldots+p_{ii}(\lambda_i+k_i)+\ldots+p_{is}(\lambda_s+k_s)+\ldots \\
&\qquad \ldots p_{i,\,n/2-1}(\lambda_{n/2-1}+k_{n/2-1})+p_i=0 \\
&\vdots \\
&[s] \quad p_{s1}(\lambda_1+k_1)+\ldots+p_{si}(\lambda_i+k_i)+\ldots+p_{ss}(\lambda_s+k_s)+\ldots \\
&\qquad \ldots+p_{s,\,n/2-1}(\lambda_{n/2-1}+k_{n/2-1})+p_s=0 \\
&[n/2] \quad p_{n/2,\,1}(\lambda_1+k_1)+\ldots+p_{n/2,\,i}(\lambda_i+k_i)+\ldots \\
&\qquad \ldots+p_{n/2,\,s}(\lambda_s+k_s)+\ldots+p_{n/2,\,n/2-1}(\lambda_{n/2-1}+k_{n/2-1})+\ldots+p_{n/2}=0
\end{aligned} \tag{22}$$

* This is done here only to facilitate the writing of the mathematical proofs. In actual computing practice the elements remain in their usual arrangement, so that the elements of the transfer matrix do not have to be re-assembled.

Using all equations (22) except equation (22, s) we obtain the following solution for k_i

$$k_i = x_i = -\lambda_i + \frac{\Delta_i}{\Delta} * \tag{23}$$

where

$$\Delta_i = \begin{vmatrix} p_{1,i+1} & p_{1,i+2} & \cdots & p_{1,n/2-1} & p_1 & p_{11} & \cdots & p_{1,i-1} \\ p_{2,i+1} & p_{2,i+2} & \cdots & p_{2,n/2-1} & p_2 & p_{21} & \cdots & p_{2,i-1} \\ \vdots & & & & & & & \\ p_{s-1,i+1} & \cdots & & & p_{s-1} & \cdots & & p_{s-1,i-1} \\ p_{s+1,i+1} & \cdots & & & p_{s+1} & \cdots & & p_{s+1,i-1} \\ \vdots & & & & & & & \\ p_{n/2,i+1} & \cdots & & & p_{n/2} & \cdots & & p_{n/2,i-1} \end{vmatrix}$$

and

$$\Delta = \begin{vmatrix} p_{11} & p_{12} & \cdots & p_{1i} & \cdots & p_{1,n/2-1} \\ p_{21} & p_{22} & \cdots & p_{2i} & \cdots & p_{2,n/2-1} \\ \vdots & & & & & \\ p_{s-1,1} & \cdots & & p_{s-1,i} & \cdots & p_{s-1,n/2-1} \\ p_{s+1,1} & \cdots & & p_{s+1,i} & \cdots & p_{s+1,n/2-1} \\ \vdots & & & & & \\ p_{n/2,1} & \cdots & & p_{n/2,i} & \cdots & p_{n/2,n/2-1} \end{vmatrix}$$

We put $\lambda_i^{[1]} = \lambda_i + k_i \quad (i \neq s)$

and get $\lambda_i^{[1]} = \dfrac{\Delta_i}{\Delta}$

i.e. independent of the first estimates λ_i. This holds also for $\lambda_i^{[1]} = \lambda_s + k_s$, as will be shown in the following.

We obtain a certain number k_s, which we call y_s, from equation (22, s) by inserting for all k_i $(i \neq s)$ their solution (23)

$$y_s = -\lambda_s - \left\{ \frac{1}{p_{ss}} \left(p_s + p_{s1}\frac{\Delta_1}{\Delta} + p_{s2}\frac{\Delta_2}{\Delta} + \ldots + p_{s,s-1}\frac{\Delta_{s-1}}{\Delta} + \right. \right.$$
$$\left. \left. + p_{s,s+1}\frac{\Delta_{s+1}}{\Delta} + \ldots + p_{s,n/2-1}\Delta_{n/2-1}/\Delta \right) \right\} \tag{24}$$

Another value x_s of k_s was given by (23). We therefore take the mean value $k_s = \frac{1}{2}(x_s + y_s)$ and get

$$\lambda_s^{[1]} = \frac{1}{2}\left[\frac{\Delta_s}{\Delta} - \{\ldots\}\right]$$

which is also independent of the first estimate λ_s.

With (23) and (24) we have

$$R_s = x_s - y_s = \frac{\Delta_s}{\Delta} + \{\ldots\}$$

which is likewise independent of λ_i.

Substituting $\lambda_i^{[1]}$ $(i \neq s)$ in (23), it is obvious that

$$k_i^{[1]} = x_i^{[1]} = -\lambda_i^{[1]} + \Delta_{i/\Delta} = -\Delta_{i/\Delta} + \Delta_{i/\Delta} = 0$$

* s must be chosen so that $\Delta \neq 0$.

Vol. 2
1960-61

Equally $$k_s^{[1]} = \tfrac{1}{2}(x_s^{[1]} + y_s^{[1]}) = 0$$

because, according to (23),

$$x_s^{[1]} = -\lambda_s^{[1]} + \frac{\Delta_s}{\Delta} = \frac{1}{2}\left[\frac{\Delta_s}{\Delta} + \{\ldots\}\right] = \frac{R_s}{2}$$

and according to (24)

$$y_s^{[1]} = -\lambda_s^{[1]} - \{\ldots\} = -\frac{1}{2}\left(\frac{\Delta_s}{\Delta} + \{\ldots\}\right) = -\frac{R_s}{2}$$

Since $R_s = R_s(\omega)$ approaches zero, when $\omega \to \omega_E$, then $x_s^{[1]}$ and $y_s^{[1]}$ each go to zero, which is also true for x_s and y_s, if the estimate λ_i is correct for $\omega \to \omega_E$. This will practically be the case, if for the λ_i's to be used for $\omega = \omega_r$ the corrected $\lambda_i^{[1]} = \lambda_i + k_i(\omega_{r-1})$ of the proceeding computing step are taken and if the step $\omega_r - \omega_{r-1}$ is relatively small. Unless these conditions are violated, the equation for the natural frequency criterion $R_s(\omega)$ will be a difference of small numbers instead of becoming—especially in the case of large ω's—a difference of very large numbers.

Whereas in the above theoretical considerations it was assumed that the transfer matrices were multiplied with each other in the usual fashion in order to facilitate the mathematical proofs, in actual computing practice the matrices are multiplied one after another with the columns of the initial state vector (21). In this way we obtain finally at the end m of the body under consideration

$$\mathbf{z}_m = \begin{bmatrix} g_1 \\ g_2 \\ \vdots \\ g_n \end{bmatrix} + k_1 \begin{bmatrix} g_{11} \\ g_{21} \\ \vdots \\ g_{n,1} \end{bmatrix} + k_2 \begin{bmatrix} g_{12} \\ g_{22} \\ \vdots \\ g_{n,2} \end{bmatrix} + \ldots + k_i \begin{bmatrix} g_{1i} \\ g_{2i} \\ \vdots \\ g_{n,i} \end{bmatrix} + \ldots + k_s \begin{bmatrix} g_{1s} \\ g_{2s} \\ \vdots \\ g_{n,s} \end{bmatrix}$$

$$+ \ldots + k_{n/2-1} \begin{bmatrix} g_{1,\,n/2-1} \\ g_{2,\,n/2-1} \\ \vdots \\ g_{n,\,n/2-1} \end{bmatrix}$$

On account of the boundary conditions at $m, n/2$ terms

$$g_i + k_1 g_{i1} + k_2 g_{i2} + \ldots + k_i g_{ii} + \ldots + k_{n/2-1} g_{i\ n/2-1}$$

must be zero.

Using $n/2-1$ of these equations, excluding say the equation for $i = s$, we can calculate all correction factors

$$k_i = x_i \quad (i \neq s)$$

With equation (s) $$g_s + k_1 g_{s1} + \ldots + k_{n/2-1} g_{s,\,n/2-1} = 0$$

substituting for k_i $(i \neq s)$ x_i and for k_s as shown before y_s, we can compute y_s. From this follows

$$k_s = \frac{x_s + y_s}{2}$$

Thus we obtain the corrected initial values

$$\lambda_i^{[1]} = \lambda_i + k_i$$

which are then employed as the λ_i in the next computing step, where a slightly higher or lower frequency is used in the transfer matrices. With this practice the elements g_i in the first column will remain rather small as compared with the usual transfer-matrix method resulting in the numerical advantages outlined above.

Likewise the eigen-modes are easily found by multiplying all columns with their respective k_i and by then adding corresponding elements of all columns.

Example

Let us consider the simple problem of free vibrations of the Myklestad beam in Fig. 14.

FIG. 14.

Vol. 2
1960-61

With the data, holding for each field and point mass alike,

$$l = 1; \quad EI = \tfrac{1}{6};$$

the transfer matrix is as follows:[12]

$$\begin{bmatrix} 1 & 1 & 3 & 1 \\ 0 & 1 & 6 & 3 \\ 0 & 0 & 1 & 1 \\ m\omega^2 & m\omega^2 & 3m\omega^2 & 1+m\omega^2 \end{bmatrix}$$

If we carry out the matrix multiplication for the case $m\omega^2 = 3$, the frequency determinant will be

$$82 \times 289 - 558 \times 42 = 262$$

which, considering the small numbers in the matrix, constitutes a difference of rather large numbers.

Since we have a fourth-order problem, equation (21) reduces to

$$\mathbf{z}_1 = \begin{bmatrix} 0 \\ 0 \\ 1 \\ \lambda_1 \end{bmatrix} + k_1 \begin{bmatrix} 0 \\ 0 \\ 0 \\ 1 \end{bmatrix}$$

Let us start with a frequency corresponding to $m\omega^2 = 1$. Since we begin with a small frequency, no numerical difficulties have to be expected even though our estimate of λ_1 may be quite inaccurate. For simplicity's sake we take $\lambda_1 = 1$, therefore

$$\mathbf{z}_1 = \begin{bmatrix} 0 \\ 0 \\ 1 \\ 1 \end{bmatrix} + k_1 \begin{bmatrix} 0 \\ 0 \\ 0 \\ 1 \end{bmatrix}$$

This state vector is then successively multiplied with the transfer matrix as follows

$$\begin{bmatrix} 0 \\ 0 \\ 1 \\ 1 \end{bmatrix}_1 + k_1 \begin{bmatrix} 0 \\ 0 \\ 0 \\ 1 \end{bmatrix}_1$$

$$\downarrow \qquad \downarrow$$

$$\begin{bmatrix} 1 & 1 & 3 & 1 \\ 0 & 1 & 6 & 3 \\ 0 & 0 & 1 & 1 \\ 1 & 1 & 3 & 2 \end{bmatrix} \rightarrow \begin{bmatrix} 4 \\ 9 \\ 2 \\ 5 \end{bmatrix}_2 + k_1 \begin{bmatrix} 1 \\ 3 \\ 1 \\ 2 \end{bmatrix}_2$$

$$\downarrow \qquad \downarrow$$

$$\begin{bmatrix} 1 & 1 & 3 & 1 \\ 0 & 1 & 6 & 3 \\ 0 & 0 & 1 & 1 \\ 1 & 1 & 3 & 2 \end{bmatrix} \rightarrow \begin{bmatrix} 24 \\ 36 \\ 7 \\ 29 \end{bmatrix}_3 + k_1 \begin{bmatrix} 9 \\ 15 \\ 3 \\ 11 \end{bmatrix}_3$$

$$\downarrow \qquad \downarrow$$

$$\begin{bmatrix} 1 & 1 & 3 & 1 \\ 0 & 1 & 6 & 3 \\ 0 & 0 & 1 & 1 \\ 1 & 1 & 3 & 2 \end{bmatrix} \rightarrow \begin{bmatrix} 110 \\ 165 \\ 36 \\ 139 \end{bmatrix}_4 + k_1 \begin{bmatrix} 44 \\ 66 \\ 14 \\ 55 \end{bmatrix}_4 = 0$$

The boundary conditions at point 4 lead to the following two equations

$$36 + k_1 \times 14 = 0$$

$$139 + k_1 \times 55 = 0$$

Take $s = 1$, then

$$y_1 = -\frac{36}{14} = -2{\cdot}571$$

$$x_1 = -\frac{139}{55} = -2{\cdot}527$$

$$x_1 - y_1 = +0{\cdot}044$$

Since $x_1 - y_1 \neq 0$, the ω used above was not an eigen-frequency.

$$k_1 = \frac{x_1 + y_1}{2} = -2{\cdot}55$$

Adding this value to λ_1 in the state vector $\mathbf{z}_1$ we obtain

$$\mathbf{z}_1^{[1]} = \begin{bmatrix} 0 \\ 0 \\ 1 \\ 1+(-2{\cdot}55) \end{bmatrix} + k_1^{[1]} \begin{bmatrix} 0 \\ 0 \\ 0 \\ 1 \end{bmatrix} = \begin{bmatrix} 0 \\ 0 \\ 1 \\ -1{\cdot}55 \end{bmatrix} + k_1^{[1]} \begin{bmatrix} 0 \\ 0 \\ 0 \\ 1 \end{bmatrix}$$

Here the superscript indicates that this is the first iteration step.

As we have seen above it is actually unnecessary to carry out the second step because it does not yield any new information.

We now proceed with the computation by choosing a new value for ω. If this is taken close to the preceding one, it can be expected that the value

$$1 + k_1 = 1 + \frac{x_1 + y_1}{2} = -1{\cdot}55$$

is a good estimate for λ_1.

Let us carry out the next matrix multiplication for $m\omega^2 = 2{\cdot}0$. Then

$$\begin{bmatrix} 0 \\ 0 \\ 1 \\ -1{\cdot}55 \end{bmatrix}_1 + k_1 \begin{bmatrix} 0 \\ 0 \\ 0 \\ 1 \end{bmatrix}_1 \qquad \begin{aligned} -w_1 &= 0 \\ \psi_1 &= 0 \\ M_1 &= 1 \\ Q_1 &= -1{\cdot}79 \end{aligned}$$

$$\downarrow \qquad \downarrow$$

$$\begin{bmatrix} 1 & 1 & 3 & 1 \\ 0 & 1 & 6 & 3 \\ 0 & 0 & 1 & 1 \\ 2 & 2 & 6 & 3 \end{bmatrix} \rightarrow \begin{bmatrix} 1{\cdot}45 \\ 1{\cdot}35 \\ -0{\cdot}55 \\ 1{\cdot}35 \end{bmatrix}_2 + k_1 \begin{bmatrix} 1 \\ 3 \\ 1 \\ 3 \end{bmatrix}_2 \qquad \begin{aligned} -w_2 &= 1{\cdot}21 \\ \psi_2 &= 0{\cdot}62 \\ M_2 &= -0{\cdot}79 \\ Q_2 &= 0{\cdot}62 \end{aligned}$$

$$\downarrow \qquad \downarrow$$

$$\begin{bmatrix} 1 & 1 & 3 & 1 \\ 0 & 1 & 6 & 3 \\ 0 & 0 & 1 & 1 \\ 2 & 2 & 6 & 3 \end{bmatrix} \rightarrow \begin{bmatrix} 2{\cdot}50 \\ 2{\cdot}10 \\ 0{\cdot}80 \\ 6{\cdot}35 \end{bmatrix}_3 + k_1 \begin{bmatrix} 10 \\ 18 \\ 4 \\ 23 \end{bmatrix}_3 \qquad \begin{aligned} -w_3 &= 0{\cdot}07 \\ \psi_3 &= -2{\cdot}27 \\ M_3 &= -0{\cdot}17 \\ Q_3 &= 0{\cdot}67 \end{aligned}$$

$$\downarrow \qquad \downarrow$$

$$\begin{bmatrix} 1 & 1 & 3 & 1 \\ 0 & 1 & 6 & 3 \\ 0 & 0 & 1 & 1 \\ 2 & 2 & 6 & 3 \end{bmatrix} \rightarrow \begin{bmatrix} 13{\cdot}55 \\ 25{\cdot}95 \\ 7{\cdot}15 \\ 33{\cdot}05 \end{bmatrix}_4 + k_1 \begin{bmatrix} 63 \\ 111 \\ 27 \\ 149 \end{bmatrix}_4 \qquad \begin{aligned} -w_4 &= -1{\cdot}96 \\ \psi_4 &= -1{\cdot}05 \\ M_4 &= 0{\cdot}59 \\ Q_4 &= -3{\cdot}15 \end{aligned}$$

Vol. 2
1960-61

That $\lambda_1 = -1{\cdot}55$ was not a poor estimate is borne out by the fact that the elements in the first column vectors do not rise appreciably with each successive matrix multiplication as was the case before,* although the step from $m\omega^2 = 1$ to $m\omega^2 = 2$ was quite large.

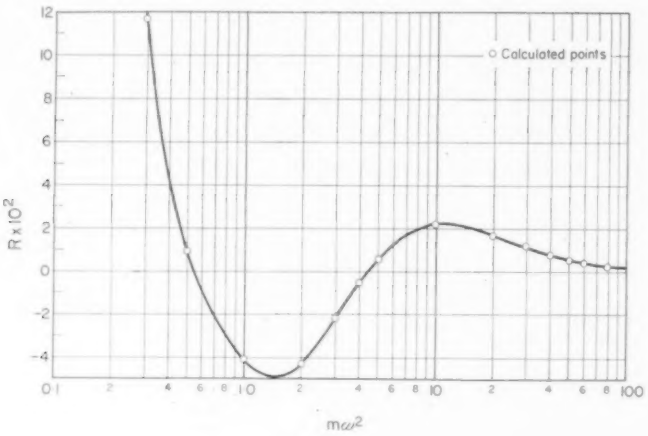

FIG. 15.

The boundary conditions at point 4 again yield the following two equations

$$7{\cdot}15 + k_1 \times 27 = 0$$

$$33{\cdot}05 + k_1 \times 149 = 0$$

from which we obtain

$$y_1 = -\frac{7{\cdot}15}{27} = -0{\cdot}265$$

$$x_1 = -\frac{33{\cdot}05}{149} = -0{\cdot}222$$

Hence

$$x_1 - y_1 = +0{\cdot}043$$

and

$$k_1 = \frac{x_1 + y_1}{2} = -0{\cdot}243$$

Multiplying the right columns in the last multiplication table with $k_1 = -0{\cdot}243$ and adding the result to the corresponding left columns we obtain the values for w, ψ, M and Q at the points 1, 2, 3 and 4. From the plots in Fig. 15 we can see that $m\omega^2 = 2$ corresponds to a frequency between the second and third eigen-frequency.

In the same way the calculation was continued for higher values of $m\omega^2$ and in every case slide-rule accuracy was sufficient.

* The numbers in the first column are less than 10 per cent the size they would assume if λ_1 had been taken equal to unity.

REFERENCES

1. N. O. Myklestad, *J. Aero. Sci.* **11**, 153 (1944).
2. M. A. Prohl, *Trans. Amer. Soc. Mech. Engrs.* **67**, 142 (1945).
3. W. T. Thomson, *Trans. Amer. Soc. Mech. Engrs.* **72**, 337 (1950).
4. H. Fuhrke. Diss., Technische Hochschule Darmstadt (1953).
5. E. Pestel, *Abh. braunschw. wiss. Ges.* **6**, 227 (1954).
6. K. Marguerre, *J. Math. Phys.* **35**, 28 (1956).
7. S. Falk, *Abh. braunschw. wiss. Ges.* **7**, 74 (1955).
8. H. Unger, *Intern Kolloquium über Probleme der Rechentechnik* pp. I41–149. Dresden (1955).
9. F. F. Ehrich, *J. Appl. Mech.* **23**, 109 (1956).
10. G. Schumpich, *Öst. Ing.-Arch.* **11**, 194 (1957).
11. E. Pestel and G. Schumpich, *Schiffstech.* **4**, 55 (1957).
12. E. Pestel, *Dynamics of Structures by Transfer Matrices.* Technical Report No. 1, Contract AF 61 (/52)-33 (1959).
13. E. Pestel, G. Schumpich and S. Spierig, *Ver. dtsch. Ing. Ber.* **35**, 11 (1959).
14. S. Falk, *Ingen.-Arch.* **24**, 216 (1956).
15. S. Falk, *Ver. dtsch. Ing. Ber.* **30**, 65 (1958).
16. S. Falk, *Ingen.-Arch.* **26**, 61 (1958).
17. S. Falk, *Ingen.-Arch.* **26**, 96 (1958).
18. E. Pestel, *Ingen.-Arch.* **27**, 250 (1959).
19. E. Pestel and O. Mahrenholtz, *Ingen.-Arch.* **28**, 255 (1959).

Vol. 2
1960-61

Int. J. Mech. Sci. Pergamon Press Ltd. 1960. Vol. 2, pp. 168–178. Printed in Great Britain

ON THE STATISTICAL ANALYSIS OF THE MOTION OF SOME SIMPLE TWO-DIMENSIONAL LINEAR VEHICLES MOVING ON A RANDOM TRACK*

F. KOZIN and J. L. BOGDANOFF
Division of Engineering Sciences, Purdue University, Lafayette, Indiana

(*Received* 24 *February* 1960)

Summary—The influence of the length parameters—base length, idealized-tire spread and track-roughness spread—on the assumed "ride" criterion of some simple two-dimensional linear vehicles is examined. This examination is made under the assumption that the vehicles move with constant horizontal velocity on a weakly stationary random track in such a way that contact is maintained with the track throughout the motion.

It is found that base length and track-roughness spread have a pronounced influence on the ride criterion throughout the range of interest in this paper. However, the idealized-tire spread only produces a marked effect on the ride criterion if the base length has been badly chosen.

As the analysis is based upon second-order statistical properties, a knowledge of all of the joint probability distributions of the random track is not required.

I. INTRODUCTION

ONE of the important military land-vehicle problems of the present day is that of increasing the speed of certain types of vehicles under off-road conditions. The present 3–5 m.p.h. range is reminiscent of the days of horse-drawn wagons and is in striking contrast to the high speeds obtained on modern highways. The low speed range is obviously due to the fact that present-day vehicles are not designed to be driven across open fields. The basic problem is thus: how must designs be modified so as to increase off-road speeds without unduly impairing speed on paved roads?

This paper is devoted to a presentation of some results obtained in an initial effort[1-3] to find solutions to the above problem. In particular, we confine our attention to examining the influence of some parameters on one aspect of vehicle ride.

Ground roughness, roughness of the surface of the sea, roughness of the atmosphere, etc., can only be defined in a statistical sense.[4, 5] Hence, our analysis is based upon statistical methods.†

We shall consider a two-dimensional linear vehicle moving with constant horizontal velocity on a straight track. Gravity is neglected. It is assumed that the vehicle has two contacts with the track; these contacts may be either point followers or idealized linear tires with finite tire spread. In each case, the contact with the track is assumed to be maintained at all times. While the

* This research was conducted by the Midwest Applied Science Corp. for the Land Locomotion Research Laboratory, Detroit Arsenal, under Contract DA-33-008-ORD-1738.

† An elementary discussion is given in Ref. 3 of the concepts and terms in probability and statistics employed below. For greater detail, see Refs. 6–8.

vehicle under discussion has only two contacts, the analysis is easily extended to include multi-contact vehicles.

The equations of motion are given for a vehicle having different properties in front and rear. However, to simplify the analysis and computations, we have confined our attention to a symmetrical vehicle, i.e. to one having the same properties in front and rear with its center of gravity midway between the two contacts. This simplification does not appear to constitute a restriction on the qualitative results of the study.

The statistical description of the track elevation is assumed to be independent of the horizontal co-ordinate origin location, and the mean value is taken as zero. Transient vehicle motion is ignored. Thus, power spectral-density methods may be employed. A spectral density* of ground roughness as computed from the results of a survey taken in an open field is included. Unfortunately, so little work has been done in characterizing ground roughness statistically that we have not employed this single density function in calculations. Instead, and until further surveys are made and analyzed, we shall employ a spectral density for the track roughness which can be adjusted to give a reasonable approximation to the one obtained from measurement and is analytically tractable. Surveys may ultimately indicate that this choice is a good one or that another analytical form is appropriate.

Vol. 2
1960-61

One of the factors which appears to limit the velocity or speed of a vehicle under off-road conditions is the driver's inability to stand the pounding he gets from the vehicle itself. As vertical acceleration of the driver's seat is one source of such pounding, the results given below pertain to the influence of certain length parameters on the variance and peak value of the power spectral density of the vertical acceleration of a point on the frame, in particular, the center of gravity. The length parameters considered are the distance between points of contact with the track, track-roughness spread and the idealized-tire spread. The influence of other parameters and other aspects of driver-pounding such as pitching of the frame will be taken up at a later time.

It is worthy of note that the results presented depend only upon second-order statistical properties of the random track. Hence, whether the ground or track is Gaussian, for example, is of no concern.

II. ANALYSIS

The schematic diagram shown in Fig. 1 defines the linear model considered. The constants have their usual meanings and the track elevation vs. horizontal distance x is denoted by $Y_0(x)$. We assume that $Y_0(x)$ is a second-order, mean-square-continuous, weakly stationary random function of x.[3] The quantity m is the mass of the frame. I_m is the moment of inertia of the frame about its center of gravity. The wheel masses are m_1 (rear) and m_2 (front), respectively. The tire spring constants and damping constants are distributed along the tire spread. κ_j, γ_j and a_j $(j = 1{\cdot}2)$ are, respectively, the spring constant per unit

* Roughly speaking, if a weakly stationary random function were to be thought of as the superposition of a great many sinusoidal components, then the average power in the frequency band $(\omega, \omega + d\omega)$ is given by $P(\omega)\, d\omega$ where $P(\omega)$ is called the power spectral-density function.

length, the damping constant per unit length and the half spread. We assume that κ_j and γ_j are even functions of ξ the distance along the tire spread as measured from the tire center. All angles are assumed small so that cosines may be replaced by 1 and sines by the angle in radians.

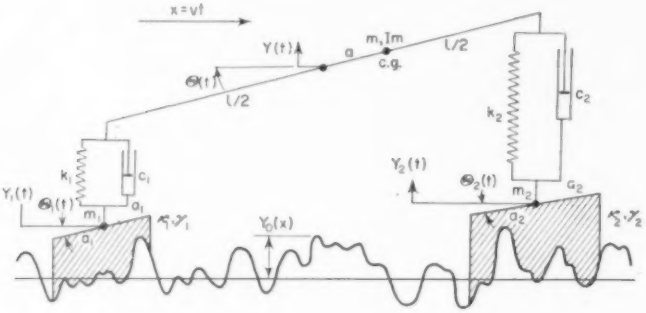

FIG. 1. Idealized vehicle.

The equations of motion are

$$\left.\begin{aligned} m(\ddot{Y}+a\ddot{\Theta}) &= -F_1-F_2 \\ I_m\ddot{\Theta} &= \left(\frac{l}{2}+a\right)F_1-\left(\frac{l}{2}-a\right)F_2 \\ m_1\ddot{Y}_1 &= F_1-F_3, \quad m_2\ddot{Y}_2 = F_2-F_4 \end{aligned}\right\} \tag{1}$$

where

$$\left.\begin{aligned} F_1 &= k_1\left[Y-\frac{l}{2}\Theta-Y_1\right]+c_1\left[\dot{Y}-\frac{l}{2}\dot{\Theta}-\dot{Y}_1\right] \\ F_2 &= k_2\left[Y+\frac{l}{2}\Theta-Y_2\right]+c_2\left[\dot{Y}+\frac{l}{2}\dot{\Theta}-\dot{Y}_2\right] \\ F_3 &= \int_{-a_1}^{a_1}\left\{\kappa_1\left[Y_1+\xi\Theta_1-Y_0\left(x-\frac{l}{2}+\xi\right)\right]+\right. \\ &\qquad \left.+\gamma_1\left[\dot{Y}_1+\xi\dot{\Theta}_1-\dot{Y}_0\left(x-\frac{l}{2}+\xi\right)\right]\right\}d\xi \\ F_4 &= \int_{-a_2}^{a_2}\left\{\kappa_2\left[Y_2+\xi\Theta_2-Y_0\left(x+\frac{l}{2}+\xi\right)\right]+\right. \\ &\qquad \left.+\gamma_2\left[\dot{Y}_2+\xi\dot{\Theta}_2-\dot{Y}_0\left(x+\frac{l}{2}+\xi\right)\right]\right\}d\xi \end{aligned}\right\} \tag{2}$$

and the derivatives and integrals are to be interpreted as mean-square derivatives and mean-square integrals.[8]

For a symmetrical vehicle, and employing the usual symbols of vibration literature, equations (1) reduce to the following:

$$\left.\begin{aligned}
&\ddot{Y}+2\zeta_y\omega_y\dot{Y}+\omega_y^2 Y-\tfrac{1}{2}(2\zeta_y\omega_y\dot{Y}_1+\omega_y^2 Y_1)-\tfrac{1}{2}(2\zeta_y\omega_y\dot{Y}_2+Y_2)=0\\
&\quad-\alpha_1\left(\frac{2\zeta_y\omega_0^2}{\omega_y}\dot{Y}+\omega_0^2 Y\right)+\ddot{Y}_1+\left(2\zeta_0\omega_0+\alpha_1\frac{2\zeta_y\omega_0^2}{\omega_y}\right)\dot{Y}_1+\\
&\quad+\omega_0^2(1+\alpha_1)Y_1+\frac{\alpha_1 l}{2}\left(\frac{2\zeta_\theta\omega_0^2}{\omega_\theta}\dot{\Theta}+\omega_0^2\Theta\right)\\
&=\omega_0^2\int_{-a}^{a}\left[\frac{\kappa}{K}Y_0\left(x-\frac{l}{2}+\xi\right)+\frac{2\zeta_0}{\omega_0}\frac{\gamma}{C}\dot{Y}_0\left(x-\frac{l}{2}+\xi\right)\right]d\xi,\\
&\quad-\alpha_1\left(\frac{2\zeta_y\omega_0^2}{\omega_y}\dot{Y}+\omega_0^2 Y\right)+\ddot{Y}_2+\left(2\zeta_0\omega_0+\alpha_1\frac{2\zeta_y\omega_0^2}{\omega_y}\right)\dot{Y}_2+\\
&\quad+\omega_0^2(1+\alpha_1)Y_2-\frac{\alpha_1 l}{2}\left(\frac{2\zeta_\theta\omega_0^2}{\omega_\theta}\dot{\Theta}+\omega_0^2\Theta\right)\\
&=\omega_0^2\int_{-a}^{a}\left[\frac{\kappa}{K}Y_0\left(x+\frac{l}{2}+\xi\right)+\frac{2\zeta_0}{\omega_0}\frac{\gamma}{C}\dot{Y}_0\left(x+\frac{l}{2}+\xi\right)\right]d\xi\\
&\frac{1}{l}(2\zeta_\theta\omega_\theta\dot{Y}_1+Y_1)-\frac{1}{l}(2\zeta_\theta\omega_\theta\dot{Y}_2+Y_2)+\ddot{\Theta}+2\zeta_\theta\omega_\theta\dot{\Theta}+\omega_\theta^2\Theta=0
\end{aligned}\right\}\tag{3}$$

where
$$K=\int_{-a}^{a}\kappa\,d\xi,\quad C=\int_{-a}^{a}\gamma\,d\xi,\quad \alpha_1=\frac{k}{K}\tag{4}$$

The angles Θ_1 and Θ_2 drop out of the second and third equations because κ and γ are assumed to be even functions of ξ.

Let $h_y(t), h_{y_1}(t), h_{y_2}(t), h_\theta(t)$ and $g_y(t), g_{y_1}(t), g_{y_2}(t), g_\theta(t)$ be the impulsive admittances of the system. Then, mean-square solutions of (3) are

$$\left.\begin{aligned}
Y(t)&=\omega_0^2\int_0^\infty\{h_y(\tau)F_1(t-\tau)+g_y(\tau)F_2(t-\tau)\}\,d\tau\\
Y_1(t)&=\omega_0^2\int_0^\infty\{h_{y_1}(\tau)F_1(t-\tau)+g_{y_1}(\tau)F_2(t-\tau)\}\,d\tau\\
Y_2(t)&=\omega_0^2\int_0^\infty\{h_{y_2}(\tau)F_1(t-\tau)+g_{y_2}(\tau)F_2(t-\tau)\}\,d\tau\\
\Theta(t)&=\omega_0^2\int_0^\infty\{h_\theta(\tau)F_1(t-\tau)+g_\theta(\tau)F_2(t-\tau)\}\,d\tau
\end{aligned}\right\}\tag{5}$$

where the integrals are mean-square Riemann integrals. The system has been started at $t=-\infty, x=vt$ and

$$\left.\begin{aligned}
F_1(t)&=\int_{-a}^{a}\left[\frac{\kappa}{K}Y_0\left(vt-\frac{l}{2}+\xi\right)+\frac{2\zeta_0}{\omega_0}\frac{\gamma}{C}\dot{Y}_0\left(vt-\frac{l}{2}+\xi\right)\right]d\xi\\
F_2(t)&=\int_{-a}^{a}\left[\frac{\kappa}{K}Y_0\left(vt+\frac{l}{2}+\xi\right)+\frac{2\zeta_0}{\omega_0}\frac{\gamma}{C}\dot{Y}_0\left(vt+\frac{l}{2}+\xi\right)\right]d\xi
\end{aligned}\right\}\tag{6}$$

Vol. 2
1960-61

We have assumed that $Y_0(x)$ is of second order, mean-square continuous and weakly stationary. Let its mean value be zero. Then

$$E\{Y_0(x)\,Y_0(x+x_0)\} = \Gamma_{Y_0}(x_0)$$

is the covariance of $Y_0(x)$. If $P_{Y_0}(\lambda)$ is the power spectral density of $Y_0(x)$, then[6, 7]

$$\left.\begin{aligned}\Gamma_{Y_0}(x_0) &= \frac{1}{2}\int_{-\infty}^{\infty} P_{Y_0}(\lambda)\,e^{i\lambda x_0}\,d\lambda \\ P_{Y_0}(\lambda) &= \frac{1}{\pi}\int_{-\infty}^{\infty} \Gamma_{Y_0}(x_0)\,e^{-i\lambda x_0}\,dx_0\end{aligned}\right\} \tag{7}$$

With

$$x = vt, \quad t' - t = \tau, \quad \lambda v = \omega \tag{8}$$

equations (7) become

$$\left.\begin{aligned}\Gamma_{Y_0}(\tau) &= \frac{1}{2}\int_{-\infty}^{\infty} \frac{P_{Y_0}(\omega)}{v}\,e^{i\omega\tau}\,d\omega \\ P_{Y_0}(\omega) &= \frac{1}{\pi}\int_{-\infty}^{\infty} \Gamma_{Y_0}(\tau)\,e^{-i\omega\tau}\,d\tau\end{aligned}\right\} \tag{9}$$

The means of $F_1(t)$ and $F_2(t)$ are zero, since the mean of $Y_0(x)$ is zero. We shall denote the various covariances of $F_1(t)$ and $F_2(t)$ by

$$\Gamma_{F_1}(\tau), \quad \Gamma_{F_1F_2}(\tau), \quad \Gamma_{F_2F_1}(\tau), \quad \Gamma_{F_2}(\tau)$$

Then, taking, for example, $Y(t)$, we find that its mean is zero, and its covariance is

$$\left.\begin{aligned}\Gamma_Y(\tau) &= \omega_0^4\int_0^{\infty}\int_0^{\infty} [h_y(\tau_1)\,h_y(\tau_2)\,\Gamma_{F_1}(\tau-\tau_2+\tau_1) + \\ &\quad + h_y(\tau_1)\,g_y(\tau_2)\,\Gamma_{F_1F_2}(\tau-\tau_2+\tau_1) + \\ &\quad + h_y(\tau_2)\,g_y(\tau_1)\,\Gamma_{F_2F_1}(\tau-\tau_2+\tau_1) + \\ &\quad + g_y(\tau_1)\,g_y(\tau_2)\,\Gamma_{F_2}(\tau-\tau_2+\tau_1)]\,d\tau_1\,d\tau_2 \\ &= \frac{1}{2}\int_{-\infty}^{\infty} \omega_0^4\,e^{i\omega\tau}[|H_y(i\omega)|^2 P_{F_1}(\omega) + \\ &\quad + H_y(-i\omega)\,G_y(i\omega)\,P_{F_1F_2}(\omega) + \\ &\quad + H_y(i\omega)\,G_y(-i\omega)\,P_{F_2F_1}(\omega) + \\ &\quad + |G_y(i\omega)|^2 P_{F_2}(\omega)]\,d\omega\end{aligned}\right\} \tag{10}$$

where $H_y(i\omega)$ and $G_y(i\omega)$ are the frequency responses corresponding to $h_y(t)$ and $g_y(t)$, respectively. The second expression on the right shows that the power spectral density of $Y(t)$ is

$$\begin{aligned}P_Y(\omega) = \omega_0^4\{&|H_y(i\omega)|^2 P_{F_1}(\omega) + H_y(-i\omega)\,G_y(i\omega)\,P_{F_1F_2}(\omega) + \\ &+ H_y(i\omega)\,G_y(-i\omega)\,P_{F_2F_1}(\omega) + |G_y(i\omega)|^2 P_{F_2}(\omega)\}\end{aligned} \tag{11}$$

Formulas similar to (10) and (11) may be written out for $Y_1(t), Y_2(t), \Theta(t)$ but we omit them to conserve space. Expressions for cross covariances and cross spectral densities may also be obtained if needed.

Covariances and spectral densities of various mean-square derivatives of $Y(t)$, $\Theta(t)$, etc., are obtained in the usual way from the covariances of $Y(t)$, $\Theta(t)$, etc.

The analysis and discussion in the remainder of the paper will be confined to two special cases of the vehicle shown in Fig. 1.

Case (a)

For this case (see Fig. 2), idealized tires are replaced by massless point followers. The power spectral densities for the vertical displacement at any

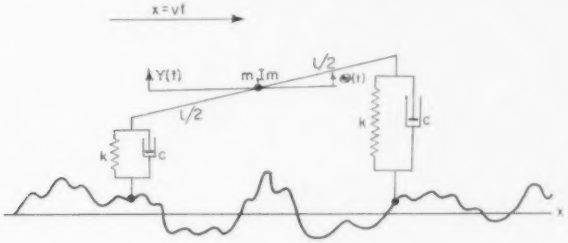

FIG. 2.

point on the frame a distance z from the center of gravity and the angular displacement $\Theta(t)$ are, respectively,

$$
\begin{aligned}
P_y(z,\omega) = \frac{1}{2l^2}&\left[\left(1-\frac{\omega^2}{\omega_y^2}\right)^2+\left(2\zeta y\frac{\omega}{\omega_y}\right)^2\right]^{-1}\left[\left(1-\frac{\omega^2}{\omega_\theta^2}\right)^2+\left(2\zeta_\theta\frac{\omega}{\omega_\theta}\right)^2\right]^{-1}\times\\
&\times\left\{l^2\left(1+\cos\frac{\omega l}{v}\right)\left[1+\left(2\zeta y\frac{\omega}{\omega_y}\right)^2\right]\left[\left(1-\frac{\omega^2}{\omega_\theta^2}\right)^2+\left(2\zeta_\theta\frac{\omega}{\omega_\theta}\right)^2\right]+\right.\\
&+8lz\sin\frac{\omega l}{v}\left[\zeta y\frac{\omega^3}{\omega_y^3}\left\{\frac{\omega^2}{\omega_\theta^2}-1-\left(2\zeta_\theta\frac{\omega}{\omega_\theta}\right)^2\right\}-\right.\\
&\left.-\zeta_\theta\frac{\omega^3}{\omega_\theta^3}\left\{\frac{\omega^2}{\omega_y^2}-1-\left(2\zeta y\frac{\omega}{\omega_y}\right)^2\right\}\right]+\\
&\left.+2z^2\left(1-\cos\frac{\omega l}{v}\right)\left[1+\left(2\zeta_\theta\frac{\omega}{\omega_\theta}\right)^2\right]\left[\left(1-\frac{\omega^2}{\omega_y^2}\right)^2+\left(2\zeta_y\frac{\omega}{\omega_y}\right)^2\right]\right\}\frac{P_{Y_0}(\omega)}{v}
\end{aligned}
\tag{12}
$$

and

$$
P_\Theta(\omega)=\frac{2\left(1-\cos\frac{\omega l}{v}\right)\left[1+\left(2\zeta_\theta\frac{\omega}{\omega_\theta}\right)^2\right]}{\left[\left(1-\frac{\omega^2}{\omega_\theta^2}\right)^2+\left(2\zeta_\theta\frac{\omega}{\omega_\theta}\right)^2\right]l^2}\frac{P_{Y_0}(\omega)}{v} \tag{13}
$$

Case (b)

Here (see Fig. 3), we replace the spring and damper above each idealized tire by a rigid link, and lump the masses of the tires in with the mass of the frame. Let

$$
\left.\begin{aligned}
\omega_0^2&=\frac{K}{m}, & 2\zeta_0\omega_0&=\frac{C}{m}, & \kappa&=\frac{K}{2a}\\
\omega_1^2&=\frac{Kl^2}{2I_m}, & 2\zeta_1\omega_1&=\frac{Cl^2}{2I_m}, & \gamma&=\frac{C}{2a}
\end{aligned}\right\} \tag{14}
$$

Vol. 2
1960-61

Then, if we write $P_Y(z,\omega)_0$ and $P_\Theta(\omega)_0$ for $P_Y(z,\omega)$ and $P_\Theta(\omega)$, respectively, when $\omega_y, \omega_\theta, \zeta_y$ and ζ_θ are replaced by $\omega_0, \omega_1, \zeta_0$ and ζ_1 we find that

$$\left.\begin{aligned} P_Y(z,\omega)_0 &= P_Y(z,\omega)\left(\frac{\sin\dfrac{\omega a}{v}}{\dfrac{\omega a}{v}}\right)^2 \\ P_\Theta(\omega)_0 &= P_\Theta(\omega)\left(\frac{\sin\dfrac{\omega a}{v}}{\dfrac{\omega a}{v}}\right)^2 \end{aligned}\right\} \tag{15}$$

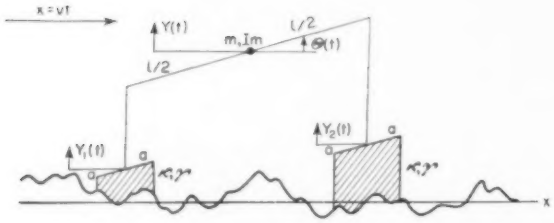

FIG. 3.

III. GROUND ROUGHNESS

Extensive surveys of airport-runways roughness and the roughness of the surface of the sea have been made recently. In these cases, statistical methods were used to characterize the roughness. The necessary surveys to determine the roughness of ground in open fields are just being undertaken. However, until these surveys are completed and the data analyzed, it is not possible to describe in a quantitative manner the statistical nature of the roughness of various types of open fields.

For the purposes of this paper, we shall employ the power spectral density

$$P_{Y_0}(\lambda) = \frac{2\sigma_{Y_0}^2}{\lambda_0\sqrt{2\pi}}\exp\left(-\frac{\lambda^2}{2\lambda_0^2}\right) \tag{16}$$

This formula contains one parameter λ_0 in addition to the variance $\sigma_{Y_0}^2$ of $Y_0(x)$. By changing λ_0, it is possible to change the amount of power in the various frequency bands. In particular, a small λ_0 means that most of the power is concentrated in the low-frequency (1/length) region; conversely, a large λ_0 means that most of the power is distributed in the high-frequency region.

IV. DISCUSSION

The power spectral densities of the vertical acceleration of the center of gravity in the two cases may be obtained in the usual manner[3,7] from (12) and (15):

$$\frac{P_{\ddot{Y}}(0,\omega)}{2\sigma_{Y_0}^2\omega_y^3} = \frac{r^4(1+\cos\alpha r\nu)\,(1+4\zeta_y^2 r^2)}{2[(1-r^2)^2+4\zeta_y^2 r^2]}\,\frac{\nu}{\beta\sqrt{2\pi}}\exp\left(-\frac{r^2\nu^2}{2\beta^2}\right) \tag{17}$$

and

$$\frac{P_{\ddot{Y}}(0,\omega)_0}{2\sigma_{\dot{Y}_0}^2\omega_y^3} = \frac{P_{\ddot{Y}}(0,\omega)}{2\sigma_{\dot{Y}_0}^2\omega_y^3}\left(\frac{\sin r\alpha(a/l)\nu}{r\alpha(a/l)\nu}\right)^2 \tag{18}$$

respectively, where

$$\left.\begin{aligned} r &= \frac{\omega}{\omega_y} = \frac{\omega}{\omega_0}, \qquad \alpha = \frac{l\omega_y}{v_0} = \frac{l\omega_0}{v_0} \\ \beta &= \frac{\lambda_0 v_0}{\omega_y} = \frac{\lambda_0 v_0}{\omega_0}, \quad \nu = \frac{v_0}{v} \end{aligned}\right\} \tag{19}$$

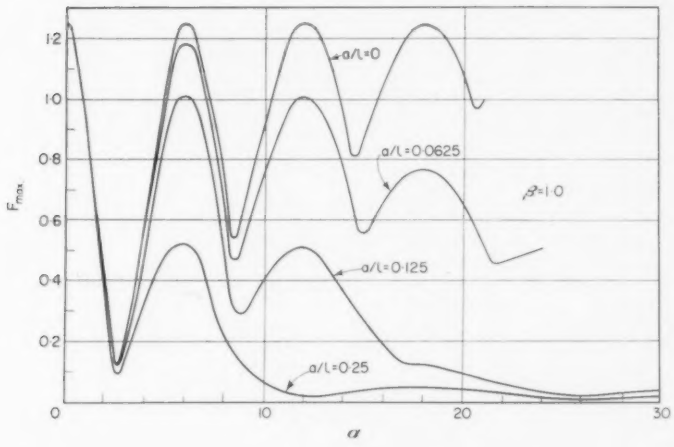

FIG. 4.

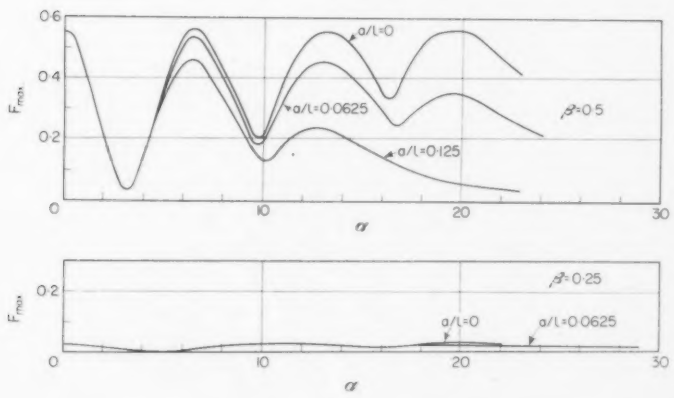

FIG. 5.

As was pointed out in the Introduction, a possible factor limiting the speed of a vehicle under off-road conditions may be provided by the peak value of $P_{\ddot{Y}}$. Graphs of the peak values of $P_{\ddot{Y}}(0,\omega)$ and $P_{\ddot{Y}}(0,\omega)_0$ as function of α, β and a/l, with $\zeta_y = 0{\cdot}25$ and $v_0/v = 1$ are presented in Figs. 4 and 5.

The curves on each figure with $a/l = 0$ correspond to the vehicle described in Case (a). They were determined from (17). The maximum peak value occurs when $\alpha = 0$ and is repeated more or less periodically as α increases. This may be interpreted as meaning that there are certain values of l, including zero, which produce the maximum in $P_{\ddot{Y}}(0, \omega)$, or perhaps the worst possible ride. There is an absolute minimum and a series of relative minima in each curve which also occur more or less periodically with increasing α. The α-values at these minima and the corresponding peak value of (17) are listed in Table 1 for

TABLE 1. $(a/l = 0)$

$\beta\alpha$	β	α	r_1	r_2	$F_{\max}$	Variance	α	Var.$_{\min}$
2·615	1·000	2·6150	0·87208	1·9055	0·13218	0·18292	2·4025	0·17594
		8·4947	0·87644	1·41562	0·54326	0·40006	8·8391	0·39670
		14·5881	0·90461	1·26904	0·81323	0·44353		
		20·6849	0·92944	1·20415	0·96733	0·45045		
1·64	0·500	3·28322	0·66681	1·25262	0·03607	0·030889	3·1103	$0{\cdot}29375^{-1}$
		9·85125	0·74239	1·16985	0·20443	0·11141		
		16·4070	0·80018	1·11375	0·33624	0·13033		
		22·9572	0·83614	1·07929	0·41396	0·13489		
1·30	0·250	5·22448	0·35658	0·85482	$0{\cdot}43176^{-2}$	$0{\cdot}22906^{-2}$		
		15·7870	0·43130	0·76536	$0{\cdot}17159^{-1}$	$0{\cdot}62364^{-2}$		
		26·4310	0·48312	0·70609	$0{\cdot}21785^{-1}$	$0{\cdot}61568^{-2}$		
		37·0734	0·51123	0·67528	$0{\cdot}23427^{-1}$	$0{\cdot}61601^{-2}$		
1·47	0·125	11·7439	0·15840	0·39160	$0{\cdot}33828^{-3}$	$0{\cdot}90839^{-4}$		
		35·9626	0·18944	0·33688	$0{\cdot}13055^{-2}$	$0{\cdot}21672^{-3}$		
		60·4045	0·21144	0·30903	$0{\cdot}16524^{-2}$	$0{\cdot}21621^{-3}$		
		84·8009	0·22353	0·29523	$0{\cdot}17769^{-2}$	$0{\cdot}21621^{-3}$		

$\beta = 1{\cdot}000,\ 0{\cdot}500,\ 0{\cdot}250$; the variances of $\dddot{Y}/2\sigma^2_{\dot{Y}_0}\omega_y^3$ are also listed. Thus, there is one α or l which for each β and ν makes the peak in $P_{\ddot{Y}}(0, \omega)$ an absolute minimum. We may regard this as meaning that for one l the ride is the "best". This means that for a track of given roughness as specified by (16) and for a given velocity (β = constant, ν = constant) there is one length which provides the best ride under our criterion. It is further noted that the "tuning" is sharp at this length.

Decreasing values of $\beta(= \lambda_0 v_0/\omega_y)$ may be interpreted as decreasing values of λ_0; this corresponds, by (16), to decreasing power in the shorter wavelengths. That is, decreasing λ_0 means the track is smoothing out at the shorter wavelengths and getting rougher at the longer ones. In view of the fact that (17) contains r^4 as a factor which reduces the contribution of (16) at the large wavelengths, we conclude that reducing β should reduce the peak values in $P_{\ddot{Y}}(0, \omega)$. Figs. 4 and 5 substantiate this deduction. Decreasing β may also be interpreted as decreasing v_0. However, decreasing v_0 raises α. Hence, we note that the peak values of $P_{\ddot{Y}}(0, \omega)$ may either decrease or increase depending upon the initial value of α. A similar remark is valid if we change β by changing $\omega_y(= \omega_0)$.

The remaining curves in Figs. 4 and 5 and the material in Tables 2 and 3 pertain to values of a/l different from zero. When $a/l \neq 0$, we have the vehicle described in Case (b). Equation (18) shows that peaks in $P_{\dot{Y}}(0, \omega)_0$ and the

TABLE 2. ($a/l = 0{\cdot}0625$; $\alpha = 2{\cdot}4199$; $\text{var.}_{\min} = 0{\cdot}17194$)

β	α	r_1	r_2	$F_{\max}$	Variance
1·000	2·62263	0·87026	1·89469	0·12937	0·17797
	8·61633	0·86494	1·38864	0·47061	0·32941
	15·0399	0·87813	1·22537	0·56038	0·26101
	21·8614	0·87985	1·13505	0·45958	0·16019
0·500	3·28754	0·66540	1·25028	$0{\cdot}35644^{-1}$	$0{\cdot}30442^{-1}$
	9·94960	0·73295	1·15669	0·18291	$0{\cdot}98343^{-1}$
	16·8283	0·77779	1·08490	0·24233	$0{\cdot}90809^{-1}$
	24·1781	0·79160	1·02468	0·20717	$0{\cdot}63089^{-1}$
0·250	5·23821	0·35562	0·85314	$0{\cdot}42699^{-2}$	$0{\cdot}22625^{-2}$
	16·2471	0·41906	0·74440	$0{\cdot}15292^{-1}$	$0{\cdot}54303^{-2}$
	29·0451	0·43967	0·64266	$0{\cdot}15172^{-1}$	$0{\cdot}40037^{-2}$
	46·6916	0·40604	0·53609	$0{\cdot}99660^{-2}$	$0{\cdot}21135^{-2}$

TABLE 3

a/l	β	α	r_1	r_2	$F_{\max}$	Variance
0·125	1·000	2·64565	0·86475	1·86236	0·12129	0·16433
		9·00860	0·82705	1·30668	0·29629	0·18323
		17·1634	0·76325	1·05946	0·12518	0·46255
		30·5288	1·04011	1·22674	$0{\cdot}41671^{-1}$	
	0·500	3·30072	0·66113	1·24325	$0{\cdot}34394^{-1}$	$0{\cdot}29128^{-1}$
		10·3040	0·70071	1·11316	0·12756	$0{\cdot}65360^{-1}$
		20·2056	0·63794	0·90973	$0{\cdot}53295^{-1}$	$0{\cdot}16724^{-1}$
		34·3205	0·92685	1·08865	$0{\cdot}18269^{-1}$	$0{\cdot}46743^{-2}$
	0·250	5·28087	0·35259	0·84789	$0{\cdot}41268^{-2}$	$0{\cdot}21791^{-2}$
	0·125	11·8899	0·15643	0·38675	$0{\cdot}32207^{-3}$	$0{\cdot}85404^{-4}$
	0·0625	24·4004	$0{\cdot}76264^{-1}$	0·18837	$0{\cdot}36379^{-4}$	$0{\cdot}46944^{-5}$
0·250	1·000	2·73902	0·84107	1·73573	$0{\cdot}92997^{-1}$	0·11705
		12·1784	0·57347	1·51011	$0{\cdot}20869^{-1}$	$0{\cdot}11872^{-1}$
		25·2673	0·75847	1·23324	$0{\cdot}14754^{-1}$	$0{\cdot}41638^{-2}$
		38·1646	0·82784	1·14838	$0{\cdot}91456^{-2}$	
	0·500	3·35713	0·64337	1·21471	$0{\cdot}29707^{-1}$	$0{\cdot}24253^{-1}$
		15·2739	0·44295	1·18485	$0{\cdot}10170^{-1}$	$0{\cdot}42424^{-2}$
	0·250	5·47804	0·33951	0·82346	$0{\cdot}35533^{-2}$	$0{\cdot}18437^{-2}$
	0·125	12·3910	0·15019	0·37071	$0{\cdot}27403^{-3}$	$0{\cdot}69482^{-4}$
	0·0625	25·4261	$0{\cdot}73227^{-1}$	0·18059	$0{\cdot}30958^{-4}$	$0{\cdot}38211^{-5}$

Vol. 2
1960-61

variance of $\ddot{Y}$ in this case should be less than when $a/l = 0$. This is borne out by the curves just referred to. Fig. 4, in particular, shows that in order for the tire spread to produce much of a reduction in the peak values of (18), α must be greater than the value for the first minimum, the reduction being greatest when α makes the peaks in (17) largest. Although a large tire spread always improves the ride, substantial gains are present only if l has been chosen poorly or if α is large.

Since $a/l = 0{\cdot}0625$ corresponds to a total idealized-tire contact equal to $\frac{1}{4}$ of l, it is clear that considerable tire contact is required if substantial reductions in $P_{\ddot{Y}}(0, \omega)_0$ are to be made for low values of α.

The tables indicate that the variance of the vertical acceleration of the center of gravity follows the trends of the peak values in (17) and (18). Much the same type of remarks could thus be made if variance of $\ddot{Y}$ had been selected as a measure of limiting speed.

Perhaps the most interesting general observation is the pronounced influence of α on the peaks in $P_{\ddot{Y}}(0, \omega)$ and $P_{\ddot{Y}}(0, \omega)_0$. Little attention appears to have been paid to this point in the past. The next observation of note is that the total contact along the track must be at least $\frac{1}{4}$ to $\frac{1}{2}$ of l before it materially reduces the peaks when α is reasonably small.

In closing, we must add words of caution concerning our results. At present they stand as interesting qualitative properties that are sound and consistent within the framework from which they were derived.

However, the question of the conclusiveness of our deductions must at present remain unanswered. One of the major reasons is that too little is known at this time about the driver's response tolerances in a quantitative manner. Furthermore, other criteria may be at least as important as the driver's comfort in limiting the speed of the vehicle on off-road conditions.

Acknowledgements—This study was conducted under the sponsorship of the Land Locomotion Research Laboratory of the Detroit Arsenal. It is a pleasure to acknowledge their support. Particular credit must be given to Col. BEKKER, Director of the Laboratory, and to Capt. EHRLICH for their efforts in calling the attention of the automotive industries to this important problem, and for their very helpful discussions and suggestions given during the course of our work.

REFERENCES

1. J. L. BOGDANOFF and F. KOZIN, Report No. 48, Land Locomotion Research Laboratory, Detroit Arsenal, Detroit (1959).
2. J. L. BOGDANOFF and F. KOZIN, Report No. 56, Land Locomotion Research Laboratory, Detroit Arsenal, Detroit (1959).
3. J. L. BOGDANOFF and F. KOZIN, Report No. 65, Land Locomotion Research Laboratory, Detroit Arsenal, Detroit (1960).
4. JAMES H. WALLS, J. C. HOUBOLT and H. PRESS, NACA Tech. Note 3305 (1954).
5. M. ST. DENIS and W. J. PIERSON, JR., *Trans. Soc. Nav. Archit., N.Y.* **61**, 280 (1953).
6. W. B. DAVENPORT, JR. and W. L. ROOT, *An Introduction to the Theory of Random Signals and Noise.* McGraw-Hill, New York (1958).
7. J. H. LANING, JR. and R. H. BATTIN, *Random Process in Automatic Control.* McGraw-Hill, New York (1956).
8. J. E. MOYAL, *J. R. Statist. Soc.* B **11**, 150 (1949).

Int. J. Mech. Sci. Pergamon Press Ltd. 1960. Vol. 2, pp. 179–194. Printed in Great Britain

AN ANALYSIS OF COLD STRIP ROLLING

D. JORTNER,* J. F. OSTERLE† and C. F. ZOROWSKI†

(*Received* 25 *February* 1960)

Summary—A method of analysis is presented for investigating the mechanics of cold strip rolling. This method takes into account the elastic deformations of the strip and the rolls and the effect of applied strip tensions, as well as the plastic strip deformations. Predictions of load and torque requirements for reducing strip of any material and dimensions are obtainable along with the pressure distributions between the rolls and the strip, the shape and length of the contact arc, and the resulting roll flattening. The only information required for the application of this method is the dimensions and elastic–plastic material properties of the roll and strip. The results of a number of numerical examples are presented and compared with experimental results to indicate limits on the accuracy of the method.

Vol. 2
1960-61

NOMENCLATURE

r, θ	polar co-ordinates with origin at center of cylinder
$r_1 \theta_1$ $r_2 \theta_2$	polar co-ordinates with origins at opposite ends of a diameter of cylinder
x, y	Cartesian co-ordinates with origin at center line of strip
ϕ	Airy stress function
σ	tensile stress
τ	shear stress
ϵ	normal strain
u	radial deformation of cylinder
v	vertical deformation of strip with respect to center line
a	radius of cylinder
h	strip height
$\Delta\theta = 2\alpha$	finite-difference angle
T	horizontal tensile load per unit width of strip
P	radial load per unit width on surface of cylinder
p	radial pressure on roll or vertical pressure on strip
P_r	normal pressure on strip
p_1, p_2, p_3	principal compressive stresses
$\sigma_1, \sigma_2, \sigma_3$	principal tensile stresses
k_t	yield stress in pure tension
k_c	yield stress in pure compression
k	yield stress in plane compression (also referred to as plane deformation or plane strain)
E	modulus of elasticity
ν	Poisson's ratio
μ	coefficient of friction
β	angle between strip surface and horizontal

* Carnegie Institute of Technology. (Now with Bettis Atomic Power Division, Westinghouse Electric Corporation.)

† Department of Mechanical Engineering, Carnegie Institute of Technology, Pittsburgh 13, Pennsylvania.

INTRODUCTION

THE conditions encountered in the arc of contact in metal rolling is a subject which has fostered a great number of theoretical and experimental investigations in the past several decades. These investigations have been prompted by a desire to learn more about the mechanics of rolling and to establish rolling theories which eliminate the necessity of depending on empirical data. The need for such a complete theory of rolling still exists. Today, there is greater emphasis being placed on the accurate prediction of rolling loads, power requirements and optimum design parameters for new systems and materials. Past experience and approximate theories dependent on empirical corrections often prove inadequate.

The purpose of this paper is to remove certain inconsistencies which exist in even the latest theories of cold rolling and thereby obtain a clearer picture of the rolling process. In existing theories of cold rolling, if roll deformations are considered they are usually computed by the method developed by Hitchcock[1]. Hitchcock's formula is valid only if the pressure distribution between roll and strip is of a certain form, namely elliptical. However, the pressure distribution on the strip corresponding to the roll deformation dictated by this formula is not elliptical or even nearly so. This inconsistency is one of the weak points in the present-day theory of cold rolling.

This paper eliminates this inconsistency by solving the rolling problem by a method which allows both the roll and strip deformations to be compatible with the pressure distribution. The method presented is a finite-difference procedure in which the strip within the arc of contact is "sliced" into sections and the appropriate equations of equilibrium and compatibility written separately for each section. These equations are then solved progressively yielding consistent pressure and deformation distributions. The use of this finite-difference technique enables the elastic regions in the strip to be treated in a more accurate way than is possible by the Ford *et al.*[2] technique which is in present use. The usual assumption is made in the following analysis, that strip and roll deformations exist only in longitudinal planes perpendicular to the roll axes, and no variations in the deformations occur across the width of the strip. The solution to this two-dimensional problem will be applicable across the strip width except for narrow regions near its edges.

The theoretical analysis is presented in three parts. The elastic roll deformations are considered first. Equations are developed for obtaining the radial deformation of any point on the roll surface for a given normal pressure distribution applied over a portion of the surface. The investigation of the elastic and plastic stresses in that portion of the strip in contact with the rolls makes up the second part. By considering finite portions of the strip in this region a series of finite-difference equations are obtained which specify the stress distribution in the strip for a given roll shape and strip-thickness requirements. In the third part the previous two results are combined into a systematic iterative procedure for finding a consistent set of results. This procedure insures compatibility of the strip and roll deformations and proper reduction of the

strip while satisfying the criteria for plastic behavior of the strip material. The results obtained from this procedure include the pressure distribution, rolling load, rolling torque, length and shape of the contact arc and the roll flattening.

To solve a given problem, only the physical properties and dimensions of the material involved, the applied front and rear tensions, and the average coefficient of friction between the rolls and strip need to be specified. Unfortunately it is necessary to use an approximate average value for the friction coefficient obtained from experimental results since very little is known quantitatively about the variation of friction in the arc of contact.

ELASTIC ROLL DEFORMATIONS

One of the most widely known and used works on roll deformations is due to Hitchcock[1]. It makes use of the Hertz solution for elastic bodies in contact. The pressure distribution is elliptical and the contact arc remains circular which is a great advantage with respect to simplicity. However, the actual pressure distribution on the roll is not elliptical and this will affect the shape of the roll surface.

Vol. 2
1960-61

According to Keller[3], for a given length of contact arc the effect of roll-shape variation on total load is small; however, variations in the length of contact can produce appreciable changes in the rolling load. It is thus desirable to predict the deformed roll shape as accurately as possible since it in turn defines the length of contact arc. To this end a solution has been developed which permits the almost exact determination of the elastic deformations of the roll in the region of the contact arc for any arbitrary normal pressure distribution.

The model used to obtain the solution of the roll-deformation problem is a cylinder in plane strain with diametrically applied concentrated loads [see Fig. 1(a)]. The solution to this problem is an influence function giving the radial deformation at any point on the surface due to concentrated loads at the ends of a diameter. With this influence function the surface deformations due to any arbitrary contact-pressure distribution can be established, provided the back-up pressure distribution has the same shape. That is, the loads at the ends of a diameter must be self-balancing.

This type of model closely approximates the condition found in a four-high mill where the back-up roll supplies the balancing load. Actually the back-up pressure will have a different distribution from the strip pressure and cannot accurately be represented by the chosen model. However, making use of St. Venant's principle, it is assumed that the actual location and distribution of the back-up pressure will have a negligible effect on the radial deformations of points on the contact arc. This assumption has been shown to be valid for conditions encountered in the rolling problem by some later work yet to be published. It is also assumed that tangential shearing stresses on the contact arc have a negligible effect on the radial deformations.

The Airy stress function for the two-dimensional plane-strain problem of the cylinder subjected to diametrically applied concentrated loads must satisfy the differential equation

$$\nabla^4 \phi = 0 \tag{1}$$

The solution to equation (1) must also satisfy the boundary conditions of a stress-free surface except for the applied loads. Such a solution is given by Timoshenko and Goodier[4] as the sum of three functions

$$\phi = -\frac{Pr_1\theta_1\sin\theta_1}{\pi} - \frac{Pr_2\theta_2\sin\theta_2}{\pi} + \frac{Pr^2}{2\pi a} \tag{2}$$

The first two functions produce simple radial compressive stress distributions about their respective origins. On the surface these combine to give a constant radial compressive stress. This is eliminated to satisfy the boundary conditions of zero surface stress by the addition of the third term of equation (2). It introduces a constant isotropic tensile stress over the entire cross-section of equal magnitude to the previously mentioned compressive stress.

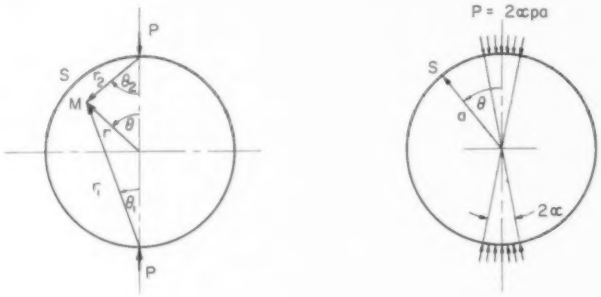

FIG. 1. Loading and geometry of roll-deformation models.

Before proceeding to the deformations, the actual expressions for the stresses are obtained from equation (2) by application of the following relationships:

$$\sigma_r = \frac{1}{r}\frac{\partial\phi}{\partial r} + \frac{1}{r^2}\frac{\partial^2\phi}{\partial\theta^2}; \quad \sigma_\theta = \frac{\partial^2\phi}{\partial r^2}; \quad \tau_{r\theta} = -\frac{\partial}{\partial r}\left(\frac{1}{r}\frac{\partial\phi}{\partial\theta}\right) \tag{3}$$

For convenience the stresses arising from the three terms of equation (2) are transformed to a central co-ordinate system (r, θ). This is accomplished by use of the geometry of the model and the transformation equations for change of stress axes.

$$\left.\begin{aligned}
\sigma_r &= -\frac{P}{\pi}\left[\frac{2(a+r\cos\theta)}{a^2+r^2+2ar\cos\theta}\left(1-\frac{a^2\sin^2\theta}{a^2+r^2+2ar\sin\theta}\right)\right. \\
&\qquad \left. + \frac{2(a-r\cos\theta)}{a^2+r^2-2ar\cos\theta}\left(1-\frac{a^2\sin^2\theta}{a^2+r^2-2ar\sin\theta}\right) - \frac{1}{a}\right] \\
\sigma_\theta &= -\frac{P}{\pi}\left[\frac{2(a+r\cos\theta)\,a^2\sin^2\theta}{(a^2+r^2+2ar\cos\theta)^2} + \frac{2(a-r\cos\theta)\,a^2\sin^2\theta}{(a^2+r^2-2ar\cos\theta)^2} - \frac{1}{a}\right]
\end{aligned}\right\} \tag{4}$$

A similar expression can be obtained for the shearing stress but it is not needed for calculating the radial deformation.

The radial deformation and strain are related to the stresses, (4), for plane deformations by the expression

$$\frac{\partial u(r,\theta)}{\partial r} = \epsilon_r = \frac{1}{E}[(1-\nu^2)\,\sigma_r - \nu(1+\nu)\,\sigma_\theta] \tag{5}$$

Integrating equation (5) from the center of the cylinder to the surface and evaluating the radial deformations at the surface gives

$$u(a,\theta) = \frac{P}{\pi E}\left\{(1-\nu^2)\left[\cos\theta \ln\left(\frac{1-\cos\theta}{1+\cos\theta}\right)+2\right] - (1-\nu-2\nu^2)\sin\theta\left[\tan^{-1}\left(\frac{1+\cos\theta}{\sin\theta}\right)+\tan^{-1}\left(\frac{1-\cos\theta}{\sin\theta}\right)\right]\right\} \tag{6}$$

This now represents the radial deformation at a surface point S, relative to roll center, due to concentrated loads on the opposite ends of a diameter of the cylinder.

Equation (6) has a singularity at $\theta = 0$, under the load, due to the infinite stress produced by the point load. To eliminate this singularity and obtain meaningful results, the radial surface deformations due to a uniform pressure over a small finite arc length are obtained by replacing the point load in equation (6) by the product of the pressure and an infinitesimal arc length and integrating over the small finite angle 2α, as shown in Fig. 1(b). This not only eliminates the infinite stresses and strains under the point load but also permits an arbitrary pressure distribution to be expressed in terms of finite increments which is more convenient for later applications.

Performing the indicated integration involving equation (6) yields the following expressions for the radial surface deformations. When the point S is outside the pressure area, $|\theta| > \alpha$, the surface deformations are given by:

$$\left.\begin{aligned} u(a,\theta,\alpha) = \frac{pa}{\pi E}\Bigg\{&(1-\nu-2\nu^2)\Bigg[\cos(\theta+\alpha)\left(\tan^{-1}\frac{1+\cos(\theta+\alpha)}{\sin(\theta+\alpha)} + \tan^{-1}\frac{1-\cos(\theta+\alpha)}{\sin(\theta+\alpha)}\right) - \cos(\theta-\alpha)\left(\tan^{-1}\frac{1+\cos(\theta-\alpha)}{\sin(\theta-\alpha)} + \tan^{-1}\frac{1-\cos(\theta-\alpha)}{\sin(\theta-\alpha)}\right)\Bigg] \\ &+(1-\nu^2)\left[\sin(\theta+\alpha)\ln\frac{1-\cos(\theta+\alpha)}{1+\cos(\theta+\alpha)} - \sin(\theta-\alpha)\ln\frac{1-\cos(\theta-\alpha)}{1+\cos(\theta-\alpha)}\right]\Bigg\} \end{aligned}\right\} \tag{7}$$

When the point S is inside the pressure area, $|\theta| < \alpha$, it is necessary to integrate through a singularity in the integrand. This is done by approaching the singularity from both sides but not going through it. The final result is

$$\bar{u}(a,\theta,\alpha) = u(a,\theta,\alpha) - \frac{pa}{\pi}(1-\nu-2\nu^2) \tag{8}$$

Vol. 2
1960-61

In eliminating the infinite strain in the deformations directly under the point load, the deformation functions u have been made dependent on the arc length 2α over which the pressure increment is distributed. For a given load P the effect of α on the deformation decays rapidly outside the loading area but increases as α decreases within the area, as would be expected. Of course the smaller α is chosen the more accurately a given pressure distribution can be represented.

Fig. 2 presents the actual influence functions used for the computation of roll shapes in the problems to be presented later. The choice of $\alpha = 0{\cdot}05°$ allowed for from 30 to 60 finite pressure areas on the contact arc.

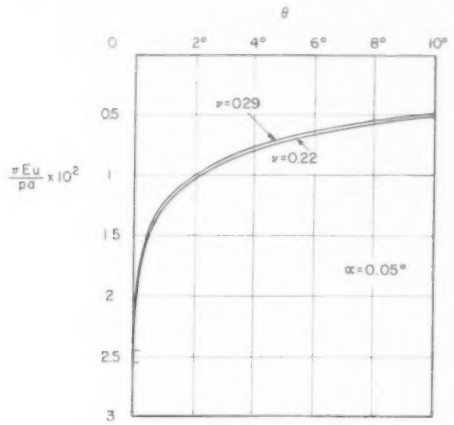

FIG. 2. Influence function for roll deformations.

With the influence function established, the deformation of a point on the surface of the cylinder due to a specific pressure distribution represented by "n" uniform finite pressure increments becomes

$$(u_j)_{\text{total}} = \frac{a}{\pi E} \sum_{i=1}^{n} \left(\frac{\pi E u}{ap}\right)_{ij} P_i \tag{9}$$

STRESS DISTRIBUTION IN STRIP

The region of contact is divided into three zones; the elastic-compression, plastic and elastic-recovery zone as indicated in Fig. 3. Little is known about the transition between these zones. In this analysis it is assumed that transition occurs abruptly across vertical plane sections. The elastic and plastic regions are analyzed separately. The purpose of the analysis is to determine the pressure distribution on the strip surface when the strip height is specified.

Ford *et al.*[2] considered the effect of the elastic regions in the strip. Their solution, however, assumed the shape of the contact arc to be circular. Furthermore, they neglected the effect of the surface shearing forces in the elastic analysis of the strip. The surface shearing forces were considered afterwards, however, in determining the variation in strip tension through the region.

The analysis presented here for the elastic region results in an exact solution for a differential element of the strip. The solution is then extended by finite-difference methods throughout the region. The only approximations in the over-all solution are those introduced by the finite-difference method and relaxed-boundary conditions at the ends of the region.

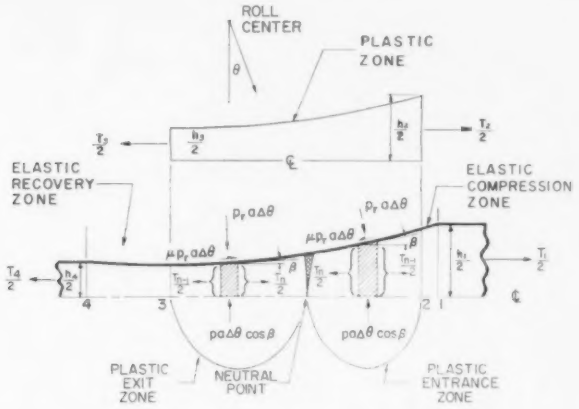

FIG. 3. Contact region of strip.

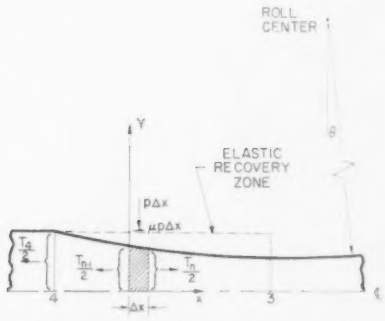

FIG. 4. Elastic-recovery zone.

The elastic-recovery zone is shown in Fig. 4. The elastic-compression zone would be a mirror image of this figure and its analysis would proceed in the same manner. It is assumed that the strip would recover elastically to a uniform height (see Fig. 4) if the vertical pressure loading were removed. It is further assumed that the surface pressure $p(x)$ varies linearly over each differential element Δx of the strip. On the element shown, the surface pressure $p(x)$ would be given by

$$p(x) = p_0 + \frac{dp}{dx}x \tag{10}$$

where the pressure derivative is a constant over the element.

Vol. 2
1960-61

The Airy stress function representing the solution to this problem must again satisfy equation (1) and the following set of boundary conditions

$$\sigma_y\left(x, \frac{h}{2}\right) = -p(x) \qquad \tau_{xy}\left(x, \frac{h}{2}\right) = \mu p(x)$$

$$\int_0^{h/2} \sigma_x(x, y)\, dy = \frac{T(x)}{2} = \frac{T_4}{2} - \mu \int_{x_4}^{x} p(x)\, dx \tag{11}$$

The third condition has been relaxed since it expresses a requirement to be satisfied not by $\sigma_x(x, y)$ itself but only by the resultant of the $\sigma_x(x, y)$ distribution. This is necessary to obtain the simple polynomial solution to be discussed.

By assuming a general fourth-order polynomial in x and y, a solution for the stress function is established. In satisfying equation (1), the boundary conditions (11) and the conditions of center-line symmetry, all the undetermined coefficients of the polynomial are established. The resulting expression is

$$\phi = \left(-\frac{x^3}{6} + \frac{\mu h x^2}{8} - \frac{\mu x^2 y^2}{2h} - \frac{\mu h y^2}{12} - \frac{\mu y^4}{6h}\right)\frac{dp}{dx} - \left(\frac{x^2}{2} + \frac{\mu x y^2}{h}\right) p_0 + \frac{T y^2}{2h} \tag{12}$$

and the stresses become

$$\sigma_x = \frac{T}{h} - \frac{2\mu p_0}{h} x + \frac{\mu}{h}\left(2y^2 - x^2 - \frac{h^2}{6}\right)\frac{dp}{dx}$$

$$\sigma_y = -p(x) + \frac{\mu}{h}\left(\frac{h^2}{4} - y^2\right)\frac{dp}{dx}$$

$$\tau_{xy} = \frac{2\mu y}{h} p(x) \tag{13}$$

At any value of x in the elastic region, the vertical displacement of the strip assuming a plane state of strain is given by

$$v = \frac{(1-\nu^2)}{E}\int_0^{h/2} \sigma_y\, dy - \frac{\nu(1+\nu)}{E}\int_0^{h/2} \sigma_x\, dy \tag{14}$$

This vertical displacement v represents the difference between the final and undeformed strip heights. Making use of this interpretation and carrying out the indicated integrations in equation (14), the following expression is obtained for the difference between the exit strip height and the strip height at any position x.

$$h_4 - h(x) = \frac{(1-\nu^2)h}{E} p(x) + \frac{(1-\nu^2)\mu h^2}{6E}\frac{dp(x)}{dx} - \frac{2\nu(1+\nu)\mu}{E}\int_{x_4}^{x} p(x)\, dx \tag{15}$$

Actually the pressure $p(x)$ is desired as a function of the strip height $h(x)$. This is conveniently obtained by transforming equation (15) into finite-difference form. The pressure gradient at the finite-difference point "n" corresponding to location x is expressed as a "backward" difference, i.e.

$$\frac{dp_n}{dx} = \frac{p_n - p_{n-1}}{\Delta x}$$

Then equation (15) can be rearranged to give

$$p_n = \frac{E(h_4 - h_n) + \dfrac{(1-\nu^2)\,h_n^2\,\mu}{6n\Delta x}\,p_{n-1} + 2\nu\Delta x(1+\nu)\,\mu \sum_{i=1}^{n-1} p_i}{\dfrac{(1-\nu^2)\,h_n^2\,\mu}{6\Delta x} + (1-\nu^2)\,h_n - 2\nu(1+\nu)\,\mu\Delta x} \tag{16}$$

Starting with $p = 0$ at h_4, equation (16) can be used for a stepwise determination of the pressure distribution in the elastic region once the strip height is specified. This equation will remain valid for determining the surface pressures up to the point where the strip stresses are such that the material yields according to the plasticity criterion yet to be established. The same procedure is applicable to the elastic-compression zone.

To remain consistent with the cylinder co-ordinates, Δx is replaced by $a\Delta\theta$. This transformation is not exact since it assumes that roll radius remains constant and $\cos\theta = 1$. However, for the conditions encountered in cold rolling the approximation is very good.

The mathematical model used for the analysis of the plastic region is based on Orowan's[5] homogeneous theory. The only important difference between this derivation and the original homogeneous theory is that this analysis allows for an arbitrary shape of the surface. Any elastic deformations in the plastic region will be neglected and the plasticity condition to be used is the von Mises–Hencky[6, 7] distortion energy theory. Mathematically this plasticity criterion is expressed in terms of the principal stresses as

$$(\sigma_1 - \sigma_2)^2 + (\sigma_2 - \sigma_3)^2 + (\sigma_3 - \sigma_1)^2 = 2k_t^2 \tag{17}$$

Assuming small displacements and neglecting elastic deformations, Poisson's ratio for plastic deformations in rolling approaches $\frac{1}{2}$, Nadai[8]. Using this value of Poisson's ratio and considering a state of plane strain, a compression yield criterion is obtained from equation (17) in the form

$$p_1 - p_3 = \frac{2}{\sqrt{3}}\,k_c = k \tag{18}$$

where p_1 and p_3 represent the maximum and minimum principal compressive stresses and k is referred to as the constrained compressive yield stress.

The vertical and horizontal normal stresses in the strip are now assumed uniform over any vertical section and equal in magnitude to the principal stresses. This is reasonable considering the surface shear is only of the order of 5 per cent of the surface pressure and zero at the center line. In terms of the notation used in the elastic-strip analysis the compression yield criterion in equation (18) becomes

$$p + \sigma_x = k \tag{19}$$

The geometry of the plastic region is illustrated in Fig. 3. This region consists of three distinct sections which can be classified as entrance, neutral and exit. In cold rolling the neutral section is usually small and for the present

Vol. 2
1960-61

will be assumed to occur at one point. In deriving the equations governing the behavior of the plastic region, the differences in loading which cause some differences in sign are denoted by the upper signs for the exit section and the lower signs for the entrance section. For the two elements shown in Fig. 3 the equations governing horizontal and vertical equilibrium respectively in finite-difference form are

$$(T_n - T_{n-1}) \pm a\Delta\theta[(p_r \sin\beta)_n + (p_r \sin\beta)_{n-1}] + \mu a\Delta\theta[(p_r \cos\beta)_n + (p_r \cos\beta)_{n-1}] \tag{20}$$

and

$$p = p_r(1 \mp \mu \tan\beta) \tag{21}$$

Equation (19) is now used to eliminate p from equation (21). The result is then combined with equation (20) making use of the following substitution as a result of the homogeneous theory:

$$T = \sigma_x h$$

This combination yields a recurrence relationship for the normal strip surface (or radial roll pressure) $[p_r]_n$ as a function of the strip-height distribution.

$$[p_r]_n = \frac{[hk]_n + [hp_r(1 \mp \mu \tan\beta) + p_r a\Delta\theta \cos\beta(\mu \pm \tan\beta) - hk]_{n-1}}{[h(1 \mp \mu \tan\beta) - a\Delta\theta \cos\beta(\mu \pm \tan\beta)]_n} \tag{22}$$

For a specified surface shape the only unknown in equation (22) is the normal surface pressure. Starting with the known values at the plastic–elastic boundaries, each of the two forms of the equation are used to calculate from the two inner elastic boundaries into the plastic region. The neutral point is determined as that point at which both solutions give equal pressures. The "exit equation" is not valid in the entrance region, and vice versa. It is to be noted that k and β are functions of h. The strip material determines k while the trigonometric functions of β are expressed in terms of h in finite-difference form, i.e.

$$[\sin\beta]_n = \frac{h_{n+1} - h_{n-1}}{4a\Delta\theta}, \text{ etc.}$$

ITERATIVE PROCEDURE FOR NUMERICAL SOLUTIONS

A procedure for obtaining a convergent equilibrium solution for rolling load, torque, etc., using the developments of the previous sections will now be discussed. A method is presented for obtaining individual solutions for the deformations and stresses in the rolls and strip by successive iterations. The numerical results presented in the paper were obtained from a specific program written for the IBM 650 computer. The method of procedure is, of course, applicable to any other digital machine and the description here is one of the logical mathematical steps and not programming methods.

The successive-approximation solution depends on using the roll-deformation and strip-stress distribution equations alternately, and continually adjusting the results to conform to the proper boundary conditions. First the roll is assumed to have a circular shape and the distance between the rolls and the

extent of the contact arc are approximated from the required strip gauge and the yield criterion. With the contact region thus established, an approximate pressure distribution can be found using the plastic- and elastic-strip solutions. A new roll shape is now determined using the calculated pressure distribution. Again the boundary conditions on strip height and the yield criterion establish a new contact region and the cycle of calculations is begun again. This iterative procedure continues until the length of contact arc and the integral of the pressure distribution converge to the desired accuracy.

In a solution, there are two basic types of operations. First, a number of calculations are made to supply starting conditions. Then the repetitive steps are developed which themselves provide the starting conditions for the following iteration. The process is then self-sustaining and only a convergence criteria is required to stop the process after any desired accuracy is achieved.

Excluding the calculation of required constants and an approximate relation for yield stress in terms of strip height, the following is a more detailed outline of necessary initial and recurrence calculations.

Vol. 2
1960-61

INITIAL CALCULATIONS

A–1. Starting values of the yield stresses k_2 and k_3 are found by assuming $h_3 \simeq h_4$ and $h_2 \simeq h_1$.

B–1. Starting values of p_2 and p_3 are found using the yield criterion [equation (19)], neglecting the changes in horizontal tension through the elastic regions.

C–1. Starting values of h_2 and h_3 are found from the elastic-strip solution [equation (16)], again neglecting changes in horizontal tension through the elastic regions and the non-uniformity of the vertical pressure distribution.

D–1. Steps A–1 to C–1 are repeated using the first approximations to obtain second approximations.

RECURRENCE CALCULATIONS (FOR ONE ITERATION)

A–2. The radial deformation of the roll is found as a function of the angle θ. This is accomplished using the influence coefficients from equations (7) and (8) and the summation equation (9). For the first trial the radial deformations are all zero (circular roll).

B–2. The strip height is calculated as a function of θ. The shape of the strip boundary has been determined in A–2 from the pressure distribution. The minimum height of the strip is h_3 whose initial value was found in D–1. The point (or angle) on the strip boundary shape at which the minimum height occurs becomes point 3, and the height at that point is set equal to h_3. The height at each other point is then adjusted an equal amount as was the height at point 3. This corresponds to moving the rolls closer together to compensate for roll flattening.

C–2. Points 1, 2 and 4 are determined since h_1 and h_4 are specified and h_2 was calculated in D–1. This determines the extent of the contact arc.

D–2. The first approximate stress distributions in the elastic regions are found from stepwise solution of equation (16). This determines the approximate

variation of horizontal force through the elastic regions, and the build-up of the pressure distribution.

E–2. Using the information of D–2, better approximations are obtained for h_2, h_3, k_2 and k_3 from the yield-criterion equation (19) and the elastic-strip-solution equation (16) considering the terms previously neglected in C–1.

F–2. The height distribution is readjusted using the latest value of h_3. The value of h_2, h_3, k_2 and k_3 from E–2 will be used as starting values for the next iteration.

G–2. The elastic-stress distribution and surface pressures are calculated a second time.

H–2. The plastic-stress distribution and surface pressures are calculated using equation (22). The calculations are begun at point 2 on the entrance side and point 3 on the exit side. The neutral point is determined where the two solutions yield the same pressure.

I–2. Summations are performed to obtain the total load, torque and other relevant quantities.

This completes one iteration. Usually between three and five iterations are required before an equilibrium state is reached.

NUMERICAL EXAMPLES AND COMPARISON WITH EXPERIMENT

The iteration procedure described was employed to investigate several numerical examples for which experimental data were available. These experiments were reported by Hessenberg and Sims[9]. Both annealed and pre-rolled strip were tested in order to determine the rolling load and torque required to produce a given per cent reduction. The applied tensions on the strip were varied to determine their effect on the load and torque requirements. The type of steel used was commercial-quality rimming steel. The coils of strip were individually tested by the method of Ford[10] to determine the yield stress as a function of per cent reduction in plane compression [see equation (18)] for each coil.

In obtaining the theoretical prediction for comparison with the experimental data, the following physical properties were assumed.

(a) The yield stress of the strip material was specified as a function of the strip thickness. The values used were taken directly from the measurements made for the particular coil of strip for which the comparison was being made. In the computer code, the portion of the yield-stress curve to be used was fitted at four points by a third-order polynomial. More refined fitting procedure could easily be used if warranted.

(b) Measurements of friction coefficients for various materials and types of lubrication, Whitton and Ford[11], indicate that in this comparison, the coefficient should be in the range 0·055–0·060. A value of 0·055 was chosen for all the cases considered here. (It was later found that a slightly higher coefficient of perhaps 0·0575 would reduce the average error in the rolling load.)

(c) The modulus of elasticity of the strip was assumed to be $29{\cdot}5 \times 10^6$ lb/in^2 and for the forged steel rolls 30×10^6 lb/in^2. Poisson's ratio of the strip was assumed to be 0·287 and for the rolls 0·29 was used.

For the comparison of predictions with experiment, sixteen cases were considered. Eight of the cases employ annealed strip and the other eight use strip which had previously been reduced by 40 per cent. Tables 1 and 2 present those comparisons and indicate the part played by roll flattening in increasing the rolling load and contact angle. The average deviation of prediction from experiment is $-4{\cdot}3$ per cent in the rolling load and $+3{\cdot}1$ per cent in the torque.

TABLE 1. PREDICTED ROLLING RESULTS FOR ANNEALED MILD STEEL

	Coil 2. Nominal reduction 30%			
	2a	2b	2c	2d
Initial strip thickness (in.)	0·0643	0·0645	0·0645	0·0642
Final strip thickness (in.)	0·0455	0·0455	0·0456	0·0453
Average applied front tension (lb/in^2)	3600	12,000	21,600	23,000
Average applied rear tension (lb/in^2)	0	12,600	6000	12,600
Experimental load (lb/in.)	27,000	22,600	23,000	20,800
Calculated load (lb/in.)	27,600	21,850	22,550	20,350
Error in load (%)	+2·2	−3·3	−2·0	−2·2
Experimental roll torque (in-lb/in.)	2780	3340	1400	2160
Calculated roll torque (in-lb/in.)	2860	3360	1420	2080
Error in torque (%)	+2·9	+0·6	+1·4	−3·7
Other calculated results				
Roll "flattening" per roll (in.)	0·00206	0·00166	0·00165	0·00150
Angle of contact (degrees)	4·1	4·1	4·0	4·0
% of angle due to roll deformation	9·8	9·8	7·5	7·5
% of load due to roll deformation	11·6	10·2	8·9	8·9
	Coil 3. Nominal reduction 50%			
	3a	3b	3c	3d
Initial strip thickness (in.)	0·0633	0·0651	0·0651	0·0646
Final strip thickness (in.)	0·0325	0·0327	0·0320	0·0327
Average applied front tension (lb/in^2)	15,800	15,600	8600	39,800
Average applied rear tension (lb/in^2)	6200	12,400	18,600	18,600
Experimental load (lb/in.)	31,600	30,000	29,000	25,000
Calculated load (lb/in.)	33,700	30,950	26,800	23,850
Error in load (%)	+6·6	+3·2	−7·6	−4·6
Experimental roll torque (in-lb/in.)	4800	5440	6640	3960
Calculated roll torque (in-lb/in.)	4940	5340	6420	3870
Error in torque (%)	+2·9	−1·8	−3·3	−2·3
Other calculated results				
Roll "flattening" per roll (in.)	0·00238	0·00204	0·00180	0·00157
Angle of contact (degrees)	5·1	5·2	5·2	5·0
% of angle due to roll deformation	7·8	7·7	7·7	8·0
% of load due to roll deformation	11·2	12·2	11·8	9·2

Vol. 2
1960-61

TABLE 2. PREDICTED ROLLING RESULTS FOR PRE-ROLLED MILD STEEL

	Coil 5. Nominal reduction 30%			
	5a	5b	5c	5d
Initial strip thickness (in.)	0·0382	0·0389	0·0383	0·0383
Final strip thickness (in.)	0·0265	0·0262	0·0262	0·0261
Average applied front tension (lb/in²)	11,000	7600	23,600	40,200
Average applied rear tension (lb/in²)	0	11,400	11,600	23,400
Experimental load (lb/in.)	33,600	32,000	29,000	21,800
Calculated load (lb/in.)	32,600	30,350	26,900	20,450
Error in load (%)	−3·0	−5·2	−7·2	−6·2
Experimental roll torque (in-lb/in.)	2500	3540	2400	2020
Calculated roll torque (in-lb/in.)	2770	3830	2500	2040
Error in torque (%)	+10·8	+8·2	+4·2	+1·0
Other calculated results				
Roll "flattening" per roll (in.)	0·00244	0·00230	0·00187	0·00154
Angle of contact (degrees)	3·4	3·5	3·3	3·2
% of angle due to roll deformation	14·7	14·3	12·1	9·4
% of load due to roll deformation	19·8	19·6	15·3	10·6

	Coil 6. Nominal reduction 50%			
	6a	6b	6c	6d
Initial strip thickness (in.)	0·0385	0·0385	0·0385	0·0387
Final strip thickness (in.)	0·0184	0·0185	0·0176	0·0182
Average applied front tension (lb/in²)	8400	8400	21,800	42,200
Average applied rear tension (lb/in²)	0	13,000	13,000	23,800
Experimental load (lb/in.)	45,600	40,800	37,400	29,600
Calculated load (lb/in.)	44,250	38,450	36,050	25,750
Error in load (%)	−3·0	−5·8	−3·6	−13·0
Experimental roll torque (in-lb/in.)	5060	5640	4940	4140
Calculated roll torque (in-lb/in.)	5110	5640	4830	4280
Error in torque (%)	−1·0	0	−2·2	−3·4
Other calculated results				
Roll "flattening" per roll (in.)	0·00334	0·00264	0·00250	0·00176
Angle of contact (degrees)	4·3	4·4	4·3	4·2
% of angle due to roll deformation	14·0	15·9	11·6	11·9
% of load due to roll deformation	18·9	22·1	18·2	14·1

The maximum deviation in the load is −13·0 per cent. In the torque it is +10·8 per cent. It was estimated by Hessenberg and Sims[9] that the experimental error is of the order of 3 per cent. Therefore it is difficult to judge the accuracy of the prediction for any particular case. However, it is felt that this method is at least as accurate and considerably more general than other methods in use.

The calculated results show a systematic tendency to exaggerate somewhat the effect of applied tensions on the rolling load. It can be seen in Tables 1 and 2 that, in general, as the average of the two applied tensions increases, there is a

tendency for the error in the calculated rolling load to become more negative. The cause of this tendency is not known.

From Table 2 it is seen that as much as 22 per cent of the rolling load can be attributed to roll flattening. It should be noted here that this percentage can easily be as high as 50 per cent for high-strength material of small thickness.

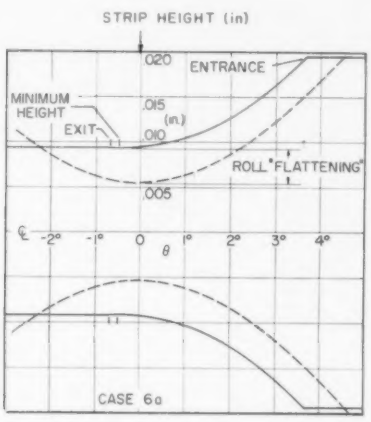

FIG. 5. Equilibrium strip-height distribution and roll flattening—case 6a.

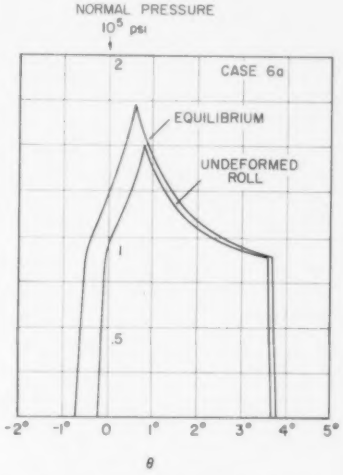

FIG. 6. Equilibrium and undeformed roll-pressure distribution—case 6a.

One of the calculated results listed in Tables 1 and 2 is the roll flattening per roll. This is defined as the difference between half the minimum strip thickness and the smaller thickness that would exist if the roll were perfectly rigid. Fig. 5 indicates the shape the roll takes for a typical case compared to the shape it would have if there were no deformation (shown dashed). The amount of roll flattening is indicated. In this example the flattening is 0·0033 in. per roll.

The effect of roll flattening on the angle of contact and rolling load is demonstrated in Fig. 6. Here, the theoretical pressure distribution on the work roll is indicated for a rigid roll and for the actual equilibrium roll deformation. It can be seen that the roll deformation lengthens the contact arc and increases the area under the pressure-distribution curve. In addition, any increase in contact arc length produces a larger increase in the rolling load.

CONCLUSIONS

This paper presents an analysis of the mechanics of cold rolling, which is more refined in many respects than previous analyses. The method could find practical application in the evaluation of new rolling mills in the conceptual design stages or the prediction of performance of existing mills with previously untried strip materials. In addition, the analysis can be used to predict the minimum strip thickness obtainable without exceeding a specified rolling load.

Vol. 2
1960-61

This limiting condition occurs when the entire region of contact becomes elastic, with the stresses satisfying the yield criterion at only one location. Another application is in the prediction of the amount of lateral-edge taper on the strip. An upper bound on the amount of taper will be equal to double the roll flattening per roll.

REFERENCES

1. J. H. HITCHCOCK, *Roll Neck Bearings.* Report of ASME Research Committee (1935).
2. H. FORD, D. R. BLAND and F. ELLIS, *J. Iron St. Inst.* **171**, 245 (1952).
3. J. D. KELLER, *Steel* **128**, 92 (1951).
4. S. TIMOSHENKO and J. N. GOODIER, *Theory of Elasticity.* McGraw-Hill, New York (1951).
5. E. OROWAN, *Proc. Instn. Mech. Engrs., Lond.* **150**, 140 (1943).
6. R. VON MISES, *Nachrichten von der Königlichen Gesellschaft der Wissenschaften zu Gottingen, math.-phys. Klasse* 582 (1913).
7. H. HENCKY, *Z. angew. Math. Mech.* **4**, 323 (1924).
8. A. NADAI, *Plasticity.* McGraw-Hill, New York (1931).
9. W. C. F. HESSENBERG and R. B. SIMS, *J. Iron St. Inst.* **168**, 155 (1951).
10. H. FORD, *Proc. Instn. Mech. Engrs., Lond.* **159**, 115 (1948).
11. P. W. WHITTON and H. FORD, *Proc. Instn. Mech. Engrs., Lond.* **169**, 123 (1955).

Int. J. Mech. Sci. Pergamon Press Ltd. 1960. Vol. 2, pp. 195–205. Printed in Great Britain

RESIDUAL STRESSES IN COLD IRONED TUBES

B. M. Botros
Ein Shams University, Cairo, Egypt, U.A.R.

(*Received* 10 *August* 1959)

Summary—Some investigations into the effect of the process variables on the pattern and magnitude of the residual stresses in the walls of ironed tubes is given. Sachs' boring method was adopted, a rotary jig being constructed to make possible the uniform inside and outside etching of aluminium tubes with caustic soda and of mild-steel tubes with nitric acid. Direct mechanical methods for measuring strains was preferred to the use of electric strain gauges.

The results indicated high compressive stresses on both tube surfaces, which changed rapidly to comparatively low tensile stresses with maximum values near the outside surface. Radial stresses are always very small.

Lubrication only slightly affects surface stresses. Lower residual stresses were found with higher reductions, tending to be negligible for reductions greater than 30 per cent.

Vol. 2
1960-61

INTRODUCTION

Residual stresses are stresses which exist in an elastic body when all external constraints are removed. The stresses considered here are macroscopic in type and are relatively large in magnitude.

It is usual to associate surface compressive residual stresses in ironed tubes with increased life, while tensile stresses are associated with decreased life. There is therefore considerable interest in methods which may reveal the magnitude and distribution of residual stresses in different products.

The present investigations were carried out to examine the effects of imposed deformation, lubrication and other variables on the pattern and magnitude of the residual stresses in the walls of both aluminium and mild steel tubes which had been ironed. It was also hoped that such information might suggest some means of controlling the residual stresses.

The tube ironing was carried out using fixed plug heads in order to prevent any change of the tube inside diameter and thus reducing the outside diameter only (Fig. 1).

Many investigators have investigated the residual stresses in drawn bars and tubes, using the split bending deflexion and the Sachs boring method.[1-15] Some comparisons carried out by Loxley[16] on hollow drawn tubes showed that the two methods give practically the same results.

The Sachs boring method of layer removal by etching was adopted for this work. A rotary jig was designed and developed to facilitate the uniform etching of layers either from the inside or the outside of the tube specimen. An etching technique was developed for aluminium as well as for mild steel. Direct mechanical methods for measuring strains were chosen in preference to using strain gauges, especially as the instruments used for measuring the length and the thickness of tube walls were accurate to within 0·0001 in. and this made possible an accuracy in the calculated stresses of more than 5 per cent.

Ford[17], in a survey of the mechanical methods for residual-stress investigation, cast doubt on the accuracy of strain gauges as used in Sachs method, because the readings had to be made at fairly long time intervals, up to several weeks, and it is not certain that the gauges will remain consistent

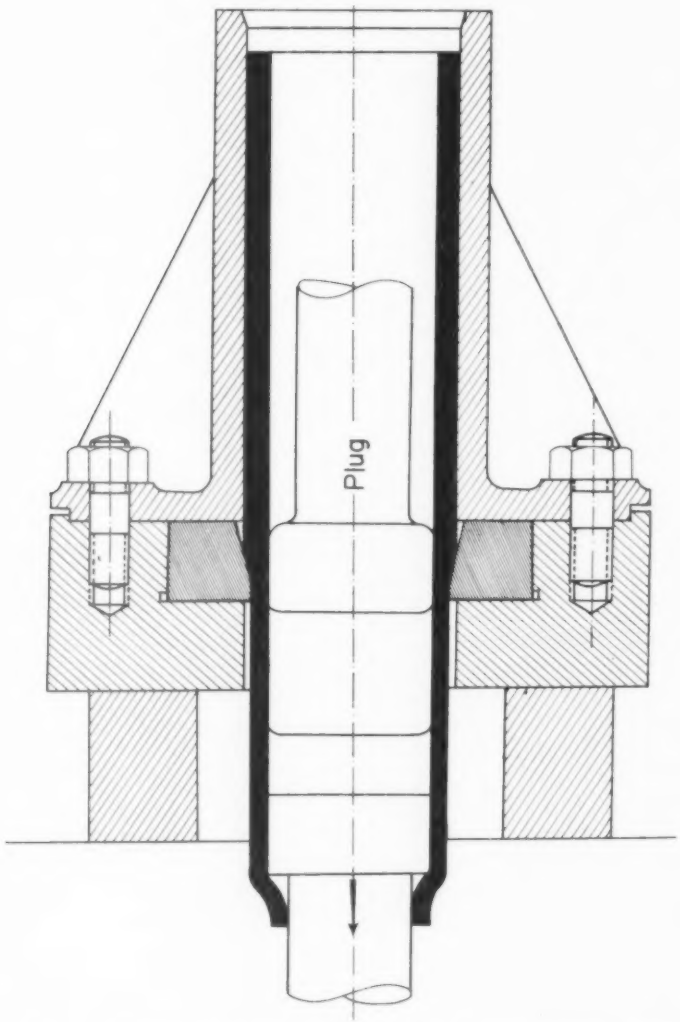

Fig. 1. Diagrammatic representation of tube-ironing technique.

over such lengths of time. Another drawback to this technique is the repeated soldering and breaking off of the strain gauges from the bridge used for measuring, which thereby exposed them to corrosion and humidity; there is also the fact of the high sensitivity of the strain gauges to temperature variations. It would be satisfactory to apply strain gauges if the boring or turning could be carried out mechanically without heat or vibration.

Boring method for measuring residual stresses

Sachs gave the following set of equations for determining the residual stresses at a point in the wall of a worked tube, when boring or pickling at the inside of the tube:

$$\sigma_l = \frac{E}{1-\nu^2}\left[(F_b - F)\frac{\partial\psi}{\partial F} - \psi\right]$$

$$\sigma_t = \frac{E}{1-\nu^2}\left[(F_b - F)\frac{\partial\theta}{\partial F} - \frac{F_b + F}{2F}\theta\right]$$

and

$$\sigma_r = \frac{E}{1-\nu^2}\cdot\frac{F_b - F}{2F}\theta$$

where:

$\sigma_l, \sigma_t, \sigma_r$ are the stresses in the longitudinal, tangential and radial directions respectively
E Young's modulus
ν Poisson's ratio
F_b total sectional area, including the bore
F current sectional area of the bore
ψ $\lambda + \nu\delta$
θ $\delta + \nu\lambda$
λ longitudinal strain $= (l - l_i)/l_i$
δ tangential strain $= (D - D_i)/D_i$
l current tube length
l_i initial tube length
D current tube outside diameter
D_i initial tube outside diameter

When turning or pickling the tube from the outside, the equations are:

$$\sigma_l = -\frac{E}{1-\nu^2}\left[(F - F_a)\frac{\partial\psi}{\partial F} + \psi\right]$$

$$\sigma_t = -\frac{E}{1-\nu^2}\left[(F - F_a)\frac{\partial\theta}{\partial F} + \frac{F + F_a}{2F}\theta\right]$$

$$\sigma_r = -\frac{E}{1-\nu^2}\frac{F - F_a}{2F}\theta$$

where F_a is the inside or bore sectional area, and F is the current or total sectional area including the bore.

The functions ψ and θ may be plotted against the bored or pickled cross-section of the cylinder, a smooth curve drawn through them and the slope of the curves $\partial\psi/\partial F$ and $\partial\theta/\partial F$ readily derived.

There are various tests that can be applied to the results to assess their reliability:

(1) On the plot of σ_l against the tube-wall thickness, the area under the curve, which represents compression, should be equal to that above the curve, which represents tension.

Vol. 2
1960-61

(2) The radial stress σ_r is zero at inner and outer surfaces and negligible elsewhere.

(3) Stresses at interior points when determined by boring, should be the same as those determined by removing the layers from the outside.

APPARATUS AND EXPERIMENTAL TECHNIQUE

The main difficulty in carrying out residual stress experiments is to remove thin uniform layers, either from the inside or the outside, without introducing other stresses as may easily happen when using such mechanical methods as grinding and machining.

The method of chemical etching was adopted for the present investigations and a successful method of removing uniform layers of metal by acid or soda pickling was developed. Rubber solution and Sellotape were found to be more effective than the stopping wax used by previous investigators.[15, 18] Mild-steel tubes were protected with two coats of rubber solution applied at 24-hr intervals and left for 12 hr before use. The rubber solution was removed from the tube after each etch and the dimensions were taken from the actual tube surface.

Aluminium tubes were protected with Sellotape which was found to be unaffected by caustic soda solution and was also easy to remove for measuring purposes. Durofix was used to seal the Sellotape edges and thus prevent them from leaving the tube surface while pickling.

The etching of mild steel was carried out with nitric acid of 1 : 3 by volume solution, and gave a removal rate of about 0·0003 in./min. Aluminium was etched in caustic soda solution of between 1 : 5 and 1 : 4 by weight, and the rate of removal at room temperature was approximately 0·0001 in./min.

(i) *Tube specimen*

Many investigators[10, 14, 19] have studied the effect of length on residual-stress determinations and have suggested that correct results can be obtained only when the ratio of the tube length to its outside diameter is not less than about 2. A tube length of about 5 in. for 2·5 in. outside diameter was therefore considered suitable to eliminate end effects. The test specimen was parted off the parent tube and the ends bevelled and squared (inserts on Figs. 2 and 3) either in a grinding machine or a lathe, making only small cuts and using excess coolant to minimize vibration and heat. The ends of the tubes were bevelled in order that the same reference could be used for all length measurements, when layer removal commenced.

(ii) *Strain measurements*

The tube outside diameter was measured by means of a calibrated micrometer to an accuracy of $\pm 0{\cdot}0001$ in. using a simple jig. Ten measurements were taken along each of four longitudinal lines equally spaced at 90° around the tube. Changes in length were measured along these four lines using a Talymin comparator, to an accuracy of $\pm 0{\cdot}0001$ in. Measurements were taken after leaving the tube in a temperature-controlled dark room for 24 hr, care being taken to avoid radiant heat from lamps or the human body.

(iii) *Perspex rotary jig*

To carry out the pickling of the specimens and to remove very thin uniform layers either from the inside or the outside surface of the tube, a rotary jig was used, see Fig. 2. The jig components, except for the seals and the driving motor, were all made of Perspex to withstand the effects of the pickling solutions. It consists of a base with two side supports and four columns, all cemented together. The columns carried a loose-top Perspex plate on which was mounted a slow-speed d.c. driving motor. A Perspex pulley was keyed to the motor shaft and a side nut prevented it from sliding axially. All these parts were kept covered with wax to protect them from the active solutions. A square hole was cut in the top plate for the driving belt and to let the solution drip into the glass container. The height of this plate was such as to allow ample room for the brush used for the outside pickling. The apparatus was easily manageable as a complete unit so

that it could be dipped into a sink full of circulating water after completing each test. The rotary parts of the apparatus which hold the tube specimens consisted of two different assemblies, one for external and the other for internal etching.

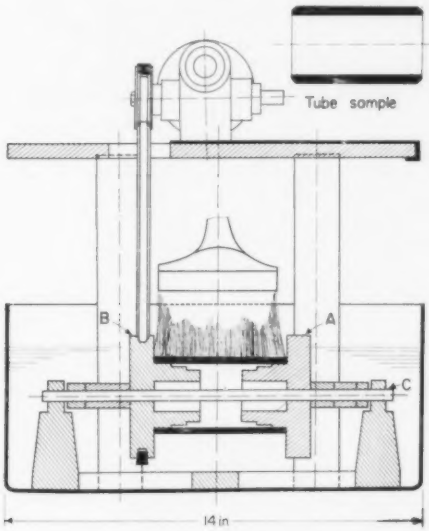

FIG. 2. Apparatus arrangement for external etching of tube.

(iv) *External etching* (*See Fig.* 2)

The assembly consists of two stepped chucks gripping the inside of the tube specimen and carried on a shaft between the two main side supports mentioned before. A pulley was formed on the side of one of these chucks engaged with the driving pulley of the motor.

In this type of etching, the specimen was fully submerged in the liquid and kept revolving at a slow speed of about 20–30 rev/min. In the case of mild-steel tubes, the surface was swept by a pure-hair brush. This prevented the formation of a dark film which was found to interfere with the etching, and to give rise to non-uniformity of the process.

Fig. 4 illustrates the uniformity of the outside etching on a mild-steel tube. The ordinate represents the radial distance through the wall thickness, while the abscissa represents the developed-tube circumference. The sequence of curves represents the average measurements of the tube-wall thickness along the specimen as the layers were removed one after the other. The pickling of mild-steel tubes from the inside presents a similar picture. The uniformity in the pickling of aluminium tubes in soda solution was found to be very satisfactory, the metal surface being smoother than in the case of the mild-steel ones.

A simple method later found to be very satisfactory concerned aluminium tubes which were to be etched from the outside. This method consists in first covering the cross-sections of the tube with wide Sellotape and sealing the edges with Durofix. The tube was then dropped into the soda solution, and due to the lightness of the material, the specimen floated. It was caused to rotate by means of a nylon brush, which also helped to remove the attacked layers.

(v) *Internal etching* (*See Fig.* 3)

The tube was carried from the outside by means of two chucks having their outside edges projecting in two stationary boxes, through which liquid flows in and out of the tube specimen.

Vol. 2
1960-61

Acid was supplied to the stationary end boxes by flexible tubes and then passed through holes which created a desirable swill in the ends of the rotating chucks. The reversed direction of flow was obtained by supplying and receiving the liquid in two glass jars that were alternately raised and lowered throughout the test (insert to Fig. 3).

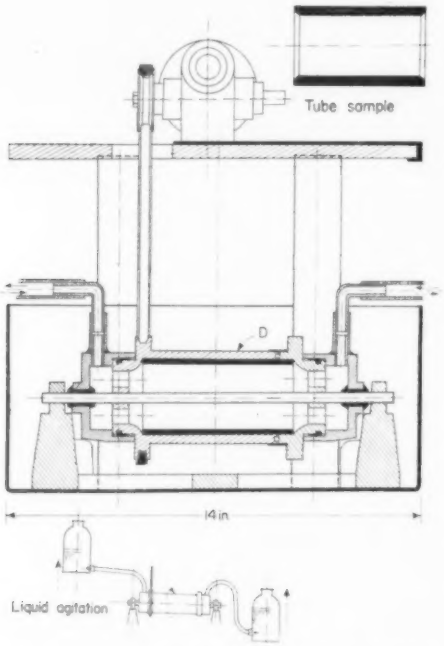

FIG. 3. Apparatus arrangement for internal etching of tube.

EXPERIMENTAL PROCEDURE

(i) *Preliminary investigations*

Specimens prepared from the "as received" aluminium and mild-steel tubes were pickled with soda solution and nitric acid, respectively. The resultant longitudinal and diametral changes were measured at each stage of layer removal, and the resultant residual stress-distribution curves are given in Fig. 5. It shows high circumferential and longitudinal compressive stresses at, or near, the outside surface, and low stresses in the inner portions of the tube wall. The radial stresses were negligible across the wall thickness.

Aluminium tubes in the "as received" condition did not show any measurable residual stresses. It was necessary, therefore, to anneal the mild-steel tubes before preparing them for ironing tests. The procedure for studying the residual stress distribution was repeated with a section of a mild-steel tube cut off after annealing. The results obtained were similar to those in Fig. 5 and the stresses were reduced, not eliminated. It was considered that any surface stresses due to machining the "as received" tubes to obtain the necessary concentricity, ovality and straightness could thus be eliminated. Both the aluminium and the mild-steel tubes were able, therefore, to be prepared free of any significant internal stresses before carrying out the ironing tests.

(ii) *Residual stresses due to ironing operations: Introduction and procedure*

The principal variables in the tube ironing which have an effect on the distribution of residual stresses are: the reduction in cross-sectional area of the tube, the lubricant used, the ratio of the tube outside radius to the wall thickness, and the particular material of the tube under test.

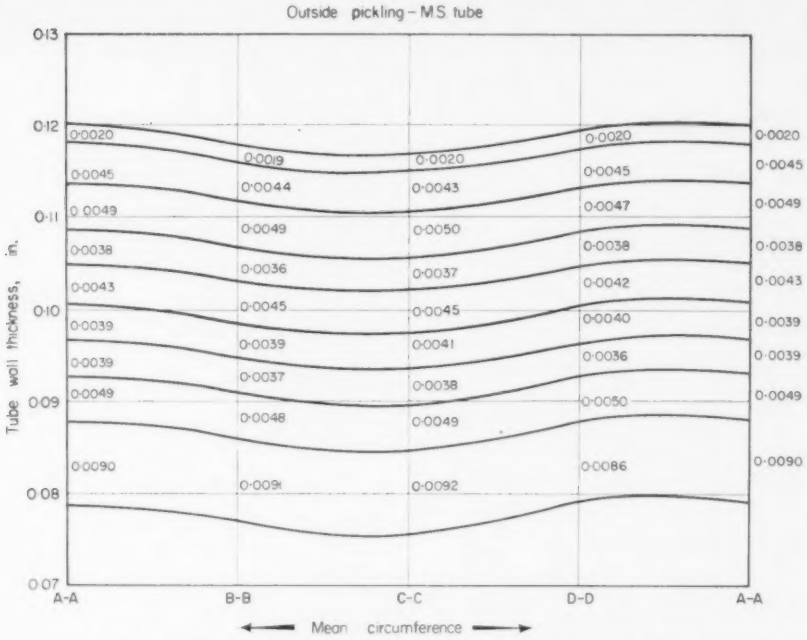

FIG. 4. Representation of the uniformity of tube pickling.

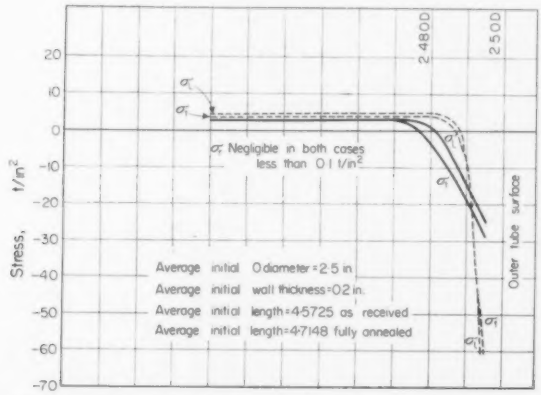

FIG. 5. Effects of anneal on residual stresses in mild-steel tubes.
- - - Mild steel, "as received"
—— Mild steel, fully annealed
} Outside pickling

In all such previous investigations on the distribution of residual stresses employing the pickling technique, only mild steel has been studied. In this work, the possibility of applying the pickling technique to other metals, such as aluminium, and the possibility of using caustic soda solution were investigated.

The procedure for the complete determination of residual-stress distribution was in each case to cut two equal specimens from a parent tube, the length of the tube being approximately twice the tube outside diameter. One of the specimens was subjected to inside pickling while the other was pickled from the outside. The resulting deformation, in each case, in both axial and tangential directions, was measured as previously described. This approach assumes, of course, that each cross-section of a parent tube is identical.

Vol. 2
1960-61

RESULTS AND DISCUSSION

The experimental results are given in Figs. 6–8 and show the distribution of longitudinal and tangential residual stresses through the tube-wall thickness. The stresses were calculated applying the Sachs equations referred to above.

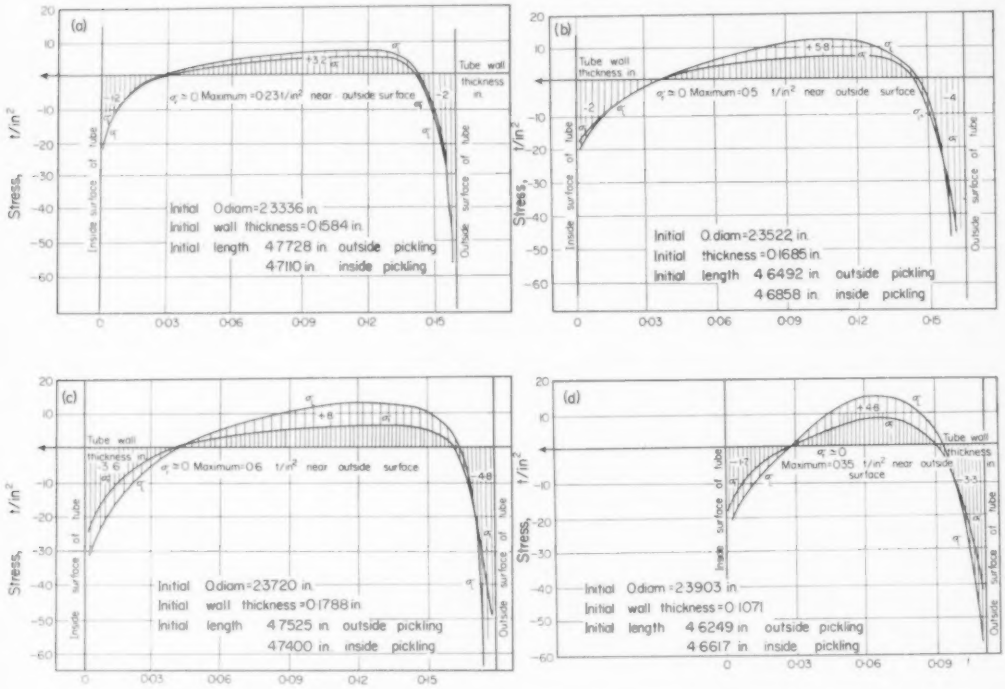
(a)
Stress, t/in²
Tube wall thickness in
Inside surface of tube
Outside surface of tube
σt ≈ 0 Maximum =0·231/in² near outside surface
Initial O.diam=2·3336 in.
Initial wall thickness=0·1584 in.
Initial length 4·7728 in. outside pickling
4·7110 in. inside pickling
(b)
Tube wall thickness in
σt ≈ 0 Maximum =0·5 t/in² near outside surface
Initial O.diam=2·3522 in.
Initial thickness=0·1685 in.
Initial length 4·6492 in. outside pickling
4·6858 in. inside pickling
(c)
Tube wall thickness in
σt ≈ 0 Maximum=0·6 t/in² near outside surface
Initial O.diam=2·3720 in.
Initial wall thickness=0·1788 in.
Initial length 4·7525 in. outside pickling
4·7400 in. inside pickling
(d)
Tube wall thickness in
σt ≈ 0 Maximum=0·35 t/in² near outside surface
Initial O.diam=2·3903 in.
Initial wall thickness=0·1071
Initial length 4·6249 in. outside pickling
4·6617 in. inside pickling

FIG. 6. Residual-stress distribution in mild-steel tubes with various percentage reductions in cross-sectional area and r_0/t_0 ratio. (a) $r_0/t_0 = 6$; 22·8%. (b) $r_0/t_0 = 6$; 17·9%. (c) $r_0/t_0 = 6$; 12·5%. (d) $r_0/t_0 = 10$; 12%.

Pickling from both the inside and the outside tube surfaces was performed so that it covered the whole cross-sectional area of the tube walls. This technique of combining the two operations helped to determine the residual-stress distribution in the boundary layers as well as in the core of the wall thickness. It is necessary in cases where there are rapid changes of direction in the stress distribution in the surface layers. It is also necessary when the greater part of the section exhibits only comparatively low residual stresses while the surface zones are under high stress.

The coincidence of the section at which σ_l and σ_t had their greatest value and the similarity of the stress gradient gave confidence in the strain measurements.

The results show similar general patterns for the stresses in both the longitudinal and the circumferential directions. High compressive stresses were indicated on both the inside and outside surfaces, with higher values on

Vol. 2
1960-61

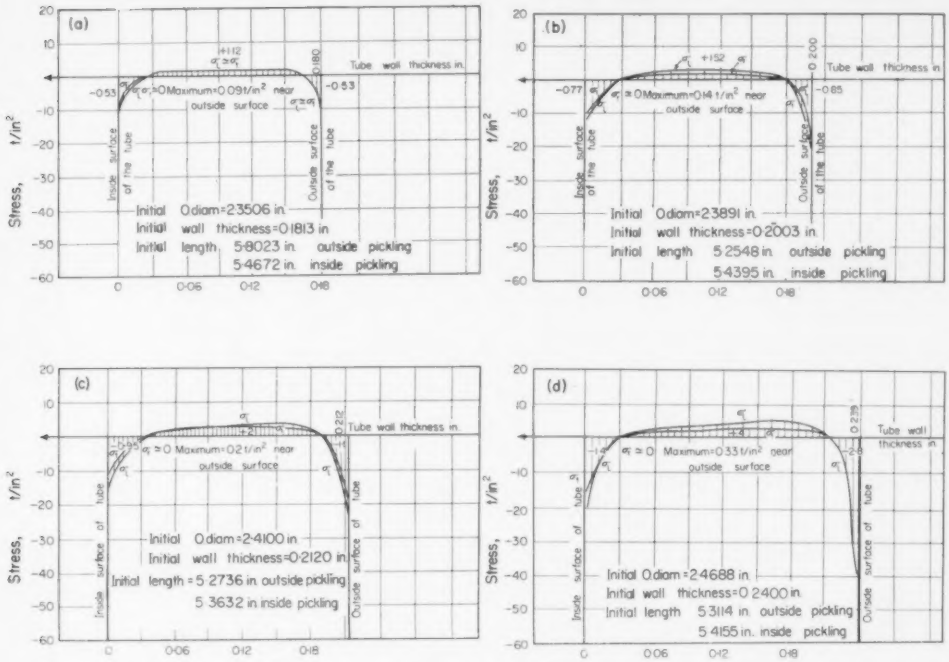

FIG. 7. Residual-stress distribution in aluminium tubes with various percentage reductions in cross-sectional area and $r_0/t_0 = 5$. (a) 29·5. (b) 21·6. (c) 17. (d) 4·4% reduction.

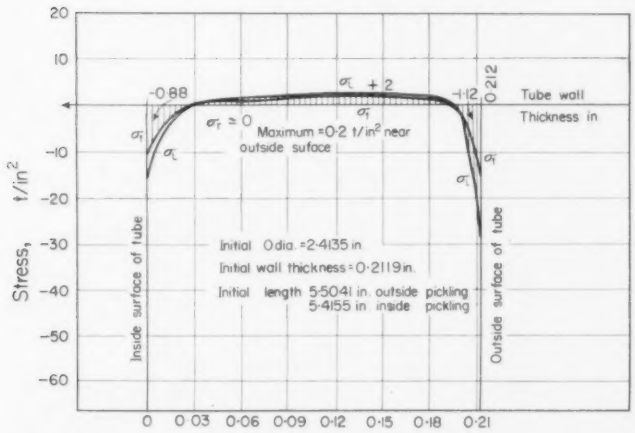
Initial O.dia.=2·4135 in.
Initial wall thickness=0·2119 in.
Initial length 5·5041 in. outside pickling
5·4155 in. inside pickling
Maximum=0·2 t/in² near outside suface
Tube wall Thickness in
Inside surface of tube
Outside surface of tube
Stress, t/in²

FIG. 8. Residual-stress distribution in an aluminium tube of $r_0/t_0 = 5$ ironed with 17 per cent reduction in sectional area using no lubricant.

the outside. The latter changed more rapidly to tensile values, and in all cases the maximum tensile stresses appeared near the outer surface; they decreased gradually towards the inside and remained mainly tensile through most of the

wall thickness. The maximum compressive stresses, however, were much larger than the maximum tensile. The magnitude of the peak tangential stresses was generally smaller than that of the longitudinal stress. The inner compressive stresses penetrated the walls slightly deeper than the corresponding outside stresses.

It is generally acknowledged that the radial stresses are of little importance[9, 10, 20] and in all tests described here nowhere exceed $0{\cdot}6\,t/\text{in}^2$ with mild steel and $0{\cdot}4\,t/\text{in}^2$ with aluminium. This is because the tube-wall thickness is generally small compared with the other dimensions so that no sizeable internal stresses can be left in that direction after relaxation. The maximum values of the radial stresses which were found to exist near the outside surfaces, are marked in Figs. 5 and 8. In all cases studied there was an "equilibrium check", since the longitudinal force on any transverse cross-section, represented by the integrated areas under the stress curves, must equal zero.

The existence of compressive stresses on the inner tube surface can be explained as follows. All metal surfaces have irregularities and when two such surfaces are placed together they will be supported on the summits of their irregularities and their real area of contact will be small. The local pressures will thus be very high, and plastic flow and deformation will occur. This is particularly true as the tube slides on the plug-head surface. Therefore, if during the ironing operation the surface layers are retarded with respect to the mass of plastic flow, they will be stretched more severely than the central core of the material passing through the die. After leaving the die the material is unloaded, thus causing the surface layers to be left with internal compressive stresses in both the longitudinal and hoop directions. As a consequence tensile stresses in the central portion of the tube will arise as a reaction to the outer compressive stresses.

Experiments with aluminium tubes were performed using graphite-in-tallow as a lubricant, and with no lubricant. From Figs. 7 and 8 it can be seen that the lubricant used had practically no influence on the residual stresses across the tube walls.

The effect of the reduction in cross-sectional area of a tube by ironing was studied in both aluminium and mild-steel tubes. From Figs. 6 and 7 it can be seen that the smaller the reduction or the total strain imposed on the tube material, the larger the stresses obtained in all three principal directions. This can be explained by observing that the metal deformation is more uniform the higher the reduction.

The final variable to be investigated was the r_0/t_0 ratio. Two mild-steel specimens with initial r_0/t_0 values of 6 and 10 were ironed through the same reduction in cross-sectional area, 12·5 per cent, using graphite-in-tallow as lubricant. The results, given in Fig. 6, show that the maximum tensile stress values were practically the same, though the surface stresses were less with the thinner tube.

The strains recorded when the surface layers are removed by pickling were lower than those from thick tubes, subjected to the same reduction in cross-sectional area.

Vol. 2
1960-61

CONCLUSIONS

The pickling process for removing metal layers, either from the inside or the outside surfaces of any tube, can be performed satisfactorily, provided sufficient care is taken.

Results of studies carried out on both aluminium and mild-steel tubes showed that compressive stresses appeared on and near both the outer and inner surfaces. The magnitudes of the compressive stresses were comparatively high and the changes to tensile values were achieved more rapidly from the outside of the tube. Surface stresses were little affected by friction and could be reduced only slightly by the use of an efficient drawing lubricant. The percentage reduction in tube cross-sectional area had the most noticeable effects; the higher the reduction imposed on the tube the lower the residual stresses left in the metal. It was concluded that internal stresses are reduced to negligible values by ironing to reductions larger than 30 per cent in cross-sectional area. This indicates the possibility of ironing tubes in such a manner as to prevent the occurrence of high residual stresses, rather than finding a way to reduce them once they are present.

Acknowledgements—The author wishes to record his gratitude to Professor H. W. Swift and Mr. F. C. Turner for their advice and facilities granted at the University of Sheffield, to Dr. J. F. Wallace for his supervision and assistance and to Mr. W. Johnson for his help with the manuscript.

Thanks are also due to the Tube Investment Ltd., The British Aluminium Co. Ltd. and Edgar Vaughan Ltd., Birmingham, for their supplies of tubes and lubricants.

This work would not have been possible without the financial assistance given by the Egyptian Government and the British Iron & Steel Research Association.

REFERENCES

1. E. Heyn, *J. Inst. Met.* **12**, 3 (1914).
2. G. Sachs, *Z. Metallk.* **19**, 352 (1927).
3. D. K. Crampton, *Trans. Amer. Inst. Min. (Metall.) Engrs., Inst. Met. Div.* **89**, 233 (1930).
4. N. Devidenkov, *Z. Metallk.* **24**, 25 (1932).
5. J. Fox, *Engineering, Lond.* **129**, 65 (1930).
6. J. Fox, *Engineering, Lond.* **136**, 375 (1933).
7. H. Buchholtz, *Stahl u. Eisen, Düsseldorf* **52**, 490 (1932).
8. *Studies in the Working of Steel Tubes.* Tube Investment Ltd. Research Report (1937).
9. G. Sachs and G. Espey, *Trans. Amer. Inst. Min. (Metall.) Engrs., Inst. Metals Div.* **147**, 348 (1942).
10. G. Sachs and G. Espey, *Trans. Amer. Inst. Min. (Metall.) Engrs., Inst. Metals Div.* **147**, 74, 348 (1942).
11. C. S. Barrett, *Proc. Exp. Stress Anal.* **11**, 147 (1944).
12. K. Heindlhofer, *Evaluation of Residual Stresses.* McGraw-Hill, New York (1948).
13. H. B. Wishart and R. K. Potter, *Trans. Amer. Soc. Metals* **41**, 692 (1949).
14. B. M. Botros. Thesis, Sheffield University (1950).
15. E. M. Loxley, *Progress Report on the Measurement of Residual Stresses in Cold Drawn Tubes.* B.I.S.R.A. Report MW/E/43/50 (1950).
16. E. M. Loxley, *The Application of the Sachs Boring Method to the Measurement and Detection of Residual Stresses in Cold Drawn Tubes.* B.I.S.R.A. Report MW/E/55/53 (1953).
17. H. Ford, *Symposium on Residual Stresses.* Institute of Metals, London (1947).
18. B. B. Hundy, *J. Iron St. Inst.* **179**, 23 (1955).
19. E. M. Loxley, *Second Report on the Detection and Measurement of Residual Stresses in Cold Drawn Tubes.* B.I.S.R.A. Report MW/E/48/51 (1951).
20. H. Ford, *Proc. Inst. Mech. Engrs., Lond.* **159**, 115 (1948).

Int. J. Mech. Sci. Pergamon Press Ltd. 1960. Vol. 2, pp. 206–211. Printed in Great Britain

UNIFORMLY LOADED RECTANGULAR PLATE SUPPORTED AT THE CORNERS

S. L. LEE* and P. BALLESTEROS†

(*Received* 16 *April* 1960)

Summary—An approximate solution for a uniformly loaded rectangular plate supported at the corners is discussed. The results of the solution are shown to be in close agreement with those obtained by numerical solutions and experimental investigation of uniformly loaded square plates supported at the corners. For the limiting case where the aspect ratio approaches zero, the resulting expressions closely approximate those derived for a uniformly loaded and simply supported strip of unit width.

NOTATION

a, b	half-side dimensions of a rectangular plate (see Fig. 1)
h	thickness of a plate
q	intensity of uniformly distributed load
w	deflection function
x, y, z	rectangular co-ordinates
C_1, C_2, etc.	constant coefficients
D	flexural rigidity of a plate, $Eh^3/12(1-\mu^2)$
E	modulus of elasticity
M_x, M_y	bending moments per unit length of sections of a plate perpendicular to the x- and y-axes respectively
M_{xy}	twisting moment per unit length of section of a plate perpendicular to the x-axis
Q_x, Q_y	shearing forces parallel to the z-axis per unit length of a plate perpendicular to the x- and y-axes respectively
R	concentrated reaction at the corner of a rectangular plate
V_x, V_y	reactions parallel to the z-axis per unit length of the boundary of a plate perpendicular to the x- and y-axes respectively
μ	Poisson's ratio
$\left[\frac{\partial^3 w}{\partial x^2 \partial y}\right]_{a,b}$	value of the partial derivative of w, twice with respect to x and once with respect to y, at the point $x = a$ and $y = b$

INTRODUCTION

THE solution for a uniformly loaded rectangular plate supported at the corners, although commonly encountered in practice, is not apparently available. Data for uniformly loaded square plates supported at the corners were given by Nadai[1] and Marcus[2]. The solutions in both cases were obtained by means of numerical methods for particular values of Poisson's ratio. Experimental investigation

* The Technological Institute, Northwestern University, Evanston, Illinois.

† Instituto Tecnologico de Monterrey, Monterrey, Mexico. (Formerly at the Technological Institute, Northwestern University, Evanston, Illinois.)

of a uniformly loaded square concrete slab, prestressed in two directions and supported in similar manner, was reported by Scordelis *et al.*[3]

An approximate solution for a uniformly loaded rectangular plate supported at the corners is presented in the following.

DEFLECTION FUNCTION

The solution of the biharmonic equation in polynomials was discussed by Girkmann[4]. It will be shown that an approximate solution for the problem under consideration can be obtained by taking the deflection function in the form

$$W = C_1 + C_2 x^2 + C_3 y^2 + C_4 x^4 + C_5 x^2 y^2 + C_6 y^4 \tag{1}$$

Locating the origin of the co-ordinate axes at the center of the rectangular plate as shown in Fig. 1, the boundary condition that there be no reactions at

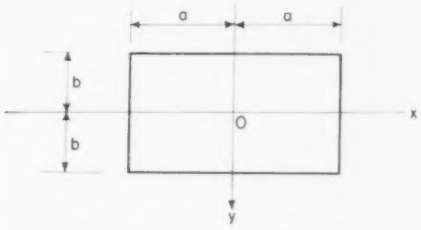

FIG. 1. Rectangular plate.

the free edges is expressed by

$$\left.\begin{aligned} [V_x]_{a,y} &= -D\left\{\left[\frac{\partial^3 w}{\partial x^3}\right]_{a,y} + (2-\mu)\left[\frac{\partial^3 w}{\partial x\,\partial y^2}\right]_{a,y}\right\} = 0 \\ [V_y]_{x,b} &= -D\left\{\left[\frac{\partial^3 w}{\partial y^3}\right]_{x,b} + (2-\mu)\left[\frac{\partial^3 w}{\partial x^2\,\partial y}\right]_{x,b}\right\} = 0 \end{aligned}\right\} \tag{2}$$

Substituting (1) in (2) and the biharmonic equation

$$\frac{\partial^4 w}{\partial x^4} + 2\frac{\partial^4 w}{\partial x^2\,\partial y^2} + \frac{\partial^4 w}{\partial y^4} = \frac{q}{D}$$

leads respectively to

$$6C_4 + (2-\mu)C_5 = 0$$

$$(2-\mu)C_5 + 6C_6 = 0$$

$$24C_4 + 8C_5 + 24C_6 = \frac{q}{D}$$

The solution of this system of equations yields

$$C_4 = C_6 = \frac{(2-\mu)q}{48(1-\mu)D}$$

$$C_5 = -\frac{q}{8(1-\mu)D}$$

for which (1) becomes

$$W = C_1 + C_2 x^2 + C_3 y^2 + \frac{q}{48(1-\mu)D}[(2-\mu)(x^4+y^4) - 6x^2 y^2] \tag{3}$$

TABLE 1. VALUES OF ϕ_1, ϕ_2, ϕ_3, ϕ_4 AND ϕ_5 TABULATED AGAINST ARGUMENTS OF b/a

b/a	ϕ_1 Eq. (6)*	ϕ_2 Eq. (8a)	ϕ_3 Eq. (8b)	ϕ_4 Eq. (9)	ϕ_5 (Eq. (10)
0	2·5525	0·5000	−0·0583	0	0·5000
0·1	2·5473	0·4994	−0·0533	0·0044	0·5012
0·2	2·5346	0·4977	−0·0383	0·0177	0·5047
0·3	2·5237	0·4947	−0·0133	0·0398	0·5105
0·4	2·5298	0·4907	0·0217	0·0707	0·5187
0·5	2·5745	0·4854	0·0667	0·1104	0·5292
0·6	2·6853	0·4790	0·1217	0·1590	0·5420
0·7	2·8958	0·4717	0·1867	0·2164	0·5572
0·8	3·2460	0·4627	0·2617	0·2827	0·5747
0·9	3·7817	0·4528	0·3467	0·3578	0·5945
1·0	4·5550	0·4417	0·4417	0·4417	0·6167

* At $b/a = 0{\cdot}328$, (6) gives a minimum value of 2·5229.

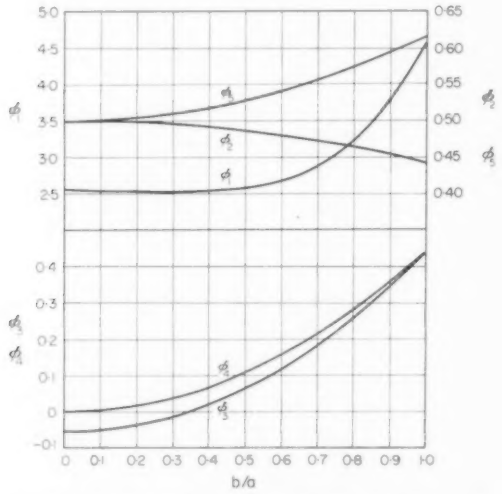

FIG. 2. Values of ϕ_1, ϕ_2, ϕ_3, ϕ_4 and ϕ_5 plotted against arguments of b/a.

It is of interest to note that (3) satisfies the condition of zero reactions at the free edges irrespective of the values of C_1, C_2 and C_3 which are determined by the boundary conditions

$$\left.\begin{aligned} \int_0^b [M_x]_{a,y}\, dy &= -D\int_0^b \left[\frac{\partial^2 w}{\partial x^2} + \mu\frac{\partial^2 w}{\partial y^2}\right]_{a,y} dy = 0 \\ \int_0^a [M_y]_{x,b}\, dx &= -D\int_0^a \left[\frac{\partial^2 w}{\partial y^2} + \mu\frac{\partial^2 w}{\partial x^2}\right]_{x,b} dx = 0 \\ [w]_{a,b} &= 0 \end{aligned}\right\} \tag{4}$$

Thus substituting (3) in (4) and solving the resulting equations,

$$C_1 = \frac{qa^2b^2}{48(1-\mu^2)D}\left[(10+\mu-\mu^2)\left(\frac{a^2}{b^2}+\frac{b^2}{a^2}\right)-2(7\mu-1)\right]$$

$$C_2 = \frac{qab}{24(1-\mu^2)D}\left[(1+5\mu)\frac{b}{a}-(6+\mu-\mu^2)\frac{a}{b}\right]$$

$$C_3 = \frac{qab}{24(1-\mu^2)D}\left[(1+5\mu)\frac{a}{b}-(6+\mu-\mu^2)\frac{b}{a}\right]$$

for which (3) becomes

$$w = \frac{qa^4}{48(1-\mu^2)D}\left\{(10+\mu-\mu^2)\left(1+\frac{b^4}{a^4}\right)-2(7\mu-1)\frac{b^2}{a^2}\right.$$
$$+2\left[(1+5\mu)\frac{b^2}{a^2}-(6+\mu-\mu^2)\right]\frac{x^2}{a^2}+2\left[(1+5\mu)-(6+\mu-\mu^2)\frac{b^2}{a^2}\right]\frac{y^2}{a^2}$$
$$\left.+(2+\mu-\mu^2)\frac{x^4+y^4}{a^4}-6(1+\mu)\frac{x^2y^2}{a^4}\right\} \qquad (5)$$

The maximum deflection at the center of the plate, for $\mu = 0{\cdot}3$, is given in terms of the aspect ratio b/a by

$$\phi_1 = \frac{Eh^3}{qa^4}[w]_{0,0} = 2{\cdot}5525\left(1+\frac{b^4}{a^4}\right)-0{\cdot}550\frac{b^2}{a^2} \qquad (6)$$

The values of ϕ_1, as well as those of ϕ_2, ϕ_3, ϕ_4 and ϕ_5 derived later, are given in Table 1 and Fig. 2 against arguments of b/a.

INTERNAL FORCES

Differentiating (5) yields the expressions for the bending moments, the twisting moment and the shearing forces:

$$\left.\begin{aligned} M_x &= \frac{qa^2}{12}\left[6-(1-\mu)\frac{b^2}{a^2}-6\frac{x^2}{a^2}+3(1-\mu)\frac{y^2}{a^2}\right] \\ M_y &= \frac{qa^2}{12}\left[6\frac{b^2}{a^2}-(1-\mu)-6\frac{y^2}{a^2}+3(1-\mu)\frac{x^2}{a^2}\right] \\ M_{xy} &= -\frac{q}{2}xy \\ Q_x &= -\frac{q}{2}x \\ Q_y &= -\frac{q}{2}y \end{aligned}\right\} \qquad (7)$$

The concentrated reaction at the corner is

$$R = 2D(1-\mu)\left[\frac{\partial^2 w}{\partial x\,\partial y}\right]_{a,b} = -qab$$

as it should be.

Vol. 2
1960-61

The bending moments at the center of the plate, for $\mu = 0{\cdot}3$, are given by

$$\left.\begin{aligned} \phi_2 &= \frac{1}{qa^2}[M_x]_{0,0} = 0{\cdot}5 - 0{\cdot}05833\frac{b^2}{a^2} \\ \phi_3 &= \frac{1}{qa^2}[M_y]_{0,0} = 0{\cdot}5\frac{b^2}{a^2} - 0{\cdot}05833 \end{aligned}\right\} \tag{8}$$

For design purposes, a better approximation for $[M_y]_{0,0}$, for $\mu = 0{\cdot}3$, may be given by

$$\phi_4 = \frac{1}{qa^2}[\bar{M}_y]_{0,0} = 0{\cdot}4417\frac{b^2}{a^2} \tag{9}$$

A glance at the values of ϕ_3 and ϕ_4 in the vicinity of $b/a = 0$ in Fig. 2 will illustrate this point.

The maximum bending moment occurs at the center of the longer edge. For $\mu = 0{\cdot}3$, this maximum value is given by

$$\phi_5 = \frac{1}{qa^2}[M_x]_{0,b} = 0{\cdot}5 + 0{\cdot}1167\frac{b^2}{a^2} \tag{10}$$

COMPARISON OF RESULTS

It is interesting to observe that, for $\mu = 0{\cdot}3$ and $b/a = 0$, (5) and (7a) become, respectively,

$$\left.\begin{aligned} \lim_{b/a\to 0}[w]_{x,0} &= \frac{qa^4}{Eh^3}\left((2{\cdot}5525 - 3{\cdot}105\frac{x^2}{a^2} + 0{\cdot}5525\frac{x^4}{a^4}\right) \\ \lim_{b/a\to 0}[M_x]_{x,0} &= 0{\cdot}5qa^2\left(1 - \frac{x^2}{a^2}\right) \end{aligned}\right\} \tag{11}$$

whereas the deflection and bending moment of a simply supported and uniformly loaded strip of unit width and span "$2a$" are, locating the origin at the center of the span, respectively

$$\left.\begin{aligned} w &= \frac{qa^4}{Eh^3}\left(2{\cdot}5 - 3{\cdot}0\frac{x^2}{a^2} + 0{\cdot}5\frac{x^4}{a^4}\right) \\ M_x &= 0{\cdot}5qa^2\left(1 - \frac{x^2}{a^2}\right) \end{aligned}\right\} \tag{12}$$

The close agreement between (11) and (12) is rather striking.

For a uniformly loaded square plate supported at the corners, numerical solution by Marcus[2] gives, for $\mu = 0{\cdot}3$,

$$\frac{D}{qa^4}[w]_{0,0} = 0{\cdot}3979 \quad (0{\cdot}4171)$$

$$\frac{D}{qa^4}[w]_{0,b} = 0{\cdot}2728 \quad (0{\cdot}2978)$$

$$\frac{1}{qa^2}[M_x]_{0,0} = 0{\cdot}4361 \quad (0{\cdot}4417)$$

$$\frac{1}{qa^2}[M_x]_{0,b} = 0{\cdot}5617 \quad (0{\cdot}6167)$$

The values given in parentheses to the right are the corresponding values obtained by means of (5) and (7a). Another numerical solution by Nadai[1] yields, for $\mu = 0{\cdot}25$,

$$\frac{D}{qa^4}[w]_{0,0} = 0{\cdot}4051$$

Experimental investigation by Scordelis *et al.*[3] of a uniformly loaded and corner-supported square concrete slab prestressed in two directions, with $a = 7{\cdot}0$ ft, $h = 5{\cdot}0$ in., $q = 62{\cdot}5$ lb/ft^2 and $E = 4{,}109{,}000$ lb/in^2, yields*

$$[w]_{0,0} = 0{\cdot}195 \text{ in.} \qquad (0{\cdot}2014 \text{ in.})$$

$$[w]_{0,7} = 0{\cdot}125 \text{ in.} \qquad (0{\cdot}1376 \text{ in.})$$

$$[M_x]_{0,0} = 1450 \text{ ft-lb/ft} \qquad (1328 \text{ ft-lb/ft})$$

$$[M_y]_{7,0} = 1890 \text{ ft-lb/ft} \qquad (1942 \text{ ft-lb/ft})$$

Vol. 2
1960-61

Taking $\mu = 0{\cdot}2$, the corresponding values obtained by means of (5) and (7a, b) are shown in parentheses.

It is seen from the foregoing that the results obtained for a square plate by means of the approximate solution are in fairly close agreement with the numerical solutions and the experimental data mentioned.

DISCUSSION AND CONCLUSION

A glance at Fig. 2 indicates that in the range $0 < b/a < 0{\cdot}4$, the values of ϕ_1 and ϕ_2, given by (6) and (8a), vary only slightly from the corresponding values for $b/a = 0$. Comparison with (12a, b) for $x = 0$ shows that, for $b/a < 0{\cdot}4$, the behaviors of $[w]_{0,0}$ and $[M_x]_{0,0}$ for the plate approach those of the simply supported strip of unit width.

It should be observed that the error in M_x becomes appreciable as x approaches a and, similarly, the error in M_y becomes appreciable as y approaches b. The error is largest in the vicinity of the corners. This should be expected as a result of the approximation expressed by (4a, b). Otherwise, the results obtained by means of the approximate solution compare favorably with known solutions at the limiting cases where the aspect ratios are respectively zero and unity. It is unfortunate that data for intermediate values of the aspect ratio are not currently available. A check at an intermediate value, say $b/a = 0{\cdot}75$, should more firmly establish the accuracy of the proposed solution.

REFERENCES

1. A. Nadai, *Z. angew. Math. Mech.* **2**, 1 (1922).
2. H. Marcus, *Die Theorie elastischer Gewebe und ihre Anwendung auf die Berechnung biegsamer Platten* p. 173. Springer, Berlin (1932).
3. A. C. Scordelis, K. S. Pister and T. Y. Lin, *J. Amer. Concr. Inst.* **28**, 241 (1956).
4. K. Girkmann, *Flachentragwerke, Einfuhrung in de Elastostatik der Scheiben, Platten und Faltwerke* p. 37. Springer, Wien (1954).

* Values are scaled from figures in Ref. 3.

PAPERS TO BE PUBLISHED IN FUTURE ISSUES

H. KUDO: Some analytical and experimental studies of axi-symmetric cold forging and extrusion

R. S. BENSON and W. A. WOODS: The energy content of exhaust pulses in the exhaust system of a supercharged two-stroke-engine model

J. H. HORLOCK and R. I. LEWIS: Shear flows in straight-sided nozzles and diffusers

O. C. ZIENKIEWICZ and R. W. GERSTNER: The method of interface stress adjustment and its uses in the solution of some flame elasticity problems

P. MONTAGUE: Load distribution in overhead stranded conductors

E. VOLTERRA: A second approximation of the method of internal constraints and its applications to problems of plates and bars

J. C. MALTBAEK: The influence of a concentrated mass on the free vibrations of a uniform beam

W. JOHNSON and H. KUDO: The cutting of metal strips between partly rough knife-edge tools

P. L. B. OXLEY: A strain hardening solution for "shear angle" in orthogonal metal cutting

W. F. RILEY and A. J. DURELLI: Stress distribution on the boundary of an elliptical hole in a large plate during passage of a stress pulse of long duration

D. J. RYLEY: Phase equilibrium in low-pressure steam turbines

H. LIPPMANN, O. MAHRENHOLTZ and W. JOHNSON: Thin elastic strips at large deflexions

W. MERCHANT and S. A. SAAFAN: On the critical pressures and buckling modes of regular polygonal prismatic tubes of 3, 4 and 5 sides

Int. J. Mech. Sci. Pergamon Press Ltd. 1961. Vol. 2, pp. 213–223. Printed in Great Britain

STRESS DISTRIBUTION ON THE BOUNDARY OF AN ELLIPTICAL HOLE IN A LARGE PLATE DURING PASSAGE OF A STRESS PULSE OF LONG DURATION

(MAJOR AXIS TANGENT TO THE WAVE FRONT)

W. F. RILEY and A. J. DURELLI

Armour Research Foundation of Illinois Institute of Technology, Chicago, Illinois

(*Received* 27 *September* 1960)

Vol. 2
1960-61

Summary—A solution to the problem of the stress distribution on the boundary of an elliptical hole in a large plate during passage of a compressive stress pulse of relatively long duration is presented. The major axis of the ellipse is tangent to the wave front. The solution was experimentally obtained by using a low-modulus model material in a combined photoelasticity and *moiré* analysis. The long-duration stress pulse was applied by loading a small region of an edge of the plate with a falling weight.

The results of the investigation indicate that the falling-weight loading generates a biaxial state of stress at every point in the plate, which varies with time. The maximum dynamic compressive stresses on the hole boundary can be computed with a fair degree of accuracy by using: (1) the equations of Inglis for the static-stress distribution on the boundary of an elliptical hole in any two-dimensional uniform and axial system of combined stress, and (2) the biaxial stresses, at the same instant of time, at a point, symmetric with respect to the center of the hole (free field stresses). The maximum dynamic tensile stresses on the hole boundary were always smaller than the values computed using the same procedure.

I. INTRODUCTION

THE experimental results presented in this paper were obtained in a program similar to the one conducted by the authors in determining the stress distribution on the boundary of a circular hole in a large plate during passage of a stress pulse of long duration.[1] In both programs, dynamic photoelasticity methods were used in conjunction with low-modulus model materials. In the current program, however, *moiré* methods were used to determine strains in place of the grid techniques previously used.

II. THEORETICAL CONSIDERATIONS

When a time-dependent load is applied at a point on one edge of a semi-infinite plate, two basic waves are produced, namely, dilatational waves and distortional waves. These waves propagate radially from the point of load application with velocities C_1 and C_2 respectively. Theoretically, the dilatational wave is produced by radial displacements which occur at the point of load application. The maximum shearing stresses associated with this wave, at every point in the field, make an angle of 45° to the wave front. This maximum shear is independent of θ (angular position of the point, measured with respect to a line perpendicular to the edge of the plate at the point of load application) and, as a consequence, it can be expected that the photoelastic fringes associated

with the dilatational wave will be circular lines with the point of load application at the center.

Theoretically, the distortional wave is produced by transverse or circumferential displacements; therefore, the maximum shearing stresses at every point in the field are in the plane of the wave front. It can be expected that the photoelastic pattern associated with a distortional wave will be quite complex since the magnitude of the maximum shear at a point is a function of the angular position θ of the point.

III. EXPERIMENTAL METHOD

The photoelastic method employed in this program utilized a low-modulus model material in conjunction with: (1) a 16-mm Fastax camera for recording the overall fringe patterns, and (2) a microflash unit for obtaining fringe patterns in the immediate vicinity of the hole. These photoelastic techniques have been described in previous papers by the authors[2–4] and will not be repeated here. The interested reader can refer to those papers.

The use of the *moiré* method for determining strains in two-dimensional problems has found increasing application in recent years. The *moiré* effect is an optical phenomenon observed when two arrays of lines are superimposed. If the arrays consist of opaque parallel lines which are not identical in spacing or orientation then *moiré* fringes will form as the lines of one array alternately fall on or between the lines of the other array (see Fig. 1). Measurements of the spacing and direction of the fringes give sufficient information for determining differences between the arrays. In a recent paper by one of the authors the techniques and equations needed to determine strains from *moiré* fringes are developed.[5] Additional techniques developed for use in dynamic applications will be described in a future paper.

IV. TEST PROCEDURE

A large plate with dimensions $0{\cdot}37 \times 12 \times 12$ in. was machined from a sheet of urethane rubber (Hysol 8705). An elliptical hole, with major and minor axes $1\frac{1}{4}$ in. and $\frac{5}{8}$ in. respectively, was machined in the plate. The location and orientation of the hole are shown in Fig. 2. The location of the hole was chosen to allow maximum time for study before reflections return from the boundary. Also the 30° orientation provides a symmetric point in the same model where free-field stresses can be simultaneously determined. The symmetric point is far enough removed from the hole so that any disturbances produced by the presence of the hole do not interfere appreciably with the free-field stress distribution. The 30° orientation also places the hole in a location where the influences of both the dilatational and distortional waves are felt. If the hole were located on the centerline of the plate, the distortional wave influence would be smaller.

The loading of the model was accomplished by dropping a weight (108 g) from a height of 16 in. on a hard plastic striker which was permanently positioned on the model (see Fig. 2). A complete record of the photoelastic fringes produced by the impact was obtained by using a 16-mm Fastax camera

Vol. 2
1960-61

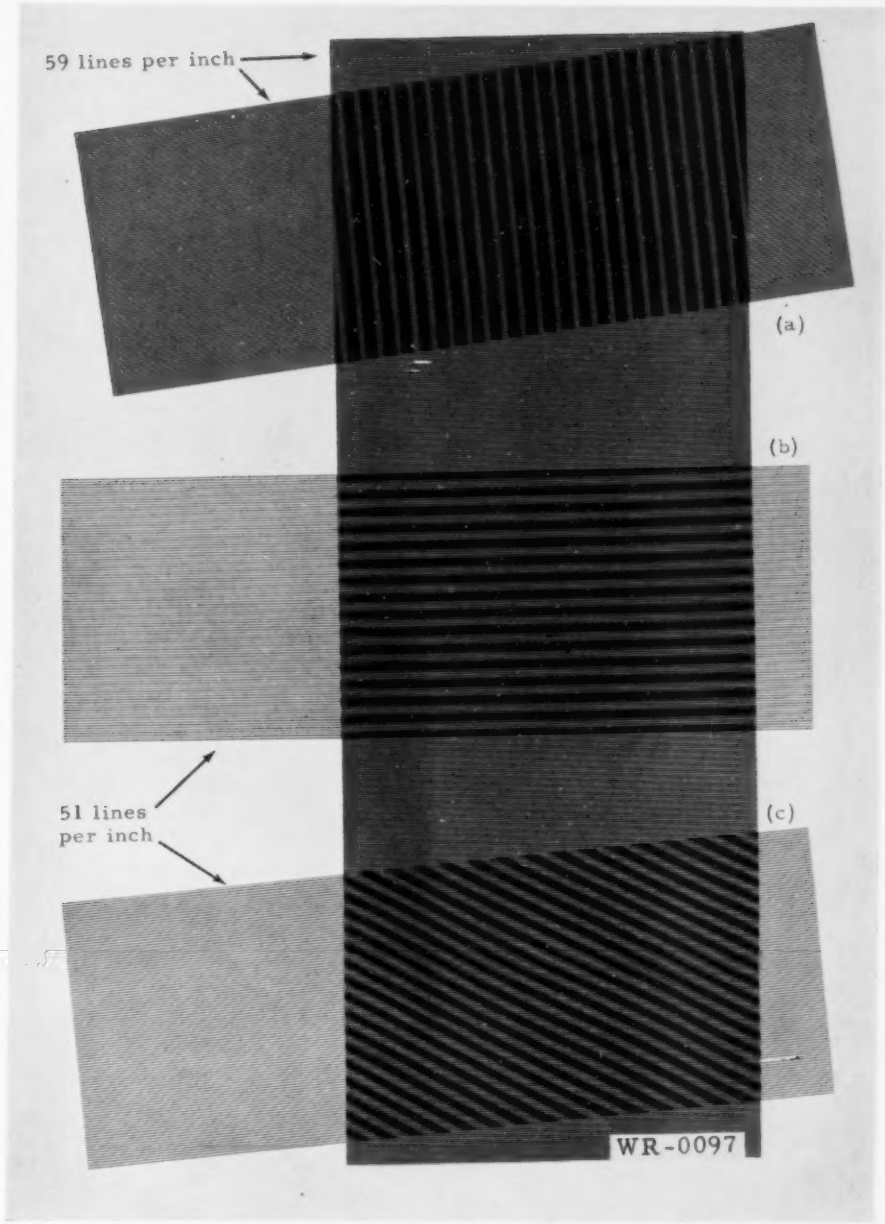

FIG. 1. Mechanism of formation of *moiré* fringes. (a) Fringes due to rotation alone. (b) Fringes due to difference in pitch alone. (c) Fringes due to combination of rotation and difference in pitch.

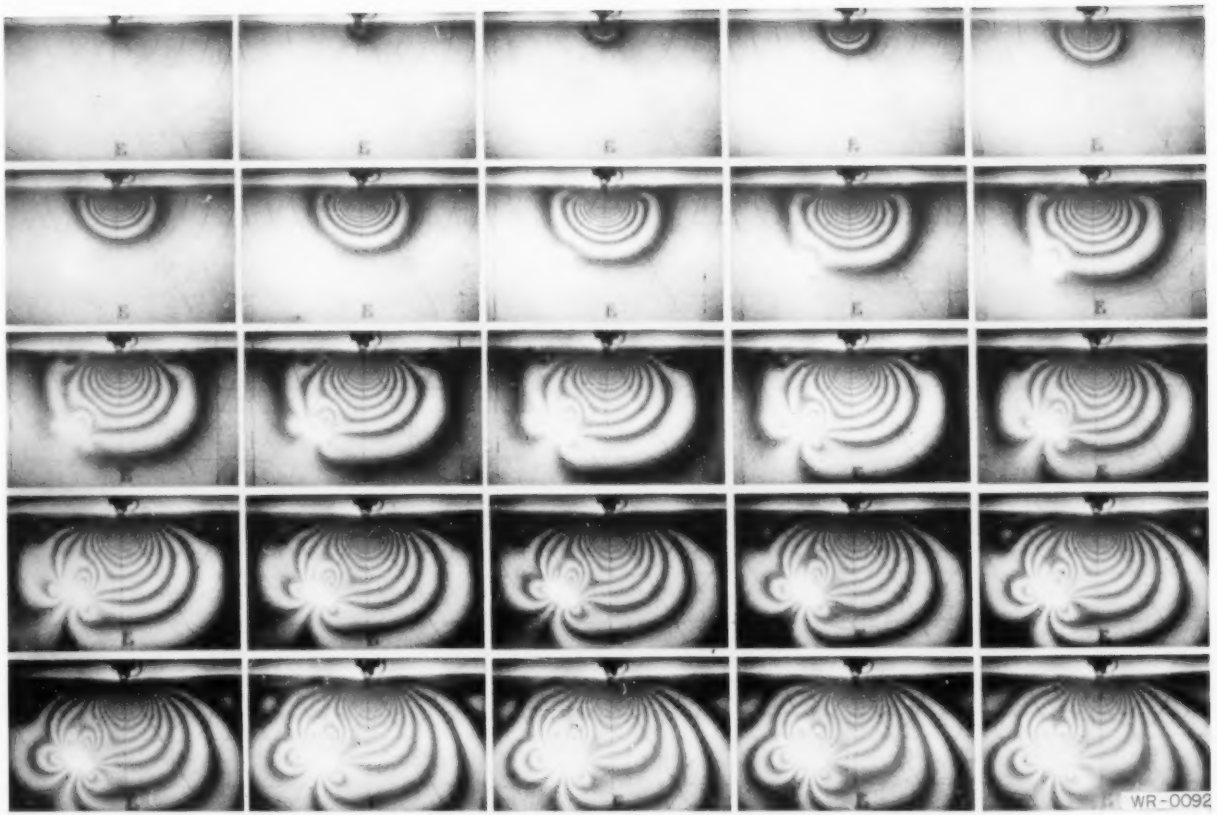

FIG. 3. Series of 25 photographs showing a compressive wave of long duration propagating past an elliptical hole in a large plate of Hysol 8705.

Vol.
1960

Vol. 2
1960-61

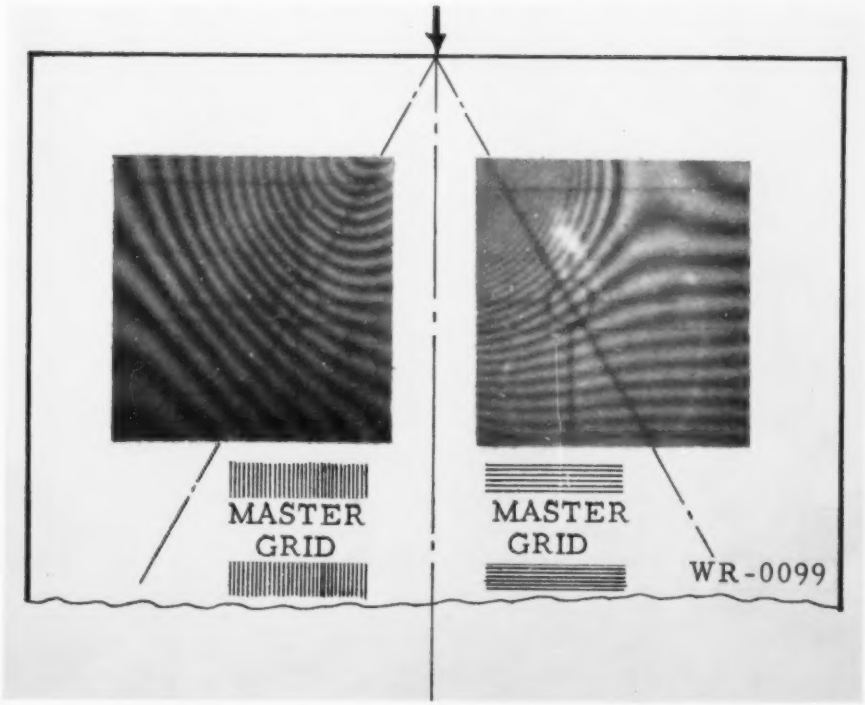

FIG. 4. Typical dynamic *moiré* patterns.

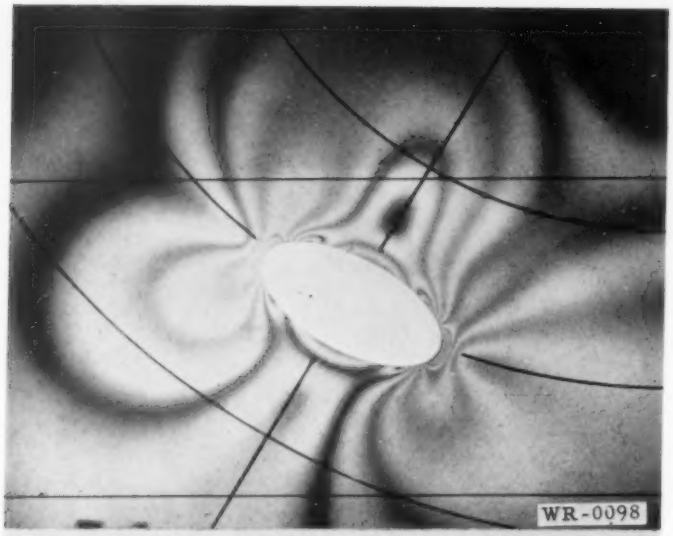

3152 Microseconds After Impact

(a)

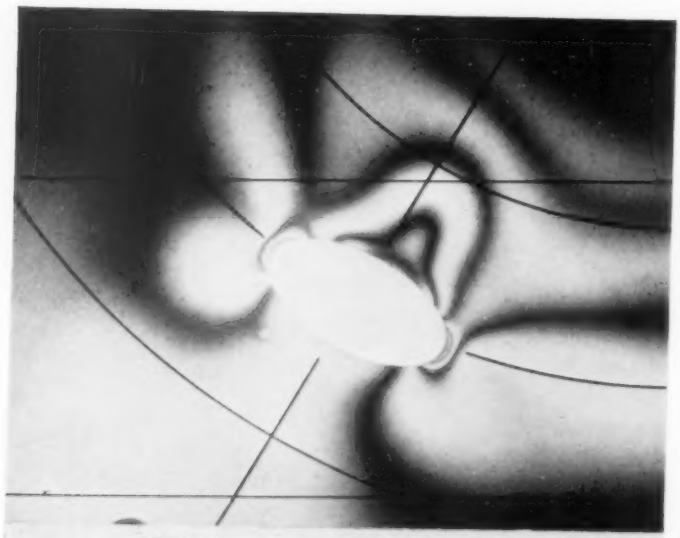

1576 Microseconds After Impact

(b)

FIG. 5. Microflash photographs showing the fringe-order distribution around the boundary of the hole 1576 and 3152 μsec after impact.

operating at 6900 frames/sec. The first 20 frames of this record together with 5 additional frames are shown in Fig. 3. The time period covered by these frames is approximately 4000 μsec. The total time duration of the pulse applied by the falling weight was approximately 12,000 μsec.

Similar Fastax records were also obtained of the *moiré* fringes in the region of the free-field symmetric point. The printed grid used in obtaining the *moiré* fringes had 1000 lines/in. Typical records are shown in Fig. 4.

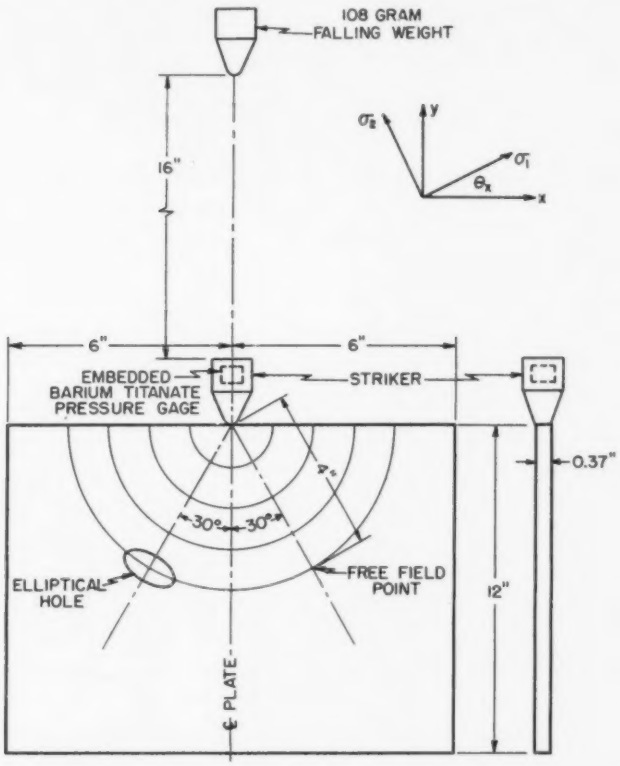

FIG. 2. Sketch of the model illustrating the loading, the location of the hole, and the symmetric free-field point.

The photoelastic fringe patterns obtained with the Fastax camera were suitable for studying the overall wave-propagation phenomena, but were not suitable for precise fringe-order determinations at the hole boundary. In order to obtain photographs suitable for these determinations a series of twenty microflash photographs were obtained at approximately 200-μsec intervals after impact. The microflash photographs were sequenced by using a specially built timer unit which was triggered with a barium titanate pressure gage embedded in the striker. Two representative photographs of the fringe distribution around the hole are shown in Fig. 5. It can readily be seen from these photographs that the fringe order at the boundary of the hole can be accurately determined.

Vol. 2
1960-61

V. ANALYSIS OF DATA

The microflash photographs used for analysis covered the interval of time from 1200 μsec after impact until 4600 μsec after impact. The beginning of the time interval was chosen when the 0·5 order fringe reached the symmetric point in the field (the wavefront reached this point about 800 μsec after

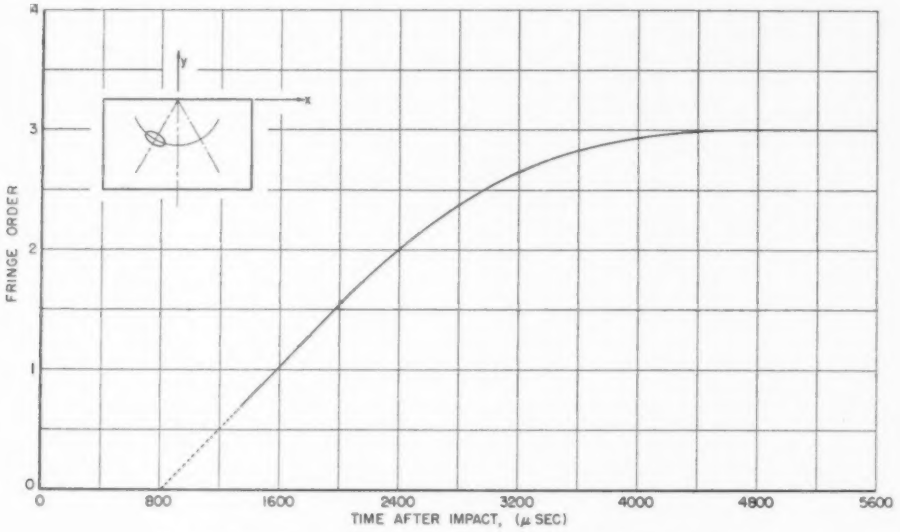

FIG. 6. Fringe order at the symmetric free-field point as a function of time after impact.

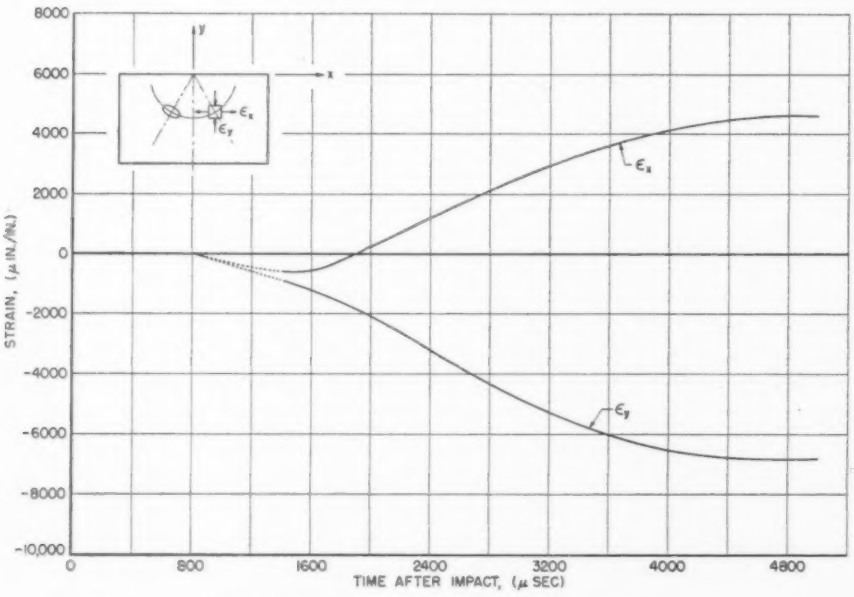

FIG. 7. Horizontal strain ϵ_x and vertical strain ϵ_y at the symmetric free-field point as a function of time after impact.

impact). This was the first instant at which the response around the hole boundary was sufficient to make fringe-order determinations. The end of the interval was chosen to insure that reflections were not influencing the distribution around the hole.

The Fastax and microflash records were then used to obtain the fringe-order distribution around the hole, the fringe order at the symmetric point in the free field and the two strains ϵ_x and ϵ_y at the symmetric point in the free field. The experimentally determined values for the fringe order as a function of time at the symmetric free-field point are shown in Fig. 6. (Similar curves for the two strains ϵ_x and ϵ_y are shown in Fig. 7.) It was possible to make very accurate fringe-order determinations. It is estimated that the two strain curves, however, may be in error by as much as 10 per cent. The data shown in Figs. 6 and 7 were then used to obtain the two principal stresses and their directions. This was accomplished through the use of equations developed in a previous paper.[1]

Vol. 2
1960-61

VI. DYNAMIC-STRESS DISTRIBUTION

The dynamic stresses around the hole were computed directly from the photoelastic data, since the radial component of the boundary stress vanished. An equivalent static stress distribution around the hole was then computed using Inglis'[6, 7] solution for an elliptical hole in an infinite plate under any system of combined stress. Static loads capable of producing a stress field equivalent to the biaxial stress field at the symmetric point were used in these calculations. The results of the static and dynamic stress determinations for a number of times after impact are shown in Figs. 8–16.*

At the center of each of these figures the magnitudes and directions of the corresponding free-field stresses are plotted. It is interesting to note that the compressive stresses at positions 90° and 270° from the radial line through the point of load application seem to build up much more rapidly than the tensile stresses which appear at positions 0° and 180°. In Fig. 8 the dynamic compressive stresses have developed to a considerable level while the tensile stresses are still zero. In Fig. 9 the tensile stresses at 0° begin to develop ahead of those at 180°. From this time on, the non-symmetric distribution slowly begins to approach the static distribution.

While the individual values of stress at all points on the boundary are of considerable significance, the maximum compressive and tensile stresses which develop are of greatest importance to the designer. In Fig. 17 the maximum tensile and compressive stresses on the boundary of the hole are compared to the maximum compressive stress (σ_2) which occurs at the symmetric point in the free field at the same instant of time. The static values of stress in this figure have been computed for the biaxial condition of stress which exists at the free-field symmetric point at the same instant of time. It can readily be seen from this figure that the dynamic compressive stresses on the hole boundary are only slightly larger than they would be in an equivalent static field. The

* In Figs. 8–16, the static distribution was computed using the Inglis equation and the biaxial state of stress at the symmetric point at the same instant of time.

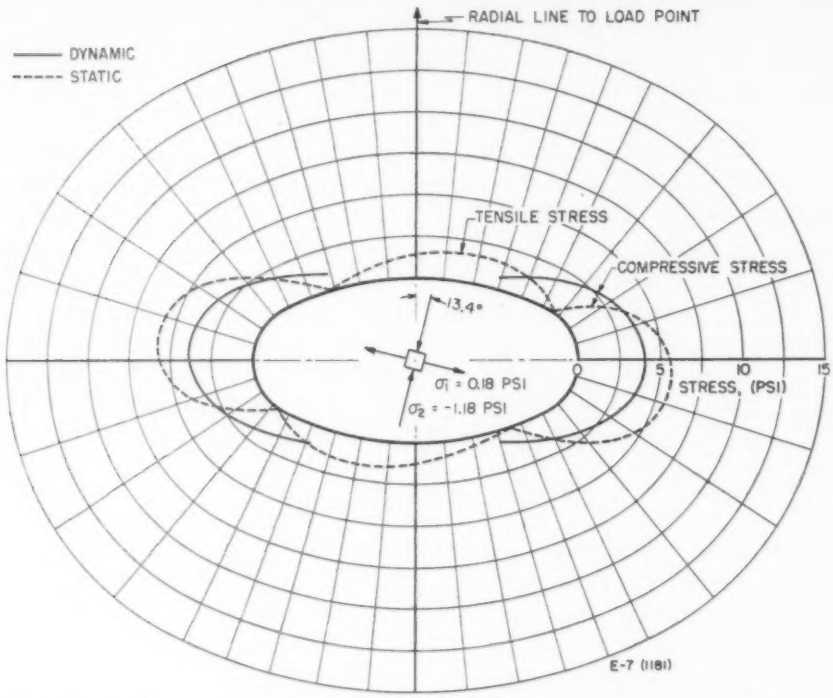

FIG. 8. Static and dynamic stress distributions on the hole boundary 1181 μsec after impact.

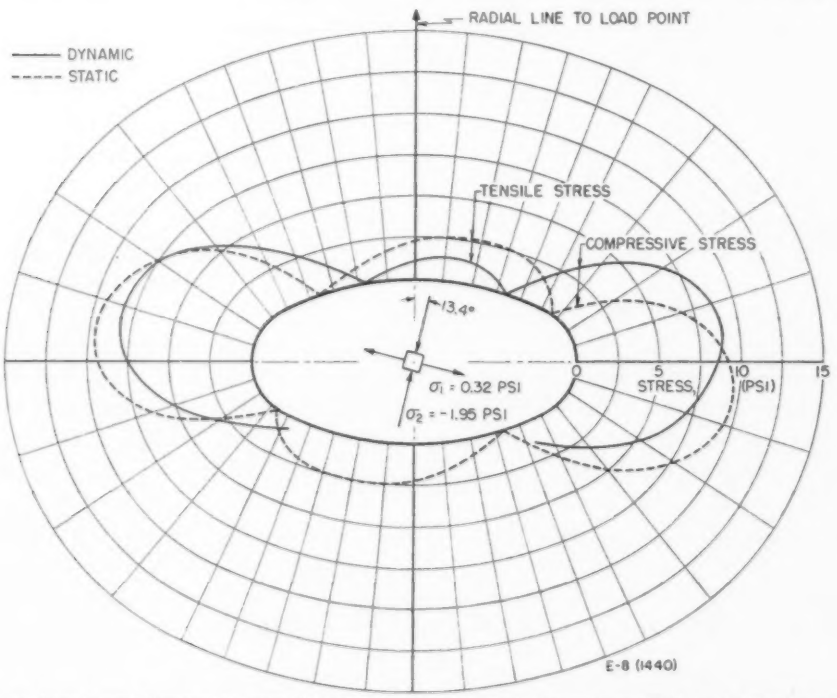

FIG. 9. Static and dynamic stress distributions on the hole boundary 1440 μsec after impact.

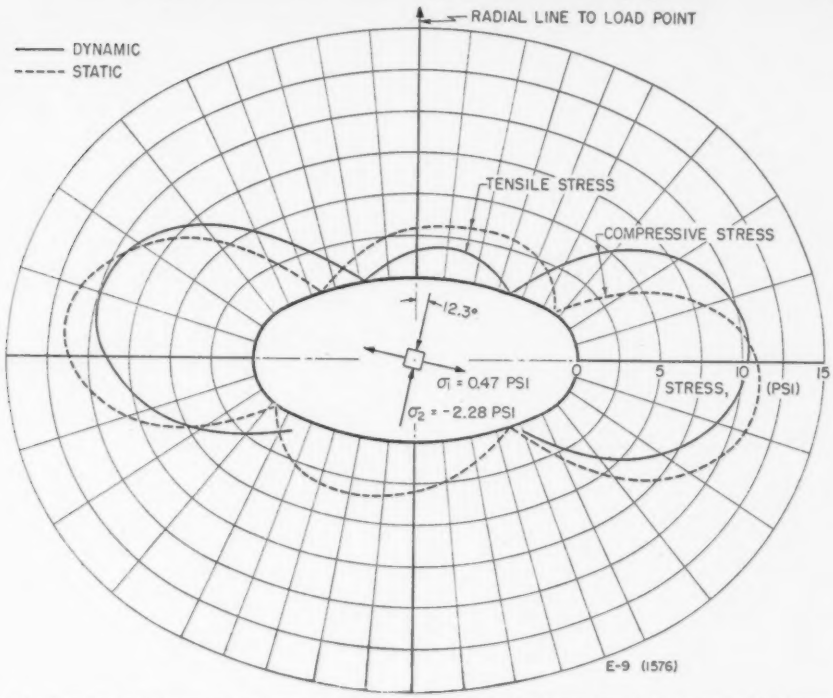

FIG. 10. Static and dynamic stress distributions on the hole boundary 1576 μsec after impact.

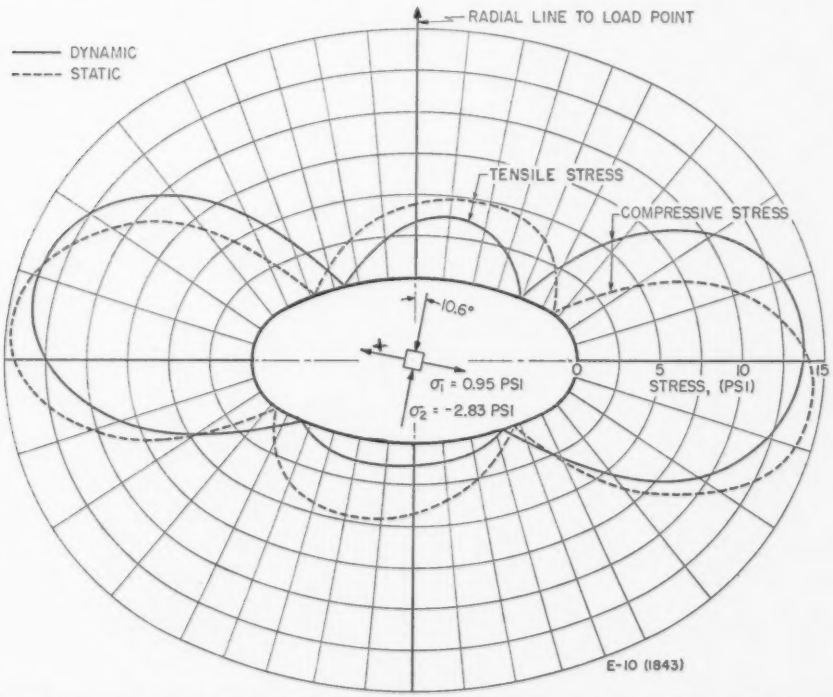

FIG. 11. Static and dynamic stress distribution on the hole boundary 1843 μsec after impact.

Vol. 2
1960-61

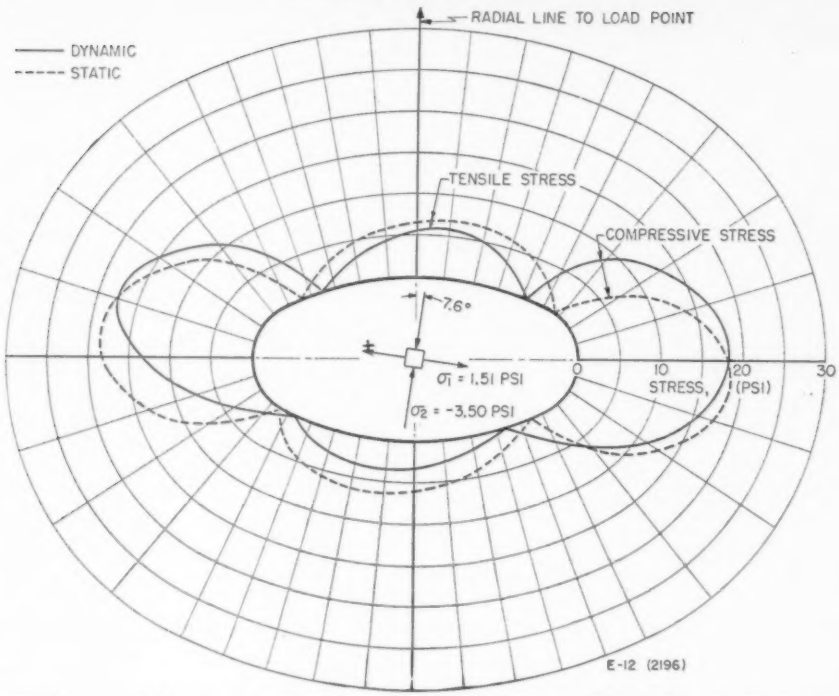

FIG. 12. Static and dynamic stress distribution on the hole boundary 2196 μsec after impact.

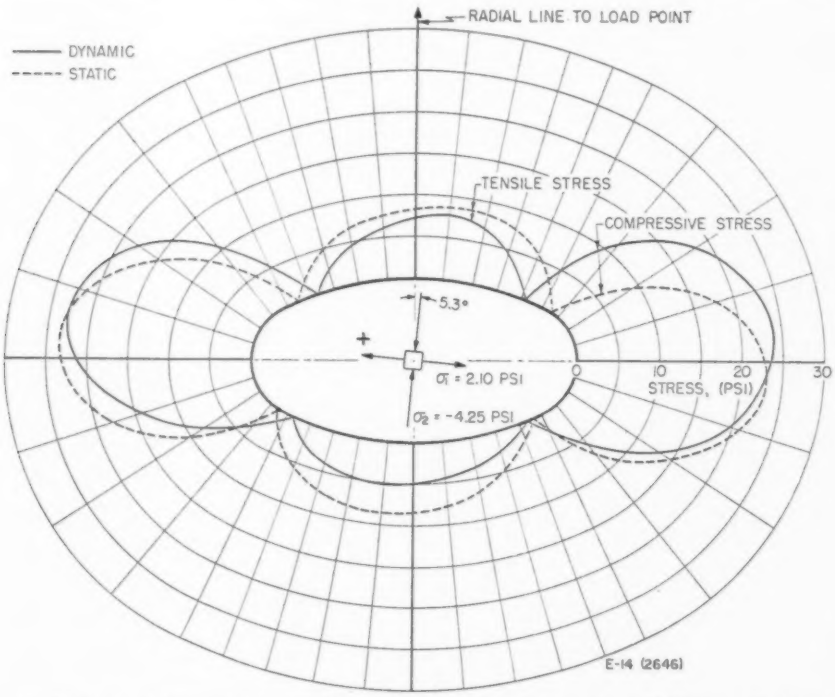

FIG. 13. Static and dynamic stress distribution on the hole boundary 2646 μsec after impact.

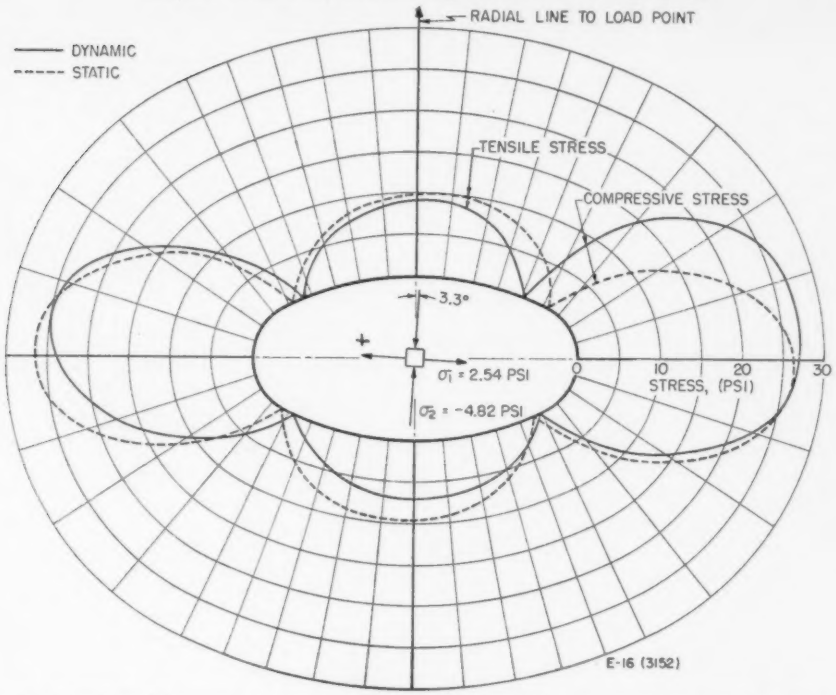

FIG. 14. Static and dynamic stress distribution on the hole boundary 3152 μsec after impact.

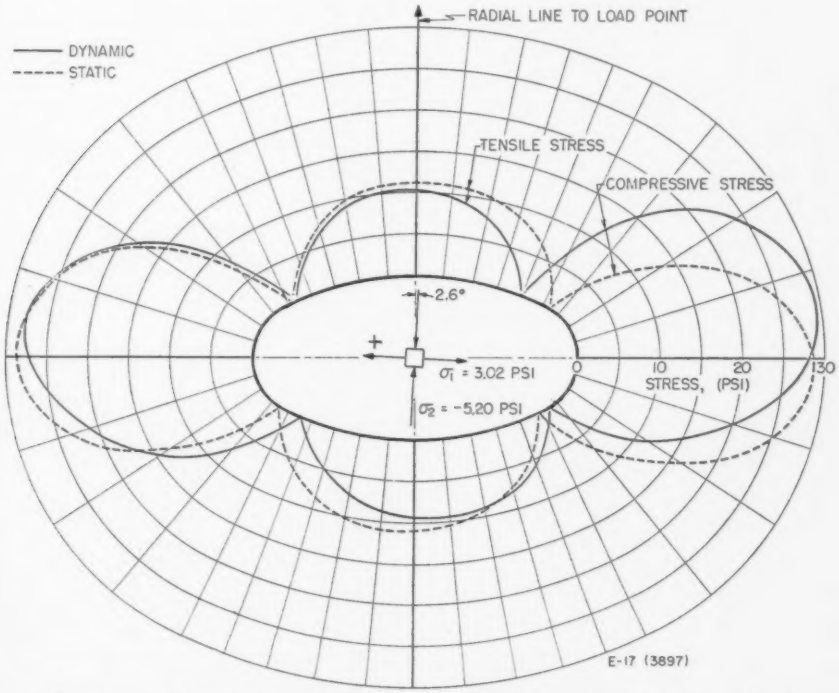

FIG. 15. Static and dynamic stress distribution on the hole boundary 3897 μsec after impact.

Vol. 2
1960-61

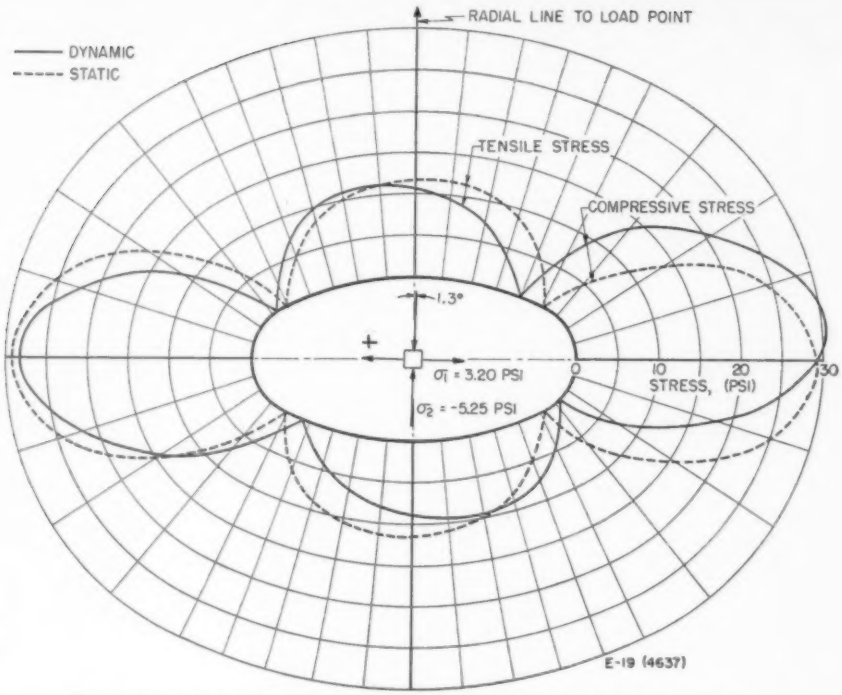

FIG. 16. Static and dynamic stress distributions on the hole boundary 4637 μsec after impact.

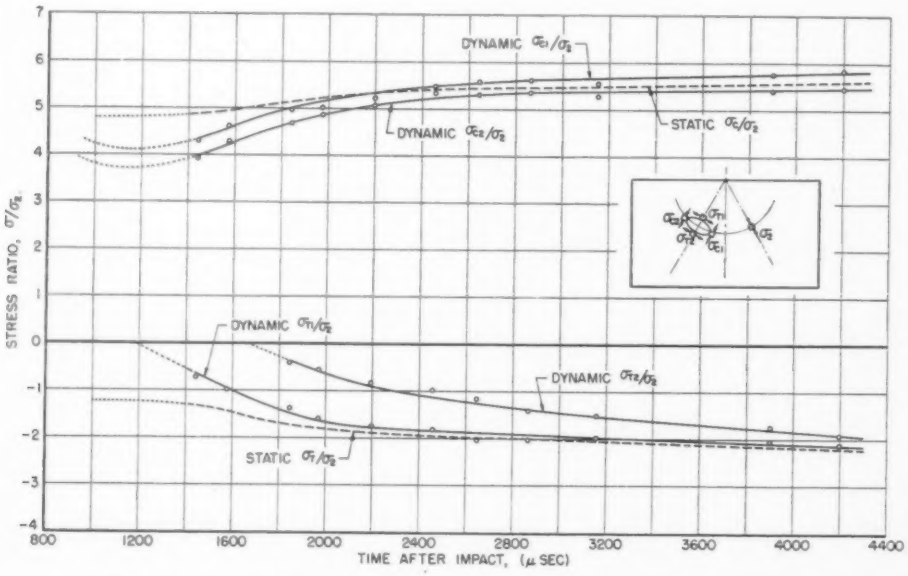

FIG. 17. Ratios of the maximum tensile and compressive stresses on the hole boundary to the free-field compressive stress at the same instant of time after impact.

differences are probably not significant. The tensile stresses developed on the hole boundary are always smaller under dynamic loading than predicted.

VII. CONCLUSIONS

The results of this investigation indicate that the maximum compressive stresses on the hole boundary can be computed with a fair degree of accuracy by employing the Inglis solution for an elliptical hole in an infinite plate and considering the free-field biaxial stress conditions. It was also established that the maximum tensile stresses are always smaller than predicted. In drawing conclusions based on this work it should be remembered that the stress pulse employed had a length approximately seventy-five times the length of the minor axis of the hole. The front of the pulse was not very steep and, therefore, the gradient of stress along a portion of the pulse equal to the minor axis of the hole was small. The results of this current study agree in general with the results obtained previously for the case of a circular hole. More recently some work has been conducted on a similar problem using a circular hole and a short-duration pulse generated by detonating a small explosive charge of lead azide. The results of this study will be reported later.

Vol. 2
1960-61

Acknowledgements—The research reported in this paper was part of a project conducted at Armour Research Foundation under the sponsorship of Air Force Special Weapons Center, Air Research and Development Command. The authors wish to express their appreciation to Mr. E. H. Wang, Chief, Structures Division, and Capt. J. T. Pantall for their encouragement and support.

REFERENCES

1. A. J. Durelli and W. F. Riley, Stress Distribution on the Boundary of a Circular Hole in a Large Plate during Passage of a Stress Pulse of Long Duration. *J. Appl. Mech.* To be published.
2. A. J. Durelli and W. F. Riley, *J. Appl. Mech.* **24**, 69 (1957); *Trans. Amer. Soc. Mech. Engrs.* **79**, 69 (1957).
3. J. W. Dally, W. F. Riley and A. J. Durelli, *J. Appl. Mech.* **26**, 613 (1959).
4. J. W. Dally, A. J. Durelli and W. F. Riley, *Proc. Soc. Exp. Stress. Anal.* **17**, 33 (1960).
5. S. Morse, A. J. Durelli and C. A. Sciammarella, *Proc. Amer. Soc. Civ. Engrs.* **86**, 105 (1960).
6. C. E. Inglis, *Trans. Instn. Nav. Archit., Lond.* **55**, 219 (1913).
7. C. E. Inglis, *Engineering, Lond.* **95**, 315 (1913).

Int. J. Mech. Sci. Pergamon Press Ltd. 1961. Vol. 2, pp. 224–230. Printed in Great Britain

THE CUTTING OF METAL STRIPS BETWEEN PARTLY ROUGH KNIFE-EDGE TOOLS

W. JOHNSON* and H. KUDO†

(*Received* 28 *September* 1960)

Summary—The results of calculations concerning the effect of friction between tools and material are presented for a pair of collinear knife-edge dies cutting a wide strip of metal of finite thickness. The friction so acts as to increase the depth of penetration required before the metal between the dies becomes wholly plastic.

1. INTRODUCTION

WHEN a circular wire is cut with a pair of pliers it is not possible to analyse at all rigorously the mechanics of the operation. With the help of a plane-strain analysis for the cutting of wide sheet of finite thickness with knife-edge dies it is possible, however, to give a meaning to the experimental results obtained when cutting circular wires or rods. This procedure has been reported on elsewhere.[1]

Hill[2] has shown how the plane-strain cutting of a strip of finite thickness resting on a perfectly smooth foundation, by a single perfectly smooth knife-edge tool, may be explained. The initial entry of the tool throws up a coronet at the sides of the tool, see Fig. 1(a), elastic stresses only extending between the knife edge and the foundation. After penetration to a critical depth, a new mode of deformation takes over and a fully plastic zone extends through the strip thickness to the foundation; compare Fig. 1(b). The penetration of the tool causes a horizontal displacement of material, no further material being raised at the upper-face surface. Hill has given results appertaining to these processes, in particular values of the critical ratio H/a for various semi-angles of the wedge α at which the first mode of deformation is superseded by the second. Fig. 1(a) and (b) actually represents only one quarter of the whole diagram when cutting with knife-edge pliers is envisaged; what was the smooth foundation in Hill's case is the horizontal centre-line of the strip in our case. It follows that for a plier analysis we can take over most of Hill's results. Our purpose is to examine the effect on the critical H/a ratio of the coefficient of friction μ between the tools and the metal. Whatever conclusions may be arrived at from these calculations should be useful as a guide to what may be expected in connexion with cutting a circular wire.

2. CALCULATIONS AND RESULTS

The slip-line field used to account for cutting and so parting the strip into horizontal outwardly, but oppositely, moving rigid blocks is $OABQO$ in

* Department of Mechanical Engineering, College of Science and Technology, University of Manchester.

† The Government Mechanical Laboratory, Suginami, Tokyo.

Fig. 1(b) (the symbols used in the equations below will be obvious from this figure). This is identical with Hill's original field, and to take into account friction between metal and tool requires us to make angle OAD less than 45°.

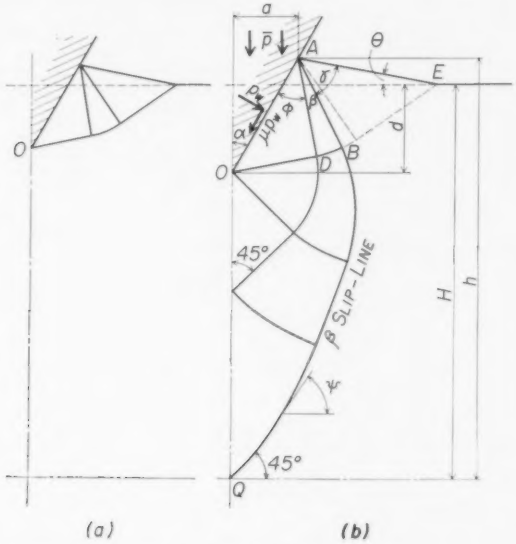

FIG. 1. (a) Cutting a semi-infinite block: first mode of deformation.
(b) Cutting a strip of finite thickness: second mode of deformation.

The total horizontal force on boundary ABQ is zero, and, using the Hencky equations, it is easy to show that the hydrostatic pressure at point D, p_D is given by:

$$\frac{p_D}{2k} = \frac{\frac{1}{2}a - I}{h} + \frac{\pi}{2} - \alpha + \phi + 2\beta \tag{1}$$

where

$$I = \int_0^h \psi \, dy$$

The mean vertical cutting pressure on the area of contact with the metal is $\bar{p}$ and

$$\frac{\bar{p}}{2k} = \frac{p_D}{2k} + \tfrac{1}{2}(\sin 2\phi + \cot\alpha \cos 2\phi) \tag{2}$$

Also,

$$\mu = \tfrac{1}{2}\cos 2\phi / (\tfrac{1}{2}\sin 2\phi + p_D/2k) \tag{3}$$

Slip-line fields for semi-angles of wedge 15°, 30°, 45°, 60° and 75° were drawn using 9° or 10° equiangular nets for making calculations.

For semi-angle $\alpha = 15°$, a full set of results is shown in Fig. 2. Fig. 2(a) shows $\bar{p}/2k$ versus h/a for various values of ϕ; Fig. 2(b) shows μ versus h/a for different values of ϕ; Fig. 2(c) shows $\bar{p}/2k$ versus μ for values of h/a, and Fig. 2(d), $\bar{p}/2k$ versus h/a for various values of μ.

Grunzweig *et al.*[3] have given the results of calculations of the pressure to indent a semi-infinite block when the indenter or tool is rough and, by a process of interpolation, their results have been made to give values of $p/2k$ versus μ

Vol. 2
1960-61

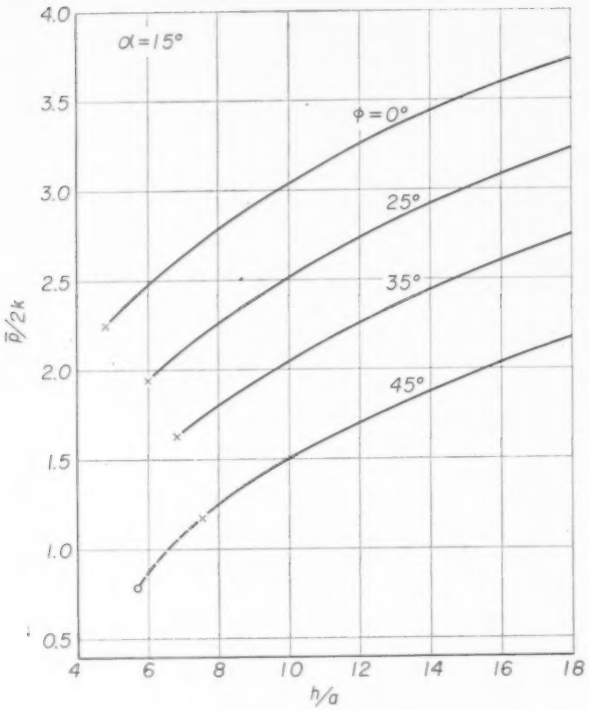
α=15°
φ=0°
25°
35°
45°
p̄/2k
h/a
4.0
3.5
3.0
2.5
2.0
1.5
1.0
0.5
4
6
8
10
12
14
16
18

FIG. 2(a).

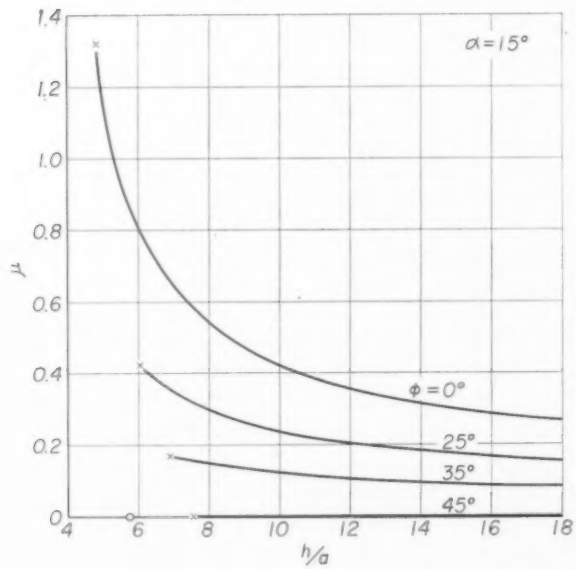
α=15°
φ=0°
25°
35°
45°
μ
h/a
1.4
1.2
1.0
0.8
0.6
0.4
0.2
0
4
6
8
10
12
14
16
18

FIG. 2(b).

Vol. 2
1960-61

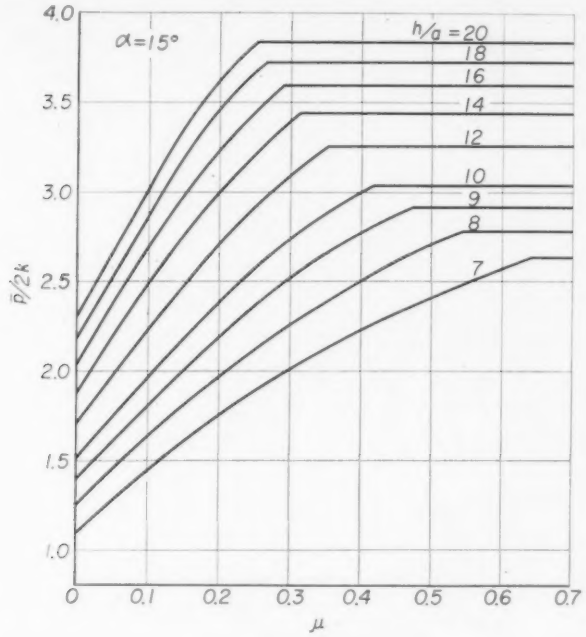

FIG. 2(c).

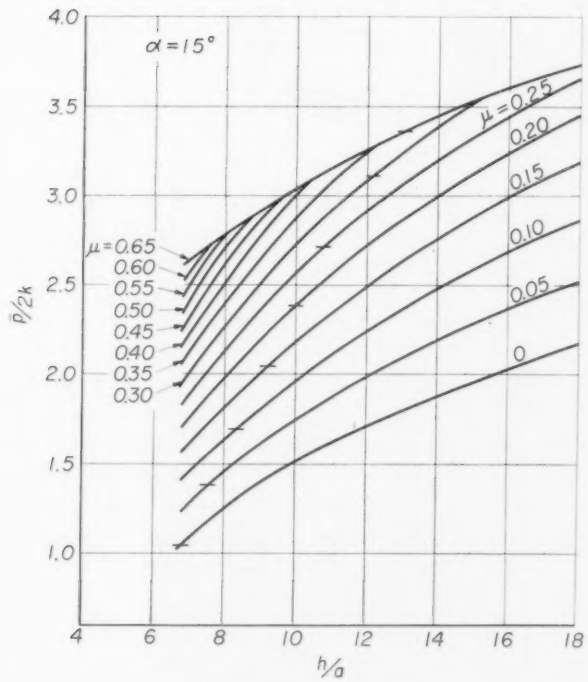

FIG. 2(d).

for various values of α for our use. Putting this information on to Fig. 2(d), for instance (note the horizontal lines of intersection with the curves for various values of μ), we are able to find the sequence of critical h/a values, i.e. the value of h/a for transition from one mode of deformation, Fig. 1(a), to the other, Fig. 1(b).

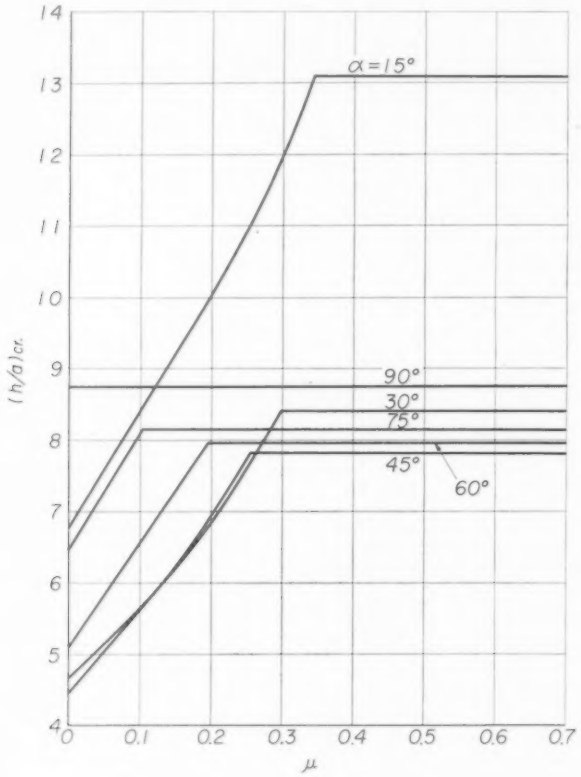

FIG. 3.

In Fig. 3 we show for the different wedge-angles how this critical ratio varies with μ for various values of α. It is found, however, that for $\alpha = 15°$ and $\mu = 0$ (i.e. $\phi = 45°$) transition does not occur even when h/a decreases to its minimum, i.e. when $\beta = 0$; the piling-up mode of deformation is retained throughout the penetration, despite the availability of the second mode. We may introduce a third mode of deformation as shown in Fig. 4(a) for a smooth tool, and for this particular case the result for $\bar{p}/2k$ versus h/a is entered on Fig. 2(a) and denoted by a circle. [A valid hodograph for this mode is shown dotted in Fig. 4(a).] For the purposes of our calculations, we have assumed a continuous curve, shown by the chain line in Fig. 2(a), to join-up the results for the two operative modes. For configurations in which h/a is smaller than that given by Fig. 4(a), we should have to develop the slip-line field as shown in Fig. 4(b).

In Fig. 5, the critical ratio (d/H) against μ is plotted for various values of α; d/H is the fraction of the original strip thickness penetrated by the apex of the wedge O, before the plastic zone penetrates the remaining thickness of the strip.

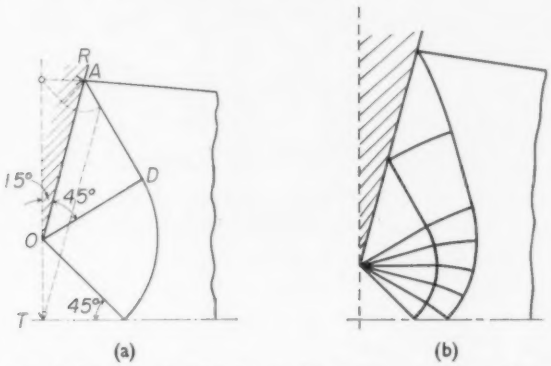

FIG. 4. (a) A third mode of deformation for a smooth small-angle wedge for a particular configuration. (b) General type of field for third mode of deformation.

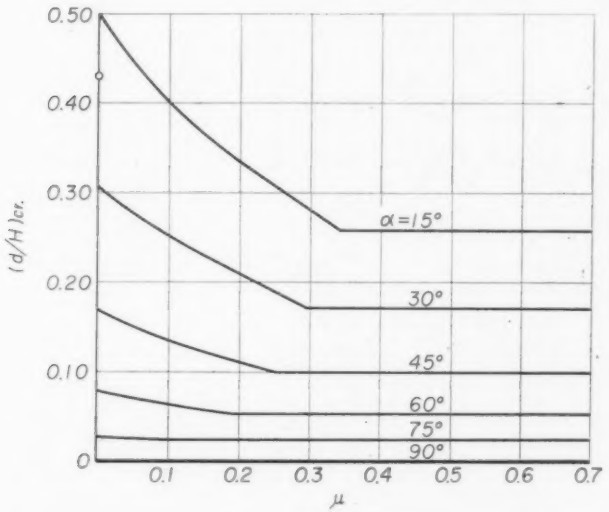

FIG. 5.

The depth of penetration d and the length of contact between the wedge tool and the material l are related by[3]

$$\left(\frac{d}{H}\right)_{cr} = \frac{d/l}{d/l - \cos\alpha + (h/a)_{cr}\sin\alpha} \tag{4}$$

For $\mu = 0$, the critical values of d/H for $\alpha = 90°$, $60°$ and $30°$ are in agreement with those given by Hill[2]. The circle on the prime ordinate in Fig. 5 is taken for $\alpha = 15°$ from Hill's paper; it is different from that obtained by us because

Vol. 2
1960-61

Hill's value is calculated for the case in which the strip lies on a smooth flat foundation being indented by one die only. When $\alpha < 30°$, this situation is modified by the ability of material on the foundation immediately below the die to rise vertically away from it.

The mean pressure $\bar{p}$ for the two modes of deformation in Fig. 1 are identical when

$$\frac{p_B}{2k} = \tfrac{1}{2} + \gamma - \tfrac{1}{4}\pi \tag{5}$$

$p_B/2k$ is the hydrostatic pressure at B [Fig. 1(b)] and γ is the angle between AB and free surface AE. The above equation is equivalent to Hill's condition[4] for the assumed rigid region BAE, in the slip-line solution for cutting, to remain rigid. The hydrostatic pressure at point Q, Fig. 1(b), is

$$\frac{p_Q}{2k} = \frac{p_D}{2k} - (2\beta + \phi + \tfrac{1}{4}\pi - \alpha) \tag{6}$$

$$= (\tfrac{1}{2}a - I)/h + \tfrac{1}{4}\pi \tag{7}$$

The vertical and horizontal normal stresses at Q are

$$\frac{\sigma_v}{2k} = -\frac{p_Q}{2k} - \tfrac{1}{2} \tag{8}$$

and

$$\frac{\sigma_h}{2k} = -\frac{p_Q}{2k} + \tfrac{1}{2} \tag{9}$$

It was found that in all cases investigated, in the slip-line field of Fig. 1(b), σ_v becomes positive when h/a is in excess of about 4·75. This indicates that the horizontal line of symmetry in Fig. 1 cannot be replaced by a flat smooth foundation if $h/a > 4{\cdot}75$. In other words, the critical value of h/a in Fig. 3 is affected if the strip is placed on a flat smooth base and cut by a knife-edge, except when the critical value of $(h/a) \leqslant 4{\cdot}75$.

If the width of the strip in the direction perpendicular to the plane of flow is not sufficiently large compared with a, a local contraction around the point Q would be expected if $h/a > 4{\cdot}75$, even when the strip is cut by only one pair of knife-edges. On the other hand, if the strip is very thick, a triaxial tensile stress is produced near the point Q inside the strip, and this facilitates brittle fracture.

REFERENCES

1. W. JOHNSON, *Appl. Sci. Res., Hague* **A7**, 65 (1958).
2. R. HILL, *J. Mech. Phys. Solids* **1**, 265 (1953).
3. J. GRUNZWEIG, I. M. LONGMAN and N. J. PETCH, *J. Mech. Phys. Solids* **2**, 81 (1954).
4. R. HILL, *J. Mech. Phys. Solids* **2**, 278 (1954).

Int. J. Mech. Sci. Pergamon Press Ltd. 1961. Vol. 2, pp. 231–250. Printed in Great Britain

THE ENERGY CONTENT OF EXHAUST PULSES IN THE EXHAUST SYSTEM OF A SUPERCHARGED TWO-STROKE-ENGINE MODEL

R. S. Benson and W. A. Woods
Mechanical Engineering Department, University of Liverpool

(*Received* 9 *March* 1960)

Vol. 2
1960-61

Summary—The paper describes a theoretical and experimental investigation of the factors which influence the magnitude of the energy content of the exhaust pulses in the exhaust system of a turbo-charged two-stroke-cycle engine. The theoretical analysis is first concerned with the development of an expression for assessing the energy content of the exhaust gas, and the concept of continuous mean power is described. The influence of wave action on the continuous mean power is then examined using the method of characteristics.

The theoretical analysis showed that there is an optimum value for the turbine nozzle area and the exhaust-pipe size to obtain the maximum available power in the exhaust gases. The analysis showed that the power available in the exhaust pulses increased with an increase in engine speed, release pressure and supercharge period, and a decrease in pipe cross-sectional area and nozzle area. In the case of the last two variables, there was an optimum size below which there was a decrease in available power.

The experimental programme covered a wide range of speeds, release pressures and exhaust-pipe-nozzle sizes. The results agreed with the qualitative trends predicted in the theoretical analysis.

INTRODUCTION

The utilization of the energy available in the exhaust gases of internal combustion engines is of practical interest in turbo-supercharged engines. This is of particular importance in the case of two-stroke-cycle engines where the gas exchange process occurs over only one-third or so of a revolution. In a previous paper[1] the results were given of a theoretical and experimental investigation of wave action in a high-pressure-charged two-stroke-cycle engine model, the turbo-charger being represented by a nozzle located at the outlet end of the exhaust pipe. In this paper the energy content of the exhaust pulses generated in the same apparatus is examined. As before, the unsteady-flow problem is analysed theoretically using unit processes in the method of characteristics. The energy content of the exhaust pulse is defined as the work that could be performed by the gas in an ideal isentropic gas turbine. By assuming that the ideal gas turbine operates under quasi-steady flow conditions it is possible to calculate the power of such a turbine. This power expressed in non-dimensional form is used as the parameter for comparing the energy content of the exhaust pulses in various exhaust systems (nozzle-pipe configurations).

APPARATUS

The engine cycle was simulated by a special pulse generator operating at cycle speeds from 750 to 1500 rev/min. A full description of the apparatus was

given in the previous paper.[1] The supercharged exhaust-pipe systems tested are given in Table 1. The release pressure range was limited by the compressor and apparatus characteristics to 30–50 lb/in² gauge. For the majority of the tests the supercharge pressure was held constant at 15 lb/in² gauge. Typical indicator diagrams were shown in the previous paper.

Table 1. Test group numbering*

Nozzle details	Speed (rev/min)	Pipe length 40 in.			Pipe length 120 in.		
		$d=1$ in.	$d=1\frac{1}{2}$ in.	$d=2$ in.	$d=1$ in.	$d=1\frac{1}{2}$ in.	$d=2$ in.
Nozzle ratio $\phi =$	750	1	13	25	37	49	61
0·563 for $d=1$ in.	1000	2	14	26	38	50	62
0·34 for $d=1\frac{1}{2}$ in.	1250	3	15	27	39	51	63
0·191 for $d=2$ in.	1500	4	16	28	40	52	64
	750	5	17	29	41	53	65
Nozzle ratio $\phi =$	1000	6	18	30	42	54	66
0·25	1250	7	19	31	43	55	67
	1500	8	20	32	44	56	68

* Each number represents a series of three tests at nominal release pressures of 50, 40, 30 lb/in² gauge.

$$\phi = \frac{\text{area of throat of nozzle}}{\text{area of pipe}}$$

d = diameter of exhaust pipe

THEORETICAL ANALYSIS

The theoretical analysis is first concerned with the development of an expression for assessing the energy content of the exhaust gases and the concept of the continuous mean power is derived. The influence of wave action on the continuous mean power is then examined by utilizing the method of characteristics.

NOTATION

a speed of sound (ft/sec)
c_p specific heat at constant pressure (ft-lb$_f$/slug per °F)
h specific enthalpy—ft-lb$_f$/slug
m mass—slug
n c/s
p pressure (lb$_f$/ft²)
s entropy (ft-lb$_f$/slug °R)
t time (sec)
u particle velocity (ft/sec)
F cross-sectional area (ft²)
L length (ft)
R gas constant (ft-lb$_f$/slug °R)
W_T turbine work (ft-lb$_f$)
$(E)_{cv}$ total internal energy of control volume (ft-lb$_f$)

α characteristic constant
θ crank angle degrees
ρ density (slug/ft^3)
γ ratio of specific heats—isentropic exponent
λ characteristic constant

Suffixes

A atmospheric
P pipe
CE cylinder end of exhaust pipe
N nozzle end of exhaust pipe
1 inlet to nozzle
2 outlet from nozzle
3 outlet from turbine
t throat of nozzle
I primary wave
II secondary wave
(see Fig. 9)

Vol. 2
1960-61

Non-dimensional parameters

$$A = \frac{a}{a_A} = \text{non-dimensional speed of sound}$$

$$P = \frac{p}{p_A} = \text{non-dimensional pressure}$$

$$U = \frac{u}{a_A} = \text{non-dimensional particle velocity}$$

$$\phi = \frac{\text{nozzle area}}{\text{pipe cross-sectional area}}$$

$$\psi = \frac{\text{supercharge port area}}{\text{pipe cross-sectional area}}$$

$$\Phi = \frac{\text{exhaust port area}}{\text{pipe cross-sectional area}}$$

Reference conditions

a_A speed of sound at atmospheric pressure corresponding to isentropic expansion from pipe pressure p and speed of sound a to atmospheric pressure p_A
p_A atmospheric pressure
a reference speed of sound
p reference pressure
F reference pipe area

ENERGY CONTENT OF EXHAUST PULSES AND CONTINUOUS MEAN POWER CONCEPT

The energy content of the exhaust pulse at the outlet end of the exhaust pipe is defined as the maximum work that can be performed by the gas in an ideal isentropic gas turbine.

The thermodynamic model for the system is shown in Fig. 1; the ideal isentropic gas turbine is placed immediately downstream of the exhaust pipe.

Applying the first law of thermodynamics to the control volume enveloping the inlet and outlet ducts of the turbine we have:

$$-\frac{dW_T}{dt} = \frac{dm_3 h_3}{dt} + \frac{dm_3}{dt}\frac{u_3^2}{2} - \frac{dm_1 h_1}{dt} - \frac{dm_1}{dt}\frac{u_1^2}{2} + \frac{d(E)_{cv(1-3)}}{dt} \tag{1}$$

For the nozzle the corresponding equation is

$$0 = \frac{dm_2 h_2}{dt} + \frac{dm_2}{dt}\frac{u_2^2}{2} - \frac{dm_1 h_1}{dt} - \frac{dm_1}{dt}\frac{u_1^2}{2} + \frac{d(E)_{cv(1-2)}}{dt} \tag{2}$$

where suffixes 1, 2 and 3 refer to the positions given in Fig. 1.

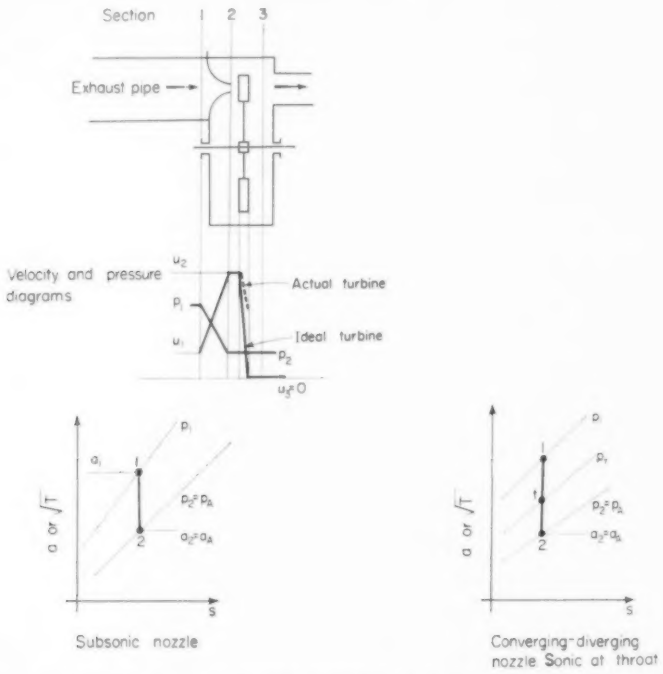

FIG. 1. Thermodynamic model turbine: u = gas velocity, p = static pressure of gas, a = velocity of sound in gas, s = entropy and T = temperature.

If the length of the gas path in the turbine is small compared with the exhaust-pipe length we may assume that at any instant of time

$$\frac{dm_1}{dt} = \frac{dm_2}{dt} = \frac{dm_3}{dt} = \frac{dm}{dt}$$

whence

$$\frac{d(E)_{cv(1-2)}}{dt} = 0 \text{ for the control volume } 1 \to 2$$

$$\frac{d(E)_{cv(1-3)}}{dt} = 0 \text{ for the control volume } 1 \to 3$$

The model shown in Fig. 1 is an ideal isentropic, purely impulse gas turbine; the pressure drop occurs in the fixed nozzle* and the kinetic energy produced in the gas stream is then transferred to the rotor.

For maximum work from the turbine $u_3 = 0$, hence, combining (1) and (2) and noting that $h_2 = h_3$,

$$\frac{dW_T}{dt} = \frac{dm}{dt}\frac{u_2^2}{2} \tag{3}$$

This is the kinetic energy of the gas stream leaving the nozzle.

For isentropic expansion

$$\frac{p}{\rho^\gamma} = \text{constant} \tag{4}$$

The equation of continuity is

$$F_1 \rho_1 u = F_2 \rho_2 u_2 \tag{5}$$

From equation (2)

$$a_1^2 + \frac{\gamma - 1}{2} u_1^2 = a_2^2 + \frac{\gamma - 1}{2} u_2^2 \tag{6}$$

The mass flow rate

$$\frac{dm}{dt} = F_1 \rho_1 u_1 \tag{7}$$

Hence combining equations (3)–(7) we have

$$\frac{dW_T}{dt} = \frac{\gamma F_1}{2} p_2 a_2 \phi \left[\frac{\frac{2}{\gamma - 1}\left[\left(\frac{p_1}{p_2}\right)^{(\gamma-1)/\gamma} - 1\right]}{1 - \phi^2 \left(\frac{p_2}{p_1}\right)^{2/\gamma}} \right]^{\frac{3}{2}} \tag{8}$$

where $\phi = \dfrac{F_2}{F_1}$.

If $a_2 = a_A$ and $p_2 = p_A$, equation (8) can be rewritten in the form

$$\frac{dW_T}{dt} = F_1 p_A a_A \pi_p \tag{9}$$

where

$$\pi_p = \frac{\gamma}{2} \phi \left[\frac{\frac{2}{\gamma - 1}\left[\left(\frac{p_1}{p_A}\right)^{(\gamma-1)/\gamma} - 1\right]}{1 - \phi^2 \left(\frac{p_A}{p_1}\right)^{2/\gamma}} \right]^{\frac{3}{2}} \tag{10}$$

for subsonic flow.

In Fig. 2 the parameter π_p is plotted against p_1/p_A for a nozzle with area ratio $\phi = 0{\cdot}25$ ($\gamma = 1{\cdot}4$).

Equation (9) gives the instantaneous power developed by the turbine† or the instantaneous power available in the gas pulse.

* In the present work the gas flow through the exhaust nozzles was subsonic in almost all the tests, and in the few tests where the flow became sonic this occurred over a very small part of the cycle. For this reason the treatment is restricted to the subsonic-flow case only.

† The corresponding expression for an ideal turbine with choked flow is given in the Appendix.

Vol. 2
1960-61

In the exhaust system of an internal-combustion engine the pressure pulses occur in a cyclic sequence, the maximum energy available per cycle is therefore

$$W_T = \oint \left(\frac{dW_T}{dt}\right).dt \tag{11}$$

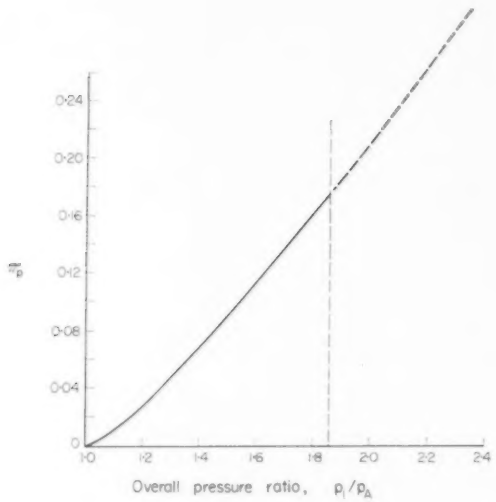

FIG. 2. $\pi_p \sim$ pressure ratio curve ($\phi = 0{\cdot}25$): ———— subsonic flow through convergent nozzle (unchoked-turbine case); — — — — choked flow through convergent–divergent nozzle (choked-turbine case); - - - - - - - sonic boundary; π_p = power function parameter, p_1 = static pressure in pipe adjacent to nozzles, p_A = atmospheric pressure and ϕ = (area of throat of nozzle)/(area of pipe).

Of more practical interest is the maximum power that can be developed by a gas turbine operating with a pulse exhaust system. If n is the number of cycles per second then the maximum power is

$$\begin{aligned} W_T n &= \left[\oint \frac{dW_T}{dt}.dt\right] \times n \\ &= \oint F_1 p_A a_A \pi_p n\, dt \end{aligned} \tag{12}$$

For an engine cycle of 360 crank angle degrees

$$\begin{aligned} W_T n &= \int_0^{360} \frac{F_1 p_A . a_A}{360\, n} \pi_p . n . d\theta \\ &= F_1 p_A \int_0^{360} \frac{a_A \pi_p\, d\theta}{360} \qquad (13) \\ &= F_1 p_A . \overline{a_A \pi_p} \qquad (14) \end{aligned}$$

where $\overline{a_A \pi_p}$ is the mean value of the product $a_A \pi_p$ over the cycle.

Vol. 2
1960-61

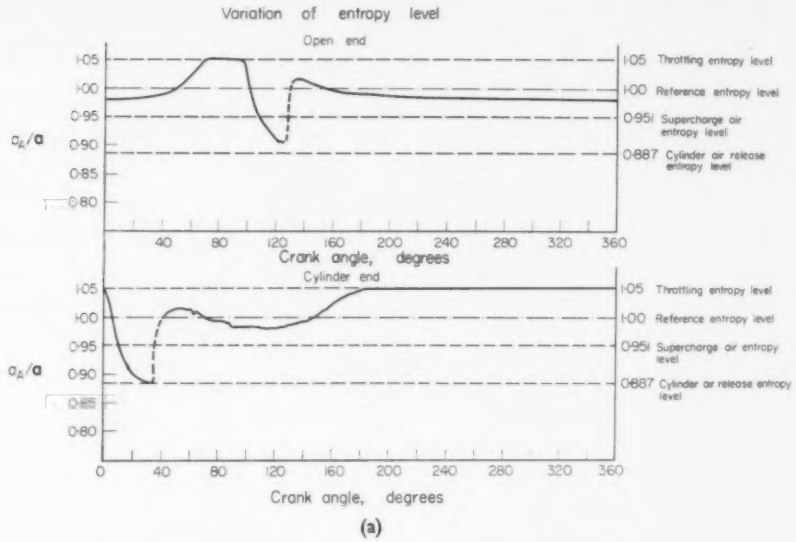

(a)

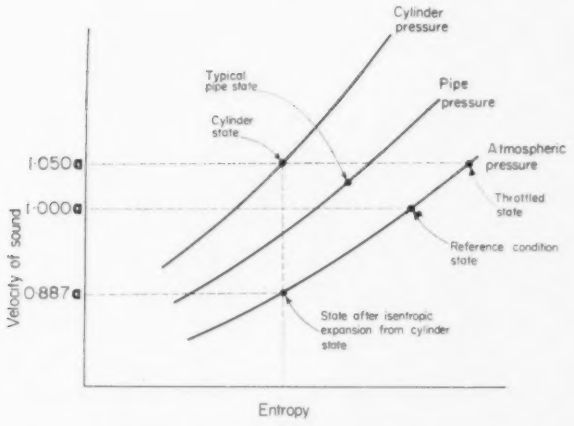

(b)

FIG. 3(a) and (b). Variation of entropy level: a_A = velocity of sound at atmospheric pressure on any given isentrope; **a** = velocity of sound at atmospheric pressure on a reference isentrope, i.e. reference speed of sound; $(a_A)/(\mathbf{a})$ = dimensionless "entropy level" [values of entropy level given on 3(a) are dimensionless].

Comparing equations (14) and (9) it will be seen that equation (14) gives the average value of the instantaneous power over the cycle. This will be called the *continuous mean power* or CMP, and is analogous to the mean indicated or effective pressure for a reciprocating-engine indicator diagram.

Hence
$$\text{CMP} = F_1 p_A \overline{a_A \pi_p} \tag{15}$$

where
$$\overline{a_A \pi_p} = \int_0^{360} \frac{a_A \pi_p}{360} d\theta \tag{16}$$

It is convenient to express equation (15) in non-dimensional form; thus

$$\frac{\mathrm{CMP}}{\mathbf{Fpa}} = \frac{F_1}{\mathbf{F}} \cdot \frac{p_A}{\mathbf{p}} \cdot \frac{\overline{a_A \pi_p}}{\mathbf{a}} \tag{17}$$

The bold-type symbols are reference conditions. Of particular significance is the ratio $\overline{a_A}/\mathbf{a}$.

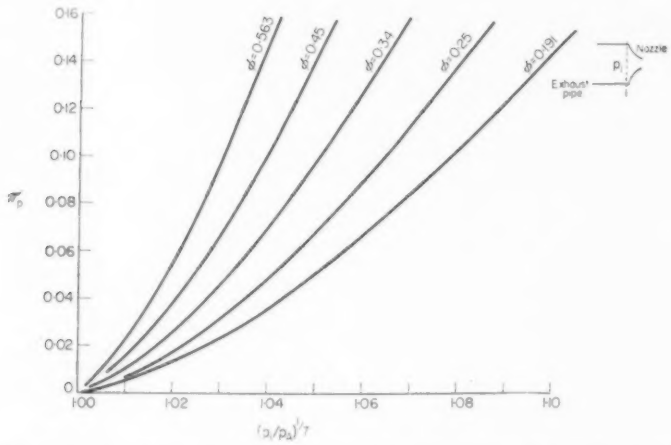

FIG. 4. $\pi_p \sim$ (pressure ratio)$^{1/7}$ across nozzle curves for various nozzle ϕ ratios (subsonic flow at nozzle throat). Power-function parameter

$$\pi_p = \frac{7}{10}\phi \left[\frac{5\left(\frac{p_1}{p_A}\right)^{2/7} - 1}{1 - \phi^2 \left(\frac{p_A}{p_1}\right)^{10/7}} \right]^{\frac{3}{2}}$$

ϕ = (area of throat of nozzle)/(area of pipe); p_1 = static pressure in pipe adjacent to nozzle; p_A = atmospheric pressure.

If the speed of sound **a** is taken at atmospheric pressure then it can be shown that the entropy in the pipe S_A and the reference entropy **s** are related by the equation

$$\frac{a_A}{\mathbf{a}} = \exp\left(\frac{S_A - \mathbf{s}}{2C_p}\right) \tag{18}$$

The ratio $a_A/\mathbf{a}$ is therefore a "measure" of the difference between the entropy of the gas stream and the reference entropy. In a pipe in which the entropy level is uniform and invariant with time, $a_A/\mathbf{a}$ is a constant. In a pipe in which there are temperature discontinuities, heat transmission or friction, $a_A/\mathbf{a}$ is variable. There can also be entropy changes caused by irreversible flows at area discontinuities. In the apparatus used in the present experiments the main causes of the entropy differences in the pipe were the pipe entry conditions and the temperature discontinuity between the high-pressure release air and the supercharge air [Fig. 3(b)]. In practice, however, these differences were not excessive as shown in Fig. 3(a) where the variation in $a_A/\mathbf{a}$

is shown for a typical test. It was considered that for the present experimental analysis **a** be made equal to the mean value of a_A.

Thus equation (17) became

$$\frac{\mathrm{CMP}}{\mathbf{Fpa}} = \frac{F_1}{\mathbf{F}} \frac{p_A}{\mathbf{p}} \frac{\overline{a_A}}{\mathbf{a}} \bar{\pi}_p \tag{19}$$

and if $\overline{a_A} = \mathbf{a} = \text{constant}$

$$\frac{\mathrm{CMP}}{\mathbf{Fpa}} = \frac{F_1}{\mathbf{F}} \frac{p_A}{\mathbf{p}} \bar{\pi}_p \tag{20}$$

The parameter π_p is a function of the pipe pressure immediately upstream of the nozzle (p_1) and the ratio of the nozzle area to the pipe area ϕ. A series of curves of π_p for various ϕ values used in these experiments is shown in Fig. 4. For a given nozzle area π_p is a function of the pulse pressure p_1, hence $\bar{\pi}_p$ is a function of the pulse magnitude and the duration of the pulse.

In the next section the effect of the wave action on the continuous mean power (CMP) is examined.

THE INFLUENCE OF WAVE ACTION ON THE CONTINUOUS MEAN POWER

The complex wave phenomena in the exhaust pipe can be examined qualitatively by the method of characteristics using unit processes to obtain the general trends of the analysis. This was demonstrated in a previous paper.[1] In this paper the same technique is used to examine the effect of wave action on the power available in the gas pulses.

The pressure–velocity relationship* across a wave can be represented by the integrated characteristic equations

$$P^{(\gamma-1)/2\gamma} = \frac{\gamma-1}{2} \frac{u}{a_A} + \alpha \quad \text{(across a wave to the right)} \tag{21}$$

$$P^{(\gamma-1)/2\gamma} = -\frac{\gamma-1}{2} \frac{u}{a_A} + \lambda \quad \text{(across a wave to the left)} \tag{22}$$

where P is non-dimensional pressure p/p_A and α and λ are the characteristic constants (Fig. 5). The pulse profile in the exhaust pipe of a high-pressure supercharged two-stroke system consists of two parts, a primary pulse produced by the exhaust blowdown and a secondary pulse produced by the supercharge air.

It was shown in the previous paper[1] that, in general, the former pulse corresponded to simple wave flow whilst the latter was associated with the

* The pressure–velocity relationships alternatively may be interpreted along a wave; in this case they are

$$P^{(\gamma-1)/2\gamma} = \frac{\gamma-1}{2}\left(\frac{u}{a_A}\right) + \alpha \quad \text{(along a wave to the left)}$$

$$P^{(\gamma-1)/2\gamma} = -\left(\frac{\gamma-1}{2}\right) \frac{u}{a_A} + \lambda \quad \text{(along a wave to the right)}$$

Vol. 2
1960-61

reflected waves. From the analysis point of view it is considered desirable to examine the two pulses separately.

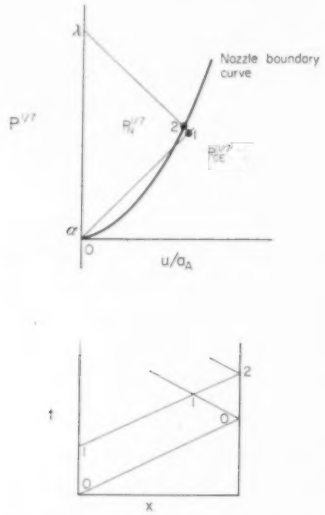

Fig. 5. Representation of characteristic constants. P = (static pressure in pipe)/(atmospheric pressure); suffix CE denotes at cylinder end of pipe; suffix N denotes at nozzle end of pipe; u = gas velocity; t = time; x = Cartesian co-ordinate of distance; a_A = velocity of sound in gas at atmospheric pressure; α and λ are characteristic constants.

(a) *Primary pulse*

Since this is associated with simple wave flow the pipe conditions at exhaust-port opening will correspond to $P^{(\gamma-1)/2\gamma} = 1$, $u/a_A = 0$. For this simple case the magnitude of the pressure pulse P_N at the nozzle end can be directly calculated from a knowledge of the nozzle-area ratio ϕ and the magnitude of the incident wave P_{CE}. This can be carried out on the state diagram shown in Fig. 5. From the calculated value of P_N the parameter π_p can be obtained from equation (10) (Fig. 4). The results from such an analysis are shown in Fig. 6. For each incident-wave pressure P_{CE} there is an optimum value of ϕ for maximum instantaneous power. The general trend shows an increase in the optimum value of ϕ with an increase in pulse amplitude P_{CE}.

The primary-pulse amplitude increases with an increase in cylinder release pressure and increase in speed, and hence for a fixed pipe size one would expect the instantaneous power to increase with these two variables. In order to examine the effect of pipe size it is necessary to consider the parameter $(F_1)/(\mathbf{F})\,\pi_p$ from equation (20), since, in this case, $(F_1)/(\mathbf{F})$ and π_p are both functions of pipe size. For a given nozzle-area ratio, $\phi = 0{\cdot}25$, and port opening area (or given crank-angle position), the effect of pipe size on the parameter $(F_1)/(\mathbf{F})\,\pi_p$ for two cylinder pressures is shown in Fig. 7. The reference area $\mathbf{F}$ is the cylinder cross-sectional area (2-in. bore). It will be clearly seen that there is an optimum pipe area depending on the cylinder pressure.

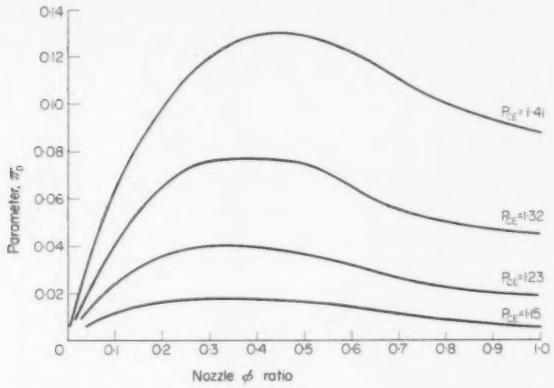

FIG. 6. $\pi_p \sim$ nozzle ϕ ratio curves for various pulses. P_{CE} = (static pressure in pipe at cylinder end)/(atmospheric pressure); π_p = power-function parameter; ϕ = (area of throat of nozzle)/(area of pipe).

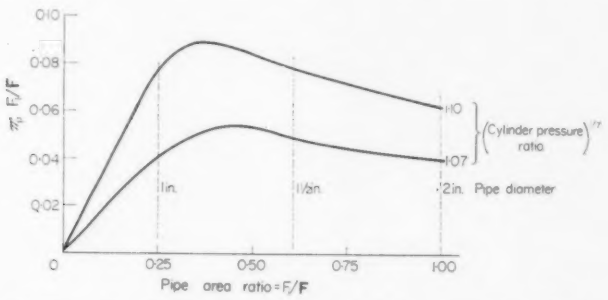

FIG. 7. $\pi_p(F_1)/(\mathbf{F}) \sim (F_1)/(\mathbf{F})$ curves for two cylinder pressures. (Nozzle area)/(pipe area) = 0·25; (exhaust pipe area)/(cylinder area) = 0·2; π_p = power-function parameter; F_1 = cross-sectional area of exhaust pipe; $\mathbf{F}$ = area of a 2-in. diameter circle (i.e. cross-sectional area of cylinder).

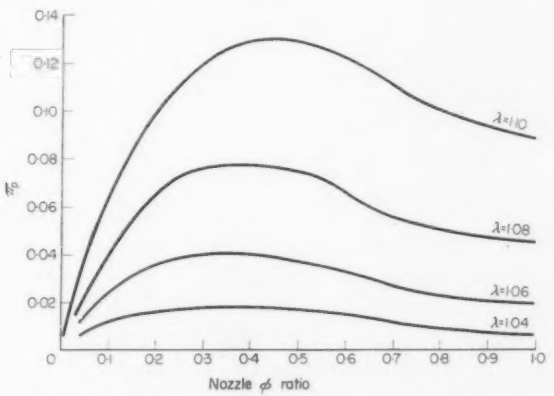

FIG. 8. $\pi_p \sim$ nozzle ϕ ratio curves for various characteristic constants. π_p = power-function parameter; ϕ = (area of throat of nozzle)/(area of pipe); λ = characteristic constant.

Vol. 2
1960-61

(b) *Secondary pulse (supercharge pulse)*

The magnitude of the secondary pulse depends on the supercharge pressure, port area, pipe area, engine speed and reflected waves from the nozzle end. If there are no reflected waves the general trend in the results would be similar to those given above for the primary pulse. The effect of increasing the supercharge pressure for these conditions would be similar to increasing the cylinder pressure. In general, however, the reflected waves will influence the magnitude of the supercharge pulse at the nozzle end.

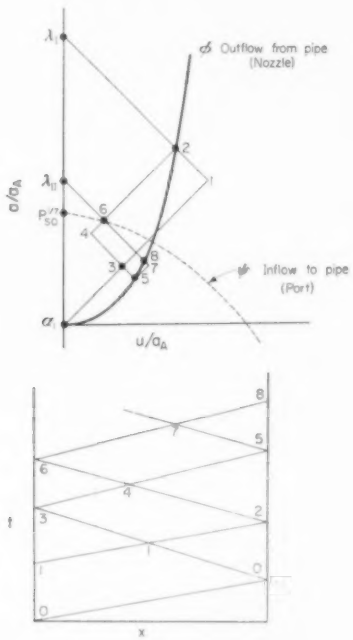

FIG. 9. Unit process for a secondary pulse. a = velocity of sound in gas; a_A = velocity of sound in gas at atmospheric pressure; t = time; u = velocity of gas; x = Cartesian co-ordinate; ϕ = (area of throat of nozzle)/(area of pipe); ψ = (area of equivalent port)/(area of exhaust pipe); P_{SO} = (stagnation pressure of supercharge air)/(atmospheric pressure); α and λ are characteristic constants; suffix I denotes a primary wave; suffix II denotes a secondary wave.

By using the unit-process technique an assessment of the effect of the reflected waves on the instantaneous power can be made. For this general case $\alpha \neq 1{\cdot}0$ and we must therefore modify the approach. Each incident pressure wave reflected at the nozzle end will lie on a λ characteristic (Fig. 5). The intersection of the characteristic and the nozzle boundary curve will give the pressure at the nozzle; hence it is possible to evaluate the variation of P_N with ϕ and thus π_p with ϕ without reference to the magnitude of the incident wave at that stage. The results of such an analysis are shown in Fig. 8 which is essentially similar to Fig. 6 with λ replacing P_{CE}.

The unit process for the secondary pulse is shown in Fig. 9. Consider a wave point 1 (Fig. 9) which is reflected at the nozzle end as 2 and then interacts with gas entering the pipe at the cylinder end to give the point 6. The wave point 6 is reflected at the nozzle to 8. The magnitude of the pressure at point 8 is the value of P_N in the supercharge pulse which controls the maximum instantaneous power. It will be seen from Fig. 9 that the magnitude of P_N will depend on the magnitude of the incident primary pulse P_{CE} (point 1), the nozzle-area ratio ϕ, the (supercharge-port area)–pipe-area ratio ψ and the supercharge

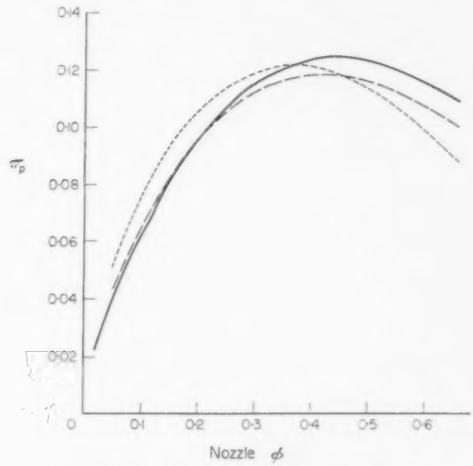

FIG. 10. $\pi_p \sim \phi$ curves for supercharge pulse at $\theta = 90°$ after EPO (discharge influenced by reflexion of blowdown pulse).
π_p = power-function parameter;
ϕ = (area of throat of nozzle)/(area of pipe);
P_{CE} = (static pressure in pipe at cylinder end)/(atmospheric pressure).
Magnitude of primary wave P_{CE}: 1·000 ——— no reflected wave; 1·072 — — —; 1·316 - - - - -

pressure P_{SO}. Calculation of the parameter π_p depends on a knowledge of the value of λ for the incident supercharge pulse. For fixed values of ϕ, ψ and $P_{SO}^{1/\gamma}$ there will be a unique relationship between the incident primary-pulse pressure P_{CE} (point 1, Fig. 9) and the supercharge-pulse pressure at the nozzle end P_N (point 8, Fig. 9). A series of calculations was carried out for the conditions pertaining in the test apparatus to examine the effect of the reflected wave on the parameter π_p. A crank angle of 90° at the supercharge port opening was selected (ψ = constant) and a constant supercharge pressure $P_{SO} = 2{\cdot}00$. The results of the analysis are shown in Fig. 10.

The analytical procedure involved the calculation of the characteristic constant λ_{II} for several incident primary-pulse pressures. Fig. 8 was then used to evaluate π_p. The results show that for each incident primary-pulse pressure P_{CE} there is an optimum nozzle-area ratio ϕ. The full line for $P_{CE} = 1$ corresponds to no reflected waves from the nozzle end.

Vol. 2
1960-61

DURATION OF PULSES

The duration of the pulses is of major importance in assessing the continuous mean power. The duration of the primary pulse is mainly controlled by the engine speed and release pressure, the speed in general being more significant. The duration of the secondary pulse, however, is more important since this pulse is of longer duration than the primary pulse. To a first-order estimate the duration of the secondary pulse can be assessed by the time the pulse is present in the exhaust pipe after the exhaust ports close (EPC). For this case the exhaust pipe is similar to a cylinder with a port at one end (i.e. the nozzle), and the pulse duration equivalent to the discharge time.

For this case the pulse duration $\Delta\theta$ can be expressed in terms of the engine speed N, the pipe length L_p, the nozzle area ratio ϕ and the speed of sound at atmospheric pressure a_A [Fig. 3(b)] as

$$\Delta\theta = \frac{NL_p}{a_A\phi} f(p) \tag{23}$$

where $f(p)$ is a function of the pressure at EPC.[2]

This expression shows that for a given pulse pressure at EPC the parameter $\bar{\pi}_p$ will increase with increase in engine speed and pipe length and decrease in nozzle ratio. Although an increase in pipe length will increase the pulse duration, at the same time there will be a reduction in pulse pressure at the nozzle end due to friction. The nett effect on the continuous mean power will depend on the incident pulse pressure P_{CE} and the pipe size (length and bore).

SUMMARY OF THEORETICAL DEDUCTIONS

The instantaneous power available in the gas at the nozzle end of the exhaust pipe is a function of the nozzle-area ratio and the upstream pressure. The available power increases with increase in engine speed and release pressure due to the increase in upstream pressure. There is an optimum nozzle-area ratio for maximum instantaneous power and this varies with the incident-pulse pressure in the pipe at the cylinder end. The continuous mean power will vary with nozzle ratio, pipe size (length and diameter). In general, the smaller the nozzle size, pipe length and bore, the greater the available power. There is, however, an optimum nozzle-area ratio and pipe-area ratio below which there will be a decrease in power.

The complexity between the factors which influence the instantaneous power and the factors which influence the continuous mean power renders it difficult to give quantitative answers except by detailed characteristic calculations. In order to ascertain whether the general qualitative picture obtained with unit processes was satisfactory, a detailed experimental programme was carried out.

EXPERIMENTAL RESULTS

The indicator diagrams taken at the nozzle end of the exhaust pipe were analysed to obtain the continuous mean power (CMP) for each test. Three

diagrams are shown in Fig. 11 where the parameter

$$\frac{F_1}{\mathbf{F}}\frac{a_A}{\mathbf{a}}\pi_p$$

is plotted against crank angle θ. A typical measured indicator diagram analysed on a constant-entropy basis is shown together with the results of a detailed constant-entropy calculation, by the method of characteristics. For these two diagrams, the above parameter simplified to $(F_1)/(\mathbf{F})\,\pi_p$. A third diagram is shown in which the calculated diagram was modified to take account of the entropy variation during the cycle. The results show that the assumption of constant entropy was reasonable.

Vol. 2
1960-61

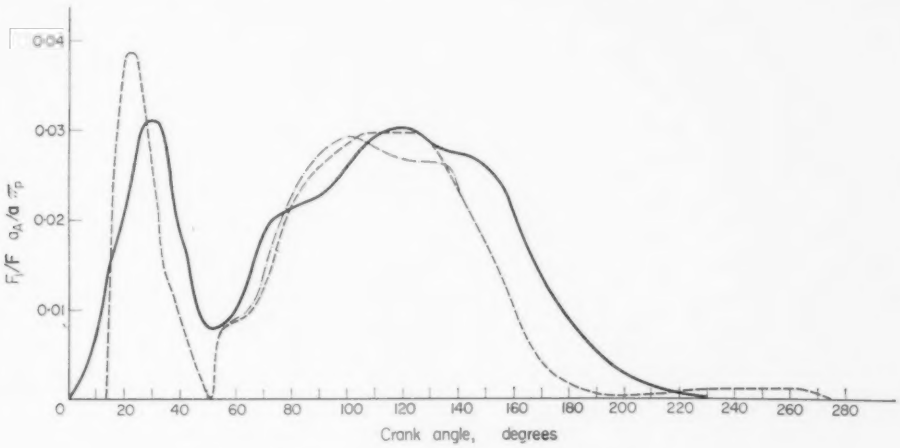

FIG. 11. Instantaneous power ~ crank-angle curves.

$\frac{F_1}{\mathbf{F}}\frac{a_A}{\mathbf{a}}\pi_p$ = combined power-function parameter.

Curve reference

$\frac{F_1}{\mathbf{F}}\frac{\overline{a_A}}{\mathbf{a}}\overline{\pi_p}$

- 0·01047 ———— derived from measured diagram constant entropy
- 0·00874 — — — — derived from measured diagram constant entropy
- 0·00866 · — · — · — derived from calculated diagram entropy

Space precludes the inclusion of all the tests, some typical results are given in Figs. 12–18. In Figs. 12–15 the experimental results are shown for various pipe sizes, nozzle-area ratios and engine speeds. All the tests showed an increase in available power with increase in release pressure, the magnitude of the increase being greater with the smaller pipe sizes. These and other results were correlated to obtain the effects of the exhaust-pipe size and nozzle configuration on the power available. In Fig. 16 the derived results are shown for a release pressure 3·75 atm absolute. For a fixed nozzle-area ratio ($\phi = 0{\cdot}25$) the power increases with an increase in speed, as would be expected; furthermore, the available power increases with decrease in pipe diameter and pipe length. The

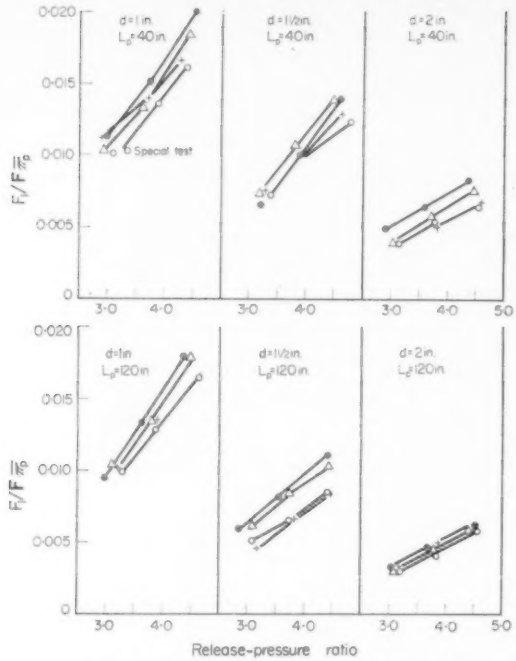

FIG. 12. Power from exhaust gas: nozzle $\phi = 0{\cdot}25$. Experimental results: d = diameter of exhaust pipe; L_p = length of exhaust pipe; $\bar{\pi}_p$ = mean value of power-function parameter; F_1 = area of exhaust pipe; $\mathbf{F}$ = area of 2-in. diameter cylinder; ϕ = (area of throat of nozzle)/(area of pipe); ○——○ 750 rev/min; +——+ 1000 rev/min; △——△ 1250 rev/min; ⊕——⊕ 1500 rev/min.

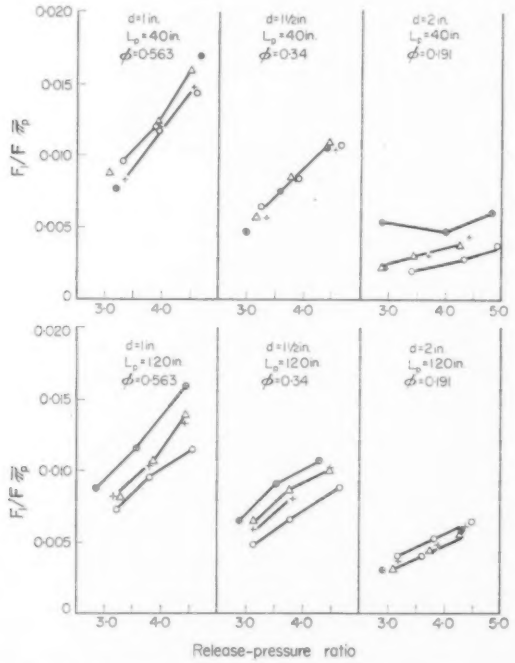

FIG. 13. Power from exhaust gas: various nozzle ϕ values. Experimental results: key as for Fig. 12.

effects of pipe length are (1) to increase the pulse duration and (2) to reduce the pulse magnitude due to friction. These results show that the second effect predominates. On the other hand, the percentage difference in available power between the two pipe lengths is greater in the larger-diameter pipe than in the smaller-bore pipe, i.e. pipe length is more important in the case of large-diameter pipes.

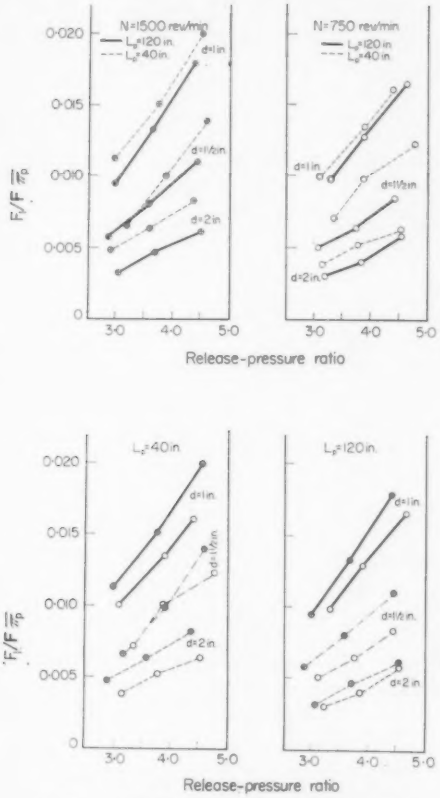

FIG. 14. Effect of pipe length and pipe diameter on power available: nozzle $\phi = 0{\cdot}25$. Experimental results: key as for Fig. 12.

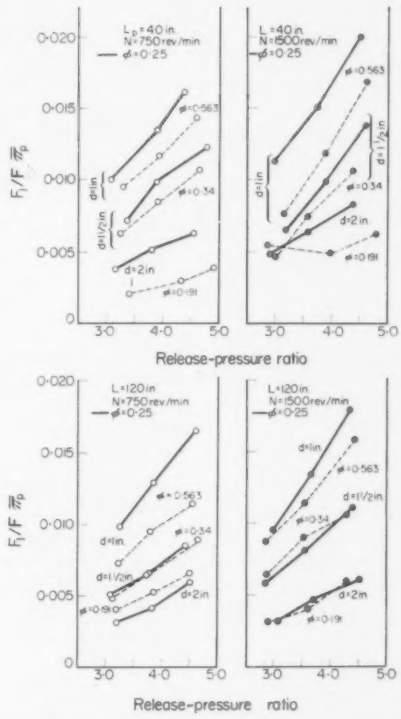

FIG. 15. Power from exhaust gas (nozzle-ratio effect). Experimental results: key as for Fig. 12.

The theoretical treatment showed that the optimum nozzle ratio would fall in a range between 0·2 and 0·5. This is clearly shown in the experimental results (Fig. 16) where for the short pipe a nozzle-area ratio $\phi = 0{\cdot}25$ gave the best results in all cases, whilst in the long pipe the optimum value of ϕ varied with pipe diameter and speed.

The effect of pipe bore on the available power is shown in Fig. 17 at two speeds. Over the range of pipes tested it was not possible to obtain the optimum pipe size. The curves are drawn through three points and it may well be that the optimum size lies between $(F_1)/(\mathbf{F}) = 0{\cdot}25$ and 0·4, but no definite conclusion can be drawn.

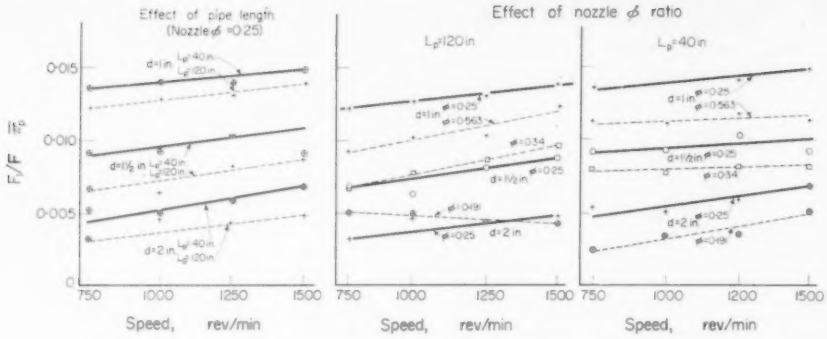

FIG. 16. The effect of speed, pipe diameter, pipe length and nozzle ratio on power available (results derived from experimental curves for release-pressure ratio 3·75). Notation as for Fig. 12.

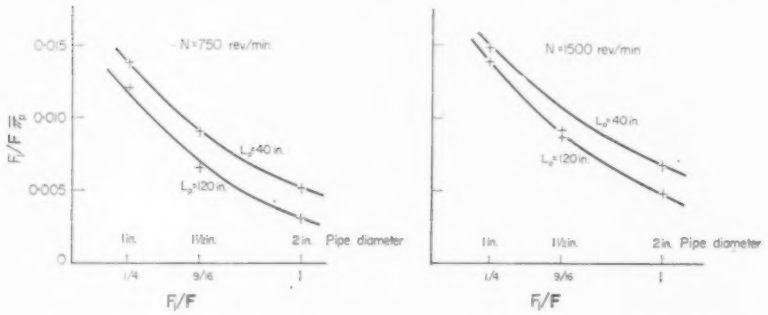

FIG. 17. The effect of pipe area on power available (results derived from experimental curves for release-pressure ratio 3·75). $\phi = 0{\cdot}25$; ϕ = (area of throat of nozzle)/(area of pipe); F_1 = area of pipe; $\mathbf{F}$ = area of 2-in. diameter cylinder; L_p = length of pipe; π_p = mean value of power-function parameter; N = speed rev/min.

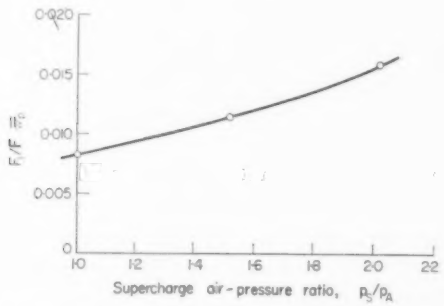

FIG. 18. Effect of supercharge air pressure on power available. Speed 1500 rev/min; nozzle ratio $\phi = 0{\cdot}563$; release-pressure ratio 4·425; pipe length 120 in.; pipe diameter 1 in.; F_1 = area of exhaust pipe; $\mathbf{F}$ = area of 2-in. diameter cylinder; ϕ = (area of throat of nozzle)/(area of pipe); p_S = supercharge air pressure; p_A = atmospheric pressure.

The majority of the tests were carried out with a supercharge pressure of 15 lb/in² gauge. The effect of the supercharge pressure was examined at 1500 rev/min with a nozzle ratio $\phi = 0{\cdot}563$ with release pressure 4·425 atm absolute. The results are shown in Fig. 18. The zero value corresponds to zero supercharge air pressure.

DISCUSSION OF RESULTS

These results confirm the general theoretical analysis; in particular, they show that a qualitative assessment of the problem can be made using unit processes.

In comparing these results with practical engine performance it should be noted that no account has been taken of the energy in the exhaust gases due to the piston motion. This, however, is not very great in a two-stroke-cycle engine. The matching of the turbo-charger and the engine will depend not only on the exhaust-pipe characteristics, but also on the engine characteristics, in particular the engine ports. In the present test both the supercharge pressure and engine ports were fixed over the speed range examined. In practice the supercharge pressure would depend on the energy available in the exhaust gas to drive the gas turbine, the overall efficiency of the turbo-supercharge unit and the design of the supercharge-air ports.

Vol. 2
1960-61

Although no account has been taken of the effect of temperature this should not vitiate the value of the tests. The essential feature in the plotting of the results has been the selection of a reference entropy level. An analysis was made of the effect of the varying entropy in the pipe associated with temperature discontinuity between the release gas and the supercharge air. This analysis showed that the maximum possible error in the instantaneous value of $a_A \pi_p$ for the exhaust blowdown period over 36 crank angle degrees was -10 per cent and for the supercharge period over 114° was $+2\frac{1}{2}$ per cent. This gave an error in the CMP over 360° of $+3$ per cent. In practice this error would probably not be obtained, for example the calculation in Fig. 11 gave an error of $\frac{1}{2}$ per cent in the CMP with the assumption of constant entropy.

For comparative purposes the non-dimensional approach enables a direct assessment of the power available in the exhaust system. It was shown in the previous paper[1] that for the supercharge period the cylinder volume may be neglected in calculating the pressure changes in the exhaust pipe. Hence the effect of different supercharge port dimensions can be examined directly by utilizing the techniques given in this and the previous paper. Although the data produced here are of fundamental interest, the methods can be extended directly into practical engine design.

CONCLUSION

The experiments and the theoretical analysis show that the energy content of the exhaust pulses in the exhaust pipe of a high-pressure-charged two-stroke-engine model increases with

(i) Increase in engine speed and release pressure.
(ii) Decrease in pipe diameter down to an optimum size.
(iii) Decrease in pipe length.
(iv) Increase in supercharge pressure.

The tests and the theory show that there is an optimum nozzle-area to pipe-area ratio for maximum power. The optimum value lies between 0·2 and 0·5.

There is an optimum pipe-area to cylinder cross-sectional-area ratio but it was not possible to ascertain the value in the present tests; it should, however, lie between 0·2 and 0·4.

Acknowledgements—The tests described in this paper were carried out in the Walker and Harrison–Hughes Laboratories of the University of Liverpool. The authors wish to acknowledge with thanks the help given by Professor W. J. Kearton in providing the facilities. The authors also wish to thank Mr. W. Miller, Superintendent of the Laboratories, Mr. J. Cowie and Mr. E. Hobson for their help and advice.

APPENDIX

For flow choked at the turbine nozzle the energy content of the exhaust gases can be determined as follows.

It will be considered that the maximum work can be performed in the turbine if the leaving velocity (u_3) is zero. For this case the stagnation enthalpy drop corresponding to isentropic expansion from nozzle inlet pressure (p_1) to turbine exhaust pressure (p_3) (equal to atmospheric pressure p_A) will give the maximum available energy in the exhaust gas.

For choked flow at the nozzle throat,

$$u_t = a_t \tag{A.1}$$

$$\frac{dm}{dt} = F_1 \rho_1 u_1 = F_t \rho_t a_t \tag{A.2}$$

$$a_1^2 + \frac{\gamma - 1}{2} u_1^2 = \frac{\gamma + 1}{2} a_t^2 \tag{A.3}$$

$$-\frac{dW_T}{dt} = \frac{dm}{dt}\left(h_3 - h_1 - \frac{u_1^2}{2}\right) \tag{A.4}$$

Combining equations (A.1)–(A.4) we obtain

$$\frac{dW_T}{dt} = F_1 p_A a_A \pi_p \tag{A.5}$$

where

$$\pi_p = \frac{\gamma}{2(\gamma - 1)} \phi \left(\frac{p_t}{p_1}\right)_{cr}^{(3\gamma-1)/2\gamma} \left(\frac{p_1}{p_A}\right)^{(3\gamma-1)/2\gamma} \left[(\gamma + 1) - 2\left(\frac{p_A}{p_t}\right)^{(\gamma-1)/\gamma}\right]$$

The critical-pressure ratio $\left(\frac{p_t}{p_1}\right)_{cr}$ is given by

$$\phi^2 = \left(\frac{p_1}{p_t}\right)_{cr}^{2/\gamma} \left[\frac{\gamma + 1}{\gamma - 1} - \left(\frac{2}{\gamma - 1}\right)\left(\frac{p_1}{p_t}\right)_{cr}^{(\gamma-1)/\gamma}\right]$$

$$\phi = \frac{\text{Throat area}}{\text{Pipe area}}$$

REFERENCES

1. R. S. BENSON and W. A. WOODS, *Int. J. Mech. Sci.* **1**, 253 (1960).
2. R. S. BENSON, *Engineer, Lond.* **199**, 546 (1955).

Int. J. Mech. Sci. Pergamon Press Ltd. 1961. Vol. 2, pp. 251–266. Printed in Great Britain

SHEAR FLOWS IN STRAIGHT-SIDED NOZZLES AND DIFFUSERS

J. H. HORLOCK* and R. I. LEWIS†

(*Received* 23 *March* 1960)

Summary—Analytical solutions are given for the shear flow through (i) a two-dimensional straight-walled duct of varying cross-sectional area, and (ii) a duct bounded by two conical surfaces. The solution for the two-dimensional flow is confirmed by experiment.

Vol. 2
1960-61

1.0 INTRODUCTION

IT IS well known that non-uniformities in the velocity of an incompressible inviscid fluid flowing through a duct become accentuated by a diffusing section, and attenuated by a contraction.[1-3]

These non-uniformities are induced by the vorticity perpendicular to the plane of flow in a two-dimensional system, or by the tangential vorticity in axisymmetric flow. The rotational velocity components so induced may be regarded as perturbations of the irrotational flow through the duct, the vector sum of rotational and irrotational velocity components resulting in a so-called "shear flow".

If the perturbations are small and the equations of motion are linearized, simple general solutions may be obtained for flow through a two-dimensional straight-walled duct, and a conical diffuser.

Particular solutions result from prescribing the manner of entry and outflow of the fluid.

2.0 NOTATION

r, θ, x; r, ϕ, θ	co-ordinates
u, v, w	velocity components
u', v'	perturbation velocities
$m = 2\pi C$	source strength per unit length
p	pressure
η	vorticity
A	area
Γ	circulation
F, Θ	functions of θ
R	functions of r
a_n, b_n, p_n, A_n, B_n, ν_n	constants
λ	radius ratio
α, β, γ, δ	function of r, p and λ
P_n, Q_n	Legendre functions
$U = C/r$	unperturbed velocity—wedge-shaped duct
$U = C/r^2$	unperturbed velocity—conical duct

* Department of Mechanical Engineering, The University, Liverpool 3.
† Engineering Department, University of Cambridge.

3.0 SHEAR FLOW THROUGH A TWO-DIMENSIONAL STRAIGHT-WALLED CHANNEL

3.1. *General analysis*

In a flow system the velocity may be regarded as the vector sum of irrotational and rotational components. The former is created by a suitable distribution of sources, sinks or vortices, while the latter component is induced by the vorticity vector perpendicular to the plane containing the velocity components.

Consider the flow of an incompressible inviscid fluid through a duct with straight walls (Fig. 1). The projections of the walls meet at OO'. Flow through such a duct may be regarded as the perturbed flow from a line source, or into a line sink situated at OO'. If a system of plane polar co-ordinates is adopted with OO' as the origin (Fig. 1), the velocity components in the direction of r and θ for a perturbed source flow are

$$u = \frac{C}{r} + u'$$
$$v = v' \tag{1}$$

where $m = 2\pi C$, the source strength per unit length, and u', v' are the rotational perturbations.

The equations of motion are

$$-\frac{1}{\rho r}\frac{\partial p}{\partial \theta} = u\frac{\partial v}{\partial r} + \frac{v}{r}\frac{\partial v}{\partial \theta} + \frac{uv}{r}$$
$$-\frac{1}{\rho}\frac{\partial p}{\partial r} = u\frac{\partial u}{\partial r} - \frac{v^2}{r} + \frac{v}{r}\frac{\partial u}{\partial \theta} \tag{2}$$

The vorticity normal to the r, θ plane is

$$\eta = \frac{\partial v'}{\partial r} + \frac{v'}{r} - \frac{1}{r}\frac{\partial u'}{\partial \theta} \tag{3}$$

and the equation of continuity

$$\frac{\partial u'}{\partial r} + \frac{u'}{r} + \frac{1}{r}\frac{\partial v'}{\partial \theta} = 0 \tag{4}$$

If u' and v' are small, their second-order products may be neglected. The linearized equations of motion are then

$$-\frac{1}{\rho C}\frac{\partial p}{\partial \theta} = \frac{\partial v'}{\partial r} + \frac{v'}{r} \tag{5}$$

$$-\frac{1}{\rho C}\frac{\partial p}{\partial r} = \frac{1}{r}\frac{\partial u'}{\partial r} - \frac{u'}{r^2} - \frac{C}{r^3} \tag{6}$$

Eliminating pressure derivatives,

$$\frac{\partial^2 v'}{\partial r^2} + \frac{1}{r}\frac{\partial v'}{\partial r} - \frac{v'}{r^2} - \frac{1}{r}\frac{\partial^2 u'}{\partial r\,\partial \theta} + \frac{1}{r^2}\frac{\partial u'}{\partial \theta} = 0$$

which may be integrated with respect to r giving

$$\frac{\partial v'}{\partial r} + \frac{v'}{r} - \frac{1}{r}\frac{\partial u'}{\partial \theta} = F(\theta) \text{ (a function of } \theta \text{ only)}$$

Hence from (3)
$$\eta = F(\theta) \tag{7}$$

So that within the approximations made the vorticity remains constant along the radial lines of the potential flow.

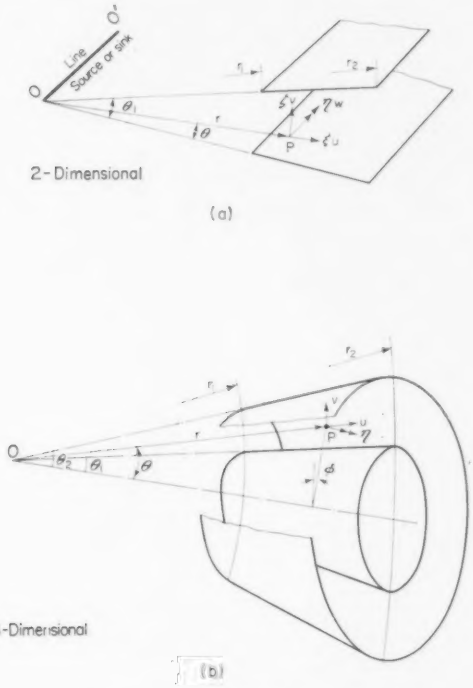

FIG. 1. Co-ordinate systems.

This result may be explained by consideration of the circulation Γ around a fluid element of area dA.

$$\Gamma = \left(\frac{\partial v'}{\partial r} + \frac{v'}{r} - \frac{1}{r}\frac{\partial u'}{\partial \theta}\right) r\, d\theta\, dr = \eta\, dA$$

By Kelvin's theorem the circulation around a closed curve bounding this element remains constant. Since dA is unchanged for an incompressible fluid, η is constant along streamlines. If the perturbed streamline pattern departs only slightly from the unperturbed, the velocities induced by a "streamline" distribution of η will differ only slightly from those induced by a radial distribution.

A solution for u' and v' may be obtained from the continuity equation with no further assumptions. Differentiating (3) and (4)

$$\frac{\partial \eta}{\partial r} = \frac{\partial^2 v'}{\partial r^2} + \frac{1}{r}\frac{\partial v'}{\partial r} - \frac{v'}{r^2} - \frac{1}{r}\frac{\partial^2 u'}{\partial r\, \partial \theta} + \frac{1}{r^2}\frac{\partial u'}{\partial \theta} = 0$$

and

$$\frac{1}{r^2}\frac{\partial^2 u'}{\partial r\, \partial \theta} + \frac{1}{r^2}\frac{\partial u'}{\partial \theta} + \frac{1}{r^2}\frac{\partial^2 r'}{\partial \theta^2} = 0$$

Eliminating $(\partial^2 u')/(\partial r\,\partial\theta)$ from these equations and using (3) and (7)

$$\frac{\partial^2 v'}{\partial r^2}+\frac{3}{r}\frac{\partial v'}{\partial r}+\frac{v'}{r^2}+\frac{1}{r^2}\frac{\partial^2 v'}{\partial\theta^2}=\frac{2F(\theta)}{r} \tag{8}$$

Assuming a solution of the form

$$v' = F(\theta)\,R(r)$$

where $R(r)$ is a function of r only, (8) may be written

$$\frac{r^2 R''+3rR'+R-2r}{R}=-\frac{F''}{F}=p_n^2$$

where p_n is a constant.

Equation (8) thus separates into two ordinary equations

$$\begin{aligned} r^2 R''+3rR'+(1-p_n^2)R &= 2r \\ F''+p_n^2 F &= 0 \end{aligned} \tag{9}$$

The second has as its general solution the Fourier series

$$F(\theta)=\sum_{n=1}^{n=\infty}\{a_n\sin p_n\theta+b_n\cos p_n\theta\}$$

where $p_n = n\pi/\theta_1$, $\theta_1>\theta>0$ and θ_1 is arbitrary. The solution of (9) for the nth term in the series is

$$R(r)=\frac{1}{r}[A_n r^{p_n}+B_n r^{-p_n}]+\frac{2r}{4-p_n^2}$$

and the complete solution of (9) is

$$v'=\sum_1^\infty\left\{\frac{1}{r}[A_n r^{p_n}+B_n r^{-p_n}]+\frac{2r}{4-p_n^2}\right\}\{a_n\sin p_n\theta+b_n\cos p_n\theta\} \tag{10}$$

3.2. *Wall boundary conditions*

If the duct walls coincide with $\theta = 0$ and θ_1, then at these positions v' must be zero, and b_n is zero. Using (4) to obtain u' the solution becomes

$$v'=\sum_1^n\left\{\frac{1}{r}[A_n r^{p_n}+B_n r^{-p_n}]+\frac{2r}{4-p_n^2}\right\}a_n\sin p_n\theta \tag{11}$$

$$u'=-\sum_1^n\left\{\frac{1}{r}[A_n r^{p_n}-B_n r^{-p_n}]+\frac{p_n r}{4-p_n^2}\right\}a_n\cos p_n\theta \tag{12}$$

This solution contains:

(a) A potential flow term specified by A_n which becomes important as $r\to\infty$ (for $p_n>1$, i.e. $\theta_1<\pi$).

(b) A potential flow term specified by B_n which becomes important as $r\to 0$.

(c) A term governed by the vorticity, which becomes more significant as $r\to\infty$, but is important everywhere.

While it may be reasonable to reject (a) and (b) within the finite region of the duct, they will be retained until particular solutions have been obtained.

3.3. *Inlet and outlet boundary conditions*

Of the three constants A_n, B_n and a_n, the latter is determined by the angular distribution of vorticity,

$$\eta = \sum_1^n a_n \sin p_n \theta$$

A_n and B_n can be obtained by specifying inlet and outlet boundary conditions at radii r_1 and r_2 respectively. Two possibilities are considered.

3.4. *Constant static pressure at inlet and outlet*

The boundary conditions corresponding to the case of diffusion between regions of constant pressure at r_1 and r_2 are

$$\frac{\partial p_1}{\partial \theta} = \frac{\partial p_2}{\partial \theta} = 0$$

or, from (5), $\dfrac{\partial}{\partial r}(rv') = 0$ at r_1 and r_2.

Vol. 2
1960-61

Applying these boundary conditions term by term in the general solution, and considering the nth term, with suffixes dropped for convenience,

$$Apr_1^{p-1} - Bpr_1^{-p-1} + \frac{4r_1}{4-p^2} = 0, \text{ inlet,}$$

$$Apr_2^{p-1} - Bpr_2^{-p-1} + \frac{4r_2}{4-p^2} = 0, \text{ outlet,}$$

from which A_n and B_n can be found, and

$$u' = \left\{\frac{4\alpha - p^2}{4-p^2}\right\} \frac{ar}{p} \cos p\theta \tag{13}$$

$$v' = \left\{\frac{4\beta + 2p}{4-p^2}\right\} \frac{ar}{p} \sin p\theta \tag{14}$$

where
$$\alpha = \frac{(\lambda^{p+2}-1)\left(\dfrac{r}{r_1}\right)^{p-2} + (\lambda^{p-2}-1)\left(\dfrac{r}{r_2}\right)^{-p-2}}{(\lambda^{2p}-1)},$$

and
$$\beta = \frac{-(\lambda^{p+2}-1)\left(\dfrac{r}{r_1}\right)^{p-2} + (\lambda^{p-2}-1)\left(\dfrac{r}{r_2}\right)^{-p-2}}{(\lambda^{2p}-1)}$$

The values attainable for each term in the series for u' and v' may be compared by a study of the functions within the curly brackets.

At inlet and outlet

$$u_1' = r_1 \sum_1^n \frac{a_n}{p_n} \cos p_n \theta$$

$$u_2' = r_2 \sum_1^n \frac{a_n}{p_n} \cos p_n \theta \tag{15a}$$

or at a given angular position

$$\frac{u_2'}{u_1'} = \frac{r_2}{r_1} = \lambda \tag{15b}$$

The shape of the perturbation in the through-flow velocity profile is the same but its magnitude increases in proportion to λ. Because the mean velocity also decreases in this ratio,

$$\frac{u_2'}{U_2} = \lambda^2\left(\frac{u_1'}{U_1}\right)$$

where $U = (m)/(2\pi r) = C/r$ is the mean through-flow velocity, and the fractional perturbation of the flow increases as λ^2. This marked change in the through-flow velocity profile for quite small area ratios is observed experimentally, and is illustrated in Figs. 2 and 3.

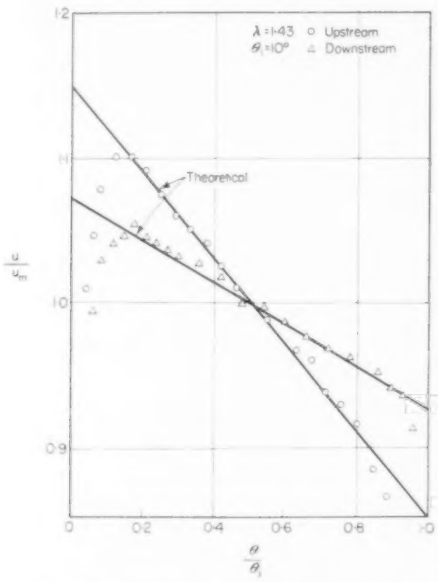

Fig. 2. Shear flow through a two-dimensional converging duct.

The experiments were carried out using a two-dimensional duct 9·5 in. long, with an inlet section 5 in. wide by 10 in. deep. The vertical walls could be adjusted to form a contraction or diffuser of the desired angle.

In the first experiment an almost linear shear profile, generated by an array of $\frac{1}{8}$-in. diameter steel rods situated 10 in. upstream of the duct inlet, was passed through a contraction ($\lambda = 1{\cdot}43$, $\theta_1 = 10°$, $U_1 = 55{\cdot}9$ ft/sec). The profile observed at outlet is compared in Fig. 2 with that predicted theoretically, and agrees to within 1·5 per cent away from the boundary layers. The maximum value of (u_1'/U_1) was about 0·1.

For the second experiment a pronounced concave profile, generated by a 2-in. wide strip of wire gauze suspended 10 in. upstream of inlet, was passed through a diffuser ($\lambda = 1{\cdot}47$, $\theta_1 = 15°$, $U_1 = 81{\cdot}3$ ft/sec). A preliminary check was made with the walls parallel, to see if the shear flow was in equilibrium. Negligible change occurred in the profile between inlet and outlet. It was found that, with 15° of divergence and the concave profile, separation was

limited to a small region in each corner. Although the perturbations exceeded 30 per cent of the mean velocity at exit, the theoretical prediction of (u_2'/U_2) exceeded the measured value by only 7 per cent. The spread of the separated zones would tend to be suppressed under the influence of the distribution of main-stream vorticity, which would continue to induce higher velocities near the side walls, and transverse velocities (towards the walls) throughout the duct.

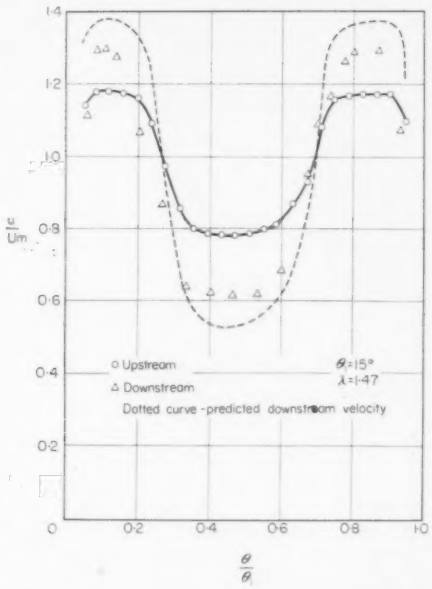

FIG. 3. Shear flow through a two-dimensional diverging duct.

In practice it is impossible to achieve exactly the inlet and outlet boundary conditions assumed in the theory, although in the experiments described above the variation of static pressure across the inlet and outlet sections was very small indeed. The duct was preceded by a 10-in. parallel section, and, at outlet, discharged into the laboratory.

Within the duct the u' profile may become distorted, as the function $(4\alpha - p^2)/(4 - p^2)$ of equation (13) may be different from unity. The departure of this function from unity is influenced independently by p and λ.

Smaller values of p are obtained (i) in a duct of wide divergence and (ii) with a profile in which the perturbation velocity varies cosinusoidally across the duct. (A value of $p = 1$ may be obtained in a duct in which $\theta_1 = \pi$ and $\eta = a_1 \sin\theta$.) Large values of p apply to flows which have high local rates of shear (the higher-order terms of the series for the vorticity are important), or to flows in narrow channels ($\theta_1 < 20°$). The parameter λ represents the area ratio r_2/r_1.

3.4.1. *The effect of varying p (channel divergence θ_1 and shear gradient at a fixed area ratio λ).* For a value of $\lambda = 1{\cdot}5$, coefficients in the series for u' and v'

are shown in Fig. 4(a) and (b). The greatest departure of $(4\alpha - p^2)/(4 - p^2)$ from unity occurs when $p = 1$, corresponding to the first term of the series ($n = 1$), and the maximum possible angle of divergence ($\theta_1 = \pi$). (This is true for all values of λ.) In the example considered ($\lambda = 1{\cdot}5$) even the maximum departure from unity (0·085) is still small and for $0 < \theta_1 < \pi$ it is sufficient to assume that

$$u_1' = \sum_1^n \frac{ar}{p_n} \cos p_n \theta \tag{16}$$

It is worth noting that, for $p = 1$, v' becomes quite large at inlet and remains greater than u' throughout. For a shear flow in which the first term of the series is important (a cosine variation of u') v' would assume proportions three times as great as u' in a duct with a "wedge" angle θ_1 of 180°.

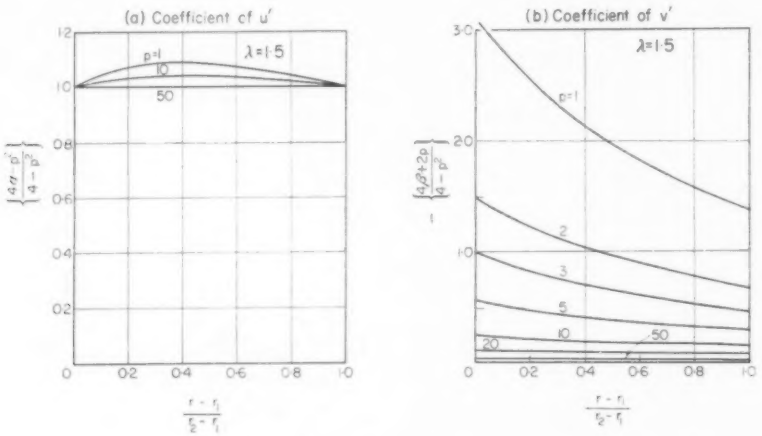

Fig. 4. Variation of u' and v' with p—constant-pressure inlet.

For more practical diffuser angles, say $\theta_1 < 20°$, v' is always less than a quarter of u' [see Fig. 4(b)], and negligible compared with the mean flow for all types of shear flow. Streamlines would in fact depart very little from the radial direction.

For higher rates of shear, high-order terms of the series become more important and v' becomes small compared with u'.

3.4.2. *The effect of variation of area ratio* (λ) *at a fixed* p. The striking effect of increasing the area ratio (λ) at a fixed p may be seen from Figs. 5–7, in which values of 1, 3 and 10 have been taken for p.

As the area ratio is increased, the distortion of the profile within the duct is severely increased, particularly just after entry. However, it should be remembered that for large area increases, since the mean non-uniformities increase as λ^2, the allowable perturbations at inlet must be strictly limited (as $1/\lambda^2$) to justify the approximate form of the equations of motion. The distortions will be less perceptible.

For $p = 1$, v' continues to be greater than u' as λ increases.

For $p = 3$, v' and u' are of the same order.

For $p = 10$, v' has diminished to about one-fifth of u'.

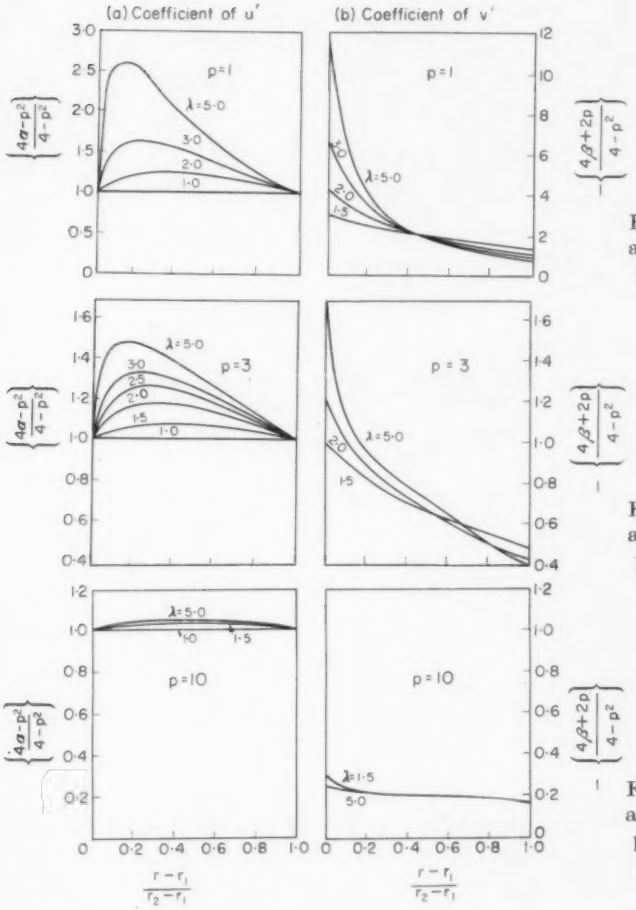

FIG. 5. Variation of u' and v' with λ—constant-pressure inlet and outlet.

FIG. 6. Variation of u' and v' with λ—constant-pressure inlet and outlet.

FIG. 7. Variation of u' and v' with λ—constant-pressure inlet and outlet.

It should be noted that for small values of λ (i.e. if the duct does not extend close to the origin or to infinity), the potential-flow terms of equations (11) and (12) (A_n and B_n) contribute an insignificant amount to the solution. As $\lambda \to 1$, $u' \to (ar/p)\cos p\theta$, which is the form to which (12) would be reduced if A_n and B_n approached zero, and p became very large. The terms governed by A_n and B_n in (12) may be rejected only as $\lambda \to 1$ and/or $p \to \infty$.

3.5. *Radial entry and constant static pressure at outlet*

The fluid may be guided radially into the duct and ejected into a region of constant static pressure. The required boundary conditions at inlet and outlet

are

$$\left.\begin{aligned} v' &= 0 \text{ at } r_1 \\ \frac{\partial}{\partial r}(v'r) &= 0 \text{ at } r_2 \end{aligned}\right\} \quad \text{for a diverging duct in which } U \text{ is positive}$$

$$\left.\begin{aligned} v' &= 0 \text{ at } r_2 \\ \frac{\partial}{\partial r}(v'r) &= 0 \text{ at } r_1 \end{aligned}\right\} \quad \text{for a converging duct in which } U \text{ is negative}$$

The solutions for u' and v' are

$$u' = \sum_1^n \left(\frac{2\gamma - p^2}{4 - p^2}\right) \frac{ar}{p} \cos p\theta \tag{17}$$

$$v' = \sum_1^n \left(\frac{2\delta + 2p}{4 - p^2}\right) \frac{ar}{p} \sin p\theta \tag{18}$$

in which

$$\gamma = \frac{(p + 2\lambda^{p+2})\left(\frac{r}{r_1}\right)^{p-2} - (p\lambda^{p-2} - 2)\left(\frac{r}{r_2}\right)^{-p-2}}{(\lambda^{2p} + 1)}$$

$$\delta = -\frac{(p + 2\lambda^{p+2})\left(\frac{r}{r_1}\right)^{p-2} + (p\lambda^{p-2} - 2)\left(\frac{r}{r_2}\right)^{-p-2}}{(\lambda^{2p} + 1)}$$

for the diverging duct, and

$$\gamma = \frac{(p\lambda^{p+2} + 2)\left(\frac{r}{r_1}\right)^{p-2} + (2\lambda^{p-2} - p)\left(\frac{r}{r_2}\right)^{-p-2}}{(\lambda^{2p} + 1)}$$

$$\delta = -\frac{(p\lambda^{p+2} + 2)\left(\frac{r}{r_1}\right)^{p-2} - (2\lambda^{p-2} - p)\left(\frac{r}{r_2}\right)^{-p-2}}{(\lambda^{2p} + 1)}$$

for the converging duct.

Again, the individual and comparative behaviour of u' and v' for ducts of varying angle and area ratio may be studied by examining the functions within the curly brackets (see Figs. 8–11).

A simple expression for u' at inlet and outlet [such as equation (15a)] cannot be obtained. For large values of θ_1 the profile at outlet may differ considerably from that at inlet and that within the duct.

In *all* cases v' is reduced to a fraction of u' over the complete range of λ and p.

3.5.1. *Effect of varying p at a fixed area ratio (divergent duct).* For an area ratio λ of 1·5 and small p (as for wide-angled ducts and cosinusoidally sheared flows), $(2\gamma - p^2)/(4 - p^2)$ departs widely from unity for values of p up to 10, particularly at entry [see Figs. 9(a), 10(a) and 11(a)]. When $p = 1$ ($\theta_1 = 180°, n = 1$) this effect is amplified by increasing λ [Fig. 9(a)]. With larger values of p, this effect is reversed, and when $p = 10$ the departure of

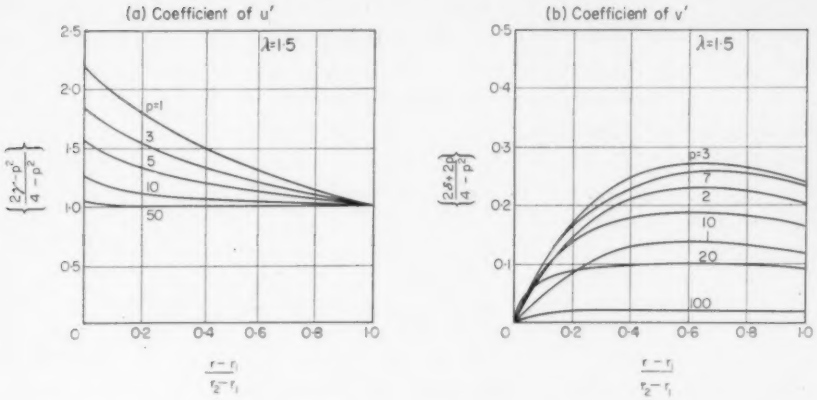

FIG. 8. Variation of u' and v' with p—radial inlet, constant-pressure outlet.

Vol. 2
1960-61

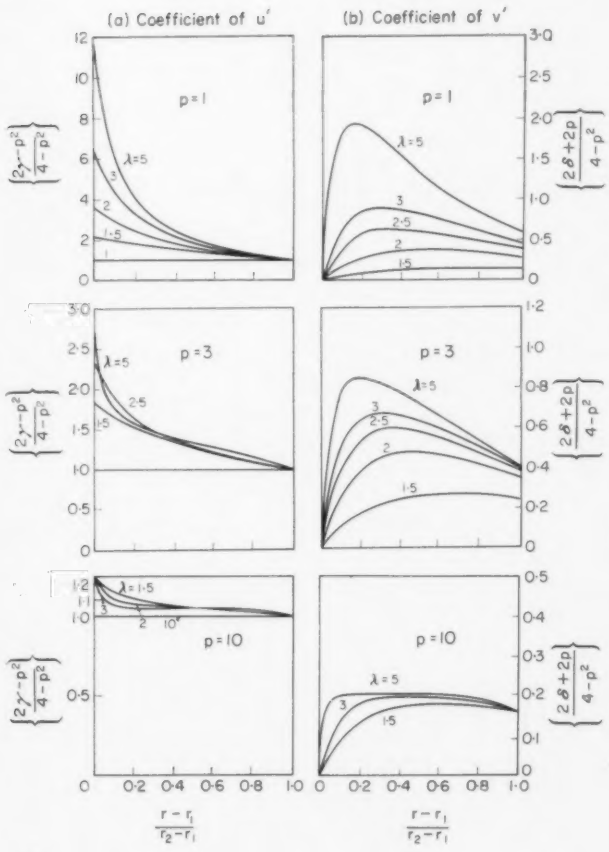

FIG. 9. Variation of u' and v' with λ—radial inlet, constant-pressure outlet.

FIG. 10. Variation of u' and v' with λ—radial inlet, constant-pressure outlet.

FIG. 11. Variation of u' and v' with λ—radial inlet, constant-pressure outlet.

$(2\gamma - p^2)/(4 - p^2)$ from unity is reduced by increasing λ [Fig. 11(a)]. In comparison with the corresponding solution of Section 2.4, v' is reduced, and u' is increased.

If the vorticity distribution is sinusoidal and $\theta = 180°$ ($p = 1$) the maximum value of u' is proportional to $(2\gamma - p^2)/(4 - p^2)$.

From a comparison of the velocities at inlet and outlet it is now apparent that u' is actually attenuated for this wide-angled duct. Taking a typical case when $\lambda = 3$, it is found that

$$u_2' = 0{\cdot}47\, u_1'$$

and

$$\frac{u_2'}{U_2} = 1{\cdot}41 \frac{u_1'}{U_1}$$

whereas with constant static pressure at inlet and outlet

$$\frac{u_2'}{U_2} = 9 \frac{u_1'}{U_1}$$

The throughflow (u'/U_2) profile does steepen, but the effect of the inlet radial constraint is to limit its growth.

For narrow-angled ducts or for high local rates of shear v' becomes negligible (p large), and u' approximates to

$$u' = \sum_1^n \frac{a_n r}{p_n} \cos p_n \theta$$

as in the first solution 2.1.

4.0 SHEAR FLOW BETWEEN CONICAL SURFACES

4.1. *General analysis*

Axi-symmetric shear flow through an annular passage bounded by conical walls with a common vertex (e.g. through a conical diffuser) may be treated in a similar manner, adopting spherical polar co-ordinates with the origin at the vertex [Fig. 1(b)]. If the tangential, or swirling, component of the velocity is everywhere zero, the equations of motion are

$$-\frac{1}{\rho r}\frac{\partial p}{\partial \theta} = u\frac{\partial v}{\partial r} + \frac{v}{r}\frac{\partial v}{\partial \theta} + \frac{uv}{r} \quad \text{radially}$$

$$-\frac{1}{\rho}\frac{\partial p}{\partial r} = u\frac{\partial u}{\partial r} + \frac{v}{r}\frac{\partial u}{\partial \theta} - \frac{v^2}{r} \quad \text{axially} \tag{19}$$

The tangential component of vorticity is

$$\eta = \frac{\partial v}{\partial r} + \frac{v}{r} - \frac{1}{r}\frac{\partial u}{\partial \theta} \tag{20}$$

As in the two-dimensional case the flow may be regarded as the perturbed flow from a point source of strength $m = 4\pi C$ situated at O, and velocity components in the r, θ direction are

$$u = C/r^2 + u', \quad v = v'$$

If u' and v' are small, the approximate equations of motion become

$$-\frac{1}{\rho r}\frac{\partial p}{\partial \theta} = \frac{C}{r^2}\frac{\partial v'}{\partial r} + \frac{Cv'}{r^3} \tag{21}$$

$$-\frac{1}{\rho}\frac{\partial p}{\partial r} = \frac{C}{r^2}\frac{\partial u'}{\partial r} - \frac{2Cu'}{r^3} - \frac{2C^2}{r^5} \tag{22}$$

Proceeding as before, (20), (21) and (22) reduce to

$$\frac{\partial \eta}{\partial r} = \frac{\eta}{r} \quad \text{or} \quad \frac{\eta}{r} = \Theta \tag{23}$$

where Θ is a function of θ only. The quantity η/r remains constant approximately along conical surfaces. This result, which is similar to (7), may be understood by considering an elementary ring of fluid of radius r and cross-sectional area dA, concentric with the axis. By Kelvin's theorem the strength of such a vortex ring drifting along with the stream must remain constant.

$$\eta\, dA = \text{constant}$$

For incompressible flow, the volume of the fluid in the ring is constant ($r\, dA$ = constant). Hence η/r is constant along stream surfaces, concentric with the axis. For small values of u' and v' the stream surfaces will depart only a first-order amount from conical surfaces, and the induced velocity components due to an assumed conical vorticity distribution will be subject only to a second-order error.

The equation of continuity is

$$\frac{\partial u'}{\partial r} + \frac{2u'}{r} + \frac{1}{r}\frac{\partial v'}{\partial \theta} + \frac{v'}{r}\cot\theta = 0 \tag{24}$$

and from (20) and (23)

$$\frac{\partial^2 v'}{\partial r^2} + \frac{4}{r}\frac{\partial v'}{\partial r} + \frac{2v'}{r} + \frac{1}{r^2}\frac{\partial}{\partial \theta}(v'\cot\theta) + \frac{1}{r^2}\frac{\partial^2 v'}{\partial \theta^2} = \frac{4\eta}{r} = \frac{4\Theta}{r} \tag{25}$$

Assuming a solution of the form

$$v' = R\Theta$$

where R is a function of r only, equation (25) reduces to two ordinary equations

$$\Theta'' + \frac{d}{d\theta}(\Theta\cot\theta) + k_n\,\Theta = 0 \tag{26}$$

$$R'' + \frac{4}{r}R' + \frac{2-k_n}{r^2}R = 4 \tag{27}$$

Expressing equation (26) in terms of the independent variable $x = \cos\theta$,

$$(1-x^2)\frac{d^2\Theta}{dx^2} - 2x\frac{d\Theta}{dx} + \left(k_n - \frac{1}{1-x^2}\right)\Theta = 0$$

which is Legendre's associated equation of the first order, the solution of which is

$$\Theta = \sum_1^n \left[a_n \frac{d}{d\theta}\{P_n(\cos\theta)\} + b_n \frac{d}{d\theta}\{Q_n(\cos\theta)\}\right]$$

Vol. 2
1960-61

where $P_n(\cos\theta)$ and $Q_n(\cos\theta)$ are Legendre polynomials of the first and second kind, and $k_n = n(n+1)$.

The solution of (27) is then

$$R = Ar^{n-1} + Br^{-n-2} + 4r^2/(12-k_n)$$

and the general solution of (25)

$$v' = \sum_1^n \left\{ A_n r^{n-1} + B_n r^{-n-2} + \frac{4r^2}{12-k_n} \right\} a_n \{P'_n + \nu_n Q'_n\} \tag{28}$$

From the continuity equation

$$u' = -\sum_1^n \left\{ nA_n r^{n-1} - (n+1) B_n r^{-n-2} + \frac{k_n r^2}{12-k_n} \right\} a_n \{P_n + \nu_n Q_n\} \tag{29}$$

in which $b_n/a_n = \nu_n$.

4.2. *Wall boundary conditions*

ν_n is determined by the condition of v' being zero at the walls. If the inner and outer walls coincide with θ_1 and θ_2 ($\theta_1 < \theta_2 < \pi/2$) then

$$P'_n(\cos\theta_1) + \nu_n Q'_n(\cos\theta_1) = 0$$
$$P'_n(\cos\theta_2) + \nu_n Q'_n(\cos\theta_2) = 0$$

and

$$\begin{vmatrix} P'_n(\cos\theta_1) & Q'_n(\cos\theta_1) \\ P'_n(\cos\theta_2) & Q'_n(\cos\theta_2) \end{vmatrix} = 0 \tag{30}$$

Since

$$\eta = \sum_1^n a_n \{P_n(\cos\theta) + \nu_n Q_n(\cos\theta)\}$$

any distribution of vorticity may be matched by a process similar to Fourier analysis.

For flow through a conical diffuser, since $Q_n(\cos\theta)$ is infinite for $\theta = 0$, $\nu_n = 0$. Legendre polynomials, of the first kind only, may be chosen with derivatives which vanish at $\theta = \theta_1$.

4.3. *Inlet and outlet boundary conditions*

Inlet and outlet boundary conditions may be imposed as in the two-dimensional case. For simple diffusion between regions of constant static pressure at r_1 and r_2

$$\frac{\partial p_1}{\partial \theta} = \frac{\partial p_2}{\partial \theta} = 0$$

and

$$\frac{\partial}{\partial r}(vr) = 0$$

The solution for the nth term becomes

$$u' = -r^2 \left(\frac{12\alpha - k_n}{12 - k_n} \right) a_n \{P_n(\cos\theta) + \nu_n Q_1(\cos\theta)\} \tag{31}$$

$$v' = -r^2 \left(\frac{12\beta - 4}{12 - k_n} \right) a_n \{P'_n(\cos\theta) + \nu_n Q'_n(\cos\theta)\}$$

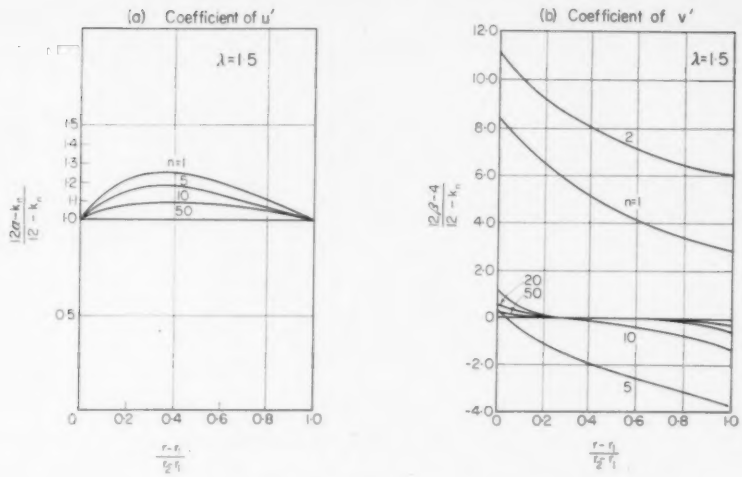

FIG. 12. Variation of u' and v' with n—conical duct.

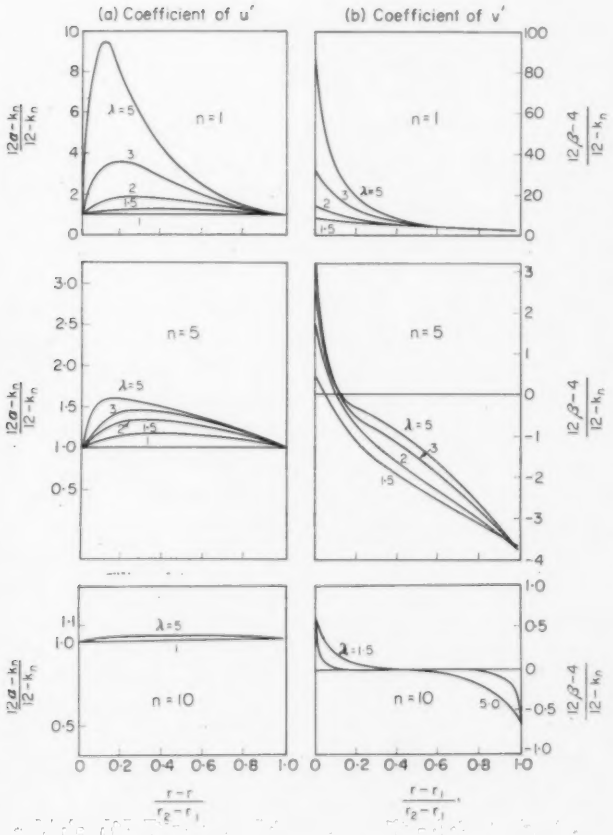

FIG. 13. Variation of u' and v' with λ—conical duct.

FIG. 14. Variation of u' and v' with λ—conical duct.

FIG. 15. Variation of u' and v' with λ—conical duct.

Vol. 2
1960-61

where

$$\alpha = \frac{(\lambda^{n+4}-1)\left(\frac{r}{r_1}\right)^{n-3} + (\lambda^{n-3}-1)\left(\frac{r_2}{r}\right)^{n+4}}{(\lambda^{2n+1}-1)}$$

$$\beta = \frac{-(n+1)(\lambda^{n+4}-1)\left(\frac{r}{r_1}\right)^{n-3} + n(\lambda^{n-3}-1)\left(\frac{r_2}{r}\right)^{n+4}}{(\lambda^{2n+1}-1)}$$

A result similar to (15) is obtained for the u' velocity profiles at inlet and exit.

$$\frac{u_1'}{r_1^2} = \frac{u_2'}{r_2^2}$$

or

$$\frac{u_2'}{U_2} = \lambda^4 \frac{u_1'}{U_1}$$

Again the profile steepens as the square of the area ratio λ^2.

The manner in which the coefficients of u' and v' depend on n and λ may be seen from Figs. 12–15, and is very similar to solution (i) of the two-dimensional case. For large values of n, greater than 10, approximately,

$$u' = -\Sigma r^2 a_n \{P_n(\cos\theta) + \nu_n Q_n(\cos\theta)\}$$

$$v' = 0$$

For simple conical diffusers ($\nu_n = 0$) in which the angle of diffusion would not normally exceed 20° because of separation losses, this is a good approximation. For example, the first zero of $P_n(\cos\theta)$ occurs at $2\theta = 20° 12'$ when $n = 13$. For this value of n, $[12\alpha - n(n+1)]/[12 - n(n+1)]$ is very close to unity.

5.0 CONCLUSIONS

Analytical solutions have been given for non-uniform flows through conical and two-dimensional straight-walled ducts, with experimental confirmation of the two-dimensional flow.

Non-uniformities in the through-flow velocity are increased with increasing cross-sectional area, and are decreased with decreasing cross-sectional area. The magnitudes of the perturbations in through-flow and transverse velocities (u', v') respectively are dependent upon the nature of the boundary conditions imposed upon the flow. With radial constraint on flow direction at inlet, the transverse perturbations (v') are small compared with the through-flow perturbations. With constant static pressure at inlet and outlet the relative magnitudes of u' and v' depend upon the vorticity distribution and the channel divergence. For all boundary conditions, if the channel divergence is small $(\theta_1 < 20°)$, transverse velocities may be neglected and the through-flow velocity profile varies as the square of the area ratio $[u'/U\alpha(\text{area ratio})^2]$.

REFERENCES

1. R. C. Pankhurst and D. W. Holder, *Wind Tunnel Technique*. Pitman Press, Bath (1952).
2. L. Prandtl, *Herstellung Einwandfreier Luftströme* (*Windkanäle*). *Handbüch der Experimentalphysik* Vol. IV. M.B.H., Leipzig (1932).
3. S. Corrsin, *J. Aero. Sci.* **19**, 135 (1952).

Int. J. Mech. Sci. Pergamon Press Ltd. 1961. Vol. 2, pp. 267–276. Printed in Great Britain

THE METHOD OF INTERFACE STRESS ADJUSTMENT AND ITS USES IN THE SOLUTION OF SOME PLANE ELASTICITY PROBLEMS

O. C. ZIENKIEWICZ and R. W. GERSTNER
Civil Engineering Department, Northwestern University

(*Received* 21 *April* 1960)

Summary—A method of solution of plane elasticity problems, which utilizes known, closed-form solutions and a finite-difference correction technique, is presented. The method, which simplifies the required computation, is particularly adaptable to problems involving semi-infinite media, singularities, and thermal discontinuities. Some applications are included.

Vol. 2
1960-61

INTRODUCTION

THE finite-difference treatment of plane elasticity problems is often complicated and tedious because of the necessity of accurately computing the stress functions in order to obtain reasonably accurate stress values. In addition, the preliminary calculation of the boundary conditions is in itself a major operation which adds to the computational difficulties. When problems involving semi-infinite media are encountered, special difficulties arise and extensive preliminary calculations are required. To avoid some of these, a new method was developed by the authors in connection with an investigation of stress distributions in prestressed structures.[1] In this study all the difficulties mentioned above were present and in addition the existence of singularities, notoriously troublesome to deal with by an orthodox finite-difference approach, complicated the problem.

The method presented here presupposes that it is possible to find simple, closed-form solutions (hereafter called the "particular solutions") which are capable of satisfying all the equilibrium conditions within the body under investigation, and which, in addition, satisfy the elastic compatibility conditions everywhere except on some interface line within the body. To obtain the complete solution in such a case it is only necessary to perform a "correction" computation, which, when superimposed on the original solutions, restores the continuity on the interface. This corrective solution which imposes a system of internal, self-equilibrating stresses has zero stress values on all external boundaries and, by St. Venant's principle, leads to stresses which tend to zero with increasing distance from the interface. In general it will be found that the numerical values of the corrective stresses are small as compared with the complete stress values, and therefore only a limited accuracy is required in their computation.

The method of formulating the problem is similar to the technique described earlier by the authors,[2] in which interface conditions between media of different elasticities were treated. In fact, the interface chosen to separate the sections

of the body for which the closed-form solutions are obtainable may also separate the sections in which the elastic constants differ, without introducing additional complication.

The same techniques may be used with success in problems of thermoelastic stress distribution in which a discontinuity of thermal properties or temperature occurs.

GENERAL FORMULATION

Consider the two-dimensional case of an elastic body separated by an interface dividing the body into two portions each of which may have different elastic properties (Fig. 1). The loading on the body may be quite arbitrary,

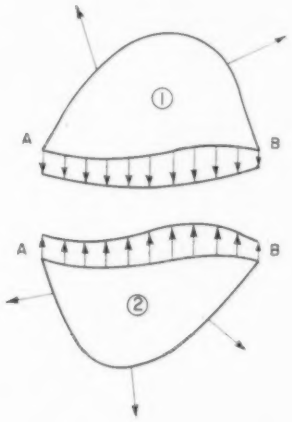

FIG. 1.

provided that it is possible to obtain for the two sections stress distributions which satisfy elasticity conditions, and which are self-equilibrating at all points along the interface AB. There are no additional restrictions on the stress distribution along AB. If such a particular solution can be obtained, the conditions of equilibrium and compatibility are satisfied everywhere except on the interface where a discontinuity of displacements will, in general, occur.

The stresses must now be adjusted so that the displacements of the two pieces give a perfect fit along the interface AB, i.e.

$$u_1 = u_2 - \alpha y + \beta \tag{1}$$

$$v_1 = v_2 + \alpha x + \gamma \tag{2}$$

where u and v denote displacements in the x and y directions respectively, subscripts 1 and 2 refer to portions 1 and 2 of the body, and α, β and γ are arbitrary constants. This adjustment of the stress distribution will be achieved by the corrective solution which gives discontinuities on the interface equal and opposite to those of the particular solution without imposing any external loading.

Although a general formulation of the corrective solution is possible for any shape of the dividing interface, only the case of a straight interface will be considered here—because of simplicity and also because the straight interface occurs more frequently in practice. As was shown by the authors,[2] the necessary and sufficient conditions for the continuity of displacement along AB can be given now in an alternative form as

$$\left(\frac{\partial u}{\partial x}\right)_1 = \left(\frac{\partial u}{\partial x}\right)_2 \tag{3}$$

$$\left(\frac{\partial^2 v}{\partial x^2}\right)_1 = \left(\frac{\partial^2 v}{\partial x^2}\right)_2 \tag{4}$$

where the x-axis is parallel to AB. In general the particular solution will not satisfy the preceding equations but will result in displacements u' and v' which give

$$\left(\frac{\partial u}{\partial x}\right)_1' = \left(\frac{\partial u}{\partial x}\right)_2' + M(x) \tag{5}$$

$$\left(\frac{\partial^2 v}{\partial x^2}\right)_1' = \left(\frac{\partial^2 v}{\partial x^2}\right)_2' + N(x) \tag{6}$$

where the "lack of fit" functions $M(x)$ and $N(x)$ can easily be calculated from the known stresses of the particular solutions. If the prime superscript is used also to denote the stresses from the particular solutions along the interface, then

$$M(x) = A_1(\sigma'_{x1} - B_1\sigma'_{y1}) - A_2(\sigma'_{x2} - B_2\sigma'_{y2}) \tag{7}$$

$$N(x) = 2A_1(1+B_1)\frac{\partial \tau'_{xy1}}{\partial x} - \frac{\partial}{\partial y}[A_1(\sigma'_{x1} - B_1\sigma'_{y1})] - 2A_2(1+B_2)\frac{\partial \tau'_{xy2}}{\partial x} + \frac{\partial}{\partial y}[A_2(\sigma'_{x2} - B_2\sigma'_{y2})] \tag{8}$$

in which $A = \dfrac{1}{E}$, $B = \nu$ for plane stress

and $A = \dfrac{(1-\nu^2)}{E}$, $B = \dfrac{\nu}{1-\nu}$ for plane strain

To obtain the corrective stresses it is necessary to obtain a solution in which discontinuities with values of $-M(x)$ and $-N(x)$ are introduced along the line AB. This solution will not introduce any external forces on the body.

If ϕ and θ represent the Airy stress function (for the solution described above) in regions 1 and 2 respectively, the following conditions have to be satisfied on the interface due to the self-equilibrating nature of the stresses.

$$\phi = \theta \tag{9}$$

$$\frac{\partial \phi}{\partial y} = \frac{\partial \theta}{\partial y} \tag{10}$$

Writing the displacement relations for the corrective solution in a form similar to equations (5) and (6) (the signs of the $M(x)$ and $N(x)$ terms are reversed),

Vol. 2
1960-61

and expressing these in terms of the stress function, we have

$$A_1\left[\frac{\partial^2\phi}{\partial y^2}-B_1\frac{\partial^2\phi}{\partial x^2}\right]=A_2\left[\frac{\partial^2\theta}{\partial y^2}-B_2\frac{\partial^2\theta}{\partial x^2}\right]-M(x)=0 \tag{11}$$

$$A_1\left[\frac{\partial^3\phi}{\partial y^3}+(2+B_1)\frac{\partial^3\phi}{\partial x^2\,\partial y}\right]=A_2\left[\frac{\partial^3\theta}{\partial y^3}+(2+B_2)\frac{\partial^3\theta}{\partial x^2\,\partial y}\right]-N(x)=0 \tag{12}$$

In addition, the governing biharmonic equation must be satisfied by the functions in their respective regions and also on the interface. Therefore, on the interface

$$\nabla^4\phi=0 \tag{13}$$

$$\nabla^4\theta=0 \tag{14}$$

The manipulation of equations (9–14), when expressed in finite-difference form, to obtain the special finite-difference equations for the stress function on and near the interface has been discussed.[2] The resulting special equations are identical to equations (24) and (25) of that reference except for the appearance of additive terms involving $M(x)$ and $N(x)$. If the elastic properties of the two regions are different, then these terms are somewhat lengthy, and their full form is given in the Appendix. For the particular case where regions 1 and 2 have the same elastic properties, these equations result simply in the usual approximation to the biharmonic equation

$$20\phi_0-8\Sigma\phi_1+2\Sigma\phi_5+\Sigma\phi_9+F=0 \tag{15}$$

with $F=\dfrac{a^3N(x)}{A}$ for points on the mesh line coinciding with the interface

$F=\dfrac{-a^2M(x)}{2A}$ for points on the mesh line above the interface

$F=\dfrac{+a^2M(x)}{2A}$ for points on the mesh line below the interface.

In the preceding equation, ϕ stands for the real value of either stress function at the appropriate point. It is necessary, however, to calculate fictitious values of ϕ and θ near the boundary for the subsequent stress computation.

The displacement adjustment may now be carried out using conventional relaxation procedures. The stress function has zero slopes on all external boundaries, and, if the initial values of the stress function are taken as zero, it can be seen from equation (15) that initial residuals appear at mesh points along the interface as well as at points on the two mesh lines adjacent to the interface. The liquidation of these residuals will usually be confined to an area close to the interface. Stresses from the corrective solution are added to those of the particular solution to obtain the final values.

The simplicity of the initial setting up of the corrective solution can now be appreciated. The only subsidiary calculation required is to find the $M(x)$ and $N(x)$ values at appropriate points.

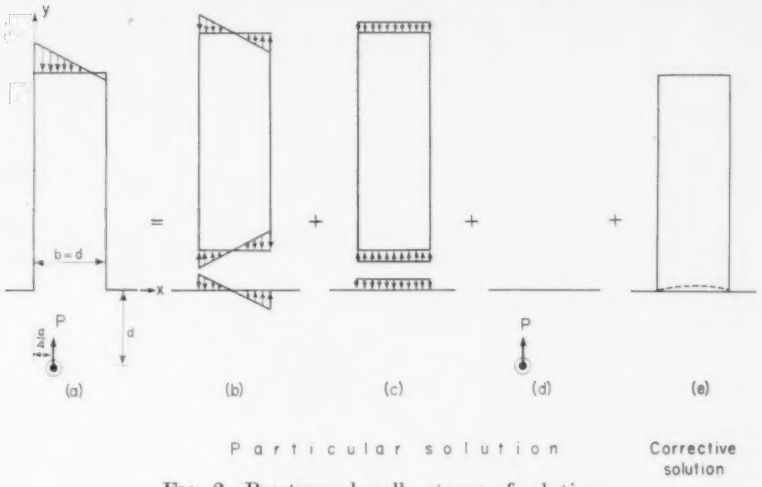

FIG. 2. Prestressed wall—stages of solution.

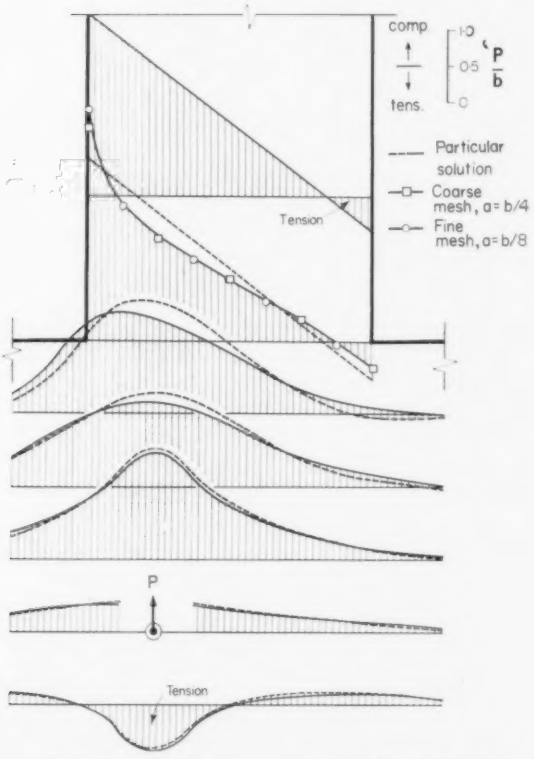

FIG. 3. Vertical stresses—example of Fig. 2.

An example

The problem shown in Fig. 2(a) is presented as a numerical example. This situation represents a prestressed wall with the prestressing force linearly distributed over the top of the wall and resisted by a concentrated force within

Vol. 2
1960-61

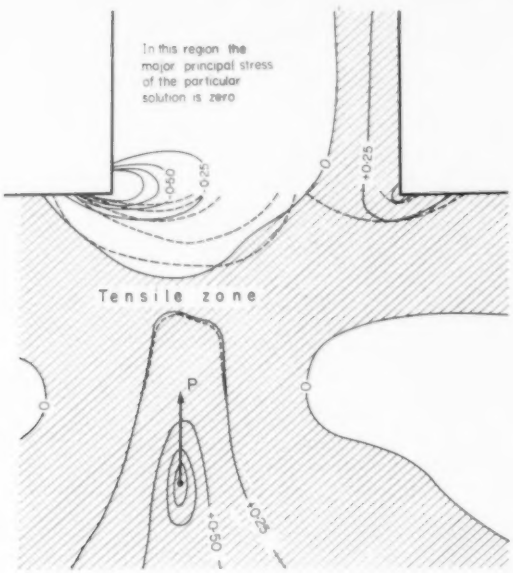

FIG. 4(a). Contours of equal major principal stress ($\sigma \times P/b$):— — — — principal stresses—particular solution; ———— principal stresses—complete solution.

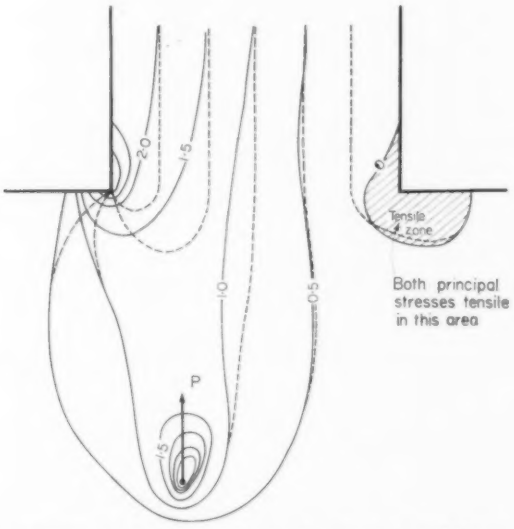

FIG. 4(b). Contours of minor principal stress ($\sigma \times P/b$):— — — — principal stresses—particular solution; principal stresses—complete solution.

the foundation. For the particular solution the vertical stresses within the wall were assumed to vary linearly, and the horizontal and shear stresses to be zero (a trivial but exact solution). With the interface taken as the line separating

the wall from the foundation, the particular solution for the latter region results from the linear surface loadings shown in Fig. 2(b) and (c), and the internal concentrated force shown in Fig. 2(d). The stress distributions from these loadings can be computed from known elasticity solutions.[3–5]

In this example the wall was assumed to have the same elastic properties as the foundation, and Poisson's ratio was assumed to be zero. This simplifies appreciably the computation of the $M(x)$ and $N(x)$ values.

Fig. 3 shows a plot of the vertical stresses. It is of particular interest to observe how quickly the uncorrected stresses of the particular solution (shown by dashed lines) approach the true stresses (full lines) on sections progressively farther away from the interface. Also of interest is the fact that the corrective stresses computed on a very coarse mesh are almost indistinguishable from the fine mesh values.

Vol. 2
1960-61

The last two observations illustrate several important advantages of the method. In many instances it is unnecessary to perform any correction whatsoever. If a correction is deemed necessary, a coarse relaxation mesh will often give sufficient accuracy, since a relatively low degree of precision in the correction calculation still enables good accuracy to be attained for the entire problem. It is quite simple to ascertain the degree of precision being achieved in the computation since a very rough calculation will soon indicate the order of magnitude of the correction.

Fig. 4(a) and (b), showing contours of maximum and minimum principal stresses, concludes the example. Again, the close agreement between the principal stresses from the particular solution (dashed lines), and those of the complete solution (full lines), should be noted.

FURTHER APPLICATIONS—THERMAL DISCONTINUITIES

Precisely the same techniques may be used to determine the stresses in a wall under hydrostatic or gravity loading, where the method has considerable advantage over the techniques used previously[6] and reduces the amount of computation required.

On occasion it may be impossible to obtain an exact particular solution. If, however, it is known that an approximate solution (e.g. one derived by the engineering bending theory) is valid with some small error, then it is possible to obtain the complete solution within the limits of that error.

Another instance where the method is always rewarding is the case of stress distributions resulting from steady-state temperature variations in bodies where sharp discontinuities, of temperature or elastic and thermal properties of the material, occur at an interface. It is known[7] that no stresses are developed within a homogeneous and singly connected region subject to two-dimensional heat flow if the temperature field obeys

$$\nabla^2 T = 0$$

It then follows that the particular solution in the regions separated by the discontinuity is zero. However, on the line of the discontinuity (assumed straight and parallel to the x-axis as before) a lack of fit due to the initial

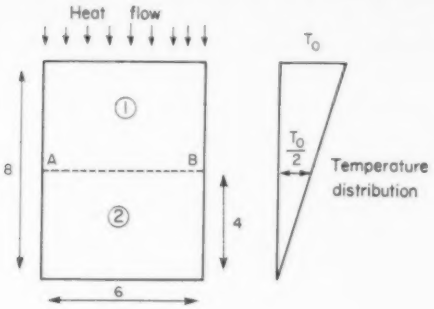

$$\alpha_1 = 2\alpha \quad \alpha_2 = \alpha$$
$$E_1 = E_2 \quad \nu_1 = \nu_2$$

FIG. 5. Thermal stress problem with discontinuous coefficient of expansion α.

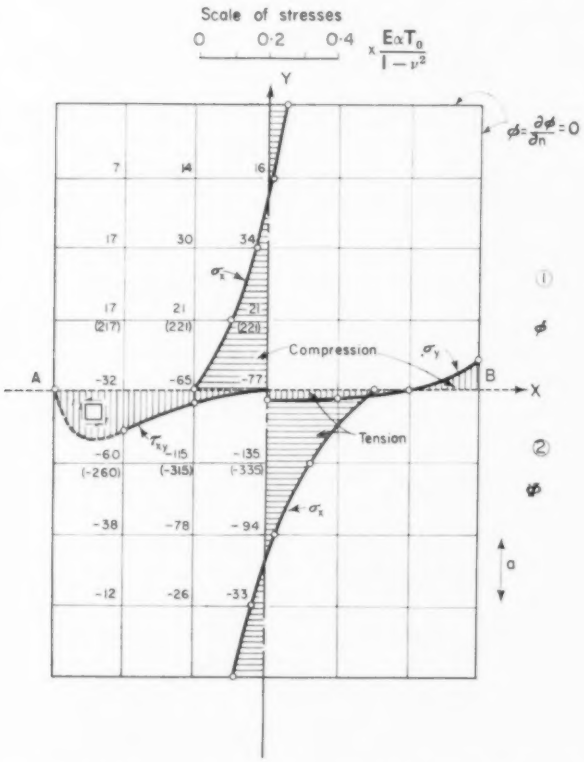

FIG. 6. Thermal stresses on the interface and axis of symmetry—example of Fig. 5. (The numbers are values of stress function divided by $(a^2 E\alpha T_0)/[800(1-\gamma^2)]$. Figures in parentheses are appropriate fictitious values.)

thermal strain occurs, as given by

$$\left(\frac{\partial u}{\partial x}\right)_1' - \left(\frac{\partial u}{\partial x}\right)_2' \equiv M(x) = \alpha_1 T_1 - \alpha_2 T_2 \tag{16}$$

and

$$\left(\frac{\partial^2 v}{\partial x^2}\right)_1' - \left(\frac{\partial^2 v}{\partial x^2}\right)_1' \equiv N(x) = \frac{\partial}{\partial y}(\alpha_1 T_1) - \frac{\partial}{\partial y}(\alpha_2 T_2) \tag{17}$$

The restoration of continuity by a corrective solution follows exactly the same procedure as before, the only departure being that now the final stress system is merely that due to the correction.

As an example of such an application, consider the simple case of a linear temperature distribution through the rectangular prism shown in Fig. 5. The elastic properties of the material and the thermal conductivity are assumed uniform throughout, but the coefficient of expansion of part 1 is taken to be twice that of part 2.

Vol. 2
1960-61

The results shown in Fig. 6 are obtained by relaxation of three lines of initial residuals [given by equation (15)] on and near the interface AB with zero values of ϕ and its slopes on all external boundaries. This simple example illustrates the applicability of the general procedure to this and other problems of thermal stresses. It is of interest that the techniques developed earlier for such a class of problems by one of the authors[8] resulted in identical approximations for the simple case of a temperature discontinuity. However, the earlier method gives less accurate results in other applications, and in any case gives only rough results for the stresses at the discontinuity itself. The present method gives very precise answers in this critical region.

In Fig. 6, in addition to the final results, the actual computed values of the stress functions ϕ and θ are shown, and the fictitious values of ϕ inside region 2 on the first mesh line and the corresponding values of θ inside region 1 should be noted. These fictitious values are determined directly from interface relations [equation (11)] after the relaxation is accomplished.

CONCLUSION

The novel method of attack on the wide range of problems described in this paper is shown to be very effective and labor-saving whenever it can be applied. In addition to the advantages already enumerated, the philosophy of the approach (best illustrated in the example of a prestressed wall, in which a reasonable, statically correct, system of stresses is taken as the starting point of the computation) follows the method used effectively in structural analysis and often permits the effect of the corrective stress system to be localized.

REFERENCES

1. O. C. Zienkiewicz and R. W. Gerstner, *Proc. Amer. Soc. Civ. Engrs.* **87**, P.O.1 (1961).
2. O. C. Zienkiewicz and R. W. Gerstner, *Int. J. Mech. Sci.* **2**, 93 (1960).
3. S. D. Carothers, *Proc. Roy. Soc.* **A97**, 119 (1920).
4. E. Melan, *Z. angew. Math. Mech.* **12**, 343 (1932).
5. J. Dundurs, Dissertation, Northwestern University (1958).
6. O. C. Zienkiewicz, *J. Instn. Civ. Engrs.* **27**, 244 (1947).
7. S. Timoshenko, *Theory of Elasticity*. McGraw-Hill, New York (1951).
8. O. C. Zienkiewicz, *Min. Proc. Instn. Civ. Engrs.* **4**, 88 (1955).

APPENDIX

For the case when the two regions separated by the interface have different elastic properties, the special finite-difference equations for the stress function on and near the interface are identical to equations (24) and (25) of Ref. 2, except for the appearance of the additive terms involving $M(x)$ and $N(x)$.

For a point on the interface the following terms are added to the left side of equation (24):

$$\frac{-a^2 M_0(x)}{(A_1+A_2)^2}(2A_2-2A_1+2A_1 B_1-2A_2 B_2)$$

$$\frac{-a^2 M_1(x)}{(A_1+A_2)^2}(A_2 B_2-A_1 B_1)-\frac{a^2 M_3(x)}{(A_1+A_2)}(A_2 B_2-A_1 B_1)$$

$$\frac{+2a^3 N_0(x)}{A_1+A_2}$$

For a point one mesh above the interface the following term is added to the left side of equation (25):

$$-\frac{a^2 M_0(x)}{A_1+A_2}$$

while a change of sign in the preceding term is necessary in the appropriate equation for a point one mesh below the interface. In the preceding equations the subscripts 0, 1 and 3 used with the $M(x)$ and $N(x)$ terms refer to points numbered 0, 1 and 3 using the usual relaxation nomenclature.

It can be seen that if both regions have the same elastic properties (i.e. $A_1 = A_2$ and $B_1 = B_2$) the additive terms given above reduce to those shown in equation (15).

Int. J. Mech. Sci. Pergamon Press Ltd. 1961. Vol. 2, pp. 277–293. Printed in Great Britain

LOAD DISTRIBUTION IN OVERHEAD STRANDED CONDUCTORS

P. MONTAGUE
Department of Engineering, University of Manchester

(*Received* 27 *May* 1960)

Summary—The paper attempts to forecast the load taken by each strand of a steel-cored aluminium conductor at different total cable loads, by considering the fundamental load–strain characteristics of the steel and aluminium elements.

Vol. 2
1960-61

INTRODUCTION

THE long-term problem requiring solution involves the prediction of the time-sag characteristics of overhead lines. Since this sag is almost certainly due mainly to creep in the aluminium strands of the cable, and creep cannot be

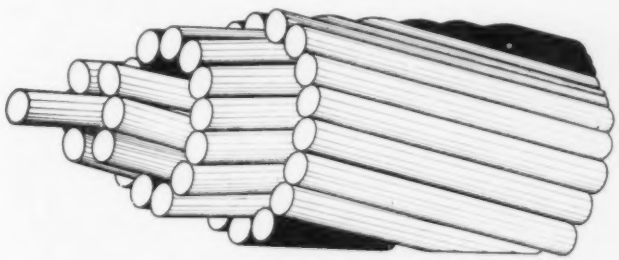

FIG. 1. Detail of cable.

tackled without a knowledge of the loads involved, it is necessary first to establish the proportion of total cable load carried by the various strands. The main interest here is in the 37-strand steel-cored aluminium conductor. With strands of 0·110 in. diameter this cable is commonly used throughout Great Britain in overhead-line work. It consists of a central steel core wire, surrounded immediately by a helix-layer of six more steel wires, on top of which are two more layers of aluminium wires, also laid in helix form. The first aluminium helix contains twelve wires and the second contains eighteen wires. Each successive helix is laid so that its wires cross those of the layer below, this type of construction being known as contra-lay. Fig. 1 shows a detail of the cable. All strands are of equal diameter.

In 1941 the British Electrical and Allied Industries Research Association issued a report (referred to below as F/T139) by Tuck and Double[1] describing experimental work designed to find the proportion of load taken by the steel in S.C.A. conductor of 37/0·102 in. strand construction, i.e. 37 strands, each of 0·102 in. diameter, 7 being steel and the remaining 30 being aluminium. This work established the distribution of load between the steel as a whole and the

aluminium as a whole, but did not attempt to find the detailed load distribution, e.g. within the aluminium helices.

It has been found that by working from the tensile load–strain characteristic curves of single aluminium and steel wires, a value of the effective modulus and values of load distribution can be derived, which agree reasonably well with the experimental values for 37/0·102 in. S.C.A. conductor presented in F/T139.

PRELIMINARY TESTS

Since, in the method described in the next section, the estimation of load at any strain in a particular strand of the cable is to be deduced from curves obtained by separate tensile tests on that strand, it was necessary not only to perform such tests, but to establish that the curves obtained were representative of the wire in its stranded condition.

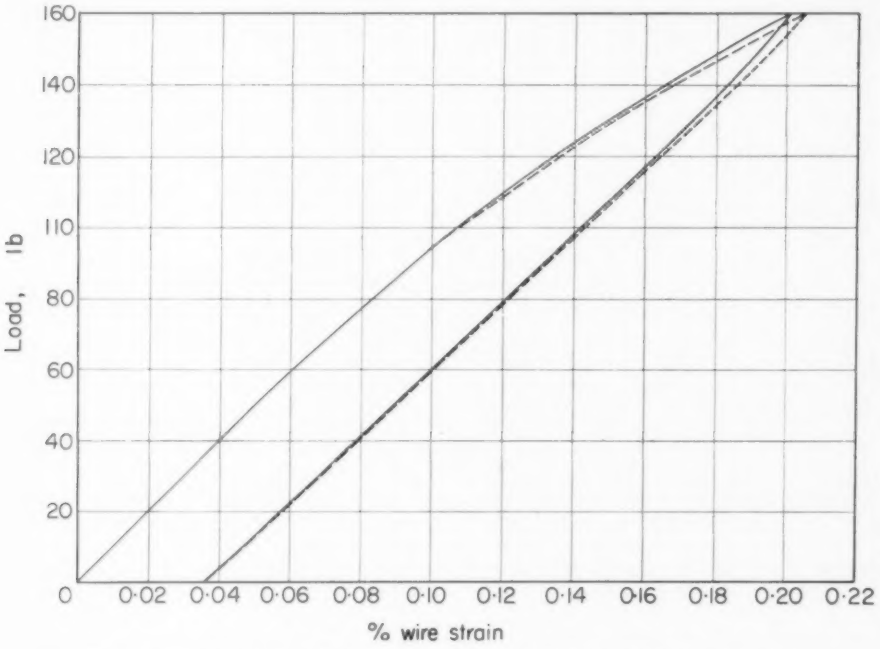

FIG. 3. Comparison of stranded and unstranded 0·110-in. diameter aluminium wire during first loading cycle (———— stranded; — — — — — — unstranded).

By tensile testing a length of wire in its unstranded condition side by side with a length of stranded wire originally from the same coil, it was possible to decide whether the difference in cold work experienced by the two wires was of significance in changing the load–strain characteristics. If there was a significant difference between the behaviour of wire which had simply been straightened from coil form for testing, and that of wire which had been formed into a helix and then unformed again for testing, it follows that any separate test would not adequately represent the behaviour of the stranded wire in the cable.

Each wire in a length of 37/0·110-in. S.C.A. conductor was individually numbered corresponding to the coil from which it had been stranded on to the cable. Unstranded samples from each coil, also numbered, enabled comparative tests to be carried out. A length of each aluminium wire was extracted from the cable and straightened for tensile testing. The straightening was done between staggered rollers as shown in Fig. 2. Since,

Vol. 2
1960-61

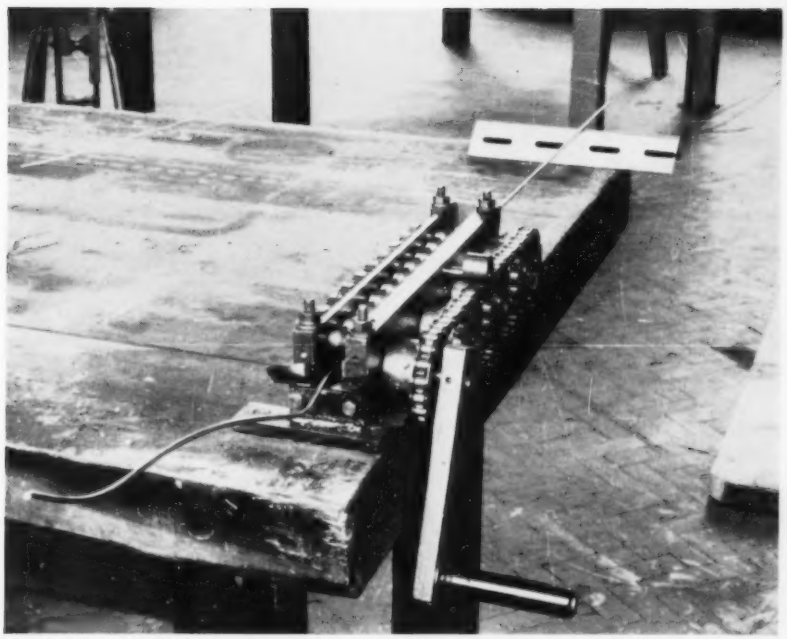

FIG. 2. Staggered rollers for straightening wire.

Vol
196

in the stranding process, the wires are bent into their helical shape (i.e. they are not twisted about their own axis), rollers were used in order to *un*bend them, i.e. an attempt was made to reverse the stranding operation. In this way the amount of cold work performed on the wires during straightening was to some extent controlled. Also, it was felt wise to straighten the wire without resort to pulling, which would jeopardize the subsequent tensile tests, where the first loading cycle is all-important. In fact, even with soft material such as commercially pure aluminium, a considerable axial load is required to straighten it from helix form.

The unstranded wire had to be straightened too, since it was in coil form. Thus, before testing, two samples of wire, originally from the same coil, had been subjected to different amounts of cold work, this difference being greater than that between the straightened, unstranded wire and the wire as stranded on the cable.

Each strand from the cable was tested through several tensile loading cycles to strains varying from 0·05 to 0·3 per cent, and the corresponding unstranded wires given precisely the same treatment.

A typical first-cycle aluminium load–strain curve is shown in Fig. 3, indicating the close similarity between the behaviours of the stranded and unstranded samples. However, it should be noted that, as the strain increases, that in the unstranded wire is greater than that in the stranded wire. This point is referred to later.

Vol. 2
1960-61

No appreciable variation in behaviour was noted between stranded wires from different helices of the cable, although they had been bent to different radii of curvature in stranding.

In view of these tests it was decided to use the load–strain curves of the stranded wires as a basis for the derivation of the load distribution in the cable.

At 0·1 per cent strain, the mean nominal stress value for the stranded aluminium wires was found to be $10{\cdot}02 \times 10^3$ lb/in^2, the variations on this figure being from $9{\cdot}83 \times 10^3$ lb/in^2 to $10{\cdot}2 \times 10^3$ lb/in^2. The mean value of E, Young's modulus, in the second loading cycle was $10{\cdot}03 \times 10^6$ lb/in^2 and on the third cycle $10{\cdot}05 \times 10^6$ lb/in^2.

The steel wires were tested only in their unstranded form, as the difficulties of straightening the stranded form are considerable. In this cold-drawn condition, the tensile load–strain characteristic for the steel is slightly non-linear.

METHOD—ASSUMPTIONS AND LIMITATIONS

If the entire cable is supposed to have a certain linear strain due to an unknown axial load, knowing the geometrical properties of the constituent wires, a close approximation to the corresponding linear strain of each one can be easily calculated. Knowing also the load–strain characteristic of each wire, both of steel and aluminium, the tensile load in each wire corresponding to the particular wire-strain is known. The addition of the components of all the individual wire loads in the axial direction of the cable is considered to be the external load on the cable required to produce the given cable strain.

By taking a series of cable strains, from zero to any desired value, working out the individual wire strains and noting the consequent loads in the wires, a curve can be plotted of total cable load against cable strain. This can obviously be done for as many cycles of cable loading as may be desired, provided the curves for a similar number of loading cycles are available for the individual wires.

The procedure outlined above consists essentially of relating the tensile load, in the wires of the stranded cable under load, to the tensile load in individual wires under separate tests by equating the tensile strains. This procedure would be perfectly valid if either of two conditions existed: (i) that the elements of the cable remained elastic, or (ii) that the strands of the cable were in a state

of pure tension. Unfortunately, neither of these two conditions does exist. As will be seen later, the aluminium wires very quickly became non-elastic under load. Also, as will be shown, the wires in the cable are subjected not only to tension, but also to shear, bending and twisting. Whereas the presence of shear, bending and twisting would not affect the tensile load–strain characteristic if the wires remained purely elastic, this is no longer true when they become non-elastic. Thus, the question arises of the effect of shear, bending and torsion on the tensile behaviour of a plastic specimen. It is a question which cannot easily be answered with the present available knowledge on the subject. It remained therefore to justify the method used by demonstrating that the magnitude and influence of the shear, bending and twisting loads are small and negligible in the presence of the tensile load. This has been done by analysing the elastic case of the helical wire under these loads, finding their relative magnitude and assuming that they will be of the same order in the plastic case.

RELATION BETWEEN CABLE-STRAIN AND WIRE-STRAIN

Consider a length l of cable, as shown in Fig. 4(a), extended under load a distance e. If the ends of the cable are restrained against rotation about the cable axis, point A on one strand moves in the axial direction of the cable to point A'. Fig. 4(b) shows one strand wound round a central core-wire of constant diameter, centre X. If point O is at the centre of the helix strand, OS is the direction of the helix at O, and OL is perpendicular to XO and to the axial direction of the centre strand, then the angle $LOS = \alpha$, which is defined as the helix angle.

In Fig. 4(c) the strand is shown unwound over the length l of the cable. The initial length of the strand will be s, where $s = OA$. With the application of tensile load to the cable, since rotation is completely prevented by the grips, the strand assumes the position OA', i.e. it is extended amount δs and rotated through angle $\delta\alpha$.

Now $$e = \delta l_1 + \delta l_2$$

and $$\delta l_2 \simeq (s+\delta s)\,\delta\alpha\cos\alpha \simeq s.\delta\alpha\cos\alpha$$

thus $$e = \delta s.l/s + \delta\alpha.s.\cos\alpha$$

hence $$e/l = \delta s/s + \delta\alpha\cot\alpha \quad \text{since} \quad s/l = 1/\sin\alpha$$

i.e. $$\epsilon_c = \epsilon_s + \delta\alpha\cot\alpha$$

where ϵ_c is the cable-strain and ϵ_s the strand-strain.

Now $$s\delta\alpha \simeq A'B \simeq e\cos\alpha$$

therefore $$\delta\alpha\cot\alpha = e\cos^2\alpha/s\sin\alpha$$
$$= e\cos^2\alpha/l = \epsilon_c\cos^2\alpha$$

Thus, $$\epsilon_c \simeq \epsilon_s + \epsilon_c\cos^2\alpha$$

i.e. $$\epsilon_s \simeq \epsilon_c\sin^2\alpha$$

This relationship between ϵ_c and ϵ_s is correct to second-order quantities. ϵ_s is due entirely to axial tensile load in the strand, but the fact that the strand must rotate through the angle $\delta\alpha$ to its final position means that bending and twisting have also taken place. Thus, the extended strand is in a complex state of stress and not in simple tension. It has been assumed, of course, that the diameter of the helix remains constant. This assumption seems reasonable since, on dismantling an overhead conductor which has been in service for many years, no evidence is found of nicking or indentation where the wires of one helix cross those of the underlying helix. With contra-lay, there are obviously regular points at which a wire in an outer helix crosses the wires lying beneath it, and, with a soft material such as aluminium, some evidence of high radial pressure at these points would be expected

to show. The lack of such evidence points rather to the suggestion that "tubing" takes place, i.e. each complete helix-layer acts as a tube with high lateral pressure between the strands. There is geometrical evidence to support this suggestion since, owing to the helices, a cross-section through the cable shows a circular centre strand surrounded by a number of ellipses, their longer axes being greater than the wire diameter. Thus, if a straight centre wire surrounded by six wires in helix form is considered, due to the increased lateral dimension of the helix wires in cross-section, they cannot all touch the core wire if all seven are of equal diameter. They will touch each other and thus be prevented from exerting high radial pressure on the core, causing the tubing effect. Referring to Fig. 4(c), if the load taken by any strand in the axial direction of the cable is P, then F, the direct load on the strand, is $P \sin \alpha$, and Q, the shear load on the strand, is equal to $P \cos \alpha$.

Vol. 2
1960-61

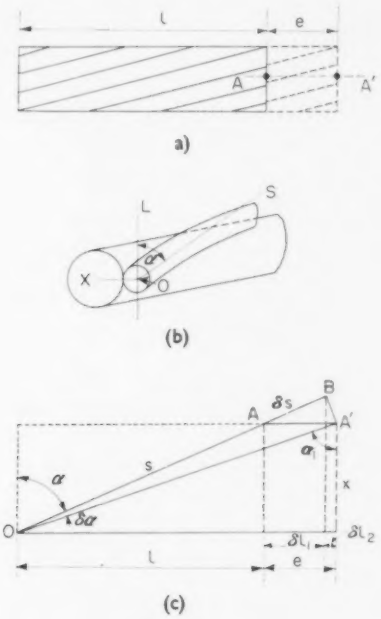

FIG. 4.

If r is the radius of the helix XO, then, in the unstrained condition, the strand curvature is $\cos^2 \alpha/r = 1/R_1$ and the twist per unit length of strand $= \sin \alpha \cos \alpha/r$.

After the strain has taken place and the strand has assumed its new position OA', its curvature is

$$\cos^2 (\alpha+\delta\alpha) = 1/R_2$$

and

$$\cos (\alpha+\delta\alpha) = \cos \alpha_1 = x/(s+\delta s)$$

so that

$$1/R_2 = \frac{1}{r}\frac{x^2}{(s+\delta s)^2}$$

Twist per unit length of strand $= \sin \alpha_1 \cos \alpha_1/r$

$$= \frac{1}{r}\frac{(l+e)}{(s+\delta s)}\frac{x}{(s+\delta s)} = \frac{1}{r}\frac{x(l+e)}{(s+\delta s)^2}$$

The change in curvature is

$$(1/R_1 - 1/R_2) = \frac{1}{r}\frac{x^2}{s^2} - \frac{1}{r}\frac{x^2}{(s+\delta s)^2}$$

$$= \left(\frac{x}{s}\right)^2 \frac{1}{r}\frac{2\epsilon_s}{(1+2\epsilon_s)} = \frac{\cos^2 \alpha}{r}\frac{2\epsilon_s}{1+2\epsilon_s}$$

Similarly, the change in twist/unit length of the strand is

$$\frac{\sin\alpha\cos\alpha}{r}\frac{2\epsilon_s-\epsilon_c}{1+2\epsilon_s}$$

The bending moment required to change curvature

$$M = EI\frac{\cos^2\alpha}{r}\frac{2\epsilon_s}{1+2\epsilon_s}$$

and the torque required to change the twist/unit length

$$T = GJ\frac{\sin\alpha\cos\alpha}{r}\frac{2\epsilon_s-\epsilon_c}{1+2\epsilon_s}$$

Putting F, Q, M and T into terms of ϵ_c by using the relationship

$$\epsilon_s = \epsilon_c\sin^2\alpha$$

we have that

$$F = AE\epsilon_c\sin^2\alpha$$

where

A = area of the strand

$$Q = AE\epsilon_c\sin\alpha\cos\alpha$$

$$M = \frac{EI}{r}\sin^2\alpha\cos^2\alpha\frac{2\epsilon_c}{1+2\epsilon_c\sin^2\alpha}$$

$$T = \frac{GJ}{r}\sin\alpha\cos\alpha\epsilon_c\frac{1-2\sin^2\alpha}{1+2\epsilon_c\sin^2\alpha}$$

where E, G, I and J refer to the strand.

To consider the elastic case, the following values are used:

$A = 0{\cdot}0095$ in^2 $\qquad E = 2{\cdot}5G = 10\times10^6$ lb/in^2

$I = 0{\cdot}0718\times10^{-4}$ in^4 $\qquad J = 2I$

$\alpha = 80°$ $\qquad r = 0{\cdot}22$ in.

$\epsilon_c = 0{\cdot}001$

The expressions above show M and T to be very small in magnitude compared with F; when $\epsilon_c = 0{\cdot}001$, $F = 92$ lb, direct stress $= 9690$ lb/in^2, $Q = 16{\cdot}22$ lb, shear stress $= 1710$ lb/in^2, $M = 0{\cdot}0191$ lb-in. The direct stress due to bending is 146 lb/in^2; $T = 0{\cdot}042$ lb-in. The shear stress due to torsion is 161 lb/in^2. Thus, the stresses due to M and T are negligible compared with those due to F. The angle α varies from one helix to the next in the cable. The British Standard 215 Part 1, 1956, allows the manufacturer some latitude to accommodate the stranding machines.

α is defined by the lay-ratio where

$$\text{lay-ratio} = \frac{\text{axial length of complete helix}}{\text{mean diameter of the helix}}$$

Table 1 gives the limits which apply to the 37-strand conductor, and the consequent tolerances on the helix angle.

TABLE 1

Helix	Lay-ratio	Helix angle
Steel core	20–30	80° 58′–83° 59′
12-Wire helix	14–21	77° 02′–81° 24′
18-Wire helix	11·25–14	73° 48′–77° 02′

The following work is based on the lower limits of lay-ratio, i.e. on a tight cable.

Vol. 2
1960-61

MODULUS OF ELASTICITY AND LOAD-RATIO 37/0·102-in. S.C.A. CONDUCTOR

In the Report F/T139, dealing with 37/0·102-in. S.C.A. conductor, the modulus of elasticity was measured experimentally, and the load distribution between the total steel area and the total aluminium area determined by the use of a magnetic-flux method. (This method relates the change in permeability of the steel to its tensile load.) The "load-ratio" was found for varying total cable-loads, where

$$\text{load-ratio} = \frac{\text{load carried by steel}}{\text{total cable load}}$$

The procedure outlined above will therefore be applied first to the 37/0·102-in. S.C.A. conductor to correlate the experimental evidence of F/T139.

The following symbols are used:

ϵ_c = strain of cable in its axial direction
$\epsilon_{s_0} = \epsilon_c$ = strain of centre straight strand (steel)
ϵ_{s_1} = strain of any strand in the first helix (steel)
ϵ_{s_2} = strain of any strand in the second helix (aluminium)
ϵ_{s_3} = strain of any strand in the third helix (aluminium)

and P_{s_0}, P_{s_1}, P_{s_2}, P_{s_3} are the strand loads in the direction of their own axes. Then

$$\epsilon_{s_1} = \epsilon_c \sin^2 \alpha_1; \quad \epsilon_{s_2} = \epsilon_c \sin^2 \alpha_2; \quad \epsilon_{s_3} = \epsilon_c \sin^2 \alpha_3$$

where α_1, α_2 and α_3 are the respective helix angles, and are taken as 80° 58′, 77° 02′ and 73° 48′.

The load along the cable axis due to P_{s_1} is $P_{s_1}/\sin \alpha_1$, so that the total load taken by the first helix in the direction of the cable will be $P_1 = 6P_{s_1}/\sin \alpha_1$, and the corresponding loads in the second and third helices will be $P_2 = 12P_{s_2}/\sin \alpha_2$ and $P_3 = 18P_{s_3}/\sin \alpha_3$, respectively. The total steel load (P_{ST}) is

$$P_{ST} = P_{s_0} + 6P_{s_1}/\sin \alpha_1$$

and the total aluminium load (P_{AL}) is

$$P_{AL} = 12P_{s_2}/\sin \alpha_2 + 18P_{s_3}/\sin \alpha_3$$

P_{ST} and P_{AL} are taken in the direction of the cable, so the total cable-load (P_C) is

$$P_C = P_{ST} + P_{AL}$$

and

$$\text{the load-ratio} = P_{ST}/P_C$$

In Table 2 values of ϵ_{s_1}, ϵ_{s_2} and ϵ_{s_3} are given corresponding to values of ϵ_c from 0 to 0·003. For example, an axial strain of 0·001 on the cable produces strains in strands of the first, second and third helices of 0·000975, 0·00095 and 0·000922 respectively, using the relationship $\epsilon_s = \epsilon_c \sin^2 \alpha$. Fig. 5 shows a typical load–strain curve for the 0·110-in. diameter aluminium strand, and Fig. 6 a typical load–strain curve for the 0·110-in. diameter steel strand. The same curves can be used for the 0·102-in. diameter strands simply by multiplying the load-ordinates at any particular strain by the ratio of the areas of the two types of strand.

Now, by considering a series of strains on the cable, referring to Table 2 for the strand strains, and applying to load–strain curves for the aluminium and steel wires, a corresponding series of loads can be deduced for the various strands, viz. P_{s_0}, P_{s_1}, P_{s_2} and P_{s_3}. From these individual wire loads at various cable-strains, the total cable-load can be calculated.

TABLE 2

$\epsilon_C = \epsilon_{s_0}$	ϵ_{s_1}	ϵ_{s_2}	ϵ_{s_3}
0	0	0	0
0·0002	0·000195	0·000190	0·0001844
0·0006	0·000586	0·000570	0·000553
0·0010	0·000975	0·000950	0·000922
0·0014	0·001366	0·001330	0·001291
0·0018	0·001757	0·001710	0·001660
0·0022	0·002145	0·002090	0·002030
0·0026	0·002535	0·002470	0·002395
0·0030	0·002927	0·002850	0·002766

For example, Figs. 5 and 6 show typical load–strain curves for the 0·110-in. aluminium and steel wires respectively. As mentioned above, these can be used also for finding the load in 0·102-in. strands at any particular strain, by multiplying the load ordinate on the graph by A_2/A_1 where A_1 = area of a 0·110-in. diameter strand and A_2 = area of a 0·102-in. diameter strand. Fig. 5 shows three cycles of loading to find P_{s_3} in the 37/0·102-in. S.C.A. conductor loaded to $P_C = 7500$ lb, and similar cycles to find P_{s_2} for three cycles of loading in the 37/0·110-in. S.C.A. conductor loaded to $P_C = 11{,}500$ lb. Fig. 6 shows the corresponding cycles for P_{s_1} in both cables.

Similar cycles must be plotted in each case for P_{s_0} and P_{s_3}, since the cyclic curves for each helix will not be exactly the same owing to the slight difference in strain of each helix at a given cable strain.

Thus, the 37/0·102-in. S.C.A. conductor was taken through a series of loading cycles, the cable-load P_C being calculated as outlined previously, i.e.

$$P_C = P_{ST} + P_{AL} = P_{s_0} + 6P_{s_1}/\sin\alpha_1 + 12P_{s_2}/\sin\alpha_2 + 18P_{s_3}/\sin\alpha_3$$

Table 3 gives the helix loads and the load-ratios for the "uploading" legs of the first and third cycles with the 37/0·102-in. S.C.A. conductor, derived in this way. The helix loads in Table 3 are shown graphically in Fig. 7, where the difference in distribution of load between the steel and aluminium from the first loading to the third loading is shown clearly. This is due to the large permanent set suffered by the aluminium (see Fig. 5) at the end of the first loading cycle, and, to a much lesser degree, to the further permanent set after the second cycle. The permanent set continues to reduce rapidly with succeeding cycles. Thus, in Fig. 7 the steel takes the entire load in the third cycle until a cable strain exceeding 0·03 per cent is reached, when the aluminium commences to take some of the load. The effect of this can be seen on the load–strain cycles for the whole cable shown in Fig. 8, where the sudden change of

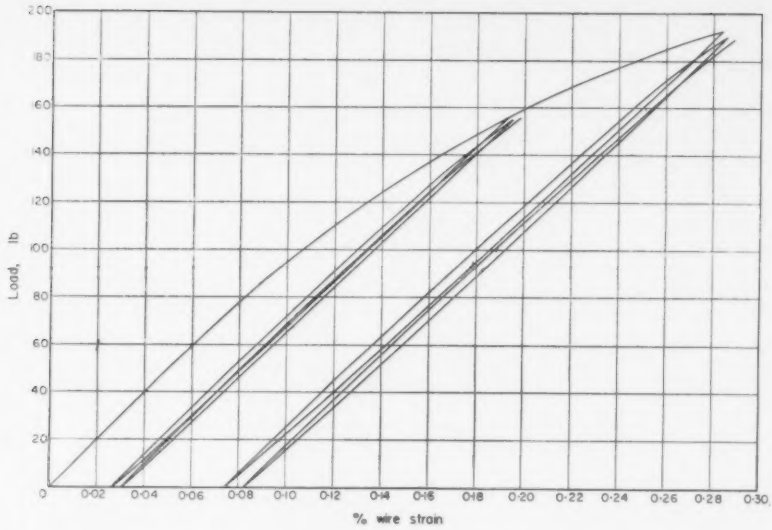

FIG. 5. Aluminium loading cycles for single wire used in the derivation of P_{s_2} for 37/0·102-in. (small cycles shown) and 37/0·110-in. (large cycles shown) S.C.A. conductors.

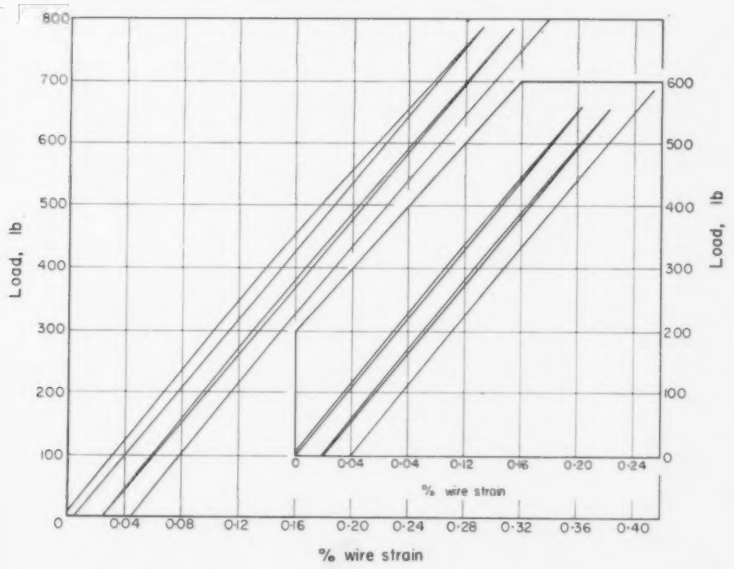

FIG. 6. Steel loading cycles for single wires used in the derivation of P_{s_2} for 37/0·102-in. (small cycles shown) and 37/0·110-in. (large cycles shown) S.C.A. conductors. Second and third cycles are moved 0·02 per cent strain to the right for clarity.

Vol. 2
1960-61

TABLE 3. DERIVED LOAD DISTRIBUTION IN 37/0·102-in. S.C.A. CONDUCTOR FOR FIRST AND THIRD LOADINGS

	ϵ_c	P_{s_0}	Steel helix load (lb)	Inner alum. helix load (lb)	Outer alum. helix load (lb)	Load-ratio
First loading	0	0	0	0	0	
	0·0002	54	318	206	300	0·4235
	0·0004	104	611	416	605	0·4115
	0·0006	151	898	606	894	0·4115
	0·0010	247	1468	969	1435	0·4160
	0·0014	340	2036	1273	1898	0·4283
	0·0018	431	2570	1525	2280	0·4410
	0·0020	477	2830	1636	2442	0·4480
	0·0022	520	3095	1737	2600	0·4540
Third loading	0	0	0	0	0	
	0·0002	43	264	0	0	1·0
	0·0004	93	564	100	126	0·7450
	0·0006	141	846	286	418	0·5830
	0·0010	237	1416	678	999	0·4970
	0·0014	332	1953	1060	1567	0·4660
	0·0018	428	2550	1420	2110	0·4580
	0·0020	472	2800	1580	2350	0·4550

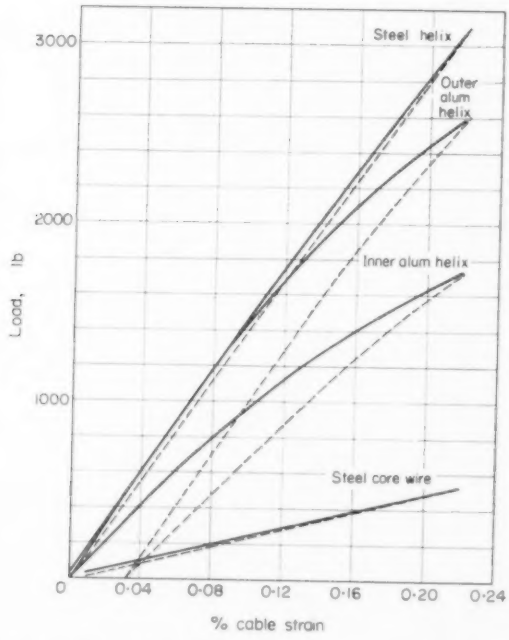

FIG. 7. Derived load distribution in 37/0·102-in. S.C.A. conductor for first and third loadings to P_C = 7500 lb (———— denotes first loading; — — — — denotes third loading).

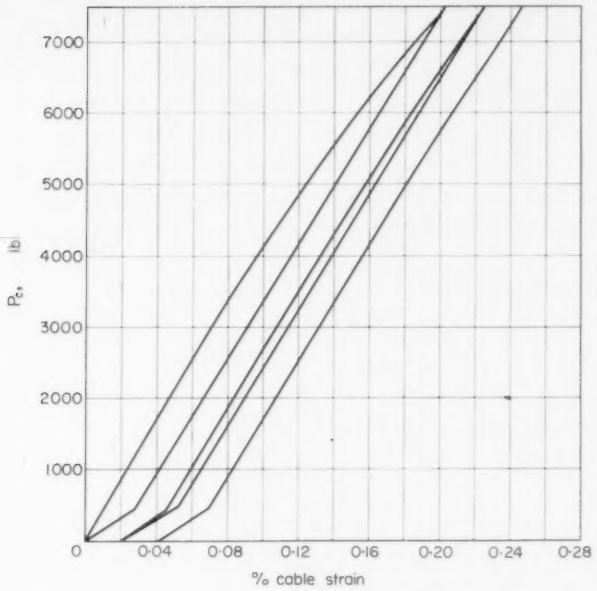

FIG. 8. Derived loading cycles for 37/0·102-in. S.C.A. conductor. Second and third cycles are moved 0·02 per cent strain to the right for clarity.

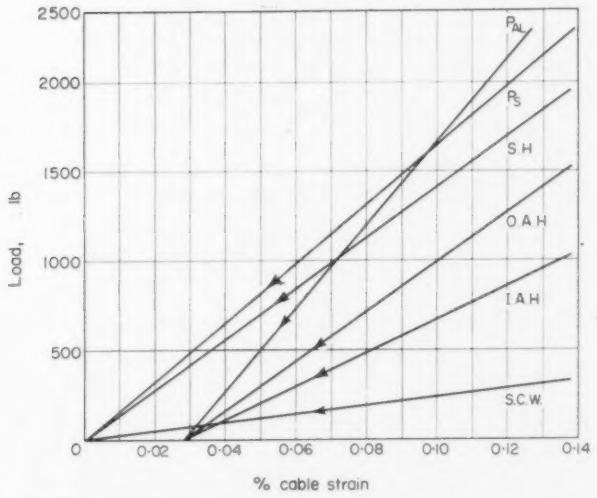

FIG. 9. Derived load distribution at end of first loading cycle for 37/0·102-in. S.C.A. conductor (S.H. = steel helix; O.A.H. = outer aluminium helix; I.A.H. = inner aluminium helix; S.C.W. = steel core wire).

slope on every curve, except the first up-loading, indicates the aluminium beginning or ceasing to take load. The condition at the end of the first load–strain cycle for the 37/0·102-in. S.C.A. conductor is clear from Fig. 9. The aluminium ceases to take load at 0·0285 per cent cable-strain, after which the steel carries the total load. At this point, the aluminium strands become slack on the cable, and remain so until the next loading cycle has raised the cable-strain to 0·0285 per cent again, when the aluminium has tightened and proceeds to carry load. This accounts for the great differences between the load-ratio values for the first up-loading and every subsequent one, as shown in Fig. 10 where the load-ratio values of Table 3 are shown graphically.

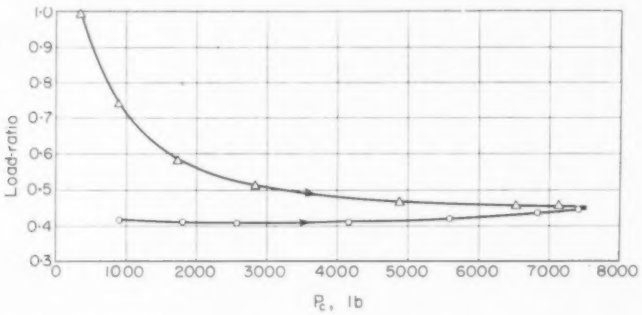

FIG. 10. Derived load-ratios for first and third loadings on 37/0·102-in. S.C.A. conductor (○ denotes first loading, △ denotes third loading).

The effective modulus of elasticity E for the 37/0·102-in. S.C.A. conductor calculated from Fig. 8 is $12{\cdot}7 \times 10^6$ lb/in². This figure is based on the total nominal area of the cable at right-angles to the load. F/T139 gives the values of E measured on two samples of 37/0·102-in. S.C.A. conductor. Sample B, stranded at 73·5°F and tested at 50°F, gave a value for E of $12{\cdot}1 \times 10^6$ lb/in². E is very little affected by temperature change, a temperature difference of 60°F causing only 2·5 per cent change in the measured E value. Sample A, stranded at an unknown temperature, but presumably in the region 70–75°F, gave a measured value of E at 47°F of $12{\cdot}3 \times 10^6$ lb/in². This difference of about 4 per cent between the measured and derived values of E may be due to the assumption of an ideal cable, initially straight. (The experimental values quoted from F/T139 were obtained with the cable in a horizontal position, and a small amount of sag between supports was present.) Also, F/T139 quotes the standard value of E for the aluminium in the cable as $9{\cdot}7 \times 10^6$ lb/in². As seen before, the value found experimentally for the derivation of E in the present case was $10{\cdot}05 \times 10^6$ lb/in².

Fig. 11 compares the load-ratio values obtained on samples A and B with those derived above (Table 3). Also on Fig. 11 is a derived load-ratio curve using the values of α_1, α_2 and α_3 given for sample A in F/T139. These were

$$\alpha_1 = 81^\circ\ 6'; \quad \alpha_2 = 82^\circ\ 18'; \quad \alpha_3 = 78^\circ\ 30'$$

α_1 is negligibly different from the value previously assumed, whereas α_2 and α_3 are considerably larger than those previously used (Table 1). The value of E calculated using the α-values shown above was again $12{\cdot}7 \times 10^6$ lb/in^2, but the load-ratios on the third loading were different, as shown in Fig. 11. Thus, the true comparison is between the derived curve for sample A and the experimental curve for sample A. No adjustment for temperature is required.

It will be noticed from Fig. 11 that the derived load-ratio curves lie below the experimental curves. This is almost certainly due to the bedding down of the aluminium helices in the experimental cases, whereas the derived curves have assumed an initially tight cable. In practice, it is noticed that on the first

Vol. 2
1960-61

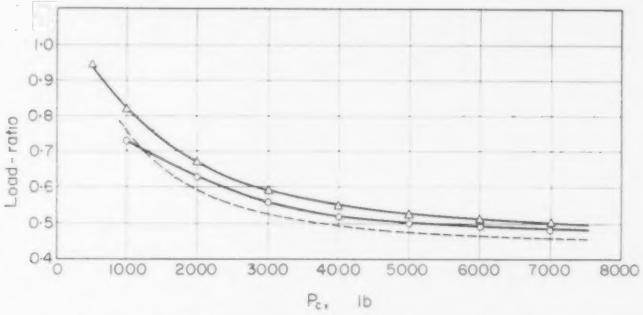

FIG. 11. Comparison between experimental and derived load-ratios at the third loading (△ denotes sample B, F/T139; ○ denotes sample A, F/T139; — — — — — denotes derived curve for sample A).

loading, a new cable is characterized by a hesitancy for the load–strain curve to rise according to the true cable-stiffness, i.e. the curve is initially of very small slope. This is partly due to the cable straightening under load, but also to the "bedding down" of the aluminium sheath, so that at first the steel is taking almost all the load. The steel therefore has a "start" over the aluminium in beginning to carry load. The effect of this "start" would carry through subsequent cycles and would necessarily mean a higher load-ratio with further loadings than that derived with the assumption of an initially tight cable.

Sample A in F/T139 was 140 ft long and the load-ratio curve in Fig. 11 represents the mean values obtained at five positions along the cable at 70°F. Sample B was 530 ft long and the curve shown represents the mean of values obtained at three positions along the cable at 72°F.

MODULUS OF ELASTICITY AND LOAD-RATIO 37/0·110-in. S.C.A. CONDUCTOR

Since reasonable correlation was found between experimental and derived curves for the 37/0·102-in. S.C.A. conductor, it was felt justifiable to produce corresponding curves for the 37/0·110-in. S.C.A. conductor, in which the main interest is centred.

Fig. 12 shows three cycles of loading for the 37/0·110-in. S.C.A. conductor loaded to $P_C = 11{,}500$ lb. The effective elastic modulus calculated from this

graph is $12{\cdot}7 \times 10^6$ lb/in^3, i.e. the same as for the 37/0·102-in. S.C.A. conductor. Since E is defined here as increment of stress/increment of strain, and is derived from linear portions of the graphs when the cables have settled down, the values should obviously be the same for the same ratio of steel to aluminium construction, with similar geometry. It should be noted that the derived results for the 37/0·110-in. S.C.A. conductor are based on the same α-values as those originally assumed for the 37/0·102-in. S.C.A. conductor (Table 1).

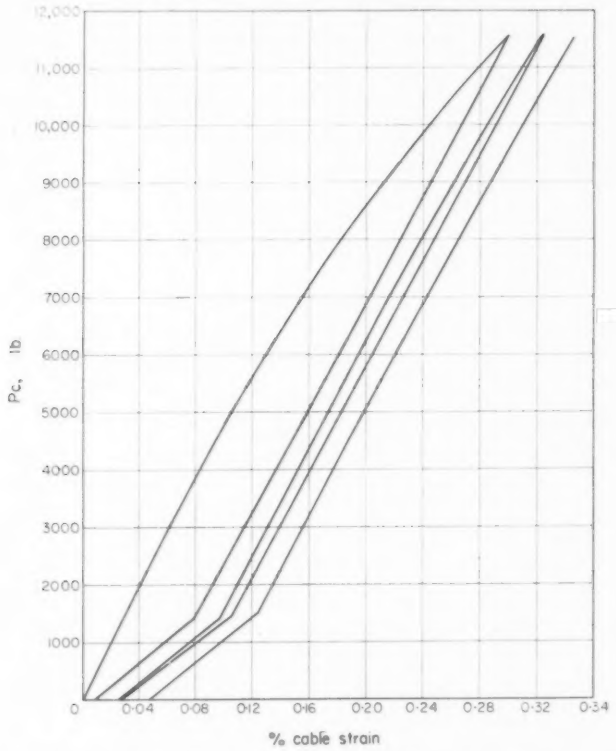

FIG. 12. Derived loading cycles for 37/0·110-in. S.C.A. conductor. Second and third cycles are moved 0·02 per cent strain to the right for clarity.

Table 4 gives the helix loads and load-ratios for up-loading in the first and third loading cycles of the 37/0·110-in. S.C.A. conductor, these helix loads and load-ratios being plotted in Figs. 13 and 14 respectively. It will be noticed that the load-ratio reaches unity at a higher relative load in this case than in the previous case of the 37/0·102-in. S.C.A. conductor. This is because a P_C value of 11,500 lb on the 37/0·110-in. S.C.A. conductor represents a considerably higher aluminium stress than does a P_C value of 7500 lb on the 37/0·102-in. S.C.A. conductor. Thus, as is evident from Fig. 5, there is a much greater permanent set in the aluminium after the first loading cycle, so that it ceases to take load at a higher strain when off-loading.

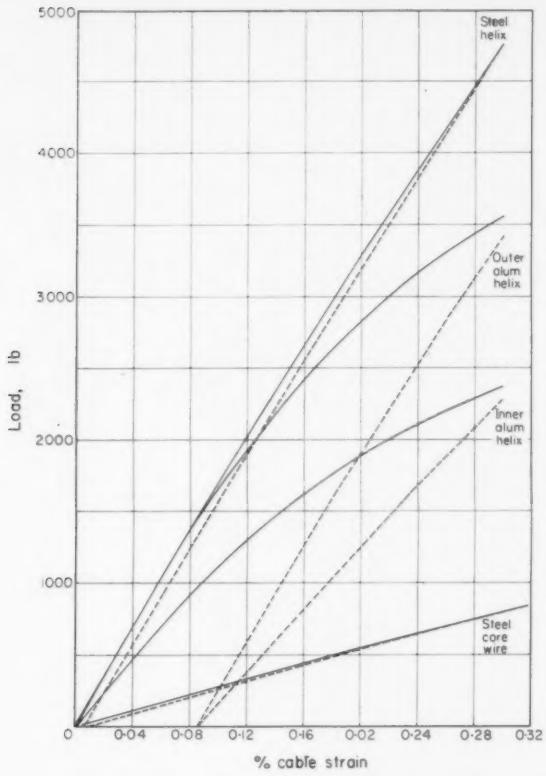

FIG. 13. Derived load distribution in 37/0·110-in. S.C.A. conductor for first and third loadings to P_C = 11,500 lb (———— denotes first loading; — — — — — denotes third loading).

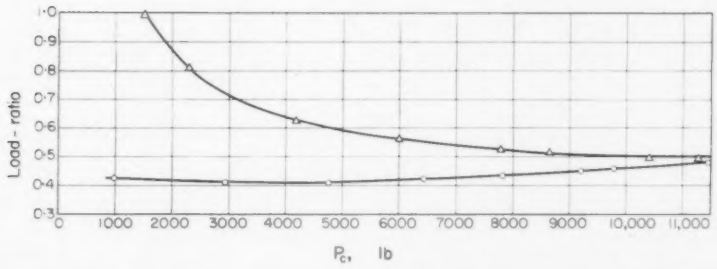

FIG. 14. Derived load-ratios for first and third loadings on 37/0·110-in. S.C.A. conductor (○ denotes first loading; △ denotes third loading).

A P_C value of 11,500 lb on the 37/0·110-in. S.C.A. conductor represents 65·6 per cent of the ultimate strength of the conductor and is considerably higher than the maximum working load of 8000 lb. The procedure described above can obviously be followed to find the load distribution at any desired value of P_C. If the cable is not to be carried through a series of cycles of loading,

but simply loaded to some particular value of P_C and left at this, then the load-ratio values for the first loading give the load distribution immediately on loading. It cannot be said that this load distribution will be the same some time after loading; this will almost certainly be untrue due to creep having taken place in the aluminium. But the initial distribution establishes a basis for the consideration of this creep and the consequent interaction between the steel and aluminium strands.

TABLE 4. DERIVED LOAD DISTRIBUTION IN 37/0·110-in. S.C.A. CONDUCTOR FOR FIRST AND THIRD LOADINGS

	ϵ_c	P_{s_0}	Steel helix load (lb)	Inner alum. helix load (lb)	Outer alum. helix load (lb)	Load-ratio
First loading	0	0	0	0	0	
	0·0002	63	370	239	349	0·4230
	0·0006	176	1046	704	1040	0·4120
	0·0010	287	1710	1125	1670	0·4165
	0·0014	395	2370	1477	2205	0·4285
	0·0018	502	2995	1770	2650	0·4415
	0·0022	605	3600	2020	3023	0·4540
	0·0024	657	3893	2120	2180	0·4620
	0·0028	757	4485	2300	3455	0·4765
	0·0030	807	4785	2375	3570	0·4840
Third loading	0	0	0	0	0	
	0·0002	41	247	0	0	1·0
	0·0006	146	924	0	0	1·0
	0·0008	212	1259	0	0	1·0
	0·0010	267	1590	172	274	0·8060
	0·0014	379	2250	615	942	0·6270
	0·0018	489	2893	1042	1590	0·5620
	0·0022	594	3520	1470	2230	0·5265
	0·0024	649	3840	1675	2540	0·5160
	0·0028	753	4465	2100	3140	0·4990
	0·0030	805	4780	2287	3430	0·4940

CONCLUSIONS

The method described is regarded as approximate because of its assumption that the tensile behaviour of the aluminium strands in their non-elastic state under a complex stress system can be predicted from purely tensile tests. However, it appears that the accuracy of the load distribution found by using the method is reasonably close to the true situation. It is clear, too, that before applying this procedure to any particular cable the geometry of that cable must be measured, i.e. the true values of α must be used. Also a previous test on a short length of cable, to establish the amount of bedding down, would be useful towards arriving at a more accurate estimate of the load distribution.

No account has been taken here of temperature change and its effect on the modulus of elasticity and on the load-ratio in the conductor. The E value, as previously pointed out, is not greatly influenced by temperature, but there is no doubt that the load distribution is. Varney's[2] method for the adjustment of

the load-ratio was used in F/T139, and showed excellent correlation with experimental results. There seems no reason why it should not be applied with equal success to the curves for individual helices derived here. The method consists essentially of giving the load–strain curves a bodily movement to the right along the strain-axis to take account of the different expansion coefficients of steel and aluminium.

No consideration has been given either to the time element, viz. the effect of holding a load over a long period of time to find its influence on the load distribution. This is the point where creep in the aluminium becomes of great importance. The continuously increasing sag, which a conductor suffers during its lifetime, must be either predicted or prevented. There seems to be some chance that a possible prevention (or part-prevention) may be effected by careful cold-working of the aluminium before it goes into service on the cable, since a certain amount of cold-working drastically reduces its creep-rate. The other factors affecting the creep properties of the aluminium are its composition and its heat treatment, and here also improvements may be possible. Any treatment, however, must be aware of its possible effect on the resistivity of the aluminium conductor.

Vol. 2
1960-61

It has been noted that the derived load-ratio curves for the 37/0·102-in. S.C.A. conductor are higher than the experimental curves. The effect of cold work on the aluminium wires was described in the discussion of the preliminary tests, and it was seen that the wire which had been subjected to the smaller amount of cold work showed a slightly greater strain for any given tensile load. The curves for the formed and straightened wires were used as a basis in deriving the load-ratio curves, but it is true that these wires had been subjected to more cold work than those on the cable, i.e. they had been straightened. The effect of this extra amount of cold work on the characteristic load–strain curves would be a further contributory factor towards indicating a slightly lower load-ratio than the true one.

Acknowledgements—The author is grateful to Professor W. Johnson and Dr. J. Halling for their help in preparing the paper for publication.

REFERENCES

1. W. D. Tuck and E. W. W. Double, *Distribution of Tensile Stress in Composite Conductors—Interim Report.* Technical Report Reference FT/139, British Electrical and Allied Research Association (1941).
2. T. Varney, *Graphic Method for Sag-Tension Calculations.* A.C.S.R. (1927).

Int. J. Mech. Sci. Pergamon Press Ltd. 1961. Vol. 2, pp. 294–310. Printed in Great Britain

THIN HEAVY ELASTIC STRIPS AT LARGE DEFLEXIONS

H. LIPPMANN*, O. MAHRENHOLTZ* and W. JOHNSON†

(*Received* 19 *July* 1960)

Summary—The deflected forms taken up by an elastic strip of uniform thickness and constant width hanging under its own weight as (i) a cantilever, (ii) a heart-shaped loop and (iii) with position-fixed ends in the same horizontal plane, are presented, the results having been obtained using an analogue computer. Some comparisons with small-deflexion theory are drawn. Results showing deflected form are also given for a uniformly thick strip whose width tapers uniformly (triangular strip) and for a long, thin, heavy wire held at its top end and deflected by a uniform horizontal wind pressure.

INTRODUCTION

HISTORICALLY, Galileo first considered the small deflexions of an initially straight cantilever carrying a transverse end load, and Euler discussed at length the forms assumed by a straight weightless, flexible rod carrying a concentrated thrust.[1] Engineers customarily only treat of beams or structures undergoing small deflexions and infinitesimally small strains, and especially when calculating deflexions, they start from Bernouilli's assumption that curvature is proportional to bending moment. The equation of the curve of small deflexions is then obtained by justifiably assuming that the slope $\dot{y}$ is, in comparison with unity, negligible and thus $(1+\dot{y}^2) \simeq 1$ in the standard expression for curvature. When the deflexions are not small, this assumption cannot be made and the solution of the appropriate differential equation is difficult and usually a series solution is sought. The exceptions are Euler's elastic curves, of which Love[2] treats at length, the rods considered being weightless and subject to a concentrated load.

When the rod or strip carries a uniformly distributed load, the equation is more difficult to solve than that derived for the concentrated end load. Again, a particular solution in series form and a numerical solution have been obtained (see below).

Five different situations are investigated of heavy, uniformly thick strips, carrying in effect uniformly distributed loads, or hanging under their own weight: (i) a simple cantilever of uniform width, (ii) a heart-shaped loop of uniform width, (iii) a beam whose ends are fixed in a horizontal line, (iv) a strip triangular in plan and (v) a thin wire hanging under its own weight but subject to a uniform horizontal wind pressure. (i) and (ii) have been previously solved numerically by Bickley[3], such results being useful in the textile industry for ascertaining the stiffness of cloth. His solutions have now been checked using an analogue computer, and extended. The work and results should also be useful to teachers as an extension of the treatment of simple beam theory, even

* Technische Hochschule, Hannover, Germany.
† Mechanical Engineering Department, College of Science and Technology, Manchester 1.

if the results can be referred to only in a qualitative way. The remaining three sections have not, as far as the authors are aware, previously been investigated.

FIG. 1. Diagram for deflexion of a simple cantilever carrying a uniformly distributed load.

Vol. 2
1960-61

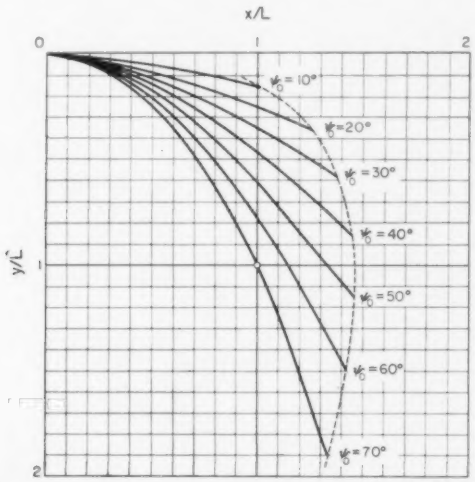

FIG. 2. Deflected forms of a cantilever for increasing values of L. (ψ is the angle at the point at the end of the curve.)

Recapitulating the results of elementary beam theory for a uniformly wide and thick-strip cantilever, in the notation of Fig. 1, Δ the vertical deflexion is given by

$$\Delta = (wl^4/8EI)/(1-\nu^2)$$

where w is the weight per unit volume, l the length of the strip, ν is Poisson's ratio and E and I have their usual meanings. The horizontal movement of the cantilever end is

$$h = (1-\nu^2)\, w^2 l^7/112E^2 I^2 \equiv 1{\cdot}75\Delta^2/l$$

For a concentrated end load the expressions are

$$\Delta = (1-\nu^2)\, Wl^3/3EI, \quad h = (1-\nu^2)\, Wl^5/15E^2 I^2 \equiv 3\Delta^2/5l$$

A simple experiment using, say, a strip of paper, in which the projecting length of strip s is steadily increased, would provide a sequence of pictures such as those given in Fig. 2. It will be noted that for a given material there exists

a maximum span, when the end of the strip starts to approach the vertical through the support.

The presence of horizontal deflexions has, of course, only secondary effects in infinitesimal-displacement theory.

BASIC EQUATIONS

The basic equations set up in this section apply only to the first three problems and require modification in the case of the last two.

A strip of undeformed length l is fixed at A and at the end O is acted on by moment M_0 and component forces F_x, F_y; the body force $w.\delta s$ acts on every element of length δs, in the positive y-direction, see Fig. 4; s is the arc length to point P on the beam measured from O, and OA is the line of centroids of the cross-sections. Let the co-ordinates of s be $x(s), y(s)$ with respect to origin A and denote by ψ the angle between the tangent to the curve at P and the x-axis. $M(s)$ is the total moment at P and $\kappa(s)$ the curvature of the beam at P. By definition, $\kappa(s) = -\dot{\psi}(s)$ where $\cdot \equiv d/ds$, and let $\kappa(0) = \kappa_0$ and $\kappa(l) = \kappa_A$.

The basic physical assumption to be made is, $\kappa = \alpha M$, where α is a constant; $\alpha = 1/E_1 I = (1-\nu^2)/EI$; E is Young's modulus and I is the second moment of area of the section about a horizontal axis through its centroid. The term $(1-\nu^2)$ arises because the strip bends under conditions of plane strain being, relative to its thickness, very wide. At P, the moment is

$$M = M_0 - F_x[y(0)-y(s)] + F_y[x(0)-x(s)] + \int_0^s w\,d\bar{s}[x(\bar{s})-x(s)] \tag{1}$$

Differentiating (1) with respect to s, it is found that

$$-\ddot{\psi} = \alpha\{F_x\dot{y} - F_y\dot{x} - ws\dot{x}\} \tag{2}$$

and since $\dot{x} = -\cos\psi$ and $\dot{y} = -\sin\psi$,

$$\ddot{\psi} + [\alpha F_y + \alpha ws]\cos\psi - \alpha F_x \sin\psi = 0 \tag{3}$$

This equation requires to be solved in conjunction with the boundary conditions appropriate to the particular problem under consideration.

For the case when the cantilever, initially straight, is built-in horizontally at A and hangs under its own weight only, a numerical step-by-step solution has been presented by Bickley[3]; this method is long and tedious. A series solution was obtained by Rohde[4] and her method was extended to treat of beams having some initial non-inflexional curvature by Seames and Conway[5]. A very complicated method using a power series has been given by Sato[6].

The problems described below are mainly different only in their boundary conditions. This class of problem is less easy and quick to solve, using a digital computer rather than an analogue computer, for, in the latter case, different values of the parameters can be generated simply by potentiometric variation. In all cases, the strip studied can be given its correct position, inclination and curvature by visual potentiometric means. The generation process for one curve requires about 10 sec, and the results are correct at best to the third significant figure.

Vol. 2
1960-61

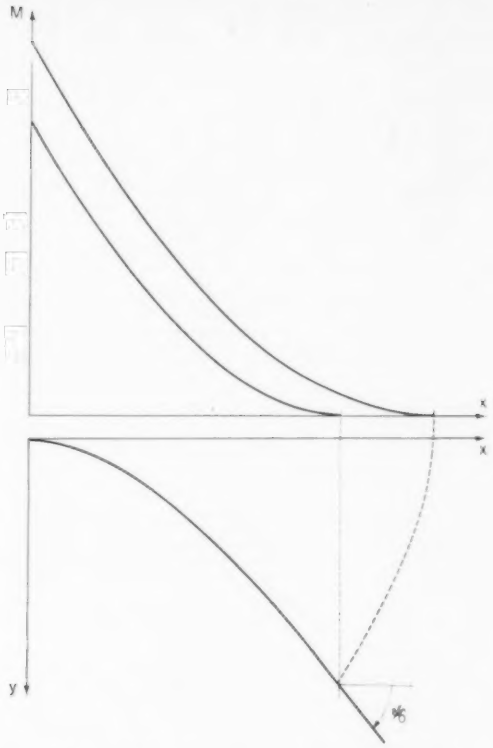

FIG. 3. Comparison of bending-moment diagrams for a quasi-straight strip and a heavily deflected one.

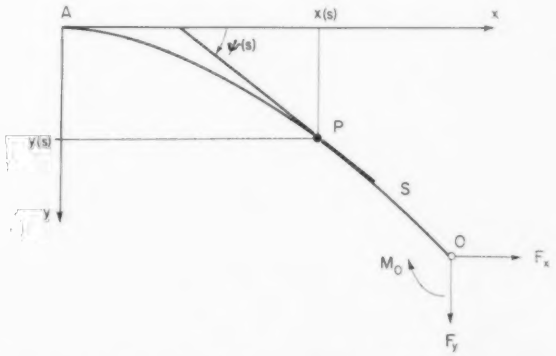

FIG. 4. Showing forces and moments on a curve of deflexion in its equilibrium position.

In the following sections, the arrangement of the computing elements for the first three problems is described, some of Bickley's results are reproduced and further solutions presented of the bending under its own weight of an initially straight beam. Incidentally, it is to be remarked that the treatment

of an initially curved beam would present little added complication. If the initial curvature is $\kappa_0(s)$, $-\dot{\kappa}_0$ is substituted as some given function on the right-hand side of equation (3).

Following Bickley, write

$$L = (\alpha w)^{-\frac{1}{4}} \tag{4}$$

L is termed the bending length. Put $\sigma = s/L, f_x = F_x/wL, f_y = F_y/wL, m = M/wL^2$ and writing $' = d/d\sigma$, we obtain the dimensionless equation,

$$\psi'' + (\sigma + f_y)\cos\psi - f_x \sin\psi = 0 \tag{5}$$

Finally, from Fig. 4, it follows that

$$\left.\begin{aligned} \frac{x}{L} &= \frac{x(0)}{L} - \int_0^\sigma \cos\psi \, d\sigma \\ \frac{y}{L} &= \frac{y(0)}{L} - \int_0^\sigma \sin\psi \, d\sigma \end{aligned}\right\} \tag{6}$$

COMPUTING SYSTEM

The analogue computer used throughout was a Telefunken RA 463/2. Fig. 5 shows diagrammatically the arrangement of the elements involved and the circuit required for treating the first three problems. The following meanings attach to the various symbols.

Wire, showing current direction.

Generated constant voltage representing $f(\sigma) = +1, \quad f(\sigma) = -1$.

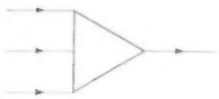

A sign-reversing amplifier: the voltages on the left are added and the sign is reversed.

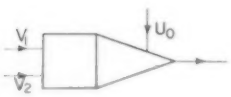

The voltages on the left are integrated with respect to σ, added to some initial value U_0 and the sign reversed. Assuming simply $t \simeq \sigma$,

$$U = -\left(U_0 + \int_0^\sigma \Sigma V_i \, d\sigma\right)$$

The stress is multiplied by a constant factor $a \geqslant 0$.

In reality, $0 \leqslant a \leqslant 1$. To obtain $a > 1$, the voltage must be multiplied by a foregoing $\triangleright$ or $\square\!\!\triangleright$ for any integer $n \geqslant 1$. For simplicity, take any non-negative value for a and assume $n = 1$ everywhere.

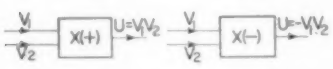

Here, for simplicity, U, V_i etc. are assumed to be dimensionless. In reality, $+V_1$, $-V_1$, $+V_2$, $-V_2$ are needed for the product $V_1 V_2$.

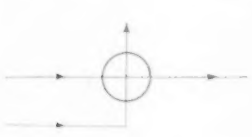

Vertical and horizontal deflexions of the electronic beam on a scale in the oscilloscope. There are two oscilloscopes in the computer.

Besides the elements shown above, there are several kinds of function generators for given functions $f(\sigma)$ and these could have been used for any initially curved beam.

Note that the equations

$$d(\cos\psi)/d\sigma = -\psi' \sin\psi$$

and

$$d(\sin\psi)/d\sigma = \psi' \cos\psi$$

have been used to generate the functions $\cos\psi$, $\sin\psi$ for equation (5).

All the curves presented below have been redrawn, to allow for parallax, using values from the curves presented by the oscilloscopes.

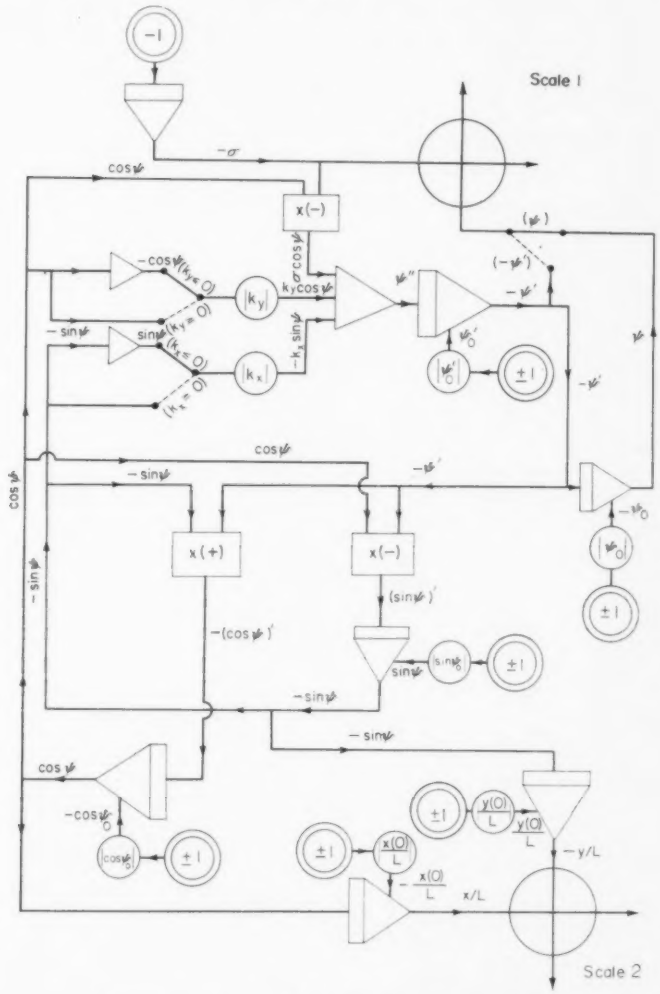

FIG. 5. Analogue circuit for first three problems.

BICKLEY'S RESULTS: PROBLEMS (i) AND (ii)

(i) *Cantilever*

Comparison of our results with those of Bickley show agreement to within 0·5 per cent; these are shown in Fig. 2. Here, of course, $f_x = f_y = M_0 = 0$ and

only the value of $\psi(0)$ was given; l/L (i.e. the computing time), $x(0)$ and $y(0)$ have to be varied until $\sigma = l/L$ and $x(l/L) = y(l/L) = \psi(l/L) = 0$.

(a) Referring to Figs. 1 and 2, it is seen that for a given value of L (i.e. of w, E_1 and I), the parameters characterizing the co-ordinates of the end of the strip which is most distant from the vertical through O are

$$\psi \simeq 47°, \quad x_0/y_0 \simeq 1{\cdot}40, \quad x_0/l \simeq 0{\cdot}79, \quad l/L \simeq 1{\cdot}84$$

Thus, $l \simeq 1{\cdot}84\,(E_1 I/w)^{\frac{1}{3}}$. Also, we have that $h \simeq 0{\cdot}21\,l$ and for comparison with the expression for small deflexions, $h \simeq w^2 l^7/190\,E_1^2 I^2$.

Further, $y_0 = \Delta \simeq 0{\cdot}56\,l \simeq wl^4/11\,E_1 I$ and hence $h \simeq 0{\cdot}66\Delta^2/l$.

(b) For the simple cantilever when $\psi_0 = 50°$, a bending-moment diagram along a horizontal scale has been drawn in Fig. 3. The bending-moment diagram for a beam of the same l and w but of much larger $E_1 I$ value, so that only a small deflexion is created, is also included in order to show the effect of the deformed shape at finite deflexion.

(ii) *Heart-shaped loops*

Agreement between our Fig. 6 and Bickley's results (his Fig. 5) was not so good, especially at the highest and lowest points of the curves. Here, only the right-hand halves of the curves were computed and f_x was used as a parameter, as by Bickley. m_0 [i.e. $\psi'(0)$], l/L and $y(0)$ had to be chosen so that for $\sigma = l/2L$,

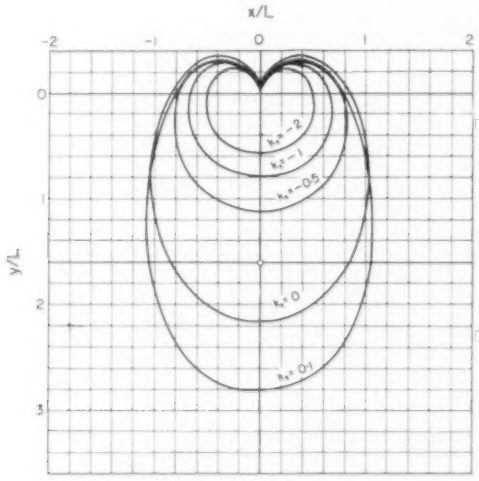

FIG. 6. Deflected forms of heart-shaped loops.

$x(l/2L) = y(l/2L) = 0, \psi(l/2L) = -\pi/2$; also $f_y = 0$ and $\psi(0) = \pi$. With this arrangement of the computing elements, it was not feasible to draw the curve $f_x = 0{\cdot}2$, since the differences in the values of m_0 were less than three significant figures (as Bickley also pointed out).

THE ELASTIC CATENARY: PROBLEM (iii)

A heavy inextensible perfectly flexible strip of length l/L is position-fixed at the points 0 and 1 to span a gap l_0/L as shown in Fig. 7. The equation of the

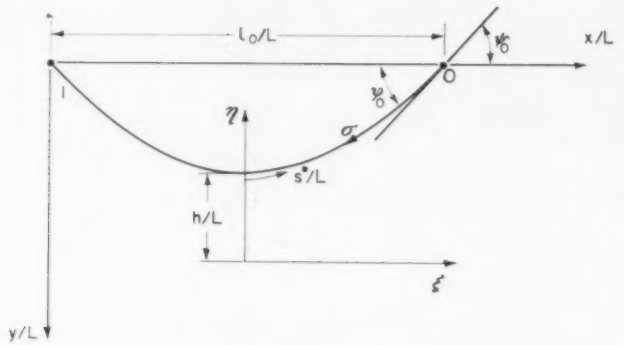

FIG. 7. Diagram of catenary.

catenary in an orthogonal ξ/η system with suitably chosen h is

$$\eta = h \cosh \xi/h \tag{7}$$

or, in terms of arc length s^*, measured from the vertex as parameter,

$$\xi = h \sinh^{-1} s^*/h$$

$$\eta = h\sqrt{[1+(s^*/h)^2]} \tag{8}$$

and the angle $\phi_0 = -\psi_0$ is defined by

$$\tan \phi_0 = \sinh \xi_0/h = \sinh l_0/2h$$

See, for instance, Ref. 7. Thus for any given angle ψ_0 or length l/L a particular catenary may be drawn. Note that,

$$s^*_{\max}/L = l/2L \geqslant l_0/2L \tag{9}$$

It is of interest to compare the forms of the inextensible catenaries and the inextensible flexible Euler curves. The latter is the equivalent of a uniform beam carrying a uniformly distributed load position-fixed at its ends. The governing equation of the catenary is described by (5) by putting $m_0 = 0$; also $f_y = F_y/wL = -l/2L$. Curves obtained by using the computer for values of $l_0/L = 0{\cdot}5$, 1, 2 and 4 are shown in Fig. 8. For the extreme cases $l_0/L = 0{\cdot}5$ and 4·0, catenaries have been inserted for facilitating comparison with the Eulerian bending curves. In each case the comparison has taken two forms:

(i) Both curves have the same length but different ψ_0 values.

(ii) Both curves have the same value of ψ_0 but different lengths.

Examining the curves, it is observed that, in case (i) there are discernible differences between the catenaries and the Eulerian curves only for the longest strips ($\psi_0 = 80°$); and in case (ii) for $\psi_0 \leqslant 60°$, the curves almost coincide.

Vol. 2
1960-61

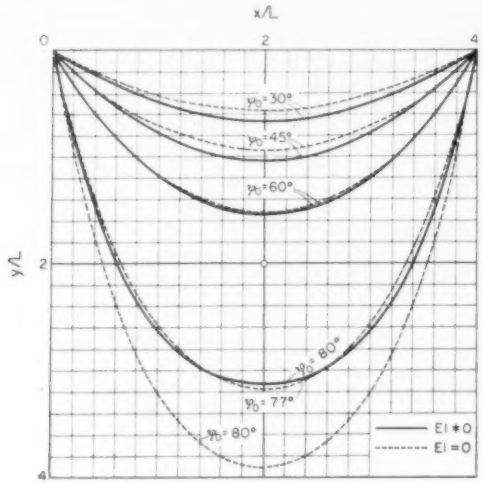

(a)

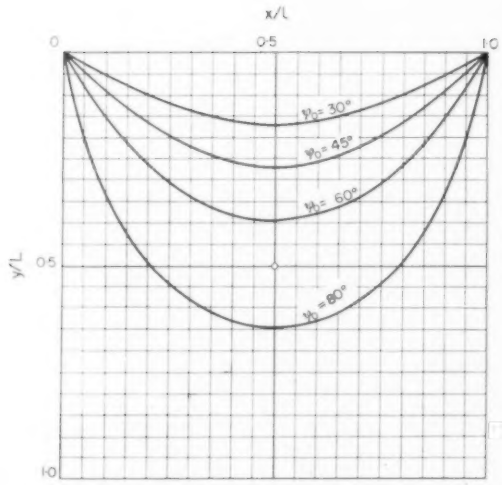

(b)

FIG. 8. Deflected form of position-fixed strip for various ratios of l_0/L: (a) 0·5 (b) 1.

Vol. 2
1960-61

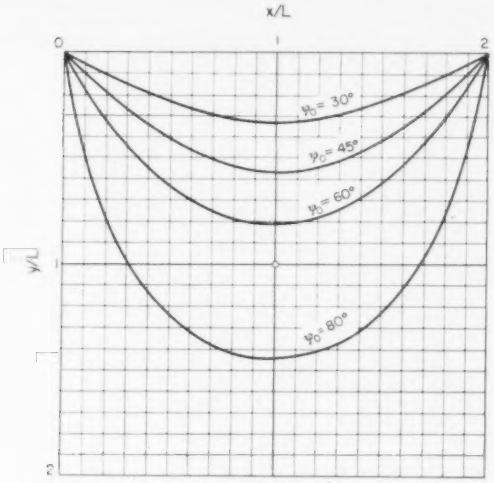

(c)

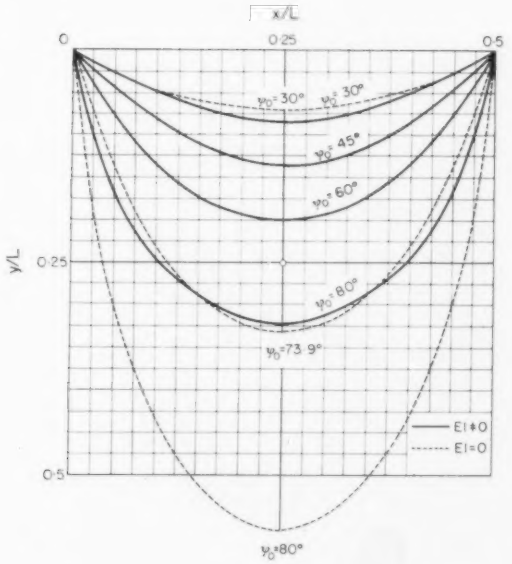

(d)

FIG. 8. Deflected form of position-fixed strip for various ratios of l_0/L: (c) 2 (d) 4.

A CANTILEVER, TRIANGULAR IN PLAN

We formulate the problem generally by considering a trapezoidal strip of uniform thickness and linearly varying width, $b = b(s)$, see Fig. 9. Denote by

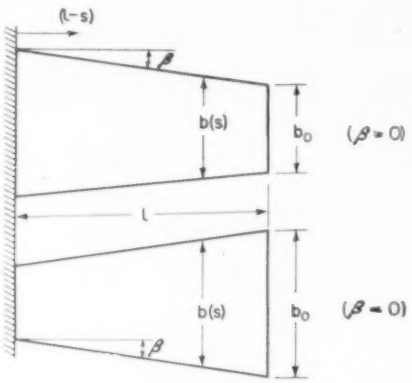

FIG. 9. Trapezoidal strip.

Γ the weight per unit area so that

$$w(s) = \Gamma b(s), \quad 0 \leqslant s \leqslant l \tag{10}$$

Following (1), we have

$$M = M_0 - F_x[y(0) - y(s)] + F_y[x(0) - x(s)] + \int_0^s w(\tilde{s})\,[x(\tilde{s}) - x(s)]\,d\tilde{s}$$

and because $\dot{x} = -\cos\psi, \quad \dot{y} = -\sin\psi, \quad (\cdot \equiv d/ds)$

$$\dot{M} = \cos\psi\left[\int_0^s w\,ds + F_y\right] - F_x \sin\psi \tag{11}$$

Now $\alpha M = \kappa$ but α is no longer a constant and hence

$$\dot{M} = \frac{\dot{\kappa}}{\alpha} + \left(\frac{\dot{1}}{\alpha}\right)\kappa = -\frac{\ddot{\psi}}{\alpha} - \left(\frac{\dot{1}}{\alpha}\right)\dot{\psi}$$

Substitution in equation (11) yields

$$\frac{1}{\alpha}\ddot{\psi} + \left(\frac{\dot{1}}{\alpha}\right)\dot{\psi} + \cos\psi\left[\int_0^s w\,ds + F_y\right] - \sin\psi F_x = 0 \tag{12}$$

Now $\alpha = 1/E_1 I$ and thus $I = d^3(b_0 + 2s\tan\beta)/12$ and $w = \Gamma(b_0 + 2s\tan\beta)$. Writing $L = (\alpha w)^{-\frac{1}{4}} = d(E/12\Gamma)^{\frac{1}{4}}$ and $\sigma = s/L$, $' \equiv d/d\sigma$, $0 \leqslant \sigma \leqslant l/L$ we have

$$Lw(L\sigma)\psi'' + L^2\dot{w}(L\sigma)\psi' + \left[L\int_0^\sigma w(L\sigma)\,d\sigma + F_y\right]\cos\psi - F_x\sin\psi = 0$$

Put

$$\left.\begin{aligned} &p = \Gamma b_0/w_m, \quad q = 2\Gamma L\tan\beta/w_m, \quad f_x = F_x/Lw_m \\ &f_y = F_y/Lw_m \quad \text{and} \quad m = M/L^2 w_m \end{aligned}\right\} \tag{13}$$

where w_m is a factor of proportionality, and obtain from (12)

$$(p + q\sigma)\psi'' + q\psi' + \left[\int_0^\sigma (p + q\sigma)\,d\sigma + f_y\right]\cos\psi - f_x\sin\psi = 0 \tag{14}$$

which equation holds in place of (5). Note that $p=1$, $q=0$ for a rectangular strip and $p=0$, $q\neq 0$ for a triangular strip, or generally $p/q = b_0/2L\tan\beta$.

Computer programme

For programming purposes, we used a modified form of equation (14), as

$$[(p+q\sigma)\psi']' + \left[\int_0^\sigma (p+q\sigma)\,d\sigma + f_y\right]\cos\psi - f_x\sin\psi = 0 \qquad (14a)$$

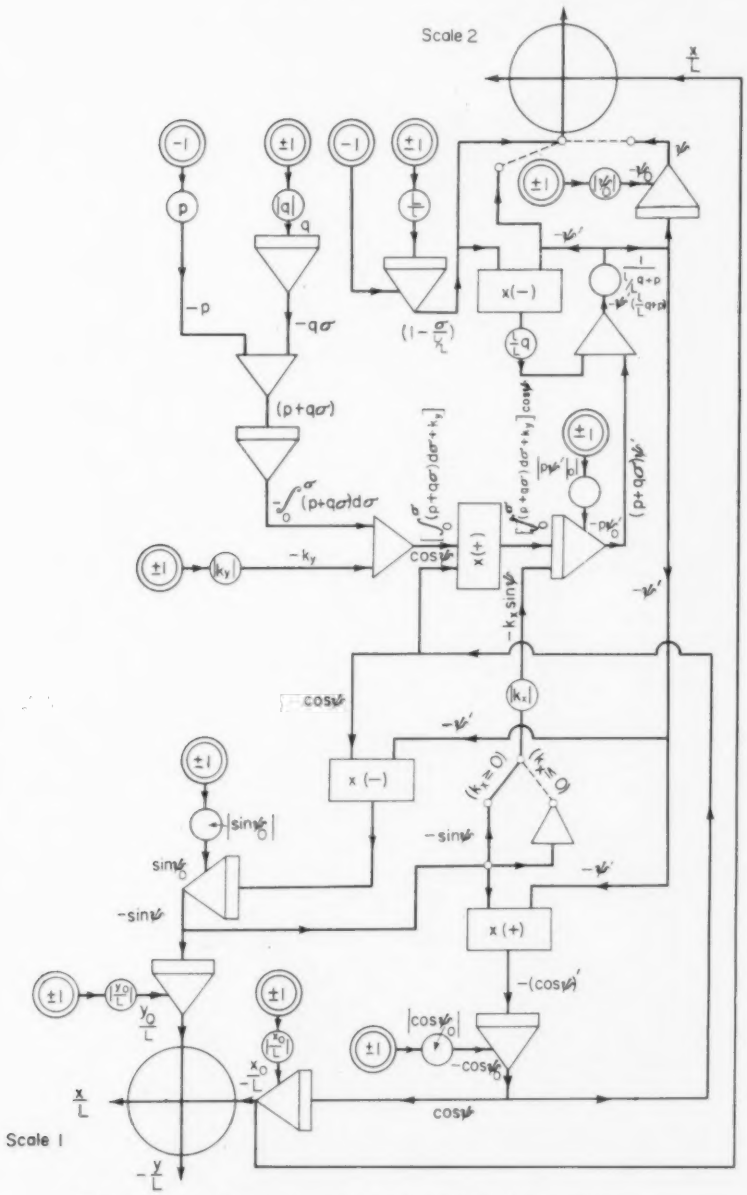

FIG. 10. Analogue circuit for triangular-plan cantilever.

Vol. 2
1960-61

The initial angle was taken as an independent parameter, so that for $\sigma = l/L$ the boundary conditions are $x/L = 0 = y/L$; $\psi' = 0$. The circuit used is shown in Fig. 10.

(Note that from equation (14a) we obtain $(p+q\sigma)\psi'$ though we need ψ' for determining $\sin\psi$ and $\cos\psi$. Division on the analogue computer is troublesome and not possible for $(p+q\sigma) = 0$—which is the case at the apex of the triangle. Division was avoided by means of the artifice shown in Fig. 10.)

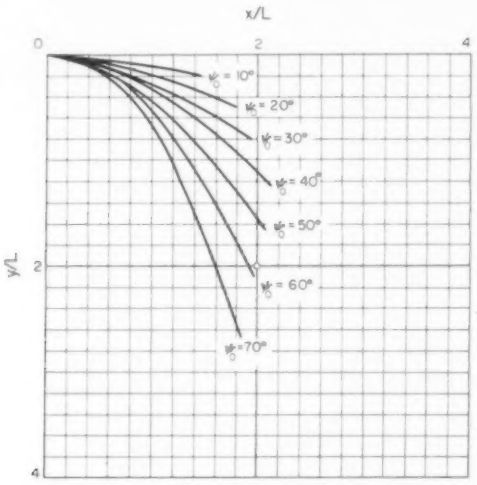

FIG. 11. Showing deflected forms for various values of ψ_0 of triangular cantilever.

TABLE 1

ψ_0	10°	20°	30°	40°	50°	60°	70°
x_0/L	1·46	1·80	1·95	2·138	2·082	2·000	1·854
y_0/L	0·189	0·482	0·808	1·250	1·652	2·105	2·696
l/L	1·47	1·86	2·17	2·46	2·73	3·03	3·44

TABLE 2

ψ_0	10°	20°	30°	40°	50°	60°	70°
x_{01}/x_{02}	0·68	0·70	0·70	0·67	0·70	0·71	0·72
y_{01}/y_{02}	0·70	0·73	0·72	0·68	0·69	0·71	0·71
l_{01}/l_{02}	0·68	0·71	0·69	0·69	0·70	0·71	0·71

The photographs taken were redrawn to correct for parallax errors—as indeed applies to all those figures presented above—and are shown in Fig. 11; some of the important proportions are given in Table 1.

In Table 2 a comparison is made of corresponding values for the rectangular strip referred to by subscript 1, and the triangular strip referred to by subscript 2 for the same value of ψ_0. It is interesting to note that the various quantities for the triangular strip can, to within about 3 per cent, be evaluated by multiplying those for the rectangular strip by 0·7. In the limit for very small deflexions, $l_{01}/l_{02} = (3)^{-\frac{1}{2}} \simeq 0{\cdot}694$.

A THIN HEAVY WIRE HANGING VERTICALLY AND SUBJECT TO HORIZONTAL WIND PRESSURE

In Fig. 12(a) an element of a thin heavy wire of length δs is shown subject to a wind force δF acting horizontally, which is proportional to $\delta s \sin\psi$, i.e. the

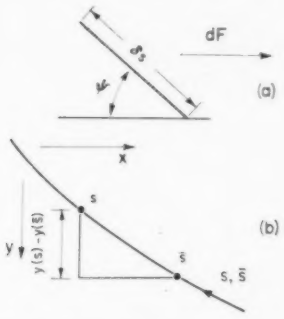

FIG. 12. (a) Element of wire subject to horizontal wind force.
(b) Portion of wire to show calculation of M^*.

wire length normal to the wind; all aerodynamical lift is neglected. Thus the moment M^* effected by the wind alone is, see Fig. 12(b),

$$M^* = -c^* \int_0^s [y(\bar{s}) - y(s)] \sin\psi \, d\bar{s}$$

where c^* is the wind force per unit length. Thus,

$$\dot{M}^* = -c^* \sin\psi \int_0^s \sin\psi \, d\bar{s} = -c^* L \sin\psi \int_0^\sigma \sin\psi \, d\sigma$$

where ψ, L and σ have the same meanings as before. We introduce the dimensionless number $\bar{c} = c^*/w$, where w is the weight per unit length of the wire, and thus

$$\begin{aligned} \dot{M}^* \alpha L^2 &= -\bar{c} \alpha w L^3 \sin\psi \int_0^\sigma \sin\psi \, d\sigma \\ &= -\bar{c} \sin\psi \int_0^\sigma \sin\psi \, d\sigma \end{aligned} \tag{15}$$

The right-hand side of (15) must be added to the left-hand side of (5). Thus, since $f_x = f_y = 0$, we get

$$\psi'' + \sigma \cos\psi - \bar{c} \sin\psi \int_0^\sigma \sin\psi \, d\sigma = 0 \tag{16}$$

Equation (16) requires to be solved with $\psi' = 0$ at $\sigma = 0$. The circuit for handling this equation is shown in Fig. 13.

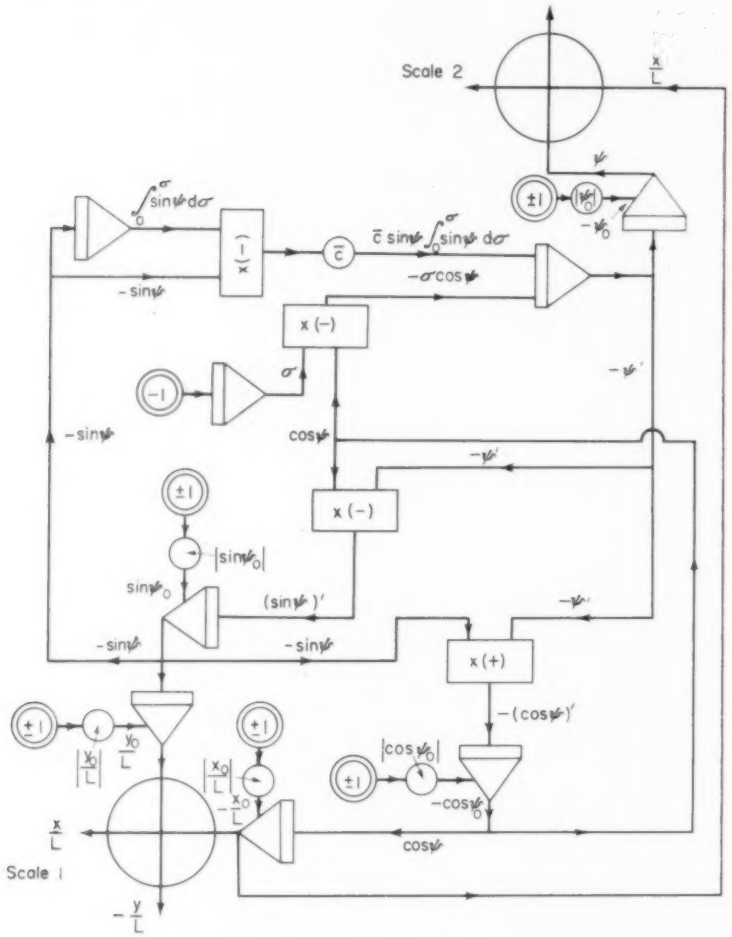

FIG. 13. Analogue circuit for hanging wire deflected due to wind pressure.

Experimental

To verify the results obtained by the computer, a steel wire of length 969 mm and diameter 3 mm was placed in a wind tunnel and caused to deflect.

A bending experiment with small deflexions gave $EI = 7{\cdot}96 \times 10^4$ kp/mm^2; the specific weight was $\Gamma = 7{\cdot}75 \times 10^{-6}$ kp/mm^3 and $w = \pi d^2 \Gamma/4 = 5{\cdot}55 \times 10^{-5}$ kp/mm. Thus $L = (EI/w)^{\frac{1}{3}} = 1127$ mm, and hence $l/L = 0{\cdot}860$.

Now, $c^* = cd\Delta p$, where Δp is related to the wind speed by

$$\Delta p = \rho v^2/2 \tag{17}$$

ρ being the density of the air and v its speed. Assuming the wire to hang as a

straight cylinder, the force on the wire is

$$F = A\Delta p.c$$

where A is the projected area of the wire and c is obtained empirically by reference to standard tables.[7] Constant c is actually dependent on the Reynolds number, $Re = vd/\nu$, ν being the kinematic viscosity of the air. The value $\bar{c} = c^*/w$ is denoted by $\bar{c}_{exp}$.

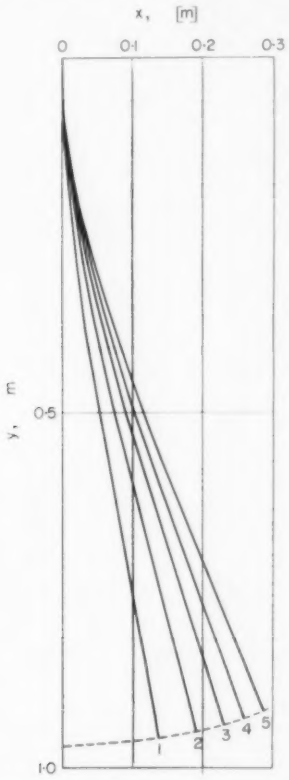

FIG. 14. Experimentally obtained curves of deflexion for hanging wire subjected to a steady horizontal wind pressure.

Table 3 shows, for each of five speeds, the measured values of Δp, the speeds obtained using equation (17) with $\rho = 0{\cdot}123\,\mathrm{kp/sec^2\,m^{-4}}$, the Reynolds number (with $\nu = 15{\cdot}1 \times 10^{-6}\,\mathrm{m^2\,sec^{-1}}$), the values of c as from Ref. 7 and the numbers $\bar{c}_{exp}$. The photographed bending curves have been redrawn in Fig. 14; they are pictures of the instantaneous situation of the wire since it was vibrating with a frequency of about one vibration per second with an amplitude of about the diameter of the wire itself. Throughout the experiment the wire never became plastic, since it always returned to its original position when the wind pressure ceased.

In Fig. 14 the experimentally obtained bending curves are shown and certain measured co-ordinates for each configuration are also presented in Table 3.

Vol. 2
1960-61

Computation

The computational process was directly related to the experiment, i.e. l/L was taken as given. The procedure was to reproduce the end points x_{end} and y_{end} as well as possible and then to determine what value of $\bar{c}$ is needed. Starting with $x_0 = x_{end}$, the endeavour was to obtain curves so that ψ would be 90° at $\sigma = l/L$ for the given l/L.

TABLE 3

	Expt. no. 1		Expt. no. 2		Expt. no. 3		Expt. no. 4		Expt. no. 5	
Δp (kp/m²)	32·7		45·7		56·2		64·6		73·2	
v (m/sec)	23·1		27·3		30·3		32·4		34·6	
Re ($\times 10^{-3}$)	4·59		5·42		6·02		6·44		6·87	
c (Ref. 7)	0·96		1·00		1·02		1·03		1·04	
$\bar{c}_{exp}$	1·83		2·46		3·08		3·58		4·08	
$\bar{c}_{comp}$	2·00		2·82		3·47		4·05		4·64	
x_{end}(m)†	0·136		0·188		0·227		0·2565		0·286	
y_{end}(m)†	0·957		0·948		0·940		0·930		0·920	
x_0(m)‡	0·1348		0·1882		0·2275		0·2565		0·285	
y_0(m)‡	0·9583		0·946		0·943		0·9262		0·918	
y(m)	x_{exp} (m)	x_{comp} (m)	x_{exp} (m)	x_{comp} (m)	x_{exp} (m)	x_{comp} (m)	x_{exp} (m)	x_{comp} (m)	x_{exp} (m)	x_{comp} (m)
0·2	0·010	0·0095	0·015	0·0148	0·019	0·0168	0·021	0·0201	0·024	0·022
0·3	0·0215	0·0209	0·032	0·0308	0·039	0·036	0·044	0·0424	0·050	0·0473
0·4	0·036	0·0353	0·052	0·0502	0·062	0·0604	0·072	0·0702	0·080	0·0785
0·5	0·0535	0·0518	0·074	0·0731	0·089	0·0882	0·1035	0·1022	0·115	0·115
0·6	0·0705	0·0690	0·097	0·0980	0·120	0·1186	0·137	0·1375	0·155	0·154
0·7	0·087	0·0876	0·124	0·1242	0·150	0·1503	0·171	0·1738	0·195	0·1952
0·8	0·1055	0·1066	0·150	0·1513	0·183	0·1827	0·209	0·2112	0·236	0·237
ψ_0 (degrees)	78·8†	79·1‡	75·0†	74·9‡	71·7†	71·6‡	69·2†	69·4‡	67·6†	67·0‡

† Experimental value.
‡ Computed value.

Computed forms of the bending lines were practically identical with the experimental ones and are as shown in Fig. 14. A detailed comparison of numerical values for the two curves is given in Table 3. Computed values of $\bar{c}$, i.e. $\bar{c}_{comp}$, differ from experimental ones by about 10 per cent as displayed in Table 3.

Acknowledgements—We wish to thank Professors J. Diamond and E. Pestel for facilitating our co-operation and for their encouragement.

REFERENCES

1. S. P. TIMOSHENKO, *History of Strength of Materials*. McGraw-Hill, New York (1953).
2. A. E. LOVE, *The Mathematical Theory of Elasticity*. Cambridge University Press (1923).
3. W. G. BICKLEY, *Phil. Mag.* **17**, 603 (1934).
4. F. V. ROHDE, *Quart. Appl. Math.* **11**, 337 (1953).
5. A. E. SEAMES and H. D. CONWAY, *J. Appl. Mech.* **24**, 289 (1957).
6. K. SATO, *Ingen.-Arch.* **27**, 195 (1959).
7. *Hütte, des Ingenieurs Taschenbuch* (28th Ed.). Ernst, Berlin (1955).

Int. J. Mech. Sci. Pergamon Press Ltd. 1961. Vol. 2, pp. 311–315. Printed in Great Britain

LETTERS TO THE EDITOR

On "On the response of the singly free linear oscillator"

(*Received* 25 *October* 1960)

CONCERNING a recent letter by CROSSLEY and GERMAN (Vol. 1, p. 396), suppose we take the authors' problem and look at it in a different way.

We know at steady state the mass vibrates at the frequency of the moving support. Let us find a spring length to give the natural frequency equal to this value. From $\omega_0 = (k/m)^{\frac{1}{2}}$ and $\omega_1 = (k_1/m)^{\frac{1}{2}}$, we get $L/l = k/k_1 = (\omega_0/\omega_1)^2$ which defines the relationship of L to ω_1. Suppose the length determined is shorter than the original length. This happens when $\omega_1 > \omega_0$. Attach the modified oscillator with the new spring length to the lower side of a thin board and at the same time attach a segment of the same kind of spring with a length equal to the original length less the new length on the upper side of the board. Set the oscillator in motion and move the upper end of the spring segment above the board in harmony with the mass below. Now if we can take the board away, connect the two parts together and do not disturb the motion, we obtain the original system with a moving support. The condition for the success in doing so is that the junction point should be held in equilibrium at all times. This requires that the support and the mass must move out of phase and the ratio of the magnitude of their motion must equal the ratio of the length of their springs.

If the length determined is longer than the original length (this happens when $\omega_1 > \omega_0$), instead of attaching a segment of the same kind of spring to the upper side of the board, attach a segment of "antispring" (spring with a negative modulus) to the lower side of the board. Following the same argument as before, we conclude that in this case the support and the mass must move in phase while the ratio of the magnitude of their motion must equal the ratio of the length of their springs as before. For either case the following relationship is correct.

$$\frac{x}{y} = \frac{L}{L-l}$$

It is seen that if $L = l$, the ratio x/y blows up. That means resonance occurs. But for $L = l$, $\omega_1 = \omega_0$. A statement then can be made to the effect that when the support frequency coincides with the resonant frequency, the node falls on the support. It appears to be a paradox for a node to be on a moving support. However, after a little reflection, this apparent paradox will be resolved.

If the mass of the spring in the oscillator is taken into consideration, we then have a problem of an infinite degree of freedom. However, it is still true that whenever the support frequency reaches a particular resonant frequency

Vol. 2
1960-61

of the oscillator (now a continuous system) the last node falls on the support (while other nodes fall on their natural spots corresponding to that particular natural frequency as calculated from the partial differential equation). As soon as the support frequency exceeds this particular frequency, a new node appears above the support. All nodes move down as the support frequency increases. When the new last node hits the support another resonant frequency (the next higher one) is reached.

H. H. Pan

College of Engineering
New York University
New York

Further comments on "Losses and efficiencies in axial-flow turbines"

(*Received* 3 *January* 1961)

In my review of losses and efficiencies in axial-flow turbines,[1] the effect of Reynolds number on losses was given in Fig. 12 of the paper. Results obtained by Dollin, Soderburg, Ackeret, Kearton and Cheshire were shown and it was stated that, with the exception of Cheshire's results, the Reynolds number was based upon the hydraulic mean diameter at the throat.

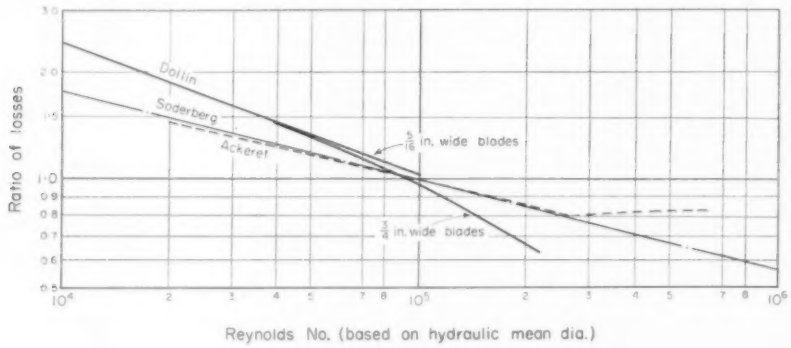

Fig. 1.

Mr. J. L. Jefferson, of Messrs. C. A. Parsons & Co. Ltd., has pointed out to me that Mr. Dollin's results were originally given in the form of loss plotted against a Reynolds number based on hydraulic mean depth (area/periphery) at the throat section. Mr. Jefferson has replotted Mr. Dollin's results against Reynolds number based on hydraulic mean *diameter* [(4 × area)/periphery] (see Fig. 1). Two sets of results are shown for blades of different widths, and the losses at any Reynolds number are expressed as a ratio of loss to the mean of the losses at a Reynolds number of 10^5. Also replotted in Fig. 1 are Soderburg's correlation and Ackeret's results (which were originally plotted against Reynolds number based on hydraulic radius [(2 × area)/periphery]). All are now plotted against hydraulic mean diameter.

These three sets of results come more closely into line, and confirm that below a Reynolds number (based on hydraulic mean diameter) of 10^5, the losses vary approximately inversely as the 1/5 power of the Reynolds number.

J. H. Horlock

Department of Mechanical Engineering
University of Liverpool

REFERENCE

1. J. H. Horlock, *Int. J. Mech. Sci.* **2**, 48 (1960).

Vol. 2
1960-61

Note on "The uniformly loaded rectangular plate supported at the corners"

(*Received* 16 *January* 1961)

Lee and Ballesteros obtained an approximate solution for a uniformly loaded rectangular plate supported at the corners.[1] Their solution apparently gives good results. Galerkin had solved the problem of a uniformly loaded rectangular plate with its four edges resting on elastic beams which are rigidly supported at their ends, the corners of the plate.[2] (This is mentioned in Timoshenko and Woinowsky-Krieger's book.[3]) By putting the flexural rigidity of these beams equal to zero, Galerkin obtained the solution for the case of a plate supported at the corners. Of course, Galerkin's works are not readily accessible in the Western world.

Lee and Ballesteros' solution does not satisfy exactly the zero-moment condition at the edges. The moments at the edges obtained from equation (7) in their paper are as follows:

$$[M_x]_{a,y} = (1-\mu)\frac{qa^2}{12}\left[3\left(\frac{y}{a}\right)^2 - \left(\frac{b}{a}\right)^2\right] \tag{1}$$

$$[M_y]_{x,b} = (1-\mu)\frac{qa^2}{12}\left[3\left(\frac{x}{a}\right)^2 - 1\right] \tag{2}$$

Suppose we like to remove these moments so as to make the solution exact, we may seek a solution for a plate subjected to applied moments equal and opposite to the above moments and superimpose this solution to the Lee and Ballesteros' solution. The following assumed form will meet our need:

$$w = \sum_{n=1,3,5,\ldots}^{\infty}\left(A_n \cosh\frac{n\pi y}{2a}\cos\frac{n\pi x}{2a} + B_n \cosh\frac{n\pi x}{2b}\cos\frac{n\pi y}{2b} + C_n\, y \sinh\frac{n\pi y}{2a}\cos\frac{n\pi x}{2a} + D_n\, x \sinh\frac{n\pi x}{2b}\cos\frac{n\pi y}{2b}\right) \tag{3}$$

The above assumed form satisfies the homogeneous biharmonic equation. It is symmetric with respect to x-, y-axes and gives zero deflections at the corners. To determine the coefficients, A_n, B_n, C_n, D_n we use the following

boundary conditions:

$$-D\left[\frac{\partial^2 w}{\partial x^2}+\mu\frac{\partial^2 w}{\partial y^2}\right]_{a,y}=-(1-\mu)\frac{qa^2}{12}\left[3\left(\frac{y}{a}\right)^2-\left(\frac{b}{a}\right)^2\right] \tag{4}$$

$$-D\left[\frac{\partial^2 w}{\partial y^2}+\mu\frac{\partial^2 w}{\partial x^2}\right]_{x,b}=-(1-\mu)\frac{qa^2}{12}\left[3\left(\frac{x}{a}\right)^2-1\right] \tag{5}$$

$$-D\left[\frac{\partial^3 w}{\partial x^3}+(2-\mu)\frac{\partial^3 w}{\partial x\,\partial y^2}\right]_{a,y}=0 \tag{6}$$

$$-D\left[\frac{\partial^3 w}{\partial y^3}+(2-\mu)\frac{\partial^3 w}{\partial x^2\,\partial y}\right]_{x,b}=0 \tag{7}$$

Upon substitution of w from (3), (4–7) become

$$\sum_{n=1,3,5,\ldots}^{\infty}\left\{\left[\left(\frac{n\pi}{2b}\right)^2 B_n+2\left(\frac{n\pi}{2b}\right)D_n\right]\cosh\frac{n\pi a}{2b}+\left(\frac{n\pi}{2b}\right)^2 aD_n\sinh\frac{n\pi a}{2b}\right\}\cos\frac{n\pi y}{2b}$$
$$=\frac{qa^2}{12D}\left[3\left(\frac{y}{a}\right)^2-\left(\frac{b}{a}\right)^2\right] \tag{8}$$

$$\sum_{n=1,3,5,\ldots}^{\infty}\left\{\left[\left(\frac{n\pi}{2a}\right)^2 A_n+2\left(\frac{n\pi}{2a}\right)C_n\right]\cosh\frac{n\pi b}{2a}+\left(\frac{n\pi}{2a}\right)^2 bC_n\sinh\frac{n\pi b}{2a}\right\}\cos\frac{n\pi x}{2a}$$
$$=\frac{qa^2}{12D}\left[3\left(\frac{x}{a}\right)^2-1\right] \tag{9}$$

$$\sum_{n=1,3,5,\ldots}^{\infty}\left\{\left[(\mu-1)\left(\frac{n\pi}{2b}\right)^3 B_n+(\mu+1)\left(\frac{n\pi}{2b}\right)^2 D_n\right]\sinh\frac{n\pi a}{2b}\right.$$
$$\left.+(\mu-1)\left(\frac{n\pi}{2b}\right)^3 aD_n\cosh\frac{n\pi a}{2b}\right\}\cos\frac{n\pi y}{2b}$$
$$=\sum_{n=1,3,5,\ldots}^{\infty}\left\{\left[(\mu-1)\left(\frac{n\pi}{2a}\right)A_n+2(\mu-2)\left(\frac{n\pi}{2a}\right)^2 C_n\right]\cosh\frac{n\pi y}{2a}\right.$$
$$\left.+(\mu-1)\left(\frac{n\pi}{2a}\right)^3 C_n y\sinh\frac{n\pi y}{2a}\right\} \tag{10}$$

$$\sum_{n=1,3,5,\ldots}^{\infty}\left\{\left[(\mu-1)\left(\frac{n\pi}{2a}\right)^3 A_n+(\mu+1)\left(\frac{n\pi}{2a}\right)^2 C_n\right]\sinh\frac{n\pi b}{2a}\right.$$
$$\left.+(\mu-1)\left(\frac{n\pi}{2a}\right)^3 bC_n\cosh\frac{n\pi b}{2a}\right\}\cos\frac{n\pi x}{2a}$$
$$=\sum_{n=1,3,5,\ldots}^{\infty}\left\{\left[(\mu-1)\left(\frac{n\pi}{2b}\right)B_n+2(\mu-2)\left(\frac{n\pi}{2b}\right)^2 D_n\right]\cosh\frac{n\pi x}{2b}\right.$$
$$\left.+(\mu-1)\left(\frac{n\pi}{2b}\right)^3 D_n x\sinh\frac{n\pi x}{2b}\right\} \tag{11}$$

The right-hand members in the above four equations may be expanded in cosine series. By means of the first two equations, A_n and B_n can be eliminated from the last two equations. It is observed that the last two equations will involve double series. The evaluation of C_n and D_n may be performed along

the same pattern as in the case of plate clamped at all four edges.[4] After C_n and D_n have been determined, A_n and B_n may then be evaluated through the first two equations.

The above-described procedure to superimpose a series solution to Lee and Ballesteros' solution is very close to what Galerkin had done. In fact Galerkin took a deflection function w as a sum of two parts. The first part is an algebraic equation satisfying $\nabla^4 w_1 = p/D$, and the second part, which satisfies $\nabla^4 w_2 = 0$, is in a series form containing trigonometric functions and hyperbolic functions as above.

The writer likes to emphasize that the existence of Galerkin's works does not diminish the value of Lee and Ballesteros' solution, as it can be seen that the labor involved in evaluating the coefficients in Galerkin's solution for any particular problem is very great.

Finally, to give further support to the accuracy of Lee and Ballesteros' solution, numerical values based on Galerkin's solution for a square plate are listed in the following. Here μ is taken to be 0·3.

$$\frac{D}{qa^4}[w]_{0,0} = 0{\cdot}4237 \quad (0{\cdot}4171)$$

$$\frac{D}{qa^4}[w]_{0,b} = 0{\cdot}2888 \quad (0{\cdot}2978)$$

$$\frac{1}{qa^2}[M_x]_{0,0} = 0{\cdot}4436 \quad (0{\cdot}4417)$$

$$\frac{1}{qa^2}[M_x]_{0,b} = 0{\cdot}6108 \quad (0{\cdot}6167)$$

The above are taken from one of Galerkin's tables and have been corrected for the Poisson ratio and plate's width. The values within the parentheses are Lee and Ballesteros' values.

H. H. Pan

College of Engineering
New York University
New York

REFERENCES

1. S. L. Lee and P. Ballesteros, *Int. J. Mech. Sci.* **2**, 206 (1960).
2. B. G. Galerkin, *Collected Works* Vol. 2, p. 15. Izdatelstvo Akademii Nauk SSSR Moscow (1953).
3. S. T. Timoshenko and S. Woinowsky-Krieger, *Theory of Plates and Shells* p. 218. McGraw-Hill, New York (1959).
4. L. W. Kantorowitsch and W. I. Krylow, *Näherungsmethoden der Höheren Analysis* p. 63. VEB, Berlin (1956).

Vol. 2
1960-61

Int. J. Mech. Sci. Pergamon Press Ltd. 1961. Vol. 2, pp. 316–318. Printed in Great Britain

BOOK REVIEWS

J. BLAKEY and M. HUTTON: **Engineering Mathematics.** Blackie, Glasgow, 1960. 603 pp., 40s.

THIS book is designed to meet the mathematical requirements of undergraduate students in engineering. It is essentially a revision of a previous work (*University Mathematics* by J. BLAKEY) in which the co-ordinate and solid geometry have been attenuated to allow the inclusion of chapters on the numerical solution of equations, statistics, relaxation methods and Laplace transforms. In the main, the book presents a traditional treatment of the basic content of most engineering mathematics syllabi. The presentation is clear, and important results are emphasized with heavy type, thus facilitating its use for reference purposes. In general each chapter provides adequate worked examples to illustrate the text, and student exercises are included at the conclusion of each chapter.

In so far as the complete mathematical requirements of an engineering undergraduate may be contained in one volume this book is reasonably successful, but the absence of any treatment of such subjects as vector methods, Bessel functions, elliptic integrals and tensors is a serious limitation. The order of the chapters is somewhat confusing and leads to unnecessary segregation, e.g. the chapters on numerical solution of equations and relaxation methods are separated by a chapter on statistics, and the chapters on areas, solids of revolution, etc., and moments of inertia are widely separated by chapters on the solution of differential equations. The usefulness of the new chapters might have been increased by a relatively small extension of their content, e.g. the chapter on relaxation does not illustrate the method for non-rectangular meshes, curved boundaries or change of mesh size, such artifices being dismissed as techniques rather than principles.

J. HALLING

B. SPAIN: **Analytical Quadrics.** Pergamon Press, Oxford, 1960. 135 pp., 30s.

THIS is a very good book on three-dimensional geometry suitable for a student who needs to reach a high standard in pure mathematics, though not, perhaps, for the pure mathematician who should base these results on the broader projective picture.

The book is attractively presented with clear diagrams and interesting examples, all of which are neatly solved in an Appendix.

An attractive feature of the book is the display of the connexion between matrices and the classification of quadrics which is here given its proper importance. An adequate introduction to the techniques of homogeneous co-ordinates and the invariant circle at infinity are given. A major criticism is that vector methods are not used in the early chapters. Students at this standard have many reasons for thinking vectorially, and the formulae for lines and planes become obvious when considered as scalar and vector products. The introduction of vector methods need not have made the book longer because some of the results proved in the text could have been left as easy exercises for the reader.

H. B. SHUTRICK

W. ABBOTT: **Machine Drawing and Design** (7th Ed.). Blackie, Glasgow, 1960. 281 pp., 21s.

THE seventh edition of this textbook for mechanical engineering students scores over its predecessors in its features on economic considerations and the selection of materials and safe stresses. Dr. Abbott's special interest in the problems of dimensioning and tolerancing has produced particularly valuable sections. The monograph on the special demands of cast parts might well be matched in the future by similar pages on fabrication and components machined from stock.

The usual matter on design elements includes expanded texts on chains and belts, a useful summary of the method of gear analysis recommended in BS 436, as well as an excellent new paragraph on ball and roller bearings. Many brief calculations illustrate

both the analytic and the synthetic approach to design. Components of reciprocating mechanisms and turbines have been singled out for a fuller treatment.

In dealing with both Drawing and Design in 281 pages, Dr. Abbott rightly abstains from quoting many empirical formulae with their associated data. While all relevant British Standards are named, no unnecessary numerical extracts are copied into the book. The economy resulting from an assumption of the reader's knowledge of the theories of machines and stresses is welcome when confined to fundamentals. All the same, the intention to provide an "intermediate" course may have been achieved too literally. The student may find the forty-three pages dealing with methods of projection and BS 308 too short, even though they are backed by exceptionally good exercises. Equally he may have to turn elsewhere for examples of more advanced analysis. The inclusion of no more than one or two special designs, involving, say, high temperatures or stresses in high-speed mechanisms, would fully meet this criticism.

Contrary to its intention, Fig. 4, p. 17, shows how easily the confusing habit of mixing projections can be avoided. Many illustrations retained from the earlier editions do not follow the line conventions of BS 308, and their dimensioning (in placing, figuring and lines) does not set a good example. Numerous new figures have, however, been added for this enlarged edition.

Considered as a whole, the book is well proportioned in both contents and size.

G. R. Schiffer

Vol. 2
1960-61

A. D. Galanin: **Thermal Reactor Theory** (2nd Ed.) (translated by J. B. Sykes). Pergamon Press, Oxford, 1960. 412 pp. + xiv. 100s.

This book is intended to be used as an advanced textbook and handbook of mathematical reactor physics; in this intention the author succeeds very well.

After an introduction of only seven pages, devoted to neutron chain reactions and energy production in fission, the author proceeds directly to a discussion of neutron diffusion and slowing down (Fermi Age Theory in Chapter I!). This is followed by critical-size calculations using one-group theory.

In a logical sequence the book continues with the two-group formulation for a homogeneous reactor, and its modification for heterogeneous reactors, including discussion of critical size with and without reflectors. Perturbation methods are discussed for both one-group and two-group formulations.

Following reactor statics come discussions of reactor kinetics due to fuel burn-up and poisoning, delayed neutrons, and temperature effects. The book ends with a substantial chapter on the transport equation, including approximate solutions and modifications to diffusion theory, and a slight chapter on the general theory of heterogeneous reactors.

The general theory presented in this book is complete and consistent, but some particular applications are not fully covered. As the author points out, light-water-moderated reactors require more accurate treatment than is permitted by the two-group theory developed here. Numerical methods are discussed in a very few pages. Control-rod calculations performed in Russia appear no more reliable than those done elsewhere. Readers will no doubt find other applications ignored or only partially treated.

The list of contents is rather detailed. The index appears short, having approximately as many entries as the list of contents; this may be due to the logical system in which the author presents his material. References are given at the end of each chapter in which they are used. In the nine separate lists thus occurring, "Glasstone and Edlund" is mentioned seven times. In general the references appear to indicate a reading of relevant Western literature. In his reading of the book, the reviewer was never conscious of the fact that he was reading a translation; this implies careful work by the translator.

To sum up, this book is a logical and careful presentation of thermal reactor theory using one-group and two-group methods; the applications discussed are selective and illustrative rather than extensive. There is no similar book in English known to the reviewer which presents the material given here. Eastern European visitors to this country express a high opinion of the original Russian book, which this translation confirms.

P. H. Price

Tables of Thermodynamic and Transport Properties. Pergamon Press, Oxford, 1960. 491 pp., £7.

THIS collection of tables comprises the thermodynamic and transport properties of air, argon, carbon dioxide, carbon monoxide, hydrogen, nitrogen, oxygen and water vapour; and is a revised edition of data compiled by the American National Bureau of Standards.

Such information is of paramount importance in fluid and thermodynamic research, and for the user of the book the most important feature must be the ease or otherwise of the exact state conditions at which the gas properties are required.

For the above gases, actual properties are given up to various temperatures (3000°K for air, argon, O_2 and N_2) and pressures 0·01 to 100 atm. The origins and correlation of data are given at the commencement of each section.

Ideal-gas thermodynamic functions are given at 1 atm and temperatures up to 5000°K. The temperature subdivisions are such as to permit linear interpolation, first differences being tabulated to facilitate this. The pressure subdivisions are arranged to enable interpolation formulae to be applied when linear interpolation is not sufficiently accurate.

The printing of the actual copy reviewed is disconcertingly non-uniform from page to page, varying from dense black to faint grey, leading to some indistinctness of figures.

G. S. CANTLE

SYDNEY GOLDSTEIN: **Lectures on Fluid Mechanics** (with special lectures by J. M. BURGERS). Interscience, New York, 1960. 309 pp., $6.60.

THIS book covers the twelve lectures in Fluid Mechanics with two additional special lectures delivered to the Seminar in Applied Mathematics at Boulder, Colorado, 1957, arranged by the American Mathematical Society.

To the reader who has both experience in Fluid Mechanics and who is mathematically equipped, the book forms a welcome addition to the library. The fundamentals and various topics are treated with the lucidity and compactness characteristic of the authors.

In addition to the chapters dealing with inviscid fluids and the Navier–Stokes equations, further chapters are included on the basic equations for the dynamics of fluids with electric and magnetic forces, to prepare the reader for some problems of Magneto–Gas-dynamics centring on the shock-wave problem. The reader is guided through Boundary-layer Theory for incompressible fluids and gases, and the chapter on the Dynamics of Inviscid Gases selects slender-body theory as the main topic.

Turbulence and Stability are rightly considered to be unamenable to shortened analytical treatment and the reader is referred to the classical publications in these subjects. Surface and tidal waves and aerofoil theory are similarly omitted.

Throughout the book, physical arguments are propounded clearly, and vector and tensor notations are used to formulate equations. Experimental results are omitted but many references are given and five useful appendices are included.

J. K. ROYLE

Vol. 2
1960-61